JAN KRIEFT

INVESTIGATION OF SPIN-CALORIC AND SPIN-ORBIT TORQUE MATERIALS BY VECTORIAL SPIN SEEBECK MEASUREMENTS AND AN ADVANCED X-RAY MAGNETIC REFLECTIVITY ANALYSIS

BIELEFELD UNIVERSITY
FACULTY OF PHYSICS

PUBLISHED BY BIELEFELD UNIVERSITY
FACULTY OF PHYSICS

Thin Films & Physics of Nanostructures

Center for Spinelectronic Materials & Devices

November 2020

Declaration Of Authorship

This thesis and the work presented in it are my own and it has been generated by me as the result of my own original research.

(Jan Krieft)

Reviewers:

Prof. Dr. Günter Reiss

Prof. Dr. Gabi Schierning

Contents

"Oooh, look at me, I looked up a quote!"

xkcd

Introduction

Motivation

The human civilization has been recording, manipulating, saving, retrieving and communicating information since the first development of writing in ancient Mesopotamia more than 5000 years ago. Following these early steps, the storage and processing technologies have seen groundbreaking advancements especially with the emergence of the Information Age in the 20th century. The rapid growth of accessible information and knowledge, the associated automation and digitization fundamentally changed all aspects of science, economies, culture, and ultimately the way people think.

In its core, this technological progress is associated with the development of the transistor technology. In particular the implementation of the metal-oxide-semiconductor field-effect transistor (MOSFET), the first compact transistor that could be miniaturized and mass-produced. It revolutionized the emerging computer technologies and became the fundamental construction stone of all modern electronics.

Based on this key invention, the computer technology, our communication and consequently our economic wealth essentially resets upon the transport of electric charges in semiconductors. However, the potential of this technology is going to reach its physical limits in the near future, since it has become increasingly complex to miniaturize the established components any further due to source-to-drain leakage.[1] But there is hope in another option to record, transmit, and store information which is to utilize an electron's spin, instead of its charge.

Merely one decade after its emergence from discoveries in the late 1980s, this so called spin electronics has become a backbone of the industry in terms of hard-disk reading and magnetic sensor applications. In particular the discovery of the tunnel magnetoresistance (TMR) by Julliere[2] and the giant magnetoresistance (GMR) by Fert[3] and Grünberg[4] significantly increased the scientific relevance in the field of nanoelectronics. The evolution from the pioneering quantum-mechanical tunneling experiments by Meservey and Tedrow[5] to the industry applications of the GMR was ultimately seen as the birth of spintronics[6] and thus was awarded the 2007

[1] T. N. Theis and H.-S. P. Wong. The end of Moore's law: A new beginning for information technology. *Comput. Sci. Eng.*, **19**(2):41 (2017)

[2] M. Julliere. Tunneling between ferromagnetic films. *Phys. Lett. A*, **54**(3): 225–226 (1975)

[3] M. N. Baibich, J. M. Broto, A. Fert, F. N. Van Dau, F. Petroff, P. Etienne, G. Creuzet, A. Friederich, and J. Chazelas. Giant magnetoresistance of (001)Fe/(001)Cr magnetic superlattices. *Phys. Rev. Lett.*, **61**(21):2472 (1988)

[4] G. Binasch, P. Grünberg, F. Saurenbach, and W. Zinn. Enhanced magnetoresistance in layered magnetic structures with antiferromagnetic interlayer exchange. *Phys. Rev. B*, **39**: 4828–4830 (1989)

[5] P. M. Tedrow and R. Meservey. Spin-dependent tunneling into ferromagnetic nickel. *Phys. Rev. Lett.*, **26**(4): 192 (1971)

[6] S. Wolf, D. Awschalom, R. Buhrman, J. Daughton, S. Von Molnar, M. Roukes, A. Y. Chtchelkanova, and D. Treger. Spintronics: a spin-based electronics vision for the future. *Science*, **294**(5546):1488–1495 (2001)

Nobel Prize in Physics.

In more recent years, the 2016 Nobel Prize in Physics was awarded for the discovery of topological phases of matter which in combination with the electric manipulation of the spin state has the potential to pave the way for future applications in materials science, solid-state electronics, and information technology.[7] Today, the development of spin-logic and torque-based devices enables further scaling and increases the information density. The ability of spintronic devices to utilize an electric current and a spin-transfer torque to switch the magnetization has resulted in the recent rise of the magnetoresistive random-access memories (MRAM) out of its niche role and into the focus of the major semiconductor companies as a non-volatile memory with ultrafast and power efficient switching.[8] More importantly, this demonstrates the spintronics future potential to revolutionize all areas of information processing by enhancing the efficiency of data storage and transfer. It is already leveraging upcoming key technologies such as antiferromagnetic storage, neuromorphic engineering and quantum computing.

Over the past decade in the field of spintronics, there has been considerable interest in magnetic Heusler compounds based on the wide range of magnetic properties and their susceptibility to manipulation by elemental substitution.[9] In particular half-Heusler alloys are currently attracting growing attention due to their non-centrosymmetric $C1_b$ magnetic structure with broken inversion symmetry.[10] This characteristic, in combination with a pronounced spin-orbit coupling, is of particular interest in current spintronic research. Most fundamentally, the inverse spin galvanic effect (ISGE) can directly generate a non-equilibrium spin polarization which subsequently induces a spin-orbit torque (SOT) on the magnetization. Phenomena like the ISGE take advantage of the relativistic momentum transfer between electron and spin just as another key mechanism of spin-orbitronics in form of the so called spin Hall effect (SHE).[11] Here, an electric current transforms into a spin current due to a spin-orbit interaction in combination with either intrinsic material asymmetries or spin-dependent scattering which results in an interface spin accumulation.

In this framework, the half-Heusler PtMnSb is an outstanding candidate for future SOT applications due to its unusual magneto-optical properties and electronic structure.[12] This alloy exhibits a half-metallic band structure and a considerable magneto-optic Kerr effect (MOKE).[13] In addition, strong intrinsic spin-orbit torque effects have been observed in this system. When these are combined with the half-metallic band structure of PtMnSb, a pronounced spin polarization is generated which is very useful in the optimization of magnetoresistive effects.

Few years ago, a novel spin Hall magnetoresistance (SMR) was discovered which is best described as an inverted GMR effect. This unidirectional SMR (USMR)[14] is observed in a bilayer consisting of a ferromagnet and a heavy metal where the inversion symmetry

[7] J. E. Moore. The birth of topological insulators. *Nature*, **464**(7286):194 (2010); and D. Pesin and A. H. MacDonald. Spintronics and pseudospintronics in graphene and topological insulators. *Nat. Mater.*, **11**(5):409 (2012)

[8] A. Antonyan, S. Pyo, H. Jung, and T. Song. Embedded MRAM Macro for eFlash Replacement. In *2018 IEEE International Symposium on Circuits and Systems (ISCAS)*, pages 1–4. IEEE, (2018)

[9] F. Casper, T. Graf, S. Chadov, B. Balke, and C. Felser. Half-Heusler compounds: novel materials for energy and spintronic applications. *Semicond. Sci. Tech.*, **27**(6):063001 (2012)

[10] C. Ciccarelli, L. Anderson, V. Tshitoyan, A. J. Ferguson, F. Gerhard, C. Gould, L. W. Molenkamp, J. Gayles, J. Železný, L. Šmejkal, Z. Yuan, J. Sinova, F. Freimuth, and T. Jungwirth. Room-temperature spin-orbit torque in NiMnSb. *Nat. Phys.*, **12**: 855–860 (2016)

[11] Y. Kato, R. C. Myers, A. C. Gossard, and D. D. Awschalom. Observation of the spin Hall effect in semiconductors. *Science*, **306**(5703):1910–1913 (2004)

[12] R. A. De Groot, F. M. Mueller, P. G. Van Engen, and K. H. J. Buschow. New class of materials: half-metallic ferromagnets. *Phys. Rev. Lett.*, **50**(25): 2024 (1983)

[13] J. Bobo, P. Johnson, M. Kautzky, F. Mancoff, E. Tuncel, R. White, and B. Clemens. Optical spectroscopy investigations of half metallic ferromagnetic Heusler alloy thin films: PtMnSb, NiMnSb, and CuMnSb. *J. Appl. Phys.*, **81**(8):4164–4166 (1997)

[14] C. O. Avci, K. Garello, A. Ghosh, M. Gabureac, S. F. Alvarado, and P. Gambardella. Unidirectional spin Hall magnetoresistance in ferromagnet/normal metal bilayers. *Nat. Phys.*, **11**(7):570–575 (2015)

is broken by either the interface or an intrinsic lack of inversion symmetry in the crystal structure or local environment of the magnetic material. In this inversion-asymmetric system, the resistivity of the heavy metal layer depends on the relative orientation of the magnetization of the ferromagnet to the spin-Hall-effect induced spin polarization at the interface.

The next logical step is to combine both fundamental ways of symmetry breaking which is realized in PtMnSb/Pt bilayers due to their lack of inversion symmetry by both the interface and the local half-Heusler environment. This bilayer system is investigated as a central focus of this work, foremost to promote the understanding of spin-orbit torques in bulk non-centrosymmetric crystals.

Therefore, the first experimental chapter of this work sets a focus on the preparation and optimization of half-Heusler PtMnSb alloy thin films and corresponding Pt capped bilayer systems for the application in spintronic devices. The structural and magnetic properties are studied in-depth to optimize the fabrication conditions and gain high quality thin films with epitaxial growth.

However, the nonmagnetic Pt in these bilayers is close to the Stoner criterion and has the ability to become magnetic in the proximity to the ferromagnetic PtMnSb. This magnetic proximity effect (MPE) is another key aspect in spintronics and of particular importance since it can prevent the generation of pure spin currents or induce secondary magnetoresistive effects.[15] In order to distinguish these SOT phenomena from magnetic-proximity induced effects, which spin polarize both the Pt in the Pt film and also within the half-Heusler compound, an in-depth magnetooptical characterization based on x-ray resonant magnetic reflectivity (XRMR)[16] is performed.

The XRMR technique allows to study the spin polarizations of buried magnetic layers which are not accessible by standard x-ray magnetic circular dichroism (XMCD) measurements. However, the in-depth analysis of the structural and magnetic depth profiles of the complexer half-Heusler bilayers turns out to be a challenge since there is no standard procedure to analyze XRMR asymmetry ratios. A central aspect of this work is therefore the development of a step-by-step guide to take advantage of the excellent magnetic sensitivity and depth resolution of XRMR which should be universally applicable to allow for the precise evaluation of even minimal spin polarization depth profiles. By means of three specific systems, where Pt is integrated in the sample in an increasingly complex manner from simple bilayer over multilayered stacks to the PtMnSb half-Heusler compound, chapter 4 of this work discusses a recipe procedure for the determination of an optimal XRMR asymmetry ratio simulation. This includes an iterative optimization approach based on various fitting algorithms as well as a detailed analysis of the asymmetry ratio features and the multidimensional error landscape. Finally, the last chapter 5 of this thesis addresses the XRMR investigation of the half-Heusler

[15] D. Meier, D. Reinhardt, M. van Straaten, C. Klewe, M. Althammer, M. Schreier, S. T. B. Goennenwein, A. Gupta, M. Schmid, C. H. Back, J.-M. Schmalhorst, T. Kuschel, and G. Reiss. Longitudinal spin Seebeck effect contribution in transverse spin Seebeck effect experiments in Pt/YIG and Pt/NFO. *Nat. Commun.*, **6**:8211 (2015); and M. Althammer, S. Meyer, H. Nakayama, M. Schreier, S. Altmannshofer, M. Weiler, H. Huebl, S. Geprägs, M. Opel, R. Gross, D. Meier, C. Klewe, T. Kuschel, J.-M. Schmalhorst, G. Reiss, L. Shen, A. Gupta, Y.-T. Chen, G. E. W. Bauer, E. Saitoh, and S. T. B. Goennenwein. Quantitative study of the spin Hall magnetoresistance in ferromagnetic insulator/normal metal hybrids. *Phys. Rev. B*, **87**(22):224401 (2013)

[16] S. Macke and E. Goering. Magnetic reflectometry of heterostructures. *J. Phys. Condens. Matter*, **26**(36):363201 (2014)

structure and interface quality as well as the element specific spin polarization depth profiles based on the previously established procedures. The obtained XRMR results are tested for reliability and compared to additional qualitative and quantitative studies of the magnetic PtMnSb characteristics to confirm the results of the previously established XRMR simulation procedure. This precise determination of the magnetooptical depth profiles opens the route for further exploration and a potential application of spin-orbit torques in devices based on non-centrosymmetric Heusler alloys.

The rise of the field of spintronics interconnects the conventional charge based electronics with the intrinsic spin of the electron. In the broader sense, as most prominently shown by the rapidly increasing energy consumption for heat transport in modern electronic data processing centers, this field of research is also intrinsically tied to the field of thermoelectricity. A decade ago, the discovery of the spin Seebeck effect (SSE),[17] which specifies the generation of a spin voltage as a result of a temperature gradient, introduced the new fields of spin caloric transport.[18] Here, the longitudinal spin Seebeck effect (LSSE)[19] is the most prominent caloritronic effect, enabling an easy and versatile generation of spin currents based on heat. In an insulating material without any mobile charge carriers, the spin is transported by magnonic spin waves which propagate nearly free off dissipation and consequently are a candidate to reduce the steadily growing energy consumption of reading and writing information.

The LSSE is commonly utilized to generate a pure spin current in a ferri- or ferromagnetic insulator (FMI) such as Yittrium Iron Garnet (YIG) or Nickelferrite (NFO). These FMIs represent a promising class of material for the implementation in spin caloric devices since the insulating character suppresses inadvertent charge currents which possibly prevent the detection of spin currents due to the induction of additional magnetoresistive effects. Such as the generation of pure spin currents, the detection is equally more complex compared to their electric counterparts. One particular robust method is the conversion by the inverse spin Hall effect (ISHE).[20] Here, a material with a significant spin Hall angle, usually a heavy 4*d* and 5*d* transition metals such as Pd or Pt, is subjected to the spin current. Once again, a MPE has the potential to generate unintended charge related parasitic effects, underlining the importance of a reliable technique to study the element specific interfacial magnetic properties.

In order to design spin caloritronic devices, it is of particular interest to examine the magnetization reversal process of these thin films. This is also of a more general interest, since the current day mass storage capabilities are realized based on the switching of magnetic memory, predominantly in hard drives. However, the study is usually realized by magnetooptical means via combinations of magneto-optic Kerr effects[21] which are not applicable to key spintronic FMIs due to their vanishingly small Kerr rotation in

[17] K.-i. Uchida, S. Takahashi, K. Harii, J. Ieda, W. Koshibae, K. Ando, S. Maekawa, and E. Saitoh. Observation of the spin Seebeck effect. *Nature*, **455**(7214):778–781 (2008)

[18] G. E. W. Bauer, E. Saitoh, and B. J. van Wees. Spin caloritronics. *Nat. Mater.*, **11**(5):391–399 (2012)

[19] K.-i. Uchida, H. Adachi, T. Ota, H. Nakayama, S. Maekawa, and E. Saitoh. Observation of longitudinal spin-Seebeck effect in magnetic insulators. *Appl. Phys. Lett.*, **97**(17): 172505 (2010)

[20] E. Saitoh, M. Ueda, H. Miyajima, and G. Tatara. Conversion of spin current into charge current at room temperature: Inverse spin-Hall effect. *Appl. Phys. Lett.*, **88**(18):182509 (2006)

[21] C. Daboo, J. A. C. Bland, R. J. Hicken, A. J. R. Ives, M. J. Baird, and M. J. Walker. Vectorial magnetometry with the magneto-optic Kerr effect applied to Co/Cu/Co trilayer structures. *Phys. Rev. B*, **47**:11852–11859 (1993)

the visible light range. Therefore, a magnetometry technique based on the vectorial observation of the spin Seebeck effect has been developed as part of this thesis. It utilizes the LSSE and ISHE voltage detection as an alternative to magnetooptical instruments to visualize the complete reversal process of the magnetization, demonstrating a spin caloric technique with broad applicability. This method is demonstrated in the study of NFO on lattice-matched substrates such as $MgGa_2O_4$ in the experimental chapter 3. These substrates show significantly improved magnetic properties as well as enhanced SSE and enhanced spin transport characteristics with potential applications in high-frequency microwave and spintronics devices.[22]

Most of the results discussed in this thesis have already been published in various peer-review journals. These articles are explicitly referenced in the corresponding chapters.

[22] A. V. Singh, B. Khodadadi, J. B. Mohammadi, S. Keshavarz, T. Mewes, D. S. Negi, R. Datta, Z. Galazka, R. Uecker, and A. Gupta. Bulk single crystal-like structural and magnetic characteristics of epitaxial spinel frrite thin films with elimination of antiphase boundaries. *Adv. Mater.*, **29** (30):1701222 (2017)

1
Theoretical Foundations

Synchrotron Radiation Techniques

Since the famous experiments by Walter Friedrich, Paul Knipping and Max von Laue[1] as well as Lawrence and William Henry Bragg,[2] the analysis of condensed matter by x-ray radiation is the most important characterization technique for any kind of solid states. Here, x-ray reflectivity (XRR) is a well-established powerful tool to determine layer thickness, analyze the density depth profile, and characterize the quality of interfaces.[3] Measuring the intensity of the specular reflected light above the critical angle of total reflection one can observe an interference pattern known as Kiessig fringes containing precise information on all structural and optical parameters of heterostructures.[4]

Following this pioneering research, various x-ray based techniques were developed to characterize the structure of materials or molecules. Next to the standard procedure for structure determination of solid bodies, the x-ray diffractometry (XRD), methods like fiber or powder diffraction small-angle x-ray scattering (SAXS) for non crystalline samples have been developed. For the characterization of the electronic structure one can resort to x-ray absorption spectroscopy (XAS) methods revealing for instance aspects of the x-ray absorption near-edge structure (XANES) probing photo absorption cross sections of electronic transitions.

X-ray fluorescence spectroscopy or related techniques such as x-ray photoelectron (XPS) or energy dispersive X-ray spectroscopy (EDX) are widely used to analyze the composition and chemical characterize condensed matter samples. These x-ray based methods are the backbone of non destructive structural and elemental characterization and provide fundamental inside into the material properties independent of surface accessibility.

Nowadays various modern synchrotron radiation facilities offer a broad spectrum of advanced photon science beamlines to investigate the structure of condensed matter and in particular provide element specific characterization of the magnetic properties of

[1] W. Friedrich, P. Knipping, and M. Laue. Interferenzerscheinungen bei Röntgenstrahlen. *Ann. Phys.*, **346**(10): 971–988 (1913)

[2] W. H. Bragg and W. L. Bragg. The reflection of X-rays by crystals. *Proc. R. Soc. Lond. A*, **88**(605):428–438 (1913)

[3] V. Holy, J. Kubena, I. Ohlidal, K. Lischka, and W. Plotz. X-ray reflection from rough layered systems. *Phys. Rev. B*, **47**(23):15896 (1993); M. Tolan. *X-ray Scattering from Soft-Matter Thin Films: Materials Science and Basic Research*. Springer, Berlin (1999); and J. Daillant and A. Gibaud. *X-ray and Neutron Reflectivity: Principles and Applications*, volume 770. Springer, Berlin (2008)

[4] H. Kiessig. Untersuchungen zur Totalreflexion von Röntgenstrahlen. *Ann. Phys.*, **402**(6):715–768 (1931); and H. Kiessig. Interferenz von Röntgenstrahlen an dünnen Schichten. *Ann. Phys.*, **402**(7):769–788 (1931)

materials. In principle, electromagnetic radiation is emitted by an electric or magnetic force acting on a charged particle in motion. This directly changes the direction of motion or the particles energy. For a non-relativistic particle we call the emitted radiation cyclotron emission, particles moving at relativistic velocities emit so called synchrotron radiation. The first observation of visible radiation of this type was made in 1946 by Elder *et al.*[5] at the General Electric synchrotron accelerator following the theoretical predictions by Iwanenko and Pomeranchuk.[6] The easiest way to realize a synchrotron radiation source is by forcing electrons by a magnetic field to travel in a curved path. In a modern synchrotron light source two approaches are used to send relativistic electrons into a magnetic field. The first one sustains a steady bunch of charged particles in a closed cycle in a storage ring of the accelerator and provides constant synchrotron radiation by passing through the magnetic field every cycle for up to many hours. In contrast the second approach is the one time linear acceleration of particles into an arrangement of magnets requiring constant supply of electrons yet providing the advantages of a free-electron laser, e.g., high brightness, very short wavelengths and a continuous tunability.

[5] F. Elder, A. Gurewitsch, R. Langmuir, and H. Pollock. Radiation from electrons in a synchrotron. *Phys. Rev.*, **71**(11):829 (1947)

[6] D. Iwanenko and I. Pomeranchuk. On the maximal energy attainable in a betatron. *Phys. Rev.*, **65**(11-12):343 (1944)

X-ray magnetic circular dichroism

A widely-used technique for the investigation of condensed matter and thin film systems as well as magnetic heterostructures in particular is based on the x-ray magnetic circular dichroism (XMCD). This method relies on the detection of x-ray absorption spectra in contrast to the x-ray resonant magnetic scattering (XRMS) which utilizes the resonance effect of the light-matter magnetic interaction and offers an unparalleled element, valence and site specific analysis to probe magnetic structures on the nanoscopic length scale.[7]

The first XMCD experiment was carried out by Schütz *et al.* in 1987.[8] This was based on a calculation of the magneto-optical absorption spectrum by Erskine and Stern in 1975.[9] In an XMCD experiment a difference spectrum of two x-ray absorption spectra is recorded with left and right circularly polarized light while the probed sample is usually placed in a magnetic field and is in essence caused by an anisotropy of the spin distribution. Alternatively the magnetic field applied to the sample can be switched between a parallel and antiparallel orientation relative to a fixed photon helicity. This spectrum contains information on the magnetic properties and in particular the spin and orbital magnetic moment. Through the utilization of synchrotron radiation the photon energies can be tuned to the resonant abortion edge of the investigated material which makes this method highly element specific. At the resonance energy of the utilized absorption process the dichroism is most pronounced. Hence, XMCD experiments are performed at x-ray energies around the absorption edges of the

[7] G. van der Laan. Soft x-ray resonant magnetic scattering of magnetic nanostructures. *C. R. Phys.*, **9**(5-6): 570–584 (2008)

[8] G. Schütz, W. Wagner, W. Wilhelm, P. Kienle, R. Zeller, R. Frahm, and G. Materlik. Absorption of circularly polarized x-rays in iron. *Phys. Rev. Lett.*, **58**(7):737 (1987)

[9] J. L. Erskine and E. Stern. Calculation of the M_{23} magneto-optical absorption spectrum of ferromagnetic nickel. *Phys. Rev. B*, **12**(11):5016 (1975)

element or compound in question.

By applying the so called sum rules we are able to separate and quantitatively evaluate the orbital and the spin magnetic moments. Originally these x-ray sum rules were established by Thole *et al.*[10] as well as Carra *et al.*[11] and subsequently experimentally verified.[12]

If we use fully circularly polarized light to excite an electron, e.g., from a $2p_{3/2}$ (L_3 edge) or $2p_{1/2}$ (L_2 edge) spin-orbit-split core-state of the probed absorbing element the electron transition probabilities are determined by the Clebsch-Gordon coefficients. The spin polarization of the excited electrons can be found by a simple summation of all possible excitations weighted by their probabilities whereas the orbital polarization of the excited electrons is independent of the core level. The absorption process requires the conservation of angular momentum and in case of circularly polarized incident light it has to be transfered to the excited electron where it can be partially converted to the spin via the spin-orbit coupling and cause a spin polarization. Since the L_3 and L_2 edges are p states spitted by the exchange interaction the spin-orbit coupling $l + s$ and $l - s$ leads to an opposite spin polarization for both edges.

For example electrons excited from the $2p_{3/2}$ state with a helicity $+1$ carry a spin of $m_s = +1/2$ in 62.5 % of the time while a spin of $m_s = -1/2$ is carried with a probability of only 37.5 %. Considering the $2p_{1/2}$ initial state the absorption leads to an excited $m_s = -1/2$ spin state with a probability of 75 %. The remaining electrons carry a $m_s = +1/2$ spin in the final state. The dipol operator cannot act on spin and thus does not allow for a spin flip during excitation.[13] This shows that a nonzero spin polarization of the excited state is only realized due to a spin-orbit splitting of the core state. A switch of the light from right- to left-handed circularly leads to a sign change of the excited spin polarization. Therefore, an exchange split valence shell with different occupation of spin-up and spin-down electrons serves as a detector for the spin of the excited electrons. This is illustrated in the schematics shown in Fig. 1.1 for the L edge transition.

Furthermore, one has to consider the number of unoccupied final states regarding the excitation process where a nonzero spin or orbital momentum is inducing a dichroism effect. Here, the magnetic properties of the measured system become accessible because the transmission probability depends on the degree of spin polarization of the excited electrons and moreover on the number of empty spin-up or -down states above the Fermi level. Focusing on the excitation of $2p_{3/2}$ state electrons into the $3d$ band with right polarized light we can compare fully spin-polarized final states and unpolarized states with no magnetization.

In a simplified picture the system is magnetically saturated where no unoccupied states of one spin orientation are accessible as shown in Fig. 1.2(a). Here, the transition probability of spin-down electrons is zero while the spin-up transition probability is relatively high as illustrated in Fig. 1.1. If the magnetization

[10] B. Thole, P. Carra, F. Sette, and G. van der Laan. X-ray circular dichroism as a probe of orbital magnetization. *Phys. Rev. Lett.*, **68**(12):1943 (1992)

[11] P. Carra and M. Altarelli. Dichroism in the x-ray absorption spectra of magnetically ordered systems. *Phys. Rev. Lett.*, **64**(11):1286 (1990)

[12] C. Chen, Y. Idzerda, H.-J. Lin, N. Smith, G. Meigs, E. Chaban, G. Ho, E. Pellegrin, and F. Sette. Experimental confirmation of the X-ray magnetic circular dichroism sum rules for iron and cobalt. *Phys. Rev. Lett.*, **75**(1):152 (1995)

[13] J. Stöhr and H. Siegmann. *Magnetism: From fundamentals to Nanoscale Dynamics. 2006*. Springer Berlin, Germany

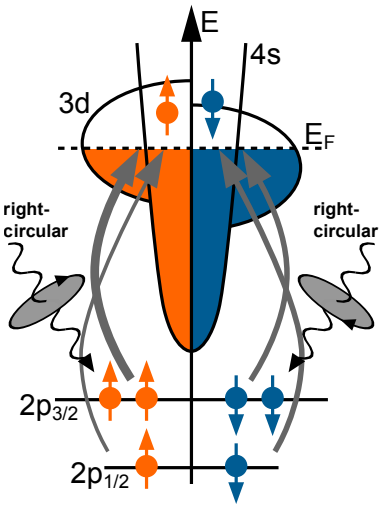

Figure 1.1: Schematic illustration of the XMCD effect for the L edge $2p$-$3d$ transition as corresponding to the resonant absorption process in a $3d$ transition metal.

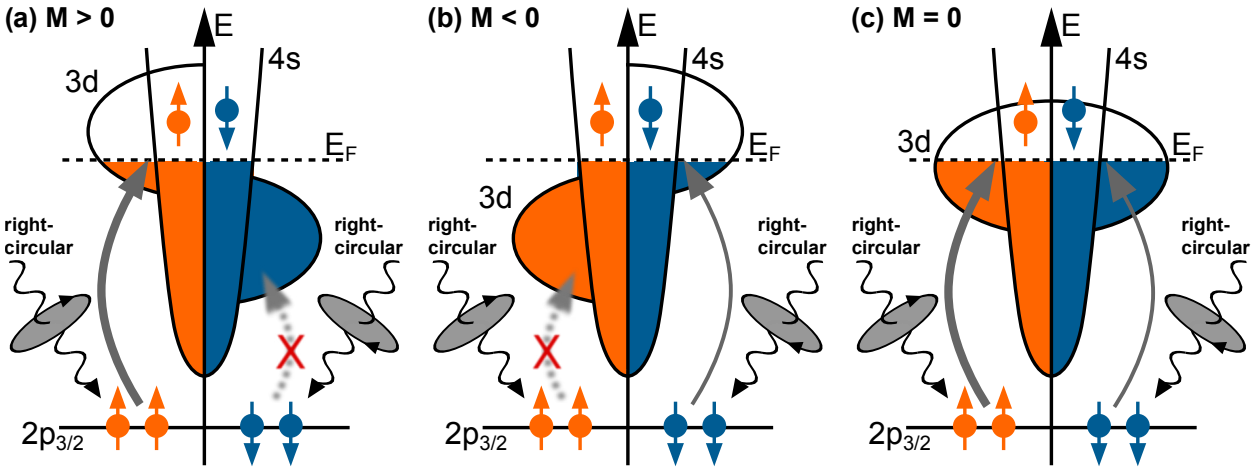

Figure 1.2: (a) Schematic illustration of the excitation of a $2p_{3/2}$ state electron into the $3d$-band of a transition metal ferromagnet with a magnetization chosen such that the $3d$ spin-down band is filled. (b) and (c) illustrate the reversed magnetization direction and zero magnetization, respectively.

is reversed (Fig. 1.2(b)), we see a switch in the spin polarization of final states and a smaller transition probability according to the transition probabilities listed above for the $2p_{3/2}$ state. The difference in this absorption process is the origin of the magnetic circular dichroism at this edge. For a maximal effect, the spin of the incident photon has to be aligned with the direction of magnetization. As also illustrated in Fig. 1.1, the transitions at the L_2 edge yield an XMCD with a switched sign and different transition probabilities. No dichroism can be observed when the magnetization of the probed system is zero as shown in Fig. 1.2(c). The combined transition probability is independent of the x-ray polarization and therefore no dichroism occurs. This dependency of the XMCD signal on the magnetization allows for a measurement of element-specific field-dependent magnetization curves.[14]

The intensity of the XMCD signal has the following dependency,

$$I_{\mathrm{XMCD}} = I_+ - I_- \propto \mu_+ - \mu_- \propto P_{\mathrm{cir}} \vec{M} \cdot \vec{L}_{\mathrm{ph}} \propto P_{\mathrm{cir}} M_{\mathrm{p}} \cos(\theta), \qquad (1.1)$$

where $I_\pm$ represents the experimentally measured intensity for a parallel or antiparallel configuration of the photon polarization and the magnetization direction. The absorption coefficients $\mu_\pm$ correspond to the Lambert-Beer law for optical absorption and μ_+ refers to the same sign of spin polarization for excited electrons from the $2p_{1/2}$ initial state and unoccupied final states. The degree of circular photon polarization (DCP) is given by P_{cir}, $\vec{M}$ denotes the magnetization vector and $\vec{L}_{\mathrm{ph}}$ the direction of the photon angular momentum. M_{p} is the magnitude of the magnetization in the direction of the photon angular momentum taking into account the angle θ between those directions.

For the explicit calculation of the spin and orbital moment of the investigated element the sum rules have to be applied. Due to the spin-orbit coupling the spin polarization of electrons originating from the initial states $2p_{3/2}$ and $2p_{1/2}$ show opposite signs in relation to the equal signs for the orbital polarization which allows us to separate the spin and orbital contributions to the dichroic

[14] E. Beaurepaire, F. Scheurer, G. Krill, and J.-P. Kappler. *Magnetism and Synchrotron Radiation*, volume 34. Springer Berlin, Germany (2001)

response. These rules derived by Thole[15] and Carra[16] for spin-orbit split absorption edges calculate the spin $\mu_s = -2\mu_B\langle S_z\rangle/\hbar$ and orbital magnetic moment $\mu_l = -2\mu_B\langle L_z\rangle/\hbar$ per unoccupied final state n_h. To derive the sum rules, various assumptions and approximations have to be made yet the calculation of magnetic moments through a sum-rule analysis shows reasonable results and relying on the density matrix formalism the sum rules are applicable beyond the atomic framework.[17]

Following the experimental confirmation by Chen *et al.*[18] the effective spin magnetic moment and the orbital magnetic moment are given by

$$\frac{\mu_s^{\text{eff}}}{n_h} = \frac{-3p+2q}{r}\cdot\mu_B \qquad \text{and} \tag{1.2}$$

$$\frac{\mu_l}{n_h} = -\frac{2q}{3r}\cdot\mu_B. \tag{1.3}$$

Here, the integral for the L_3 edge is denoted by the p value, the integral over the whole range $L_3 + L_2$ is given by the value q and r is the XAS integral with

$$p = \int_{L_3} (\mu_+ - \mu_-)\,\mathrm{d}E, \tag{1.4}$$

$$q = \int_{L_3+L_2} (\mu_+ - \mu_-)\,\mathrm{d}E, \tag{1.5}$$

$$r = \frac{1}{2}\int_{L_3+L_2} (\mu_+ + \mu_-)\,\mathrm{d}E, \tag{1.6}$$

where the L_3 and L_2 absorption edges must be clearly separated energetically. At this point, a two-step background function with thresholds set to the inflection points on the low energy side of the L_3 as well as L_2 resonance is introduced to accounts for the absorption into delocalized electron states. The step heights of this background function are set to 2/3 (L_3) and 1/3 (L_2) of the average absorption in the post-edge region based on the unequal number of initial state electrons. The steps of this function are broadened to factor in the experimental resolution and core-hole lifetime. The integral r is then obtained by determining the area between the measured absorption and this predefined two-step function. This sum rule based calculation of the spin and orbital moments gives reasonable results and is especially applicable for the analysis of transition metal elements.

For the analysis of a conventional thin film sample it is feasible to measure the absorption directly by the intensity of transmitted x-rays. However, this method has its limits when the investigated layers are deposited on thick supportive structures or substrates. In this cases the absorption is measurable by detecting fluorescence photons or an electric current generated as a direct result of the x-ray absorption process. Option one is to measure the absorption coefficient in the so called fluorescence yield (FY) mode via the detection of emitted photons which are emitted as a direct consequence of core electrons being excited by the absorption of an x-ray

[15] B. Thole, P. Carra, F. Sette, and G. van der Laan. X-ray circular dichroism as a probe of orbital magnetization. *Phys. Rev. Lett.*, **68**(12):1943 (1992)

[16] P. Carra, B. Thole, M. Altarelli, and X. Wang. X-ray circular dichroism and local magnetic fields. *Phys. Rev. Lett.*, **70** (5):694 (1993)

[17] H. Wende and C. Antoniak. X-ray magnetic dichroism. In *Magnetism and Synchrotron Radiation*, pages 145–167. Springer, Berlin, Germany, (2010)

[18] C. Chen, Y. Idzerda, H.-J. Lin, N. Smith, G. Meigs, E. Chaban, G. Ho, E. Pellegrin, and F. Sette. Experimental confirmation of the X-ray magnetic circular dichroism sum rules for iron and cobalt. *Phys. Rev. Lett.*, **75**(1):152 (1995)

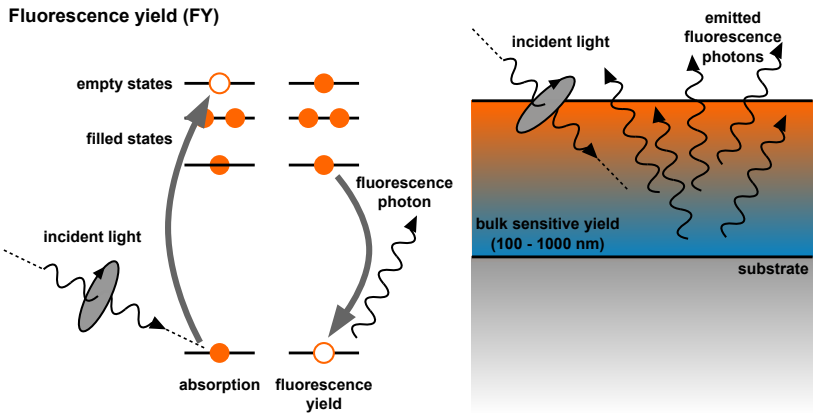

Figure 1.3: Schematic illustration of the FY mode and the corresponding excitation and fluorescence process. An incident x-ray photon is absorbed and transfers its energy to an electron followed by an electron transitioning into the now empty ground state emitting a (less energetic) fluorescence photon. The FY mode is bulk sensitive typically probing the top few micrometer of a sample depending on the energy of incident x-ray.

photon. This core electron leaves an inner-shell vacancy which is subsequently filled by an electron from an energetically higher state and thus resulting in a release of energy. This energy can be transferred to another electron which is then ejected from the atom as an Auger electron or it is released in the form of an emitted photon contributing to the fluorescence yield. The emitted Auger electrons on the other hand can generate more secondary electrons in a cascading way exceeding the energy threshold to leave the sample. The detection of emitted electrons is called total electron yield (TEY) mode and usually supported by an external electric field, e.g., a positively charged electrode in close proximity to the sample. The detected current based on the drained electrons is subsequently interpreted as a probe of the absorption coefficient in relation to a normalized reference for the intensity of the incident x-ray beam.

Since the decay length of hard x-rays is usually on the order of a few micrometers in a solid state material even in the more energetic hard x-ray regime it is beneficial to detect an x-ray absorption spectra indirectly. The direct absorption is accessible when a significant number of the incident photons are transmitted through the investigated material which premises a sample cut smaller than the decay length of the used x-ray light. Therefore, the XAS usually has to be detected indirectly by the following techniques. In the FY mode fluorescence photons are emitted after the a vacancy in a core state is filled by an electron from an outer shell. The intensity of the emitted fluorescence photons is counted at each energy of the impinging photons and is proportional to the number of the absorbed x-ray photons. The fluorescence yield is thereby defined as the de-excitation probability of an excited atom by emitting a fluorescence photon. Especially in the hard x-ray regime in the FY mode the whole film volume is probed. This process and the corresponding schematic of energy levels involved in the fluorescence are illustrated in Fig. 1.3.

An alternative method to measure an x-ray absorption spectrum is the TEY mode. Here, the number of emitted electrons, including photoelectrons, electrons generated through the Auger process and

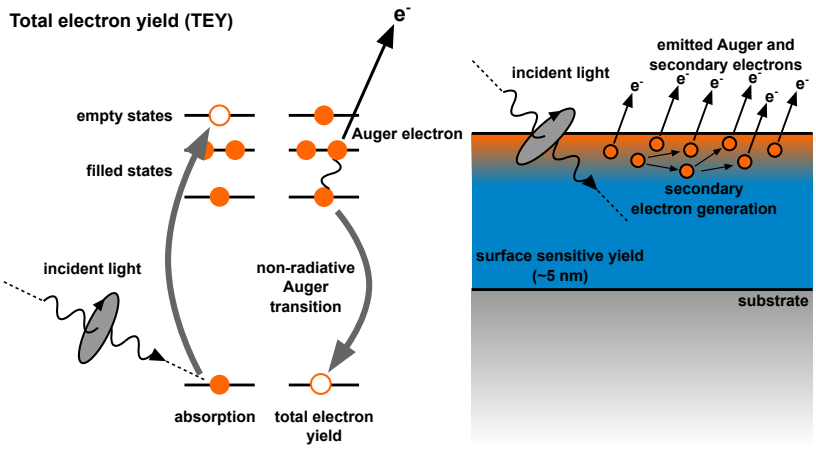

Figure 1.4: Schematic illustration of the TEY mode and the corresponding excitation and Auger process. An incident x-ray photon is absorbed and its energy is transfered to an electron which is excited or emitted as a photo electron. The formed core hole is filled by non radiative de-excitation by an electron of an upper level. The energy can be transferred to another electron, which is ejected from the atom as an Auger electron. Only electrons in close proximity to the surface can be emitted rendering TEY surface sensitive.

further secondary electrons is detected.

The Auger electrons with a relatively high energy are usually scattered inelastically mostly in the sub-nanometer range and therefore quickly transfer the energy to secondary electrons. As soon as the electrons have reached an energy range of below 10 eV the increasing mean free path lets them in many cases escape the sample in a much higher number than the Auger electrons. Therefore, if only Auger electrons are detected the absorption coefficient is probed for the immediate surface of the sample. If in contrast all emitted electrons are detected the secondary electrons yield information on the top few nanometer. In both cases the Auger electron yield is proportional to the number of primarily excited electrons which makes the total electron yield proportional to the absorption coefficient. The probability of an electron decaying to a core state via the Auger process is much higher than through the fluorescence process, yet the probing of a much larger volume in the FY mode compensated this disadvantage in intensity. In the FY mode the influence of the surface to the signal is almost negligible which is beneficial if the focus of the study lies on the bulk of the sample and not on surface contamination or interface properties. The characteristic probing depth of both modes is illustrated in Figs. 1.3 and 1.4.

In an XMCD experiment the absorption is measured in at least one of this modes, usually both for more information on the surface quality and bulk like sample properties. The quantitative evaluation is done subsequently where spin and orbital contributions to the circular dichroism signal are separable for excitations of $2p_{1/2}$ and $2p_{3/2}$ states due to spin polarizations with opposing signs and orbital polarization yielding dichroic contributions of equal sign. The spectra acquired in the TEY mode are usually the basis for a sum rule analysis of XMCD signal. However, this is not reliable for FY measurements since these can suffers from self-absorption effects and misrepresent the intrinsic XAS.[19]

In addition, fluorescence yield spectra can be acquired in trans-

[19] L. Tröger, D. Arvanitis, K. Baberschke, H. Michaelis, U. Grimm, and E. Zschech. Full correction of the self-absorption in soft-fluorescence extended X-ray-absorption fine structure. *Phys. Rev. B*, **46**(6):3283 (1992); and F. M. De Groot. Dips and peaks in fluorescence yield X-ray absorption are due to state-dependent decay. *Nat. Chem.*, **4**(10):766–767 (2012)

mission, measuring the incoming as well as the transmitted x-ray intensity through the sample. When the x-ray light is absorbed in an insulator such as the substrate material, it generates high-energy electrons which by means of electron-electron scattering produce conduction electrons and valence holes. Subsequently, these electron-hole pairs radiatively recombine via defect states and emit luminescence light. This alternative detection method to obtain XAS and XMCD spectra is the so called the luminescence yield (LY) measurement where the x-ray beam is transmitted through the thin film sample and is subsequently converted into the visible light fluorescence of the substrate. The luminescence signal is detected with a photo-diode behind the sample and can be displayed as a function of the x-ray photon energy. The signal is free of saturation or self-absorption effects. Thus, the luminescence measurement is a bulk sensitive direct x-ray transmission probe.[20]

X-ray resonant magnetic reflectivity

The combination of the XRR and XMCD principles creates a powerful technique linking the structural and optical depth profiles of the reflectivity experiment with the element specific magnetic information,[21] thus enabling the detailed investigation of magnetooptical depth profiles in thin film systems. This x-ray resonant magnetic reflectometry (XRMR) technique measures the intensity of the specular reflection and uses a change of the circular polarization or of an applied external magnetic field to gain a contrast providing the spin depth profile of a material element-selectively.[22]

The XRMR method is based on a scattering experiment, where the photo emission, which follows the relaxation after the absorption process, is observed in the low angle regime. This process is illustrated in Fig. 1.5 the same resonant excitation featured in the previous XMCD related schematics (Figs. 1.1 and 1.2). The resonant absorption of an incident photon leads to a resonant scattering process at the absorption edge combining magnetic dichroism with specular reflectivity. Thus, XMCD can be regarded as a special case of this resonant magnetic scattering.

In general, XRMR is a powerful method to directly determine the spin depth profile of a material element-selectively. Especially for the investigation of the static magnetic proximity effects (MPE) interfaces buried underneath multiple other thin film and cover layers have to be probed independently of each other and in great detail. Only a few studies report using XMCD to identify the number of proximity-induced spin-polarized layers by utilizing a thickness-variation series and therefore a wide set of samples.[23]

The XMCD yield profoundly depends on the thickness of the investigated thin film sample. Depending on the measurement method either only the average spin polarization of the surface or a large bulk section of the investigated material is probed. Hence, thick samples with high dichroism contributions of the film volume

[20] M. Kallmayer, H. Schneider, G. Jakob, H. Elmers, B. Balke, and S. Cramm. Interface magnetization of ultrathin epitaxial $Co_2FeSi(110)/Al_2O_3$ films. *J. Phys. D: Appl. Phys.*, **40**(6):1552 (2007); and M. Meinert, J.-M. Schmalhorst, G. Reiss, and E. Arenholz. Ferrimagnetism and disorder of epitaxial $Mn_{2-x}Co_xVAl$ Heusler compound thin films. *J. Phys. D: Appl. Phys.*, **44**(21): 215003 (2011)

[21] G. van der Laan, B. T. Thole, G. A. Sawatzky, J. B. Goedkoop, J. C. Fuggle, J.-M. Esteva, R. Karnatak, J. Remeika, and H. A. Dabkowska. Experimental proof of magnetic x-ray dichroism. *Phys. Rev. B*, **34**(9):6529 (1986); G. Schütz, W. Wagner, W. Wilhelm, P. Kienle, R. Zeller, R. Frahm, and G. Materlik. Absorption of circularly polarized x-rays in iron. *Phys. Rev. Lett.*, **58**(7):737 (1987); C. Chen, F. Sette, Y. Ma, and S. Modesti. Soft-x-ray magnetic circular dichroism at the $L_{2,3}$ edges of nickel. *Phys. Rev. B*, **42**(11):7262 (1990); G. van der Laan and B. Thole. Strong magnetic x-ray dichroism in $2p$ absorption spectra of $3d$ transition-metal ions. *Phys. Rev. B*, **43**(16):13401 (1991); P. Carra, B. Thole, M. Altarelli, and X. Wang. X-ray circular dichroism and local magnetic fields. *Phys. Rev. Lett.*, **70**(5):694 (1993); J. Stöhr. X-ray magnetic circular dichroism spectroscopy of transition metal thin films. *J. Electron Spectrosc. Relat. Phenom.*, **75**:253–272 (1995); and J. Stöhr. Exploring the microscopic origin of magnetic anisotropies with X-ray magnetic circular dichroism (XMCD) spectroscopy. *J. Magn. Magn. Mater.*, **200**(1-3):470–497 (1999)

[22] J. Tonnerre, L. Sève, A. Barbara-Dechelette, F. Bartolomé, D. Raoux, V. Chakarian, C. Kao, H. Fischer, S. Andrieu, and O. Fruchart. Soft x-ray resonant magnetic reflectivity study of thin films and multilayers. *J. Appl. Phys.*, **83**(11):6293–6295 (1998); J. Geissler, E. Goering, M. Justen, F. Weigand, G. Schütz, J. Langer, D. Schmitz, H. Maletta, and R. Mattheis. Pt magnetization profile in a Pt/Co bilayer studied by resonant magnetic x-ray reflectometry. *Phys. Rev. B*, **65** (2):020405 (2001); and D. Lee, S. Sinha, D. Haskel, Y. Choi, J. Lang, S. Stepanov, and G. Srajer. X-ray resonant magnetic scattering from structurally and magnetically rough interfaces in multilayered systems. I. Specular reflectivity. *Phys. Rev. B*, **68**(22):224409 (2003)

[23] W. Antel Jr, M. Schwickert, T. Lin, W. O'Brien, and G. Harp. Induced ferromagnetism and anisotropy of Pt layers in Fe/Pt (001) multilayers. *Phys. Rev. B*, **60**(18):12933 (1999)

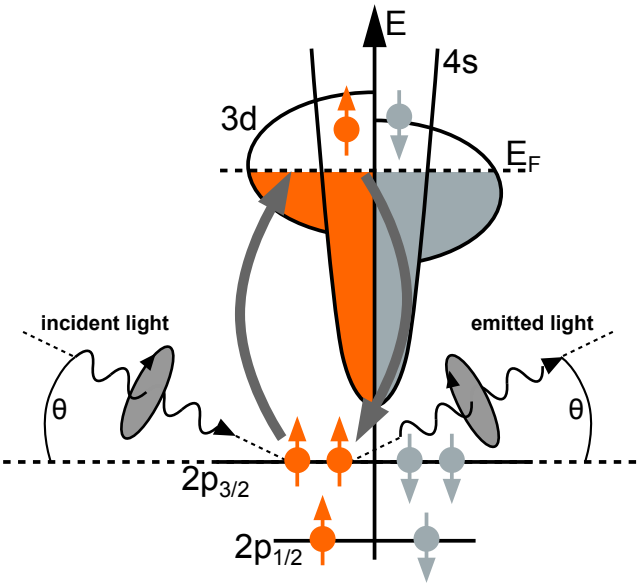

Figure 1.5: Schematic illustration of the resonant scattering process for the L edge 2*p*-3*d* transition in a 3*d* transition metal. The spin-down electrons do contribute to the scattering process as well but are shown grayed out for reasons of clarity.

do not allow for the specific analysis of interface effects. For example, the interface spin polarization of thin films is not resolvable via XMCD if the thickness of these layers exceeds a few nanometer.[24] Regarding the investigation of the MPE in Pt with XMCD techniques, thin film systems with particularly small thickness are required since thicker Pt films only yield disappearing signals and thus merely make it possible to estimate an upper limit for the induced Pt magnetic polarization.[25] In addition, the sum rules necessary to extract the magnetic moments from this questionably obtainable dichroism signals are partially violated, e.g., for Co-Pt systems.[26]

In contrast, the XRMR technique interconnects the magnetic characterization with the conventional XRR depth profiling and thus adds an excellent spatial resolution, on the order of 1 Å, to the circular-dichroic measurement.[27] Furthermore, XRMR combines the excellent capability of off-resonant XRR to determine film thickness, interlayer roughness, electron densities and the complex refractive indices, with the element specific magnetic information obtained at the corresponding absorption edge due to the XMCD or linear dichroism (XMLD) affecting the intensity of the absorbed and reflected light. Thus, XRMR allows to study buried and consecutive magnetic layers on a single sample. This magnetic information is not necessarily accessible by the standard XMCD measurements even when these studies are based on a wide set of samples with a variation of layer thickness.[28]

The XRMR technique is highly sensitive in the detection of magnetic moment depth profiles when asymmetry signals even down to a ratio of about 0.01 are detectable as it is the case for observations at the L_3 edges of ferromagnetic materials[29]or materials close to the Stoner criterion[30] in direct proximity to a ferromagnet.[31] The proximity to a ferromagnet increases the exchange interaction of

[24] M. Suzuki, H. Muraoka, Y. Inaba, H. Miyagawa, N. Kawamura, T. Shimatsu, H. Maruyama, N. Ishimatsu, Y. Isohama, and Y. Sonobe. Depth profile of spin and orbital magnetic moments in a subnanometer Pt film on Co. *Phys. Rev. B*, **72**(5):054430 (2005)

[25] S. Geprägs, S. Meyer, S. Altmannshofer, M. Opel, F. Wilhelm, A. Rogalev, R. Gross, and S. T. Goennenwein. Investigation of induced Pt magnetic polarization in $Pt/Y_3Fe_5O_{12}$ bilayers. *Appl. Phys. Lett.*, **101**(26):262407 (2012)

[26] C. Ederer, M. Komelj, M. Fähnle, and G. Schütz. Theory of induced magnetic moments and x-ray magnetic circular dichroism in Co-Pt multilayers. *Phys. Rev. B*, **66**(9):094413 (2002)

[27] T. Kuschel, C. Klewe, P. Bougiatioti, O. Kuschel, J. Wollschläger, L. Bouchenoire, S. Brown, J. Schmalhorst, D. Meier, and G. Reiss. Static Magnetic Proximity Effect in Pt Layers on Sputter-Deposited $NiFe_2O_4$ and on Fe of Various Thicknesses Investigated by XRMR. *IEEE Trans. Magn.*, **52**: 4500104 (2016)

[28] C. Klewe, T. Kuschel, J.-M. Schmalhorst, F. Bertram, O. Kuschel, J. Wollschläger, J. Strempfer, M. Meinert, and G. Reiss. Static magnetic proximity effect in $Pt/Ni_{1-x}Fe_x$ bilayers investigated by x-ray resonant magnetic reflectivity. *Phys. Rev. B*, **93** (21):214440 (2016)

[29] C. Kao, J. Hastings, E. Johnson, D. Siddons, G. Smith, and G. Prinz. Magnetic-resonance exchange scattering at the iron L II and L III edges. *Phys. Rev. Lett.*, **65**(3):373 (1990); J. Tonnerre, L. Sève, D. Raoux, G. Soullié, B. Rodmacq, and P. Wolfers. Soft X-ray resonant magnetic scattering from a magnetically coupled Ag/Ni multilayer. *Phys. Rev. Lett.*, **75**(4):740 (1995); and S. Roy, C. Sanchez-Hanke, S. Park, M. Fitzsimmons, Y. Tang, J. Hong, D. J. Smith, B. Taylor, X. Liu, M. Maple, A. E. Berkowitz, C.-C. Kao, and S. K. Sinha. Evidence of modified ferromagnetism at a buried Permalloy/CoO interface at room temperature. *Phys. Rev. B*, **75**(1):014442 (2007)

[30] E. C. Stoner. Collective electron ferromagnetism II. Energy and specific heat. *Proc. Royal Soc. A*, **169**(938): 339–371 (1939)

[31] L. Sève, N. Jaouen, J. Tonnerre, D. Raoux, F. Bartolomé, M. Arend, W. Felsch, A. Rogalev, J. Goulon, C. Gautier, and J. F. Bérar. Profile of the induced 5*d* magnetic moments in Ce/Fe and La/Fe multilayers probed by x-ray magnetic-resonant scattering. *Phys. Rev. B*, **60**(13):9662 (1999)

a material close to the Stoner criterion like Pt and therefore can increase the Stoner parameter converting a paramagnet into a ferromagnet for a few atomic layers. This effect is discussed in-depth in section 1.4 of this chapter. Here, XRMR is advantageous over the XMCD method since it can identify buried magnetic layers with high resolution on single samples while these magnetic information is not accessible by the conventional XMCD measurements.[32]

Due to the high sensitivity it is in general possible to use XRMR to extract interfacial magnetization depth profiles with subnanometer resolution. This is for instance demonstrated in the study of manganite-based heterostructures, though the measured reflectivity spectra must be fitted with great care to obtain the magnetization depth profiles, e.g., by radically minimizing the number of free parameters for instance through independently measuring thickness and roughness parameters.[33] In addition, it is often necessary to verify or support the obtained structural and magnetic depth profile by additional methods such as determining the ratio of optical parameters from XMCD measurements[34] and by implementing robust analysis procedures to ensure the XRMR method is sensitive enough to distinguish between different cases.

The x-ray reflectivity is usually measured in the standard $\theta - 2\theta$ scattering geometry where θ is the angle between the incident beam and the thin film plane. The fundamental principle is to reflect a beam of incident light from a flat surface and probe the yield of light reflected under a specular condition. According to the Fresnel equations the reflected intensity is easy to determine theoretically though it interface roughness modifies the intensity depending on the density profile. This effect is superimposed with the interference of the reflected light originating from the various probed interfaces which creates an oscillation pattern observed in reflectivity experiment. This interference pattern is called Kiessig fringes and holds comprehensive information on layer thickness and all structural as well as optical parameters of thin film systems. The reflectivity R is defined as the ratio between the intensity of incoming and reflected light. It can be determined in relation to the reflection coefficient r by the relation $R = |r|^2$. In a thin film system with an interface separating layer $i-1$ from layer i this coefficient is given by the Fresnel equation

$$r = \frac{k_{i-1} - k_i}{k_{i-1} + k_i}, \tag{1.7}$$

where k_i is the perpendicular wave vector in layer i use the convention $k_i = (2\pi/\lambda)\left(n_i^2 - \cos^2\theta\right)^{1/2}$ and n_i is the refractive index of material i.[35]

For a layer in the probed thin film system having a thickness d the position of the Kiessig fringe minima is given by $m\lambda = 2d\sin\theta$ with an integer m. The amplitude of those oscillations depends on the density contrast between the layers while the interface roughness reduces the overall reflectivity. The crystal structure

[32] T. Kuschel, C. Klewe, J.-M. Schmalhorst, F. Bertram, O. Kuschel, T. Schemme, J. Wollschläger, S. Francoual, J. Strempfer, A. Gupta, M. Meinert, G. Götz, D. Meier, and G. Reiss. Static magnetic proximity effect in $Pt/NiFe_2O_4$ and Pt/Fe bilayers investigated by x-ray resonant magnetic reflectivity. *Phys. Rev. Lett.*, **115**(9):097401 (2015); and C. Klewe, T. Kuschel, J.-M. Schmalhorst, F. Bertram, O. Kuschel, J. Wollschläger, J. Strempfer, M. Meinert, and G. Reiss. Static magnetic proximity effect in $Pt/Ni_{1-x}Fe_x$ bilayers investigated by x-ray resonant magnetic reflectivity. *Phys. Rev. B*, **93** (21):214440 (2016)

[33] A. Verna, B. A. Davidson, Y. Szeto, A. Y. Petrov, A. Mirone, A. Giglia, N. Mahne, and S. Nannarone. Measuring magnetic profiles at manganite surfaces with monolayer resolution. *J. Magn. Magn. Mater.*, **322**(9-12):1212–1216 (2010)

[34] S. Brück, S. Macke, E. Goering, X. Ji, Q. Zhan, and K. M. Krishnan. Coupling of Fe and uncompensated Mn moments in exchange-biased Fe/MnPd. *Phys. Rev. B*, **81**(13):134414 (2010)

[35] D. De Boer, A. Leenaers, and W. Van den Hoogenhof. Glancing-incidence x-ray analysis of thin-layered materials: A review. *X-Ray Spectrometry*, **24**(3):91–102 (1995)

can be disregarded in the specular regime as long as the scattering vector $q = 2k \sin\theta$ is significantly smaller than the reciprocal lattice vector. With the incident light wavenumber $k = 2\pi/\lambda$ the scattering vector is often expressed as $q = |k - k_0| = 4\pi \sin\theta/\lambda$. A detailed derivation is given in the Eqs. (1.69) to (1.73).

The basic theory to analyze the reflection and transmission of an electromagnetic wave interacting with an interface was established by Fresnel in the frame of a mechano-elastic model.[36] In a model where the electrons are elastically bonded to the atomic core, the interactions of x-rays with this matter is specifiable in a quantitative way. The fundamental principles of motion operating on an electron in an electromagnetic field E results in the relation

[36] A. Fresnel. *Mémoires de l'Académie*, **11**: 393 (1823)

$$m\frac{\mathrm{d}^2 r}{\mathrm{d}t^2} + h\frac{\mathrm{d}r}{\mathrm{d}t} + kr = -eE, \tag{1.8}$$

where h and k are the friction and spring coefficients. Following the oscillations of the incident light, the displacement of the electron in relation to the average location can be written as

$$r = \frac{-e}{m\left(\omega_0^2 - \omega^2\right) + i\omega\frac{h}{m}} E e^{i\omega t}. \tag{1.9}$$

Here the value $\omega_0 = \sqrt{k/m}$ is the so called eigen pulsation of the electron i.e. the corresponding time-dependent transversal displacement in relation to the core. Its important to note that this value is significantly smaller than the angular frequency of hard x-ray light since $\omega_0 \approx 10^{15}\,\mathrm{rad/s} \ll \omega = 1.2 \times 10^{19}\,\mathrm{rad/s}$. According to this relation we can approximate

$$r \approx \frac{eE}{m\omega^2}, \tag{1.10}$$

in case the energy is far away from an absorption edge of the material and therefore the dielectric polarisation can be expressed as

$$P = \epsilon_0 \chi E = -\frac{\rho_e^2 E}{m\omega^2}, \tag{1.11}$$

with the dielectric susceptibility χ and the number of electrons per unit volume or electron density ρ_e. The former can be expressed as

$$\chi = \epsilon_r - 1 = -\frac{\rho_e e^2}{\epsilon_0 m\omega^2}, \tag{1.12}$$

where ϵ_r is the relative permittivity or dielectric constant. The complex refractive index for electromagnetic radiation $n = \sqrt{\epsilon_r \mu_r}$ generally depends on the frequency and is widely used in optics for example in Fresnel equations. In case of a nonmagnetic material μ_r is close to 1 and therefore we can write the complex refractive index with the real and imaginary part ϵ_1 and ϵ_2 of the relative permittivity as

$$n \approx \sqrt{\epsilon_r} = \sqrt{\epsilon_1 + i\epsilon_2} = \sqrt{1 + \chi}. \tag{1.13}$$

Furthermore with this assumption $\chi \ll 1$ one can express the index of refraction as

$$n = 1 - \frac{\rho_e e^2}{2m\epsilon_0 \omega^2}. \tag{1.14}$$

Here, it is beneficial to introduce a length that characterizes the electron interactions at the atomic scale primarily with electromagnetic radiation, the classical electron radius:

$$r_e = \frac{1}{4\pi\epsilon_0}\frac{e^2}{m_e c^2} = 2.82 \times 10^{-15}\,\mathrm{m}. \tag{1.15}$$

Following this and if there is no absorption process involved, the refractive index can be rewritten as

$$n = 1 - \frac{r_e \rho_e \lambda^2}{2\pi}. \tag{1.16}$$

This is subsequently applicable to crystallized materials as outlined by A. Gibaud.[37] The electron density ρ_e can be written as

$$\rho_e = \sum_k \frac{Z_k}{V_m}, \tag{1.17}$$

[37] A. Gibaud and G. Vignaud. Specular reflectivity from smooth and rough surfaces. In *X-ray and Neutron Reflectivity*, pages 85–131. Springer, Berlin, Germany, (2009)

if the unit cell volume V_m and the number of electrons of atom k in this unit cell Z_k is known. This number has to be modified to correctly include the absorption precesses as resulting from a quantum mechanical description by the real f' and imaginary f'' part of the anomalous atomic form factor at the wavelength λ. Besides through summing up over all atoms in the unit cell, it is possible determine the electron density via the mass density ρ and its stoichiometric composition. Taking the number of atoms x_k of each species k and their molar mass M_k into account, the electron density can also be determined by

$$\rho_e = N_\mathrm{A} \cdot \rho \frac{\sum_k x_k \frac{Z_k + f'_k + i f''_k}{M_k}}{\sum_k x_k}, \tag{1.18}$$

with the Avogadro number N_A. Based on those equations and because for x-ray radiation the complex refractive index deviates only slightly from unity with a real part that is usually smaller than 1 the refraction index is normally written as

$$n = 1 - \delta + i\beta, \tag{1.19}$$

with the dispersive correction δ written as

$$\delta = \frac{r_e}{2\pi}\lambda^2 \rho_e = \frac{r_e}{2\pi}\lambda^2 N_\mathrm{A} \cdot \rho \frac{\sum_k x_k \frac{Z_k + f'_k}{M_k}}{\sum_k x_k} \tag{1.20}$$

as well as the absorptive correction β expressed as

$$\beta = \frac{r_e}{2\pi}\lambda^2 N_\mathrm{A} \cdot \rho \frac{\sum_k x_k \frac{f''_k}{M_k}}{\sum_k x_k}. \tag{1.21}$$

The real part describes the dispersion of radiation as it interacts with matter, while the imaginary part accounts for the absorption

of radiation. Typical values for δ are usually in the range of 10^{-5} to 10^{-6} and one order of magnitude smaller for β, which is proportional to the absorption coefficient of the probed material and can be probed directly by recording an absorption spectrum.

In an alternative notation the Eqs. (1.16) and (1.18) can be combined to directly relate the refraction index with the corresponding complex scattering amplitude specific for the atomic number

$$f(E) = f_0 + f'(E) + if''(E), \tag{1.22}$$

which depends the on x-ray energy E with the coherent scattering factor f_0 valid for off-resonant energies, and the dispersive and absorptive scattering factors f' and f'' becoming especially important near an absorption edge. Therefore, the refraction index can be written as

$$n = 1 - \frac{r_e \lambda^2}{2\pi} \sum_k n_k f_k(E). \tag{1.23}$$

The real and imaginary parts of many analytic complex functions are connected by the Kramers-Kronig relations which allows us to calculate the real part from the imaginary part of the scattering amplitude or vice versa

$$f'(E) = \frac{2}{\pi} \oint \frac{E_0 \cdot f''(E)}{E_0^2 - E^2} \, \mathrm{d}E \tag{1.24}$$

$$f''(E) = -\frac{2}{\pi} \oint \frac{E \cdot f'(E)}{E_0^2 - E^2} \, \mathrm{d}E. \tag{1.25}$$

The refraction index $n = 1 - \delta(E) + i\beta(E)$ therefore is energy dependent through the attenuation of the incident light due to absorption and the corresponding phase shift. The real part of the correction in n is given by

$$\delta(E) = \frac{r_e \lambda^2}{2\pi} \left(f_0 + f'(E)\right) \tag{1.26}$$

and the imaginary part by

$$\beta(E) = \frac{r_e \lambda^2}{2\pi} f''(E), \tag{1.27}$$

respectively. This energy dependence illustrates that this absorptive and dispersive correction are crucially depending on the x-ray wavelength in addition to the material properties such as the electron density.[38]

[38] M. Born and E. Wolf. *Principles of optics: Electromagnetic theory of propagation, interference and diffraction of light*. Elsevier (2013)

Since the refractive index of x-rays is usually less than unity, the incident light is subject to total external reflection under the condition that the angle of incidence θ is is smaller than the critical angle θ_c. This angle is determined by

$$\cos\theta_c = n = 1 - \delta \tag{1.28}$$

if no absorption is occurring at the reflecting surface. The off-resonant wavelength dependent absorption ($\sim 10^{-8}$) is negligible in

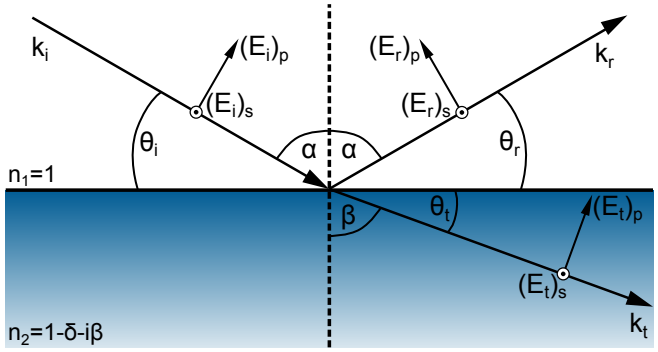

Figure 1.6: Reflection and refraction of an incident wave traveling in the plane of incidence with different indices of refraction n_1 and n_2.

most cases. Following this relation in a small-angle approximation with

$$\cos\theta_c \approx 1 - \theta_c^2/2 \tag{1.29}$$

the critical angle is defined by

$$\theta_c \approx \sqrt{2\delta} = \sqrt{\frac{r_e\lambda^2}{\pi} N_A \frac{(Z+f')}{A}\rho}. \tag{1.30}$$

If one uses the typical values for δ to calculate this angle it becomes obvious that it is rather small and total external reflection only becomes important at grazing angles of incidence. At larger angles $\theta > \theta_c$ of incident, the reflectivity decreases quickly as the x-ray beam penetrates inside the film.

When a simple flat film layer is probed reflection occurs at the top and bottom interfaces of this film leading to the angle dependent Kiessig fringes due to the interference of light reflected from both surfaces. On account of the low reflectance or reflectivity R in relation to the amplitude coefficient r of interfaces between neighboring layers one can approximate

$$R = |r|^2 \propto \frac{1}{\sin^4\theta} \approx \frac{1}{\theta^4} \tag{1.31}$$

and thus the contributions of multiple reflections are neglectable. Regarding the Kiessig fringes the interference maximum, the measured intensity contains information of the thickness of the probed layer due to the difference in path length

$$\Delta = m \cdot \lambda = 2d \cdot sin\theta_m \qquad \text{with } m \in \mathbb{N}. \tag{1.32}$$

This is the famous Bragg equation which can be rewritten as

$$d = \frac{m\lambda}{2\sin\theta_m} = \frac{2\pi m}{2\sin\theta_m \cdot \frac{2\pi}{\lambda}} = \frac{2\pi m}{|q|}. \tag{1.33}$$

including the wave vector q parallel to the reciprocal lattice vector and the diffraction order m.

In detail the transmission and reflection coefficients can be derived by identifying the continuity conditions of the electric and magnetic fields at the interfaces by considering an electromagnetic plane wave propagating in the plane of incidence.[39]

[39] J. Daillant and A. Gibaud. *X-ray and Neutron Reflectivity: Principles and Applications*, volume 770. Springer, Berlin (2008)

Figure 1.6 shows the idealized case of a perfectly smooth interface where the medium is sufficiently thick for the transmitted beam to be completely absorbed. For materials with approximately the same permeability the Fresnel equations can be approximated for polarized light with the electric field vector parallel (p),

$$t_p = \left(\frac{E_t}{E_i}\right)_p = \frac{2n_1 \cos\alpha}{n_2 \cos\alpha + n_1 \cos\beta} \tag{1.34}$$

$$r_p = \left(\frac{E_r}{E_i}\right)_p = \frac{n_2 \cos\alpha - n_1 \cos\beta}{n_2 \cos\alpha + n_1 \cos\beta} \tag{1.35}$$

$$\tag{1.36}$$

and perpendicular (s) to the scattering plane

$$t_s = \left(\frac{E_t}{E_i}\right)_p = \frac{2n_1 \cos\alpha}{n_1 \cos\alpha + n_2 \cos\beta} \tag{1.37}$$

$$r_s = \left(\frac{E_r}{E_i}\right)_p = \frac{n_1 \cos\alpha - n_2 \cos\beta}{n_1 \cos\alpha + n_2 \cos\beta}. \tag{1.38}$$

$$\tag{1.39}$$

In these equations, r_p (r_s) and t_p (t_s) are the reflection and transmissions coefficients for p (s) polarized light in relation to the plane of incidence. As illustrated in Fig. 1.6, n_1 and n_2 specify the complex refractive indices of the materials on the relevant side of the interface. Utilizing the complementary angles depicted here, θ_i and α and θ_t and β respectively, one can rewrite Eq. (1.39) with the assumption of air or vacuum ($n_1 = 1$) as the ambient medium to become

$$r_s = \frac{\sin\theta - n\sin\theta_t}{\sin\theta + n\sin\theta_t}. \tag{1.40}$$

It can be shown that for small grazing incident angles of x-ray radiation $r_p \approx r_s \approx r$. Now Snell's law $\cos\theta = n\cos\theta_t$ can be applied and the angle dependent reflection coefficient can be determined by the equation

$$r(\theta) = \frac{\sin\theta - \sqrt{n^2 - \cos^2\theta}}{\sin\theta + \sqrt{n^2 - \cos^2\theta}}. \tag{1.41}$$

According to Eq. (1.29) for small incident angles the refractive index can be written as

$$n^2 = 1 - 2\delta = 1 - \theta_c^2 \tag{1.42}$$

and in the same approximation the previous Eq. (1.41) is transformed to

$$r(\theta) = \frac{\theta - \sqrt{\theta^2 - \theta_c^2}}{\theta + \sqrt{\theta^2 - \theta_c^2}}. \tag{1.43}$$

The reflection coefficient results from the relation shown in Eg. 1.31 as follows

$$R(\theta) = \left|\frac{\theta - \sqrt{\theta^2 - \theta_c^2}}{\theta + \sqrt{\theta^2 - \theta_c^2}}\right|^2. \tag{1.44}$$

If a reflectometry measurement is performed on a material which significantly absorbs x-ray light, e.g., during a resonant scan, the

refractive index includes the complex value and the Fresnel reflectivity has to be stated as

$$R(\theta) = \left| \frac{\theta - \sqrt{\theta^2 - \theta_c^2 - 2i\beta}}{\theta + \sqrt{\theta^2 - \theta_c^2 - 2i\beta}} \right|^2 . \tag{1.45}$$

or written for an equally transfer of the wave-vector q_z in direction of the interface normal this changes to

$$R(\theta) = \left| \frac{q_z - \sqrt{q_z^2 - q_c^2 - \frac{32i\pi^2\beta}{\lambda^2}}}{q_z + \sqrt{q_z^2 - q_c^2 - \frac{32i\pi^2\beta}{\lambda^2}}} \right|^2 , \tag{1.46}$$

with the critical scattering vector q_c.

In ordinary hard x-ray reflectometry this wave-vector transfer is much larger than q_z and the measured reflectivity curve approaches

$$R = \frac{q_c^4}{16q^4} \tag{1.47}$$

asymptotically as presented in Fig. 1.7.

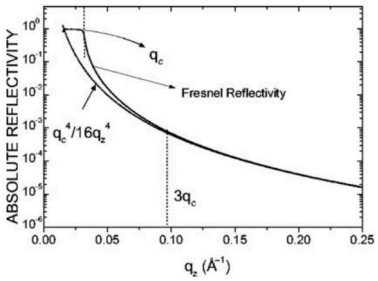

Figure 1.7: Calculated reflectivity of a flat silicon wafer and asymptotic law. This figure was taken from Ref. [Daillant and Gibaud, 2008]

If the value of q_c is experimentally measured, one can directly determine the value of the electron density of the probed material with

$$q_c = 3.75 \times 10^{-2} \sqrt{\rho_e}, \tag{1.48}$$

where ρ_e is the electron density in the units $e^- / \text{Å}^3$.[40]

The x-ray reflectometry is a potent tool to investigate multilayer structures. When multiple stacked thin films are subjected to x-ray radiation the reflected and transmitted electromagnetic waves interact depending on the polarization according to the reflection and transmission coefficients presented in Eqs. (1.36) - (1.39) based on the Fresnel equations. At every multilayer interface in a horizontally stratified stack the electromagnetic wave is reflected. Therefore, the combined reflection processes are discussed in a multiple scattering formalism introduced by Parratt.[41] As illustrated in Fig. 1.8, every interface interacts with four partial beams for every polarization of light, one pair incoming and going out on the upper side and one pair coming in as reflected light from below and transmitted or reflected into deeper layers. One can derive the continuity conditions for those partial electromagnetic waves as

$$E_i^r e^{ik_i z} = r \cdot E_i^t e^{-ik_i z} + (1 - r) \cdot E_{i+1}^r e^{ik_{i+1} z}, \tag{1.49}$$

$$E_i^t e^{-ik_{i+1} z} = -r \cdot E_{i+1}^r e^{ik_{i+1} z} + (1 + r) \cdot E_{i+1}^t e^{-ik_i z}. \tag{1.50}$$

The ratio of reflected to incident wave amplitude of every layer is defined as

$$R_i = \frac{E_i^r}{E_i^t} \tag{1.51}$$

which based on the continuity conditions (Eq. 1.50) results in the useful recursion formula with the thickness of the ith layer d_i

$$R_i = \frac{r_i + R_{i+1} e^{2ik_{i+1} d_{i+1}}}{1 + r_i R_{i+1} e^{2ik_{i+1} d_{i+1}}}, \tag{1.52}$$

[40] F. de Bergevin. The interaction of x-rays (and neutrons) with matter. In *X-ray and Neutron Reflectivity*, pages 1–57. Springer, (2009)

[41] L. G. Parratt. Surface Studies of Solids by Total Reflection of X-Rays. *Phys. Rev.*, **95**(2):359 (1954)

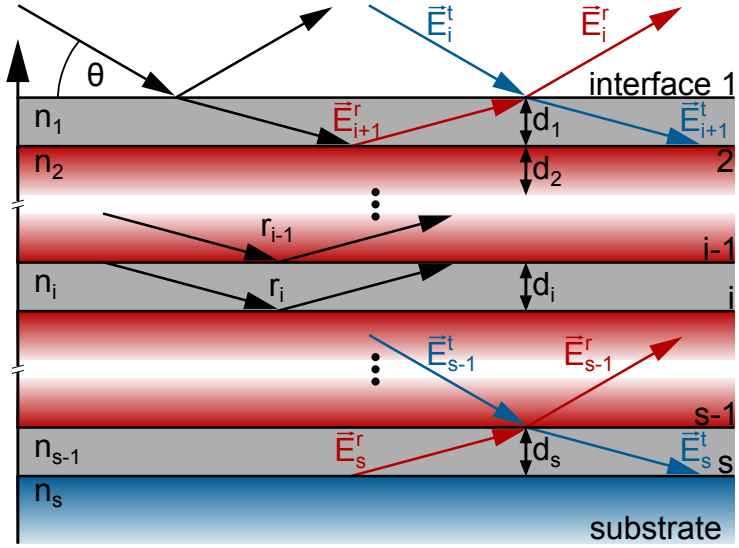

Figure 1.8: Schematic view of a multilayer system illustrating the scattering of the partial electromagnetic waves resulting from multiple scattering events in a stack of s layers of thicknesses d_s. The definition of the transmitted ($\vec{E}_i^t$, red) and reflected ($\vec{E}_i^r$, blue) electromagnetic wave vectors of the propagating electric fields is shown relative to the interface.

while k_i represents the normal component of the wavevector in this layer. Since this formalism is based on the Fresnel equations s and p polarized light has to be treated independently. Here it is noteworthy that R_i in addition to the reflection of the incident beam at an interface r_i includes the equally polarized light coming from the layers below describing the overall electric field ratio in the layer. The ratio of reflected to incident intensity I_r / I_0 can be obtained by

$$\frac{I_r}{I_0} = \left| \frac{E_0^r}{E_0} \right|^2 = |R_0|^2 . \tag{1.53}$$

The main scheme of the Parratt formalism for a multilayer system is illustrated in Fig. 1.8 for a stack of stack of s layers of thicknesses d_s.

The multilayer system featured in Fig. 1.8 shows a stack with perfectly flat interfaces. In real heterostructures interfaces are usually not atomically smooth and therefore show a finite roughness which results in a reduced reflection at this in no longer discrete transition between two individual layers. This effect is originating in the continuous change of the index of refraction at a rough interface with a gradual change in the optical properties. Further imperfections and interface defects increase the diffusive scattering and decrease the reflectance at the interface. The diffuse scattering is also associated with a loss of energy in the specular direction though this effect is negligible while the roughness is not significantly larger than the wavelength.[42]

When a reflectometry experiment is probing the total intensity of the reflected light, it becomes obvious that this value is profoundly influenced by the overall roughness of the contributing interfaces even in the sub-nanometer roughness regime. To work with the Parratt formalism in analyzing reflectometry data, this intensity loss has to be modeled accurately. Otherwise any simulated reflectivity curve will be orders of magnitude off target in relation to the experimental results. Therefore the roughness of the interfaces has

[42] Y. Fujii. Recent Developments in the X-Ray Reflectivity Analysis for Rough Surfaces and Interfaces of Multilayered Thin Film Materials. *J. Mater.*, **2013** (2013)

to to accurately modeled to be implemented into the calculation of reflectivity coefficients.

This gradual transition of two materials with different optical properties has to be modeled with an interface profile function $\varsigma(z)$ and the reflectivity change can be approximated when we multiply the Fresnel coefficients with the Fourier transform of the profile derivative $\mathrm{d}\varsigma(z)/\,\mathrm{d}z$.[43]

[43] D. Stearns. The scattering of x-rays from nonideal multilayer structures. *J. Appl. Phys.*, **65**(2):491–506 (1989)

Névot and Croce[44] introduced a modeling of optical profile of the interface roughness based on the error function which is encountered in integrating the normalized form of the Gaussian function. The Fresnel coefficients included in the continuity conditions (Eqs. (1.49) and (1.50)) have to be modified to incorporate the exponentially dampening of the electromagnetic waves caused by the interface roughness in the form

[44] L. Névot and P. Croce. Caractérisation des surfaces par réflexion rasante de rayons X. Application à l'étude du polissage de quelques verres silicates. *Rev. Phys. Appl.*, **15**(3):761–779 (1980)

$$r_{i,i+1}^{\text{rough}} = r_{i,i+1} e^{-k_{z,i} \cdot k_{z,i+1} \cdot \sigma^2} \tag{1.54}$$

with a roughness factor σ which is defined as the root mean square (rms) of the vertical interface roughness.[45] This wave vector dependent effective Fresnel coefficients are then used to describe an interface within the Parratt approach and usually produce satisfying results. More complex interface layouts can be simulated by slicing the interface region of a stack into numerous single layers with no inherent roughness to simulate a real chemical profile by the variation of the optical properties of each layer.

[45] S. Macke and E. Goering. Magnetic reflectometry of heterostructures. *J. Phys. Condens. Matter*, **26**(36):363201 (2014)

However, this modeling approach of specular reflectometry data cannot be used to distinguish between different roughness types with subnanometer resolution because the reflectivity is always measured over a larger area of at least the focus size. Therefore, any model describing the interface roughness is only related to the averaged electron density distribution along the interface normal.[46]

[46] H. Zabel. X-ray and neutron reflectivity analysis of thin films and superlattices. *Appl. Phys. A*, **58**(3): 159–168 (1994)

For the investigation of magnetic properties through these scattering processes, all magnetooptical material parameters have to be taken into account. When a magnetic material is probed the basic scattering amplitude is extended by a magnetic scattering factor which for example includes the magnetic contribution to the circular dichroism in a resonant magnetic scattering process at an absorption edge. The process of resonant magnetization-sensitive x-ray scattering in the vicinity of the L_2 and L_3 absorption edges was theoretically described by Hannon *et al.* as a result of electric multipole transitions arising from exchange scattering.[47]

[47] J. Hannon, G. Trammell, M. Blume, and D. Gibbs. X-ray resonance exchange scattering. *Phys. Rev. Lett.*, **61** (10):1245 (1988)

The x-ray scattering at an atom is treated in this context in the far field as a decaying spherical wave and thus the scattered field E_f amplitude is written as

$$E_f = -r_e f\left(q, \omega_0, \vec{e}_f, \vec{e}_i\right) \frac{e^{ik_0 r}}{r} E_i. \tag{1.55}$$

Here, the incident electric field amplitude E_i is interacting with the scattering factor f depending on the momentum transfer q, the x-ray energy or angular frequency ω_0 and the complex polarization

vectors $\vec{e}_i$ and $\vec{e}_f$ of the incident and the scattered beam. The atomic scattering factor of Eq. (1.22) is amended in the dipole approximation to combine the different scattering types and includes the magnetic scattering process with the magnetic scattering factors m' and m'' providing the dispersive and the absorptive correction according to

$$f\left(q,\omega,\vec{e}_f,\vec{e}_i\right) = -\left(\vec{e}_f^{\,*}\cdot\vec{e}_i\right)\cdot\left[f_0(q)+f'(\omega)+if''(\omega)\right] + i\left(\vec{e}_f^{\,*}\times\vec{e}_i\right)\cdot\vec{b}\cdot\left[m'(\omega)+im''(\omega)\right]. \tag{1.56}$$

In this formula $\vec{b}$ is the unit vector of the film magnetization defining the direction of the magnetic moment. Here, the magnetic scattering alters the scattered polarization and therefore this process is a part of the anisotropic scattering. When the magnetization direction is defined in spherical coordinates as

$$\vec{b} = \begin{pmatrix} \sin\theta_M \sin\varphi_M \\ \sin\theta_M \cos\varphi_M \\ \cos\theta_M \end{pmatrix} \tag{1.57}$$

with the azimuthal angle θ_M and polar angle φ_M Eq. (1.56) can be transformed into the simple tensor form

$$f\left(q,\omega,\vec{e}_f,\vec{e}_i\right) = \vec{e}_f\cdot\boldsymbol{F}\cdot\vec{e}_i \tag{1.58}$$

with the scattering tensor

$$\boldsymbol{F} = \left[f_0(q)+f'(\omega)+if''(\omega)\right]\mathbb{1} + i\left[m'(\omega)+im''(\omega)\right] \times \begin{pmatrix} 0 & \cos\theta_M & -\sin\theta_M\sin\varphi_M \\ -\cos\theta_M & 0 & \sin\theta_M\cos\varphi_M \\ \sin\theta_M\sin\varphi_M & -\sin\theta_M\cos\varphi_M & 0 \end{pmatrix}. \tag{1.59}$$

Based on this tensor the scattering characteristics of a magnetic atom can be calculated depending on the initial $\vec{e}_i$ and final light polarization $\vec{e}_f$.[48]

The scattering tensor notation is often used to calculate macroscopic magnetic quantities of the investigated system.[49] For instance the electric susceptibility tensor χ_e can be determined by the sum over all elements j of the material system with the corresponding atomic density ρ_j as per

$$\chi_e = \frac{4\pi}{k_0^2} r_e \sum_j \rho_j \boldsymbol{F}_j. \tag{1.60}$$

In the same manner, the relative dielectric permittivity tensor, approximated for optically transparent materials, is then defined as

$$\epsilon_r = 1+\chi_e \approx n^2 = (1-\delta+i\beta)^2 \approx 1-2\delta+2i\beta. \tag{1.61}$$

However, this equation is only valid for optical isotropic system, e.g., in a cubic structure defined by the dielectric tensor

$$\epsilon = n^2 \cdot \begin{pmatrix} 1 & 0 & 0 \\ 0 & 1 & 0 \\ 0 & 0 & 1 \end{pmatrix}. \tag{1.62}$$

[48] J. Fink, E. Schierle, E. Weschke, and J. Geck. Resonant elastic soft x-ray scattering. *Rep. Prog. Phys.*, **76** (5):056502 (2013); and S. Macke and E. Goering. Magnetic reflectometry of heterostructures. *J. Phys. Condens. Matter*, **26**(36):363201 (2014)

[49] R. G. Newton. Optical theorem and beyond. *Am. J. Phys.*, **44**(7):639–642 (1976)

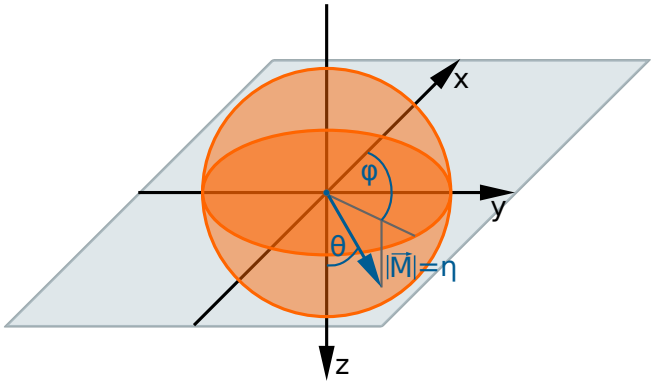

Figure 1.9: Schematic illustration of the magnetization direction in spherical polar coordinates with an absolute value according to the magnetooptical constant defining the dielectric tensor.

In order to account for a magnetization of the system this tensor has to be modified as determined by the scattering tensor presented in Eq. (1.59) is given by

$$\epsilon = n^2 \cdot \begin{pmatrix} 1 & i\eta \cdot \cos\theta_M & -i\eta \cdot \sin\theta_M \sin\varphi_M \\ -i\eta \cdot \cos\theta_M & 1 & i\eta \cdot \sin\theta_M \cos\varphi_M \\ i\eta \cdot \sin\theta_M \sin\varphi_M & -i\eta \cdot \sin\theta_M \cos\varphi_M & 1 \end{pmatrix}, \tag{1.63}$$

with the magnetooptical constant η defined by the magnetization vector

$$\vec{M} = \eta \cdot \begin{pmatrix} \sin\theta_M \cos\varphi_M \\ \sin\theta_M \sin\varphi_M \\ \cos\theta_M \end{pmatrix} \tag{1.64}$$

according to the illustration in Fig. 1.9.

The magnetic terms of the scattering tensor m' and m'' are also linked by the Kramers-Kronig relation the same manner as the nonmagnetic scattering factors presented in Eqs. (1.24) and (1.25).

For the incorporation of magnetism into the analysis of reflectivity measurements, one should take into account that the Parratt formalism in its original form is only applicable for optical isotropic system. As mentioned above, the σ and π polarizations are treated independently of each other and yield self-contained results. In order to introduce circularly polarized light and thus the ability to evaluate magnetic scattering, the intensities of both linear polarizations are averaged. This independence of the popularizations in the Parratt formalism demands the calculation of four separate light channels within the formalism, incident σ (π) light to final σ (π) polarized wave as well as left (right) circularly polarized light to a final polarization of the same helicity. However, these limitations of the formalism do not impede a detailed simulation of the magnetic reflectivity since light channels with different input and output polarizations are usually not accessible via a standard measurement as they would require polarization filters and have small scattering amplitudes. The optimal condition for a high magnetic contrast in an experiment of this kind is therefore the utilization of fully left or right circularly polarized light. In contrast, no magnetic scattering is contained in pure σ and π polarization channels. The left and right circular light channels feature a sign change for the magnetic

scattering which is equivalent to a switch of the magnetization. This can therefore be interpreted as the magnetooptical description of the XMCD effect.

If the small angle approximation is valid, e.g., for the resonant magnetic scattering experiments in the hard x-ray regime, where the typical scattering angle is close to grazing incident, the scattering amplitude given in Eq. (1.56) can be reduced to

$$\begin{aligned} f(q,\omega) = &- \left[f_0(q) + f'(\omega) + if''(\omega)\right] \\ &+ p_c \cdot \vec{b} \cdot \left[m'(\omega) + im''(\omega)\right]. \end{aligned} \tag{1.65}$$

The DCP is directly factored in by the coefficient p_c which is, in contrast, included in the complex polarization vectors in the complete dipole approximation. In the same manner as the optical parameters of the refraction index δ and β are defined in Eq. (1.26) and (1.27) the magnetooptical corrections to the refraction index $\Delta\delta$ and $\Delta\beta$ are expressed as

$$\Delta\delta(E,M) = \frac{r_e\lambda^2}{2\pi} \cdot m'(E,M) \tag{1.66}$$

for the dispersive correction as well as

$$\Delta\beta(E,M) = \frac{r_e\lambda^2}{2\pi} \cdot m''(E,M) \tag{1.67}$$

for the absorptive correction. These parameters specify the changes to the optical parameters uniquely depending on the magnetization of the probed material. The changes in reflectivity induced by these magnetooptical parameters $\Delta\delta$ and $\Delta\beta$ in relation with a switch of photon helicity or orientation of the magnetization are a powerful characteristic to investigate magnetic depth profiles in thin film systems. Since the intensity in x-ray reflectometry measurements decays over several orders of magnitude the change in reflectivity due to a switch of magnetization or photon helicity has to be weighted by the overall intensity. Therefore, instead of the simple difference signal the asymmetry ratio

$$\Delta I = \frac{I_+ - I_-}{I_+ + I_-} \tag{1.68}$$

is used to analyze resonant magnetic reflectivity experiments. This asymmetry ratio is thereby the basis for the analysis of the magnetooptical depth profile and is usually simulated based on a spatial distribution of the magnetooptical parameters to fit the experimental results.

Simulation of XRR and XRMR measurements

The software tool ReMagX has been especially developed by the Max Planck Institute for Intelligent Systems (formerly MPI-MF) to fit magnetic resonant reflectivity curves from thin film samples and in the process factor in magnetic contributions.[50]

[50] S. Macke. ReMagX - x-ray magnetic reflectivity tool. www.remagx.org

This software is designed to simulate standard nonmagnetic x-ray reflectivity based on the Parratt formalism for variable energies. The focus of ReMagX is the simulation of the reflectivity from magnetic multilayer systems probed with circularly polarized x-rays. This additional element selective magnetic contrast for the standard x-ray reflectometry allows for the simulation of chemical and magnetic depth profiles and goes beyond the potential of commercially available x-ray diffraction softwares.[51]

The standard procedure for modeling reflectivity curves of thin films is based on layers of different materials or compounds with a homogeneous density. In this work, the usual approach of thin film modeling utilizes a specific list of the various layered materials or compounds, where thickness, roughness of the interfaces and the optical constants are the defining parameters. Beside the layer specific fitting (LSF) mode, ReMagX supports this advanced element specific fitting (ESF) mode to simulate separate density and magnetic depth profiles. In chapter 4, a step-by-step evaluation method is presented to combine the advantages of the ESF mode with a detailed analysis of both the asymmetry ratio features as well as χ^2 landscapes, which illustrate the goodness of the fits, in order to determine a global best fit of the XRR and XRMR measurements. The goal is to create a robust and consistent representation of the structural and magnetic depth profiles for all bi- and multilayer systems discussed in this work.

Element specific simulations are based on separate depth profiles for each element with specific scattering factors.[52] This method enables the user to model entirely different depth profiles for each element of a thin film or heterostructure. It can also be extended to describe a depth profile based on an exclusive magnetic scattering factor (no nonmagnetic scattering contribution) and, thus, facilitates the simulation of a layer independent magnetization. Therefore, separate layer depth profiles are used for each element in the ESF mode with specific scattering factors f_1 and f_2. Here, the magnetic depth profile is modeled using a separate dummy element having the scattering factors set to zero and the magnetic scattering factor $f_\mathrm{m} = f_{1\mathrm{m}} + if_{2\mathrm{m}}$ providing the magnetooptical properties. For comparison, the asymmetry ratio is also fitted in the classical LSF mode, simulating the magnetooptical $\Delta\delta$ and $\Delta\beta$ depth profiles and specifying the magnetization dependent changes in the optical parameters of the refractive index.

Because of the limitations of the Parratt formalism the simulation of a dichroism by a change of light polarization is impossible. Consequently, in the Parratt formalism the magnetic dichroism is implemented by changing the magnetization of the analyzed thin film. This approach is not sufficient to enable the full accuracy of the simulation at an magnetic absorption edge. Therefore, a full matrix based magnetooptical representation can be used. The magnetic asymmetry is simulated relying on a Zak matrix[53] formalism which simulates the reflectivity based on a layered sample approach. Here,

[51] S. Macke, A. Radi, J. E. Hamann-Borrero, A. Verna, M. Bluschke, S. Brück, E. Goering, R. Sutarto, F. He, G. Cristiani, M. Wu, E. Benckiser, H.-U. Habermeier, G. Logvenov, N. Gauquelin, G. A. Botton, A. P. Kajdos, S. Stemmer, G. A. Sawatzky, M. W. Haverkort, B. Keimer, and V. Hinkov. Element specific monolayer depth profiling. *Adv. Mater.*, **26**(38): 6554–6559 (2014)

[52] J. Hannon, G. Trammell, M. Blume, and D. Gibbs. X-ray resonance exchange scattering. *Phys. Rev. Lett.*, **61** (10):1245 (1988)

[53] J. Zak, E. Moog, C. Liu, and S. Bader. Universal approach to magneto-optics. *J. Magn. Magn. Mater.*, **89**(1-2):107–123 (1990)

the sample is divided into thin layers where each section has optical and magnetooptical properties corresponding to the density and magnetic depth profile perpendicular to the layer stack. The Zak matrix based algorithm works with an arbitrary polarization of incident light and deals with any orientation of magnetization in the material at which the dichroism is implemented by the switch of the light polarization. In this formalism, the interface roughness can in the same way be considered as a Gaussian distribution centered at the interface modifying the optical depth profile accordingly.

The relevant fitting parameters for a standard reflectometry experiment are the thicknesses of the layers in the investigated system and the rms roughness of all corresponding interfaces. Additionally, the optical constants (dispersive δ and absorptive part β) of all layers are parameters of the simulation process. In case of the XRMR analysis the magnetooptical constants $\Delta\delta$ and $\Delta\beta$ are parameters of the fit and usually these have to be bound to a certain spatial distribution which is different from the optical depth profile since a chemically uniform material is not necessarily magnetized uniformly especially when interface or proximity effects are investigated. This independent magnetic depth profile is added to or subtracted from the normal optical depth profile in the simulation process.

The software ReMagX uses the momentum transfer in the direction of the film normal (z direction) to display and simulate reflectivity and asymmetry curves. Hence, the reflectometry curves have to be modified to comply with the requirements of this software tool. Depending on the laboratory refractometer or synchrotron beamline software the z component of the scattering vector or momentum transfer characterize the angle at which the scattered radiation is detected. Therefore, the scattering angle θ has to be converted into the scattering vector q.

The momentum vector of a plane wave is defined by the absolute value of the wave vector k according to

$$k = |\vec{k}| = \frac{\omega}{c} = \frac{2\pi}{\lambda}, \tag{1.69}$$

with the angular frequency ω and wavelength λ. This wave vector is proportional to the momentum vector $\vec{p}$ with the reduced Planck constant $\hbar$ written as

$$\vec{p} = \hbar\vec{k}. \tag{1.70}$$

As shown in Fig. 1.10 in an elastic scattering experiment, the difference of the incoming and outgoing momenta is given by $\vec{q}$. Following the equation

$$\vec{q} = \vec{p}_{\text{out}} - \vec{p}_{\text{in}}, \tag{1.71}$$

the scattering vector is defined by

$$\sin\theta = \frac{\frac{1}{2}|\vec{q}|}{|\vec{p}_{\text{in}}|} \tag{1.72}$$

and therefore the momentum transfer is for an elastic scattering process

$$|\vec{q}| = 2|\vec{p}_{\text{in}}| \cdot \sin\theta = \frac{4\pi}{\lambda} \cdot \sin\theta. \tag{1.73}$$

The magnitude of the transfered momentum or scattering vector $\vec{q}$ is an alternative representation of the scattering angle taking into account the incident wavelength.

In the vectorial notation, an incident electromagnetic wave in vacuum can be written as

$$\vec{E}\,(\vec{r},t) = \vec{E}_0 e^{i\vec{k}_{\text{in}}\cdot\vec{r}-i\omega t} \tag{1.74}$$

with the wave vector

$$\vec{k}_{\text{in}} = k_0 \begin{pmatrix} 0 \\ \cos\theta \\ \sin\theta \end{pmatrix} \tag{1.75}$$

propagation in the scattering plane spanned by the y and z coordinates. Therefore, the scattering vector is in the same way defined as the wave vector difference before and after scattering

$$\vec{q} = \vec{k}_{\text{in}} - \vec{k}_{\text{out}} = k_0 \begin{pmatrix} 0 \\ \cos\theta \\ \sin\theta \end{pmatrix} - k_0 \begin{pmatrix} 0 \\ \cos\theta \\ -\sin\theta \end{pmatrix} = \begin{pmatrix} 0 \\ 0 \\ 2k_0 \sin\theta \end{pmatrix}. \tag{1.76}$$

Furthermore, the data is normalized and usually adjusted by a footprint correction. At grazing incidence due to the limited size of the sample an over-illumination can occur where the investigated structure does not fully intercept the width of the incident beam. Depending on the beam size and the surface dimensions of the sample an incident angle is calculated as of the beam is totally reflected on the sample. The intensity measured at smaller incident angles has to be corrected to fit an accurate simulation. One can assume a rectangular beam with the sizes h and b which is parallel to the surface of the sample. At an incident angle θ the footprint F of the beam on the surface of the sample is given by

$$F = \frac{h \cdot b}{\sin\theta}. \tag{1.77}$$

The length of the footprint in beam direction $f = h/\sin\theta$ corresponds to the illumination length on the sample surface. At an incident angle of

$$\theta_{\text{m}} = \sin^{-1}\frac{h}{l} \tag{1.78}$$

this length matches the sample surface dimension in beam direction l. In general, below this angle the intensity of the reflected beam is reduced by

$$\Delta I = \frac{\sin\theta}{\sin\theta_{\text{m}}} \tag{1.79}$$

relative to a measurement with a probed area smaller than the sample size.

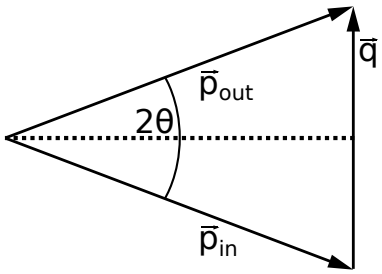

Figure 1.10: Elastic scattering experiment at a scattering angle 2θ with the momentum of the incoming wave $\vec{p}_{\text{in}}$ and $\vec{p}_{\text{out}}$ of the scattered wave. The absolute values of the momenta are equivalent in an elastic process where the scattering vector or momentum transfer is defined by the difference vector $\vec{q}$.

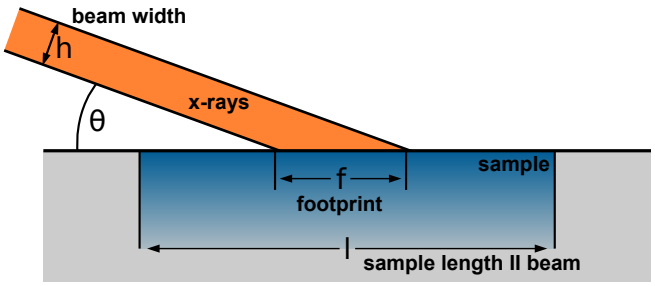

Figure 1.11: Geometrical footprint correction. The intensity of the reflected beam has to be corrected in the footprint region due to over-illumination of the sample depending to angle of incidence.

For example, at the critical angle $\theta_c \approx 0.2°$ of silicon at an energy of 8 keV using a typical x-ray beam with $h = 100\,\mu m$, the length of the footprint on the sample surface along the direction of the beam propagation is $f \approx 30\,mm$.[54] For this reason the sample has to be at least of this size to totally reflect a beam at this incident angle. For smaller samples the reflected intensity must be corrected according to the degree of sample illumination.

In a standard approach of evaluation XRR or magnetic XRMR data, a starting point is usually the analysis of an off-resonant non-magnetic XRR measurement to gather all important informations on the structural sample properties like in particular the layer thicknesses and interface roughnesses. It is usually a good starting point to make an educated guess of the real multilayer system based on the growth process in relation to the objectives of the sample preparation. The starting point for the thickness t of each layer can be calculated via knowledge of deposition rate and time and alternatively it can be easily approximated from the oscillation width Δq of the reflectivity curve according to $t = 2\pi/\Delta q$. The starting value for the roughnesses can either be set to zero for a smoothly grown system or approximated with a good guess, e.g., a few angstrom for polished substrate interfaces up to several nanometer rms roughness for inter diffusive capping layers.

In order to complete the set of starting parameters, the optical parameters δ and β far away from resonant absorption edges are transferable from the available literature. The atomic scattering factors and x-ray properties of all elements into consideration are gathered in nuclear data tables most famously by Henke *et al.*[55] or Chantler *et al.*[56] summing up x-ray energy-dependent photoabsorption, scattering, transmission, and reflection properties. With those collection of structural and optical parameters the simulated reflectivity curve should start to resemble the actual measurement if there is no significant influence from any resonant scattering process.

All experimental parameters such as energy and angular resolution, polarization and beam energy have to be preset in any fitting routine. Based on this rough fit the optimal parameters for the real samples are determined by the fitting algorithms where the fitting intervals have to be constrained to physically reasonable value to narrow down the parameter space the algorithms are working on. Using the software ReMagX, the off-resonant data is either directly

[54] A. Gibaud and G. Vignaud. Specular reflectivity from smooth and rough surfaces. In *X-ray and Neutron Reflectivity*, pages 85–131. Springer, Berlin, Germany, (2009)

[55] B. L. Henke, E. M. Gullikson, and J. C. Davis. X-ray interactions: photoabsorption, scattering, transmission, and reflection at $E = 50$ - $30,000$ eV, $Z = 1$ - 92. *Atomic data and nuclear data tables*, **54** (2):181–342 (1993)

[56] C. T. Chantler. Theoretical form factor, attenuation, and scattering tabulation for $Z = 1$ - 92 from $E = 1$ - 10 eV to $E = 0.4$ - 1.0 MeV. *J. Phys. Chem. Ref. Data*, **24**(1):71–643 (1995)

fitted with the Nelder-Mead algorithm which can get stuck in local error minima. Additionally, a preparatory heuristic optimization algorithm can be used, sampling the whole parameter space and therefore setting up the Nelder-Mead algorithm to work downhill in the χ^2 landscape as final fitting step.

When the structural parameters are determined by the off-resonant fitting process the same density depth profile with equivalent layer thicknesses and interface roughnesses has to be valid for the simulation of the XRR data taken at or close to an absorption edge. This minimizes the parameter space for the determination of the optical parameters δ and β by fitting the resonant reflectivity curve. Alternatively, if XAS data is available, e.g., by performing XMCD measurements at the edges in question, the spectrum can be adjusted to the tabulated off-resonant tables of the XAS related refractive index and subsequently a Kramers-Kronig transformation can be performed to calculate the real part of the signal. The parameters δ and β identified this way are then excellent starting parameters for a fit of the resonant XRR data. If necessary, the modeled chemical composition and the resulting optical depth profile of the analyzed structure has to be corrected to include, e.g., contaminations like carbon hydrates, water adsorption or surface oxidation and reach a satisfactory fit with reliable optical constants.

As soon as this model is converged and a satisfying goodness of the fit as been reached, the constructed structural model is used as a basis for the XRMR analysis where a magnetic model of the thin film system is determined. In general, an explicit view on the complete parameter space, stretched out by all structural and optical parameters of the reflectivity simulation, is even more important for an accurate simulation in case of an inclusion of magnetic reflectivity Here, when the energy of the x-ray light source is tuned to the resonance energies of the probed elements, samples can be probed element-specifically.

A standard recipe procedure for the data analysis of XRR consecutive XRMR measurements is outlined in Fig. 1.12.[57] Depending on the anticipated magnetic properties the magnetic model is designed independently of the chemical depth profile which acts comparable to a supporting structure providing relative boundary values, e.g., for interface positions inside the structure. As a consequence, one usually assumes a homogeneous magnetization of a ferromagnetic layer in the boundaries defined by the chemical depth profile. The roughness of this layer is not necessarily identical to the structural roughness of the corresponding interface yet this value often represents a decent starting point for any simulation.

In magnetic heterostructures the magnetooptical depth profile at interfaces is increasingly complex, mainly depending on a plurality of magnetic interface related effects, e.g., magnetic dead layers, exchange- or magnetic proximity effects, enhanced interface saturation magnetization and others. The most flexible way to model these effective magnetization depth profiles is by an intelligent

[57] C. Klewe, T. Kuschel, J.-M. Schmalhorst, F. Bertram, O. Kuschel, J. Wollschläger, J. Strempfer, M. Meinert, and G. Reiss. Static magnetic proximity effect in Pt/$Ni_{1-x}Fe_x$ bilayers investigated by x-ray resonant magnetic reflectivity. *Phys. Rev. B*, **93** (21):214440 (2016)

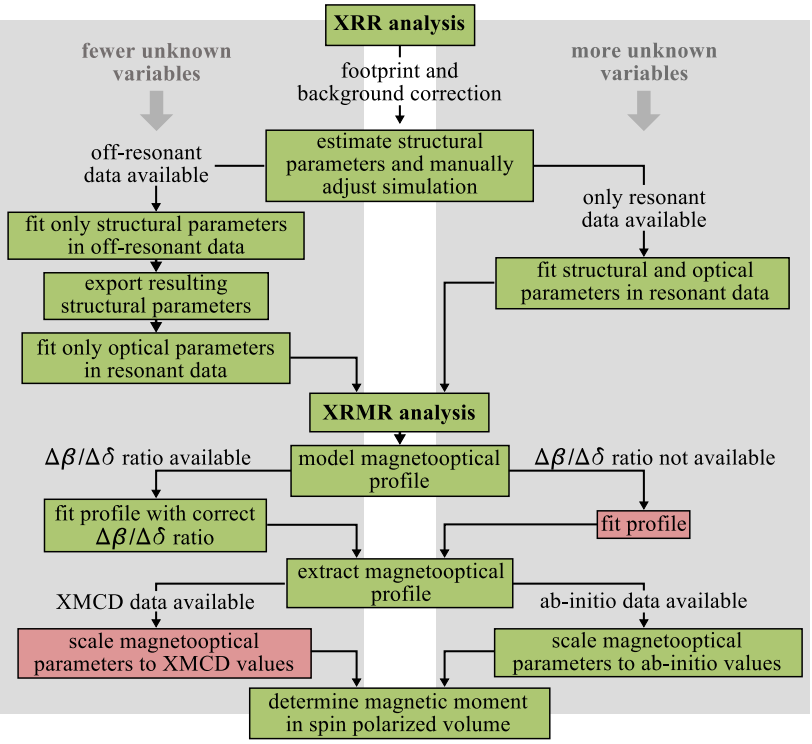

Figure 1.12: Recipe procedure for the evaluation of XRR and XRMR data to determine magnetic moments in the sample volume. The green blocks correspond to the general standard procedure, while the red boxes indicate alternative approaches. This procedure was first described in [Klewe et al., 2016].

multi-slicing of the chemical model and fitting of the magnetooptical parameters of each sublayer within reasonable intervals.

However, this usually generates a vast parameter space which need to be carefully constrained so the algorithm converges to realistic solutions. Here, a separate parameterized magnetic model similar to the structural model merely based on the thickness and roughness of the magnetic depth profile is usually more adequate. Alternatively, the software ReMagX features a Gaussian magnetooptical depth profile to define artificial variations of the sample magnetization like for example reduced magnetization at an interface or proximity induced magnetism in nonmagnetic layers. Either absolute or relative values of the parameters $\Delta\delta$ and $\Delta\beta$ are modeled with Gaussian function and usually bound to an optical depth profile of a certain layer so that the corresponding magnetic moment scales with the atomic density of the layer. Relative to the z-position, in direction of the normal of the layer surface, the density d of the optical layer is defined by

$$d(z) = \frac{1}{4}\left(1 - \mathrm{erf}\left(\frac{z_\mathrm{t} - z}{\sigma_\mathrm{t}}\right)\right)\left(1 + \mathrm{erf}\left(\frac{z_\mathrm{b} - z}{\sigma_\mathrm{b}}\right)\right), \tag{1.80}$$

where z_t is the top position of the magnetic layer and z_b the bottom position, respectively. The rms roughness values of the top and bottom boundary is given by σ_t and σ_b. In the case of a bound profile, the artificial magnetization depth profile, e.g. the Gaussian function, scales with this optical function to calculate the magnetooptical depth profile. If the profile is unbound, the artificial profile directly defines the profile of the magnetic parameters $\Delta\delta$ and $\Delta\beta$ impended

of the chemical structure.

The thickness and roughness parameters of an artificial magnetic depth profile or the variance and center position of a Gaussian function are optional parameters in REMAGX and are used to simulate the magnetooptical depth profile just as the corresponding $\Delta\delta$ and $\Delta\beta$ values, while the structural parameters remain unchanged. Here, the best fit is defined by the χ^2 value in relation to the experimental asymmetry ratio and the resulting ratio of $\Delta\delta/\Delta\beta$ can be compared with *ab initio* calculations. This allows for an approximation of the magnetic moments per atom in the spin polarized material. If no *ab initio* data is available, the Kramers-Kronig transformed XAS signal can be used to correlate the magnetooptical parameters and redetermine magnetic moments of the material investigated by resonant scattering. This determination of the magnetic moment is summarized in the bottom half of the flow chart of Fig. 1.12 following the XRR and XRMR analysis.

When it comes to analyzing reflectivity data obtained for complex multilayer systems with structures possessing imperfect interfaces or on systems with significant contamination or oxidation, even this advanced fitting technique is still no guarantee for a successful simulation of the asymmetry ratio. Chapter 4 of this work specifies and utilizes an extended analysis approach, including χ^2 mapping, to avoid discrepancies within the results and to reduce the need for further measurements, which is a common problem in diverse studies based on XRMR experiments. This strategy is beneficial for the simulation of reflectivity curves depending on many free parameters which may impede the simplex approach by developing numerous local minima. Furthermore it is shown that the in-depth analysis of XRMR data requires a more elaborated simulation especially for the investigation of complex heterostructures with non-trivial magnetic depth profiles.

The necessary steps to resolve this issues are outlined in sections 4, in order to present a general solution of unifying the various prior approaches to analyze magnetic reflectivity results of magnetic thin film systems. It is explicitly shown where the standard analysis procedures are limited throughout literature and an analysis approach beyond the standard methods is discussed on the basis of Pt L_3 XRMR measurements of increasingly complex thin film systems.

Experimental details of the XRR and XRMR analysis

WITHIN THE FRAMEWORK of the XRR and XRMR analysis, the required structural information is obtained from the XRR intensity I and the magnetic information from the XRMR asymmetry ratio ΔI. During the reflectivity measurement the angle of incidence θ is changed and the intensity of the reflected light $I_\pm$ is detected to calculate the magnetic asymmetry $\Delta I = (I_+ - I_-)/(I_+ + I_-)$ at each

angle of incidence as introduced in Eq. (1.68).

The magnetic contrast necessary for the XRMR experiment is achieved in two ways either by flipping a saturating external magnetic field and, thus, the magnetization of the thin film system or by switching the helicity of the circularly polarized light. As discussed in-depth in chapter 5.1, both methods independently result in slightly different x-ray reflectivity curves when varying the magnetization direction relative to the x-ray polarization due to a change in the optical constants of the spin polarized material based on the refractive index $n = 1 - \delta + i\beta$. Thus, the dispersion and absorption coefficients δ and β are modified by the fraction $\Delta\delta$ and $\Delta\beta$ defined by the magnetooptical index $\Delta n = \Delta\delta - i\Delta\beta$ of the circular dichroism for different magnetization directions. In a geometry, in which the x-ray light is propagating parallel to the magnetization, the complex refractive index is generally expressed by

$$n_{\pm} = 1 - (\delta \mp \Delta\delta) + i\,(\beta \mp \Delta\beta)\,. \tag{1.81}$$

In case of magnetization as well as helicity switching, the asymmetry ratio is detected for both x-ray polarizations or magnetization orientations, respectively. For instance, in case of helicity switching the intensity is collected for right I_+ and left I_- circular polarization for each angle of incidence θ and for the sample magnetization parallel to the scattering vector. The magnetic asymmetry ratio ΔI can thus be calculated at each angle. The same measurement can also be repeated with the sample magnetization being reversed. The new asymmetry ratio should thus be equal but opposite in sign. The final asymmetry ratio can thus be extracted by calculating the half difference between the two measurements $A_c = 1/2 \cdot (A_+ - A_-)$. This method allows to subtract non-magnetooptical effects such as source movements.

The obtained reflectivity measurements are not analytically translatable into the fundamental magnetooptical depth profile. Therefore, an iterative simulation has to be conducted to calculate an expected reflectivity curve based on a magnetooptical modulation of the analyzed thin film system. The result is then successively optimized to achieve a good agreement between measured and simulated reflectivity and in the same way between experimentally obtained and simulated magnetic asymmetry.

The nonmagnetic reflectivity is simulated as a function of the scattering vector $q = 4\pi/\lambda \sin(\theta)$ using the recursive Parratt algorithm[58] and a Névot-Croce[59] roughness model. This approach is fine to determine the structural and optical depth profiles, but not sufficient to obtain a fully accurate model of the asymmetry ratio. Therefore, a full matrix-based magnetooptical representation is employed here. The asymmetry ratio is simulated relying on a Zak matrix[60] formalism which simulates the roughness by adaptively slicing the interface into a series of segments. As a result, the sample is divided into thin layers where each section has optical

[58] L. G. Parratt. Surface Studies of Solids by Total Reflection of X-Rays. *Phys. Rev.*, **95**(2):359 (1954)

[59] L. Névot and P. Croce. Caractérisation des surfaces par réflexion rasante de rayons X. Application à l'étude du polissage de quelques verres silicates. *Rev. Phys. Appl.*, **15**(3):761–779 (1980)

[60] J. Zak, E. Moog, C. Liu, and S. Bader. Universal approach to magneto-optics. *J. Magn. Magn. Mater.*, **89**(1-2):107–123 (1990)

and magnetooptical properties corresponding to the density and magnetic depth profile spread vertically through the layer stack. A detailed step-by-step guide to the basics of analyzing reflectivity measurements is presented in the review by Macke and Goering on magnetic reflectivity of heterostructures.[61]

[61] S. Macke and E. Goering. Magnetic reflectometry of heterostructures. *J. Phys. Condens. Matter*, **26**(36):363201 (2014)

The quality of the asymmetry ratio simulation is always determined by the sum of the squared error

$$\chi^2 = \sum_i (A_{i,\text{meas.}} - A_{i,\text{sim.}})^2 \tag{1.82}$$

of every asymmetry ratio data point A_i. The goodness of fit of the specular reflectivity is defined as

$$\chi^2 = \sum_i (\log I_{i,\text{meas.}} - \log I_{i,\text{sim.}})^2 , \tag{1.83}$$

since the detected intensity I_i decays by orders of magnitude as a function of the scattering vector q.

In the standard XRR and XRMR fitting procedure, the χ^2 value is minimized utilizing a downhill simplex algorithm, also known as Nelder-Mead method or amoeba method, to achieve an optimal agreement between experimental data and simulated fit.[62] This algorithm represents a numerical approach to converge to the minimum of an objective function with a finite number of parameters in a multidimensional space given by the experimental variables. This search method for nonlinear optimization problems, where derivatives are unknown, has one particular problem, namely that this is a heuristic algorithm which is not guaranteed to be optimal since it can converge to non-stationary points.[63]

[62] J. A. Nelder and R. Mead. A simplex method for function minimization. *Comput. J.*, **7**(4):308–313 (1965)

[63] K. I. McKinnon. Convergence of the Nelder–Mead Simplex Method to a Nonstationary Point. *SIAM J. Optim.*, **9**(1):148–158 (1998)

[64] J. C. Lagarias, J. A. Reeds, M. H. Wright, and P. E. Wright. Convergence properties of the Nelder–Mead simplex method in low dimensions. *SIAM J. Optim.*, **9**(1):112–147 (1998)

Therefore, this method of least squares based on simple optimization is not sufficient to define a good fit. Due to the often complex sample structure and variety of free parameters, χ^2 usually has a multi-dimensional landscape with numerous local minima impeding simple downhill algorithms.[64] For more complex thin films with plenty of structural parameters to take into account, a second more sophisticated optimization algorithm is required. Hence, the asymmetry ratio simulation and its corresponding χ^2 landscape have to be analyzed in great detail to obtain reliable solutions for non-trivial magnetic depth profiles.[65]

[65] J. Tiilikainen, J.-M. Tilli, V. Bosund, M. Mattila, T. Hakkarainen, J. Sormunen, and H. Lipsanen. Accuracy in x-ray reflectivity analysis. *J. Phys. D: Appl. Phys.*, **40**(23):7497 (2007)

It is especially important to set reasonable constraints to the fitting parameters and to use the most probable starting configuration determined from the sample growth. Furthermore, it is most appropriate to employ a procedure sampling the complete configured parameter landscape like a metaheuristic algorithm or comparable higher-level optimization procedure. Therefore, aside from the standard simplex optimization algorithm, an evolution approach based on a generic algorithm fitting routine[66] was implemented in REMAGX.

[66] J. Tiilikainen, V. Bosund, J.-M. Tilli, J. Sormunen, M. Mattila, T. Hakkarainen, and H. Lipsanen. Genetic algorithm using independent component analysis in x-ray reflectivity curve fitting of periodic layer structures. *J. Phys. D: Appl. Phys.*, **40**(19):6000 (2007); J. Tiilikainen, J. Tilli, V. Bosund, M. Mattila, T. Hakkarainen, V.-M. Airaksinen, and H. Lipsanen. Nonlinear fitness–space–structure adaptation and principal component analysis in genetic algorithms: an application to x-ray reflectivity analysis. *J. Phys. D: Appl. Phys.*, **40**(1):215 (2006); and A. Ulyanenkov and S. Sobolewski. Extended genetic algorithm: application to x-ray analysis. *J. Phys. D: Appl. Phys.*, **38**(10A):A235 (2005)

Experimental details of the XMCD analysis

In order to obtain information on the magnetic properties of a sample and support the XRMR experiments, it is instrumental to analyze the corresponding magnetic circular dichroism spectra. The interaction of the magnetic material with the circularly polarized light can be evaluated based on the complex index of refraction as given by Eq. (1.81) to determine the magnetooptical parameters based on the XAS. Here, the photon spin is aligned parallel or antiparallel to the magnetic moments of the sample, defining the substantial magnetization dependent changes in the absorption spectra. Accordingly, the circular dichroism is defined as

$$\Delta n = 1/2 \cdot (n_+ - n_-) = \Delta\delta - i\Delta\beta. \tag{1.84}$$

This dichroism specifies the phase change $\Delta\delta$ in the relation of right- and left-handed polarized waves and thus is expressed as a rotation of the polarization plane. As discussed in chapter 1.1.2, the second magnetooptical parameter $\Delta\beta$ defines the polarization dependent absorption. When the x-ray light is transmitting through a magnetooptically active material of a thickness d, this magnetic dichroism generates an elliptical polarized beam. This process is specified by the complex Faraday equation which is given by

$$\phi + i \tan\epsilon \approx i\frac{d \cdot \pi}{\lambda} \cdot \frac{\epsilon_{xy}}{\sqrt{\epsilon_{xx}}} \tag{1.85}$$

with λ being the optical wavelength. ϵ_{xy} expresses the off-diagonal absolute permittivity which is the magnetooptically active component due to it being antisymmetric in magnetization.

For linearly polarized transmitted light the ellipticity ϵ as well as the rotation angle ϕ are directly connected to the magnetooptical parameters given by the first order approximation

$$\phi = \frac{2\pi}{\lambda} \cdot d \cdot \frac{\Delta\delta}{\tan\theta} \tag{1.86}$$

with the angle of the incident beam θ relative to the sample surface.[67]

[67] P. Oppeneer. *Handbook of Magnetic Materials*, volume 13. Elsevier, Amsterdam (2001)

The magnetooptical parameter $\Delta\beta$ is determined utilizing circularly polarized light in the XMCD experiments based on the asymmetry of the absorption spectra A defined by

$$A = \frac{T_+ - T_-}{T_+ + T_-}. \tag{1.87}$$

Here, the transmissions coefficients T of the circularly polarized beams with the magnetic field oriented parallel or antiparallel to the incident direction are written as

$$T_\pm = \exp\left(\frac{-4\pi \cdot d \cdot (\beta_0 \pm \Delta\beta)}{\lambda}\right). \tag{1.88}$$

In addition, the relation $A \approx \tan 2\epsilon$ is valid[68] under the condition

[68] H.-C. Mertins, F. Schäfers, X. Le Cann, A. Gaupp, and W. Gudat. Faraday rotation at the $2p$ edges of Fe, Co, and Ni. *Phys. Rev. B*, **61**(2) (2000)

of small permittivity values ϵ leading to the equation

$$A \approx \tan 2\epsilon = 2\frac{2\pi}{\lambda} \cdot d \cdot \frac{\Delta\beta}{\tan\theta}. \tag{1.89}$$

This equation includes the angle of incidence θ based on the effective thickness of the probed material $d/\sin\theta$ in combination with the effective magnetic field $B\cos\theta$ which defines the angular dependence of the interaction of the left or right polarized x-ray light with the magnetic field or magnetization, respectively. Analog to the XRMR asymmetry ratio, the asymmetry of the XMCD spectrum is determined based on the normalized difference of the x-ray intensity for both photon helicities I_+ and I_-. The normalized XMCD asymmetry

$$A = \frac{I_+ - I_-}{I_+ + I_-}, \tag{1.90}$$

is measured in transmission or via TEY measurements derived from the intensity difference of the circularly polarized light. This XAS based value is directly related to the imaginary component of the Faraday equation as presented in Eq. (1.89) which connects the asymmetry to the magnetic absorption parameter.

Magnetic proximity effects

When neighboring magnetic and nonmagnetic film layers are in direct physical proximity to each other the interfacial magnetic properties in the latter can be influenced due to a magnetic exchange coupling effect. It was first shown theoretically by Zuckermann[69] that a weak itinerant ferromagnet has the ability to induce a magnetization into an adjacent paramagnetic material due to the magnetic proximity effect. This phenomenon was then studied experimentally confirming the predicted magnetic characteristics, for instance by investigating the origin of the magnetization of nonmagnetic Pd in contact with Fe in Fe/Pd multilayer systems.[70] Similarly, the spin polarization of Pd atoms in Ni/Pd magnetic multilayers has been reported by Yang *et al.*[71] as well as the magnetic proximity effect in nonmagnetic V in multilayer systems with ferromagnetic Fe.[72]

Besides this classical combination of a nonmagnetic or paramagnetic material with a ferromagnetic system, these layers were also combined with antiferromagnetic materials, especially in multilayer systems, exhibiting a significant difference in the magnetic ordering temperatures of the neighboring materials. This difference controls the coupling effect in a way that the material with the higher ordering temperature is enhancing the magnetic ordering temperature second component.[73] This enhancement of the ordering parameter has led to the name of this phenomenon since a proximity of the atomic states of the two adjacent magnetic compounds is the main cause of the magnetic ordering.[74] Today, the term magnetic proxim-

[69] M. Zuckermann. The proximity effect for weak itinerant ferromagnets. *Solid State Commun.*, **12**(7):745–747 (1973)

[70] O. Rader, E. Vescovo, J. Redinger, S. Blügel, C. Carbone, W. Eberhardt, and W. Gudat. Fe-induced magnetization of Pd: The role of modified Pd surface states. *Phys. Rev. Lett.*, **72**(14): 2247 (1994)

[71] T. Yang, B. Liu, F. Pan, J. Luo, and K. Tao. Polarization of Pd atoms in Ni/Pd magnetic multilayers. *J. Phys. Condens. Matter*, **7**(6):1121 (1995)

[72] M. Schwickert, R. Coehoorn, M. Tomaz, E. Mayo, D. Lederman, W. O'Brien, T. Lin, and G. Harp. Magnetic moments, coupling, and interface interdiffusion in Fe/V (001) superlattices. *Phys. Rev. B*, **57**(21):13681 (1998)

[73] K. Lenz, S. Zander, and W. Kuch. Magnetic proximity effects in antiferromagnet/ferromagnet bilayers: The impact on the Néel temperature. *Phys. Rev. Lett.*, **98**(23):237201 (2007)

[74] P. Jensen, H. Dreyssé, and M. Kiwi. Magnetic reordering in the vicinity of a ferromagnetic/antiferromagnetic interface. *Eur. Phys. J. B*, **46**(4):541–551 (2005)

ity effect (MPE) is usually associated with a change of the magnetic interface properties of a material when it is coupling, and usually inducing a magnetic moment, in direct proximity to a material featuring a different long-range magnetic ordering.

In recent years, these MPEs have demonstrated their great potential for technological applications, in particular since a variety of novel properties are expected in the corresponding heterostructure systems which are not present in the constituent compounds and potentially useful for dissipation-less spintronics. However, this requires a detailed analysis of the interface properties in magnetic heterostructure which are under consideration for interface-related spin devices. In particular, a spin-polarized interface layer created by an MPE can support or hamper spin transport effects such as the SSE and has to be taken into account if pure spin currents have to be identified.

Additionally, the so called non-equilibrium MPE was introduced lately as an explanation for the induction of the spin Hall magnetoresistance (SMR), initially by Nakayama *et al.* in a metallic Pt film which is attached to an electrically insulating magnet.[75] Here, the resistance of the metal film depends on the magnetic properties of the adjacent, electrically insulating ferromagnet. However, the SMR in the Pt layer is not caused by a statically induced magnetization but by non-equilibrium spin currents and appears only in the vicinity of the attached YIG on the scale of the spin diffusion length. Hence, both effects induce the generation of a spin polarization at the interfaces of a paramagnetic thin film metal in vicinity to a ferromagnet, yet both effects are caused by very different causations, which will be further discussed in the following sections.

[75] H. Nakayama, M. Althammer, Y.-T. Chen, K.-i. Uchida, Y. Kajiwara, D. Kikuchi, T. Ohtani, S. Geprägs, M. Opel, S. Takahashi, R. Gross, G. E. W. Bauer, S. T. B. Goennenwein, and E. Saitoh. Spin Hall magnetoresistance induced by a nonequilibrium proximity effect. *Phys. Rev. Lett.*, **110** (20):206601 (2013)

The static magnetic proximity effect

The theory of the static magnetic proximity effect generated at the interface of a ferromagnetic and an antiferromagnetic material has been introduced by Kiwi *et al.*[76] working on superconducting properties of nonmagnetic alloys of simple metals with transition-metal impurities. This was based on an experimental study by Hauser who studied the penetration depth of the spin polarization of a magnetic metal into a nonmagnetic metal or alloy with a high exchange-enhanced spin susceptibility utilizing the superconducting proximity effect.[77] The superconducting transition temperature was used as an indicator for the magnetization of a Pd layer. More precisely, a reduction of the transition temperature is observed when Pd thickness is decreased which proves that the Pd film in close proximity with a ferromagnetic Fe or antiferromagnetic Cr layer is magnetized and exhibits a spin polarization at the interface.

The static magnetic interface coupling causing the MPE at the interface of thin film system is in general created by two different processes. The first is the interfacial coupling via band hybridization and the second mechanism is the Rudermann-Kittel-Kasuya-Yosida

[76] M. Kiwi and M. Zuckermann. The Proximity Effect for Weak Itinerant Ferro-and Antiferro-Magnets. In *Proc. of the 19-th Conf. on Magnetism and Magnetic Materials*, volume 18, page 347, (1973); and M. Kiwi. Origin of the magnetic proximity effect. *Mater. Res. Soc. Symp. Proc.*, **746** (2002)

[77] J. Hauser. Magnetic proximity effect. *Phys. Rev.*, **187**(2):580 (1969)

(RKKY)[78] exchange interaction which can significantly influence the interface magnetism. Both coupling mechanisms decisively depend on the materials electronic properties and especially on the electronic states at the Fermi energy.

First of all, the principal dependence of the magnetic moments is closely linked to the degree of band hybridization at the interface. Moreover, the magnetic ordering is attributed to the density of states at the Fermi level and the given inter-atomic correlated band occupation.[79] In this context, one can follow Stoner's description of band ferromagnetism where the so-called Stoner criterion[80] is defined as the product of the exchange interaction integral and the density of states at the Fermi level. This product must be larger than unity in order to describe a ferromagnet. Here, for example the ferromagnet Fe is far above one, while the paramagnetic Pt, integral material of this work, is slightly below. The proximity to a ferromagnet increases the exchange interaction of the adjacent paramagnetic material and consequently increases the Stoner parameter converting the paramagnet into a ferromagnet for a few atomic layers. Although the Stoner description is quite known, it is just a rough model identifying ferromagnetic materials and is not able to correctly describe the strength of the MPE, the number of spin-polarized atomic interface layers or the spin or orbital nature of the MPE.

In a quantum-mechanical explanation, the ferromagnetism of the 3*d* transition metals has its origin in the exchange interaction which reduces the electrostatic energy of the electrons and leads to a parallel ordering of the magnetic moments. This effect is based on the Pauli exclusion principle since the fermionic electrons with the same spin cannot also be in the same spatial state according to the spin-statistic theorem. As a result, parallel aligned electrons can get promoted to a higher kinetic energy state. However, the orbital wave-function overlap of unpaired valence electrons is reduced for a parallel spin alignment and the charge distributions are more separated reducing the Coulomb repulsion. In case this reduction of the Coulomb energy is larger than the increased kinetic energy due to the higher occupied state, the parallel spin alignment is energetically favorable leading to a spontaneous ferromagnetism. This difference in energy is referred to as exchange energy.

In the Stoner model ferromagnetism is induced by the rigid displacement of energy bands corresponding to the spin-up and spin-down bands. This is illustrated in the band model in Fig. 1.13 where electrons from the spin-down band are transferred to the spin-up band if their respective energy is within a range $E_F - \Delta E$ from the Fermi level. In approximation of a constant DOS close to E_F the number of electrons in this interval is close to $N(E_F)\Delta E/2$. More precisely, the dispersion relations $E(k)$ for spin-up and spin-

[78] M. A. Ruderman and C. Kittel. Indirect exchange coupling of nuclear magnetic moments by conduction electrons. *Phys. Rev.*, **96**(1):99 (1954); T. Kasuya. A theory of metallic ferro- and antiferromagnetism on Zener's model. *Prog. Theor. Phys.*, **16**(1):45–57 (1956); and K. Yosida. Magnetic properties of Cu-Mn alloys. *Phys. Rev.*, **106**(5):893 (1957)

[79] B. Cox, R. Tahir-Kheli, and R. Elliott. Thin films of itinerant-electron ferromagnets on a nonmagnetic metallic substrate. *Phys. Rev. B*, **20**(7):2864 (1979)

[80] E. C. Stoner. Collective electron ferronmagnetism. *Proc. Royal Soc. A*, **165**(922):372–414 (1938)

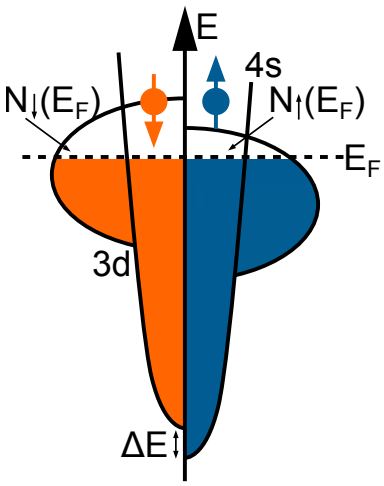

Figure 1.13: Schematic illustration of the spin-split DOS of a 3*d* transition metal. The exchange interaction splits the energy of both spin-states by ΔE. The states at the Fermi energy E_F are spin-polarized and the high DOS at the Fermi level $N(E_F)$ leads to a fulfilled Stoner criterion and thereby a spontaneous ferromagnetic order.

down electrons can be written as

$$E_{\uparrow}(k) = \varepsilon(k) - I_{\mathrm{F}} \frac{N_{\uparrow} - N_{\downarrow}}{N} \qquad \text{and} \tag{1.91}$$

$$E_{\downarrow}(k) = \varepsilon(k) + I_{\mathrm{F}} \frac{N_{\uparrow} - N_{\downarrow}}{N}, \tag{1.92}$$

where I_{F} is the Stoner parameter and $N_{\uparrow\downarrow}$ represents the density of states of spin-up and spin-down electrons, respectively. The dispersion relation of electrons with a disregarded electron-electron interaction is given by $\varepsilon(k)$. The polarization of the system is defined as $p = (N_{\uparrow} - N_{\downarrow})/N$ and can be determined through band structure calculations in relation to the total energy of the system. In case the minimal total energy is found for $p = 0$ the system manifests in a paramagnetic ground state. As a result of the exchange splitting, the change of the kinetic energy of the system is

$$\Delta E_{\mathrm{kin}} = \frac{1}{2} N(E_{\mathrm{F}}) \cdot (\Delta E)^2 \tag{1.93}$$

in the constant DOS approximation. The reduction of Coulomb energy associated with this increase of kinetic energy can be expressed with the Stoner parameter accounting for the effective exchange interaction and written as

$$\Delta E_{\mathrm{pot}} = -\frac{1}{2} I_{\mathrm{F}} \cdot \left(N(E_{\mathrm{F}})(\Delta E)\right)^2 . \tag{1.94}$$

Therefore, the change energy due to the exchange splitting is given by

$$\Delta E = \Delta E_{\mathrm{kin}} + \Delta E_{\mathrm{pot}} = \frac{1}{2} N(E_{\mathrm{F}})(\Delta E)^2 \cdot \left(1 - I_{\mathrm{F}} N(E_{\mathrm{F}})\right) . \tag{1.95}$$

This shows that polarized ground states emerge for $I_{\mathrm{F}} \cdot N(E_{\mathrm{F}}) \geq 1$, where $N(E_{\mathrm{F}})$ is the density of states at the Fermi level. This term expression of the Stoner criterion provides a practical rule to determine the spontaneous magnetization of a magnetic system. However, a polarized state can potentially be energetically favorable over the paramagnetic state before this criterion is in effect. For the $3d$ transition metals Fe, Ni, and Co the Stoner criterion product is larger than unity which turns them into a ferromagnetic material below the Curie-temperature. Here, the Fermi level is crossing the $3d$ bands, as illustrated in Fig. 1.13, which yield a high DOS and thus fulfill the Stoner criterion.[81] The occurrence of spontaneous ferromagnetism is highly depending on the DOS at the Fermi energy since the exchange interaction is comparable for all $3d$ transition metals. In contrast to the $3d$ ferromagnets with high $N(E_{\mathrm{F}})$ contribution, materials with completely filled $3d$ bands below E_{F}, e.g., Cu, do not fulfill the Stoner criterion.

[81] J. Stöhr and H. C. Siegmann. Magnetism. *Solid-State Sciences. Springer, Berlin, Heidelberg*, **5** (2006)

However, the band hybridization at the interface and occupancy of these states at the Fermi level is only determining the magnetic coupling of the first few monolayers in the paramagnetic material. In strongly exchange enhanced Pauli paramagnets, such as Pd and Pt, induced spin polarizations generated by the static MPE are

quite common since they are in close vicinity to the Stoner criterion. Here, the exchange enhancement corresponding to the MPE modifies the wave-vector dependent susceptibility, which is of the RKKY type for free electrons.[82] If the distance from the ferromagnetic interface is exceeding this distance the exchange coupling mediated via the RKKY interaction is additionally defining the state of magnetism in the extended interface region. This interaction describes the indirect exchange of localized magnetic moments, e.g., *d* band electron spins of a metal, and the respective coupling of the magnetic moments via the polarized spin states of conduction electrons. Thus, the Stoner description leads to a pronounced exponentially decaying contribution to the exchange coupling that is quite pronounced in relation to the RKKY oscillations, which continue to determine the interaction at long distances.

Regarding the paramagnetic metals utilized in this work, Pt does not fulfill the Stoner criterion with $I_{\mathrm{F}} \cdot N(E_{\mathrm{F}}) = 0.59$ in the fcc as well as $I_{\mathrm{F}} \cdot N(E_{\mathrm{F}}) = 0.65$ in the hcp phase. The used Pd has a value much closer to the criterion with $I_{\mathrm{F}} \cdot N(E_{\mathrm{F}}) = 0.849$ in the fcc phase. Both materials are close enough to be easily spin polarized due to the static MPE.[83] This has been experimentally proven for Pt and Pd,[84] while other MPE candidates show indications of a static MPE due to theoretical predictions or spin transport experiments. Those promising materials, which are not yet systematically investigated, include Rh, La, Ce, Gd, Ta, W, Ir, and Au.[85]

The generation of MPE based spin-polarized interface layers can significantly influence spin transport effects like SMR or SSE. Here, the additional ferromagnetism in nominal paramagnetic metal layers such as Pt have to be taken into consideration when the spin transport is discussed in the corresponding heterostructures, possibly challenging the classical explanatory approaches. For example, a magnetoresistance effect in a nominally nonmagnetic metal thin film in contact with a ferromagnetic insulator or metal shows resistivities which is distinctly different from all other known magnetoresistance effects and can only be explained based on the induced magnetic moments at the interface.[86]

The density of states of a ferromagnetic insulator is usually gaped at the Fermi level and following the Stoner criterion no static MPE should be present in metal in contact with this system. However, an intermixing of the nonmagnetic metal and the ferromagnetic insulator at the interface, corresponding to a significant roughness, impurities and lattice imperfections can induce interface states around the Fermi level and facilitate a static MPE. Similarly, SMR experiments show that a spin polarization in a normal metal due to a static MPE is likely to induce a parasitic effect like an enhanced anisotropic magnetoresistance.[87] The SMR in general is the first realization of the second class of MPEs, the non-equilibrium magnetic proximity effects, which is discussed below.

[82] P. Fulde. *Electron correlations in molecules and solids*, volume 100. Springer Science & Business Media (2012)

[83] M. Sigalas and D. Papaconstantopoulos. Calculations of the total energy, electron-phonon interaction, and Stoner parameter for metals. *Phys. Rev. B*, **50**(11):7255 (1994)

[84] V. Moruzzi and P. Marcus. Magnetism in fcc rhodium and palladium. *Phys. Rev. B*, **39**(1):471 (1989)

[85] V. Moruzzi and P. Marcus. Magnetism in fcc rhodium and palladium. *Phys. Rev. B*, **39**(1):471 (1989); L. Sève, N. Jaouen, J. Tonnerre, D. Raoux, F. Bartolomé, M. Arend, W. Felsch, A. Rogalev, J. Goulon, C. Gautier, and J. F. Bérar. Profile of the induced 5*d* magnetic moments in Ce/Fe and La/Fe multilayers probed by x-ray magnetic-resonant scattering. *Phys. Rev. B*, **60**(13):9662 (1999); R. Bansal, N. Chowdhury, and P. Muduli. Proximity effect induced enhanced spin pumping in Py/Gd at room temperature. *Appl. Phys. Lett.*, **112**(26):262403 (2018); F. Wilhelm, P. Poulopoulos, H. Wende, A. Scherz, K. Baberschke, M. Angelakeris, N. Flevaris, and A. Rogalev. Systematics of the Induced Magnetic Moments in 5*d* Layers and the Violation of the Third Hund's Rule. *Phys. Rev. Lett.*, **87**(20):207202 (2001); and J. Moodera and R. Meservey. Magnetic proximity effect in thin films of Ni on nonmagnetic metals. *Phys. Rev. B*, **29**(6):2943 (1984)

[86] Y. Lu, J. Cai, S. Huang, D. Qu, B. Miao, and C. Chien. Hybrid magnetoresistance in the proximity of a ferromagnet. *Phys. Rev. B*, **87**(22): 220409 (2013)

[87] J. Li, M. Jia, Z. Ding, J. Liang, Y. Luo, and Y. Wu. Pt-enhanced anisotropic magnetoresistance in Pt/Fe bilayers. *Phys. Rev. B*, **90**(21):214415 (2014)

Non-equilibrium magnetic proximity effects

The main difference of the non-equilibrium magnetic proximity effect in relation the static MPE is the dependency on the application of an external perturbation to drive the system out of an equilibrium in order to generate a spin polarization. This is fundamentally different from the static MPE, where the spin polarization is arising spontaneously due to the exchange splitting of the band structure satisfying the Stoner criterion.

Here, the perturbation in question can be created by an electrical current or a thermal gradient. This perturbation does not influence the band structure of the nonmagnetic metal, however it manipulates the occupation of the spin-up and spin-down bands and which can be expressed as a relative modification of the chemical potential for both sides of the spin-split DOS. As illustrated in the DOS schematic of Fig. 1.14, this shift induces a spin-polarization due to the mismatch of occupied states in the spin-up and spin-down band.

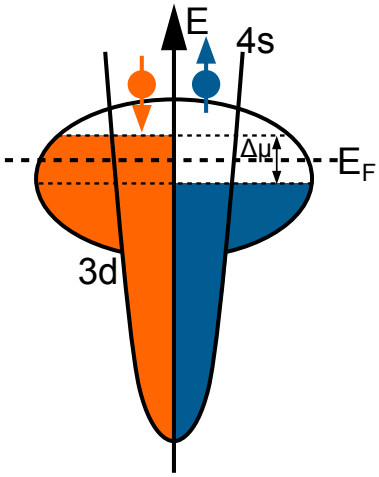

Figure 1.14: Schematic illustration of the DOS of a 3*d* transition metal generating a spin polarization by means of a shifted chemical potential in the spin-up and spin-down DOS. The band occupation of the spin-up band is shifted by $\Delta\mu$ in the chemical potential around the Fermi energy in relation to the spin down-band.

This effect differs fundamentally from the classical ferromagnetism since it does not require any form of exchange splitting but an external perturbation. The SMR effect is related to the absorption and reflection of a spin current flowing along the direction normal to the ferromagnetic insulators (FMI) interface in contact with a non-ferromagnetic metal (NM). Here, a charge current is driven through the normal metal, which exhibits a large spin-orbit coupling, to generate a transverse spin current via the spin Hall effect (SHE). The emergence of the SHE is discussed in more detail in the following section. This spin current then causes a spin accumulation at the interface of the normal metal acting as the perturbation inducing the spin-polarization. The spin-current is absorbed via a spin torque generation or reflected depending on the orientation of the FMI magnetization direction with respect to the polarization of the spin current.

Depending on the ratio of absorbed and reflected spin-current a charge current is induced via the inverse spin Hall effect (ISHE) in the non-ferromagnetic metal. Thus, the spin current acts as dissipation channel for charge transport, which mediated by the ISHE affects the longitudinal resistance of the metal. Therefore, this spin accumulation at the interface and injection of a spin current into neighboring metal layer can be defined as a non-equilibrium MPE since the result of this proximity to the ferromagnet significantly change the electronic properties.

This definition of a non-equilibrium magnetic proximity effect is also applicable to the LSSE used in parts of this work. Here, a thermal gradient injects a magnon-induced spin current perpendicular to the film plane and usually generates a spin accumulation in a non-ferromagnetic material. This way, the LSSE manipulates the magnetic properties of the metal in direct contact with the ferromagnetic material, e.g., in a NM/FMI bilayer system as used in the

vectorial LSSE experiments. Again, the injection of a spin current into the adjacent metal can be interpreted as a non-equilibrium MPE.

Spin Hall effect

THE UTILIZATION OF SPIN and charge degrees of freedom is an important aspect to control equilibrium and non-equilibrium material properties within the field of spintronics. Here, in particular the generation, manipulation, and detection of spin currents is fundamental to understand this spin-orbit coupling phenomena and design promising applications. A key role in the spin current generation is incumbent upon the SHE which describes the creation of a transverse pure spin current polarized perpendicular to the plane defined by the charge and spin current in a material possessing a significant spin-orbit coupling.[88]

The SHE is based on the coupling of charge and spin currents due to the spin-orbit interaction and was already predicted by Dyakonov and Perel in 1971.[89] One year later, the spin Hall effect was experimentally observed by Chazalviel and Solomon in InSb.[90] In 1975, it was measured quantitatively in Ge[91] with a level of precisions that still rivals our contemporary measurements. However, it took three decades until this effect was experimentally revived by Kato *et al.*[92] and Wunderlich *et al.*[93] following an experimental proposal by Hirsch[94] to generate and detect a spin current in a paramagnetic metal which introduced the term "spin Hall effect".

Here, a pure spin current is defined as a pure transport of spins with zero net charge transport. In the process either the charges carrying the spins are flowing in opposite directions for opposing spin directions or the angular momentum is transported through the collective motion of a magnonic spin wave. The different types of spin, charge and spin-polarized currents are summarized in Fig. 1.15.

The SHE is closely connected to the more general family of spin-dependent Hall effect. Much of the mechanisms and descriptions are similar to the anomalous Hall effect (AHE), where the charge carriers are asymmetrically deflected depending on their spin orientation due to relativistic spin-orbit coupling.[95] However, in contrast to the AHE and ordinary Hall effect, the SHE is independent of the magnetization as well as of the external magnetic field and is merely subjected to the coupling of charge and spin currents depending on the strength of the spin-orbit interaction.

Since all spin-dependent Hall effects, namely AHE, SHE, and ISHE, are based on the same three distinct microscopic mechanisms, the skew-scattering contribution, the side jump, and the intrinsic mechanism, it is beneficial to view the AHE as a special case of the SHE in a ferromagnetic metal. In case of an AHE in this respective system, the spin-split band structure induces a spin polarization of

[88] J. Sinova, S. O. Valenzuela, J. Wunderlich, C. Back, and T. Jungwirth. Spin hall effects. *Rev. Mod. Phys.*, **87**(4):1213 (2015)

[89] M. I. Dyakonov and V. I. Perel. Current-induced spin orientation of electrons in semiconductors. *Phys. Lett. A*, **35**(6):459–460 (1971)

[90] J. Chazalviel and I. Solomon. Experimental evidence of the anomalous Hall effect in a nonmagnetic semiconductor. *Phys. Rev. Lett.*, **29**(25):1676 (1972)

[91] J. Chazalviel. Spin-dependent Hall effect in semiconductors. *Phys. Rev. B*, **11**(10):3918 (1975)

[92] Y. Kato, R. C. Myers, A. C. Gossard, and D. D. Awschalom. Observation of the spin Hall effect in semiconductors. *Science*, **306**(5703):1910–1913 (2004)

[93] J. Wunderlich, B. Kaestner, J. Sinova, and T. Jungwirth. Experimental observation of the spin-Hall effect in a two-dimensional spin-orbit coupled semiconductor system. *Phys. Rev. Lett.*, **94**(4):047204 (2005)

[94] J. E. Hirsch. Spin hall effect. *Phys. Rev. Lett.*, **83**(9):1834 (1999)

[95] N. Nagaosa, J. Sinova, S. Onoda, A. H. MacDonald, and N. P. Ong. Anomalous hall effect. *Rev. Mod. Phys.*, **82**(2):1539 (2010)

the charge current which results in a spin-dependent asymmetric scattering of charge carriers and ultimately in a charge current flowing transverse to the initially applied electric field and perpendicular to the magnetization direction. Here, the spin-asymmetric scattering of conduction electrons is caused by the spin-orbit interaction at local potentials created by crystal defects and impurities.[96] When considering the spin and charge transport in a nonmagnetic metal such as Pt and Pd to analyze the SHE in detail, one has to take the key mechanisms into account, which are discussed in the next section.

[96] C. Chien. *The Hall effect and its applications*. Springer Science & Business Media (2013)

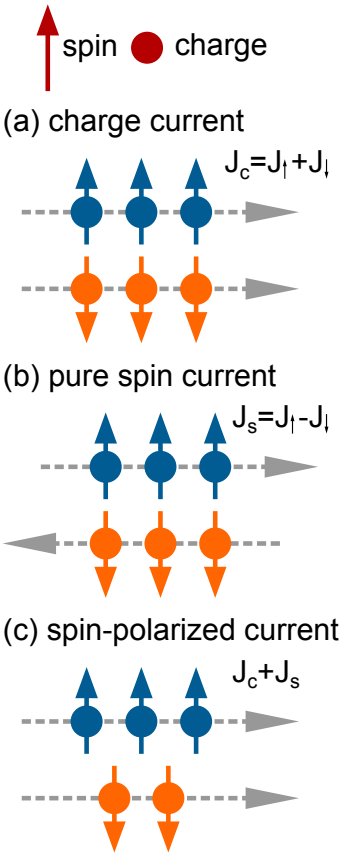

Figure 1.15: An electron carries a spin and a negative charge. (a) The electrons travel in the same direction independently of the spin orientation generating a conventional charge current. (b) Electrons with contrary spin orientations traveling in opposite directions create a pure spin current. (c) Spin-polarized currents are generated due to an imbalance of spin-up and spin-down electrons flowing in the same direction.

The side-jump and skew-scattering contribution

The main difference of the side-jump and skew-scattering mechanisms in relation to the intrinsic contribution is their focus on the asymmetric scattering events as a contribution to the SHE. Due to the spin-orbit interaction, an asymmetric scattering cross section is generated which was first discussed with regard to the skew scattering process of magnetized conduction electrons on impurity atoms by Smit in 1958.[97] Here, the Hall effect arises from the spontaneous magnetization of the itinerant electrons due to a transverse polarization which is induced by the spin-orbit interaction. In the process the scattered electrons create an effective magnetic field in their frame of reference which interacts with the magnetic spin-moment of the charge carrier. This energetically favors a preferred scattering direction in case of a predominant spin orientation of the conduction electrons or in case of the SHE yields a transverse spin-current, respectively.

Figure 1.16 illustrates the skew-scattering in an intrinsic and extrinsic model. In the intrinsic case, the scattered electron with an angular moment $\vec{L}$ has an energetically preferable path, black scattering direction in Fig. 1.16(a), in vicinity of the impurity ion due to the coupling of effective magnetic field and electron moment $\vec{\mu}_s$. An identical result is obtained when the skew-scattering is modeled based on ions exhibiting a localized magnetic moment. This extrinsic case, presented in Fig. 1.16(b), is characterized by the coupling of ion moment $\vec{\mu}_\sigma$ with effective magnetic field generated in the ion frame of reference. Thus, the orientation of the ionic magnetic moments within the crystal system is responsible for the asymmetric scattering, in contrast to the orientation of the electron spin in the intrinsic case. In both cases a skew-scattering contribution to the Hall conductivity is generated.

The SHE induced by spin-orbit scattering in nonmagnetic metals can be derived in its basic formalism describing the spin and charge current conversion in nonlocal devices.[98] In this formalism, nonmagnetic impurities in a metal generate an additional electric potential $V(\vec{r})$ and thus the electric field $\vec{E} = -(1/e)\nabla V(\vec{r})$. The electrons scattered at this impurity with a momentum $\hat{p}$ is subjected

[97] J. Smit. The spontaneous Hall effect in ferromagnetics II. *Physica*, **24**(1-5): 39–51 (1958)

[98] S. Takahashi and S. Maekawa. Spin current, spin accumulation and spin Hall effect. *Sci. Technol. Adv. Mater.*, **9**(1): 014105 (2008)

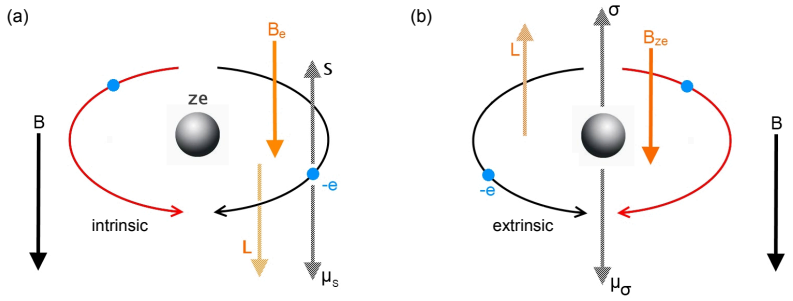

Figure 1.16: Schematic illustration of the (a) intrinsic and (b) extrinsic spin-orbit coupling of an electron and an ion with the charge $z \cdot e$.

to the effective magnetic field

$$\vec{B}_{\text{eff}} = -(1/mc)\,\hat{p} \times \vec{E}, \tag{1.96}$$

which precipitates the spin-orbit coupling

$$V_{\text{so}} = -\mu_B \vec{\sigma} \cdot \vec{B}_{\text{eff}} = \eta_{\text{so}} \vec{\sigma} \cdot [\nabla V(\vec{r}) \times \nabla / i] \tag{1.97}$$

with the Pauli spin operator σ and the spin-orbit coupling parameter η_{so}. This facilitates the calculation of the total potential generated by the impurity $U(\vec{r})$ which is the sum of the standard potential and the spin-orbit contribution $U(\vec{r}) = V(\vec{r}) + V_{\text{so}}(\vec{r})$.

Following the modified derivation of the formalism,[99] the electrons with a wave vector $\vec{k}$ and spin σ are specified by the state $\left|\vec{k}\sigma\right\rangle$. Consequently, the scattering process of conduction electrons at the center of impurity is defined by a scattering amplitude $U^{\sigma',\sigma}_{\vec{k}',\vec{k}} = \left\langle \vec{k}'\sigma' \middle| U \middle| \vec{k}\sigma \right\rangle$ that can be written as

$$U^{\sigma',\sigma}_{\vec{k}',\vec{k}} = V_{\text{imp}} \left[\delta_{\sigma',\sigma} + i\eta_{\text{so}} \boldsymbol{\sigma} \cdot \left(\vec{k} \times \vec{k}' \right) \right] \sum_i e^{i\left(\vec{k}-\vec{k}'\right)\cdot\vec{r}_i}, \tag{1.98}$$

including the Pauli matrix $\boldsymbol{\sigma}$. The sum accounts for the matrix elements of a weak δ-function potential due to the impurities at position $\vec{r}_i$, which is given by

$$V(\vec{r}) \approx V_{\text{imp}} \sum_i \delta\left(\vec{r} - \vec{r}_i\right). \tag{1.99}$$

Utilizing this matrix element, one can use the electron velocity operator $\hat{v} = \mathrm{d}\vec{r}/\,\mathrm{d}t$ to calculate the electron velocity $\vec{v}^{\sigma}_{\vec{k}}$ in consideration of the spin-orbit potential to derive an anomalous velocity contribution to the Hall effect, which is equivalent to the side-jump model.[100]

Thus, this anomalous velocity can be determined by the matrix element $\vec{v}^{\sigma}_{\vec{k}} = \left\langle \vec{k}^*\sigma \middle| \hat{v} \middle| \vec{k}^*\sigma \right\rangle$ of the velocity operator between the scattering states

$$\left|\vec{k}^*\sigma\right\rangle = \left|\vec{k}\sigma\right\rangle + \sum_{\vec{k}'} \left|\vec{k}'\sigma\right\rangle \frac{V_{\text{imp}} \sum_i e^{i\left(\vec{k}-\vec{k}'\right)\cdot\vec{r}_i}}{E_{\vec{k}} - E_{\vec{k}'} + i\delta}, \tag{1.100}$$

at which $\left|\vec{k}\sigma\right\rangle$ is the one-electron state with the momentum $\vec{k}$, the spin σ, and a kinetic energy of $E_{\vec{k}} = (\hbar k)^2/2m - E_{\text{F}}$. The matrix

[99] J. Sakurai and J. Napolitano. *Modern Quantum Mechanics*. Cambridge University Press (2017)

[100] S. Lyo and T. Holstein. Side-jump mechanism for ferromagnetic Hall effect. *Phys. Rev. Lett.*, **29**(7):423 (1972)

element yields a velocity of

$$\vec{v}_{\vec{k}}^{\sigma} = \hbar\vec{k}/m + \omega_{\vec{k}}^{\sigma}, \tag{1.101}$$

where the ordinary velocity is defined by the de Broglie relations and the anomalous velocity is given by

$$\omega_{\vec{k}}^{\sigma} = \alpha_{\mathrm{H}}^{\mathrm{SJ}} \left(\sigma \times \hbar\vec{k}/m \right). \tag{1.102}$$

Here, $\alpha_{\mathrm{H}}^{\mathrm{SJ}}$ is a dimensionless coupling parameter characterizing the side-jump contribution

$$\alpha_{\mathrm{H}}^{\mathrm{SJ}} = \frac{m\eta_{\mathrm{so}}}{\hbar\tau_{\mathrm{tr}}} = \frac{\hbar\overline{\eta}_{\mathrm{so}}}{2E_{\mathrm{F}}\tau_{\mathrm{tr}}} = \frac{\overline{\eta}_{\mathrm{so}}}{k_{\mathrm{F}}l}, \tag{1.103}$$

with a transport relaxation time τ_{tr} depending on the concentration of impurities in the material, the Fermi momentum k_{F}, the mean free path $l = v_{\mathrm{F}}\tau_{\mathrm{tr}}$ and the dimensionless spin-orbit coupling parameter $\overline{\eta}_{\mathrm{so}} = k_{\mathrm{F}}^2\eta_{\mathrm{so}}$. In order to calculate the side-jump contribution to the SHE induced spin-orbit scattering one can introduce a current operator

$$\hat{J}_{\sigma} = e\sum_{\vec{k}} \left(\hbar\vec{k}/m + \omega_{\vec{k}}^{\sigma} \right) a_{\vec{k}\sigma}^{\dagger} a_{\vec{k}\sigma} \tag{1.104}$$

based on the electron distribution function $f_{\vec{k}\sigma} = \left\langle a_{\vec{k}\sigma}^{\dagger} a_{\vec{k}\sigma} \right\rangle$ with spin σ and energy $E_{\vec{k}}$. The total charge current, defined as $\vec{J}_{\mathrm{q}} = \vec{J}_{\uparrow} + \vec{J}_{\downarrow}$, can then be written as

$$\vec{J}_{\mathrm{q}} = \vec{J}'_{\mathrm{q}} + \alpha_{\mathrm{H}}^{\mathrm{SJ}} \left[\hat{z} \times \vec{J}'_{\mathrm{s}} \right]. \tag{1.105}$$

In an analog way, the total spin current $\vec{J}_{\mathrm{s}} = \vec{J}_{\uparrow} - \vec{J}_{\downarrow}$ is derived by

$$\vec{J}_{\mathrm{s}} = \vec{J}'_{\mathrm{s}} + \alpha_{\mathrm{H}}^{\mathrm{SJ}} \left[\hat{z} \times \vec{J}'_{\mathrm{q}} \right], \tag{1.106}$$

with

$$\vec{J}'_{\mathrm{q,s}} = e\sum_{\vec{k}} \frac{\hbar\vec{k}}{m} \left(f_{\vec{k}\uparrow} - f_{\vec{k}\downarrow} \right). \tag{1.107}$$

This illustrates the additional contribution by the side-jump mechanism to the charge current and moreover the induced spin Hall current due to an effective spin separation. The Eqs. (1.105) and (1.106) can be written in the more common form describing the spin current generated by a charge current density $\vec{J}_{\mathrm{q}}$ via the SHE

$$\vec{J}_{\mathrm{s}} = \alpha_{\mathrm{SH}} \left(-\frac{\hbar}{2e} \right) \vec{J}_{\mathrm{q}} \times \vec{s}, \tag{1.108}$$

with a spin polarization $\vec{s}$ oriented perpendicular to $\vec{J}_{\mathrm{s}}$ and $\vec{J}_{\mathrm{q}}$ and an efficiency parameter of the charge-current conversion, the spin Hall angle $\alpha_{\mathrm{SH}} = \sigma_{\mathrm{SH}}/\sigma$ defined by the ratio of the spin Hall conductivity σ_{SH} and electric conductivity σ.[101] The spin Hall angle is the key parameter in describing the spin-charge conversion by quantifying the conversion efficiency between charge and spin

[101] M. Althammer, S. Meyer, H. Nakayama, M. Schreier, S. Altmannshofer, M. Weiler, H. Huebl, S. Geprägs, M. Opel, R. Gross, D. Meier, C. Klewe, T. Kuschel, J.-M. Schmalhorst, G. Reiss, L. Shen, A. Gupta, Y.-T. Chen, G. E. W. Bauer, E. Saitoh, and S. T. B. Goennenwein. Quantitative study of the spin Hall magnetoresistance in ferromagnetic insulator/normal metal hybrids. *Phys. Rev. B*, **87**(22):224401 (2013)

currents. In particular material of the heavy 5*d* transition metal group like Pt have been reported to show high spin Hall angles and a pronounced SHE.[102]

Since the amount of spin current that is reflected at an interface induces a charge current via the ISHE, this effect can be specified by the counterpart of Eq. (1.108), describing the analog charge current generation due to an arising transverse spin current

$$\vec{J}_{\mathrm{q}} = \alpha_{\mathrm{SH}} \left(\frac{2e}{\hbar} \right) \vec{J}_{\mathrm{s}} \times \vec{s}. \tag{1.109}$$

Typically, the measurement of the spin Hall angle is closely entangled with the determination of the spin diffusion length. This second important parameter in spin transport experiments, therefore critical for spintronic applications, quantifies the decay behavior of pure spin current along with the propagation. The spin Hall angle and the spin diffusion length are usually measured by nonlocal magnetotransport[103] or spin pumping[104] and spin-torque[105] based ferromagnetic resonance experiments.

In general, this charge current production based on a spin current utilizing the ISHE, in combination with the SHE, enables a reciprocal conversion between spin and charge currents, which is fundamental for the generation and observation of spin currents in spintronics devices. Particularly, in experiments using spin pumping to inject pure spin currents, the ISHE is has been established as a valuable detection method, e.g., in heavy paramagnetic metals such as Pt and Pd where the strong spin-orbit interaction allows for an efficient conversion of pumped spin currents into a detectable voltage.[106]

In addition to the side-jump contribution to the SHE presented in Eq. (1.103), the second main scattering mechanism is the so-called skew scattering contribution originating from asymmetrical scattering of conduction electrons due to the spin-orbit interaction. The skew-scattering contribution is explained within the classical Boltzmann transport theory, whereas the side-jump contribution has to be discussed in a non-classical framework. Berger *et al.* examined the scattering process in a quantum mechanical consideration in 1970 introduction the side-jump mechanism relying on spin-orbit coupling which is illustrated in Fig. 1.17 in comparison to the skew-scattering process. Here, a wave package is laterally displaced at the defect on the order of by $\Delta y \approx 10^{-11}\,\mathrm{m} - 10^{-10}\,\mathrm{m}$.[107]

Essentially, this scattering process at material impurities critically depends on the spin momentum of the conduction electrons.[108] Here, the electrons move relative to the impurity charge which induces a magnetic field in the electron frame of reference perpendicular to the direction of the conduction electron flow. This inhomogeneous field creates a Zeeman energy gradient which exerts a force on the charge carriers depending on their magnetic moment. The process also modifies the distribution function of the electrons which can be calculated according to the steady state

[102] L. Liu, T. Moriyama, D. Ralph, and R. Buhrman. Spin-torque ferromagnetic resonance induced by the spin Hall effect. *Phys. Rev. Lett.*, **106**(3):036601 (2011)

[103] S. O. Valenzuela and M. Tinkham. Direct electronic measurement of the spin Hall effect. *Nature*, **442**(7099):176 (2006)

[104] O. Mosendz, J. Pearson, F. Fradin, G. Bauer, S. Bader, and A. Hoffmann. Quantifying spin Hall angles from spin pumping: Experiments and theory. *Phys. Rev. Lett.*, **104**(4):046601 (2010)

[105] L. Liu, T. Moriyama, D. Ralph, and R. Buhrman. Spin-torque ferromagnetic resonance induced by the spin Hall effect. *Phys. Rev. Lett.*, **106**(3):036601 (2011)

[106] E. Saitoh, M. Ueda, H. Miyajima, and G. Tatara. Conversion of spin current into charge current at room temperature: Inverse spin-Hall effect. *Appl. Phys. Lett.*, **88**(18):182509 (2006)

[107] L. Berger. Side-jump mechanism for the Hall effect of ferromagnets. *Phys. Rev. B*, **2**(11):4559 (1970)

[108] N. F. Mott. The scattering of fast electrons by atomic nuclei. *Proc. R. Soc. Lond. A*, **124**(794):425–442 (1929)

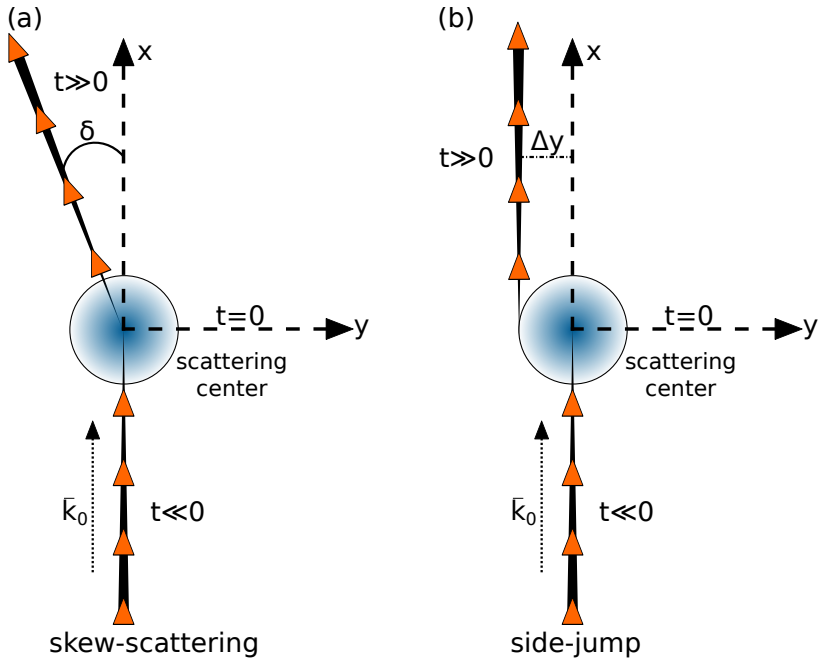

Figure 1.17: Schematic illustration of (a) skew-scattering and (b) side-jump in comparison. The trajectory of the conduction electrons is indicated before ($\vec{k}_0 \parallel x$) and after the scattering event at an impurity potential as a results of the spin-orbit coupling ($\vec{\mu}_s \parallel z$).

Boltzmann transport equation

$$\vec{v}_{\vec{k}} \cdot \nabla f_{\vec{k}\sigma} + \frac{e\vec{E}}{\hbar} \cdot \nabla_{\vec{k}} f_{\vec{k}\sigma} = \left(\frac{\partial f_{\vec{k}\sigma}}{\partial t}\right)_{\text{scatt}}, \tag{1.110}$$

with the external electric field $\vec{E}$. The term on the right is referred to as a collision term describing impurity scattering and can be separated into a scattering-in term $\left(\vec{k}'\sigma' \to \vec{k}\sigma\right)$ and a scattering-out term $\left(\vec{k}\sigma \to \vec{k}'\sigma'\right)$, respectively. Considering the scattering probability from the initial $\left|\vec{k}\sigma\right\rangle$ state to the final $\left|\vec{k}'\sigma\right\rangle'$ state with a scattering probability

$$P^{\sigma'\sigma}_{\vec{k}'\vec{k}} = (2\pi/\hbar)\, n_{\text{imp}} |\left\langle \vec{k}'\sigma' \middle| \hat{T} \middle| \vec{k}\sigma \right\rangle|^2 \delta\left(\vec{E}_{\vec{k}} - \vec{E}_{\vec{k}'}\right) \tag{1.111}$$

based on the scattering $\hat{T}$-matrix,[109] the term can be written as

$$\left(\frac{\partial f_{\vec{k}\sigma}}{\partial t}\right)_{\text{scatt}} = \sum_{\vec{k}'\sigma'} \left[P^{\sigma\sigma'}_{\vec{k}\vec{k}'} f_{\vec{k}'\sigma'} - P^{\sigma'\sigma}_{\vec{k}'\vec{k}} f_{\vec{k}\sigma}\right] \tag{1.112}$$

$$= \sum_{\vec{k}'\sigma'} P^{\sigma'\sigma(1)}_{\vec{k}'\vec{k}} \left(f_{\vec{k}'\sigma'} - f_{\vec{k}\sigma}\right) + \sum_{\vec{k}'\sigma'} P^{\sigma'\sigma(2)}_{\vec{k}'\vec{k}} \left(f_{\vec{k}'\sigma'} + f_{\vec{k}\sigma}\right), \tag{1.113}$$

separating the first-order symmetric $P^{\sigma'\sigma(1)}_{\vec{k}'\vec{k}}$ and the second-order asymmetric contributions $P^{\sigma'\sigma(2)}_{\vec{k}'\vec{k}}$. Here, Fermi's golden rule describes the transition rate of the state as a result of a weak perturbation. This transition rate is proportional to the density of states and to the strength of the coupling between the initial and final states of the system.[110] The transition probability, as presented in Eq. (1.111), is therefore proportional to the square of the transition

[109] A. Fert. Transport in magnetic alloys: Scattering asymmetries (anisotropic scattering, skew scattering, side-jump). *Physica B+C*, **86**:491–500 (1977); and J. M. Ziman. *Electrons and phonons: the theory of transport phenomena in solids*. Oxford university press (2001)

[110] E. Fermi. *Nuclear physics: a course given by Enrico Fermi at the University of Chicago*. University of Chicago Press (1950)

matrix element and the density of the final state according to the first order in perturbation theory.

In order to solve the Boltzmann transport equation presented in Eq. (1.110), one can separate the distribution function such as $f_{\vec{k}\sigma} = f^{(0)}_{\vec{k}\sigma} + g^{(1)}_{\vec{k}\sigma} + g^{(2)}_{\vec{k}\sigma}$ with the non-directional distribution function $^{(0)}_{\vec{k}\sigma}$ and the directional contributions to the distribution functions $g^{(1)}_{\vec{k}\sigma}$ and $g^{(2)}_{\vec{k}\sigma}$ which are attributed to the first-order and the second-order transitions.[111] The transport- τ_{tr} and spin-flip relaxation time τ_{sf} can now be derived via the symmetric part of the separated collision term in Eq. (1.113) which can be written as

[111] J. Kondo. Anomalous Hall effect and magnetoresistance of ferromagnetic metals. *Prog. Theor. Exp. Phys*, **27**(4): 772–792 (1962)

$$\sum_{\vec{k}'\sigma'} \left[P^{\sigma\sigma'(1)}_{\vec{k}\vec{k}'} f_{\vec{k}'\sigma'} - P^{\sigma'\sigma(1)}_{\vec{k}'\vec{k}} f_{\vec{k}\sigma} \right] = \frac{g^{(1)}_{\vec{k}\sigma}}{\tau_{\mathrm{tr}}} - \frac{f^{(0)}_{\vec{k}\sigma} - f^{(0)}_{\vec{k}-\sigma}}{\tau_{\mathrm{sf}}}. \tag{1.114}$$

Here, the transport relaxation time is defined by

$$\frac{1}{\tau_{\mathrm{tr}}} = \sum_{\vec{k}'\sigma'} P^{\sigma\sigma'(1)}_{\vec{k}\vec{k}'} = \frac{1}{\tau^{(}_{\mathrm{tr}}0)} \left(1 + 2\overline{\eta}^2_{\mathrm{so}}/3\right), \tag{1.115}$$

while the spin-flip relaxation time is given by

$$\frac{1}{\tau_{\mathrm{sf}}} = \sum_{\vec{k}'} P^{\uparrow\downarrow(1)}_{\vec{k}\vec{k}'} = \frac{\overline{\eta}^2_{\mathrm{so}}}{3\tau^{(0)}_{\mathrm{tr}}} \left(1 + \cos^2\theta\right), \tag{1.116}$$

where θ describes the angle between $\vec{k}$ and the x-axis. The collision term in Eq. (1.114) is used to solve the Boltzmann equation in the steady state presented in Eq. (1.110) which is transformed into

$$\vec{v}_{\vec{k}} \cdot \frac{\partial f_{\vec{k}\sigma}}{\partial \vec{r}} + \frac{e\vec{E}}{\hbar} \cdot \frac{\partial f_{\vec{k}\sigma}}{\partial \vec{k}} = \frac{g^{(1)}_{\vec{k}\sigma}}{\tau_{\mathrm{tr}}} - \frac{f^{(0)}_{\vec{k}\sigma} - f^{(0)}_{\vec{k}-\sigma}}{\tau_{\mathrm{sf}}}. \tag{1.117}$$

In this equation the momentum relaxation on account of impurity scattering is given by the first term on the right hand side.[112] Here, the solution providing the first-order of the directional distribution function is given by

[112] J.-P. Ansermet. Perpendicular transport of spin-polarized electrons through magnetic nanostructures. *J. Phys. Condens. Matter*, **10**(27):6027 (1998); and S. Zhang. Spin Hall effect in the presence of spin diffusion. *Phys. Rev. Lett.*, **85**(2):393 (2000)

$$g^{(1)}_{\vec{k}\sigma} \approx -\tau_{\mathrm{tr}} \left(\vec{v}_{\vec{k}} \cdot \nabla + \frac{e\vec{E}}{\hbar} \cdot \nabla_{\vec{k}} \right) f^{(0)}_{\vec{k}\sigma}. \tag{1.118}$$

The non-directional function can be expanded with the Fermi distribution function $f_0(E_{\mathrm{F}})$ as

$$f^{(0)}_{\vec{k}\sigma} \approx f_0(E_{\vec{k}}) - \sigma \frac{\partial f_0(E_{\vec{k}})}{\partial E_{\vec{k}}} \delta E_{\mathrm{F}}(\vec{r}), \tag{1.119}$$

since it is in a local equilibrium with the Fermi energy shifted by $\sigma\delta E_{\mathrm{F}}(\vec{r})$ from the global equilibrium. Based on this approximation Eq. (1.118) can be written as

$$g^{(1)}_{\vec{k}\sigma} \approx \tau_{\mathrm{tr}} \frac{\partial f_0(E_{\vec{k}})}{\partial E_{\vec{k}}} \vec{v}_{\vec{k}} \cdot \nabla \mu^{\sigma}_{\mathrm{N}}(\vec{r}), \tag{1.120}$$

where $\mu^{\sigma}_{\mathrm{N}}(\vec{r}) = E_{\mathrm{F}} + e\phi + \sigma\delta E_{\mathrm{F}}$ is the electrochemical potential and $\phi(\vec{E} = -\nabla\phi)$ the electric potential. Thereby, this derivation allows

for the actual calculation of the spin diffusion equation by applying Eqs. (1.119) and (1.120) into the Boltzmann transport equation (Eq. (1.117)) and summing over all $\vec{k}$ to get to the spin diffusion equation

$$\nabla^2 \delta\mu_{\mathrm{N}} = \frac{1}{\lambda_{\mathrm{N}}^2}\delta\mu_{\mathrm{N}} \tag{1.121}$$

considering the spin-diffusion length $\lambda_{\mathrm{N}} = \sqrt{D\tau_{\mathrm{sf}}}$ with the diffusion constant $D = (1/3)\tau_{\mathrm{tr}} v_{\mathrm{F}}^2$ and spin relaxation time given by $\tau_{\mathrm{sf}}^{-1} = \langle \tau_{\mathrm{sf}}^{-1}\theta \rangle_{\mathrm{av}} = 4\overline{\eta}_{\mathrm{so}}^2/(9\tau_{\mathrm{tr}}^{(0)})$. The second order of the Boltzmann transport function following Eq. (1.113) can be written as

$$\sum_{\vec{k}'\sigma'} \left[P_{\vec{k}\vec{k}'}^{\sigma\sigma'(1)} \left(g_{\vec{k}\sigma}^{(2)} - g_{\vec{k}'\sigma'}^{(2)} \right) - P_{\vec{k}'\vec{k}}^{\sigma'\sigma(2)} \left(g_{\vec{k}\sigma}^{(2)} + g_{\vec{k}'\sigma'}^{(2)} \right) \right] = 0. \tag{1.122}$$

It can be shown that this second-order term yields the so-called skew scattering contribution which is given by

$$g_{\vec{k}\sigma}^{(2)} = -\alpha_{\mathrm{H}}^{\mathrm{SS}} \tau_{\mathrm{sf}} \frac{\partial f_0(E_{\vec{k}})}{\partial E_{\vec{k}}} \left(\boldsymbol{\sigma} \times \vec{v}_{\vec{k}} \right) \cdot \nabla \mu_{\mathrm{N}}^{\sigma}(\vec{r}). \tag{1.123}$$

Here, $\alpha_{\mathrm{H}}^{\mathrm{SS}}$ is the dimensionless skew scattering parameter strongly depending on the wave vector defined by

$$\alpha_{\mathrm{H}}^{\mathrm{SS}} = (2\pi/3)\, \overline{\eta}_{\mathrm{so}} N(0) V_{\mathrm{imp}}. \tag{1.124}$$

This emphasizes the two main contribution to the SHE based on the spin-orbit scattering mechanisms to the spin Hall conductivity $\sigma_{\mathrm{H}} = \sigma_{\mathrm{H}}^{\mathrm{SJ}} + \sigma_{\mathrm{H}}^{\mathrm{SS}}$ in relation to the electrical conductivity σ_{N}, in particular the side-jump contribution $\sigma_{\mathrm{H}}^{\mathrm{SJ}} = \alpha_{\mathrm{H}}^{\mathrm{SJ}} \sigma_{\mathrm{N}}$ and the skew-scattering contribution $\sigma_{\mathrm{H}}^{\mathrm{SS}} = \alpha_{\mathrm{H}}^{\mathrm{SS}} \sigma_{\mathrm{N}}$, which are summarized as

$$\sigma_{\mathrm{H}}^{\mathrm{SJ}} = \frac{e^2}{\hbar} \eta_{\mathrm{so}} n_{\mathrm{e}} = \frac{2e^2}{3\pi\hbar} k_{\mathrm{F}} \overline{\eta}_{\mathrm{so}} \qquad \text{and} \tag{1.125}$$

$$\sigma_{\mathrm{H}}^{\mathrm{SS}} = \left(\frac{2\pi}{3} k_{\mathrm{F}} l N(0) V_{\mathrm{imp}} \right) \cdot \sigma_{\mathrm{H}}^{\mathrm{SJ}}. \tag{1.126}$$

Here, the electron density is denoted as $n_{\mathrm{e}} \sim N(0)E_{\mathrm{F}}$. These equations show that the skew-scattering contribution to the SHE is dominating the spin Hall conductivity in case of a high spin-orbit coupling parameter and carrier density $(k_{\mathrm{F}} l)|N(0)V_{\mathrm{imp}}| \gg 1$. From this follows that the side-jump contribution is dominant in case the approximation $(k_{\mathrm{F}} l)|N(0)V_{\mathrm{imp}}| \ll 1$ is valid. The final Eqs. (1.125) and (1.126) can be converted to approximate the spin Hall resistivity $\rho_{\mathrm{H}} \approx \sigma_{\mathrm{H}}/\sigma_{\mathrm{N}}^2$ in relation to the resistivity ρ_{N} utilizing the skew-scattering $a_{\mathrm{SS}} = (2/pi/3)\overline{\eta}_{\mathrm{so}} N(0) V_{\mathrm{imp}}$ and side-jump specific $b_{\mathrm{SJ}} = (2/pi/3)\overline{\eta}_{\mathrm{so}}(e^2/h)k_{\mathrm{F}}$ coefficients. Hence, the spin Hall resistivity is characterized by a linear side-jump and a quadratic skew-scattering term in ρ_{N} based on these specific coefficients

$$\rho_{\mathrm{H}} = a_{\mathrm{SS}} \rho_{\mathrm{N}} + b_{\mathrm{SJ}} \rho_{\mathrm{N}}^2. \tag{1.127}$$

In comparison to the skew-scattering, the side-jump mechanism is also based on an asymmetric scattering process at centers of impurity as outlined above. When the conduction electrons are viewed

as a wave function scattered at an impurity potential the spin-orbit coupling causes an instantaneous side-jump of the conduction electron trajectory where the magnitude of the shift is closely related to the spin momentum of the charge carrier. Therefore, the spin dependent scattering events at centers of impurity are generally a combination of both mechanisms yielding a localized transversal current density contributing to the SHE.

The intrinsic contribution

Beside both asymmetric scattering mechanisms, an intrinsic contribution to the SHE has to be considered which is not directly originating in asymmetric scattering events. As opposed to the discussed mechanisms, the intrinsic contribution generates a transverse current density to the electron motion which is accumulated in between the scattering events independent of the impurity potential and density. All three distinct mechanisms have been first identified in context of the anomalous Hall effect and are based on coherent band mixing effects due to the external electric field and the impurity potential.[113] However, the intrinsic contribution has to be discussed in a semiclassical theory focused on the induced inter-band coherence which is captured by a momentum-space Berry-phase related contribution to the anomalous velocity.[114] This mechanism characterized by the topological properties of the electronic structure, in particular of the Bloch states, was primarily introduced by Karplus and Luttinger in 1954,[115] yet the relationship between momentum space Berry phases and anomalous transverse velocities has became a subject of research recently due to the experimental impact of the AHE in the field of spintronics.[116]

The intrinsic contribution mainly depends on the band structure and originates from the non-equilibrium electron dynamics of the Bloch electrons under acceleration in an electric field which allows them to undergo a spin-precession due to the induced electric field around an effective magnetic field $B(k)$ depending on the wave vector. In the presence of this electrical current the Fermi surface is displaced along the current direction in momentum space which in turn generates an additional spin-orbit field acting on the election spins. In reaction to this non-equilibrium current induced field, the spins tilt depending on their momentum creating a spin-current in the direction perpendicular to the electron trajectory. Here, the

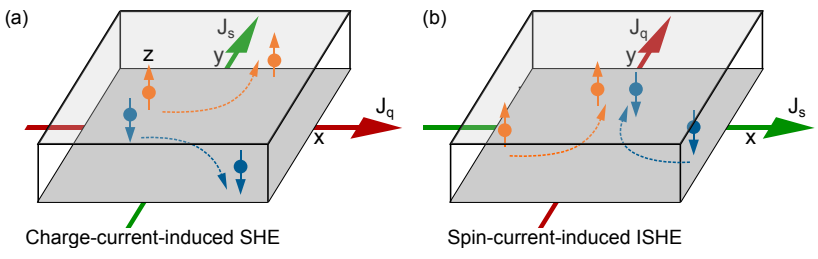

Figure 1.18: Schematic illustration of the (a) charge-current-induced SHE where the charge current J_q is flowing along the x-direction inducing the spin current J_s along the y-direction with the polarization parallel to the z-axis. The SHE is contrasted with the (b) spin-current-induced ISHE. The spin current J_s is flowing along the x-direction with the polarization parallel to the z-axis inducing a charge current J_q in the y-direction.

[113] N. Nagaosa, J. Sinova, S. Onoda, A. H. MacDonald, and N. P. Ong. Anomalous hall effect. *Rev. Mod. Phys.*, **82**(2):1539 (2010)

[114] J. Sinova, S. O. Valenzuela, J. Wunderlich, C. Back, and T. Jungwirth. Spin hall effects. *Rev. Mod. Phys.*, **87**(4):1213 (2015)

[115] R. Karplus and J. Luttinger. Hall effect in ferromagnetics. *Phys. Rev.*, **95** (5):1154 (1954)

[116] G. Sundaram and Q. Niu. Wave-packet dynamics in slowly perturbed crystals: Gradient corrections and Berry-phase effects. *Phys. Rev. B*, **59**(23): 14915 (1999); and T. Jungwirth, Q. Niu, and A. MacDonald. Anomalous Hall effect in ferromagnetic semiconductors. *Phys. Rev. Lett.*, **88**(20):207208 (2002)

change in momentum turns the spins out of the equilibrium spin texture or the alignment with the effective field, respectively. This turning of the spins favors opposite directions on diametrically opposed positions on the Fermi surface creating an effective spin current contribution to the SHE.[117]

The intrinsic contribution is therefore proportional to the integration over the Fermi surface of the Berry's curvature of all occupied bands which directly links it to the topological properties of the Bloch states. In materials which exhibit a strong spin-orbit coupling of these bands, the intrinsic contribution is dominating the AHE or SHE in comparison to the side-jump and skew-scattering mechanics. It can be shown by density function theory (DFT) calculations for Pt and other 4*d* and 5*d* transition metals that the largest contributions to the spin Hall conductivity are emerging in case separate bands are combined near the Fermi energy by means of a pronounced spin-orbit coupling.[118] However, the exact contribution of each discussed spin-current generating mechanism is depending on various material parameters and is still an open field of research.[119] Since this spin-orbit coupling phenomena is mainly discussed in this work with regard to the ISHE and more broadly the LSSE, this aspect is only of minor importance.

The conversion of a charge current into a transverse spin current via the SHE and the inverse conversion by means of the ISHE is schematically summarized in Fig. 1.18. In both cases the charge and spin current directions J_q and J_s, as well as both current directions and the electron spin orientation are orthogonal in relation to each other as specified by the Eqs. (1.108) and (1.109).

Spin Seebeck effect

The discovery of the SSE has attracted a lot of interest in the field of spin caloritronics in recent years.[120] This is, to a certain extent, due to the fact that the generated spin voltage enables the thermal injection of a spin current, usually from a ferromagnetic material, into an adjacent nonmagnetic layer over a macroscopic length scale significantly longer than the spin-flip diffusion length of conduction electrons. Following the initial demonstration of the effect by Uchida *et al.* in 2008, the SSE has been observed in a number of different material systems ranging from metallic ferromagnets[121] to magnetic insulators,[122] emphasizing the universality of the effect with regard to ferromagnetism.

Based on the ISHE, the spin current injected via the SSE can subsequently be converted into transverse charge voltage in the nonmagnetic layer of a suitable bilayer structure. In an insulating magnetic system the contribution to the SSE from conduction electrons is eliminated. Here, the spin current is carried by magnons exhibiting a significantly larger decay length than an electron mediated spin current. A conduction electron spin current usually

[117] J. Sinova, D. Culcer, Q. Niu, N. Sinitsyn, T. Jungwirth, and A. MacDonald. Universal intrinsic spin Hall effect. *Phys. Rev. Lett.*, **92**(12):126603 (2004)

[118] G.-Y. Guo, S. Murakami, T.-W. Chen, and N. Nagaosa. Intrinsic spin Hall effect in platinum: First-principles calculations. *Phys. Rev. Lett.*, **100** (9):096401 (2008); and T. Tanaka, H. Kontani, M. Naito, T. Naito, D. S. Hirashima, K. Yamada, and J. Inoue. Intrinsic spin hall effect and orbital Hall effect in 4*d* and 5*d* transition metals. *Phys. Rev. B*, **77**(16):165117 (2008)

[119] W.-K. Tse and S. D. Sarma. Intrinsic spin Hall effect in the presence of extrinsic spin-orbit scattering. *Phys. Rev. B*, **74**(24):245309 (2006); and G. Vignale. Ten years of spin Hall effect. *J. Supercond. Nov. Magn.*, **23**(1):3 (2010)

[120] K.-i. Uchida, S. Takahashi, K. Harii, J. Ieda, W. Koshibae, K. Ando, S. Maekawa, and E. Saitoh. Observation of the spin Seebeck effect. *Nature*, **455** (7214):778–781 (2008); K.-i. Uchida, H. Adachi, T. Ota, H. Nakayama, S. Maekawa, and E. Saitoh. Observation of longitudinal spin-Seebeck effect in magnetic insulators. *Appl. Phys. Lett.*, **97**(17):172505 (2010); M. Weiler, M. Althammer, F. D. Czeschka, H. Huebl, M. S. Wagner, M. Opel, I.-M. Imort, G. Reiss, A. Thomas, R. Gross, and S. T. B. Goennenwein. Local Charge and Spin Currents in Magnetothermal Landscapes. *Phys. Rev. Lett.*, **108**(10): 106602 (2012); D. Meier, T. Kuschel, L. Shen, A. Gupta, T. Kikkawa, K. Uchida, E. Saitoh, J. M. Schmalhorst, and G. Reiss. Thermally driven spin and charge currents in thin NiFe2O4/Pt films. *Phys. Rev. B*, **87**(5): 054421 (2013); D. Meier, D. Reinhardt, M. van Straaten, C. Klewe, M. Althammer, M. Schreier, S. T. B. Goennenwein, A. Gupta, M. Schmid, C. H. Back, J.-M. Schmalhorst, T. Kuschel, and G. Reiss. Longitudinal spin Seebeck effect contribution in transverse spin Seebeck effect experiments in Pt/YIG and Pt/NFO. *Nat. Commun.*, **6**:8211 (2015); and K.-i. Uchida, H. Adachi, T. Kikkawa, A. Kirihara, M. Ishida, S. Yorozu, S. Maekawa, and E. Saitoh. Thermoelectric Generation Based on Spin Seebeck Effects. *Proc. IEEE*, **104**(10, SI):1946–1973 (2016)

[121] S. Bosu, Y. Sakuraba, K.-i. Uchida, K. Saito, T. Ota, E. Saitoh, and K. Takanashi. Spin Seebeck effect in thin films of the Heusler compound Co_2MnSi. *Phys. Rev. B*, **83**(22):224401 (2011)

[122] K.-i. Uchida, J. Xiao, H. Adachi, J.-i. Ohe, S. Takahashi, J. Ieda, T. Ota, Y. Kajiwara, H. Umezawa, H. Kawai, G. E. W. Bauer, S. Maekawa, and E. Saitoh. Spin seebeck insulator. *Nat. Mater.*, **9**(11):894 (2010)

decays over several hundred nanometers[123] while a magnon spin current can propagate over several millimeters.[124] When this is propagation to the interface of the ferromagnetic material, localized spins at the interface are excited and due to the $s-d$ exchange interaction the spin current can be injected into the nonmagnetic metal and therefore detected by the ISHE.[125]

In the standard SSE measurement geometry a nonmagnetic metal is deposited on top of the SSE generating magnetic layer, usually as a probing stripe with a finite width w in the direction of the gradient. An external magnetic field is utilized to align the magnetic moments in an in-plane direction. Then a temperature gradient is applied, preferably in the same direction, inducing a spin voltage across the interface to the nonmagnetic metal. Subsequently, this process induces a spin current I_s into the metal layer which is partially converted via the ISHE into a charge voltage

$$V_q = \theta_H |e| \cdot I_s \frac{\rho}{w}, \tag{1.128}$$

with the spin Hall angle θ_H and the electrical resistivity ρ of the metal. Here, the spatial dependence of the SHE is detectable by changing the position of the nonmagnetic metal stripe in relation to the SSE material.

In general, the SSE is induced by a non-equilibrium between the magnon system in the ferromagnetic material and the conduction electron system in the nonmagnetic material as discussed in the section 1.4.2 on the non-equilibrium magnetic proximity effects.

Furthermore, in an experimental SSE setup as discussed here additional an anomalous Nernst effect (ANE), referring to the generation of an electric voltage perpendicular to both the magnetization and an applied temperature gradient, might be present. For instance in a bilayer system featuring a nonmagnetic Pt layer covering an magnetic insulator, the distinctive magnetic proximity effect at the interface can yield an ANE contaminating the spin-current detection. Although this additional effect has been demonstrated to be small, e.g., in a YIG/Pt bilayer system,[126] methods have been developed to separate the voltage generated by the SSE from the ANE contribution and in particular from the ANE produced by spin polarized Pt based on the MPE.[127]

The longitudinal spin Seebeck effect

In the conventional setup for measuring the SSE, consisting of a ferromagnet and a nonmagnetic metal stripe attached to detect the thermally generated and injected spin current, the temperature gradient is applied in-plane in a direction perpendicular to the metal stripes. The spin current is injected in an out-of-plane direction and the spin-polarization vector is aligned parallel to the magnetization of the ferromagnetic material. The spin current is converted by the ISHE into an electric field along the direction of the stripes as discussed in the previous chapter. Thus, the direction of the detected

[123] F. Jedema, H. Heersche, A. Filip, J. Baselmans, and B. Van Wees. Electrical detection of spin precession in a metallic mesoscopic spin valve. *Nature*, **416**(6882):713 (2002)

[124] Y. Kajiwara, K. Harii, S. Takahashi, J.-i. Ohe, K.-i. Uchida, M. Mizuguchi, H. Umezawa, H. Kawai, K. Ando, K. Takanashi, S. Maekawa, and E. Saitoh. Transmission of electrical signals by spin-wave interconversion in a magnetic insulator. *Nature*, **464**(7286): 262 (2010)

[125] S. Takahashi, E. Saitoh, and S. Maekawa. Spin current through a normal-metal/insulating-ferromagnet junction. *J. Phys.: Conf. Ser.*, **200**(6): 062030 (2010)

[126] T. Kikkawa, K.-i. Uchida, Y. Shiomi, Z. Qiu, D. Hou, D. Tian, H. Nakayama, X.-F. Jin, and E. Saitoh. Longitudinal spin Seebeck effect free from the proximity Nernst effect. *Phys. Rev. Lett.*, **110**(6):067207 (2013)

[127] P. Bougiatioti, C. Klewe, D. Meier, O. Manos, O. Kuschel, J. Wollschläger, L. Bouchenoire, S. D. Brown, J.-M. Schmalhorst, G. Reiss, and T. Kuschel. Quantitative disentanglement of the spin Seebeck, proximity-induced, and ferromagnetic-induced anomalous Nernst effect in normal-metal–ferromagnet bilayers. *Phys. Rev. Lett.*, **119**(22):227205 (2017)

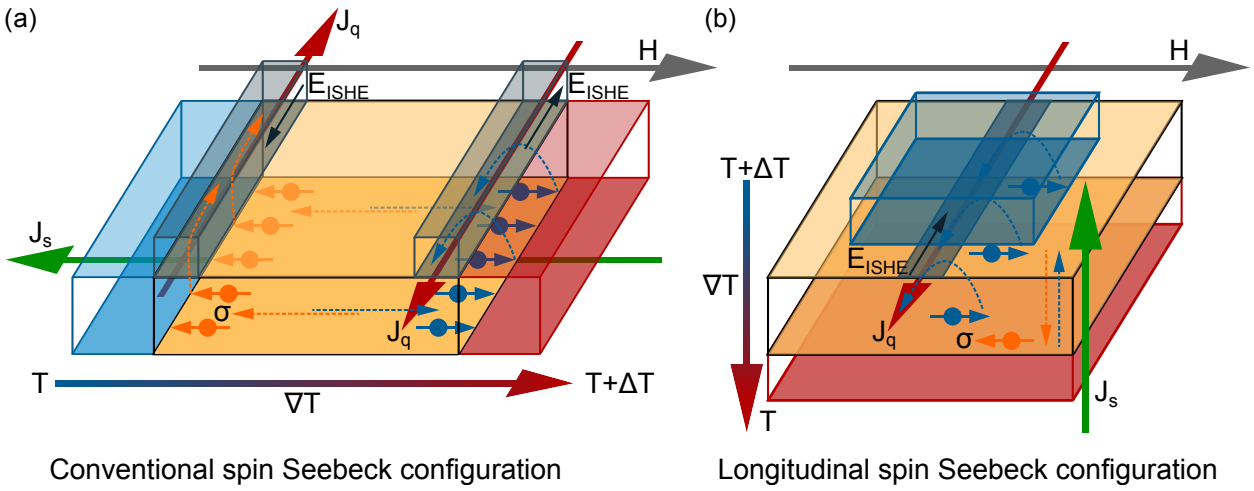

Figure 1.19: Illustration of the spin Seebeck effect in the (a) conventional and (b) longitudinal configuration. In both cases the temperature gradient ∇T excites a spin current in an antiparallel direction. Metal stripes on top are used for the detection of the thermally induced spin current, E_{ISHE} denotes the direction of the ISHE generated electromotive force in the stripes. The spin polarization vector σ of the spin current lies along the magnetization direction oriented by the external magnetic field $\vec{H}$. In the LSSE configuration, the temperature gradient ∇T is applied out-of-plane generating a direct flow of $\vec{J}_s$ into the detection layer.

spin current is perpendicular to the applied temperature gradient.

In contrast to this method, which was utilized for the primary observation of the SSE, in the longitudinal setup the thermally generated spin current is injected directly into the normal metal layer along an out-of-plane temperature gradient. This longitudinal SSE, first observed by Uschida *et al.* in the YIG/Pt system, is then detected by the ISHE in the metal in an equal measure.[128]

In order to generate a similar electromotive force by the ISHE, the sample has to be magnetized in a direction perpendicular to the temperature gradient. The LSSE setup technically only requires a bilayer thin film system consisting of a ferromagnet and a normal metal layer which makes it simple and more versatile in comparison to the conventional SSE setup. Therefore, the longitudinal setup has significantly extended the applicability of the SSE in the field of spin caloritronics in recent years.[129]

The conventional spin Seebeck setup, which was used for the first reports on this effect, is schematically illustrated in Fig. 1.19(a). Here, the temperature gradient ∇T is applied in-plane along the ferromagnetic layer exciting a pure spin current. However, in this configuration, the observed voltages can also be attributed to the LSSE generated by a contact induced parasitic out-of-plane temperature gradient, which depends on the material, interface area and temperature of the electrical contact tips or bonding wires on the attached metal stripes.[130] Thus, the LSSE induced spin current flows into these contacted, for instance, Pt stripes and is converted into a charge current by the ISHE.

In contrast, Fig. 1.19(b) shows the non-parasitic longitudinal spin Seebeck configuration, where the excited spin current is propagating directly into the detection layer deposited on the ferromagnetic layer. As discussed above, this provides a more robust detection of the spin current by the ISHE since an in-plane temperature gradient is insignificant allowing for the isolation of pure a SSE from other parasitic effects. Thus, the SSE is nowadays commonly used in the

[128] K.-i. Uchida, H. Adachi, T. Ota, H. Nakayama, S. Maekawa, and E. Saitoh. Observation of longitudinal spin-Seebeck effect in magnetic insulators. *Appl. Phys. Lett.*, **97**(17): 172505 (2010)

[129] K.-i. Uchida, M. Ishida, T. Kikkawa, A. Kirihara, T. Murakami, and E. Saitoh. Longitudinal spin Seebeck effect: from fundamentals to applications. *J. Phys. Condens. Matter.*, **26**(34): 343202 (2014); and Z. Li, J. Krieft, A. V. Singh, S. Regmi, A. Rastogi, A. Srivastava, Z. Galazka, T. Mewes, A. Gupta, and T. Kuschel. Vectorial observation of the spin Seebeck effect in epitaxial NiFe2O4 thin films with various magnetic anisotropy contributions. *Appl. Phys. Lett.*, **114**(23):232404 (2019)

[130] D. Meier, D. Reinhardt, M. van Straaten, C. Klewe, M. Althammer, M. Schreier, S. T. B. Goennenwein, A. Gupta, M. Schmid, C. H. Back, J.-M. Schmalhorst, T. Kuschel, and G. Reiss. Longitudinal spin Seebeck effect contribution in transverse spin Seebeck effect experiments in Pt/YIG and Pt/NFO. *Nat. Commun.*, **6**:8211 (2015)

longitudinal configuration especially to study metallic ferromagnetic thin film systems.

The PtMnSb half-Heusler material system

THE MANIPULATION OF THE MAGNETIZATION by SOTs has in recent years been studied on a large-scale due to its potential for efficiently writing information in magnetic memories. Thereby, a current induces a non-equilibrium spin-polarization, which is exchange coupled to the ordered local moments and exerts a torque depending on the systems crystal symmetry. In particular, attention is given to non-centrosymmetric systems with space inversion asymmetry, where SOTs emerge even in single-layer materials. The half-metallic half-Heusler PtMnSb is a promising candidate for further investigations of this intrinsic SOTs. This spin phenomenon is highly relevant for modern spintronic devices based on electrical switching of magnetic moments.

Half-Heusler compounds are magnetic inter-metallics with a face centered cubic (fcc) crystal structure and a composition of XYZ. The components X and Y are typically transition metals while component Z is usually from the p-block of the periodic table. These compounds exhibit properties which are generally not associated with the individual materials, as most famously shown for the first studied Heusler compound Cu_2MnAl[131] which is ferromagnetic at room temperature in contrast to the individual non-ferromagnetic elements.

[131] F. Heusler. Über magnetische Manganlegierungen. *Verh. Dtsch. Phys. Ges.*, **5**:219 (1903)

Many Heusler alloys have properties highly beneficial for spintronic applications, in particular ferro-, antiferro-, and ferrimagnetism, half- and semimetallicity, semiconductivity or even superconducting and topological characteristics. On these grounds the half-Heusler alloys have been subject of increased attention as a new material class for the study of spintronic effects in recent years.

Alternatively, the half-Heusler structure can be accurately described as a ternary stuffed variant of the classical electron closed-shell semiconductors which crystallize in a zincblende (ZnS-type) lattice as for instance GaAs. Hence, in the half-Heusler the eight valence electrons are distributed among three atoms instead of two while the third atom occupies the octahedral vacancies in the ZnS-type lattice. Consequently, this results in the formation of a rocksalt-like sublattice characterized by ionic bonding interaction.[132] The different crystal lattices involved in this sublattice relation are illustrated in Fig. 1.20.

[132] F. Casper, T. Graf, S. Chadov, B. Balke, and C. Felser. Half-Heusler compounds: novel materials for energy and spintronic applications. *Semicond. Sci. Tech.*, **27**(6):063001 (2012)

This graphic illustration includes the half-Heusler material PtMnSb which crystallizes in a non-centrosymmetric structure corresponding to the space group $F\bar{4}3m$. Within this structure, the Sb atoms are placed on the Wyckoff positions 4a $(0,0,0)$ and the Mn atoms on the 4b $(1/2,1/2,1/2)$ position to form the ionic NaCl-type sublattice as shown in the Fig. 1.20. In the same manner,

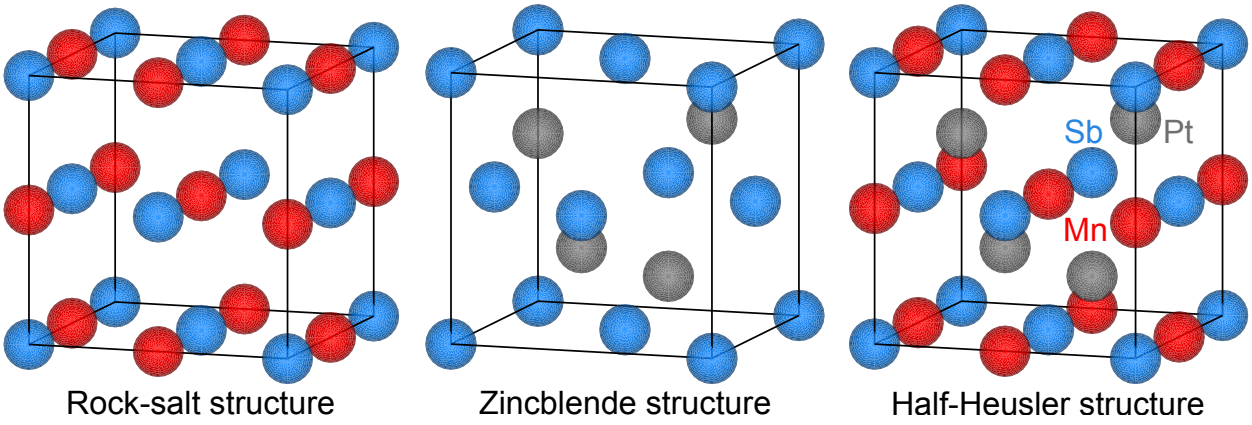

Figure 1.20: Half-Heusler materials are derived from a combination of the rocksalt-type and a zincblende-type lattice.

the Sb atoms on 4a and Pt atoms on 4c $(1/4, 1/4, 1/4)$ build the covalent ZnS-type structure which combines to the presented half-Heusler structure. The positioning of the atoms in this lattice structure is highly dependent on the size difference between the involved atoms and the inter atomic interaction which can be roughly characterized by an atom's electronegativity.[133]

Thus, PtMnSb actually crystallizes in a special atomic order for a half-Heusler compound where the most electropositive element Mn and the atom with intermediate electronegativity Sb forms the NaCl-type sublattice. Additionally, the Sb and the most electronegative element Pt form the covalent ZnS substructure.

It follows that in this structure the elements of the alloy are forming solid phases with four interlocking cubic face-centered crystal sublattices. Here, one sublattice is unoccupied in case of the XYZ half-Heusler system while the magnetism in this alloy is caused by a super-exchange mechanism between the neighboring magnetic atoms. The magnetic ions usually occupy the NaCl-sublattice and therefore their distance is rather large what facilitates a magnetic interaction based on a super-exchange mechanism. In this process, an electron can move between neighboring metal ions retaining its spin. This electron movement between the positions on the sublattices is made easier when no spin flip is needed for the electrons in order to correspond to Hund's rules in the final state of movement on the accepting lattice position.

This ability of electronic delocalization is usually accompanied by a reduction of the kinetic energy and thus energy minimization leads to a ferromagnetic alignment of neighboring magnetic atoms participating in the exchange process. In many Heusler materials as well as in the PtMnSb structure the magnetic ion in this process is manganese, which is placed at the centers of the cubic substructure.

SOTs in heavy metal/ferromagnet bilayers are used to electrically manipulate and switch the magnetization in the magnetic layer.[134] In particular, the SHE in the heavy metal layer as well as electron scattering at the interface[135] are responsible for transferring the spin-moment required for the SOT via a spin current from the

[133] T. Graf, C. Felser, and S. S. Parkin. Simple rules for the understanding of Heusler compounds. *Prog. Solid State Ch.*, **39**(1):1–50 (2011)

[134] I. M. Miron, K. Garello, G. Gaudin, P.-J. Zermatten, M. V. Costache, S. Auffret, S. Bandiera, B. Rodmacq, A. Schuhl, and P. Gambardella. Perpendicular switching of a single ferromagnetic layer induced by in-plane current injection. *Nature*, **476** (7359):189–193 (2011); L. Liu, C.-F. Pai, Y. Li, H. W. Tseng, D. C. Ralph, and R. A. Buhrman. Spin-torque switching with the giant spin Hall effect of tantalum. *Science*, **336**(6081):555–558 (2012); L. Neumann, D. Meier, J. Schmalhorst, K. Rott, G. Reiss, and M. Meinert. Temperature dependence of the spin Hall angle and switching current in the nc-W (O)/CoFeB/MgO system with perpendicular magnetic anisotropy. *Appl. Phys. Lett.*, **109**(14):142405 (2016); and C. O. Avci, A. Quindeau, C.-F. Pai, M. Mann, L. Caretta, A. S. Tang, M. C. Onbasli, C. A. Ross, and G. S. Beach. Current-induced switching in a magnetic insulator. *Nat. Mater.*, **16**(3): 309 (2017)

[135] V. P. Amin and M. D. Stiles. Spin transport at interfaces with spin-orbit coupling: Phenomenology. *Phys. Rev. B*, **94**:104420 (2016). DOI: 10.1103/PhysRevB.94.104420

heavy metal to the adjacent magnetic layer.

Materials with non-centrosymmetric spin configurations can even be electrically controlled by an intrinsic SOT without any additional heavy metal layer. This has recently been demonstrated in the field of antiferromagnetic spintronics for the room-temperature antiferromagnet CuMnAs.[136] In ferromagnetic crystals with broken inversion-symmetry, the inverse spin galvanic effect can generate current-induced fields to reversibly manipulate the magnetization.[137] In addition, the Rashba interaction induced by asymmetric interface layers or films lacking structure inversion symmetry makes this electrical method of magnetization manipulation a realistic candidate for room-temperature spintronic applications.[138]

Among these potential non-centrosymmetric crystals are several ferromagnetic Heusler compounds which are promising SOT candidates. For example, an intrinsic SOT has been found in the room-temperature ferromagnet half-Heusler compound NiMnSb.[139] This shows that this specific family of half-metal Heusler alloys with C1b structure is particularly interesting for SOT studies because of their robust magnetic properties and lack of inversion symmetry.

Based on these considerations, co-sputter-deposited thin films of the room-temperature ferromagnet PtMnSb, which belongs to the same Heusler class of materials,[140] have been prepared and investigated in this work. Using symmetry arguments regarding the crystal structure in connection with *in principle* analogies, which can be found in related microscopic calculations, one can expect a large intrinsic SOT.

PtMnSb thin films were first studied in the early 1980s in the form of magnetooptical recording media,[141] due to their very large magnetooptical Kerr effect.[142] At that time the PtMnSb system has been reported to show the highest magnetooptical Kerr effect at room temperature of all so far known metallic systems and thus has been subject to broad study since it represented a promising candidate for magnetooptical recording.

As result of this studies, the electronic structure of PtMnSb as well as of isoelectronic Heusler compounds like NiMnSb or PdMnSb has been subject to investigation. As a consequence, this directly led to the prediction of the first half-metallic ferromagnetic material (NiMnSb) by de Groot *et al.* in 1983.[143] Here, a half-metal defined as a material which acts as a conductor to electrons of only one spin orientation while it is an insulator or semiconductor for electrons of the opposite spin orientation. In other words, the valence band in a half-metal is partially filled for one spin orientation as in a common metal whereas a gap between a full valence and an empty conduction band exists in the density of states for the other spin orientation resulting in a conducting behavior only for either the majority or minority spin channel. In the NiMnSb system a minority band gap is formed by the *d* states inside a larger band gap of the NiSb-substructure according to the results of theoretical

[136] T. Jungwirth, X. Marti, P. Wadley, and J. Wunderlich. Antiferromagnetic spintronics. *Nat. Nanotechn.*, **11** (3):231–241 (2016); and P. Wadley, B. Howells, J. Železnỳ, C. Andrews, V. Hills, R. P. Campion, V. Novák, K. Olejník, F. Maccherozzi, S. S. Dhesi, S. Y. Martin, T. Wagner, J. Wunderlich, F. Freimuth, Y. Mokrousov, J. Kuneš, J. S. Chauhan, M. J. Grzybowski, A. W. Rushforth, K. W. Edmonds, B. L. Gallagher, and T. Jungwirth. Electrical switching of an antiferromagnet. *Science*, **351**:587–590 (2016)

[137] S. D. Ganichev, E. L. Ivchenko, V. V. Bel'Kov, S. A. Tarasenko, M. Sollinger, D. Weiss, W. Wegscheider, and W. Prettl. Spin-galvanic effect. *Nature*, **417**(6885):153–156 (2002); and A. Y. Silov, P. A. Blajnov, J. H. Wolter, R. Hey, K. H. Ploog, and N. S. Averkiev. Current-induced spin polarization at a single heterojunction. *Appl. Phys. Lett.*, **85**(24):5929–5931 (2004)

[138] A. Chernyshov, M. Overby, X. Liu, J. K. Furdyna, Y. Lyanda-Geller, and L. P. Rokhinson. Evidence for reversible control of magnetization in a ferromagnetic material by means of spin–orbit magnetic field. *Nat. Phys.*, **5**(9):656–659 (2009); and I. M. Miron, G. Gaudin, S. Auffret, B. Rodmacq, A. Schuhl, S. Pizzini, J. Vogel, and P. Gambardella. Current-driven spin torque induced by the Rashba effect in a ferromagnetic metal layer. *Nat. Mater.*, **9**(3):230–234 (2010)

[139] C. Ciccarelli, L. Anderson, V. Tshitoyan, A. J. Ferguson, F. Gerhard, C. Gould, L. W. Molenkamp, J. Gayles, J. Železnỳ, L. Šmejkal, Z. Yuan, J. Sinova, F. Freimuth, and T. Jungwirth. Room-temperature spin-orbit torque in NiMnSb. *Nat. Phys.*, **12**: 855–860 (2016)

[140] K. Watanabe. On New Ferromagnetic Intermetallic Compounds PtMnSn and PtMnSb. *J. Phys. Soc. Jap.*, **28**(2):302–307 (1970); and R. A. De Groot, F. M. Mueller, P. G. Van Engen, and K. H. J. Buschow. New class of materials: half-metallic ferromagnets. *Phys. Rev. Lett.*, **50**(25):2024 (1983)

[141] P. G. Van Engen, K. H. J. Buschow, R. Jongebreur, and M. Erman. PtMnSb, a material with very high magneto-optical Kerr effect. *Appl. Phys. Lett.*, **42** (2):202–204 (1983)

[142] H. Akasaka and M. Sato. Process and apparatus for simultaneous erasure and recording in magneto-optical recording, (1989). US Patent 4,853,912

[143] R. A. De Groot, F. M. Mueller, P. G. Van Engen, and K. H. J. Buschow. New class of materials: half-metallic ferromagnets. *Phys. Rev. Lett.*, **50**(25): 2024 (1983)

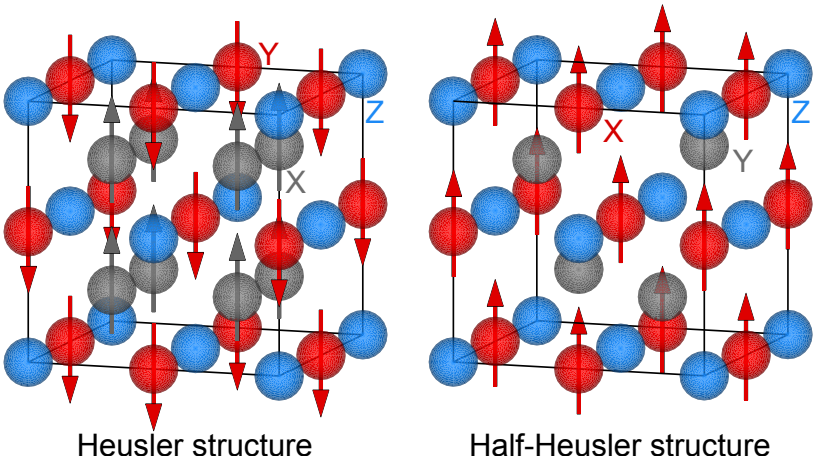

Figure 1.21: The Heusler structure (X_2YZ) manifests two magnetic sublattices which are either ferromagnetically or antiferromagnetically coupled as displayed here. Only one magnetic sublattice exists in the Half-Heusler structure (XYZ) since only the atoms on the octahedral sites exhibit a localized magnetic moment.

band structure calculations. These also indicate a Mn character of the spin-polarized states at the Fermi level.[144] Thus, the origin of the half-metallic characteristics of this group of half-Heusler materials is a strong d-band hybridization regarding the two transition elements, resulting in a large band gap between the bonding and antibonding degenerates.[145]

Within the bulk NiMnSb system, a fully spin-polarized state has been experimentally determined, however at the surface due to the segregation of Mn atoms and the elevated oxygen affinity the system loses it half-metallic characteristics.[146] This half-metallic band structure and the consequential high spin polarization is advantageous for the design of magnetoresistance applications. Since the systems are isoelectronic one has to assume that the local magnetic moments in the PtMnSb half-Heusler are distributed in a similar way as for the NiMnSb structure. However, the Pt does primarily not carry any magnetic moment in contrast to the Ni atoms and the band structure is not indicating anomalous magnetic structures.

The NiMnSb system was studied using magnetic circular dichroism which revealed that the major portion of the magnetic moment is located at the Mn site. Furthermore, a reduction of the Mn as well as the Ni moments was observed around 80 K indicating a loss of coupling between Mn and Ni.[147] For a comparison of both half-Heusler systems the higher nuclear charge of Pt with respect to Ni has to be considered. This leads to an energy shift of the minority spin electrons due to relativistic effects which have to be carefully accounted for when performing band structure calculations.[148]

In general, the half-Heulser materials feature only one magnetic sublattice since merely the atoms on the octahedral sites carry a magnetic moment. This aspect is illustrated in Fig. 1.21 where the magnetic structure of a regular Heulser is compared to the half-Heusler structure exhibiting only one magnetic sublattice.

Magnetic half-Heusler materials can only be found when the X site is occupied by Mn or an rare earth material since the rare earth

[144] H. C. Kandpal, C. Felser, and R. Seshadri. Covalent bonding and the nature of band gaps in some half-Heusler compounds. *J. Phys. D: Appl. Phys.*, **39**(5):776 (2006)

[145] I. Galanakis, P. Mavropoulos, and P. H. Dederichs. Electronic structure and Slater–Pauling behaviour in half-metallic Heusler alloys calculated from first principles. *J. Phys. D: Appl. Phys.*, **39**(5):765 (2006)

[146] G. Bona, F. Meier, M. Taborelli, E. Bucher, and P. Schmidt. Spin polarized photoemission from NiMnSb. *Solid State Commun.*, **56**(4):391–394 (1985); and K. Hanssen, P. Mijnarends, L. Rabou, and K. Buschow. Positron-annihilation study of the half-metallic ferromagnet NiMnSb: Experiment. *Phys. Rev. B*, **42**(3):1533 (1990)

[147] C. Borca, T. Komesu, H.-K. Jeong, P. A. Dowben, D. Ristoiu, C. Hordequin, J. Nozieres, J. Pierre, S. Stadler, and Y. Idzerda. Evidence for temperature dependent moments ordering in ferromagnetic NiMnSb (100). *Phys. Rev. B*, **64**(5):052409 (2001)

[148] J. Wijngaard, C. Haas, and R. De Groot. Origin of the difference in the magneto-optical Kerr effect between PtMnSb and NiMnSb. *Phys. Rev. B*, **40**(13):9318 (1989)

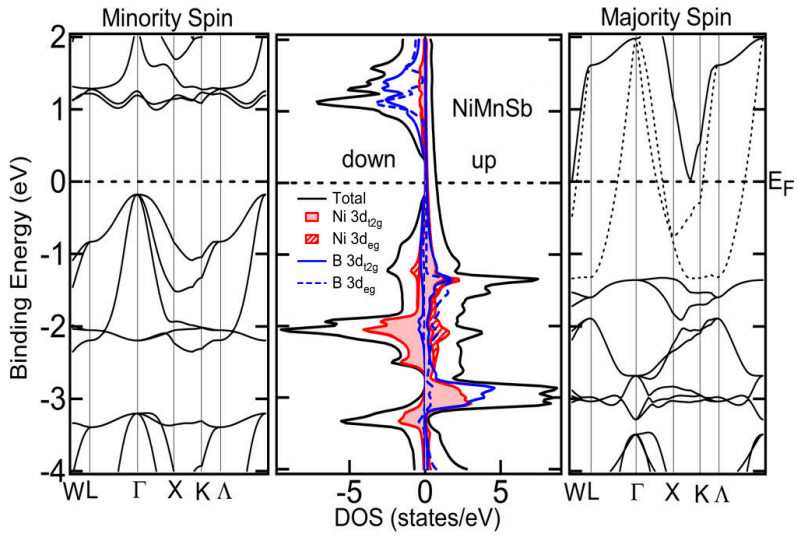

Figure 1.22: The spin-polarized total DOS and band structure (black line) as well as atom projected DOS of NiMnSb in the cubic lowest energy structure. The atom projected DOS of the Ni atom is plotted with red color (solid line for Ni $3d_{t2g}$, dashed line for Ni $3d_{eg}$) and that of the B atom (Mn) is plotted in blue solid (B $3d_{t2g}$) and dashed lines (B $3d_{eg}$). Bands crossing the E_F are plotted in dotted lines. DOS calculation from [Baral and Chakrabarti, 2019].

materials are strongly localized and do not contribute to the density of states at the Fermi level and due to the localized nature of the $3d$ and $4f$ electrons of Mn, which carry the magnetic moment.[149] However, a minor induced magnetic moment can be determined experimentally on Nickel in the NiMnSb half-Heusler and on the late transition metals like Platinum in general.

In contrast, the full Heusler compounds can exhibit different magnetic structures. Due to the two different magnetic substructures ferromagnetic, ferrimagnetic, and antiferromagnetic Heusler compounds can be found.[150] This is due to the fact that the two X atoms are occupying the tetrahedral sites and thus are enabling a magnetic interaction between these X atoms and in consequence facilitate the formation of a second magnetic sublattice as seen in Fig. 1.21 which can be more delocalized.

The spin-polarized valence-band density of states (DOS) and corresponding band structure of the NiMnSb alloy is presented in Fig. 1.22. In the spin-up channel, shown on the right side of the figure, the DOS at the Fermi energy and at higher binding energy is essentially composed of $3d_{t2g}$ states of Ni and Mn. The states close to the Fermi energy are consisting of both $3d_{eg}$ and $3d_{t2g}$ states of Ni and Mn. With regard to the band structure, this calculation by Baral *et al.* shows a three-fold degeneracy and highly dispersive spin-up bands which cross the Fermi level at more than one K point in the Brillouin-zone and features a pronounced gap in the spin-down band. The spin-polarized band structure reveals that the half-metallic gap, which is defined as the energy between the Fermi level and the maximum value of the valence band energy, is about 0.15 eV. The energy difference between the valence-band maximum and the conduction-band minimum for the minority spin is the so called spin-down gap which is about 0.46 eV for NiMnSb according to the *ab initio* study presented in Fig. 1.22. These values are in good agreement with various other band-structure and DOS

[149] T. Graf, C. Felser, and S. S. Parkin. Simple rules for the understanding of Heusler compounds. *Prog. Solid State Ch.*, **39**(1):1–50 (2011)

[150] J. Balluff, K. Diekmann, G. Reiss, and M. Meinert. High-throughput screening for antiferromagnetic Heusler compounds using density functional theory. *Phys. Rev. Mater.*, **1**(3): 034404 (2017)

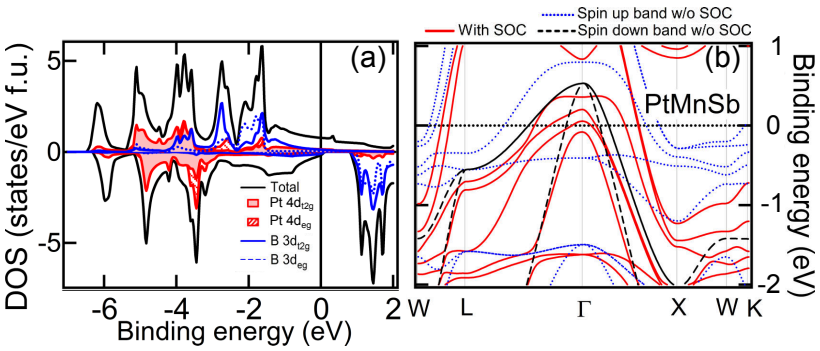

Figure 1.23: (a) The spin-polarized total DOS and the atom projected DOS of PtMnSb in the cubic lowest energy structure without including spin-orbit interaction. The total DOS (solid black) and the atom projected DOS of the Pt atom are plotted (solid red for Pt $4d_{t2g}$ and dashed red for Pt $4d_{t2g}$). The DOS of the B atom (Mn) is plotted in blue solid (B $3d_{t2g}$) and dashed lines (B $3d_{eg}$). (b) The band structure of PtMnSb with and without including spin-orbit interaction. The spin-up and spin-down bands without spin-orbit interaction are plotted with a blue dashed line and black dashed line and the bands with spin-orbit interaction are plotted with a solid red line. DOS and band structure calculation from [Baral and Chakrabarti, 2019].

calculations within literature.[151]

The detailed analysis of magnetic and electronic NiMnSb structure shows that this material is fully spin polarized in the cubic lowest energy phase. However, this value can be reduced significantly with tetragonal distortion and thus it is important to counter possible lattice distortion to maintain half-metallic and magnetic properties to make half-Heusler materials applicable for spintronic devices. Due to the addressed similarities these results for the NiMnSb half-Heusler allows also to draw conclusions regarding structural, electronic, and magnetic properties when equivalent calculations and methods of analysis are applied. In comparison, only few theoretical works deal with *ab initio* calculations of Pt-based alloys, yet PtMnSb has been under investigation due to its history regarding the magnetooptical Kerr effect.[152]

However, it is important to notice that the results of first-principles calculations for this specific alloy are controversially discussed. The first band-structure calculation by de Groot *et al.* based on an augmented-spherical-wave method resulted in the characteristics of a fully half-metallic ferromagnet.[153] These results were backed by band-structure calculation performed by Ebert *et al.* utilizing a linear muffin-tin-orbital (LMTO) approach[154] and further self-consistent tight-binding calculations within the atomic-sphere approximation by Offernes *et al.* studying typical half-Heusler phase.[155] Considered together, these conclusions partially contradict the most recent *ab initio* study of PtMnSb by Baral *et al.* which are presented in Fig. 1.23.

Based on first-principles calculations this graphic shows spin-polarized total DOS and band structure of PtMnSb. Studies of the detail the electronic structure of Pt-based cubic lowest energy structure alloys like the one presented here reveal that these have primarily metallic characteristics. The width of the valence band is about 6.6 eV and near the Fermi level E_F the spin-up DOS is mainly build up of the $3d_{t2g}$ and $3d_{eg}$ states of the manganese atoms as well as a tiny contribution from the higher platinum states. The band gap in this study is located hardly above the Fermi level which classifies this half-Heusler as metallic in nature. This is in accordance with LMTO method calculations by Galanakis *et al.*

[151] I. Galanakis, P. Dederichs, and N. Papanikolaou. Origin and properties of the gap in the half-ferromagnetic Heusler alloys. *Phys. Rev. B*, **66**(13): 134428 (2002); M. Ghimire, Sandeep, T. Sinha, and R. Thapa. First principles study of the electronic and magnetic properties of semi-Heusler alloys NiXSb (X= Ti, V, Cr and Mn). *J. Alloys Compd.*, **509**(41):9742–9752 (2011); and Y. Wu, B. Wu, Z. Wei, Z. Zhou, C. Zhao, Y. Xiong, S. Tou, S. Yang, B. Zhou, and Y. Shao. Structural, half-metallic and elastic properties of the half-Heusler compounds NiMnM (M= Sb, As and Si) and IrMnAs from first-principles calculations. *Intermetallics*, **53**: 26–33 (2014)

[152] P. G. Van Engen, K. H. J. Buschow, R. Jongebreur, and M. Erman. PtMnSb, a material with very high magneto-optical Kerr effect. *Appl. Phys. Lett.*, **42** (2):202–204 (1983)

[153] R. A. De Groot, F. M. Mueller, P. G. Van Engen, and K. H. J. Buschow. New class of materials: half-metallic ferromagnets. *Phys. Rev. Lett.*, **50**(25): 2024 (1983)

[154] H. Ebert and G. Schütz. Theoretical and experimental study of the electronic structure of PtMnSb. *J. Appl. Phys.*, **69**(8):4627–4629 (1991)

[155] L. Offernes, P. Ravindran, and A. Kjekshus. Electronic structure and chemical bonding in half-Heusler phases. *J. Alloys Compd.*, **439**(1-2):37–54 (2007)

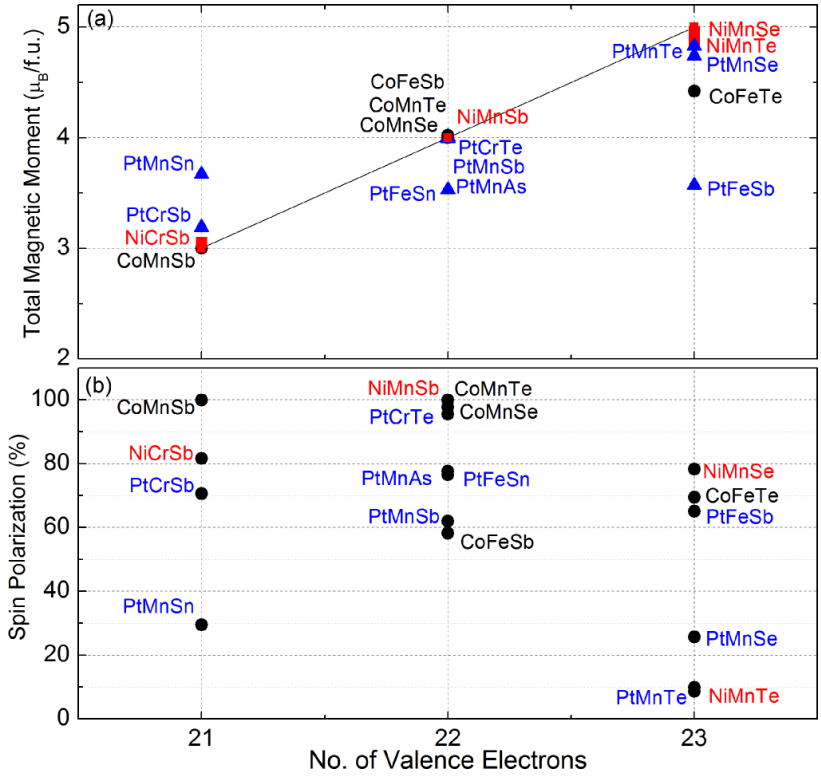

Figure 1.24: The total magnetic moment (a) and spin polarization of various half-Heusler alloys in cubic lowest energy structures (b) as a function of total number of valence electrons per formula unit adopted from [Baral and Chakrabarti, 2019].

showing that the spin-down gap is located shortly above the Fermi level.[156]

However, investigations by Habbak *et al.* based on first-principles DFT with the full potential local orbital method using the local spin-density approximation as the exchange-correlation potential indicate that PtMnSb is half-metallic with spin-down band gap 0.832 eV and a magnetic moment of $4\,\mu_B$. Utilizing the general gradient approximation, PtMnSb is not found to be half-metallic in this study. Therefore, it depends on the exact parameters of the first-principles calculations, e.g. the approximation used for the exchange-correlation functional, whether this half-Heusler is considered metallic or half-metallic in theory. The calculation presented here in Fig. 1.23 is based on the full potential method and is close agreement with two previously mentioned *ab initio* studies.

With regard to the band structure of PtMnSb it turns out that the spin-orbit coupling (SOC) has a significant effect near the Fermi level. The SOC generates a split of the threefold degenerate spin-down bands above the Fermi level which are divided into one band below E_F the other two above the Fermi level (cf. Fig. 1.23(b)). This band-structure calculation suggests that the PtMnSb system is metallic with or without including SOC which is not conform with additional band-structure calculations by Youn *et al.*, investigating the electronic structures and Fermi surfaces, showing that PtMnSb is in a half-metallic state under the premise that SOC is included into the calculation. In this study semi-relativistic calculation

[156] I. Galanakis, P. Dederichs, and N. Papanikolaou. Origin and properties of the gap in the half-ferromagnetic Heusler alloys. *Phys. Rev. B*, **66**(13): 134428 (2002)

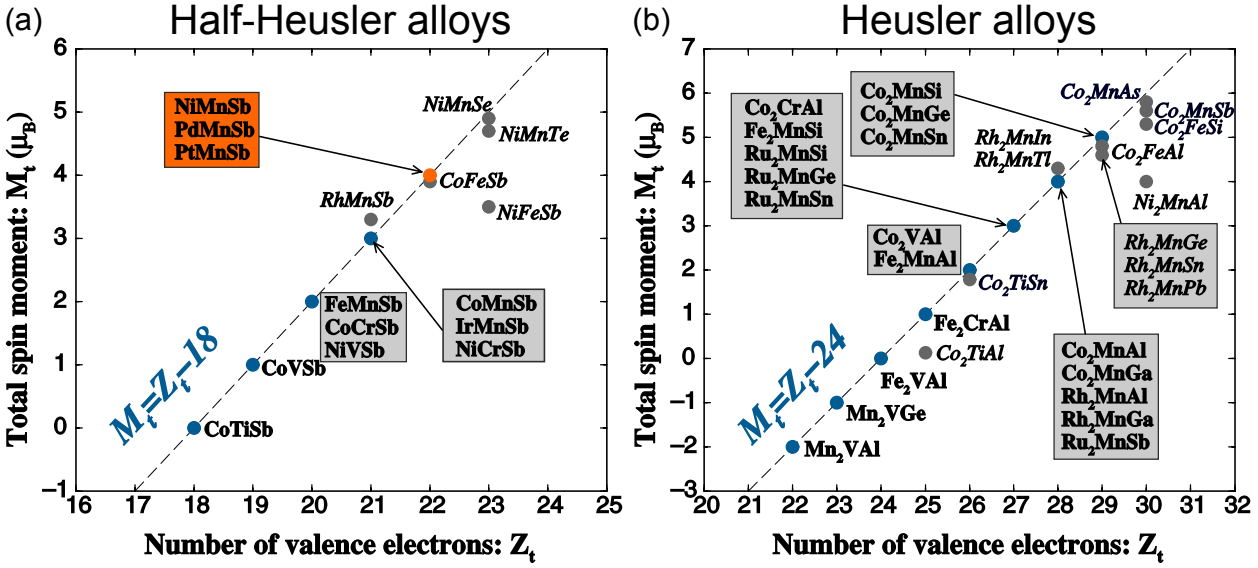

Figure 1.25: Calculated total spin moment per unit cell as a function of the total number Z_t of valence electrons per unit cell for various half (a) and full (b) Heusler alloys. The dashed line represents the Slater-Pauling behavior. Modified figure from [Galanakis et al., 2006].

yield a normal-metallic PtMnSb in a total energy LMTO method approach but PtMnSb becomes half-metallic once the spin-orbit interaction is explicitly taken into account. Therefore, the effects of the spin-orbit interaction on the band structure and Fermi surface are found to be substantial in PtMnSb.[157]

The total spin magnetic moment and spin polarization as a function of the number of valence electrons of the energetically stable half-Heusler alloys is illustrated in Figs. 1.24(a) and (b), respectively. In these systems, a ferromagnetic configuration is assumed, where the moments of the atoms on the different sites are oriented in the same direction. In the study referred to here, the total moments of these alloys are calculated to be exactly or very close to $3\,\mu_B$, $4\,\mu_B$, or $5\,\mu_B$ corresponding to the number of valence electrons and thus scaling linearly with the atomic number half-metallic alloys. In these materials, for instance in the PtMnSb structure, the atom on the Mn position usually carries the maximum magnetic moment while the total magnetic moment follows the Slater-Pauling rule.[158]

Figure 1.25(a) shows a general scheme of the spin magnetic moments per formula unit for the half-Heusler alloys calculated by Galanakis *et al.* which is presented as a function of the total number of valence electrons. The dashed line represents the Slater-Pauling behavior for the total spin moment $M_t = Z_t - 18$ obeyed by most half-Heusler compounds. In this plot, obtained by relativistic calculations with full-potential version of the screened Korringa-Kohn-Rostoker (KKR) method,[159] the value $M_t = 0$ corresponds to the semi-conducting phase and the value $M_t = 5\,\mu_B$ to the maximal moment when all five majority d states are filled. This work shows that all Mn based half-Heuslser compounds, highlighted in Fig. 1.25(a), have a total spin moment which scales accurately with the total charge. For the sake of completeness, Fig. 1.25(b) illustrates the Slater-Pauling behavior of full Heusler alloys.

[157] S. Youn and B. Min. Effects of the spin-orbit interaction in Heusler compounds: Electronic structures and Fermi surfaces of NiMnSb and PtMnSb. *Phys. Rev. B*, **51**(16):10436 (1995)

[158] I. Galanakis, P. Mavropoulos, and P. H. Dederichs. Electronic structure and Slater–Pauling behaviour in half-metallic Heusler alloys calculated from first principles. *J. Phys. D: Appl. Phys.*, **39**(5):765 (2006)

[159] N. Papanikolaou, R. Zeller, and P. Dederichs. Conceptual improvements of the KKR method. *J. Phys. Condens. Matter*, **14**(11):2799 (2002)

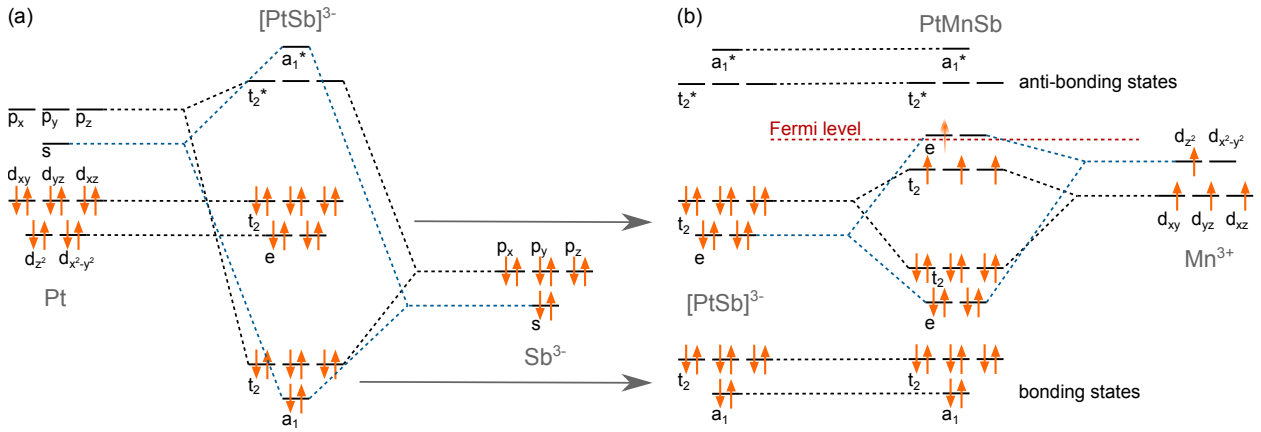

Figure 1.26: Schematic illustration of the hybridization of PtMnSb. (a) The covalent zinc blende sublattice $[PtSb]^{3-}$ is formed from the atomic Pt and Sb states. These $[PtSb]^{3-}$ hybrid orbitals then interact with the Mn^{3+} states shown in (b) forming two sets of bonding and anti-bonding orbitals. In case PtMnSb is found to be a half-metallic ferromagnet it is energetically favorable to single occupy the anti-bonding hybrid orbitals close to the Fermi level, giving rise to a magnetic moment of $4\,\mu_B$. Otherwise, if not only majority Mn d states are observed, the single occupancy of the hybrid orbitals close to E_F dissolves leading to a lower spin polarization at the Fermi level as indicated by the fading spin state in (b).

Furthermore, based on this method, the spin polarization P at the Fermi level and in the middle of the spin-down gap (E_M) can be calculated. For PtMnSb these turn to be a spin polarization $P = 66.5\,\%$ at E_F and a spin polarization of $P = 94.5\,\%$ in the middle of the gap.[160] This confirms that the alloy PtMnSb exhibits a spin-down gap but is not half-metallic since the Fermi level is slightly below the gap. This is in relative good agreement with the study constituting Fig. 1.24 where the total moment of PtMnSb likewise is presented to be $4\,\mu_B$ and the spin polarization at E_F is calculated to be shortly above 60 %.

The spin magnetic moments at the different lattice sites in PtMnSb can be estimated based on the atom-projected DOS. Therefore, the spin-projected charge density inside every Wigner-Seitz polyhedron containing the atom can be integrated within the KKR method. These polyhedra are the same for every atom in the C1b structure and yield spin magnetic moments of 0.092:3.889:-0.081 for the Pt:Mn:Sb sites in the half-Heulser structure where Pt is ferromagnetically coupled to Mn with a small induced magnetic moment, while the Sb atom is antiferromagnetically coupled to the Mn.[161] Additionally, the hybridization between the neighboring Mn atoms is weak due to the large atomic distance of about 4 Å in these half-Heusler alloys. Thus, the unoccupied minority-spin state band-width is viewed as to be rather narrow in PtMnSb.

Here, a model based on a molecular orbital approach is useful to visualize the explicit electronic structure of PtMnSb and understand the interactions of the Mn d states which determine the magnetic characteristics. Therefore, the hybridization of the atoms that occupy the positions in the zinc blende sublattice is the starting point in a close examination of the majority and minority Mn d states. This process is illustrated in Fig. 1.26(a) where the s and the p states of Pt and Sb hybridize so they are able to create one set of bonding and one set of anti-bonding a_1 and t_2 orbitals manifesting in the shown [PtSb]-substructure.

Here, the s and p states of Sb are fully occupied and hybridize with the unoccupied s and p states of Pt to generate a lower energy

[160] I. Galanakis, P. Mavropoulos, and P. H. Dederichs. Electronic structure and Slater–Pauling behaviour in half-metallic Heusler alloys calculated from first principles. *J. Phys. D: Appl. Phys.*, **39**(5):765 (2006)

[161] I. Galanakis, P. Dederichs, and N. Papanikolaou. Origin and properties of the gap in the half-ferromagnetic Heusler alloys. *Phys. Rev. B*, **66**(13): 134428 (2002)

set of bonding a_1 and triple-degenerated t_2 orbitals just as a set of unoccupied high-energy anti-bonding a_1^* and triple-degenerated t_2^* orbitals. The 5*d* orbitals of Pt show the octahedral splitting yet those orbitals are not forming hybrid orbitals with antimony. The $[PtSb]^{3-}$ substructure created by this chemical bonding then interacts with the Mn^{3+} ion states.

The fully occupied 5*d* orbitals of Pt form two sets of double degenerate *e* and triple degenerate *t* orbitals together with the empty Mn 3*d* orbitals as depicted in the center of Fig. 1.26(b). One of these sets has a bonding and one an anti-bonding character resulting in a covalent interaction. The bonding orbitals are doubly occupied and therefore filled with a total of 18 valence electrons. In the case of the half-metallic PtMnSb state the remaining four valence electrons are located in the anti-bonding hybrid orbitals in an energetically favorable state of single occupation. These four unpaired electrons near the Fermi level correspond magnetic moment of $4\,\mu_B$.

This hybridization scheme can be confirmed by theoretical calculations which show that the valence band has Pt character for both spin directions and only majority Mn *d* states are observed yet the conduction band exhibits also minority Mn *d* states. This is presented in the spin-polarized total DOS shown in Fig. 1.23(a). In combination the hybridization and band structure calculation result in a justified single occupancy of the hybrid orbitals yielding a high spin polarization at the Fermi level up to 100 % in case of a half-metallic behavior. However, as discussed above, depending of the method of DOS and band structure calculation, not only majority Mn *d* states are observed (cf. Fig. 1.23). This affects the magnetic moment of the PtMnSb alloy which has evidently been found both, slightly lower and marginally above the integer value which is in agreement with the nearly and fully half-ferromagnetic character of PtMnSb.

Since the total magnetic moment is merely the difference between the number of spin-up occupied states and the spin-down occupied states, the single occupancy of the hybrid orbitals close to E_F starts to fade out in the nearly half-metallic state as indicated by the blurred spin state in Fig. 1.23(b) going along with a lower spin polarization at the Fermi level. A simplified schematic density of states of PtMnSb in a d^4 configuration, referring to the occupied *d*-states located at the Fermi level, is shown in Fig. 1.27.

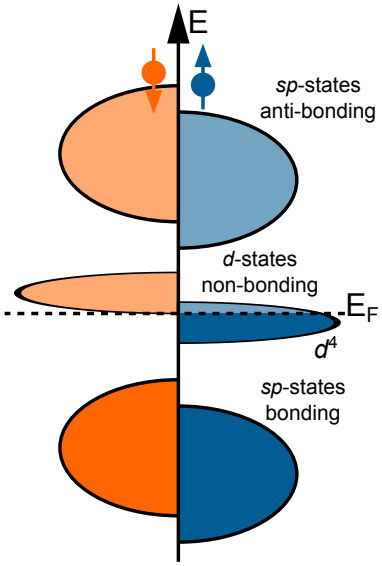

Figure 1.27: Schematic DOS of PtMnSb in a d^4 configuration with a rare band structure which is insulating in the minority but metallic in the majority spin band.

The Pt 5*d* states present a splitting between the d_{z^2} and $d_{x^2-y^2}$ orbitals in relation to the d_{xy}, d_{yz} and d_{xz} orbitals which is typical for a tetrahedral surrounding. These formed states then create hybrid orbitals with the 3*d* states of the Mn atom resulting in two sets of *e* and t_2 orbitals. Subsequently, the $d_{x^2-y^2}$ and d_{z^2} orbitals are able to couple and produce a pair of degenerate bonding and anti-bonding *e* orbitals. In the same manner, the d_{xy}, d_{yz} and d_{xz} orbitals results in two sets of triple-degenerated t_2 orbitals as displayed in Fig. 1.26(b). The band gap which is created this way

is responsible for the half-metallic properties whereat a minor case of atomic disorder can significantly change the density of states in the vicinity of the Fermi level. This can precede a loss of the half-metallic properties and alter the prevailing magnetism.

These calculated values are to be checked experimentally since the literature regarding PtMnSb *ab initio* calculations is at least debatable as discussed here since the results differ depending on methods of calculation within the density functional theory, the validity of approximations as well as the effects of spin-orbit coupling. For example, the values of the spin magnetic moment at the Mn site are obtainable via experiments of Kimura *et al.* by performing sum rule calculations based on their x-ray magnetic circular dichroism spectra.[162]

Based on the band structure calculation by Youn *et al.* they refer to the spin-polarized DOS of PtMnSb indicating a large intra-atomic exchange splitting of the Mn 3*d* states which results in an almost occupied majority- and just as unoccupied minority-spin state as presented above. The obtained values for the number of 3*d* electrons is $n_d = 5.36$ and the magnetic moment of the Mn 3*d* states is $3.78\,\mu_B$ per Mn atom. The sign of the magnetic circular dichroism (MCD) result in this work suggests an induced magnetic moment on the Pt site where the Pt 5*d* orbital is parallel to the majority Mn 3*d* state. Information about the orbital angular momentum were obtained utilizing the magnetic sum rules. The estimated value is reported to be less than 0.05 of the obtained spin angular momentum which is expected since the majority-spin state of the Mn 3*d* state is almost occupied as already discussed.

The total photoelectron yield XAS and MCD spectra in the Mn 2*p* core (L_2 and L_3) excitation regions of a PtMnSb bulk sample are presented in Fig. 1.28 as recorded by Kimura *et al.* with a magnetic field of $\sim 1.1\,T$ applied to the sample. Clear multiplet structures have been found in the Mn 2*p* x-ray absorption spectra of PtMnSb as show by the spectrum as well as sharp peak structure and a doublet structure at the Mn $2p_{3/2}$ and $2p_{1/2}$ core excitation energies. Furthermore, a shoulder structure can be observed in the antiparallel measurement configuration on the larger energy side of the $2p_{3/2}$ peak. In the dichroism spectrum a distinctive positive signal is followed by a small negative one at the L_3 edge and a small negative signals with double-peak structures can be found following the L_2 absorption edge. This common features can also be observed in the Mn 2*p* x-ray absorption spectra of gas-phase Mn and impurity Mn diluted in noble-metal hosts.[163] The application of sum rules to this spectrum yields a Mn spin moment of $4.02\,\mu_B$ for PtMnSb agreeing nicely with the calculated results and the nearly half-ferromagnetic character.

The Figs. 1.29 and 1.30 visualize the calculated Mn 2*p* and Mn 3*p* XAS and XMCD spectra for the Mn various transition playing a key role in generating the measured XMCD spectra of PtMnSb exemplarily depicted in Fig. 1.28 at the L_2 and L_3 edge and M_2 and

[162] A. Kimura, S. Suga, T. Shishidou, S. Imada, T. Muro, S.-Y. Park, T. Miyahara, T. Kaneko, and T. Kanomata. Magnetic circular dichroism in the soft-x-ray absorption spectra of Mn-based magnetic intermetallic compounds. *Phys. Rev. B*, **56**(10):6021 (1997)

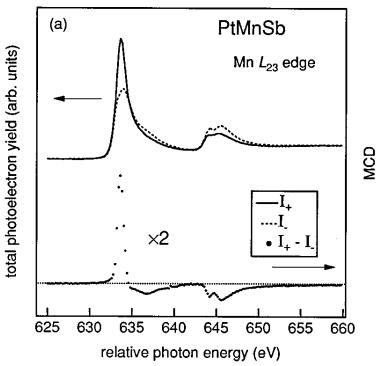

Figure 1.28: Mn 2*p* XAS and MCD spectra of PtMnSb. The solid curve (dashed curve) indicates the absorption intensity with the directions between the magnetization and the photon spin parallel (antiparallel) as denoted by I_+ (I_-). The dots show the MCD spectrum. From [Kimura et al., 1997].

[163] U. Arp, F. Federmann, E. Kallne, B. Sonntag, and S. Sorensen. Absorption resonances in the 2*p* threshold of manganese atoms. *J. Phys. B*, **25**(18): 3747 (1992)

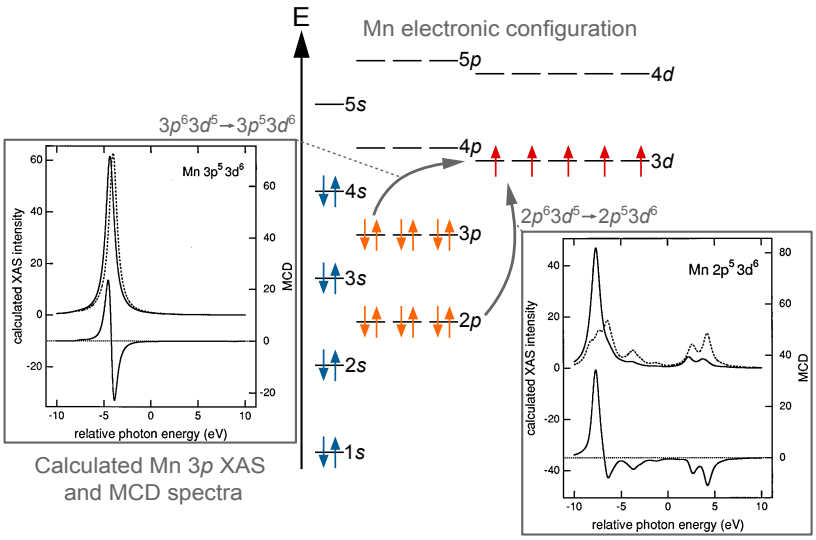

Figure 1.29: Calculated Mn $2p$ and Mn $3p$ XAS and MCD spectra for the Mn $2p^63d^5 \rightarrow 2p^53d^6$ transition (on the right) as well as the $3p^63d^5 \rightarrow 3p^53d^6$ transition (on the left), where the solid (dashed) curve indicates the I_+ (I_-) spectrum. The lower curve represents the MCD spectrum ($I_+ - I_-$) in both cases. The presented multiplet spectra have been calculated by [Kimura et al., 1997] under the assumption of a magnetized high-spin Mn $3d^5$ configuration in the ground state. The electronic transitions and the spin state, corresponding to the configuration of a Mn atom in the ground state ([Ar]$3d^54s^2$) are schematically illustrated .

M_3 edge, respectively, exhibiting rather common XAS features. The first set of XAS and MCD multiplet spectra calculated by Kimura *et al.* are part of the illustration in Fig. 1.29. Here, the Mn $2p$ XAS multiplet spectra are shown on the right hand side which have been calculated under the assumption of a magnetized high-spin Mn $3d^5$ configuration in the ground state.

The results are based on first-principles atomic multiplet and band structure calculations including the spin-orbit interaction. In the process this spectra calculation has been performed for incident light of plus and minus helicity, providing the absorption intensities I_+ and I_-, with the same quantization axis as the spin.[164] Utilizing a Hartree-Fock related method, $d-d$ and d-core Slater integrals and spin-orbit constants for the $3d$ and core levels can be determined and subsequently utilized it the calculation of the related XAS and MCD transitions spectra. The calculated spectrum presented in Fig. 1.29, representing the $2p^63d^5 \rightarrow 2p^53d^6$ transition (on the right), qualitatively reproduces the essential features of the experimental spectra of the PtMnSb half-Heusler alloy.

The Pt $5d$ states are considered to be almost occupied for both spin directions. This results in a weak hybridization between the minority-spin Mn $3d$ and the Pt $5d$ states. In the same manner, the hybridization between the neighboring Mn atoms is weak as discussed above. Therefore, the transitions at this absorption edge based on the spin Mn $3d^5$ configuration can be viewed in terms of the Mn atom in the ground state occupation as schematically illustrated in the center of Fig. 1.29. Additionally, the calculated Mn $3p$ XAS and MCD spectra for the spin Mn $3d^5$ configuration is presented on the left side of this graphical illustration. The $3p^63d^5 \rightarrow 3p^53d^6$ transition exhibits a simple dispersive structure. This structure is consistent with the XAS and MCD spectra which have been experimentally obtained at the M_2 and M_3 absorption edge of PtMnSb as shown in Fig. 1.31. The Mn $2p$ XAS and MCD

[164] A. Kimura, S. Suga, T. Shishidou, S. Imada, T. Muro, S.-Y. Park, T. Miyahara, T. Kaneko, and T. Kanomata. Magnetic circular dichroism in the soft-x-ray absorption spectra of Mn-based magnetic intermetallic compounds. *Phys. Rev. B*, **56**(10):6021 (1997)

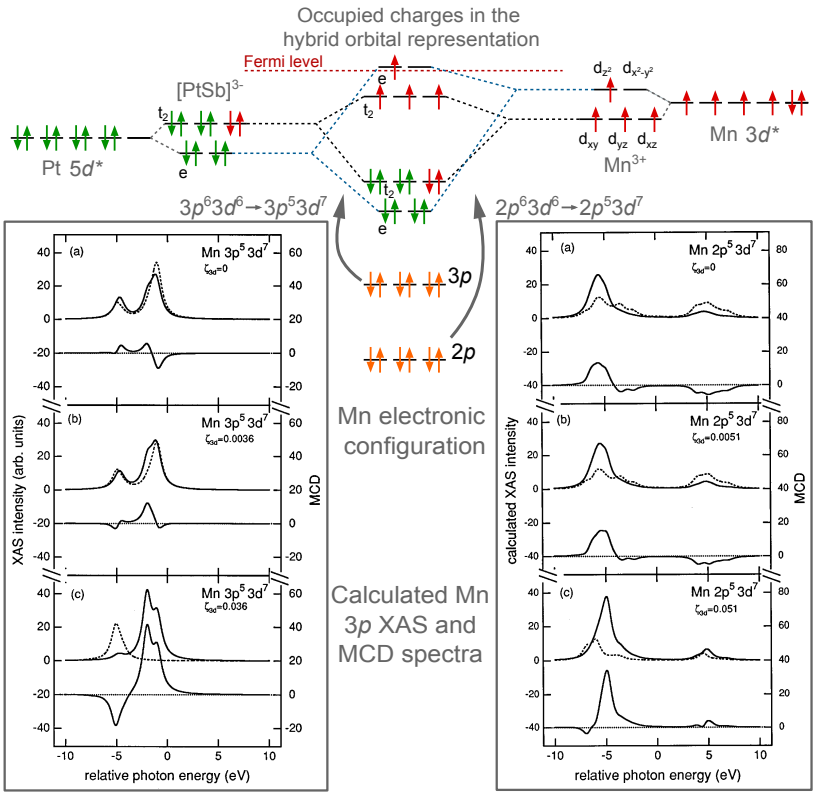

Figure 1.30: Calculated Mn $2p$ and Mn $3p$ XAS and MCD spectra for the Mn $2p^6 3d^6 \rightarrow 2p^5 3d^7$ transition (on the right) as well as the $3p^6 3d^6 \rightarrow 3p^5 3d^7$ transition (on the left), where the solid (dashed) curve indicates the I_+ (I_-) spectrum. The calculation does not consider the crystal-field terms of the Mn $3d$ state and the spin-orbit interaction of the Mn $3d$ state is set to (a) 0, (b) 10 % of full Hartree-Fock (HF), and (c) full HF values. The lower curve in each subfigure (a)-(c) represents the MCD spectrum ($I_+ - I_-$). The presented multiplet spectra have been calculated by [Kimura et al., 1997] under the assumption of a magnetized high-spin Mn $3d^6$ configuration in the ground state. The schematic illustration in the center shows Mn electronic configuration as presented with regard to the hybridization of PtMnSb. This visualizes the obtained values of the Mn $3d$ electron occupation through band structure calculations ($n_d^* \uparrow = 4.72$ and $n_d^* \downarrow = 0.85$).

spectra are equally consistent in terms of the main absorption features. The sharp peak observed for the $2p_{3/2}$ contribution followed by a tail towards higher energies is reproduced in the calculation as well as distinctive doublet structure of the $2p_{1/2}$ contribution prominently displayed in the MCD spectrum of Fig. 1.28.

The details of the x-ray absorption spectra have to be interpreted based on the band structure calculations and in particular should incorporate the obtained quantity of the Mn $3d$ electrons within the PtMnSb band model. The spin-polarized DOS as obtained by first-principles electronic structure calculations of the Heusler compounds by Youn *et al.* indicates a large intra-atomic exchange splitting of the Mn $3d$ states.[165] This implicates a nearly occupied majority-spin state and equivalently a nearly unoccupied minority-spin state accounting for a high spin-polarization at the Fermi level. Although the hybridization between neighboring Mn atoms is weak, the hybridization of the Mn $3d$ and Pt $5d$ states is significant as illustrated in the schematics of Fig. 1.26.

Table 1.1 summarizes the results of the electronic structure analysis by utilizing a linearized-muffin-tin orbital band approach particularly with regard to the band occupation and site specific magnetic moment. The total electron number in the $3d$ majority-spin state is $n_d^* \uparrow = 4.72$ and in the $3d$ minority-spin state $n_d^* \downarrow = 0.85$ accounting for a combined Mn $3d$ state occupation of $n_d = 5.57$ carrying the main part of the magnetic moment of 3.97 μ_B on the Mn sites. The specific value for the magnetic moment of the Mn

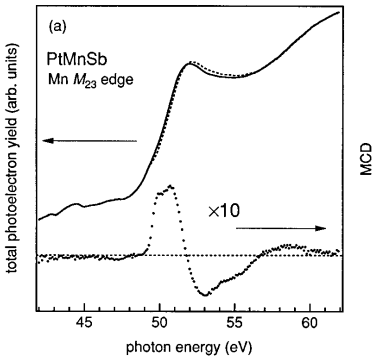

Figure 1.31: Mn $3p$ XAS and MCD spectra of PtMnSb. The solid curve (dashed curve) indicates the absorption intensity with the directions between the magnetization and the photon spin parallel (antiparallel) as denoted by I_+ (I_-). The dots show the MCD spectrum. From [Kimura et al., 1997].

[165] S. Youn and B. Min. Effects of the spin-orbit interaction in Heusler compounds: Electronic structures and Fermi surfaces of NiMnSb and PtMnSb. *Phys. Rev. B*, **51**(16):10436 (1995)

Occupied charges

Site	Spin	Q_s	Q_p	Q_d	Q_{tot}	M
Pt	↑	0.42	0.42	4.25	5.09	0.08
	↓	0.42	0.49	4.10	5.01	
Mn	↑	0.31	0.35	4.72	5.38	3.97
	↓	0.26	0.30	0.85	1.41	
Sb	↑	0.75	1.05	0.15	1.95	-0.09
	↓	0.74	1.15	0.15	2.04	
empty	↑	0.19	0.27	0.12	0.58	0.04
	↓	0.18	0.25	0.11	0.54	

Table 1.1: Occupied charges Q_l and magnetic moments M of the ferromagnetic half-Heusler PtMnSb at the experimental lattice constant obtained with electronic structure calculations under consideration of the spin-orbit interaction by [Youn and Min, 1995].

$3d$ states is calculated to be $\mu_d = (n_d^* \uparrow - n_d^* \downarrow)\mu_B = 3.87\,\mu_B$. This specific d state occupation has a significant influence on the atomic multiplet calculation since the XAS and MCD spectra is determined by all excited dipole transitions. Therefore, the experimentally obtained spectra and the specific line shapes are explained more accurately if the atomic multiplets for the $2p^5 3d^7$ configuration are included to evaluate the L_2 and L_3 absorption edge transitions.

These calculated spectra are presented on the right side of Fig. 1.30 showing the characteristic features of both types of absorption and circular dichroism spectra. In relation to the corresponding transition probability, these calculated intensities contribute to qualitatively explain the experimentally obtained spectra in their main features. The same argument is valid for the calculations of the $M_{2,3}$ edge transitions illustrated on the left side of Fig. 1.30 ($2p^5 3d^7$ configuration) also for different Hartree-Fock values determining the spin-orbit interaction strength. In any case, the electron occupation of the Mn $3d$ band as well as the strength of the spin-orbit interaction has to be accurately modeled with respect to the half-Heusler band structure and occupation and in particular include the intra-atomic exchange splitting, hybridization and bandwidth of the Mn $3d$ states, SOC and further interference effects of the transitions, e.g., Fano resonances[166] to explain the experimental XAS and MCD spectra in all detail.

[166] U. Fano. Effects of configuration interaction on intensities and phase shifts. *Phys. Rev.*, **124**(6):1866 (1961)

The $NiFe_2O_4$ Nickelferrite material system

Nickel ferrite, $NiFe_2O_4$ or shortened NFO thin films are a promising alternative to yttrium iron garnet ($Y_3Fe_5O_{12}$) which is one of the most widely studied materials in spin caloritronics[167] and magnon spintronics.[168] Especially Pt/YIG bilayers are utilized in experiments targeted on the study or exploitation of the SSE, which refers to the generation of a spin current from a thermal gradient and enables the thermal injection of spin currents from the ferromagnetic insulator YIG into the attached nonmagnetic Pt metal. Due to the extremely low magnetic damping of YIG its spin

[167] G. E. W. Bauer, E. Saitoh, and B. J. van Wees. Spin caloritronics. *Nat. Mater.*, **11**(5):391–399 (2012)

[168] A. Chumak, V. Vasyuchka, A. Serga, and B. Hillebrands. Magnon spintronics. *Nat. Phys.*, **11**(6):453 (2015)

wave properties have been extensively studied for decades[169] and the material has been widely used in microwave devices and various other applications and in articular studies regarding the SSE, coherent spin pumping,[170] spin Hall magnetoresistance (SMR)[171] and nonlocal magnon spin transport.[172]

The Pt/YIG material system has also been used to introduce the longitudinal spin Seebeck effect (LSSE), the generation of a spin current parallel to a temperature gradient that is usually aligned out-of-plane.[173] In direct consequence of these LSSE studies NFO thin films have been introduced in similar LSSE experiments[174] demonstrating the versatility of NFO for applications in high-frequency microwave and spintronics devices.[175]

This high level of practicability is in particular due to the fact that oxides exhibiting magnetic and insulating properties simultaneously are able to realize an effective spin-filter effect where spin-polarized electron currents are generated via a spin-dependent tunneling process. The spinel ferrite NFO combines both those fundamental features at room temperature making it particularly interesting for the observation of pure spin current effects.

$NiFe_2O_4$ crystallizes in the cubic spinel structure with the corresponding space group $Fd\bar{3}m$. Here, spinels are a material class characterized by the general formula AB_2O_4, where A and B are divalent and trivalent transition metal cations which occupy some or all octahedral and tetrahedral sites in the spinel lattice.[176] The oxygen anions are typically located in a close-packed fcc sublattice in such way that each spinel unit cell holds 8 formula units AB_2O_4. Therefore, the conventional spinel unit cell includes a total of 56 atoms, 32 O^{2-} anions, 16 trivalent metal B^{3+} cations and 8 divalent A^{2+} metal cations. In the inverse spinel structure half of the trivalent B^{3+} cations are located on the tetrahedral sites of the spinel lattice while the divalent A^{2+} cations are located on the octahedral sites just as the remaining half of trivalent B^{3+} cations. The $NiFe_2O_4$ spinel system forms this ideal inverse spinel lattice structure with a bulk lattice constant of $a = 8.338\,\text{nm}$.[177] For a visualization of this complex unit cell a schematic representation of this inverse spinel NFO structure is shown in Fig. 1.32.[178]

The $NiFe_2O_4$ is part of the group of ferrimagnetic spinels with a Curie temperature T_C significantly above room temperature. In NFO a ferrimagnetic ordering based upon the exchange interaction between the cations on the tetra- and octahedral positions in the spinel structure can be observed in the bulk state up to a temperature of $T_C = 865\,\text{K}$.[179] This magnetic ordering is dominated by superexchange interactions between the tetra- and octahedrally coordinated cations on the two antiferromagnetically coupled sublattices as illustrated in Fig. 1.32. In very thin NFO films an enhanced saturation magnetization is observed. This effect is attributed to a cationic inversion from an inverse to a to some extent normal spinel lattice which is usually accompanied by redistribution of Fe cations. Consequently, the magnetic moment of the thin film is increased

[169] V. Cherepanov, I. Kolokolov, and V. L'vov. The saga of YIG: Spectra, thermodynamics, interaction and relaxation of magnons in a complex magnet. *Phys. Rep.*, **229**(3):81–144 (1993)

[170] Y. Tserkovnyak, A. Brataas, and G. E. Bauer. Enhanced Gilbert damping in thin ferromagnetic films. *Phys. Rev. Lett.*, **88**(11):117601 (2002)

[171] H. Nakayama, M. Althammer, Y.-T. Chen, K.-i. Uchida, Y. Kajiwara, D. Kikuchi, T. Ohtani, S. Geprägs, M. Opel, S. Takahashi, R. Gross, G. E. W. Bauer, S. T. B. Goennenwein, and E. Saitoh. Spin Hall magnetoresistance induced by a nonequilibrium proximity effect. *Phys. Rev. Lett.*, **110** (20):206601 (2013)

[172] E. Saitoh, M. Ueda, H. Miyajima, and G. Tatara. Conversion of spin current into charge current at room temperature: Inverse spin-Hall effect. *Appl. Phys. Lett.*, **88**(18):182509 (2006)

[173] K.-i. Uchida, H. Adachi, T. Ota, H. Nakayama, S. Maekawa, and E. Saitoh. Observation of longitudinal spin-Seebeck effect in magnetic insulators. *Appl. Phys. Lett.*, **97**(17): 172505 (2010)

[174] D. Meier, T. Kuschel, L. Shen, A. Gupta, T. Kikkawa, K. Uchida, E. Saitoh, J. M. Schmalhorst, and G. Reiss. Thermally driven spin and charge currents in thin NiFe2O4/Pt films. *Phys. Rev. B*, **87**(5):054421 (2013); D. Meier, D. Reinhardt, M. van Straaten, C. Klewe, M. Althammer, M. Schreier, S. T. B. Goennenwein, A. Gupta, M. Schmid, C. H. Back, J.-M. Schmalhorst, T. Kuschel, and G. Reiss. Longitudinal spin Seebeck effect contribution in transverse spin Seebeck effect experiments in Pt/YIG and Pt/NFO. *Nat. Commun.*, **6**:8211 (2015); and J. Shan, P. Bougiatioti, L. Liang, G. Reiss, T. Kuschel, and B. J. van Wees. Nonlocal magnon spin transport in NiFe2O4 thin films. *Appl. Phys. Lett.*, **110**(13):132406 (2017)

[175] U. Lüders, A. Barthelemy, M. Bibes, K. Bouzehouane, S. Fusil, E. Jacquet, J.-P. Contour, J.-F. Bobo, J. Fontcuberta, and A. Fert. $NiFe_2O_4$: A versatile spinel material brings new opportunities for spintronics. *Adv. Mater.*, **18**(13): 1733–1736 (2006)

[176] E. Verwey and E. Heilmann. Physical properties and cation arrangement of oxides with spinel structures I. Cation arrangement in spinels. *J. Chem. Phys.*, **15**(4):174–180 (1947)

[177] O. Madelung, U. Rössler, and M. Schulz. Ternary compounds, organic semiconductors. *Landolt-Börnstein–Group III Condensed Matter*, **41** (2000)

[178] M. Hoppe, S. Döring, M. Gorgoi, S. Cramm, and M. Müller. Enhanced ferrimagnetism in auxetic $NiFe_2O_4$ in the crossover to the ultrathin-film limit. *Phys. Rev. B*, **91**(5):054418 (2015)

[179] V. Brabers. Progress in spinel ferrite research. *Handb. Magn. Mater.*, **8**: 189–324 (1995)

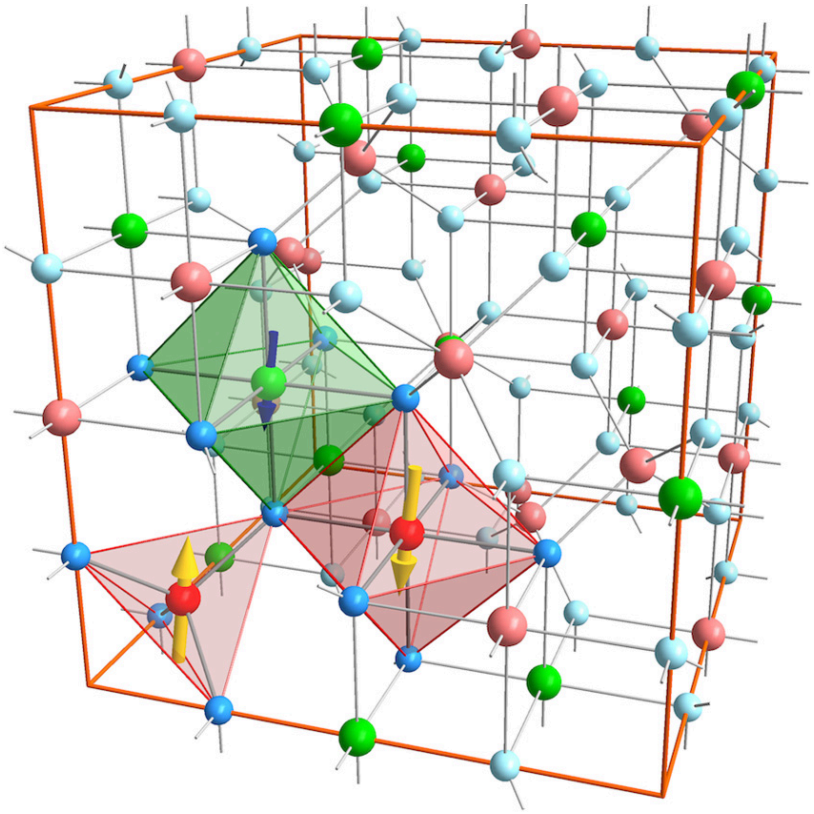

Figure 1.32: Schematic illustration of the inverse spinel lattice of $NiFe_2O_4$. The Ni^{2+} cations are shown in green merely occupying the octahedral lattice sites while the red Fe^{3+} cations are equally allocated to the tetrahedral as well as to the octahedral lattice sites. The O^{2-} anions are depicted in blue on the locations within the ace centered cubic lattice structure. The magnetic moments of the Fe^{3+} cations are compensated based on an antiferromagnetic coupling of the tetra- and octahedral positions. Ni^{2+} cations on consistent lattice sites exhibit a ferromagnetic coupling and account for the net macroscopic magnetization of $2\,\mu_B$ per formula unit. The image is adopted from [Hoppe et al., 2015].

in relation to the bulk value and the saturation magnetization M_S as a function of NFO film thickness below a value of 3 nm.[180] The bulk magnetization values which can be found in literature vary between 270 kA/m and 300 kA/m[181] and are primarily built on the Ni^{2+} cations on the octahedral sites which account for the moment of about $2\,\mu_B$ per formula unit.

The cations located on the tetrahedral A-site couple antiferromagnetically due to their super-exchange interaction via an overlap of the Fe $3d$ orbitals with the intermediate oxygen $2p$ orbitals. In contrast, the cations on the octahedral B-sites are connected at a 90° angle to the bridging nonmagnetic anion connecting to the next-to-nearest neighboring ion which induces a ferromagnetic super-exchange interaction. However, these couplings are overruled by the stronger super-exchange interaction connecting both sublattices by an antiferromagnetic coupling between the atoms on octahedral and tetrahedral sublattice sites.[182] The result of this coupling process is illustrated in Fig. 1.33 in terms of the $3d$ level splitting and occupation. The sublattices on different sites are ordered ferromagnetically, where the A-sites are occupied by the Fe^{3+} cations with 5 unpaired $3d$ electrons yielding a magnetic moment of $5\,\mu_B$ per formula unit. The B-sites, on the other hand, are occupied by the same amount Fe^{3+} $3d$ electrons and additionally by the Ni3+ cations contributing 2 unpaired $3d$ electrons which ferromagnetically couple with a magnetic moment of $7\,\mu_B$ per formula unit. The

[180] U. Lüders, M. Bibes, J.-F. Bobo, M. Cantoni, R. Bertacco, and J. Fontcuberta. Enhanced magnetic moment and conductive behavior in $NiFe_2O_4$ spinel ultrathin films. *Phys. Rev. B*, **71** (13):134419 (2005)

[181] U. Lüders, A. Barthelemy, M. Bibes, K. Bouzehouane, S. Fusil, E. Jacquet, J.-P. Contour, J.-F. Bobo, J. Fontcuberta, and A. Fert. $NiFe_2O_4$: A versatile spinel material brings new opportunities for spintronics. *Adv. Mater.*, **18**(13): 1733–1736 (2006)

[182] S. J. Kim, W. C. Kim, C. S. Kim, and S. W. Lee. Moessbauer studies of superexchange interactions in $NiFe_2O_4$. *J. Korean Phys. Soc.*, **36**(6):430–434 (2000)

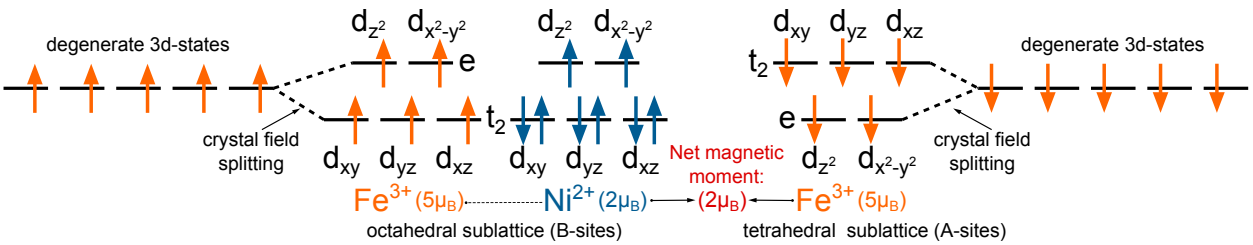

Figure 1.33: Occupation of the magnetic sublattices in the inverse spinel structure of $NiFe_2O_4$. The crystal field splitting of the degenerate 3*d* levels is illustrated for the Ni^{2+} and Fe^{3+} cations on their respective lattice sites.

discussed coupling of both sublattices reduces the net magnetic moment per formula unit to $2\,\mu_B$ which is close to the experimentally obtained value for NFO bulk material.[183]

Band structure calculations of the NFO system confirm the characteristic electronic structure and magnetic properties of a ferrimagnetic insulator. The total density of states for the $NiFe_2O_4$ inverse spinel structure has been calculated by Szotek *et al.* within the density functional theory using the self-interaction corrected local spin density (SIC-LSD) approximation.[184]

In agreement with experiments, DFT calculations confirm the ground state of $NiFe_2O_4$ to be insulating and of the inverse spinel structure. The corresponding spin decomposed DOS is shown in Fig. 1.34 with an energy gap of $\sim$ 1 eV at the Fermi level. The exchange splitting of the conduction band shown to be 1.21 eV.

As the labeled states composing the DOS of Fig. 1.34 show, the wide valence band in the center is created mainly out of oxygen 2*p* states while the conduction band is generated out of unoccupied 3*d* states of the iron atoms. Here, the majority states, shown in the upper half of the DOS schematics, are generated by cations located on the tetrahedral lattice sites, solely taken by the Fe^{3+} ions, while the minority states are formed by the atoms on the octahedral sublattice. The main contributing ions and the respective sites are indicated at each band of the DOS diagram.

Furthermore, the insulating characteristics and more generally the transport properties of NFO thin films are highly sensitive to the structural integrity of the inverse spinel system. A potential electronic transport in spinel ferrites can possibly be implemented through charge carriers which are exchanged between the divalent and trivalent cations on equal lattice sites. One option is the introduction of metal ions on octahedral lattice sites in the form Fe^{2+} or Ni^{3+} while the material system is fabricated.[185] In the same way an off-stoichiometric composition, e.g., by means of incomplete oxidation during a reactive sputtering process, can integrate Fe^{2+} into the sublattices instead of trivalent Fe cations and thus facilitate a hopping conduction process. This promotes a charge transport between Fe^{2+} and Fe^{3+} cations as well as Ni^{2+} and Ni^{3+} cations via hopping of electrons or holes.[186] Such an interchange process of charge carriers requires only a small amount of energy since the electrons or holes are traveling along the cations on the octahedral sites without altering the energy state of the sublattices

[183] V. Brabers. *Handbook of magnetic materials*, volume 8. Elsevier, New York, NY, USA (1995)

[184] Z. Szotek, W. Temmerman, D. Ködderitzsch, A. Svane, L. Petit, and H. Winter. Electronic structures of normal and inverse spinel ferrites from first principles. *Phys. Rev. B*, **74**(17): 174431 (2006)

[185] H. Lord and R. Parker. Electrical resistivity of nickel ferrite. *Nature*, **188** (4754):929 (1960)

[186] L. d. Van Uitert. Dc resistivity in the nickel and nickel zinc ferrite system. *J. Chem. Phys.*, **23**(10):1883–1887 (1955)

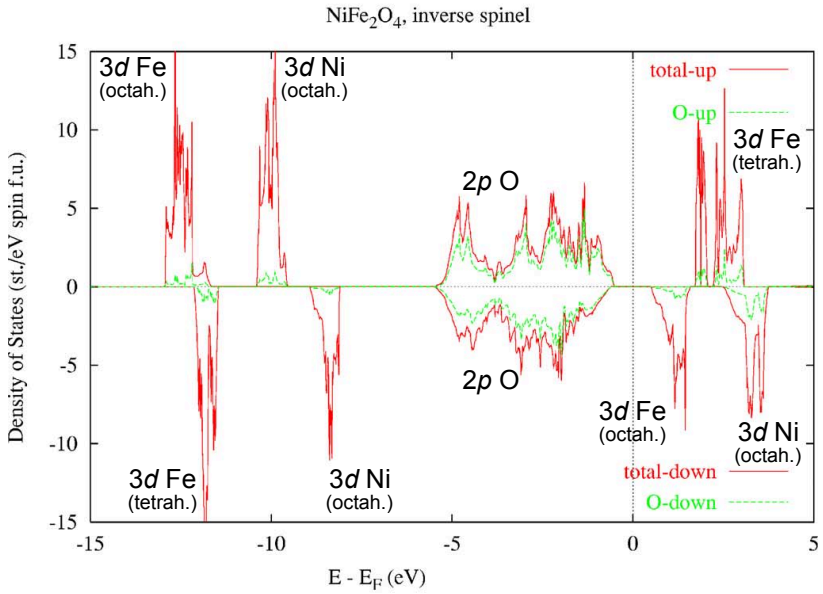

Figure 1.34: Total spin dependent densities of state (red) of $NiFe_2O_4$ per formula unit in the inverse spinel structure. The oxygen contribution to the total density of states is also shown (green). The majority contribution to the DOS is shown on the upper side of the graph, the minority DOS is presented on the bottom side. For each depicted band the main contributing ions and the respective sites are amended. The DOS calculation was performed by [Szotek et al., 2006].

significantly.[187] Therefore, the growth process has to be adjusted to fit the correct stoichiometry $NiFe_2O_4$ precisely to preserve the desired electronic transport properties of the thin film system.

[187] J. H. de Boer and E. J. Verwey. Semiconductors with partially and with completely filled 3*d*-lattice bands. *Proc. Phys. Soc.*, **49**(4S):59 (1937)

2
Fabrication and Investigation of PtMnSb thin films

The detailed investigation of structural element specific density as well as the corresponding magnetic depth profiles in any system requires samples of excellent and well defined qualities. Therefore, one aspect of this work is the study of the growth and epitaxial properties of the PtMnSb half-Heusler thin films. For this study, epitaxial PtMnSb thin films were prepared with varying film thickness on MgO(001) substrates at high temperatures in ultra-high vacuum conditions. Here, no seed layer has been utilized and additional PtMnSb/Pt bilayers have been fabricated, in general in order to study the influence of the capping on the magnetic depth profile and in particular for the investigation of the MPE. In the further course of this chapter, the fabrication and characterization of PtMnSb layers and their corresponding Pt and oxide capped bilayer systems will be discussed at length.

First of all, the specific properties of the PtMnSb films and respective bilayers are introduced in-depth. These characteristics have been investigated within this work by various techniques with a focus on their structure, stoichiometry, texture and surface topography. Furthermore, a detailed analysis based on various x-ray techniques has been performed in combination with high resolution transmission electron and atomic force microscopy to characterize the film growth and quality and provide information on the film structure, stoichiometry, and surface topography.

On the basis of this work, electrical measurements on these single films and bilayers can be performed to ultimately study spin transport properties and spin-orbit torques (SOTs).[1] Furthermore, the spin polarization depth profile of the samples is detected using x-ray resonant magnetic reflectivity.[2] Here, a Pt spin polarization in the Pt film at the interface is expected due to the magnetic proximity effect and, in addition, in the PtMnSb material itself which significantly influences the transport phenomena.

[1] K. Garello, I. M. Miron, C. O. Avci, F. Freimuth, Y. Mokrousov, S. Blügel, S. Auffret, O. Boulle, G. Gaudin, and P. Gambardella. Symmetry and magnitude of spin-orbit torques in ferromagnetic heterostructures. *Nat. Nanotechn.*, **8**(8):587–593 (2013); and C. O. Avci, K. Garello, A. Ghosh, M. Gabureac, S. F. Alvarado, and P. Gambardella. Unidirectional spin Hall magnetoresistance in ferromagnet/normal metal bilayers. *Nat. Phys.*, **11**(7):570–575 (2015)

[2] T. Kuschel, C. Klewe, J.-M. Schmalhorst, F. Bertram, O. Kuschel, T. Schemme, J. Wollschläger, S. Francoual, J. Strempfer, A. Gupta, M. Meinert, G. Götz, D. Meier, and G. Reiss. Static magnetic proximity effect in $Pt/NiFe_2O_4$ and Pt/Fe bilayers investigated by x-ray resonant magnetic reflectivity. *Phys. Rev. Lett.*, **115**(9):097401 (2015); C. Klewe, T. Kuschel, J.-M. Schmalhorst, F. Bertram, O. Kuschel, J. Wollschläger, J. Strempfer, M. Meinert, and G. Reiss. Static magnetic proximity effect in $Pt/Ni_{1-x}Fe_x$ bilayers investigated by x-ray resonant magnetic reflectivity. *Phys. Rev. B*, **93**(21):214440 (2016); and T. Kuschel, C. Klewe, P. Bougiatioti, O. Kuschel, J. Wollschläger, L. Bouchenoire, S. Brown, J. Schmalhorst, D. Meier, and G. Reiss. Static Magnetic Proximity Effect in Pt Layers on Sputter-Deposited $NiFe_2O_4$ and on Fe of Various Thicknesses Investigated by XRMR. *IEEE Trans. Magn.*, **52**:4500104 (2016)

PtMnSb fabrication methods in literature

ALLOY FILMS of the half-metallic PtMnSb have been prepared by RF sputtering from a sintered MnSb target with Pt sheets as well as from a mosaic target on a fused quartz or glas substrate followed by annealing.[3] In order to study the potential of utilizing the ferromagnet PtMnSb in GMR applications and devices, epitaxial PtMnSb(111) films on Al_2O_3(0001) have been fabricated by means of DC magnetron co-sputtering at 500 °C.[4]

In the middle of the 1990s, the growth of single-phase PtMnSb films by DC magnetron co-sputtering was studied and reported by Kautzky *et al*.[5] For the preparation of epitaxial (001) oriented PtMnSb by DC co-sputtering on a MgO substrate, identical in orientation, a (001) oriented W seed layer can be utilized. This specific growth generates by moderate in-plane strain which is shown to be insufficient to induce a perpendicular magnetization due to inverse magnetostriction.[6] In addition, ordered thin films of PtMnSb have been produced by means of solid-state phase formation. More precisely, this has been accomplished by an extensive thermal annealing of thin multilayered Pt/Mn/Sb films in a compositionally modulated stack. Moreover, films consisting of the two distinct PtMnSb and Mn_2Sb phases have been fabricated.[7] Via pulsed-laser deposition, structurally related half-Heusler compounds, for instance NiMnSb, have been grown at lower deposition temperatures.[8] In this context, it is noteworthy that epitaxial NiMnSb(001) thin films have been successfully grown on (In,Ga)As(001) using molecular-beam epitaxy (MBE).[9]

As a central aspect of this work, the sputter deposition process has been optimized in order to grow epitaxial PtMnSb. This process is discussed in the following section. Subsequently, an in-depth investigation of this half-Heusler alloy in form of a detailed structural analysis is presented. Here, the explicit focus is on the interface region of the Pt/PtMnSb bilayers which were prepared as twin samples with AlO_x/MgO capped PtMnSb films. When heterostructures based on this half-Heusler material are studied in order to realize spintronic devices based on the spin polarization in proximity to the PtMnSb, one highly important aspect is the quality of the bilayer interface. This study ensures a deeper understanding into ferromagnetic properties as well as spin-orbit torque related and magnetic proximity effects in PtMnSb films in a Pt or oxide capped bilayer system. This characterization ultimately facilitates an investigation of the SOT dependency on the utilization of an adjacent heavy metal layer and opens broader prospects for spintronic applications.[10] In this context, the preparation of PtMnSb and Pt/PtMnSb twin samples is especially useful for the quantitative disentanglement of spin caloritronic effects as for instance spin Seebeck and anomalous Nernst effects in heavy metal/ferromagnet bilayers.[11] In the following section the sample

[3] R. Ohyama, T. Koyanagi, and K. Matsubara. Magneto-optical Kerr effect of rf-sputtered PtMnSb thin films. *J. Appl. Phys.*, **61**(6):2347–2352 (1987); and E. Attaran and P. J. Grundy. The magnetic, magneto-optical and structural properties of PtMnSb thin films. *J. Magn. Magn. Mater.*, **78**(1):51–55 (1989)

[4] M. C. Kautzky, F. B. Mancoff, J.-F. Bobo, P. R. Johnson, R. L. White, and B. M. Clemens. Investigation of possible giant magnetoresistance limiting mechanisms in epitaxial PtMnSb thin films. *J. Appl. Phys.*, **81**(8): 4026–4028 (1997)

[5] M. C. Kautzky and B. M. Clemens. Epitaxial Growth of (001)- and (111)-oriented PtMnSb Films and Multilayers. In *MRS Proceedings*, volume 384, page 109. Cambridge Univ Press, (1995)

[6] M. C. Kautzky and B. M. Clemens. Structure and magneto-optical properties of epitaxial PtMnSb (001) on W (001)/MgO (001). *Appl. Phys. Lett.*, **66** (10):1279–1281 (1995)

[7] T. Matsui, N. Iketani, K. Morii, and Y. Nakayama. The effect of stacking patterns and annealing conditions on phase evolution by solid-state reactions of thin multilayered Pt/Mn/Sb films. *Mat. Chem. Phys.*, **36**(1-2):106–111 (1993)

[8] J. Giapintzakis, C. Grigorescu, A. Klini, A. Manousaki, V. Zorba, J. Androulakis, Z. Viskadourakis, and C. Fotakis. Low-temperature growth of NiMnSb thin films by pulsed-laser deposition. *Appl. Phys. Lett.*, **80**(15): 2716–2718 (2002)

[9] W. Van Roy, J. De Boeck, B. Brijs, and G. Borghs. Epitaxial NiMnSb films on GaAs (001). *Appl. Phys. Lett.*, **77** (25):4190–4192 (2000); P. Bach, A. S. Bader, C. Rüster, C. Gould, C. R. Becker, G. Schmidt, L. W. Molenkamp, W. Weigand, C. Kumpf, E. Umbach, R. Urban, G. Woltersdorf, and B. Heinrich. Molecular-beam epitaxy of the half-Heusler alloy NiMnSb on (In, Ga) As/InP (001). *Appl. Phys. Lett.*, **83**(3):521–523 (2003); and F. Gerhard, C. Schumacher, C. Gould, and L. W. Molenkamp. Control of the magnetic in-plane anisotropy in off-stoichiometric NiMnSb. *J. Appl. Phys.*, **115**(9):094505 (2014)

[10] Y. Xu, Y. Yang, K. Yao, B. Xu, and Y. Wu. Self-current induced spin-orbit torque in FeMn/Pt multilayers. *Sci. Rep.*, **6** (2016)

[11] P. Bougiatioti, C. Klewe, D. Meier, O. Manos, O. Kuschel, J. Wollschläger, L. Bouchenoire, S. D. Brown, J.-M. Schmalhorst, G. Reiss, and T. Kuschel. Quantitative disentanglement of the spin Seebeck, proximity-induced, and ferromagnetic-induced anomalous Nernst effect in normal-metal–ferromagnet bilayers. *Phys. Rev. Lett.*, **119**(22):227205 (2017)

growth of the PtMnSb thin films, which are investigated by the various means of structural and magnetic characterization techniques in the course of this work, is outlined in detail.

Sputter deposition of PtMnSb thin films

The PtMnSb films discussed in this work have been prepared by DC magnetron co-sputtering from conventional three 3-inch or 7.62 cm sources in the ultra-high vacuum (UHV) range at a base pressure of 5×10^{-10} mbar. This range is necessary to obtain a high structural quality of the fabricated thin films especially when the sample is prepared over a time period of several hours. Under high vacuum conditions even below 10^{-6} mbar the sample surface can absorb some atmospheric particles which roughly leads to the deposition of a monolayer of residual atoms every few seconds. In the UHV range this unwanted particle absorption is reduced to a residual monolayer every few days and therefore enables the deposition on contamination-free surfaces which ultimately minimizes the number of contamination events in the synthesized films.

Fundamentally, in a sputter deposition process a solid target material is bombarded with high energetic Ar^+ ions from an Ar plasma. This sputtering gas is an inert gas which allows for an efficient momentum transfer where the atomic weight of the sputtering gas should be close to the atomic weight of the target material. Here, Ar is a good compromise and is feasible for the sputtering of light and heavy elements at the same time. During this sputter deposition process atoms are ejected from the target material ideally in the direction of a substrate and impact energetically or condense on the substrates or vacuum chamber wall depending on the gas pressure during the process. The magnetron co-sputtering system used to prepare the samples for this work

The used sputtering sources feature magnetrons which utilize strong electric and magnetic fields to confine charged plasma particles in close proximity to the surface of the deposition target. An increased number of ionizing collisions, leading to a higher deposition rate, helps to sustain a plasma at lower pressures. Therefore, the process pressure is typically of the order of 10^{-3} mbar to maintain a stable plasma. If an additional reactive gas is inserted into chamber during the sputter deposition process, the sputtered particles from the target material can undergo a chemical reaction before or during the coating of the substrate. This process is called reactive sputtering and is usually based on oxygen or nitrogen addition to synthesize more complex oxidic or nitric compounds. The composition of the film is controllable through the fine-tuning of the relative pressures of the reactive and inert gases whereat the reactive gas can replace the inert gas completely.

The main deposition system used for this work was an ultra-high vacuum magnetron co-sputtering system specifically designed for

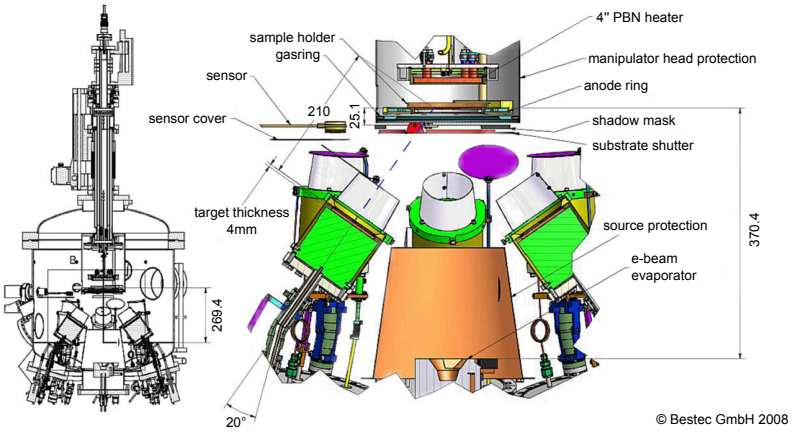

Figure 2.1: Schematic illustration of the BesTec ultra-high vacuum magnetron co-sputtering system. Revised engineering detail drawing of BesTec GmbH.

the production and optimization of functional layer systems produced by BesTec GmbH.[12] A technical illustration of the main deposition layout is depicted in Fig. 2.1, featuring a configuration of six DC and two radio frequency (RF) sputtering sources for a possible co-sputter deposition based on up to four sources simultaneously. The RF sputtering sources are primarily used to prevent a charge build-up on insulating targets through a high frequency sign change of the anode-cathode bias. Highly insulating oxide films, like the MgO layers utilized here, can be easily deposited using frequencies around the 14 MHz range. By controlling the deposition power of multiple sources separately the stoichiometry of the co-sputtered material can be precisely controlled. The sources are confocally arranged and tilted towards the substrate at an angle of 35° with respect to the surface normal with a target-to-substrate distance of 21 cm. To avoid inhomogeneous covering the substrates are usually rotated during deposition at 10 rpm. The deposition rate is an important part of process management and is controlled by a piezoelectric quartz sensor by measuring the change of resonance frequency caused by an a minimal addition of deposited mass. A crucial parameter for the fabrication of complex heterostructures and thin film systems is usually the deposition temperature. Therefore, this system included a pyrolytic boron nitride (PBN) heater which is brought close to the back side of the substrate holder during the heating process as shown at the top of Fig. 2.1. This heater is capable of keeping the substrate at a constantly controlled temperature of up to 1000 °C for deposition or post annealing processes.

The substrate temperature has a significant impact on the growth conditions and thereby the structural film properties. A variation of the deposition temperature is therefore a potent way to optimize composition, film structure and other material properties.

[12] BesTec GmbH: Vacuum systems for application in surface analysis & deposition techniques and equipment for synchrotrons.

Experimental sample growth

Within the analysis of different capping materials for the PtMnSb layer of identical thickness, twin samples were produced in a simultaneous deposition process To ensure a direct comparability. In each of these preparation cycle, two nominally identical PtMnSb (x nm) layers were grown on two polished MgO (001) substrates with a lattice mismatch of about 4 % for epitaxial growth, one of them with Pt (x nm) on top. The high-purity MgO substrate is produced by CrysTec GmbH,[13] specialized i.a. on oxidic wafer and substrates, via arc fusion growth and subsequently polished on on side. This substrate crystallizes in a cubic structure with a lattice constant of $a = 0.4212\,\text{nm}$. The standard thickness of this substrate is 1 mm and the surface prepared for deposition has a size of $10 \times 10\,\text{mm}^2$.

[13] CrysTec GmbH Kristalltechnologie. http://www.crystec.de/

Since many deposition series are discussed here and due to the constant usage of the target material and minor changes to the deposition chamber the immediate sputter parameters are subject to incremental change depending on the time of deposition within this work. The following parameters were used as a result of an optimized growth process yet they only serve as an example since especially the deposition powers are highly dependent of the target condition. The optimal sputter powers utilized for the elemental targets are 25 W for Pt, 38 W for Mn and 41 W for Sb with 10 sccm Ar gas flow at 1.9×10^{-3} mbar in order to precisely tune the correct stoichiometry with a deposition rate of 0.11 nm/sec. The deposition time was adjusted accordingly to achieve the sighted thickness of the half-Heusler thin film.

The deposition temperature for the PtMnSb thin film was 400 °C to achieve optimal growth followed by a subsequent 2 hour cool-down process to room temperature. Temperatures higher than 400 °C are incompatible with monocrystalline growth as pointed out by the structural analysis. Samples prepared at higher temperatures are not suitable for continuing investigation of the magnetic qualities or transport properties on account of the increased granular character of the thin films.

In addition to the main PtMnSb structure, the Pt layer is, in the majority of cases, deposited subsequently to the growth of the PtMnSb at room temperature with a sputter power of 100 W and an equivalent gas flow of 10 sccm Ar at 1.9×10^{-3} mbar while the substrate is consistently rotated. The deposition rate is calibrated at this optimal growth conditions to be 0.09 nm/sec. The process pressure for the RF based deposition of MgO is 1.2×10^{-2} mbar facilitating a higher crystallinity of the grown capping layer. As an experimental comparison, the Pt cover layer is deposited in a separate production series at the half-Heusler deposition temperature to prevent even minimal *in situ* oxidation.

Within the framework of the twin sample fabrication to prepare bilayer systems with Pt or oxide top layer, the PtMnSb film

on the second MgO substrate is covered by a mask prior to the Pt deposition. Subsequently and prior to atmosphere exposure, the single PtMnSb layer is capped at room temperature by 3 nm of MgO to avoid ex-situ oxidation. An additional 2 nm of Al is deposited afterwards to form a passivating oxide in order to protect the hygroscopic MgO capping layer.

Investigation of PtMnSb thin film samples

Following the deposition process outlined above, the composition of the PtMnSb films is determined by x-ray fluorescence spectroscopy (XRF). Additionally, spectral energy-dispersive x-ray spectroscopy (EDX) was used to confirm the XRF measurement by quantifying the Pt:Mn:Sb ratio. The x-ray diffraction (XRD) measurements were performed with a Philips X'Pert Pro diffractometer employing a Cu K_α source to analyze the samples crystallographic properties in a Bragg-Brentano $\theta - \theta$ configuration. In the same setup the film thickness and roughness are determined by XRR. A Bruker AFM Multimode was utilized to perform atomic force microscopy (AFM) of the surface topography. Here, specialized Bruker FMV-A probes were used in tapping mode. The thin films crystallinity, structure and composition was analyzed by means of scanning transmission electron microscopy (STEM) using a high angular annular dark field (HAADF) detector in a FEI Titan G2 60-300 fourth generation transmission electron microscope with an aberration corrected probe. This instrument is located at the Institute of Nanoscience of Aragon (INA) where HAADF imaging was used to map the thin PtMnSb layers and Pt/PtMnSb bilayer via STEM microscopy which is highly sensitive to element variations. In this context, the necessary preparation of uniformly thin TEM lamellae was performed by focused ion beam milling in a Dual Beam Helios 650 Nanolab. The atomic structure can be visualized with high quality, capturing fine details as small as a single row of atoms, to control the sample growth and interface roughness. The EDX analysis was realized by means of *in situ* STEM with an Oxford instrument.

Results and discussion

The stoichiometry of the PtMnSb was adjusted according to the EDX and XRF measurements to be close to the ideal composition. Between the different deposition series a ratio varying from 0.982:0.973:1.044 to 0.945:0.948:1.107 was compounded. These exact ratios are predominately determined by XRF with an integration time of two hours. The STEM based EDX scans enable the analysis of the thin film stoichiometry with a high spatial resolution. The STEM electron beam can be focused and moved laterally in relation

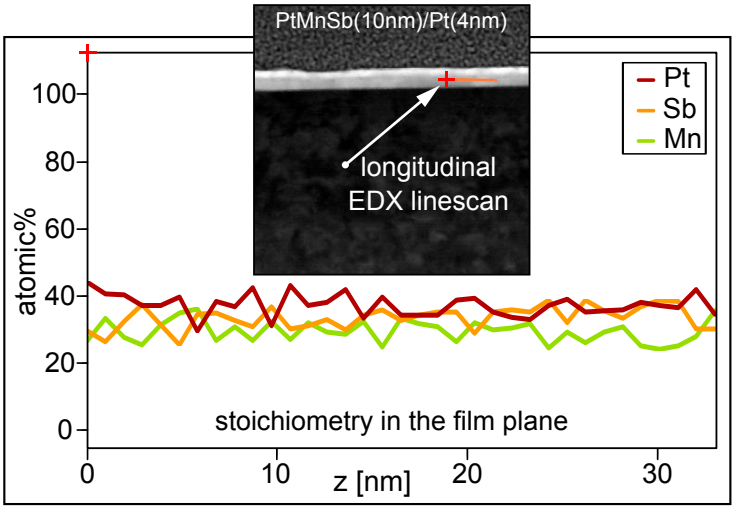

Figure 2.2: Longitudinal EDX linescan performed on the Pt(4 nm)/PtMnSb(10 nm) thin film system to confirm a homogeneous stoichiometry along the direction of the PtMnSb film. The corresponding course of the line scan is illustrated in the STEM dark field image of the sample.

to the sample cut to generate an EDX line scan profile with a nominal electron probe size in the sub-nanometer range. In the course of the line scan the energy and intensity of the x-rays emitted from the film is measured by an energy-dispersive spectrometer allowing to determine the elemental composition. The results of a line scan performed on a sample of 10 nm PtMnSb covered with a 4 nm Pt layer is exemplary shown in Fig. 2.2 confirming uniform stoichiometry along the film plane with a ratio of 1:1:1 within the margin of error.

Figure 2.3 illustrates the results of the XRD analysis. The PtMnSb (004) Bragg peak is unambiguously observable for all presented samples of varying half-Heusler thickness. The (002), (222) and (333) Bragg peaks merely emerge provided that the layer thickness exceeds about 15 nm. It turns out that the (111) Bragg peak is observable for all PtMnSb thicknesses, with the exception of the 5 nm sample where it is hardly distinctive. Hence, all films exhibit at least a polycrystalline though textured structure based on a predominant epitaxial growth in the [001] direction. This conclusion can be drawn on the basis of the peak intensity ratios and supplementary calculations of the relevant static structure factors.

Off-specular XRD experiments using an Eulerian cradle confirm the crystalline growth of the PtMnSb with (001) orientation, since corresponding sharp Bragg reflections can be detected. The Eulerian cradle is the central part of a 4-circle diffractometer designed for single crystal structure analysis which is used to extend the conventional geometry of the Philips X'Pert Pro diffractometer by adjusting the probed crystal orientation relative to incident beam and detector. Two exemplary scans performed at angles of $2\theta = 40.955°$ and $2\theta = 74.595°$ are shown in the polar plots in Figs. 2.4(a) and (b) confirming a perfect orientation of the crystallites. The result presented in these polar plots is in total agreement with a theoretical simulation of the Bragg reflexions of a PtMnSb crystal predominantly orientated along the [001] direction. The calculated x-ray diffraction patterns for the whole 2θ range in the accessible ϕ- and χ-circle planes of the Eulerian cradle are pre-

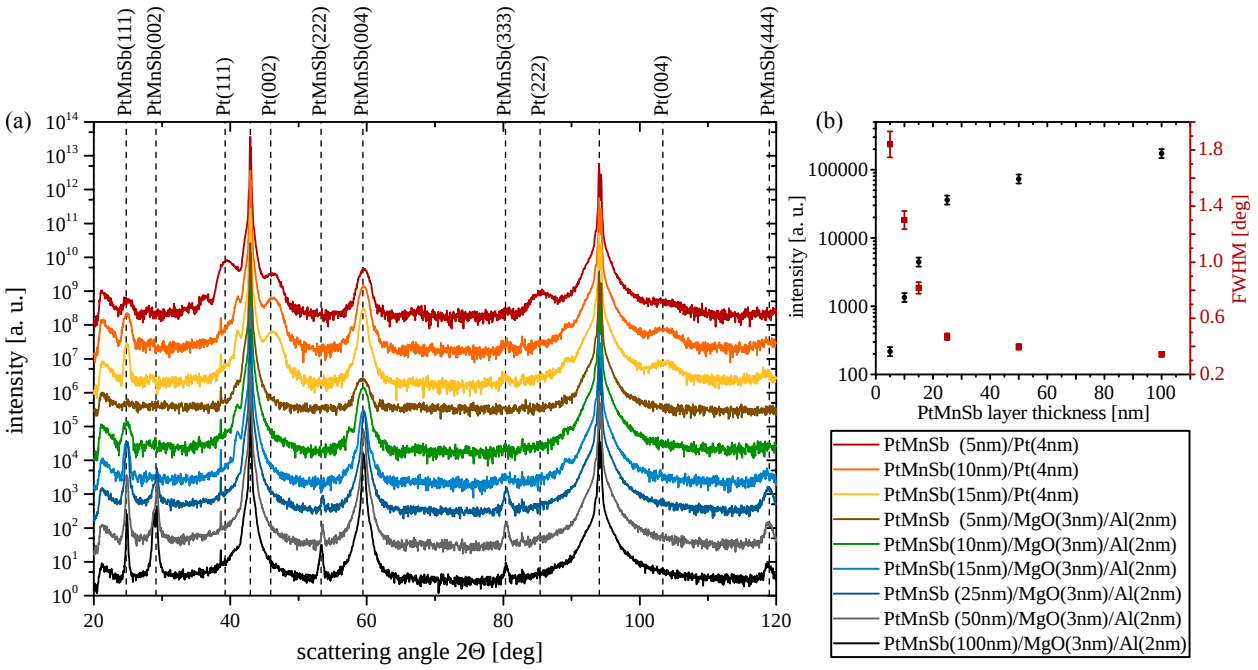

Figure 2.3: (a) XRD measurements including PtMnSb (111) and PtMnSb (004) Bragg reflections indicating two domain orientations. (b) Bragg peak intensity and FWHM of the PtMnSb (004) reflection plotted against the PtMnSb layer thickness of the AlO_x/MgO capped samples.

sented in Fig. 2.5. The patterns shown in the measured polar plots can be found in their exact position in the simulation in the color representing the selected 2θ angle.

No off-specular Bragg reflections from the (111) orientation could be detected. Consequently, the specular PtMnSb (111) reflections have to be assigned to polycrystalline material with (111) texture, while the dominant PtMnSb (004) reflection is due to a monocrystalline PtMnSb phase. Figure 2.3(b) shows both the intensity of the (004) Bragg peak as well as full width at half maximum (FWHM) plotted against the PtMnSb film thickness. Here, the flattening of the intensity increase in the range of a layer thickness between 15 nm and 25 nm indicates an increasingly polycrystalline growth which coincides with a reduction of texture. As a consequence of the direct growth on the MgO substrate, an epitaxial layer growth of Pt either in (111) or (001) orientation is determined in case of thin PtMnSb layers. When the PtMnSb layer thickness is increased, Pt is growing quasi-epitaxially on the ordered PtMnSb in (001) orientation and thus only the Pt (002) and (004) peaks are directly observable. This growth mode investigation is supported by additional TEM imaging resolving features of the crystal growth with nanometer- to atomic-resolution.

When the sample surface is imaged at a high resolution by means of an AFM measurement the topography of the sample can be measured locally and the implications of change in deposition temperature on the surface properties can be visualized. The 1 µm × 1 µm scan of a thin film prepared at 400 °C shows a locally homogeneous and smooth growth with granular character as presented in detail in Fig. 2.6(a). In contrast to this comparatively

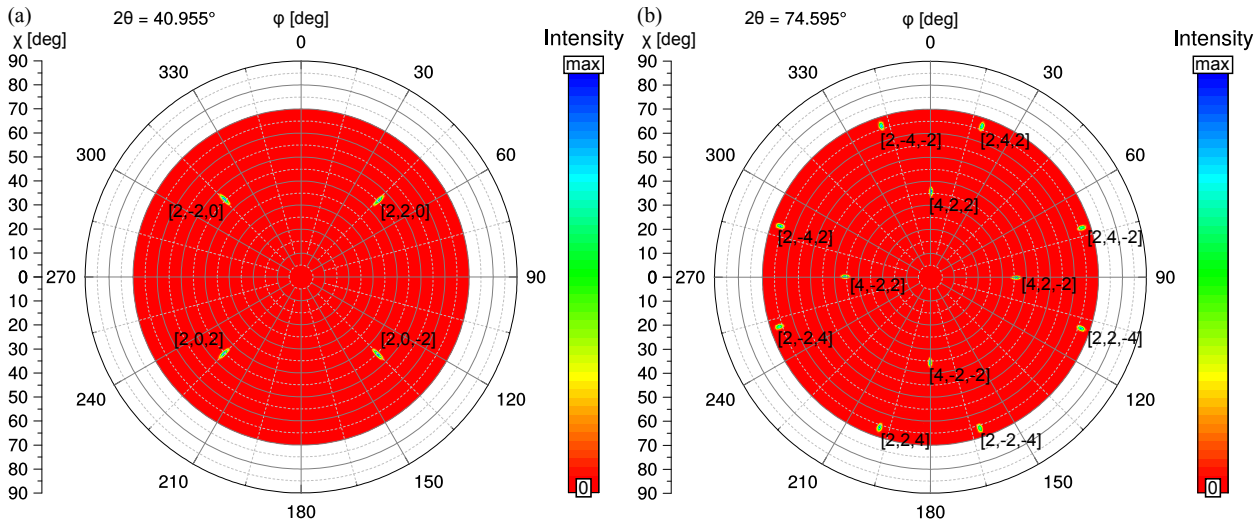

Figure 2.4: Off-specular XRD measurements in an Eulerian cradle configuration. These exemplary scans performed at angles of (a) $2\theta = 40.955°$ and (b) $2\theta = 74.595°$ confirm the crystalline growth of the PtMnSb with (001) orientation due to the detection corresponding sharp Bragg reflections. Off-specular Bragg reflections from the (111) orientation could not be found.

smooth surface of the half-Heusler material, larger grains and a more pronounced island growth is observed when the half-Heusler layer is deposited at an increased temperature of 475 °C. This is exemplarily illustrated in view of the AFM image exhibited in Fig. 2.6(b).

In general, these AFM images indicate larger grains and an increasingly significant island growth at higher deposition temperatures. The exemplary 10 nm thick PtMnSb sample of the series deposited at approximately 400 °C shows a smoother thin film consisting of significantly smaller grains with mosaicity growth which in comparison appears homogeneous. The arithmetic average roughness R_{av} is 0.71 nm and 5.02 nm for a deposition temperature of about 400 °C and 475 °C, respectively. In the former case this small value underlines the structural coherence and epitaxial growth in large regions. The corresponding line scans and height distributions shown in the associated Figs. 2.6(c) and (d), emphasize the difference in surface roughness as a result of the PtMnSb film growth.

Besides the AFM study presented here, XRR measurements and a subsequent simulation of the optical depth profile and structural parameters were performed to analyze thickness, roughness and indirectly the growth of the Heusler compound by XRR fits utilizing a layer-by-layer model.

The distinctive oscillations in the XRR curves illustrated in Fig. 2.8 represent relatively smooth surfaces for all PtMnSb layers with a thickness exceeding 5 nm. The layer roughness is determined based on the respective fits to be in the range of 0.7 nm to 1.2 nm. This precisely matches the roughness value obtained by the AFM measurements presented in Fig. 2.6.

For the analysis of the thin film system with STEM imaging the sample has to be carefully prepared by a focused ion beam (FIB) procedure to fabricate a thin electron transparent TEM lamella with

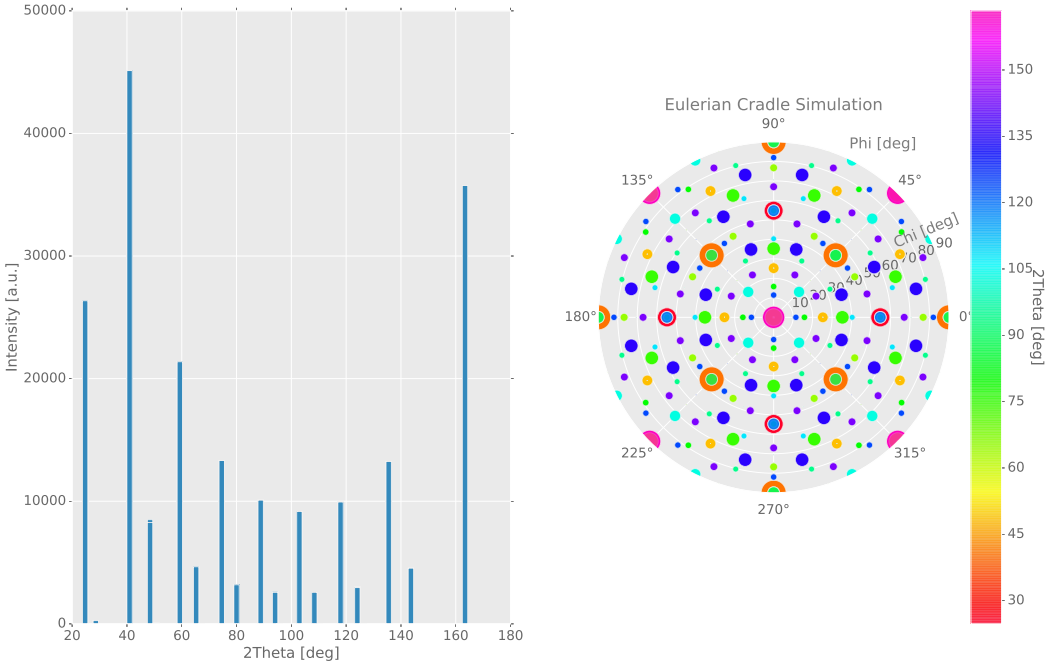

Figure 2.5: Simulation of the x-ray diffraction peak positions and intensities in the Eulerian cradle pole figures. The calculated x-ray diffraction pattern of the PtMnSb half-Heusler is illustrated on the left. The simulated results of the texture analysis performed with an Eulerian cradle on this (001) orientated structure is shown on the right. This polar plot simulation is based on the calculated diffraction pattern factoring in the position on the χ- and ϕ-circle planes used for the texture analysis. The area of the circle marks represents the relative intensity of the corresponding reflex.

a thickness of less than 100 nm. This ion beam milling allows to work *in situ* and process even materials which are not processable by conventional etching methods. The part of the structure for the STEM investigation can be chosen with extreme accuracy which a necessary prerequisite for high precision STEM-HAADF imaging of, e.g., defined interfaces regions. The FIB preparation and subsequent STEM imaging was performed at the Advanced Microscopy Laboratory (LMA) in Zaragoza. A thinned TEM lamella attached to the holder as a result of the preparation for the analysis of the Pt/PtMnSb bilayer is shown in Fig. 2.7. The sample is thinned to its final thickness and fixed via FIB-assisted chemical vapor deposition of Pt where the precursor gas is decomposed into volatile and non-volatile components by the ion beam scanning the area. This process also leads to the deposition of amorphous carbon on the surface originating from the organic platinum complex utilized as precursor.

A collection of representative STEM images of Pt/PtMnSb bilayers with a varying thickness of PtMnSb is presented in Fig. 2.10. In order to clearly separate both the PtMnSb as well as the Pt layers within the STEM pictures it is expedient to consider Figs. 2.10(d) and (e) where the PtMnSb half-Heusler and Pt fcc structure can be distinguished by structural order, brightness and the explicitly labeled crystal directions. The image allows for the conclusion that the thinnest layer, Pt/PtMnSb(5 nm) which is imaged in Figs. 2.10(a) and (b) grows epitaxially in the Volmer-Weber mode. In this growth

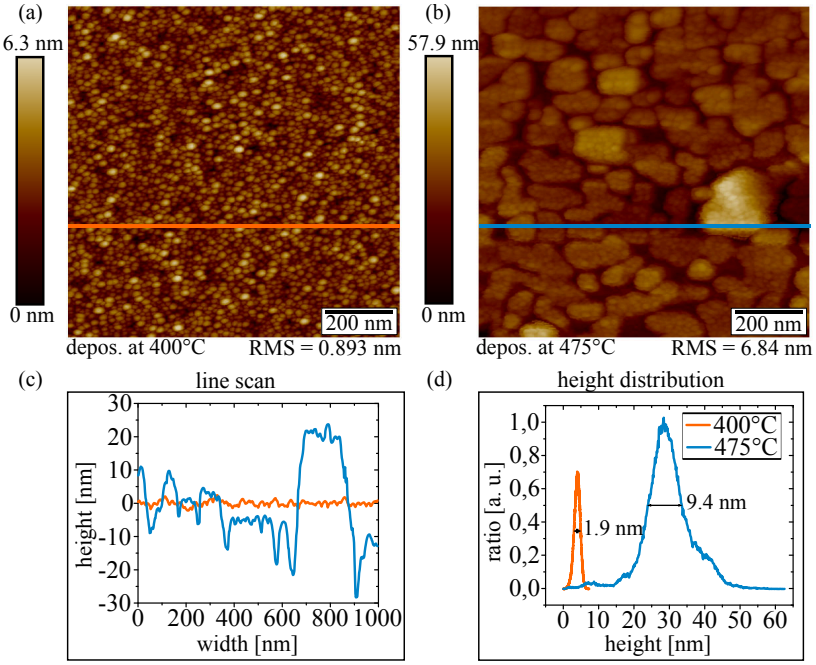

Figure 2.6: AFM images of 10 nm PtMnSb films deposited at (a) 400 °C and (b) 475 °C. Higher deposition temperature indicates larger grains and more distinct island growth. The corresponding line scan (c) and plot of the height distribution (d) emphasize the difference in roughness and PtMnSb film growth.

mode, the interactions between the deposited atoms are stronger than those of the adsorbate with the surface which leads to the formation of discrete clusters or islands before the layer is completed by infilling.

In this process, the PtMnSb forms a sharp interface with the MgO of the substrate, while the dark field images illustrate the non-wetting elemental micro and granular structure of the PtMnSb. In large regions of 20 nm to 60 nm, the images show epitaxy as well as structural coherence. Layer specific diffraction patterns are presented next to the STEM image on the right side of Fig. 2.10(b). These correspond to the structural order of the adjacent material and emphasis the local epitaxial growth on the MgO substrate.

In this calculated diffraction patterns, the red arrow points out the structural coherence in the direction of growth of this Pt/PtMnSb bilayer. Here, the Pt top layer grows over the substrate

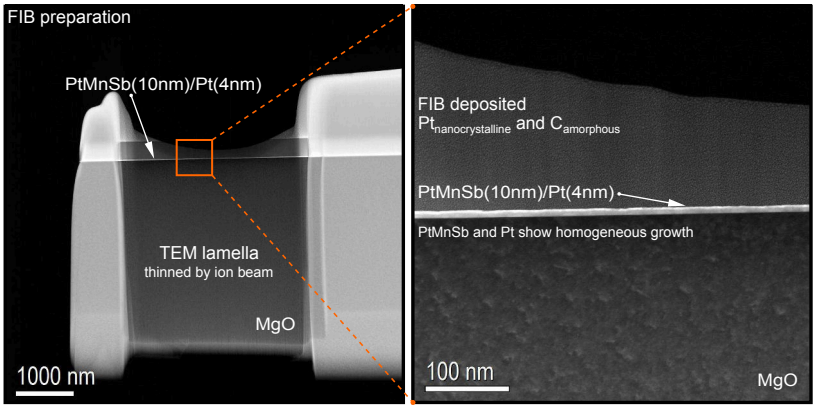

Figure 2.7: TEM dark field images illustrating the result of the FIB preparation process in form of a thinned TEM lamella. This general view of the Pt/PtMnSb(10 nm) indicates a homogeneous film grows with a minor level of roughness. The zoomed in image on the right shows the deposited film in the center in between the MgO substrate and the FIB deposited Pt and carbon. The image contrast in depending on atomic number of the film elements, light elements appear darker, heavy elements are brighter in this dark field image.

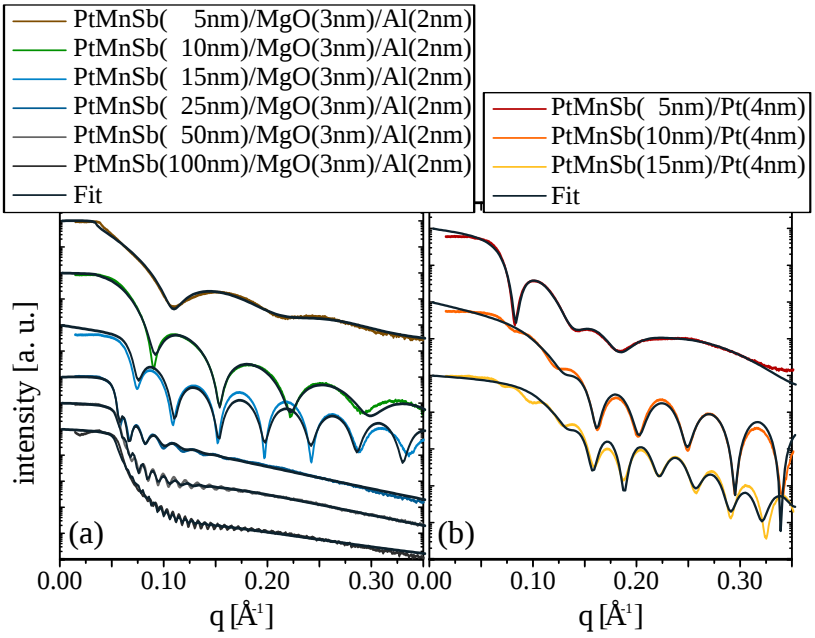

Figure 2.8: XRR measurements of (a) single PtMnSb(x nm) layers with capping and (b) Pt/PtMnSb(x nm) bilayers. XRR measurements show Kiessig oscillations which can be described by a typical Parratt layer-by-layer model using additional transition layers for the bilayer system.

in a uniform way, covering both PtMnSb islands as well as the bare MgO substrate evenly. Consequently, the Pt is growing directly on the MgO in regions without PtMnSb. Another important point in this TEM investigation lies in the detailed assessment of the interface quality within the bilayer system. This image collection reveals that the interface of Pt/PtMnSb(5 nm) is partially defective, which is shown in Fig. 2.10(b), presenting a STEM-HAADF image of an island of the nominal 5 nm film with a height of up to 9.5 nm.

Moreover, the pronounced island growth of the Pt(4 nm)/ PtMnSb(5 nm) bilayer system produces a surface roughness which is roughly of the same size and structure as the thin half-Heusler layer since the substrate is only partially covered. Figure 2.9 illustrates details of this island growth result. It is obvious that the Pt on the top is copying the PtMnSb surface structure caused by the separated islands and thus in areas without PtMnSb covering,

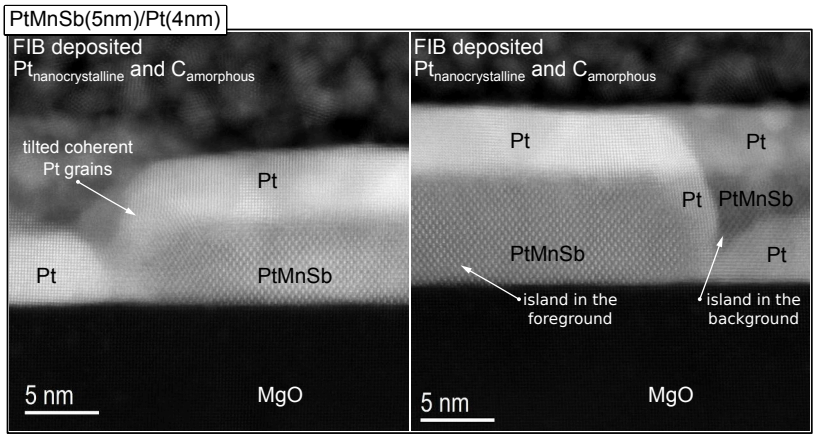

Figure 2.9: Detailed dark field STEM images of pronounced island growth of the Pt(4 nm)/PtMnSb(5 nm) bilayer system. The image on the left shows tilted mosaic Pt grains while the image on the right illustrates the increased surface roughness due to irregular substrate covering.

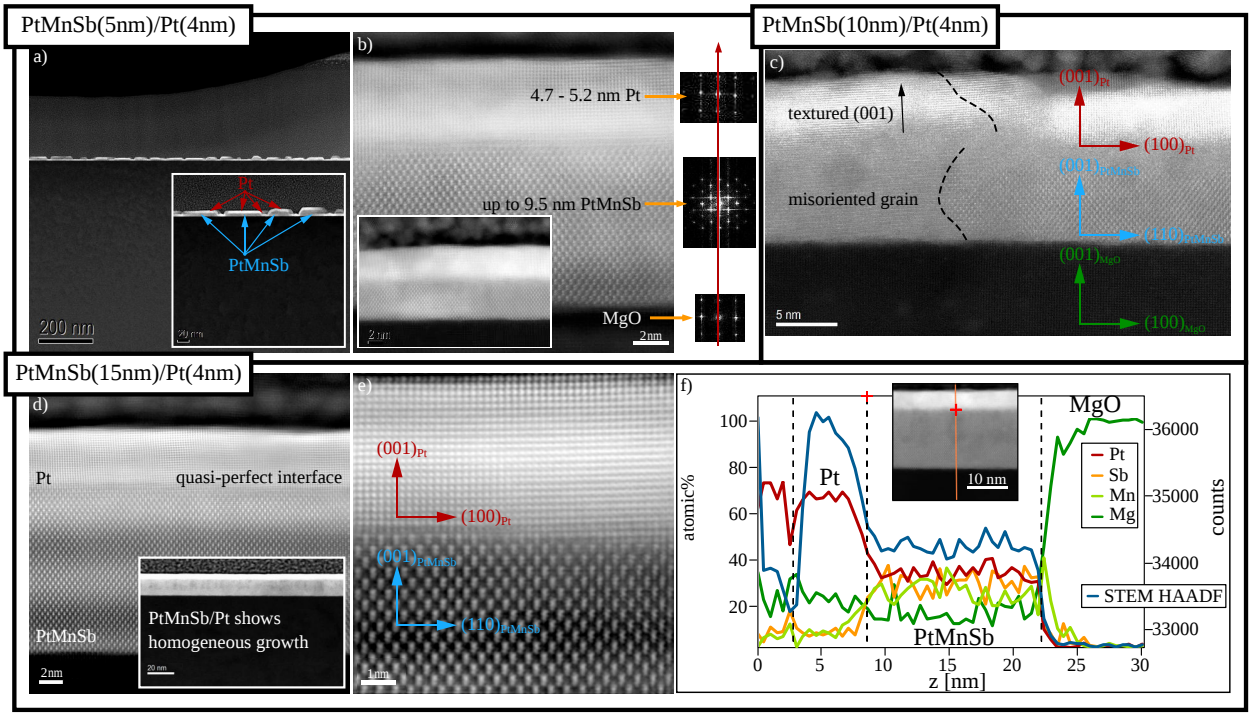

Figure 2.10: STEM-HAADF images reveal local crystalline growth of PtMnSb and Pt on the MgO substrate. (a) Films with small PtMnSb thicknesses of 5 nm show elongated islands. Inset shows a zoom-in of this bilayer. (b) STEM-HAADF image illustrates an anomaly in the Pt(4 nm)/PtMnSb(5 nm) bilayer where an island grew up to 9.5 nm. Inset shows the standard 5 nm thin film sample epitaxial growth. Red arrow across the calculated diffraction patterns indicates a coherent axis in direction of growth. (c) Thicker films of 10 nm show a small transition zone and misoriented grains. The black dotted lines are a guide to the eye for separating this misoriented grain from the epitaxial growth. (d) Films of 15 nm thickness have ultimately layer-by-layer growth, as seen in the inset showing homogeneous growth. (e) STEM-HAADF image with Wienner filtering for noise removing of the interface and the EDX linescan profile (f) reveal quasi-perfect interface matching without an interdiffusion region.

the Pt is growing directly on the MgO. The Pt layer is in general growing quasi-epitaxially on the ordered PtMnSb yet at the island boundaries a slight tilting or mosaicity of the coherent Pt grains is observable in the right image of Fig. 2.9. The Pt deposited during the FIB preparation forms a segregated mix of nanocrystalline Pt grains and amorphous carbon between those crystallites.

Furthermore, the intermediate thickness layer, Pt/PtMnSb(10 nm) is featured in the collection in Fig. 2.10(c) which shows a relatively homogeneous growth and significant lower roughness. This is due to the Frank-van der Merwe growth mode, where atomic layers of PtMnSb are attached on fully formed PtMnSb layers which results in fully formed layers.

This transition from island-based to the layer-by-layer growth can be observed at a critical layer thickness. It is highly dependent on the physical and chemical characteristics of the substrate as well as on the deposited thin film, for instance the lattice parameters and surface energies.[14] The images show a small transition zone, which manifests at the interface, where the Pt is forced into a disordered cubic structure. Partially epitaxial films with a transition zone adjusting to both crystal structures are presented by the STEM-HAADF images. These also show that areas with excess Pt tend to grow adopting the fcc structure instead of the half-Heulser structure.

EDX linescans were performed along the surface normal direction as illustrated in the insert TEM image in Fig. 2.10(f). These scans confirm that certain areas of Pt(4 nm)/PtMnSb(10 nm) exhibit a transition zone of about 2.5 nm with high Pt content on top of

[14] A. Pimpinelli and J. Villain. *Physics of Crystal Growth*, volume 19. Cambridge University Press (1998)

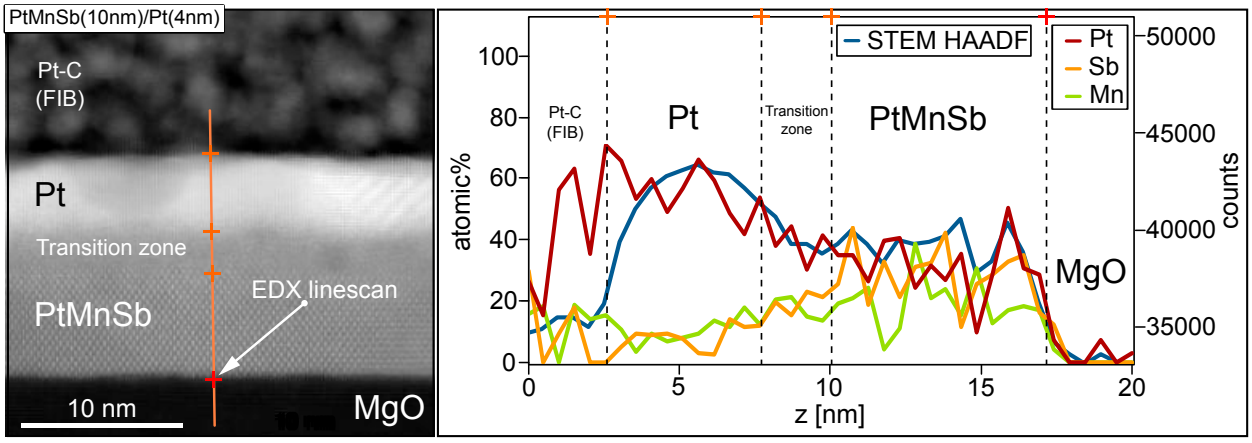

Figure 2.11: (a) STEM-HAADF image of the EDX probed area of the Pt(4 nm)/PtMnSb(10 nm) bilayer. (b) EDX linescan with drift correction enabling long time measurements for higher accuracy.

the stoichiometric PtMnSb. Figure 2.10(c) illustrates this zone in form of a large interface defect, which is represented in gray color between the bright Pt and ordered PtMnSb area. These transition or intermediate layers contain misoriented grains which are representatively shown on the left side of Fig. 2.10(c). Here, it is not possible to resolve the lattice structure of the PtMnSb half-Heusler. Therefore, these STEM image exhibits a quasi-amorphous and defective interface between the Pt and PtMnSb layer in the C1b structure.

The thickest Pt/PtMnSb(15 nm) bilayer system, which is illustrated in Figs. 2.10(d) and (e), shows quasi layer-by-layer growth. Here, the islands are closed up and the layer is fully formed with growing thickness. Consequently, the surface becomes smoother which resembles the result of layer-by-layer growth at the final stage. The interface merely exhibits minor steps and few dislocations when fitting the two lattices with an almost perfect match. A section with perfect layer-by-layer growth and a smooth interface transition is depicted in Fig. 2.10(e) where the corresponding lattice orientations are marked in the atomic structure. Consequently, one has to conclude that thin PtMnSb layers show island growth and a defective Pt/PtMnSb transition zone.

In contrast, thicker films feature homogeneous epitaxial growth and, thus, high quality interfaces can be observed. Given that the XRD analysis discloses polycrystalline characteristics in these thicker films, the homogeneous growth, primary influenced by the thicker and therefore smoother half-Heusler structure, is confined locally. However, these grains become significantly larger and more defect-free as the PtMnSb thickness increases, which is confirmed by the STEM image compilation presented here. Furthermore, Fig. 2.10(f) illustrates the transversal EDX linescans, measured with a drift correction, which confirm the fundamental composition of the Pt/PtMnSb bilayer sample as determined for the sputter deposition process by EDX and XRF analysis.

The illustration in Fig. 2.11 reveals the pronounced transition zone present in the Pt/PtMnSb(10 nm) bilayer system in greater

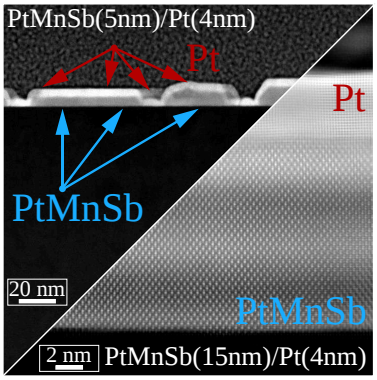

Figure 2.12: Comparison of STEM images of the Pt(4 nm)/PtMnSb(5 nm) and Pt(4 nm)/PtMnSb(15 nm) bilayer systems. The upper left half illustrates the distinctive island growth in the thin films while the bottom right half shows the quasi perfect layer-by-layer growth with a smooth interface.

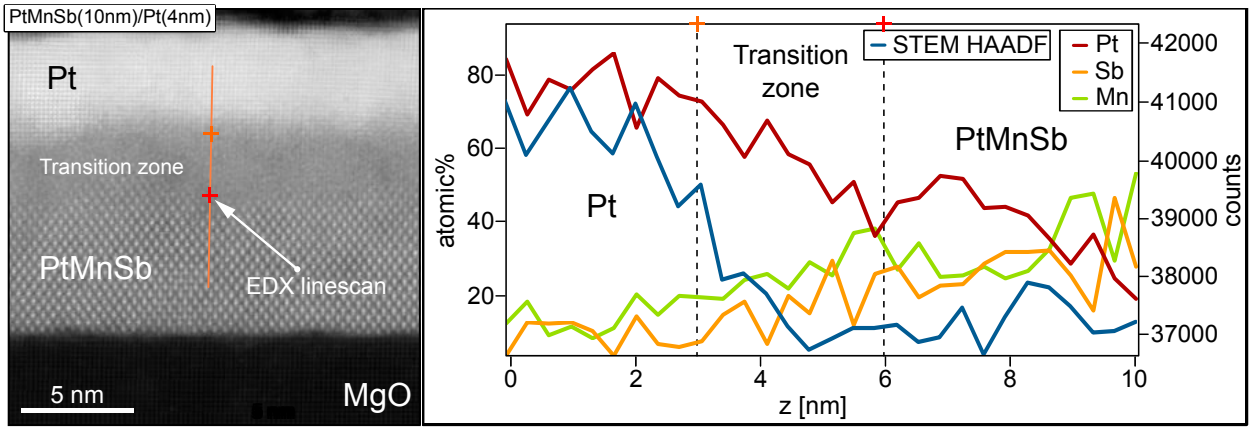

Figure 2.13: (a) STEM-HAADF image of the Pt(4 nm)/PtMnSb(10 nm) in relation to the position of the line scan. (b) EDX line scan showing the relative elemental content across the transition zone at the Pt/PtMnSb interface.

detail. Again, the composition of the PtMnSb thin film and Pt cover layer is confirmed within the tolerance of the EDX scan. Most notably is the defective interface between the crystalline PtMnSb and Pt layer which is clearly identifiable as a transition zone between the ordered layers. This region with a lateral extent of 2 nm exhibits a high platinum content as shown by results of the EDX linescan probing the stoichiometry along the film normal. Most likely the Pt is therefore compelled to adopt a different structure with respect to the half-Heusler martial forming a disordered cubic structure. This structure is indicated in the STEM images in gray color between the established Pt and PtMnSb layers shown in lighter shades of gray with a defined crystallinity.

The second transversal line scan visualized in Fig. 2.13 is essentially a zoom in into the large transition zone to investigate this interface defect in greater detail. The corresponding EDX composition results are again shown in the right side of the graphic representation. This again shows that the 10 nm PtMnSb film is not completely epitaxial. In regions where a defined transition zone has formed this structure between the Pt and PtMnSb attempts to adjust to both crystal structures as energetically favorable as possible.

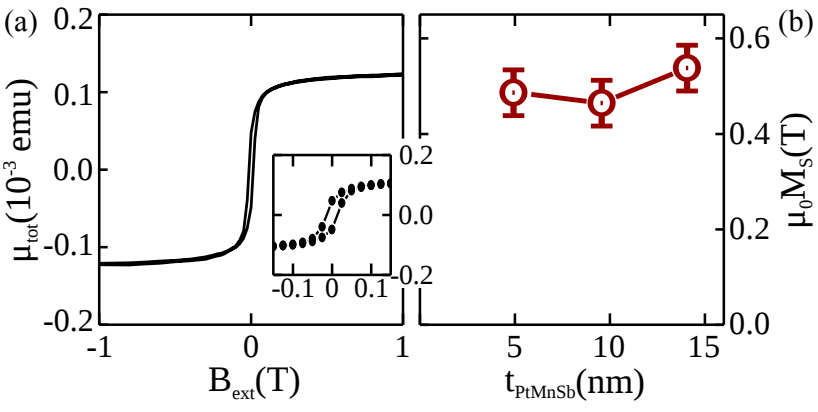

Figure 2.14: Magnetic SQUID measurements of (a) an exemplary magnetic hysteresis loop (in-plane) of the Pt(4 nm)/PtMnSb(15 nm) sample and (b) M_S of Pt(4 nm)/PtMnSb(t nm) bilayers as a function of thickness t_{PtMnSb}. The inset shows an enlargement of the low field region.

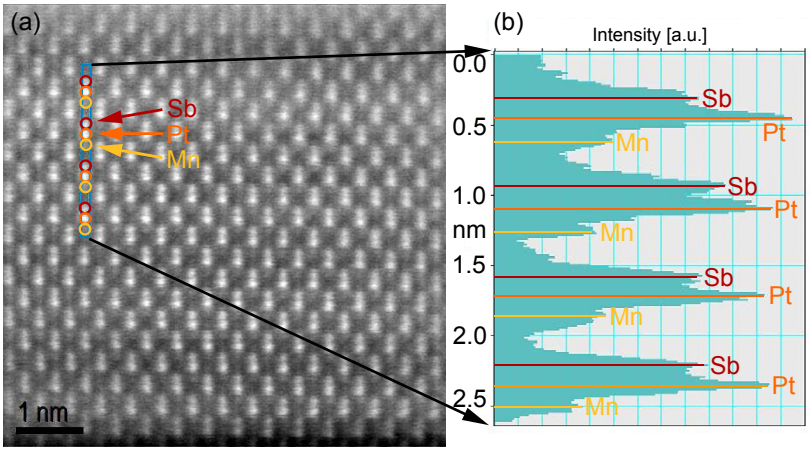

Figure 2.15: The scattering in high-angle annular dark-field imaging (HAADF) is a direct probe of the structural coherence and is highly sensitive to variations in the atomic number of atoms in the sample. The image (a) of a Pt(4 nm)/PtMnSb(5 nm) is used for an analysis of the scattering intensity (b) visualizing the atomic positions of Sb, Pt, Mn.

The excess Pt, detected by the EDX line scans, tries to copy the fcc Pt structure instead the half-Heusler structure of the PtMnSb film. The zoomed in line scan in Fig.2.13 quantifies a thickness of the Pt cover film of (4.3 ± 0.5) nm, a transition zone of (2.5 ± 0.5) nm with an elevated Pt content and a PtMnSb layer of (6.5 ± 0.5) nm. Thus, the transition zone in combination with the PtMnSb structure has a lateral extent of (9.0 ± 0.5) nm close to the calibrated thickness of the 10 nm PtMnSb thin film.

Figure 2.14 shows exemplary superconducting quantum interference device (SQUID) magnetization measurements at room temperature including a hysteresis loop of the Pt(4 nm)/PtMnSb(15 nm) bilayer which is presented on the left side in Fig. 2.14(a). The samples show an in-plane magnetization with a coercivity of about 150 Oe. An additional variance of 10 % due to an upper bound for any SQUID related artifact such as sample shape is considered for the measurements of the saturation magnetization M_S of Pt(4 nm)/PtMnSb(t nm) bilayers as a function of thickness t_{PtMnSb}. This saturation magnetization of the sample series featured in the STEM image collection is shown in Fig. 2.14(b) and the precise sample thickness was rechecked for this SQUID analysis by additional STEM measurements to determine the magnetic volume. The determined values are about 30 % below the literature bulk values for PtMnSb (570 kA/m).[15]

The crystal structure of the PtMnSb layer is visualized in the STEM images by high-angle annular dark-field imaging (HAADF). Here, an annular dark field image is produced by detecting incoherently Rutherford scattered electrons under very high angle. An advantage of this technique is that it is highly sensitive to different atomic number of atoms in the crystal lattice and can therefore provide a so called z-contrast STEM image which is shown in Fig. 2.15 along with a detailed analysis of the scattering intensity picturing the exact position of elements of a certain atomic number and in this case the different lattice sides of the PtMnSb half-Heusler.

In bright-field images in conventional TEM of the Pt(4 nm)/

[15] T. Inukai, M. Matsuoka, and K. Ono. Magneto-optical properties of vacuum-deposited PtMnSb thin films. *Appl. Phys. Lett.*, **49**(1):52–53 (1986); and E. Attaran and P. J. Grundy. The magnetic, magneto-optical and structural properties of PtMnSb thin films. *J. Magn. Magn. Mater.*, **78**(1):51–55 (1989)

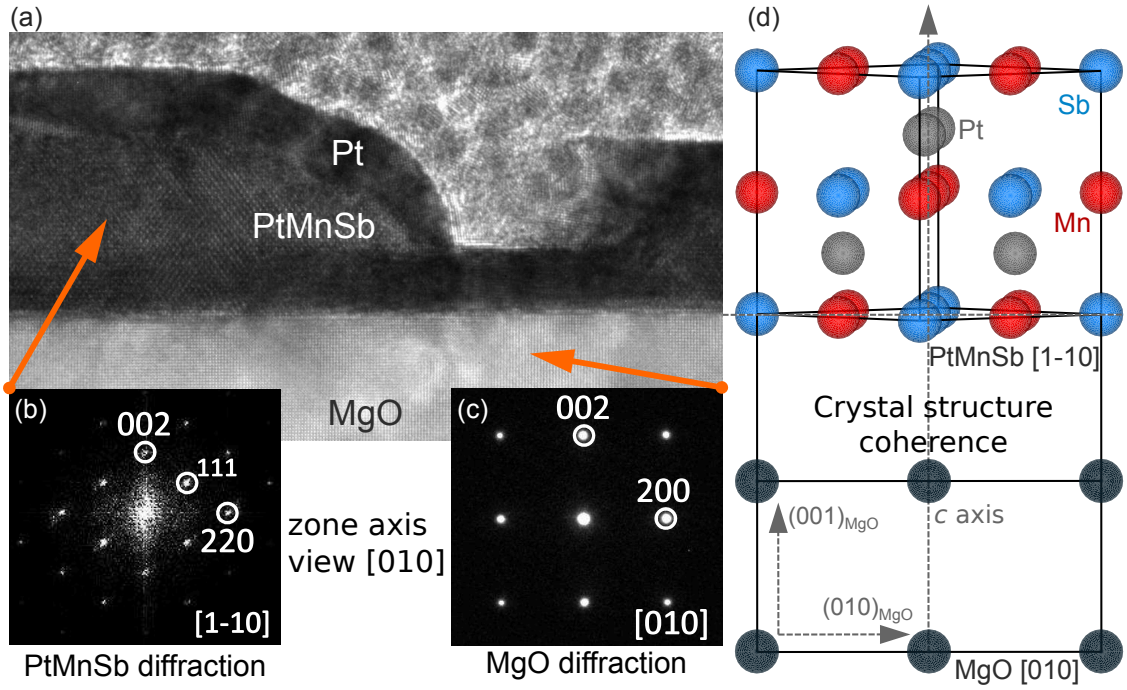

Figure 2.16: (a) Bright-field image in conventional TEM of the Pt(4 nm)/ PtMnSb(5 nm) bilayer system. The corresponding PtMnSb (b) and MgO (c) diffraction patterns in the zone axis view [010] are shown below revealing the crystal structure coherence (d) illustrated on the right.

PtMnSb(5 nm) bilayer system the island growth of the thin PtMnSb film is clearly visible. The top Pt layer adapts the grown PtMnSb framework and is deposited directly on the substrate in open areas. One bright-field image of this bilayer is shown in Fig. 2.16 in combination with corresponding PtMnSb and MgO diffraction patterns in the zone axis view [010]. Based on these diffraction patterns the crystal morphology at the interface can be determined and the crystal structure coherence, derived from this patterns, is illustrated on the right hand side of Fig. 2.16.

In Figure 2.17 an overlap of the diffraction pattern of the three major sub-structures of the Pt(4 nm)/PtMnSb(5 nm) bilayer system is presented. The view of this area electron diffraction image is perpendicular to the view presented in the bright-field image of Fig. 2.16. The bright spots represent the cubic MgO [010] structure while the smaller spots marked in the picture are diffraction patterns of the PtMnSb half-Heusler [1$\bar{1}$0] structure. The crystalline Pt top layer creates a similar cubic diffraction pattern. This can be observed in direct contrast to the ring pattern in the center of the image which corresponds to the nanocrystalline Pt deposited during the focused ion beam (FIB) sample preparation for the STEM analysis.

In comparison to the general overview of the STEM crystalline growth of PtMnSb and Pt on the MgO substrate presented in Fig. 2.10, it is beneficial to investigate the growth mode of the Pt(4 nm)/PtMnSb(10 nm) thin film in more detail. Figure 2.18 contrasts two STEM-HAADF images of this particular structure focusing on the predominant grain structure in this sample.

Figure 2.18(a) illustrates the main crystal structure with an orientation of $\mathbf{n} = [1\bar{1}0]$ of the half-Heusler forming the basis

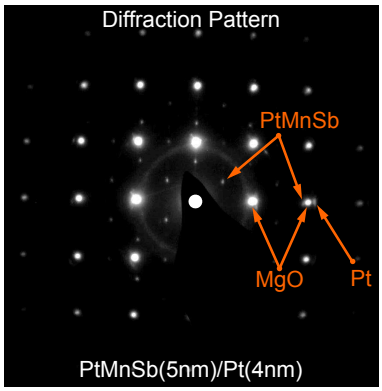

Figure 2.17: Diffraction overlap of the Pt/PtMnSb//MgO [1$\bar{1}$0], PtMnSb [010] and MgO [010] structures in a selected area electron diffraction image of the Pt(4 nm)/PtMnSb(5 nm) bilayer system. Each illuminated spot in this image corresponds to a satisfied diffraction condition based on the selected crystal structure of the sample.

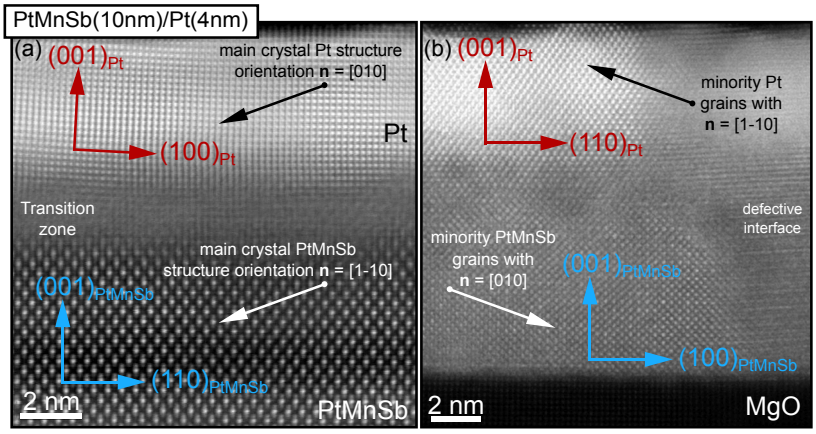

Figure 2.18: STEM-HAADF images of the Pt(4 nm)/PtMnSb(10 nm) thin film with Wiener filtering for de-noising. (a) The main crystal structure orientation of this thin film system with $\mathbf{n} = [1\bar{1}0]$ for the PtMnSb layer and $\mathbf{n} = [010]$ for the Pt layer, correspondingly. Between these structures the defective interface zone is formed (dark grey) with an expansion of ~ 2 nm. (b) STEM image of a minor grain structure reoccurring in the thin film, with a $\mathbf{n} = [010]$ orientation for the PtMnSb grains and $\mathbf{n} = [1\bar{1}0]$ image normal for the Pt grains.

for a $\mathbf{n} = [010]$ oriented Pt top layer. These two main crystalline structures are separated by the defective interface, matching both crystal structures via the Pt rich transition zone. On the left hand side of the top Pt layer the small tilting of coherent grains can be observed. Despite the epitaxial growth of the PtMnSb, the subsequent formation of a Pt rich transition zone leads to a slight yet observable mosaicity of the top Pt structure.

The image shown in Fig. 2.18(b) proofs the occurrence of some minority $\mathbf{n} = [010]$ grains in the PtMnSb layer. On top of these grains Pt grows with a $\mathbf{n} = [1\bar{1}0]$ structural orientation as indicated on the left side of the STEM image. The defective interface in this image appears to be significantly smaller compared to the majority grain orientation yet the image also shows a grain boundary on the right where no epitaxial microstructure is visible and the Pt top layer is indistinguishable from the PtMnSb film at the bottom.

The STEM-HAADF images in the compilation Fig. 2.19 are acquired with additional Wiener filtering for de-noising and higher image quality. They reveal nearly perfect interface matching without any interdiffusion region or transition zone as observed for the thinner Pt(4 nm)/PtMnSb(10 nm) sample. Both the Pt/half-Heuler as well as the substrate interfaces are sharp and only adapt the

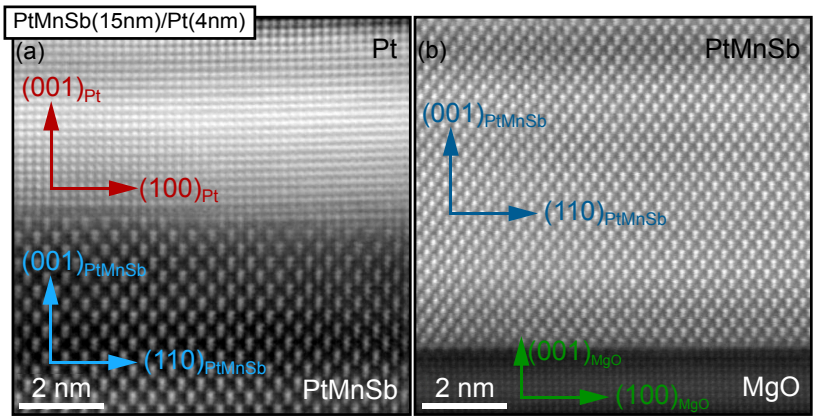

Figure 2.19: STEM-HAADF images of the Pt(4 nm)/PtMnSb(15 nm) interfaces with Wiener filtering for de-noising. (a) The quasi-perfect interface adaptation without any transition zone as seen for the PtMnSb(10 nm) sample. There are few structural fitting steps visible matching both crystalline layers. (b) Corresponding quasi-perfect substrate interface of the Pt(4 nm)/PtMnSb(15 nm) sample.

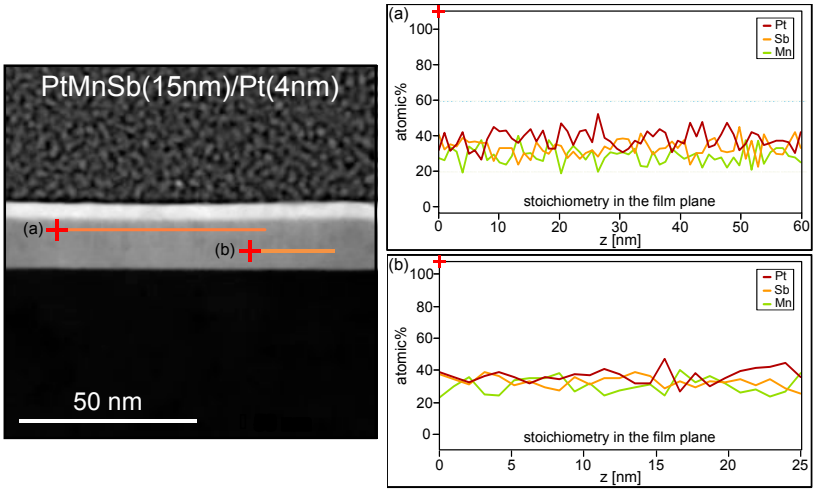

Figure 2.20: Longitudinal EDX line scans performed on the PtMnSb (15 nm)/Pt (4 nm) sample to confirm the homogeneousness of the stoichiometry. Line scan (a) shown a minimal excess of Pt due to the proximity to the Pt top layer while the line scan (b) realized deeper in the PtMnSb shows ratios of the expected half-Heusler compound.

structural differences through minimal steps and few dislocations.

The two EDX line scans presented in Fig. 2.20 illustrate the homogeneous film growth the PtMnSb thin film system. The first scan presented in scan Fig. 2.20(a) confirms the homogeneous stoichiometry along the plane of the thin film where the actual EDX scan path is indicated on the STEM dark field image. In relation to the shorter scan (b), which was performed on a path deeper into the half-Heusler layer, scan (a) reports a slightly higher Pt content than expected for a perfect half-Heulser structure which may originate in the closer proximity of the EDX path to the covering Pt top layer.

To compare the different structural properties of the PtMnSb thin films of different thickness STEM images of the Pt(4 nm)/PtMnSb(5 nm), Pt(4 nm)/PtMnSb(10 nm) and Pt(4 nm)/PtMnSb(15 nm) bilayer systems are contrasted in the compilation of Fig. 2.21. STEM image Fig. 2.21(a) is focused on a larger PtMnSb island of the irregularly grown PtMnSb (5 nm) thin film covered with Pt. This illustrated epitaxial growth of this island on the MgO substrate accompanied by a sharp interface. The top Pt layer grows epitaxially as well yet it reveals signs of slight crystal mosaicity. As indicated by the small transition zone shown in the image with a lateral extent of 0.6 nm, the Pt/PtMnSb interface is partially defective in contrast to the very sharp PtMnSb//MgO interface. In other regions of the film, especially in larger grains, there is higher structural coherence and an almost perfect Pt/PtMnSb interface with an epitaxially grown Pt top layer as seen in the top central STEM image of Fig. 2.10. Here, the thickness of PtMnSb is 5.0 nm while in other grains it can go up to $\sim$ 9.5 nm. The thickness of the Pt cover layer in this STEM image as a slight variation of 4.7 nm $-$ 5.2 nm.

In contrast, Fig. 2.21(b), depicting the Pt(4 nm)/PtMnSb(10 nm) bilayer, shows a section of the continuously grown thin film without any island formation. This has a positive effect on the overall roughness resulting in an overall homogeneous growth. However,

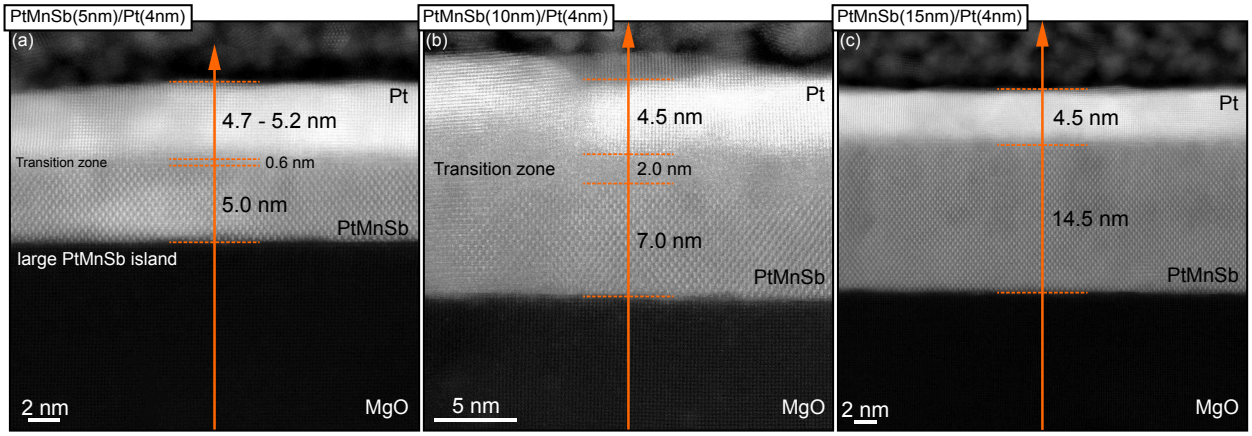

Figure 2.21: STEM-HAADF images of the (a) Pt(4 nm)/PtMnSb(5 nm), (b) Pt(4 nm)/PtMnSb(10 nm) and (c) Pt(4 nm)/PtMnSb(15 nm) thin film samples without additional filtering. For the thin PtMnSb(5 nm) sample a large PtMnSb island with epitaxial growth is shown for comparison.

in this particular region the transition zone, as analyzed by the EDX line scans, is quite pronounced. The combined thickness of this zone and the epitaxially grown PtMnSb is 9.0 nm while the ordered and [001] textured Pt cover has a thickness of 4.5 nm in the center of this STEM image. On the left side this image also shows a misoriented grain structure since the PtMnSb(10 nm) film is not completely epitaxial.

Without this supporting epitaxial micro-structure by the half-Heulser the Pt is indistinguishable across a misoriented sub-structure. The best results are achieved for the thicker Pt(4 nm)/PtMnSb(15 nm) bilayer system as depicted by the aberration corrected STEM-HAADF image on the right illustrating the quasi perfect interface matching of both interfaces with a measured PtMnSb thickness of 14.5 nm and a smooth Pt capping with a lateral extent of 4.5 nm.

Conclusion

Looking at these results in a recapitulatory way, it is shown that highly textured PtMnSb thin films and Pt/PtMnSb bilayers can be grown by co-sputter deposition on MgO (001) substrates. The PtMnSb films grow epitaxially, whereupon the degree of coherence and texture depends essentially on the half-Heusler thickness. The C1b cubic crystal structure of the half-Heusler alloys is obtained for the primary PtMnSb layer. Additionally, Pt grows as a uniform polycrystalline fcc layer in the bilayer systems, where the interface quality is significantly improving with increasing PtMnSb thickness, up to quasi-perfect matching.

Most notably, thin PtMnSb films of 5 nm grow as separate islands, while thicker films such as 15 nm and above exhibit layer-by-layer growth. In the bilayer systems, the Pt covers the PtMnSb as well as the MgO substrate, infilling the islands on the PtMnSb (5 nm) thin films. In contrast, the Pt grows epitaxially on the

smooth PtMnSb (15 nm) films, which result in fully formed bilayers. In locally-constricted regions of this thin film, the Pt grows crystalline on the PtMnSb which is illustrated by the corresponding STEM images. However, the XRD analysis reveals the polycrystalline textured character for the whole Pt/PtMnSb film, based on this film-averaging probe. In particular, PtMnSb shows a monocrystalline phase with (001) orientation which can be concluded from off-specular XRD measurements. In addition, a second polycrystalline phase with a (111) texture is found, however, the share of this phase is slightly reduced when the half-Heusler layer thickness is increased.

In conclusion, the results presented in this chapter demonstrate that heterostructures based on the PtMnSb Heusler alloy are feasible candidates to study SOT in noncentrosymmetric systems and realize spintronic devices based on this effective way to manipulate magnetization.

3
Vectorial observation of the spin Seebeck effect in epitaxial $NiFe_2O_4$ thin films

The ferromagnet PtMnSb exhibits a high spin polarization and yields large magnetoresistance ratios based on its unique half-metallic band structure with a high spin polarization of ideally 100 %, as discussed in chapter 1.7. This has facilitated the incorporation of half-Heusler compounds into spintronic devices, e.g., in order to dramatically increase the tunnel magneto resistance ratio.[1] Moreover, in addition to this application in form of ferromagnetic electrodes, this half-Heusler alloy has the ability to provide a spin-charge conversion effect.

These characteristic has increased the interest in the physical properties of the concerned Heusler materials. Due to the half-metallic DOS, where only one spin channel is available at the Fermi level in the ground state, the spin-charge conversion is considered forbidden without the assistance of magnons at a finite temperature.[2] In general, if a material is in a fully spin-polarized ground state, there should be no detectable spin current carried by conduction electrons when a temperature gradient is applied to this material. This is due to the fact that in the specific half-metallic band structure of PtMnSb for the bulk state, the minority spin band has its gap at the Fermi level. However, the minority gap can, in contrast, close as a result of the electron-magnon interactions as well as defined interface states.[3]

Additionally, a spin-charge conversion can occur based on the degradation of the perfect half-metallicity, which in case of defective or non-epitaxial growth can be a distinct structural feature of the interface region.[4] Therefore, a significant spin-charge interaction can be presumed due to a combination of bulk and interface contributions.

Thus, the spin Seebeck effect in half-metallic ferromagnets such as PtMnSb is likely to be associated with a magnon excited spin current or a spin-orbit active interface region. Due to the semiconducting properties of the minority-spin electrons, the same mechanism applies as in magnetic insulators. Here, one prominent example is Nickel ferrite which is utilized for the observation of pure spin current effects in the following chapter of this thesis.

[1] A. Bratkovsky. Tunneling of electrons in conventional and half-metallic systems: Towards very large magnetoresistance. *Phys. Rev. B*, **56**(5):2344 (1997); and C. Tanaka, J. Nowak, and J. Moodera. Magnetoresistance in ferromagnet-insulator-ferromagnet tunnel junctions with half-metallic ferromagnet NiMnSb compound. *J. Appl. Phys.*, **81**(8):5515–5517 (1997)

[2] Y. Ohnuma, M. Matsuo, and S. Maekawa. Spin transport in half-metallic ferromagnets. *Phys. Rev. B*, **94** (18):184405 (2016)

[3] M. Katsnelson, V. Y. Irkhin, L. Chioncel, A. Lichtenstein, and R. A. de Groot. Half-metallic ferromagnets: From band structure to many-body effects. *Rev. Mod. Phys.*, **80**(2):315 (2008)

[4] C. T. Tanaka, J. Nowak, and J. S. Moodera. Spin-polarized tunneling in a half-metallic ferromagnet. *J. Appl. Phys.*, **86**(11):6239–6242 (1999); and I. Galanakis. Surface properties of the half-and full-Heusler alloys. *J. Phys. Condens. Matter*, **14**(25):6329 (2002)

In context of this work, the vectorial observation technique of the spin Seebeck effect, which is discussed here based on epitaxial $NiFe_2O_4$ thin films, is in the same way applicable to the spin-charge conversion in the half-Heusler alloy films which are promising candidates for future spintronic devices. Regarding the general utility of this first vectorial magnetometry technique based on a spin caloric effect, the focus is certainly placed on the extended magnetic characterization of thin film samples which are not amenable to MOKE measurements.

Experimental and theoretical details

The Nickelferrite thin films are grown on lattice-matched substrates such as the spinel oxides $MgGa_2O_4$ (MGO) and $CoGe_2O_4$ (CGO). This strongly improves the magnetic properties, which are comparable to the benchmark material YIG.[5] In this context, both an enhanced SSE as well as improved spin transport characteristics have been demonstrated.[6] The epitaxial NFO films grown on lattice-matched substrates mainly exhibit a reduction of antiphase boundary defects. This results in enhanced signals for both electrically and thermally excited magnons, and a significantly larger magnon relaxation length which can be observed in non-local transport experiments. In Pt/NFO bilayer systems, a decent magnon spin conductivity and large spin mixing conductance at the interface can be demonstrate resulting in excellent magnon transport properties. This turns NFO and, in a broader interpretation, spinels into potential alternatives for spintronic application which are commonly based on YIG or similar garnets.

The choice of substrate material and crystal cut can thus be utilized to precisely taylor the magnetic anisotropy in the NFO thin film system. This is particularly useful in order to study the impact of the anisotropy type on the SSE since a lattice mismatch leads to strain anisotropy in addition to the magnetocrystalline anisotropy in the thin films. Thin film systems grow on different versions of this type of substrate, with varying lattice mismatch and crystal orientation, are predestined to be used for the developed a vectorial type of measurement for the SSE due to the strong magnetic properties listed above in combination with a tight control of the magnetic anisotropy. This creates a framework for the vectorial observation of the spin Seebeck effect in epitaxial NFO thin films with various magnetic anisotropy contributions which is discussed in this work. Since this vectorial magnetometry technique is based on the LSSE to study magnetization reversal processes the NFO has to be coated with a metal with a high spin Hall conductivity to act as an effective the spin-current detector.

[5] A. V. Singh, B. Khodadadi, J. B. Mohammadi, S. Keshavarz, T. Mewes, D. S. Negi, R. Datta, Z. Galazka, R. Uecker, and A. Gupta. Bulk single crystal-like structural and magnetic characteristics of epitaxial spinel frrite thin films with elimination of antiphase boundaries. *Adv. Mater.*, **29** (30):1701222 (2017)

[6] J. Shan, A. Singh, L. Liang, L. Cornelissen, Z. Galazka, A. Gupta, B. van Wees, and T. Kuschel. Enhanced magnon spin transport in $NiFe_2O_4$ thin films on a lattice-matched substrate. *Appl. Phys. Lett.*, **113**(16):162403 (2018)

Preparation and characterization of Pd/$NiFe_2O_4$ bilayers on lattice-matched substrates

The NFO films used in this work were grown by pulsed laser deposition in a similar way as described in the related studies focusing on the structural and magnetic characterization of epitaxial spinel ferrite thin films and in particular on the elimination of antiphase boundary defects[7] as well as the investigation and enhancement of the magnon spin transport in NFO thin films of excellent quality.[8]

Besides the widely utilized Pt, another material with an effective spin-charge conversion and thus a sufficiently high spin-Hall angle is Palladium (Pd).[9] It is also a member of the 4*d* and 5*d* transition metal group and has an effective spin-charge conversion and thus a sufficiently high spin-Hall angle. For this reason, Pd is also a well known SHE material and in the same way applicable as a spin-current detector. The spin Hall conductivity of the spin-current detector changes systematically in response to the number of *d* electrons in the 4*d* and 5*d* transition metal.[10] Pd has been shown to exhibit a strong spin-orbit interaction, however the spin Hall angle and therefore the spin Hall conductivity is a factor of 2-6 smaller[11] than in Pt. Nevertheless, the ISHE-signal generated by Pd is still very well suited for detecting spin currents. In addition, the utilization of Pd illustrates the broad applicability of the presented vectorial method for the observation of the SSE even in thin film systems which do not include the standard spin-detector material Pt.

The spinel ferrite NFO thin films have been grown on two different isostructural substrates, MGO with a lattice constant $a = 0.8280\,\text{nm}$ and CGO with a lattice constant $a = 0.8328\,\text{nm}$ by utilizing pulsed laser deposition. Since NFO has a nominal lattice constant of $a = 8.338\,\text{nm}$, these substrates have a lattice mismatches with $NiFe_2O_4$ of 0.78 % and 0.20 %, respectively. A larger lattice mismatch leads to a higher magnetic strain anisotropy in NFO thin films on MGO in comparison to those on CGO substrates. This was confirmed via vibrating sample magnetometry (VSM) and ferromagnetic resonance (FMR) measurements which are discussed in section 3.3.2. The fabrication and characterization of $NiFe_2O_4$ thin films were performed in close collaboration with the group of Prof. Arunava Gupta during a research stay at the University of Alabama in Tuscaloosa, AL (USA). All $NiFe_2O_4$ films were deposited on (011)- or (001)-oriented MGO and CGO substrates ($5\times5\times0.5\,\text{mm}^3$) by pulsed laser deposition (PLD) in an oxygen environment with a background pressure of 10 mTorr. The laser fluence was set to be $\sim1\,\text{J/cm}^2$. The temperature of the substrates was kept constant at 700 °C during film growth. For LSSE measurements, a 5 nm thick Pd film was deposited *in situ* by DC sputtering at 20 W power and 5 mTorr Ar pressure on top of the PLD grown NFO films.

It is noteworthy that the films grown on the near-lattice-matched substrates MGO and CGO show no antiphase boundaries (APBs)

[7] A. V. Singh, B. Khodadadi, J. B. Mohammadi, S. Keshavarz, T. Mewes, D. S. Negi, R. Datta, Z. Galazka, R. Uecker, and A. Gupta. Bulk single crystal-like structural and magnetic characteristics of epitaxial spinel frrite thin films with elimination of antiphase boundaries. *Adv. Mater.*, **29** (30):1701222 (2017)

[8] J. Shan, A. Singh, L. Liang, L. Cornelissen, Z. Galazka, A. Gupta, B. van Wees, and T. Kuschel. Enhanced magnon spin transport in $NiFe_2O_4$ thin films on a lattice-matched substrate. *Appl. Phys. Lett.*, **113**(16):162403 (2018)

[9] K. Ando and E. Saitoh. Inverse spin-Hall effect in palladium at room temperature. *J. Appl. Phys.*, **108**(11): 113925 (2010)

[10] M. Morota, Y. Niimi, K. Ohnishi, D. Wei, T. Tanaka, H. Kontani, T. Kimura, and Y. Otani. Indication of intrinsic spin Hall effect in 4*d* and 5*d* transition metals. *Phys. Rev. B*, **83**(17):174405 (2011)

[11] L. Ma, L. Lang, J. Kim, Z. Yuan, R. Wu, S. Zhou, and X. Qiu. Spin diffusion length and spin Hall angle in $Pd_{1-x}Pt_x$/YIG heterostructures: Examination of spin relaxation mechanism. *Phys. Rev. B*, **98**(22):224424 (2018); and X. Tao, Q. Liu, B. Miao, R. Yu, Z. Feng, L. Sun, B. You, J. Du, K. Chen, S. Zhang, L. Zhang, Z. Yuan, D. Wu, and H. Ding. Self-consistent determination of spin Hall angle and spin diffusion length in Pt and Pd: The role of the interface spin loss. *Sci. Adv.*, **4**(6):eaat1670 (2018)

and therefore facilitate static and dynamic magnetic properties comparable with those observed in bulk NFO. Here, the term APB refers to a planar structural defect in an ordered crystal structure where the lattices on either side of a boundary are translated by a shift vector dissimilar from the corresponding lattice vector.[12] The occurrence of APBs can significantly influence the physical properties an is in particular associated with degraded static and dynamic magnetic properties in spinel ferrites thin films.[13] A lattice mismatch between substrate and NFO film or a differences in the crystal structure usually result in some sort of structural defects. In particular, spinels such as epitaxial NFO films are vulnerable to the formation of APBs due to the presence of ordered cations in oxides with a large unit cell volume.[14]

The APBs are a result of the higher substrate symmetry in relation to the NFO film which can create a large number of nucleation sites during the start of the film growth inducing stacking defects of the atomic planes in the cationic sublattice. Furthermore, it facilitates the formation of misfit dislocations which occur on account of a large lattice mismatch.[15]

In combination, this causes a variation of the magnetic and transport properties of the spinel ferrite thin films in comparison to the properties of bulk single crystals. For example NFO thin films exhibit degraded magnetic properties, such as lower saturation magnetization in case of a high concentration of APBs. Regarding the deposition of the NFO thin films used here, the films grown on MGO and CGO substrates with (001) orientation do not show any strain relaxation or presence of APBs which has been shown by additional TEM diffraction studies. Furthermore, the surfaces of NFO films grown on MGO as well as CGO substrates by PLD are free of any adsorbate particles and have roughness values below 0.2 nm, comparable to the substrate roughness as determined by atomic force microscopy.

[12] D. Margulies, F. Parker, M. Rudee, F. Spada, J. Chapman, P. Aitchison, and A. Berkowitz. Origin of the anomalous magnetic behavior in single crystal Fe_3O_4 films. *Phys. Rev. Lett.*, **79**(25):5162 (1997)

[13] N. Li, S. Schäfer, R. Datta, T. Mewes, T. Klein, and A. Gupta. Microstructural and ferromagnetic resonance properties of epitaxial nickel ferrite films grown by chemical vapor deposition. *Appl. Phys. Lett.*, **101**(13):132409 (2012)

[14] W. Eerenstein, T. Palstra, T. Hibma, and S. Celotto. Diffusive motion of antiphase domain boundaries in Fe_3O_4 films. *Phys. Rev. B*, **68**(1):014428 (2003)

[15] M. Luysberg, R. Sofin, S. Arora, and I. Shvets. Strain relaxation in $Fe_3O_4/MgAl_2O_4$ heterostructures: Mechanism for formation of antiphase boundaries in an epitaxial system with identical symmetries of film and substrate. *Phys. Rev. B*, **80**(2):024111 (2009)

Setup for the vectorial observation of the SSE

Based on the epitaxial NFO thin films covered with the spin-current-detecting material Pd, a four-contact device was developed in this work. It acts as the technical foundation of the vectorial magnetometry method utilizing the LSSE which is ultimately suitable to study magnetic anisotropies and magnetization reversal processes.

In the setup for the LSSE measurements, illustrated in Fig. 3.1(a), the samples were sandwiched between two copper blocks. A thermally conducting and electrically insulating 250 µm thick spacer was used between the Pd layer and the upper copper block. This silicon carbide (SiC) spacer should in theory be precisely machined to fit the 5 mm^3 surface of the Pd. However, the material is cut in a way to leave out an additional 0.5 mm edge of the sample which

is not directly covered to allow for a clean bonding contact to the Pd-surface on all sides. In the process of mounting the spacer, a centering of the upper copper block is necessary, due to the fact that it is directly connected to the spacer material. Thus, positioning screws are utilized to achieve a precise stacking of sample, spacer and copper bocks.

In direct contact to the highly thermal conductive copper, one Peltier module was used to heat up the upper Cu block while the second Peltier module was used to cool down the lower Cu block in order to keep it at room temperature or 293 K. The temperature of the lower Cu block was thereby fixed at a base temperature T and the temperature of the upper Cu block was increased to $T + \Delta T$ in order to adjust a specific temperature gradient over the bilayer and substrate stack. Here, the base temperature T is set to room temperature and $\Delta T = 20$ K to generate the required constant heat flow. During the experiment, the applied temperature gradient in between the upper and lower Cu blocks can be controlled using attached K-type thermocouples. Since the vectorial observation requires an angular dependence measurements of LSSE, the experiment was constructed to be able to manually rotate the entire setup in-plane.

In order to conduct the actual LSSE measurements, the contacts of both orthogonal axis have to be connected each with a separate nanovoltmeter. Therefore, four aluminum wires are bonded in the middle of each of the four sides of Pd capped sample. This four-point contact setup and geometry used for the vectorial LSSE measurements is schematically illustrated in Fig. 3.1(b). The wires are in direct contact with the Pd layer in a way that the contacts are placed on both orthogonally aligned axes close to each edge of the surface.

Results and discussion

All films were structurally characterized following the PLD process using a Philips X'Pert diffractometer with a Cu-K$_\alpha$ source to check the film quality and quantify the lattice mismatch for the different substrates. Standard Cu-Kα θ - 2θ x-ray scans in the range of 20° – 120° show solely (h00) peaks which correspond to the

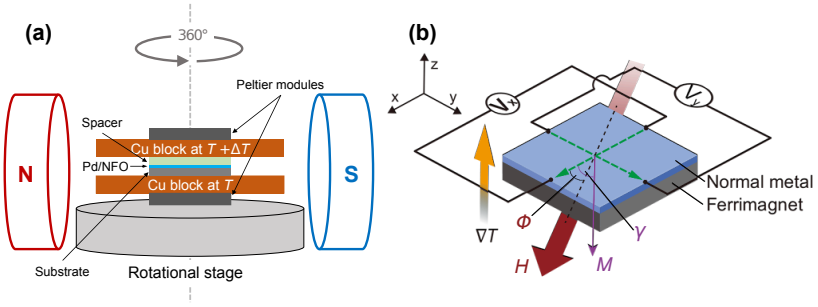

Figure 3.1: (a) Illustration of the LSSE setup. The sample is placed between two Cu blocks and a temperature gradient ∇T is applied. (b) The geometry for four-point vectorial LSSE measurements and definition of the external magnetic field and magnetization angles ϕ and γ.

respective substrates and the NFO film. Figure 3.2 provides a more detailed view on the crucial film peaks in relation to the respective substrates. It shows the XRD θ - 2θ scans in the 2θ range of 42° to 46° for NFO//MGO (001). Here, the (004) diffraction peaks of the substrate as well as the NFO film are clearly visible. The MGO and CGO (011)-oriented films can be identified by the (044) Bragg peaks which are emerging in the 2θ range of 61° to 65°. The scans reveal an increased gap between the film and substrate peak positions for both NFO//MGO samples. In contrast, the Bragg peak originating from the diffraction in the deposited thin film is nearly merged with the left shoulder of the substrate peak for the NFO//CGO sample. This clearly indicates a significantly reduced lattice-mismatch of the NFO//CGO sample in comparison to both NFO//MGO sample systems.

The out-of-plane lattice constants can be obtained from the Cu-Kα NFO (004) peak and is measured to be 0.840 nm for the NFO film deposited on MGO and 0.835 nm for NFO on the lattice-matched CGO substrate. These values are marginally larger than the bulk lattice constant $a_{\text{bulk}} = 0.8345$ nm of NFO. The film epitaxy was analyzed by ω scan at the (004) reflex for NFO films on both substrates revealing an significantly improved epitaxial growth on the lattice-matched substrates. The FWHM value at this NFO peak is below 0.04° and thus only marginally larger than the values obtained for the substrate reflexes including the instrumental broadening. Based on the determination of the out-of-plane lattice constant, it is possible to calculate the in-plane lattice constant by performing an diffraction scan in the (044) plane of the NFO film. Measurements utilizing an Eulerian full-circle cradle to get access to the in-plane dimension, as discussed in chapter 2.4, result in an in-plane value of 0.830 nm for films on MGO. Therefore, this value is almost equal to the MGO lattice constant ($a = 0.8280$ nm) and only marginally smaller than the bulk constant, implicating no necessary strain-relaxation of the epitaxial films.

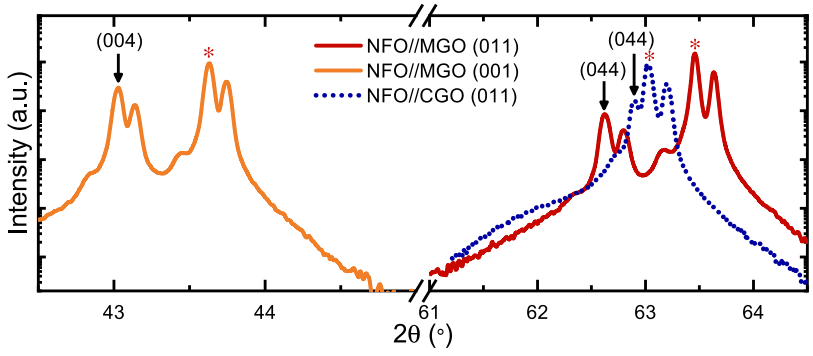

Figure 3.2: XRD θ - 2θ diffraction patterns of NFO films on different substrates (MGO (011), MGO (001), CGO (011)), respectively. The NFO peaks (↓) and labeled with the corresponding reflex and while the marker (*) is indicating the corresponding substrate peak. The splitting of the peaks for the films and substrates is originating from Cu-Kα_1 and Cu-Kα_2 radiation.

Magnetization and longitudinal spin Seebeck effect measurements

The magnetization measurements of NFO on the various substrates were performed by VSM on $\sim$ 450 nm thick NFO films. Here, thin films grown on (011)- and (001)-oriented MGO and (011)-oriented CGO substrates were analyzed to investigate the substrate specific magnetic in-plane anisotropies. The results for NFO//MGO (011) and NFO//CGO (011) samples are presented in Figs. 3.3(a) and (b), while the corresponding measurements conducted on the NFO//MGO (001)-oriented sample system are presented in Fig. 3.4.

A sharp switching of the magnetization can be observed for the NFO//MGO (011) thin film, in case the external magnetic field is applied along the [01$\bar{1}$] direction (Fig. 3.3(a)). When the external magnetic field is applied along the [100] direction, this sample demonstrates a switching behavior characteristic for the magnetic hard axis with an anisotropy field of $\sim$ 1500 Oe. Moreover, the measured SSE voltage signal V_{LSSE} along the two perpendicular directions of the sample is presented in Fig. 3.3(b). While the V_{LSSE} signal is measured along the [100] direction in the first configuration, which is shown in Fig. 3.3(c), the V_{LSSE} signal is measured along the [01$\bar{1}$] direction in the second configuration. This result is illustrated in Fig. 3.3(e).

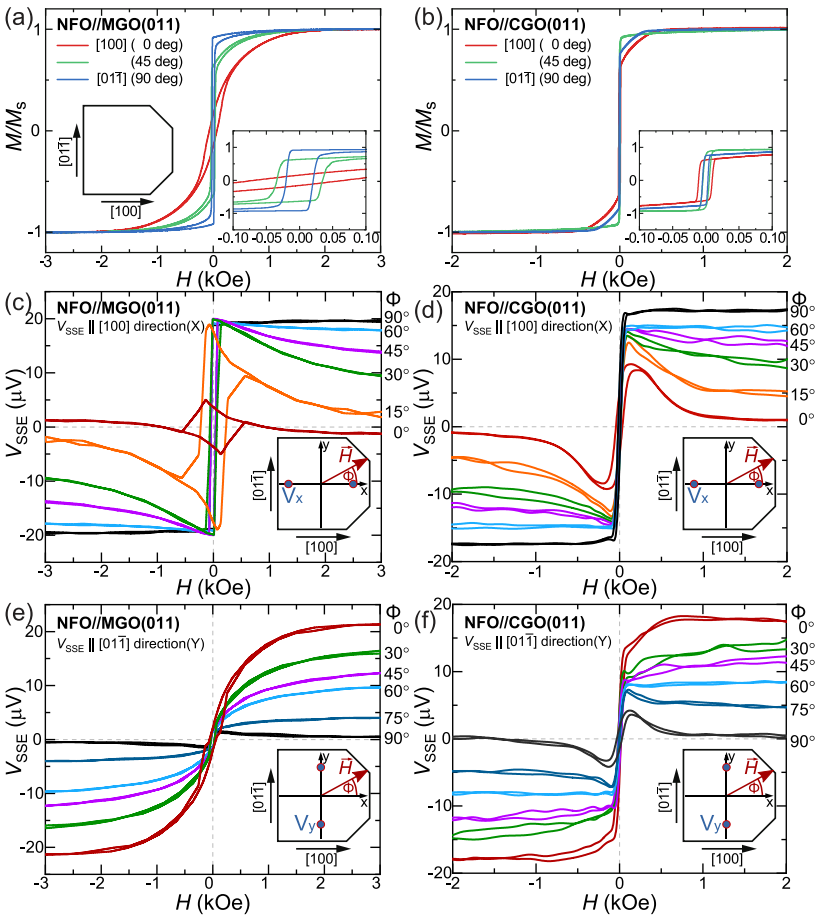

Figure 3.3: The plots (a) and (b) show the normalized in-plane magnetization versus magnetic field for NFO//MGO (011) and NFO//CGO (011). The insets are a close-up of the VSM measurements and the substrate orientation schematics of the LSSE measurements, respectively. The magnetization is measured with an external in-plane magnetic field applied in three different magnetic field direction (0° [100], 45° and 90° [01$\bar{1}$]). Graphics (c) - (f) show the LSSE measurements at various angles ϕ for (c),(e) NFO//MGO (011) and (d),(f) NFO//CGO (011) with voltage measured (c),(d) along the [100] (X) direction and (e),(f) along the [01$\bar{1}$] (Y) direction for a temperature gradient of $\Delta T = 20$ K.

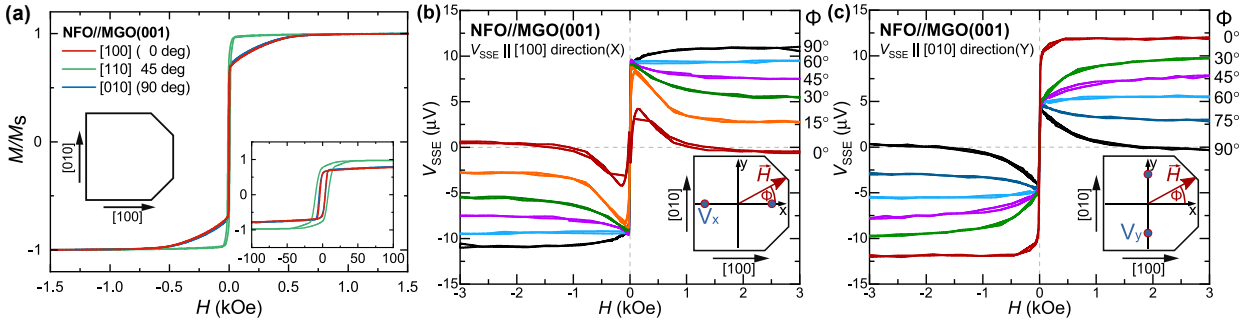

Figure 3.4: The figure (a) shows the VSM results of the normalized in-plane magnetization versus the magnetic field for NFO//MGO (001). The magnetizations are measured with the in-plane magnetic field applied in two perpendicular ([100] and [010]]) and one diagonal [110] directions. Figures (b) and (c) depict LSSE measurements at various angles along two perpendicular directions ([100] and [010]]) for NFO//MGO (001), respectively. The represented angles ϕ are the angles between the x axis and the applied field H as illustrated in schematics of Fig.3.1.

Based on the results presented in Fig. 3.4(a) one can interpret the shapes of the magnetization loops for NFO//MGO (001) thin film along both [010] and [100] directions, which implies that the thin film has a fourfold magnetic anisotropy without any additional uniaxial magnetic anisotropy. Consequently, as shown in Figs. 3.4(b) and (c), the shapes of SSE along these two perpendicular directions are highly similar.

The results of the VSM magnetization hysteresis loops sets a framework for the analysis of the LSSE signal measured at various angles for the corresponding hysteresis loops of the applied in-plane magnetic field. Figure 3.3(c) shows the results obtained in the first configuration measured along the [100] direction (X). Here, the magnetization $\vec{M}$ of the NFO film is aligned in the [01$\bar{1}$] direction, when the external magnetic field is applied along the same direction. In the event, that the polarity of the magnetic field is switched, the magnetization of the film $\vec{M}$ likewise changes to the opposite direction. Thus, a sharp switching in the V_{LSSE} signal can be observed, illustrated by the $\phi = 90°$ curve in Fig. 3.3(c). This is highly similar to the corresponding magnetization measurement in case the magnetic field is in the [01$\bar{1}$] direction, as shown in Fig. 3.3(a). In the progress of the vectorial measurement, the angle ϕ of the external magnetic field is changed with respect to the x axis in the range from 0° to 90°. This is schematically depicted in the insert of Fig. 3.3(c). For all ϕ angles in saturation, the magnetization of the NFO film $\vec{M}$ is nearly aligned in the direction of the externally applied magnetic field. In this configuration, the measured voltage generated based on the ISHE is given by

$$V_{\mathrm{LSSE}} = E_{\mathrm{LSSE}} \cdot d, \tag{3.1}$$

where d is the distance between the electrical contacts on the ISHE film and E_{LSSE} represents the electric field induced by the ISHE. This voltage generation is directly influenced by the projection of the film magnetization onto the [01$\bar{1}$] sample direction. Therefore, the electric field E_{LSSE} generated by the LSSE can be expressed as follows:

$$\vec{E}_{\mathrm{LSSE}} \propto \vec{J}_s \times \vec{\sigma}, \tag{3.2}$$

In this equation, $\vec{J}_s$ is the thermally induced spin current which is parallel to the ∇T in z direction, while $\vec{\sigma}$ describes the spin polarization vector. This is aligned along the magnetization vector of the

NFO $\vec{M}$. Therefore, Eq. 3.2 leads to the concluding proportionality relation

$$V_x \propto \sigma_y \propto M_y \ , \ V_y \propto \sigma_x \propto M_x. \tag{3.3}$$

When the angle between the external magnetic field and the [100] direction along the x axis ϕ is increased, the saturation voltage V_x is elevated corresponding to a factor of $\sin\phi$ based on the cross product relation in the generation of the ISHE.[16] Due to the increase or decrease of the external magnetic field, the projection of the magnetization in the [01$\bar{1}$] direction M_y increases or decreases. Consequently, the measured voltage signal of the ISHE also increases or decreases accordingly. When the magnetic field is decreased to zero, the magnetization is able to rotate completely into the magnetic easy axis or either partially or fully, respectively, switch into another magnetic easy axis, which reduces the projection M_y and the corresponding voltage V_x. Subsequently, the external field is increased into opposite direction. Therefore, the voltage usually switches sign and the coherent rotation of the magnetization out of the magnetic easy axis along the [01$\bar{1}$] direction ($\phi < 90°$) is accompanied by a decrease of the absolute voltage value. This is illustrated for instance in Fig. 3.3(c). For $\phi = 0°$, the saturation voltage is nearly zero as on has to expect from the cross product relation of the ISHE. Here, the small residual voltage signal, which is observed in saturation, can be explained with an alignment of the magnetization that is not completely saturated or, alternatively, by a slight misalignment of the voltage contacts along the [100] direction.

The voltage contacts along the [01$\bar{1}$] (Y) direction are utilized for LSSE measurements in the second configuration, which is illustrated in the insert of Fig. 3.3(e). When the external magnetic field is applied along the [100] direction to employ the characteristic LSSE experimental configuration (i.e. $\phi = 0°$), a similar voltage value in magnetic saturation is observed, which is comparable to the previous configuration shown in Fig. 3.3(c).

Here, the LSSE voltage signal does not show a sharp switching in case the external magnetic field decreases. Rather, the signal follows the course of the magnetization measurement in the [100] direction with low remanence, as seen in Fig. 3.3(a), and thus differs clearly from the one obtained in the first configuration. In particular, the LSSE voltage V_y increases, respectively decreases, while the projection of the magnetization onto the [100] direction M_x increases, respectively decreases, in a monotonic way until the magnetization finally switches. The measurement is detecting the same switching events as observed in the first configuration shown in Fig. 3.3(c). However, it is sensitive to the orthogonal projection of the magnetization vector.

When both independent measurements are combined to calculate the in-plane components of the magnetization vector during field reversal processes, this detection based on LSSE measurements provides a promising alternative to the various established optical

[16] E. Saitoh, M. Ueda, H. Miyajima, and G. Tatara. Conversion of spin current into charge current at room temperature: Inverse spin-Hall effect. *Appl. Phys. Lett.*, **88**(18):182509 (2006)

magnetometry methods. The VSM results for the NFO//CGO (011) thin film as a comparison with the NFO//MGO (011) sample are illustrated in Fig. 3.3(b). Here, the magnetization curves for the different external field directions once again indicate relative magnetic easy axis behavior in [01$\bar{1}$] direction and relative magnetic hard axis behavior in the [100] direction. However, it should be noted that the discrepancy between these relatively easy-axis and hard-axis loops is not as pronounced as observed in case of the NFO//MGO (011) sample system. Therefore, additional LSSE measurements were performed on this sample which are shown in Figs. 3.3(d) and (f). As expected, the LSSE measurements utilizing the contacts along these two perpendicular directions are very similar. This is consistent with the comparable magnetization results of Fig. 3.3(b).

Results of the angular-dependent FMR measurements

In addition to the LSSE measurements, further in-plane angular-dependent FMR measurements were conducted probing the sample magnetization and provide information on the anisotropy distribution in the film. Ferromagnetic resonance measurements were performed on 450 nm thick NFO films grown on (001)- and (011)-oriented MGO and CGO substrates with the external magnetic field applied in the plane of the sample. These measurements of NFO//MGO (011) thin films demonstrate the existence of a fourfold anisotropy in combination with a strong uniaxial anisotropy. These results are illustrated in Fig. 3.5(a). Here, the overall in-plane magnetic easy axis is found along the [01$\bar{1}$] direction, while the magnetic hard axis is shown to be positioned along the [100] direction. In contrast to this specific anisotropy, the NFO//CGO (011) thin films show a dominant fourfold anisotropy in combination with merely a weak uniaxial anisotropy. This combination results in a biaxial anisotropy which shows a more and a less hard axis in 0°, respectively 90°, direction. The corresponding in-plane angular dependence of the resonance field is presented in Fig. 3.5(b). Therefore, this demonstrates that complementary to the modification of the anisotropy landscape by the crystal cut, a strain anisotropy affects the overall direction and strength of the magnetic easy as well as hard axes. This anisotropy modification is observed to different degrees for the NFO//MGO (011) and NFO//CGO (011) thin films.

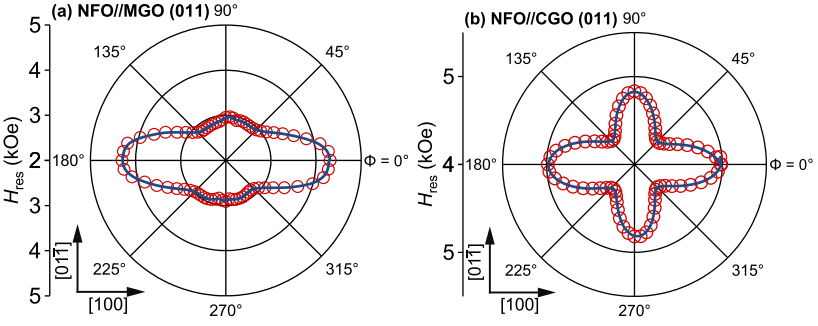

Figure 3.5: In-plane angular dependence of the resonance field, H_{res}, at 20 GHz for (a) NFO//MGO (011) and (b) NFO//CGO (011).

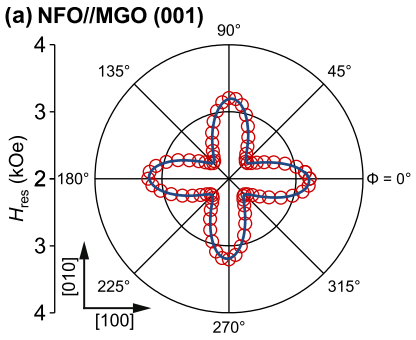

Figure 3.6: FMR measurements of the in-plane angular dependence of the resonance field, H_{res}, at 20 GHz for NFO//MGO (001).

In contrast, the NFO//MGO (001) control sample shows a pure four-fold magnetocrystalline anisotropy. The FMR results of this control sample, which is grown on the differently oriented substrate in comparison to first one discussed here, are presented in Fig. 3.6. This plot of the resonance field (H_{res}) as a function of the in-plane rotation angle ϕ demonstrates a clear four-fold symmetry for films grown on MGO (001) substrates exhibiting the [100] and [010] directions as in-plane magnetic hard axes. A deeper fit analysis of the FMR measurements is presented in the following section.

Fit analysis of the FMR measurements

The data obtained by angular-dependent FMR measurements is presented in Fig. 3.7 for NFO thin films, on the three specific substrates discussed so far. These measurements are analyzed by finding numerical solutions to the Smit-Beljers (SB) equation which offers a description of the ferromagnetic resonance in thin film systems.[17] In particular, it is utilized for a theoretical description of the dependence of the resonance field on the angle ϕ between the film normal and the external magnetic field. Therefore, the main FMR line is fitted according to the SB equation written as

[17] J. Smith and H. Beljers. Ferromagnetic resonance absorption in $BaFe_{12}O_{19}$, a highly anisotropic crystal. *Phillips Res. Rep.*, **10**(2):113–130 (1955)

$$\left(\frac{\omega}{\gamma_g}\right)^2 = \frac{1}{M_s \sin^2 v}\left[\frac{\partial^2 F}{\partial v^2}\frac{\partial^2 F}{\partial \gamma^2} - \left(\frac{\partial^2 F}{\partial v \partial \gamma}\right)^2\right], \tag{3.4}$$

where $\omega = 2\pi f$ describes the angular frequency of the microwave field and M_s the saturation magnetization. Additionally, γ_g is the gyromagnetic ratio, while v represents the polar angle with respect to the normal of the film and γ the azimuthal angle of the magnetization. The equation can subsequently be evaluated at the equilibrium, given by v_0 and γ_0, of the magnetization, which results in

$$\left.\frac{\partial F}{\partial v}\right|_{v_0} = 0 \text{ and } \left.\frac{\partial F}{\partial \gamma}\right|_{\gamma_0} = 0. \tag{3.5}$$

The total energy per unit volume can be characterized based on the famous Kittel equation[18] describing the ferromagnetic

[18] C. Kittel. On the theory of ferromagnetic resonance absorption. *Phys. Rev.*, **73**(2):155 (1948)

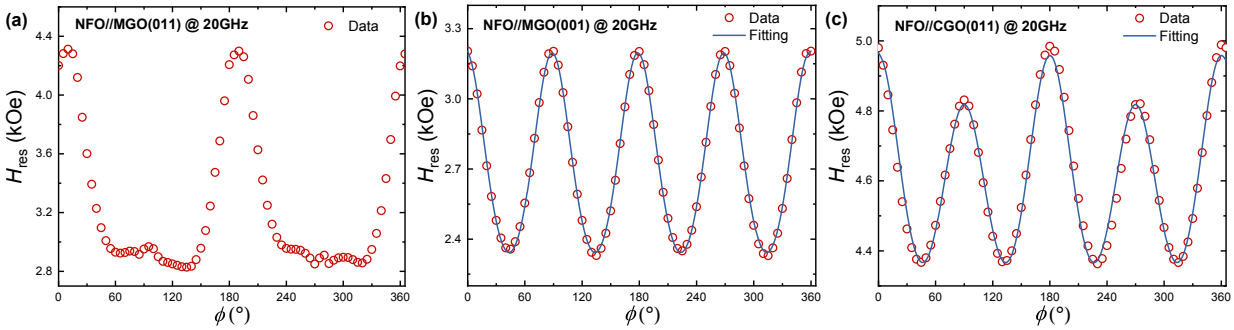

Figure 3.7: Full 360° in-plane rotation plots for (a) NFO//MGO (011), (b) NFO//MGO (001) and (c) NFO//CGO (011), respectively. The films grown on MGO (011) and CGO (011) substrate show a four-fold and a strong or weak two-fold magnetic anisotropy, while the film grown on MGO (001) substrate only shows a four-fold magnetic anisotropy. The purple lines are a fit to the data using the Smit-Beljers equation.

resonance absorption according to

$$\begin{aligned} F = & -H_0 M_s \left[\sin v_M \sin v_H \cos\left(\gamma_H - \gamma_M\right) + \cos v_M \cos v_H\right] \\ & - \left(2\pi M_s^2 - K_U^{\perp}\right) \sin^2 v_M K_U^{\parallel} \cos^2 \gamma_M \sin^2 v_M \\ & - \frac{K_1}{8}\left[3 + \cos 4\left(\gamma_M - \gamma_U\right)\right]. \end{aligned} \tag{3.6}$$

Here, the individual terms of this equation are the Zeeman energy, the uniaxial perpendicular magnetic anisotropy, the in-plane uniaxial magnetic anisotropy as well as the in-plane four-fold magnetic anisotropy energy. In case of this total energy evaluation, the polar angle of the magnetization with respect to the normal of the film is $v_M = v_H = 90°$.

The detailed constants obtained by the SB fit, Kittel equation and additional VSM measurements for all three samples NFO//MGO (011), NFO//CGO (011), and NFO//MGO (001) are summarized in Table 3.1. Here, the values presented in the upper half of the rows show the results based on the in-plane rotation measurement while the results based on the VSM measurement and Kittel plot are summarized in the rows on the bottom half. The first row is unfilled, since the obtained FMR signal for the film grown on the MGO (011) substrate was scattered around 90° and 270° and could not be fitted based on the SB equation.

The effective magnetization M_{eff} and gyromagnetic ratio defined by $\gamma_g' = \gamma_g/(2\pi)$ in this equation to specify the resonant frequency

$$\begin{aligned} f = \gamma_g' & \sqrt{\left[H_{res} + H_U^{\parallel}\cos\left(2\gamma\right) + H_4\cos\left(4\gamma\right)\right]} \\ & \cdot\sqrt{\left[H_{res} + 4\pi M_{eff} + H_U^{\parallel}\left(\cos\gamma\right)^2 + \frac{H_4}{4}\left(3 + \cos\left(4\gamma\right)\right)\right]} \end{aligned}$$

are calculated based on broadband FMR measurement along the in-plane magnetic easy axis as well as hard axis. Subsequently, the data is fitted based on the Kittel equation in the form of Eq. (3.6), were the azimuthal angle of the magnetization is set to $\gamma = 0°$ for the magnetic hard axis and $\gamma = 45°$ for the magnetic easy axis, respectively.[19]

Regarding the film grown on CGO (011), the FMR measurement is performed along the in-plane [100] and [010] direction and the resulting signal was fitted utilizing total energy formula based on

[19] C. Mewes and T. Mewes. *Handbook of Nanomagnetism*. Pan Stanford (2015)

FMR SB fit based on in-plane rotation measurement

Sample	$4\pi M_{\text{eff}}$ [kG]	$4\pi M_{\text{s}}$ [kG]	$H_U^{\perp}$ [kOe]	H_4 [Oe]	$H_U^{\parallel}$ [Oe]
NFO//MGO (011)	-	-	-	-	-
NFO//CGO (011)	4.632	2.211	2.421	-357	106 ± 8
NFO//MGO (001)	12.929	3.129	9.8	-482	-

FMR SB fit based on VSM measurement and Kittel plot

Sample	$4\pi M_{\text{eff}}$ [kG]	$4\pi M_{\text{s}}$ [kG]	H_{s} [kOe]	H_4 [Oe]	γ' [MHz/Oe]
NFO//MGO (011)	9.60 ± 0.03	3.292	12.5	-	3.09 ± 0.02
NFO//CGO (011)	4.5 ± 0.3	2.035	5.25	-364 ± 64	3.10 ± 0.01
NFO//MGO (001)	13.24 ± 0.05	2.701	15	-474 ± 3	3.076 ± 0.004

Table 3.1: Specific parameters of the SB Fit data of the FMR measurements for all three samples NFO//MGO (011), NFO//CGO (011), and NFO//MGO (001). The upper rows show the results based on the in-plane rotation measurement, the bottom rows summarize the results based on the VSM measurement and Kittel plot.

the Kittel equation (Eq. (3.6)) by fixing $\gamma = 0°$ and $\gamma = 90°$. In addition, for the film grown on MGO (011), the FMR measurement was conducted in an out-of-plane configuration. The parameters extracted from in-plane rotation measurement are in agreement with the parameters obtained from the broadband measurement and beyond this with accord with the results from the VSM measurement as summarized in in Tab. 3.1.

It is illustrated in Fig. 3.8 that the linewidth of the NFO//MGO (011) film is about 99 Oe at a frequency of 55 GHz, which is the highest among all the samples. Furthermore, the ratio of linewidth to frequency is not linear and therefore a maximum damping constant of $\alpha_{\text{max}} = 4.9 \times 10^{-3}$ is obtained for this sample. However, the linewidth of the remaining samples is significantly lower with values of about 53 Oe for NFO//CGO (011) and about 40 Oe for NFO//MGO (001), both obtained at an equivalent frequency of 55 GHz. In addition, the damping constants α_{eff} of all discussed thin films can be determined given that

$$\Delta H = \Delta H_0 + \frac{4\pi f}{\sqrt{3}\gamma_{\text{g}}} \cdot \alpha_{\text{eff}}. \tag{3.7}$$

The damping constants determined based on this relation are on the order of 10^{-4} for all samples with a minimum value of $\alpha_{\text{eff}} = (5.4 \pm 0.8) \times 10^{-4}$ for the NFO//CGO (011) layer and $\alpha_{\text{eff}} = (7.9 \pm 0.6) \times 10^{-4}$ for the NFO//MGO (001) sample, respectively.

Analysis of the LSSE voltage anisotropy

The magnetic anisotropy of the presented thin film samples can be analyzed in-depth based on the LSSE by visualizing the reversal process of the magnetization vector in dependence of the direction of the external magnetic field. Thus, the obtained LSSE voltage signals, utilized to display the LSSE hysteresis loops in Figs. 3.3(c) - (f), are henceforth be used to precisely reconstruct the magnetization

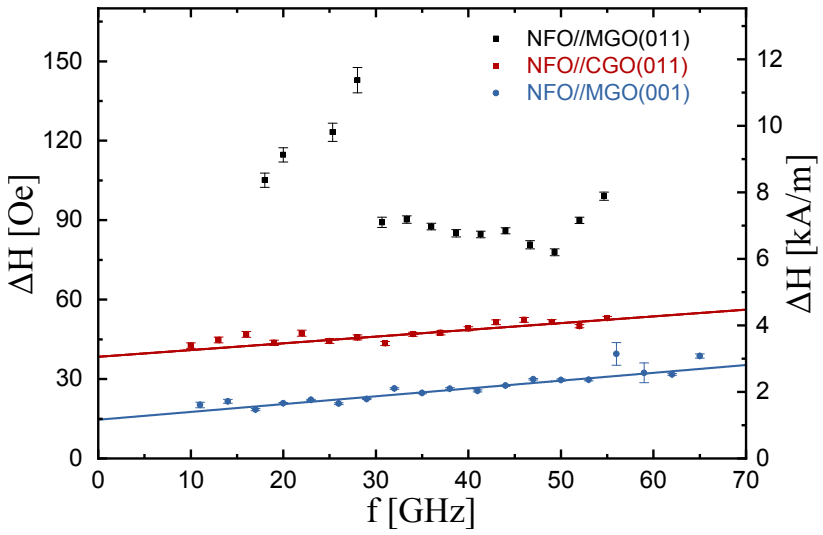

Figure 3.8: The FMR linewidth plotted against the frequency for the NFO//MGO (011), NFO//CGO (011), and NFO//MGO (001) sample. The continuous line is a fit to the data using Eq. (3.7). The data points for NFO//CGO (011) and NFO//MGO (001) at frequencies lower than 20 GHz were excluded from the fitting as the linewidth get broadened due to merging of multiple resonances with the main resonance.

reversal process. In order to calculate the status of the magnetization vector, both projections of the in-plane magnetization on the [100] and [01$\bar{1}$] directions from the vectorial LSSE measurement, M_x as well as M_y, are required. Based on Eq. (3.3), it can be expected that

$$V_x = A_x \cdot M_y \ , \ V_y = A_y \cdot M_x, \tag{3.8}$$

are valid relations. Here, the constants A_x and A_y are taking into account both material as well as specific setup parameters.

The voltage V_{SSE} anisotropy has to be analyzed in detail, since the relations presented in Eq. (3.8) are an integral part of the vectorial analysis of the LSSE signal. Only under the condition that the material and setup parameters A_x and A_y of the thin film system in question are in a first approximation identical, the magnitude and azimuthal angle of the magnetization can be correctly calculated. Otherwise, the parameters A_x and A_y would have to be obtained separately factoring in a possible LSSE voltage anisotropy.

In order to confirm the internal validity of this approximation for the discussed sample systems, one should choose a broader approach and evaluate the angular dependence of the LSSE saturation voltages V_x and V_y in detail. When sufficiently large external magnetic field is applied, the voltages V_x and V_y can be obtained in saturation. The corresponding values are described below by $V_{x,sat}$ and $V_{y,sat}$. These values can be plotted in relation to the external magnetic field angle ϕ, which is presented in Fig. 3.9. Additionally, a sine and cosine fit evaluation of the saturation voltages determined by measurements utilizing the contact along the [100] and [01$\bar{1}$] direction of the NFO//MGO (011) and NFO//CGO (011) samples has been conducted.

For this evaluation, based on the measurement geometry one can

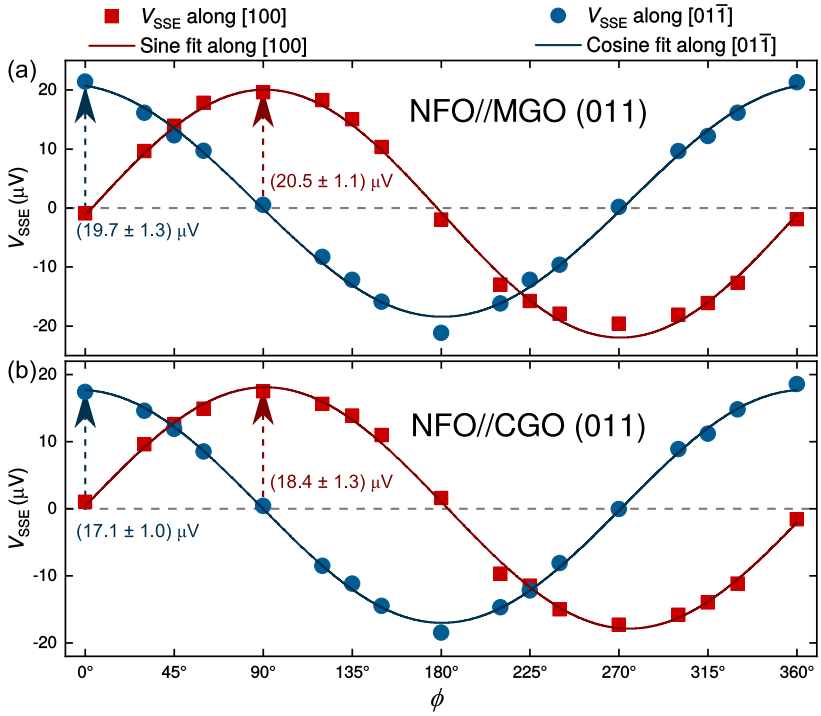

Figure 3.9: Angle dependence of the voltage V_{SSE} measured along the [100] ($V_{x,sat}$, red) and [01$\bar{1}$] ($V_{y,sat}$, blue) direction of (a) NFO//MGO (011) and (b) NFO//CGO (011) at the maximum applied external magnetic field of 3 kOe approaching the saturation value. The amplitude of the SSE voltage is specified for the corresponding fit with an error mainly influenced by the orientation of the external magnetic field (±2.5°) and the uncertainty of the fit.

assume that the relations

$$V_{x,sat} = A_x M_{y,sat} = A_x M_s \sin\phi \qquad \text{and}$$
$$V_{y,sat} = A_y M_{x,sat} = A_y M_s \cos\phi \tag{3.9}$$

are sufficient to describe the angular dependency of the saturation voltages $V_{x,sat}$ and $V_{y,sat}$. When evaluating the plots of Fig. 3.9, one can assert that both voltage amplitudes are congruent in magnitude. This substantiates the assumption of a strain-independent ISHE. The voltage signals shown in Fig. 3.9 are fitted according to Eq. (3.9) in order to determine the correct proportionality factors A_x and A_y. These are necessary to accurately convert the obtained LSSE voltages V_x and V_y into the projections of the in-plane magnetization M_x and M_y according to the relations of Eq. (3.8). In the case of the presented samples, no significant deviation of the fitted parameters can be found within the measurement accuracy and therefore $A_x \approx A_y$ has to be considered a valid assumption. For more complex systems with significantly anisotropic magnon dispersion, this quantitative determination of the proportionality factors is important in order to apply the vectorial magnetometry technique discussed here.

Moreover, this approach enables the user of this vectorial LSSE method to detect discrepancies in the saturation based on the residual of the fits. This is an easy way to check the sufficiency of the applied saturation field. In Fig. 3.9 for instance, one can merely observe a minimal deviation from both fits, which indicates a nearly saturated state at maximum field.

In summary, this analysis shows that the LSSE saturation voltages V_x and V_y in relation to the azimuthal angle of the magneti-

zation are not influenced by a significant anisotropy. However, in principle the magnetic transport and, thus, the magnitude of the generated LSSE voltages can depend on the relative orientation to the NFO crystal axes. Notably, in SMR measurements a current direction anisotropy can be observed in NFO thin films where the precise origin is still up for debate.[20]

In this SMR as well as in the SSE experiment discussed here, the spin current is always generated in out-of-plane direction propagating along the same crystallographic axis. Consequently, it is at all times independent of the direction of voltage detection. However, an anisotropy can be induced due to an anisotropic SHE or spin mixing conductance as discussed by Althammer *et al.* In the experiments presented in this chapter though, the amplitude of V_{SSE} at maximum field measured parallel to [100] direction is comparable to the voltage measured along the [01$\bar{1}$] direction for both NFO//MGO (011) as well as NFO//CGO (011), as demonstrated in Figs. 3.3(c) - (f). Thus, is has to be viewed as clear evidence for the absence of any significant anisotropy of the ISHE, such as, for instance, an anisotropy induced by strain. This is consistent with the reported immunity to electrostrain of the spin-current transport and spin-charge conversion in Pt/YIG by Wang *et al.* which is based on a robust spin-mixing conductance and magnon diffusion length at the interface.[21]

[20] M. Althammer, A. V. Singh, T. Wimmer, Z. Galazka, H. Huebl, M. Opel, R. Gross, and A. Gupta. Current direction anisotropy of the spin Hall magnetoresistance in nickel ferrite thin films with bulk-like magnetic properties. *arXiv:1811.04696*, (2018)

[21] Y. Wang, W. Lin, D. Qu, Q. Ma, Y. Zhang, Y. Li, S. Yang, and C. Chien. Voltage-Controlled Sensitivity of the Spin Seebeck Effect in $Pt/Y_3Fe_5O_{12}/MgO/(PbMg_{1/3}Nb_{2/3}O_3)_{0.7}(PbTiO_3)_{0.3}$ Multiferroic Heterostructures. *Phys. Rev. Appl.*, **10**(1):014004 (2018)

Following the analysis of the LSSE voltage anisotropy, the assumption $A_x \approx A_y$ is used to calculate all relevant quantities including the magnetization M,

$$M = \sqrt{(M_x)^2 + (M_y)^2} = \sqrt{(\frac{V_y}{A_y})^2 + (\frac{V_x}{A_x})^2} \approx \frac{1}{A_x} \cdot \sqrt{V_y^2 + V_x^2}. \tag{3.10}$$

The length of the magnetization vector is calculated based on the magnitude $|V| = \sqrt{{V_x}^2 + {V_y}^2}$, while the in-plane orientation or rather the azimuthal magnetization angle γ is given by

$$\gamma = \arctan\left(\frac{M_y}{M_x}\right) = \arctan\left(\frac{V_x}{V_y} \cdot \frac{A_y}{A_x}\right) \approx \arctan\left(\frac{V_x}{V_y}\right). \tag{3.11}$$

According to these basic relations, the magnetization reversal processes for all presented samples can be visualized.

Analysis of the magnetization reversal process based on the vectorial observation of the LSSE

The method of analysis presented in the previous section can be utilized to generate polar plots of the magnetization vector length versus the azimuthal angle γ. Figure 3.10 includes a plot compilation associated with the NFO//MGO (011) sample. It visualizes the reversal processes of the magnetization vector for certain selected external magnetic field directions ϕ, defined as illustrated in Fig. 3.1. Each polar plot shown here characterizes the progress of the obtained magnetization vector, when the external

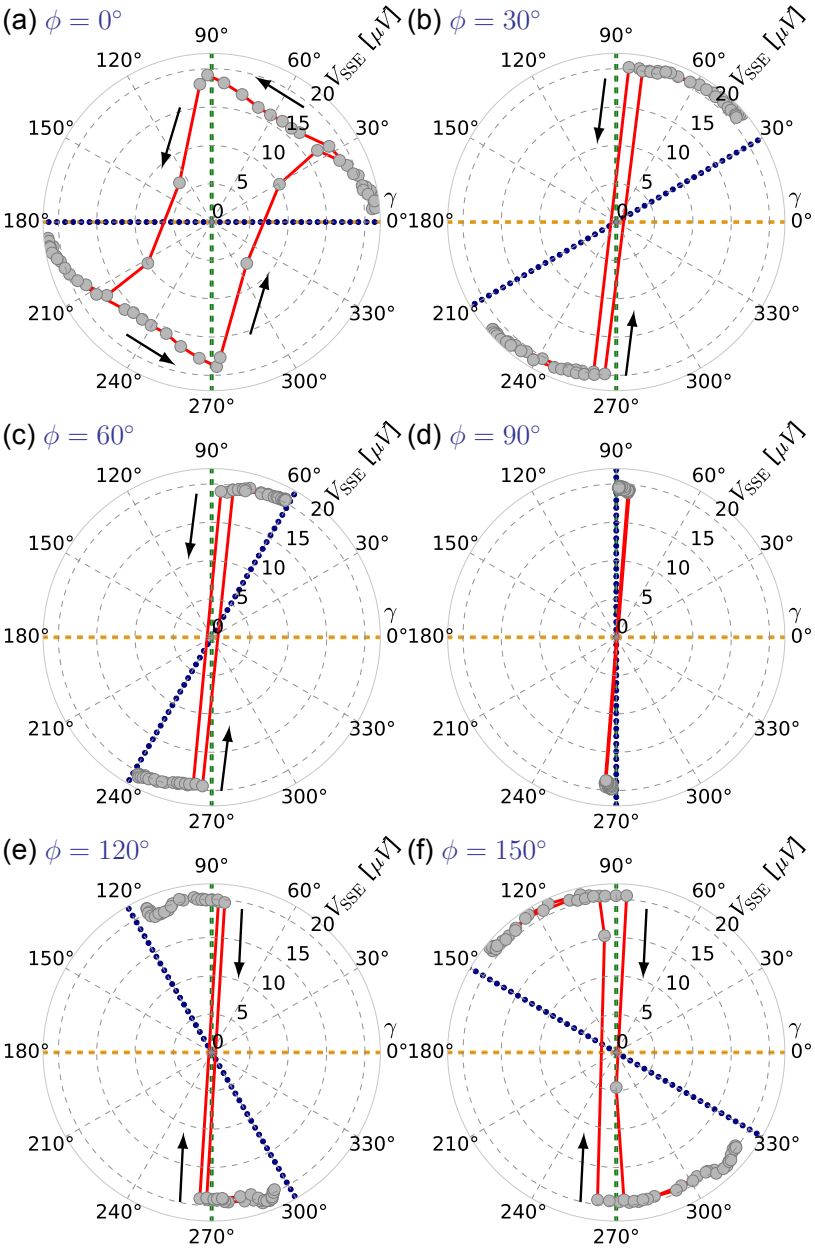

Figure 3.10: The NFO//MGO (011) reversal processes of the magnetization vector for angles of the external magnetic field (blue dotted line) ϕ from 0° to 150° ((a) - (f)) relative to the [100] in-plane direction (inset Fig. 3.3(a)). The magnitude of the magnetization vector given by $|V|$ of the combined LSSE measurements in µV is plotted against the rotation angle γ of the magnetization vector. The magnetic easy (green) and magnetic hard axes (orange) are marked by dashed lines.

magnetic field is gradually looped at a constant external magnetic field angle. Additionally, the direction of the applied external magnetic field with respect to the sample orientation is changed step-by-step, resulting in multiple polar plots, where the actual number depends on the presented angular step size. In its core, this analysis is based on the same type of magnetization measurements as shown in Fig. 3.3.

These magnetization measurements show that a defined magnetic domain state is developed at the beginning of each reversal process. Due to the sufficient external magnetic field strength, it is possible to essentially saturate the magnetization orientation in the direction of the external magnetic field. When the attention is turned to the individual reversal processes at fixed magnetic

field directions, the direct consequences of the in-plane magnetic anisotropy on the field dependent orientation of the magnetization can be studied. Here, Fig. 3.10(a) shows a prime example of a reversal process where the external magnetic field is applied along the magnetic hard axis of the NFO//MGO (011) sample at an angle of $\phi = 0°$, based on the geometry defined in Fig. 3.1(b). According to the relations of Eq. (3.3), when the external magnetic field is in saturation, V_y is maximal which represents the starting point of this particular reversal process. This outermost point of the visualized process is shown on the right side of Fig. 3.10(a). When the external magnetic field is reduced along or close to a magnetic hard axis, as it is the case here, domain splitting is induced. This is usually accompanied by a reduction of the magnitude of the magnetization vector, which can be observed in Fig. 3.10(a). When the external magnetic field is subsequently reduced further while it is still applied along the same axis, $\phi = 0°$, the magnetic moments of those domains switch or rotate towards the magnetic easy axis along [01$\bar{1}$] direction. This process is indicated by the black arrow at the top of this subplot. The preferred direction of the magnetization reversal is affected by the slight misalignment of the external magnetic field in relation to the magnetic hard axis [100] direction of this NFO sample. When the external field is increased in the opposite direction, completing the first branch of the LSSE hysteresis loop, the magnetization is forced to rotate back into the direction of the external magnetic field.

The next step is the visualization of the magnetic reversal process for additional orientations of the external magnetic field relative to the defined samples axes. For this sample, this results in the external magnetic field being no longer applied in direction of the magnetic hard axis. Therefore, the system essentially follows the coherent rotation model without transforming into multi-domains. A constant length of the magnetization vector from saturation to remanence is observed, exemplary shown in Figs. 3.10(b) and (c).

For an external magnetic field along the strong magnetic easy axis direction, which is oriented along $\phi = 90°$ as seen in Fig. 3.10(d), a simple switching of the magnetization direction by 180° is observed. This is expected in case of a magnetic loop along an easy axis direction since the LSSE hysteresis in the standard measurement geometry exhibits a minimal coercive field and high remanence.

In addition to the discussed results for this NFO//MGO (011) sample, the illustrated vectorial LSSE technique is used to visualize the magnetization reversal process of the two other corresponding samples showing a pure fourfold and a fourfold plus weak twofold anisotropy. These vector LSSE measurement results for the NFO//MGO (001) and NFO//CGO (011) samples are shown here to allow for a direct comparison between different magnetic in-plane anisotropy landscapes.

As shown in Fig. 3.11, the reversal process of NFO//CGO (011)

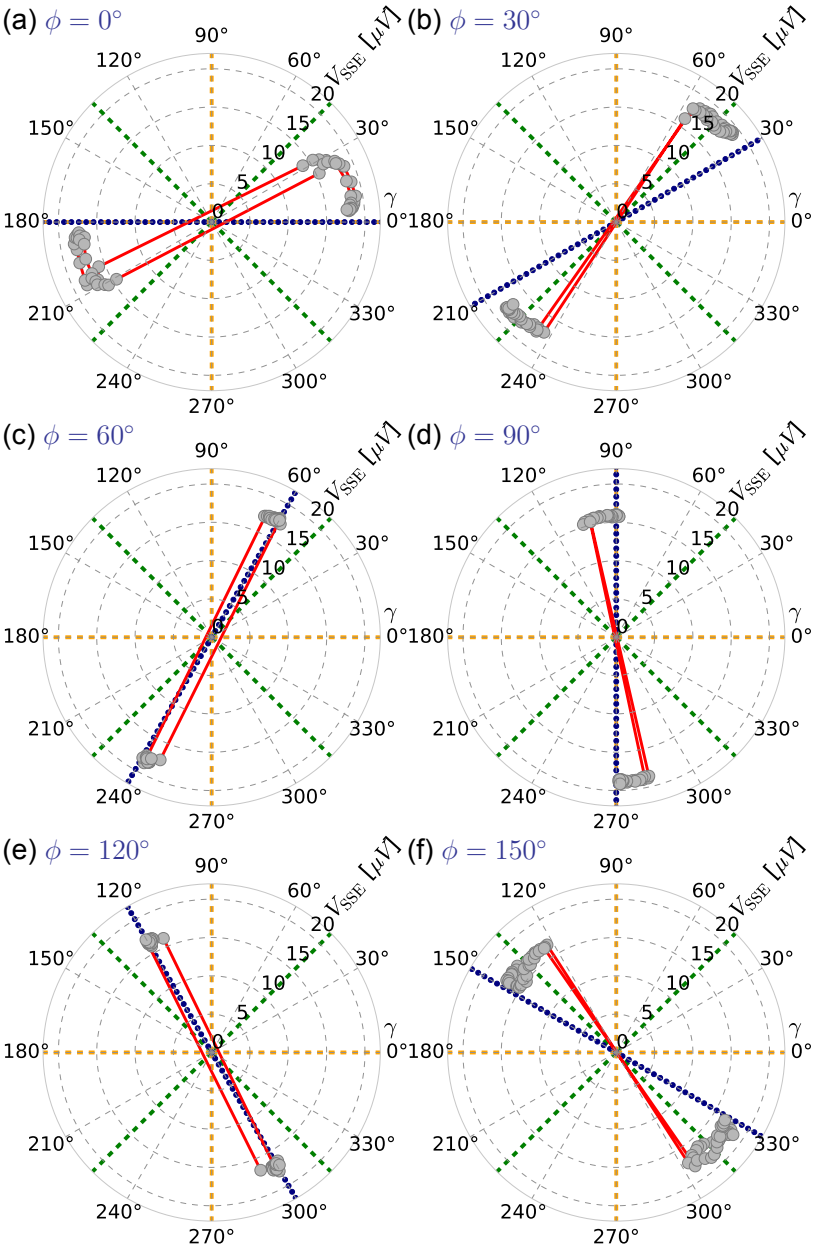

Figure 3.11: (The NFO//CGO (011) reversal processes of the magnetization vector for angles of the external magnetic field (blue dotted line) ϕ from 0° to 150° ((a) - (f)) relative to the [100] in-plane direction (see insert Fig. 3.3(a)). The magnitude of the magnetization vector given by $|V|$ of the combined LSSE measurements in µV is plotted against the rotation angle γ of the magnetization vector. The magnetic easy (green) and magnetic hard axes (orange) are marked by dashed lines.

is presented based on the same defined angle of the external magnetic field ϕ in the vectorial magnetometry setup. According to the FMR measurements, the NFO//CGO (011) sample exhibits a dominant fourfold anisotropy with a magnetic easy axes in the 45° directions relative to the magnetic harder axes in the [100] and [01$\bar{1}$] directions. The visualized reversal processes collectively show a switching of the magnetization along or in close vicinity to the magnetic easy axis. When the angles of the external magnetic field are oriented in between those magnetic easy directions, as seen in Figs.3.11(a) and (d), a coherent rotation of the magnetization vector out of the magnetic hard axis is tracked, followed by a 180° sharp switching. Subsequently, the magnetization is forced to rotate back, out of the magnetic easy axis, while the external magnetic field is

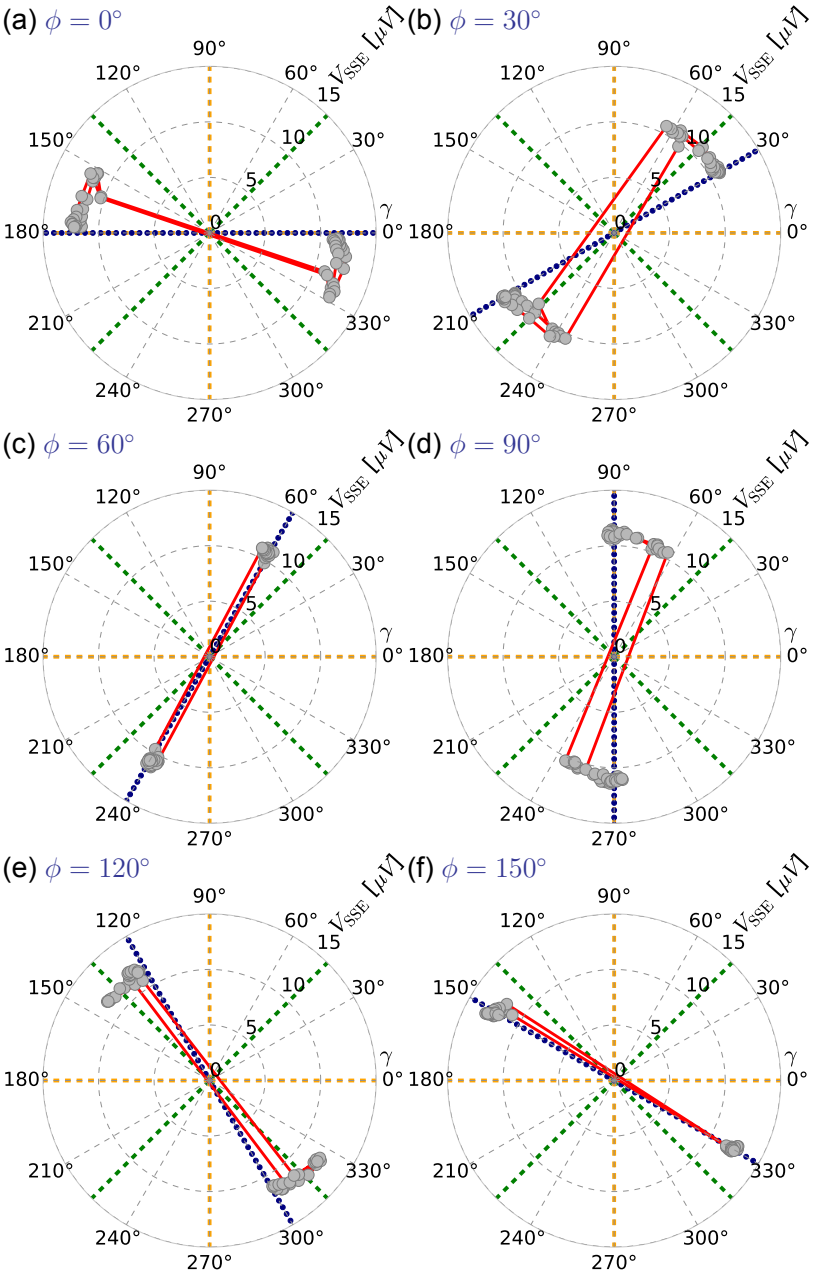

Figure 3.12: The NFO//MGO (001) reversal processes of the magnetization vector for angles of the external magnetic field (blue dotted line) ϕ from 0° to 150° ((a) - (f)) relative to the [100] in-plane direction (see the inset Fig. 3.4(a)). The magnitude of the magnetization vector given by $|V|$ of the combined LSSE measurements in µV is plotted against the rotation angle γ of the magnetization vector. The magnetic easy (green) and magnetic hard axes (orange) are marked by dashed lines.

reaching the maximum saturation value. Due to the fact that the uniaxial magnetic anisotropy is comparatively weak with regard to the uniaxial contribution of the NFO//MGO (011) sample, as indicated by the absolute value of the resonance field H_{res}, the switching already occurs when the magnetization has been rotated closer than up to $\sim 15°$ to the magnetic easy axis.

In Fig. 3.12 the reversal process of the NFO//MGO (001) sample is shown utilizing the LSSE measurements at selected angles of the external magnetic field ϕ. This is shown in Fig. 3.1(b). Analog to the NFO//CGO (011) sample presented in Fig. 3.11, the NFO//MGO (001) sample exhibits a dominant fourfold anisotropy. The magnetic easy axis is found along the $\phi = 45°$ direction, while

the magnetic harder axes are oriented along the [100] as well as [010] directions. Once more, a pronounced switching of the magnetization along or close to the magnetic easy axis is observed, comparable to the switching process of NFO//CGO (011). This is expected based on the distinctive similarity of the four-fold in-plane anisotropy. When the reversal processes are studies in detail, the absence of the additional two-fold anisotropy is shown to have a minor impact on the switching process. Again, the magnetization is in saturation at the beginning and end of the reversal process and switches in a comparable manner when the magnetization has coherently rotated up to $\sim 15^\circ$ relative to the magnetic easy axis. Here, the calculated reduction of the in-plane resonance field H_{res} is about 4 %, due to the additional weak uniaxial magnetic anisotropy of the NFO//CGO (011) sample, which is nearly insignificant in direct comparison to the NFO//MGO (001) sample. This is also apparent when Fig. 3.5(b) and Fig. 3.6(a) are directly compared.

Applicability of the vectorial LSSE based magnetometry technique

The thermally based vectorial LSSE method presented here is preferable when the magnetooptical techniques, as a method of choice for basic characterization of magnetic films, are not applicable. As opposed to the MOKE magnetometry technique, the vectorial SSE approach is notably applicable in the analysis of magnetic materials that are not amenable to magnetooptical detection based on their vanishingly small Kerr rotation. This is primarily the case for all standard vector MOKE techniques in the visible range of light when investigating materials such as ferrites, YIG[22] and in particular NFO. Apart from this wavelength dependence, it should be pointed out that a system must also posses a spin moment, e.g., an asymmetric spin-up and spin-down density of states with pronounced spin-orbit interactions to produce a Kerr rotation. This limitation highlights the demand for alternative techniques to probe magnetization reversals in an easily applicable way, especially in the expanding fields of spin caloritronics, spin orbitronics, and beyond.

[22] A. Kehlberger, K. Richter, M. C. Onbasli, G. Jakob, D. H. Kim, T. Goto, C. A. Ross, G. Götz, G. Reiss, T. Kuschel, and M. Kläui. Enhanced magneto-optic Kerr effect and magnetic properties of $CeY_2Fe_5O_{12}$ epitaxial thin films. *Phys. Rev. Appl.*, **4**(1): 014008 (2015)

Materials which are not measurable with MOKE are particularly problematic in the field of spintronics since a detailed knowledge of the magnetization reversal is key to many transport studies and storage applications based on otherwise promising materials. The vectorial SSE based magnetometry technique can fill this gap and help to obtain crucial magnetic information in case the material shows a pronounced spin Seebeck effect which is true for a wide range of materials as discussed in the review by Uchida *et al.* focusing on the thermoelectric generation based on the SSE.[23]

[23] K.-i. Uchida, H. Adachi, T. Kikkawa, A. Kirihara, M. Ishida, S. Yorozu, S. Maekawa, and E. Saitoh. Thermoelectric Generation Based on Spin Seebeck Effects. *Proc. IEEE*, **104**(10, SI): 1946–1973 (2016)

Moreover, in contrast to the vectorial magnetization technique based on SSE, which is purely based on the electrical detection, the magnetooptical instruments extracting the in-plane magnetization components have to use multiple different combinations of magne-

tooptical Kerr effects to achieve the same result.[24]. This shows the great potential of SSE-based technologies for spintronics devices and especially for the development and utilization of insulators in thermoelectric conversion. This is primarily due to the fact that this technique can support the advancement of device structures for future thermoelectric applications by exploring the magnetic switching processes and, thus, support the optimization of promising LSSE materials.

In general, the technique presented in this work has significant room for further optimization and simplification in order to facilitate a much broader applicability. Here, one easily added experimental improvement would certainly be the implementation of a lock-in detection to increase the LSSE measurement accuracy. In addition, the delicate bonding process can be substituted by the use of an insulating spacer material, processed to include defined voltage contacts. This spacer could be produced precisely for multiple applications and thus increase practicability and, more importantly, accuracy of the measurement results.

More specifically, it is technically possible to discard the bonding process to contact the sample for a lithography or printed electronics based contacting. This would increase precision and eliminate disruptive factors like defective bonds. However, since especially the lithography would include many additional manufacturing steps, this would add more complexity. Therefore, simpler spring loaded or pressed contacts are a more promising alternative. Here, one could design an insulator based spacer, in the same form shown in Fig. 3.1(a), which is preparatively coated with well-defined voltage contacts. Initial tests using printed flexible circuit boards have already been performed proving that it is possible to use this simple method to perform vectorial LSSE measurements. Since the required heat gradient can be easily applied in any lap, this method, if further optimizes, facilitates an easy application of a vectorial magnetometry technique without resorting to expensive equipment.

Additionally, one can argue that the same advantages could be gained using the SMR as a probe of the magnetic anisotropy, which would avoid having to apply heat. In principle, the SMR is applicable as a probe for the magnetization and therefore the magnetic anisotropy in a system such as the presented bilayer of nonmagnetic metal and ferrimagnetic insulator. However, due to the origin of the SMR in a combination of the SHE and the inverse SHE a different magnetic field dependency applies to the detection of the magnetization. For the SMR the observable transport properties reduce to

$$\rho_{\text{long}} \approx \rho_0 + \Delta\rho_1 \left(1 - m_y^2\right), \tag{3.12}$$

$$\rho_{\text{trans}} \approx \Delta\rho_1 m_x m_y, \tag{3.13}$$

[24] C. Daboo, J. A. C. Bland, R. J. Hicken, A. J. R. Ives, M. J. Baird, and M. J. Walker. Vectorial magnetometry with the magneto-optic Kerr effect applied to Co/Cu/Co trilayer structures. *Phys. Rev. B*, **47**:11852–11859 (1993); T. Mewes, H. Nembach, M. Rickart, and B. Hillebrands. Separation of the first-and second-order contributions in magneto-optic Kerr effect magnetometry of epitaxial FeMn/NiFe bilayers. *J. Appl. Phys.*, **95**(10):5324–5329 (2004); and T. Kuschel, H. Bardenhagen, H. Wilkens, R. Schubert, J. Hamrle, J. Pištora, and J. Wollschläger. Vectorial magnetometry using magnetooptic Kerr effect including first-and second-order contributions for thin ferromagnetic films. *J. Phys. D: Appl. Phys.*, **44**(26):265003 (2011)

where ρ_0 is the baseline resistivity of the nonmagnetic metal layer and $\Delta\rho_1/\rho_0$ is the SMR contribution with $m = (m_x, m_y, m_z)$ being a unit vector along the magnetization in the coordinate system of Fig. 3.1.[25] As Eq. (3.12) shows, there is a quadratic dependency of the SMR effect on the magnetization which leads to an ambiguousness regarding the sign of the magnetization, e.g., during a magnetization reversal process. The same sign problem also occurs due to the mixed term $m_x m_y$ in Eq. (3.13).

[25] Y.-T. Chen, S. Takahashi, H. Nakayama, M. Althammer, S. T. Goennenwein, E. Saitoh, and G. E. Bauer. Theory of spin Hall magnetoresistance. *Phys. Rev. B*, **87**(14):144411 (2013)

A systematic study of the SMR to obtain the surface magnetization in $Pt/CoFe_2O_4$ bilayer was performed by Isasa *et al.* and identifies several assumptions necessary to obtain a quantitative reconstruction of the magnetization because it is not possible to determine how $\vec{M}$ rotates with $\vec{H}$ due to the difficulty of the sign determination.[26]

[26] M. Isasa, S. Vélez, E. Sagasta, A. Bedoya-Pinto, N. Dix, F. Sánchez, L. E. Hueso, J. Fontcuberta, and F. Casanova. Spin Hall Magnetoresistance as a Probe for Surface Magnetization in $Pt/CoFe_2O_4$ Bilayers. *Phys. Rev. Appl.*, **6**(3):034007 (2016)

The vectorial LSSE method presented here, resolves this problem by unambiguously detecting the in-plane rotation of the magnetization by using an effect linear in $\vec{M}$. This is similar to the comparison of linear and quadratic MOKE effects where the quadratic terms in the in-plane magnetization do not allow to determine the sign of the individual magnetization components. Other examples are the AHE as much as the anisotropic magnetoresistance (AMR). The AHE allows for the measurements of magnetization hysteresis loops due to a strict proportionality to $\vec{M}$ while the AMR shows a quadratic dependency.

The overall accuracy of the SSE based magnetometry can be assessed referring to Fig. 3.9 where the errors of the fitted angular dependent LSSE voltages are shown. A saturated state is reached when both amplitudes of the measurements along both directions follow a sine or cosine function behavior within the range of error. Furthermore, if the magnitude of E_x and E_y are comparable the given errors indicate the accuracy of the technique.

In addition, one would directly observe further anisotropy effects (e.g. based on anisotropies of spin-mixing conductance, spin-Hall angles, etc.) in fit amplitudes deviating from each other. Since this is not the case for all samples studied so far, the accuracy can be discussed and improved as in any other magnetometry technique which primarily depend on the accessible precision of the orientation of the magnetic field. Specific influences, such as stability of the heat gradient (for SSE) or laser intensity (for MOKE) have to be discussed separately and can be further improved depending on the equipment used.

Consequently, the development of a technique for the vectorial observation of the SSE is an important subject in applied physics since it supports the advancement of device structures for future thermoelectric applications by exploring the magnetic switching processes and, thus, support the optimization of promising LSSE materials.

Conclusion

In conclusion, the experiments outlined in this chapter show that the lattice mismatch between NFO film deposited on isostructural spinel CGO (011) and MGO substrates of two different orientations ((001) and (011)) leads to a different magnetic strain anisotropy. This was determined based on VSM and FMR measurements. Additionally, the strain anisotropy decisively controls the exact form of the LSSE voltage hysteresis loops which have been determined as a function of the external magnetic field.

This work illustrates that the complete reversal process of the magnetization vector can be visualized based on the vectorial measurement of the LSSE. Here, in particular bidirectional field-dependent SSE voltage curves are used to reveal the complete magnetization reversal process, which acts as a prove of principle for a vectorial magnetometry technique based on a spin caloric effect. In general, the vectorial observation of the spin Seebeck effect is established as a promising alternative to examine the magnetization reversal process of thin films by means of the SSE and ISHE voltage detection.

The development of this novel vectorial magnetometry technique highlights the potential of SSE-based technologies for spintronics applications. Furthermore, it promotes the advancement of thermoelectric devices based on the in-depth observation of magnetic switching processes which supports the search and optimization of suitable materials in the fields spincaloritronics.

4
Advanced data analysis procedure for hard x-ray resonant magnetic reflectivity

This chapter addresses a general procedure for an in-depth analysis of hard x-ray XRMR results in order to find a robust simulation of the asymmetry ratio data and generally increase the significance of magnetic reflectivity studies on complex thin film systems. Therefore, the advantages and limits of the XRMR technique in general and the corresponding analysis procedures in particular are discussed in the context of the respective literature. The goal is to reliably obtain robust simulations of the XRMR asymmetry ratio without resorting to additional measurements or exploiting unrealistic degrees of freedom in the structural or magnetic model. Here, a universal process is established including the spectroscopic, structural and magnetic analysis which is primarily applicable for the Pt based thin films discussed in this work. In addition, it should be easily adaptable for the wide range of similar bi- and multilayer systems as well as complex heterostructures found in recent spin-orbit torque devices or sample systems for the study of other spin transport phenomena.

Hereafter, the common limitations of the prevalent analysis procedures are discussed to evaluate the most reasonable systematic steps for the refinement of the XRMR fit analysis and the corresponding modeling of the structural and magnetic thin film depth profiles. In the further course of this chapter, a detailed step-by-step recipe is outlined, based on the software tool ReMagX, to find a robust simulation of the XRMR asymmetry ratio in order to profit from the outstanding magnetic depth resolution and sensitivity of this technique. This procedure is gradually introduced in the XRMR investigation of increasingly complex thin film systems, all measured at the Pt L_3 absorption edge to identify magnetic dead layers as well as possible MPEs. The last of these three distinct systems is the PtMnSb half-Heulser structure introduce in chapter 1.7. The XRMR results of this sample system obtained in the Pt and Mn specific soft and hard x-ray regime are evaluated in-depth based on the outlined principles in the following chapter 5 of this work.

Applicable steps and limitations in the refinement of the XRMR analysis

In most studies published today, the x-ray reflectivity experiments are evaluated by a simulation and fit of the measured data utilizing the recursive Parratt formalism[1] as outlined in section 1.1.2. In this process, usually a multitude of different structural and optical parameters are fitted in the simulation and the employed algorithms have to optimize the model working with a wide parameter space. As a consequence, the choice of an appropriate fitting algorithm is a nontrivial process since various non-global optimization algorithms only converge to local optima.[2]

When the reflectivity technique is joined with the capability of synchrotron light sources to be tuned to the resonance energies of the probed elements while additionally generating highly circularly or linearly polarized x-rays, the modeling is even more challenging. On the one hand, this allows for the discussed element-specific probe since this technique is sensitive to the element's magnetic moments. One the other hand, this synchrotron based expansion of the XRR method, which thereby considers the atomic scattering as a function of the magnetic moment, substantially enlarges the probed parameter space of the XRMR simulation into the magnetooptical regime. This further complicates a robust structural and magnetic modeling of the sample. Consequently, the additional degree of localized magnetic information is in general attained at the expense of a more intricate analysis of the reflectometry data, mainly due to the fact that the magnetic depth profile and the corresponding $\Delta\delta$ and $\Delta\beta$ dimensions are appended to the probed and fitted parameter space.

So far, there are several established steps and common procedures for the analysis of XRMR asymmetry ratios as discussed in section 1.1.3. However, these are usually restricted to the experimental backbone of this technique without addressing the specific details of the magnetic modeling or the fitting process. Thus, one central aspect of this work is the consolidation of the prevalent process and optimization steps as well as the development of further modeling procedures to enhance the overall XRMR accuracy in order to fill this analytical gap. In particular, an accurate identification of the sample specific magnetic depth profile has been proven to be essential for a deeper understanding of spin transport phenomena[3] in complex multilayers and heterostructures. Important examples here are the anomalous Nernst effects in spin Seebeck experiments, contributions of the MPE in SOT devices[4] or anisotropic magnetoresistance contributions when measuring the SMR effect.[5]

In the XRMR specific literature, a multitude of possible solutions to improve the significance of the obtained results for both the specular reflectivity as well as the asymmetry ratio simulations are explicitly specified. However, these do not at all times fit

[1] L. G. Parratt. Surface Studies of Solids by Total Reflection of X-Rays. *Phys. Rev.*, **95**(2):359 (1954)

[2] A. Dane, A. Veldhuis, D. De Boer, A. Leenaers, and L. Buydens. Application of genetic algorithms for characterization of thin layered materials by glancing incidence X-ray reflectometry. *Physica B*, **253**(3-4): 254–268 (1998)

[3] S.-Y. Huang, X. Fan, D. Qu, Y. Chen, W. Wang, J. Wu, T. Chen, J. Xiao, and C. Chien. Transport magnetic proximity effects in platinum. *Phys. Rev. Lett.*, **109**(10):107204 (2012); and P. Bougiatioti, C. Klewe, D. Meier, O. Manos, O. Kuschel, J. Wollschläger, L. Bouchenoire, S. D. Brown, J.-M. Schmalhorst, G. Reiss, and T. Kuschel. Quantitative disentanglement of the spin Seebeck, proximity-induced, and ferromagnetic-induced anomalous Nernst effect in normal-metal–ferromagnet bilayers. *Phys. Rev. Lett.*, **119**(22):227205 (2017)

[4] A. Moskaltsova, J. Krieft, D. Graulich, T. Matalla-Wagner, S. Francoual, and T. Kuschel. Impact of the magnetic proximity effect in Pt on the total magnetic moment of Pt/Co/Ta trilayers studied by x-ray resonant magnetic reflectivity. *AIP Advances*, **10** (1):015154 (2020)

[5] M. Althammer, S. Meyer, H. Nakayama, M. Schreier, S. Altmannshofer, M. Weiler, H. Huebl, S. Geprägs, M. Opel, R. Gross, D. Meier, C. Klewe, T. Kuschel, J.-M. Schmalhorst, G. Reiss, L. Shen, A. Gupta, Y.-T. Chen, G. E. W. Bauer, E. Saitoh, and S. T. B. Goennenwein. Quantitative study of the spin Hall magnetoresistance in ferromagnetic insulator/normal metal hybrids. *Phys. Rev. B*, **87**(22):224401 (2013)

the obtained reflectivity and asymmetry curves within the given constraints set by the model. In addition, ambiguous results are discussed in various studies which do not allow for a clear identification of the intricacies of the magnetic model. In many cases, these discrepancies are attributed to particularly noisy signals in critical areas of the obtained asymmetry ratio.[6]

These methodical limitations are tackled in various ways which usually include the introduction of additional degrees of freedom in the optical- and magnetooptical fitting process. Alternatively, supplementary structural and magnetic information of the studied thin film system is gathered to refine model and simulation. Here, the challenge is to develop methods to ensure the unambiguousness of the obtained magnetic depth profiles and improve the XRMR fitting technique. In principle, this has been addressed in different ways in literature, in many cases explicitly tailored specifically to a particular material system in the context of the respective study. Generally speaking, little constraints on fitting parameters or a loosely defined model often facilitate a perfect simulation of the measured asymmetry ratio. However, the subsequent interpretation of the simulated magnetic depth profiles is usually ambiguous or at least inconsistent and thus of minor evidentiary value.

In order to resolve any inconsistency, different methods are used to approach the system specific limitations which are depending on both the studied material and layer structure as well as the x-ray photon energy of the experiment. For example, the investigation of interface and proximity effects in the hard x-ray regime[7] is usually based on a large number of structural parameters. These have to be constrained and should be consistent throughout the dataset, in particular where magnetic scattering factors are preset, in order to allow for a strict comparison between samples.

Wherever it is practicable, the magnetization depth profile can be split and confined to separate interface layers[8] which is comparable to the structural modeling. Therefore, it can be modeled by an inhomogeneous distribution of magnetization throughout the magnetic layer based on the introduction of additional sublayers.[9] More complex interface transitions are in many cases modeled based on multi-slicing of critical layer regions which can be considered a method of last resort when simpler, yet usually more realistic models fail to account for the obtained asymmetry ratio. The problem here is that this method facilitates a perfect agreement between experiment and simulation at the expense of a disproportionate number of free parameters, e.g., to model interfacial depth profiles. The simulated depth profiles based on a segmented layer profile must hence be interpreted very carefully, especially when making absolute statements regarding diffusion, exchange interactions, hybridization or other interface effects. It has been shown by Awaji *et al.*[10] that multiple depth profiles of magnetism should be carefully considered to eliminate all unrealistic variations in the running and only accept the most probable solution based on reasonable

[6] J. Geissler, E. Goering, F. Weigand, and G. Schütz. Interplay between chemical and magnetic roughness of Pt in a Pt/Co bilayer investigated with X-ray resonant magnetic reflectometry: Dedicated to Professor Dr. Helmut Kronmüller on the occasion of his 70th birthday. *Z. Metallkd.*, **93**(10):946–952 (2002)

[7] D.-O. Kim, K. M. Song, Y. Choi, B.-C. Min, J.-S. Kim, J. W. Choi, and D. R. Lee. Asymmetric magnetic proximity effect in a Pd/Co/Pd trilayer system. *Sci. Rep.*, **6**:25391 (2016); R. M. Rowan-Robinson, A. Stashkevich, Y. Roussigné, M. Belmeguenai, S.-M. Chérif, A. Thiaville, T. Hase, A. Hindmarch, and D. Atkinson. The interfacial nature of proximity-induced magnetism and the Dzyaloshinskii-Moriya interaction at the Pt/Co interface. *Sci. Rep.*, **7**(1):16835 (2017); and A. Mukhopadhyay, S. K. Vayalil, D. Graulich, I. Ahmed, S. Francoual, A. Kashyap, T. Kuschel, and P. S. A. Kumar. Asymmetric modification of the magnetic proximity effect in Pt/Co/Pt trilayers by the insertion of a Ta buffer layer. *arXiv:1911.12187*, (2019)

[8] E. Blackburn, C. Sanchez-Hanke, S. Roy, D. Smith, J.-I. Hong, K. Chan, A. Berkowitz, and S. Sinha. Pinned Co moments in a polycrystalline permalloy/CoO exchange-biased bilayer. *Phys. Rev. B*, **78**(18):180408 (2008)

[9] M. Przybylski, J.-M. Tonnerre, F. Yildiz, H. Tolentino, and J. Kirschner. Non-collinear magnetic profile in $(Rh/Fe_{1-x}Co_x)_2/Rh$ (001) bilayer probed by polarized soft x-ray resonant magnetic reflectivity. *J. of Appl. Phys.*, **111**(7):07C103 (2012); and M. Zwiebler, J. Hamann-Borrero, M. Vafaee, P. Komissinskiy, S. Macke, R. Sutarto, F. He, B. Büchner, G. Sawatzky, L. Alff, et al. Electronic depth profiles with atomic layer resolution from resonant soft x-ray reflectivity. *New J. Phys.*, **17**(8):083046 (2015)

[10] N. Awaji, K. Noma, K. Nomura, S. Doi, T. Hirono, H. Kimura, and T. Nakamura. Soft X-ray Resonant Magnetic Reflectivity Study on Induced Magnetism in $[Fe_{70}Co_{30}/Pd]_n$ Super-Lattice Films. *J. Phys. Conf. Ser.*, **83**(1):012034 (2007)

parameters. The principle behind this can best be described as the application of Ockham's razor.[11]

Other XRMR based investigations in the hard x-ray regime such as the study of magnetization depth profiles in exchange bias systems[12] also use programs based on the distorted-wave Born approximation.[13] The corresponding model relies on layer segmented profiles determined by an off-resonant reflectivity scan as a starting point. In order to reduce the number of free parameters, the analysis has to revert back to theoretical calculations to support the simulated magnetic depth profile and find a clear-cut result.[14] In diverse studies, in particular the charge peaks, which correspond to the resonant reflections, or only the primary features of the asymmetry ratio are incorporate into the analysis.[15] This is partly done to enable a reasonable XRMR simulation in the first place, effectively by reducing the number of fitting obstacles in the respected dataset.

Generally, a beneficial step to refine the fitting process in the first instance is to determine the sample structure by fitting reflectivity curves observed at energies far from the resonance. On the grounds of the resulting structural model, the magnetic depth profile can subsequently be established by simulating the resonant data based on the established structural parameters. The XRMR evaluation of thin film systems in both the hard x-ray[16] as well as in the soft x-ray regime[17] has been shown to be simplified by these auxiliary off-resonant XRR fits. In principle, energy-dependent XRMR measurements at constant momentum transfer can be combined with those at fixed energies to produce a reflectivity map. This sets a constraint between the dispersive- and imaginary parts and theoretically allows the spatial determination and separation of the spin and orbital magnetic moments.[18]

[11] W. H. Jefferys and J. O. Berger. Ockham's Razor and Bayesian Analysis. *Am. Sci.*, **80**(1):64–72 (1992)

[12] S. Doi, K. Nomura, N. Awaji, N. Hosoito, R. Yamagishi, and M. Suzuki. Magnetization profile of Ir in a MnIr/CoFe exchange bias system evaluated by hard x-ray resonant magnetic reflectivity. *J. Appl. Phys.*, **106**(12):123919 (2009)

[13] D. Lee, S. Sinha, D. Haskel, Y. Choi, J. Lang, S. Stepanov, and G. Srajer. X-ray resonant magnetic scattering from structurally and magnetically rough interfaces in multilayered systems. I. Specular reflectivity. *Phys. Rev. B*, **68** (22):224409 (2003)

[14] C. Ederer, M. Komelj, M. Fähnle, and G. Schütz. Theory of induced magnetic moments and x-ray magnetic circular dichroism in Co-Pt multilayers. *Phys. Rev. B*, **66**(9):094413 (2002)

[15] D. Haskel, G. Srajer, J. Lang, J. Pollmann, C. Nelson, J. Jiang, and S. Bader. Enhanced interfacial magnetic coupling of Gd/Fe multilayers. *Phys. Rev. Lett.*, **87**(20):207201 (2001); and M. Gibert, M. Viret, P. Zubko, N. Jaouen, J.-M. Tonnerre, A. Torres-Pardo, S. Catalano, A. Gloter, O. Stéphan, and J.-M. Triscone. Interlayer coupling through a dimensionality-induced magnetic state. *Nat. Commun.*, **7**:11227 (2016)

[16] C. Klewe, T. Kuschel, J.-M. Schmalhorst, F. Bertram, O. Kuschel, J. Wollschläger, J. Strempfer, M. Meinert, and G. Reiss. Static magnetic proximity effect in $Pt/Ni_{1-x}Fe_x$ bilayers investigated by x-ray resonant magnetic reflectivity. *Phys. Rev. B*, **93** (21):214440 (2016)

[17] J. Bertinshaw, S. Brück, D. Lott, H. Fritzsche, Y. Khaydukov, O. Soltwedel, T. Keller, E. Goering, P. Audehm, D. L. Cortie, W. D. Hutchison, Q. M. Ramasse, M. Arredondo, R. Maran, V. Nagarajan, F. Klose, and C. Ulrich. Element-specific depth profile of magnetism and stoichiometry at the $La_{0.67}Sr_{0.33}MnO_3/BiFeO_3$ interface. *Phys. Rev. B*, **90**(4):041113 (2014)

[18] M. Lovell and R. Richardson. Analysis methods in neutron and X-ray reflectometry. *Curr. Opin. Colloid Interface Sci.*, **4**(3):197–204 (1999); and S. Macke and E. Goering. Magnetic reflectometry of heterostructures. *J. Phys. Condens. Matter*, **26**(36):363201 (2014)

However, even when these instrumental measures outlined above are combined, the successful simulation of the magnetic depth profile cannot be ensured since the information derived from simpler models is often insufficient to adequately simulate the obtained magnetic reflectivity.[19] Polarized neutron reflectivity experiments[20] provide an opportunity to refine the XRMR based magnetization depth profiles, especially in more complex magnetic structures.[21] This combination of fundamentally different reflectivity measurements has the ability to generate results which are much more robust than the outcome of one of the individual techniques.[22]

Here, it is worth mentioning that neutron reflectivity experiments are merely sensitive to the total magnetic moment and are therefore not suited to distinguish between the magnetic moments of the specific elements. In addition, this combination of neutron and x-ray techniques is inefficient since it requires plenty of both resources as well as measurement time. These experimental limitations substantiate that a sophisticated simulation of the XRMR asymmetry ratios is required to take advantage of the powerful magnetic reflectivity technique, especially for the investigation of tiny magnetic moments, for instance within the scope of interface magnetism or the study of MPEs.

Furthermore, it has been shown by Zafar *et al.* that multiple measurements and simulations of the same material system are highly beneficial and should be used to verify the obtained magnetic depth profiles. In this context, one single XRMR measurement is easily over-interpreted since the results are rarely robust and unambiguous, especially when the magnetic reflectometry is used to investigate small-scale magnetic moments or particularly thin spin polarized layers.[23]

The broad variety of complex approaches presented here, which are used to compensate for potential limitations of the prevalent XRMR analysis procedures, illustrates the demand for a, first and foremost, reliable and consistent method to investigate the diverse Pt and Mn specific magnetic depth profiles in the bi- and multilayer thin films of this work. In addition, these studies illustrate that high quality samples, which are unambiguously transferable into a layered model system, are an important factor for a robust XRMR analysis. Hence, a homogeneous structural in-plane order and defined interface roughness enable the modeling of a real and well defined sample in the first place.[24]

When more complicated systems are the experimental focus of the XRMR study, additional structural information such as crystal growth mode, layer roughness or state of interdiffusion is required to correctly simulate a real multi layered thin film system. Since the roughness model is indistinguishable between smooth chemically diffuse or rough diffusion-free interfaces, additional surface roughness information may be necessary to accurately simulate a multilayer system. Consequently, methods such as transmission electron microscopy, [25] Rutherford backscattering spectrometry[26] or

[19] N. Hosoito, T. Ohkochi, K. Kodama, and M. Suzuki. Charge and induced magnetic structures of au layers in Fe/Au bilayer and Fe/Au/Fe trilayer films by resonant x-ray magnetic reflectivity at the Au L_3 absorption edge. *J. Phys. Soc. Jpn.*, **83**(2):024704 (2014)

[20] G. Felcher, R. Hilleke, R. Crawford, J. Haumann, R. Kleb, and G. Ostrowski. Polarized neutron reflectometer: A new instrument to measure magnetic depth profiles. *Rev. Sci. Instrum.*, **58**(4):609–619 (1987); and C. Majkrzak. Neutron scattering studies of magnetic thin films and multilayers. *Physica B*, **221**(1-4):342–356 (1996)

[21] S. Roy, M. Fitzsimmons, S. Park, M. Dorn, O. Petracic, I. V. Roshchin, Z.-P. Li, X. Batlle, R. Morales, A. Misra, X. Zhang, K. Chesnel, J. B. Kortright, S. K. Sinha, and I. K. Schuller. Depth profile of uncompensated spins in an exchange bias system. *Phys. Rev. Lett.*, **95**(4):047201 (2005); and M. Björck, G. Andersson, B. Sanyal, M. Hedlund, and A. Wildes. Segregation and interdiffusion in (Fe, Co)/Pt superlattices. *Phys. Rev. B*, **79**(8):085428 (2009)

[22] E. Kravtsov, D. Haskel, S. Te Velthuis, J. Jiang, and B. Kirby. Complementary polarized neutron and resonant x-ray magnetic reflectometry measurements in Fe/Gd heterostructures: Case of inhomogeneous intralayer magnetic structure. *Phys. Rev. B*, **79**(13):134438 (2009)

[23] K. Zafar, P. Audehm, G. Schütz, E. Goering, M. Pathak, K. Chetry, P. LeClair, and A. Gupta. Cr magnetization reversal at the CrO_2/RuO_2 interface: Origin of the reduced GMR effect. *Phys. Rev. B*, **84**(13):134412 (2011)

[24] S. Macke and E. Goering. Magnetic reflectometry of heterostructures. *J. Phys. Condens. Matter*, **26**(36):363201 (2014)

[25] M. Hytch, M. Walls, and J.-P. Chevalier. Measurement of roughness and diffuseness of interfaces. *Ultramicroscopy*, **83**(3-4):217–225 (2000)

[26] R. Nagel, C. Alof, A. Balogh, W. Arnoldbik, and D. Boerma. Study of magnetic multilayers by RBS with nanometer resolution. *Nucl. Instrum. Methods Phys. Res. B*, **183**(1-2):140–145 (2001)

atomic force microscopy[27] provide useful additional information to refine the simulation of XRMR asymmetry ratio data.

This following sections discuss XRMR results for Pt thin film samples of increasing complexity and thus serve to establish a step-by-step procedure to cover these issues systematically. In order to obtain a robust magnetic model, additional reliability checks are implemented into the analysis procedure to avoid the practice of exploiting unrealistic degrees of freedom in the simulation or the necessity to resort to additional measurements such as neutron scattering experiments. Here, a detailed analysis of the asymmetry ratio features as well as the χ^2 multidimensional maps is incorporated into a proposed step-by-step guide to improve the agreement between measurements and fit. Both of these additional optimization approaches are discussed in-depth within this chapter to establish these as convenient steps to increase the general significance of XRMR studies on bi- and multilayer thin film systems.

[27] F. J. Giessibl. Advances in atomic force microscopy. *Rev. Mod. Phys.*, **75**(3): 949 (2003)

The analysis of XRMR data discussed for Pt thin film samples of increasing complexity

THE SPIN POLARIZATION DEPTH PROFILES of Pt in different types of thin films are systematically investigated in the following sections by interface-sensitive XRMR in the hard x-ray regime at the Pt L_3 absorption edge. Subsequently, this chapter discusses the necessary analysis steps utilizing the advanced modeling techniques of REMAGX to achieve the real best fit for the XRR and XRMR scans by means of three specific systems where Pt is integrated in the sample in an increasingly complex manner from simple bilayer over multi-layered stacks to Heusler compounds that include Pt.

Initially, this development of a progressive XRMR analysis guide starts with the study of a Pt/Fe//MgO bilayer system in order to demonstrate the basic framework of the XRMR analysis. In this simple bilayer system, the magnetic depth profile induced by a MPE in Pt is investigated in different layer and element specific modeling modes. In the analysis process, the pros and cons of both modes are evaluated. The second example presented here is based on a system, where Pt is an integral part of an elaborate, multi-layered thin film stack, including a single Pt layer which is located adjacent to a MPE inducing Co layer.[28] The final example discussed in this chapter is the standard PtMnSb thin film with and without the covering Pt layer on top, representing the central sample system of this work. The significance of this half-Heusler system, which is promising system for the investigation of intrinsic SOTs, has been outlined in chapter 1.7. Here, the emphasis is on the accurate observation of the element specific magnetic depth profile which enables and supports further spincaloritronic research and the development of an optimized XRMR analysis procedure.

Apart from versatile fitting algorithms and optimization ap-

[28] R. M. Rowan-Robinson, A. Stashkevich, Y. Roussigné, M. Belmeguenai, S.-M. Chérif, A. Thiaville, T. Hase, A. Hindmarch, and D. Atkinson. The interfacial nature of proximity-induced magnetism and the Dzyaloshinskii-Moriya interaction at the Pt/Co interface. *Sci. Rep.*, **7**(1):16835 (2017); A. Mukhopadhyay, S. K. Vayalil, D. Graulich, I. Ahmed, S. Francoual, A. Kashyap, T. Kuschel, and P. S. A. Kumar. Asymmetric modification of the magnetic proximity effect in Pt/Co/Pt trilayers by the insertion of a Ta buffer layer. *arXiv:1911.12187*, (2019); and A. Moskaltsova, J. Krieft, D. Graulich, T. Matalla-Wagner, S. Francoual, and T. Kuschel. Impact of the magnetic proximity effect in Pt on the total magnetic moment of Pt/Co/Ta trilayers studied by x-ray resonant magnetic reflectivity. *AIP Advances*, **10**(1):015154 (2020)

proaches in order to improve the convergence between measured and simulated reflectivity data, the advanced element specific fitting mode of ReMagX is used to simulate separate density and magnetic depth profiles. Subsequently, the individual optimization procedures used in these increasingly sophisticated evaluations of the XRMR results are consolidated in a process flow diagram as a step towards a universally applicable XRMR analysis procedure for the specified types of Pt based bi- and multilayers as well as the wide range of comparable thin film systems. In this context, the XRMR results of the PtMnSb half-Heusler thin film system are used on the one hand to outline a general recipe procedure to analyze explicit features of the XRMR asymmetry ratios and on the other hand to obtain a robust picture of the specific magnetic depth profile which is crucial for an exact identification of magnetic dead layers as well as induced MPEs.

Experimental details of the XRR and XRMR experiments

Three different multilayers on $10 \times 10\,\mathrm{mm}^2$ MgO(001) and SiO_x/Si(001) substrates have been prepared by magnetron sputter deposition at Bielefeld University. The epitaxial Pt/Fe//MgO(001) bilayer and TaO_x/MgO/Ta/Co/Pt//SiO_x/Si(001) multilayer have been grown in an Ar^+ atmosphere in the range of 3×10^{-3} mbar at room temperature. In contrast, the PtMnSb thin films have been prepared following the sputtering process outlined in chapter 2.2 in order to achieve an optimal growth without using any seed layer.[29] These multilayer systems are used here to perform XRMR measurements on systems with increasing complexity at the same Pt absorption edge in order to obtain comparable results and facilitate the development of an advanced analysis procedure.

The asymmetry ratio of the reflectivity is measured at the Pt L_3 absorption edge using circularly polarized x-rays at room temperature. The Pt/Fe//MgO bilayer as well as the TaO_x/MgO/Ta/Co/Pt//SiO_x multilayer sample have been investigated at the P09 beamline at PETRA III (Hamburg, Germany). In this experiment, a single diamond quarter-wave plate has been utilized to generate a DCP of $(99 \pm 1)\,\%$. The reflectivity curves have been collected in the conventional $\theta - 2\theta$ scattering geometry, while an external magnetic field of $\pm 90\,\mathrm{mT}$ applied parallel to the sample surface in the scattering plane has been produced by a four-coil electromagnet following the experimental principles outlined in section 1.1.2 of this work.

The PtMnSb thin films have been investigated at the XMaS beamline BM28 at ESRF (Grenoble, France) in the same scattering geometry at room temperature.[30] The incoming x-ray photons have been converted to a DCP of $(88 \pm 1)\,\%$ via a $800\,\mu\mathrm{m}$ thick diamond phase-plate.[31] During the experiment, the helicity has been reversed at 11.5 Hz by a piezo driven device in order to sig-

[29] J. Krieft, J. Mendil, M. H. Aguirre, C. O. Avci, C. Klewe, K. Rott, J.-M. Schmalhorst, G. Reiss, P. Gambardella, and T. Kuschel. Co-sputtered PtMnSb thin films and PtMnSb/Pt bilayers for spin-orbit torque investigations. *Phys. Status Solidi Rapid Res. Lett.*, **11**(4): 1600439 (2017)

[30] S. Brown, L. Bouchenoire, D. Bowyer, J. Kervin, D. Laundy, M. Longfield, D. Mannix, D. Paul, A. Stunault, P. Thompson, M. J. Cooper, C. A. Lucas, and W. G. Stirling. The XMaS beamline at ESRF: Instrumental developments and high-resolution diffraction studies. *J. Synchrotron Radiat.*, **8**(6):1172–1181 (2001)

[31] L. Bouchenoire, S. Brown, P. Thompson, J. Duffy, J. Taylor, and M. Cooper. Performance of phase plates on the XMaS beamline at the ESRF. *J. Synchrotron Radiat.*, **10**(2):172–176 (2003)

nificantly improve the signal-to-noise ratio.[32] The measurements have been carried out at the Pt L_3 absorption edge (11 568 eV) and off-resonance (11 468 eV). Here, a magnetic field of ± 200 mT has been applied parallel to the sample surface in the scattering plane.

The Pt specific magnetic depth profiles discussed in this segment are contrasted with the Mn specific results in the following chapter 5 of this work. Due to the expected small spin magnetic moment of Pt in the PtMnSb half-Heusler system (compare section 1.7) or in case of an induced spin polarization (compare section 1.4) in the top Pt layer, the XRMR asymmetry ratio obtained at the Pt absorption edge is significantly smaller than at the Mn absorption edge. Thus, the detection of the corresponding asymmetry ratio requires a much higher integration time and where applicable a more sophisticated and in-depth analysis of the XRR and XRMR simulation, which is discussed in the following sections of this chapter, in order to achieve the same level of precision.

Here, the thickness and roughness of the modeled thin film layers are normally regarded as free fitting parameters within realistic intervals. In addition, literature values are used to maintain fixed optical constants for the first steps of the fit based optimization. For the study of the Pt/Fe bilayer system, the off-resonant XRR measurements 100 eV below the Pt absorption edge have been used to define the correct structural properties. These are conversely utilized to derive the optical constants at the resonance energy. Each layer is modeled with a homogeneous layer density and finite interface roughness based on the epitaxial growth of the sample. The resonant XRMR scans have been performed at a fixed photon energy at the maximum of the magnetic dichroism slightly below the whiteline energy of the Pt L_3 absorption edge.[33] This procedure detailed by Klewe *et al.*,[34] which is presented and discussed in chapter 1.1.3, is only applicable for uncomplex, well-defined and easy to model thin film system such as the simple Pt/Fe bilayer with smooth interfaces. In the case of structurally more sophisticated systems such as multilayers with a distinct level of inter-diffusion, interface roughness, oxidation or a overall inhomogeneity of the sample growth, the structural parameters are not immediately transferable.

The layered model of the thin film system is typically limited to the most reasonable structural parameters. These parameters are however not sufficient to describe structurally complex systems in their entirety. This is the case when there are various minor inhomogeneities which can't be independently parameterized obeying Ockham's razor principle. Therefore, the parameters of the simulation must compensate for the shortcomings of the utilized model. The sample complexity exceeding the capability of the model is necessarily compensated via minor adjustments of the structural and optical parameters. The best fits based on these type of approximated modulation are not independent of the photon energy. This impedes an immediate transferability of the structural

[32] L. Bouchenoire, S. Brown, P. Thompson, M. Cain, M. Stewart, and M. Cooper. Development of a novel piezo driven device for fast helicity reversal experiments on the XMaS Beamline. *AIP Conf. Proc.*, **879**(1): 1679–1682 (2007)

[33] G. Schütz, R. Wienke, W. Wilhelm, W. Zeper, H. Ebert, and K. Spörl. Spin-dependent x-ray absorption in Co/Pt multilayers and $Co_{50}Pt_{50}$ alloy. *J. Appl. Phys.*, **67**(9):4456–4458 (1990); J. Geissler, E. Goering, M. Justen, F. Weigand, G. Schütz, J. Langer, D. Schmitz, H. Maletta, and R. Mattheis. Pt magnetization profile in a Pt/Co bilayer studied by resonant magnetic x-ray reflectometry. *Phys. Rev. B*, **65**(2):020405 (2001); T. Kuschel, C. Klewe, J.-M. Schmalhorst, F. Bertram, O. Kuschel, T. Schemme, J. Wollschläger, S. Francoual, J. Strempfer, A. Gupta, M. Meinert, G. Götz, D. Meier, and G. Reiss. Static magnetic proximity effect in $Pt/NiFe_2O_4$ and Pt/Fe bilayers investigated by x-ray resonant magnetic reflectivity. *Phys. Rev. Lett.*, **115**(9):097401 (2015); and T. Kuschel, C. Klewe, P. Bougiatioti, O. Kuschel, J. Wollschläger, L. Bouchenoire, S. Brown, J. Schmalhorst, D. Meier, and G. Reiss. Static Magnetic Proximity Effect in Pt Layers on Sputter-Deposited $NiFe_2O_4$ and on Fe of Various Thicknesses Investigated by XRMR. *IEEE Trans. Magn.*, **52**:4500104 (2016)

[34] C. Klewe, T. Kuschel, J.-M. Schmalhorst, F. Bertram, O. Kuschel, J. Wollschläger, J. Strempfer, M. Meinert, and G. Reiss. Static magnetic proximity effect in $Pt/Ni_{1-x}Fe_x$ bilayers investigated by x-ray resonant magnetic reflectivity. *Phys. Rev. B*, **93**(21):214440 (2016)

parameters for the resonant fit. Here, it is an appropriate approach to first extract the structural parameters by modeling the resonant XRR intensity I and subsequently use these as input parameters for the XRMR analysis of the asymmetry ratio ΔI. The exact process of simulating the nonmagnetic and magnetic reflectivity is discussed at length in the following sections for each specific sample system. This includes the definition of quality for all fits of the asymmetry ratio and the specific algorithms utilized for the optimization process as well as the magnetooptical representation of the sample magnetization within the XRMR framework.

Results and Discussion

A SYSTEMATIC METHOD to accurately simulate the obtained XRMR asymmetry ratios is discussed hereafter which achieves reliable results for Pt based bi- and multilayer samples of increasing complexity without the implementation of any additional layers, supplementary measurements or unreasonable fit parameters. The focus lies on using the software package REMAGX to full capacity. The versatile implemented fitting algorithms are exploited and additional simulation methods have been developed in this work to improve convergence between measured and simulated reflectivity data and accurately determine the magnetic depth profiles at the different interfaces.

Standard Pt/Fe bilayer

For the purpose of visualizing the specific difference between the layer and independent element based simulation approaches, a direct comparison of both simulations is shown in Fig. 4.1. In this regard, the versatility of the ESF mode of REMAGX is ultimately pointed out, in particular for the element specific magnetic modeling. First of all in this chapter, the XRR intensity I and corresponding asymmetry ratio ΔI are presented for a Pt/Fe bilayer on MgO measured at the Pt L_3 edge. The fit of the obtained signal confirms the presence of a MPE induced spin polarization at the Pt/FM interface. The magnetic depth profile of the simple bilayer system is an established example of a static MPE based on an unambiguous asymmetry ratio.[35] Here, the specular reflectivity curve is illustrated in Fig. 4.1(a) together with the corresponding best-fit simulation for this Pt/Fe bilayer. Pronounced Kiessig fringes with the expected oscillation length Δq_{Fe} and faint overlaying additional Kiessig fringes with the oscillation length Δq_{Pt} are observed. These oscillations in the intensity signal allow for the determination of the Pt and Fe thickness, which are 3.0 nm and 9.5 nm, respectively, with a rms roughness value of 0.3 nm or rather 0.5 nm as well as a MgO substrate roughness of 0.2 nm. In addition, Figs. 4.1(c) and (e) show the magnetic asymmetry ratio with an amplitude of up to 4 % and

[35] T. Kuschel, C. Klewe, J.-M. Schmalhorst, F. Bertram, O. Kuschel, T. Schemme, J. Wollschläger, S. Francoual, J. Strempfer, A. Gupta, M. Meinert, G. Götz, D. Meier, and G. Reiss. Static magnetic proximity effect in $Pt/NiFe_2O_4$ and Pt/Fe bilayers investigated by x-ray resonant magnetic reflectivity. *Phys. Rev. Lett.*, **115**(9): 097401 (2015)

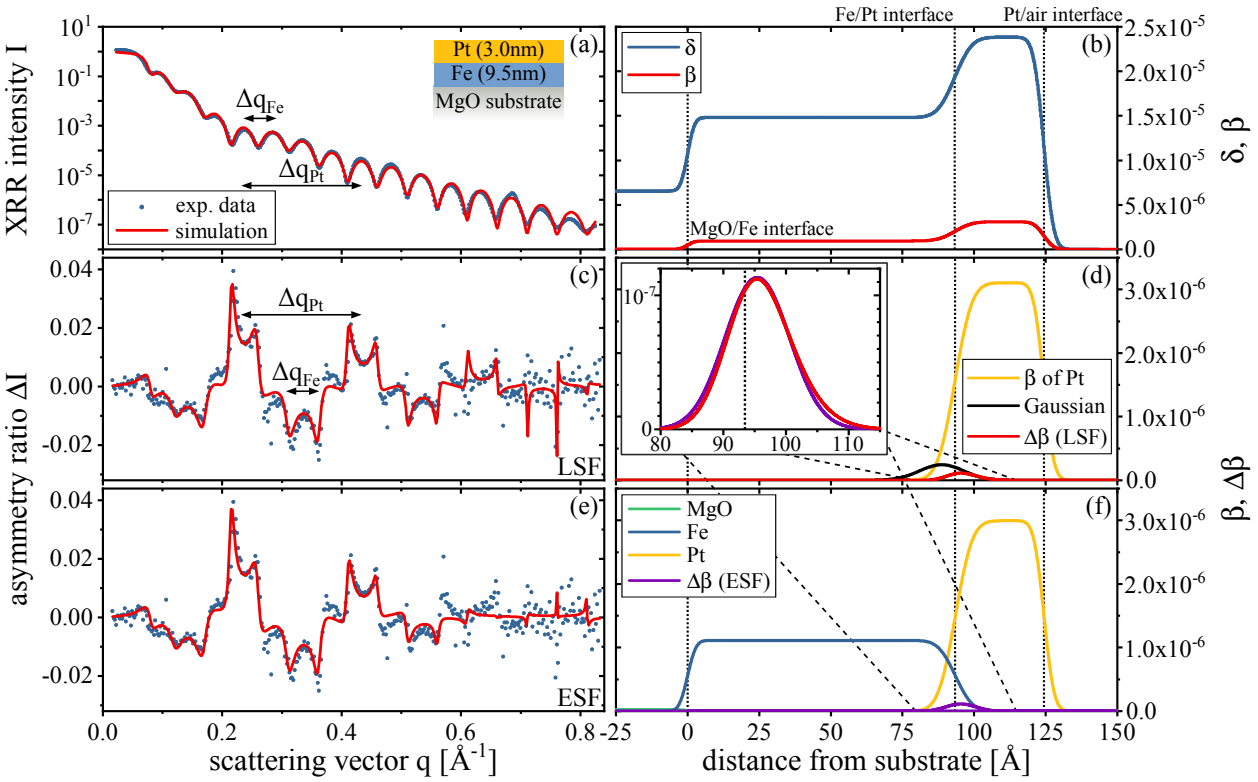

Figure 4.1: (a) XRR measurement for Pt(3.0 nm)/Fe(9.5 nm)//MgO (at 11 567.5 eV). (b) Optical δ and β depth profiles used for the asymmetry ratio simulation. (c) Corresponding asymmetry ratio $\Delta I(q)$ and simulated data using the ReMagX LSF mode. (d) Optical β and magnetooptical $\Delta\beta$ depth profile obtained with the LSF simulation. The $\Delta\beta$ depth profile is obtained from the displayed Gaussian function convolved with the β depth profile and, thus, with the roughness of the Pt/Fe interface. (e) Equivalent simulation of the asymmetry ratio $\Delta I(q)$ using the ReMagX ESF mode. (f) Optical β depth profile for each element and the magnetooptical $\Delta\beta$ depth profile corresponding to the asymmetry ratio simulation in (e). Inset in (d): Close-up comparison of the $\Delta\beta$ depth profile obtained from LSF and ESF of ReMagX.

corresponding fits generated by both the layer as well as element specific modes of ReMagX.

The optical depth profiles for the real δ and imaginary parts β derived from the reflectivity simulation are illustrated in Fig. 4.1(b). These are the basis for the simulation of the magnetic depth profile using the LSF mode, by which the magnetooptical depth profile is derived from a convolution of a Gaussian function with the optical depth profile. Therefore, the depth profiles of $\Delta\delta$ and $\Delta\beta$ are derived at the Pt/Fe interface based on the optical depth profile of the element associated with the chosen absorption edge, in this case Pt, which carries the magnetic moment under investigation.[36]

The calculation of the magnetooptical depth profile is shown in Fig. 4.1(d), where the best-fit positions the Gaussian function far into the Fe layer. However, the convolution with the interface roughness of the Pt yields a reasonable $\Delta\beta$ depth profile which is close to the Pt/Fe interface as highlighted in the inset of Fig. 4.1(d). Attention should be paid to the FWHM of the Gaussian function which is much larger than the FWHM of the resulting magnetic depth profile. Here, one should compare the black and red curve in the lowermost position of Fig. 4.1(d). The corresponding fit of the asymmetry ratio depicts a simulation where all main features are well covered in spite of an elevated noise level at higher scattering vectors q_z.

The simulation has been repeated employing the ESF mode based on separate element specific density depth profiles. In this

[36] C. Klewe, T. Kuschel, J.-M. Schmalhorst, F. Bertram, O. Kuschel, J. Wollschläger, J. Strempfer, M. Meinert, and G. Reiss. Static magnetic proximity effect in Pt/$Ni_{1-x}Fe_x$ bilayers investigated by x-ray resonant magnetic reflectivity. *Phys. Rev. B*, **93** (21):214440 (2016)

advanced fitting mode, an equivalent simulation has been obtained, which confirms that the ESF mode exhibits a similar operational level of precision as the conventional LSF approach when modeling simple magnetic layers. This can be seen by directly comparing both fitted asymmetry ratios in Figs. 4.1(c) and (e). However, the ESF mode has further advantages over the LSF mode, especially since it is way more flexible in the simulation of realistic magnetic depth profiles in sophisticated and complex magnetic systems. With regard to the magnetooptical depth profile, the focus is on the parameter $\Delta\beta$ due to the fact that the parameter $\Delta\delta$ is close to zero at the absorption edge.[37]

In the ESF mode, $\Delta\beta$ is independently modeled as a separate layer, where thickness and interface roughness parameters are used to manipulate the form and position of the magnetic depth profile. In order to model a realistic spin polarized layer at the interface, this separate magnetic layer has to be bound to a layer of an element defining the sample structure. In this model specification for the Pt/Fe bilayer, this coupling is achieved based on the assumption that the magnetic depth profile adapts the structural roughness of the interface connecting the nonmagnetic metal with the ferromagnet layer, which is thereby affecting the magnetic coupling in a decisive way.[38]

When a magnetic depth profile is simulated based on this model, using a discrete layer which adapts the roughness of the Pt density depth profile, the resulting magnetooptical $\Delta\beta$ depth profile resembles the one which is determined utilizing the LSF mode where the Gaussian function is convolved with the optical depth profile. The results of both modes are directly compared in the inset of Fig. 4.1(d). This insert highlights the $\Delta\beta$ depth profile obtained in both modes in at a distance of 100 - 115 Å from the substrate. Here, a minor increase of the $\Delta\beta$ depth profile derived in the LSF mode is observed on the right flank of the corresponding depth profile in relation to the ESF based solution. On the whole, the simulation of the asymmetry ratio, as a result of the ESF fit, merely exhibits minor deviations from the LSF result and thus shows a best fit of comparable quality. Therefore, the ESF mode should be used on a regular basis in order to profit from its versatility in both modeling independent magnetic depth profiles as well as complex magnetic alloys, heterostructures and multilayers.

In a next step, multi-dimensional χ^2 maps should be calculated and analyzed to optimize the fitting routine and ultimately determine a true global best fit. Both the computational complexity of the minimization problem as well as the dimensionality of the χ^2 objective functions the algorithms are working on, scale with the number of free parameters of the simulation. Therefore, it is expedient to exemplary focus on a simple fit of the XRR intensity for the purpose of illustration, discussing two specific parameters at once. As a start, the χ^2 values as a function of the thickness d and roughness σ parameters of the Pt layer, within the limits of

[37] T. Kuschel, C. Klewe, J.-M. Schmalhorst, F. Bertram, O. Kuschel, T. Schemme, J. Wollschläger, S. Francoual, J. Strempfer, A. Gupta, M. Meinert, G. Götz, D. Meier, and G. Reiss. Static magnetic proximity effect in $Pt/NiFe_2O_4$ and Pt/Fe bilayers investigated by x-ray resonant magnetic reflectivity. *Phys. Rev. Lett.*, **115**(9): 097401 (2015)

[38] C. Klewe, T. Kuschel, J.-M. Schmalhorst, F. Bertram, O. Kuschel, J. Wollschläger, J. Strempfer, M. Meinert, and G. Reiss. Static magnetic proximity effect in $Pt/Ni_{1-x}Fe_x$ bilayers investigated by x-ray resonant magnetic reflectivity. *Phys. Rev. B*, **93**(21):214440 (2016); and D.-O. Kim, K. M. Song, Y. Choi, B.-C. Min, J.-S. Kim, J. W. Choi, and D. R. Lee. Asymmetric magnetic proximity effect in a Pd/Co/Pd trilayer system. *Sci. Rep.*, **6**: 25391 (2016)

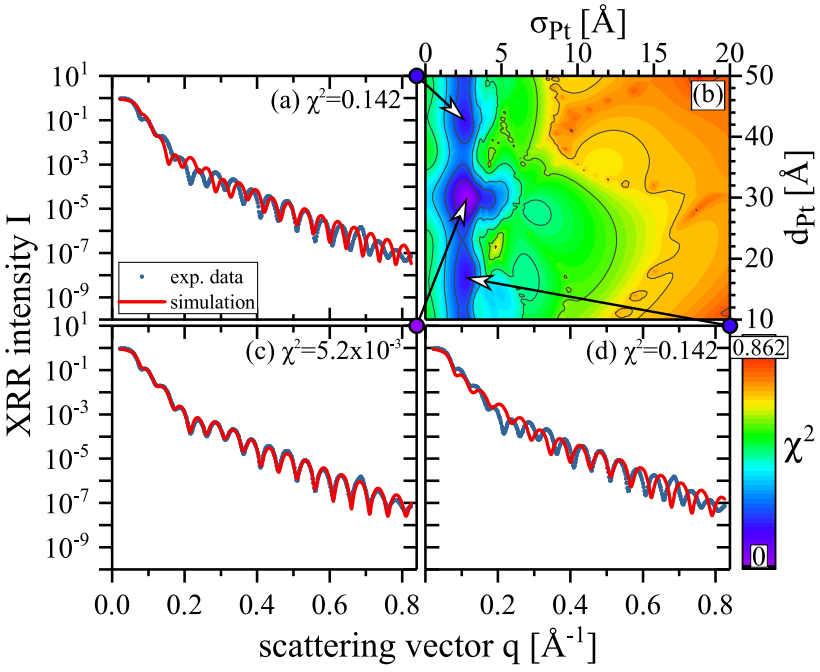

Figure 4.2: XRR measurement of Pt(3.0 nm)/Fe(9.5 nm)//MgO and various simulations of the XRR intensity I for different thicknesses d and roughnesses σ of the Pt layer. (b) 2D mapping plot of χ^2 depending on d and σ of the Pt layer. (c) shows the optimal simulation, while (a) and (d) represent local minima in the χ^2 landscape.

the fit optimization of the simulated Pt/Fe bilayer reflectivity, are presented in form of a 2D landscape in Fig. 4.2.

This compilation shows the XRR best fit at the global minimum in direct comparison to fits in both neighboring local minima which feature distinct deviations from the experimental Kiessig fringes due to a pronounced thickness variation. As a result of the relative shift of the oscillatory pattern, repeating local minima are observed at fixed multiples of d_{Pt} along this axis of the 2D plot. Along the Pt roughness axis, higher values of σ_{Pt} are going along with a significant increase of the χ^2 effective error. When a standard downhill algorithm operates on a simple objective function in a 2D space such as the one represented by this χ^2 map shown here, the reflectivity fit is easily optimized if all other parameters are already determined, especially since the local optima are obviously discarded. However, the nonlinear optimization generally has to work with a multi-dimensional χ^2 landscape which can be highly complex. In this case, all structural and optical parameters of each modeled layer increase the dimensionality of the objective function, potentially complicating the optimization problem to simulate a real multilayer system by creating additional local minima or non-stationary points.

Alternative 2D χ^2 landscapes within the same multi-dimensional landscape are further illustrated in Fig. 4.3. The reason to present this map compilation in this context is to demonstrate the general principles of an in-depth analysis of the χ^2 maps. Even though the global minimum is clearly recognizable in all presented χ^2 map, numerous local minima are observable demanding advanced metaheuristic algorithms.

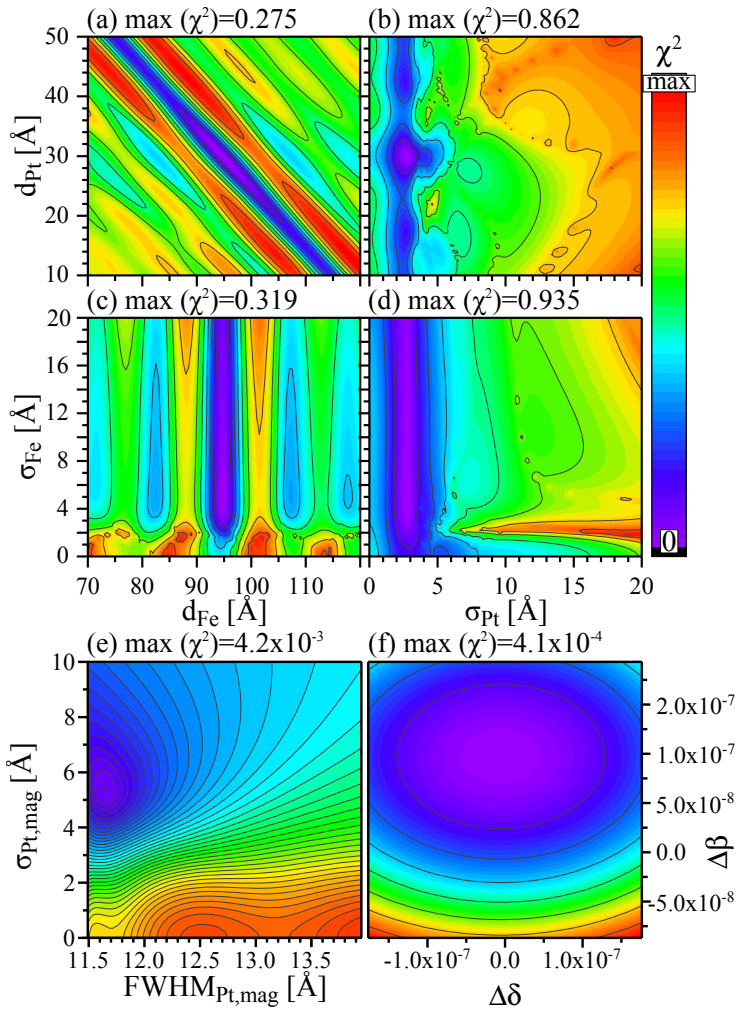

Figure 4.3: Selected 2D maps of the χ^2 value for the XRR fits of Pt(3.0 nm)/Fe(9.5 nm)//MgO. (a) χ^2 map plot varying the thickness of the Fe layer d_{Fe} and the thickness of the Pt layer d_{Pt}. (b) χ^2 map plot varying the roughness σ_{Pt} and d_{Pt}. (c) χ^2 map plot varying d_{Fe} and the roughness of the Fe layer σ_{Fe}. (d) χ^2 map plot varying σ_{Pt} and σ_{Fe}. (e) 2D plot for the magnetooptical fits of the XRMR asymmetry ratios. The FWHM of the magnetic depth profile $FWHM_{Pt,mag}$ is varied as well as the roughness $\sigma_{Pt,mag}$. (f) Corresponding 2D χ^2 plot of the magnetooptic parameters $\Delta\delta$ vs. $\Delta\beta$.

In the first subplot Fig. 4.3(a), the values of the chi-squared discrepancy are determined based on a variation of the Fe and Pt thickness parameters d_{Fe} and d_{Pt}. This dependency on layer thickness lead to a pronounced oscillatory character which results from the changed periodicity of the Kiessig fringes and the resulting shift in relation to the measured reflectivity curve. This oscillatory pattern forms bands of smeared out minima which are rotated by 45° relative to the coordinate axes. The distinct minima in this pattern are specified by multiples of d_{Fe} and d_{Pt} which are evenly arranged in relation to the global minimum, which is found in the center of the map providing the best-fit parameters.

As opposed to this plot generated by a pure variation of layer thickness, the maps illustrating the χ^2 value based on a thickness variation on one axis and the corresponding roughness parameter on the other axis present a pronounced interference like pattern. For instance, Fig. 4.3(c) shows this type of map as a function of the Fe layer thickness d_{Fe} and roughness σ_{Fe} while Fig. 4.3(d) is a function of both roughnesses σ_{Pt} and σ_{Fe}. In this compilation, Fig. 4.3(b) is the same map which has been discussed with regard to Fig. 4.2 and is included here for the sake of completeness. When

the thickness of the Fe d_{Fe} layer is increased, the χ^2 map manifests the previously identified oscillatory pattern along this axis while higher values of Pt roughness σ_{Pt} on the other hand go along with monotone increasing χ^2 values. In both maps of Figs. 4.3(c) and (d), the roughness of the upper Fe interface σ_{Fe} yields particularly broad minima along this parameter dimension. This implies a higher degree of uncertainty with respect to this value in the space of the XRR fitting process. Thus, the roughness σ_{Fe} has to be either reassured by secondary measurements or, as done here, a detailed check of χ^2 to restrict this parameter to realistic values. At large, this map compilation serves to illustrate the significance of a detailed analysis of the overall χ^2 landscape. In terms of the investigation of the magnetic depth profile, this analysis should be equally sophisticated when the asymmetry ratios are fitted.

The χ^2 maps associated with the simulation of the asymmetry ratio and thus the determination of the magnetooptical depth profiles are illustrated at the bottom of Fig. 4.3. Here, the χ^2 map shown in Fig. 4.3(e) is created by a variation of the magnetic depth profile roughness $\sigma_{\mathrm{Pt,mag}}$ in relation to the FWHM of the magnetic depth profile $\mathrm{FWHM}_{\mathrm{Pt,mag}}$. This effective thickness of the magnetic Pt depends on the thickness $d_{\mathrm{Pt,mag}}$ of the initially used magnetic layer that becomes the magnetic depth profile $\Delta\beta$ of Fig. 4.1(f) when the magnetic roughness $\sigma_{\mathrm{Pt,mag}}$ is taken into account. Here, the dependence is $\mathrm{FWHM}_{\mathrm{Pt,mag}} = 0.0198\,\mathrm{nm}^{-1} \cdot d^2_{\mathrm{Pt,mag}} + 0.0476 \cdot d_{\mathrm{Pt,mag}} + 11.5\,\mathrm{nm}$ for the Pt(3.0 nm)/Fe(9.5 nm)//MgO bilayer. This plot displays a pronounced global minimum yet no additional local minima. Therefore, in this case it is straightforward to find the optimal parameters of the magnetooptical depth profile using a simple downhill fitting algorithm. In the same way, the optimal value of the $\Delta\delta$ and $\Delta\beta$ parameter can be found in the asymmetry ratio simulation, since the 2D objective function visualized in Fig. 4.3(f) represents a clear global minimum which is best characterized as a χ^2 potential well. As a general rule, it is important to visualize multiple χ^2 maps, as illustrated in Fig. 4.3, in order to check whether there are local minima close to the global best fit in any combination of parameter plots. The reason being that these minima frequently yield good fits which are however semi-optimal solutions. This bears the potential risk of impeding the algorithm from reaching convergence in optimal simulations of the asymmetry ratio, especially when the XRMR fit is operating based on pre-established semi-optimal structural parameters.

In Fig. 4.4, the χ^2 landscape spanned by the thickness of the Pt layer d_{Pt} and the thickness of the Fe layer d_{Fe} is presented together with three reflectivity simulations at selected minima of the parameter space visualized by the χ^2 map. In particular, the global minimum associated with the best fit is directly contrasted with two adjacent local minima on this χ^2 map which is also an integral part of the selected 2D landscapes illustrated in Fig. 4.3. Both fits corresponding to the local minima are exhibiting clear

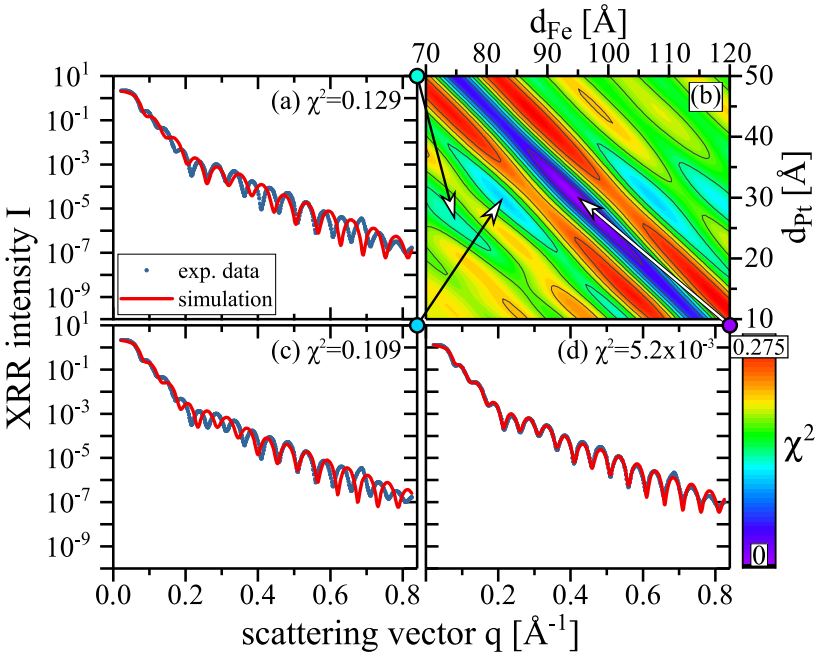

Figure 4.4: XRR measurements of Pt(3.0 nm)/Fe(9.5 nm)//MgO and various simulations of the XRR intensity I at specific locations within the (b) 2D mapping plot of χ^2 spanned by the variation of the thickness d_{Pt} of the Pt and thickness d_{Fe} of the Fe layer. (d) shows the optimal simulation, while (a) and (c) represent local minima in the χ^2 landscape.

deviations from the Kiessig oscillations based on a variation of the layer thickness. The global minimum is unambiguously located in the center of this 2D plot. Starting from the respective d_{Pt} value, further recurrent local minima are shown with equidistant steps of Δd_{Fe}. In Fig. 4.4(d), the reflectivity simulation of the best fit is illustrated while the fits of the adjacent local minima are shown in Figs. 4.4(a) and (c). It is self-evident that the simulations of the x-ray reflectivity on the left side of Figs. 4.4(a) as well as (c) are far from ideal which is also noticeable by a comparatively large value of the chi-squared discrepancy. It begins to show that these local minima fits are inaccurate based on the misrepresented Fe thickness which manifests in a displacement of the Kiessig oscillation. Consequentially, this exemplary shortcoming in the accurate determination of one thickness parameter prohibits the simulations of the asymmetry ratio constituted on this specific structural model.

The same in-depth analysis of the multidimensional χ^2 landscape for a structurally more complex system which, in the same way, involves an interface of Pt adjacent to a 3*d* ferromagnet is presented in the following section. This sample is particularly challenging because of both its fractionally inhomogeneous multilayer structure as well as intermixed oxide based capping which has a fundamental influence on the reflectivity curve. That is why a combination of fitting algorithms and an in-depth examination of the χ^2 maps is discussed in order to determine the global best-fit minimum and finally identify the MPE based magnetic depth profile in the deeply integrated Pt layer.[39]

[39] A. Moskaltsova, J. Krieft, D. Graulich, T. Matalla-Wagner, S. Francoual, and T. Kuschel. Impact of the magnetic proximity effect in Pt on the total magnetic moment of Pt/Co/Ta trilayers studied by x-ray resonant magnetic reflectivity. *AIP Advances*, **10** (1):015154 (2020)

Structurally complex multilayer including a Co/Pt interface

Figure 4.5 presents the analysis of a structurally more complex system still containing a Pt layer neighboring a 3*d* ferromagnet. In dependence of the sample fabrication or rather layer growth and capping, different density depth profiles with varying layer roughness can be expected. Thus, the simulation process is started with little information on the diffusive or oxidative condition of the individual layers. Figure 4.5(a) presents the XRR intensity plot with the best-fit simulation, obtained in the ESF mode, next to the corresponding optical depth profile which is illustrated in Fig. 4.5(b) showing the interface positions and roughness parameters of each transition between the elements or compounds. The interface position and roughness of neighboring materials is coupled comparable to the layer modeling in the LSF mode.

With regard to the partially oxidized TaO_x capping structure, a specification of multiple layers of individual elements is unnecessary, in particular, since the parameters of the intermixed elements tend to yield linear combinations of each other when simulated independently in the ESF mode. Here, it makes sense to define a single compound as a top layer representing the overall capping structure and thus reduce the number of unrestricted parameters in the XRR simulation.

Furthermore, the structural parameters are not fully transferable without modifying the off-resonant XRR fit results to the model of used in the resonant XRR and XRMR analysis. This is due to the fact that an increased sample inhomogeneity and complex oxide capping has a significant effect on the reflectivity curve which may impede the direct transferability. The reliability of the optical constants must be reviewed to guarantee that structural and optical parameters are fitted on the basis of the resonant reflectivity curve within realistic physical intervals.

The XRR intensity fit optimization with a combination of an evolutionary algorithm and a simplex fitting approach facilitates the determination of the optimal structural and optical parameters. On account of the challenging modeling of the capping layer, the XRR fit shown here is reasonably accurate yet no perfect agreement with the measured curve is reached, in particular for higher scattering vectors $q > 0.45\,\text{Å}^{-1}$. From this it follows that the simulated asymmetry ratio must be tested thoroughly in order to identify the influence of these inaccuracies given that the magnetooptical depth profile is directly connected to the determined structural parameters. The obtained asymmetry ratio and best-fit simulation are shown in Fig. 4.5(c) where every major feature of the presented curve is covered in an acceptable way by the simulation even though the experimental asymmetry ratio is on average lower than 2 %. In Fig. 4.5(e), a close-up of the Pt magnetic depth profile is shown. This profile is fixed to the right flank of the Pt density depth profile. As a consequence, the Pt magnetic depth profile

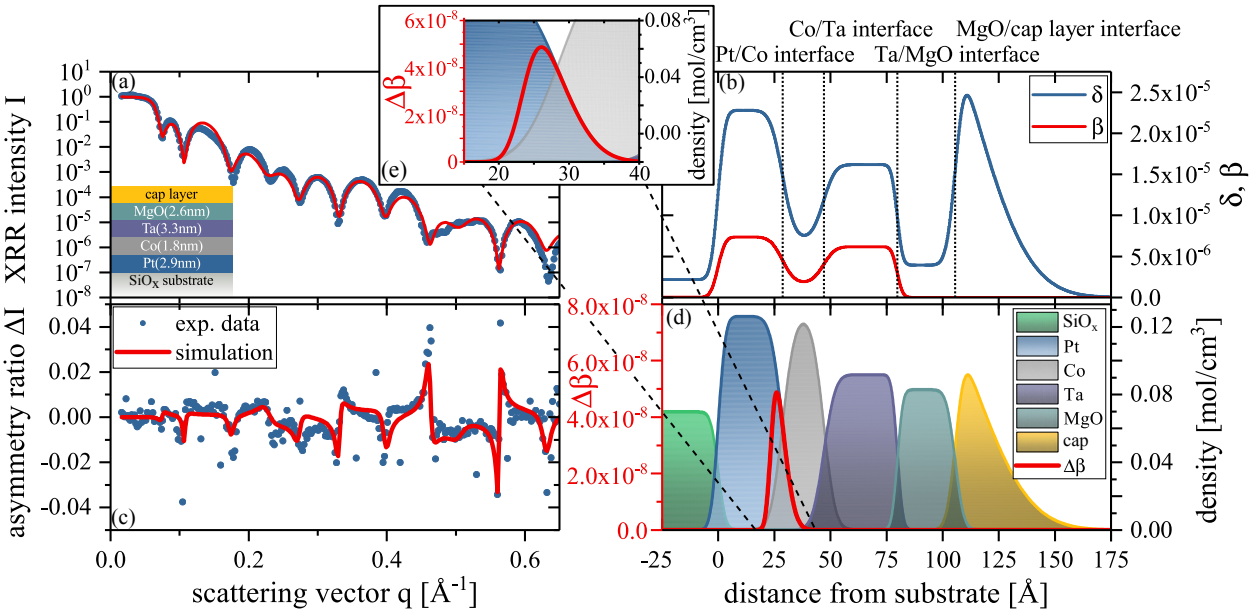

Figure 4.5: (a) XRR and (c) XRMR measurement of a TaO_x/MgO(2.6 nm)/Ta(3.3 nm)/Co(1.8 nm)/Pt(2.9 nm)//SiO_x multilayer. (b) shows the optical depth profile at the L_3 edge of Pt leading to the simulation in (a). (d) The element specific density and the magnetooptical depth profile used for the asymmetry ratio simulation in (c) obtained using the ESF mode. (e) Close-up focusing on the magnetooptical depth profile of $\Delta\beta$ which is bound to the depth profile of the Pt density at the right side of the $\Delta\beta$ depth profile.

superposes the Pt density depth profile at the interface and declines towards the substrate following the Gauss error function of a realistic magnetooptical depth profile. The form of the resulting profile is comparable to the one obtained at the Pt/Fe interface shown in Fig. 4.1(d).

When the χ^2 map of this multilayer, spanned by the thicknesses d_{Co} and d_{Pt}, is examined, the relevance of a thorough modeling of every feature of a reflectivity and asymmetry ratio is substantiated. This particular map is shown in Fig. 4.6. Generally, this map is comparable with the map presented in Fig. 4.3(a) given that it is plotted for two other thickness parameters, thereby inducing the established oscillatory pattern of local minima. In this plot, the global minimum in the center of the map is broadened along the map diagonal, similar to the global minimum in the χ^2 map of the Pt/Fe bilayer. However, based on the observed irregularity of the Kiessig fringes of this complex multilayer, the oscillatory pattern appears to be watered-down resulting in a 2D plot showing a multitude of overlaps as well as few sharp local minima.

The XRR intensity simulations presented in Figs. 4.6(a) and (c) depict a fit based on the parameters of two selected local minima. The first one shows a sharp local minimum which is located near the global minimum. The corresponding XRR simulation of the latter one is illustrated in Fig. 4.6(d), representing the best fit visualized in Fig. 4.5. The discrepancy of the fit quality between both local minima is considerably. Nevertheless, the structural parameters determined by the qualitatively worse fit are similar to those of the best fit with the exception of d_{Pt} while the objectively better fit is far from the global minimum in both mapped parameters. The corresponding reflectivity simulations of the local (Fig. 4.6(a)) and the global minimum (Fig. 4.6(d)) vary merely in in the range

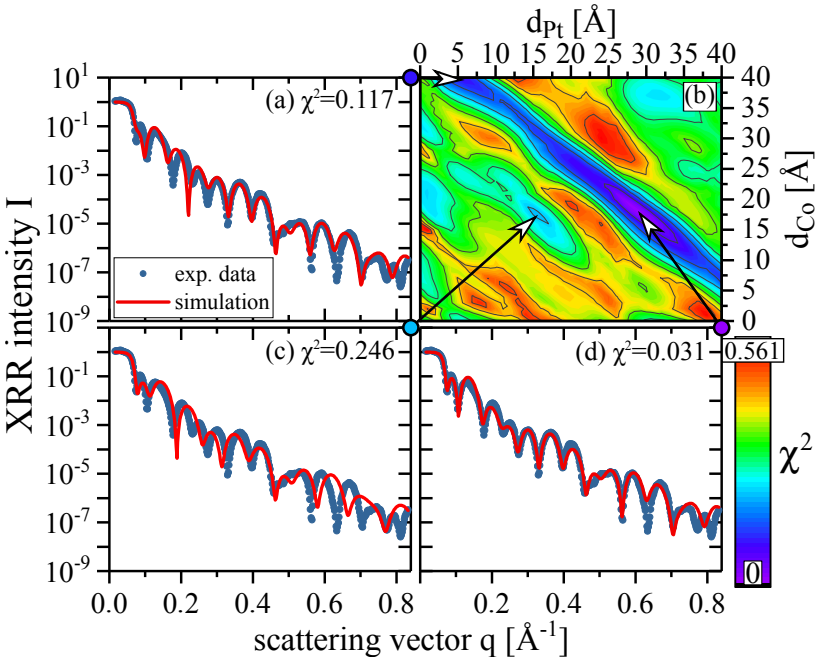

Figure 4.6: XRR intensity I and three exemplary simulations for TaO_x/MgO(2.6 nm)/Ta(3.3 nm)/Co(1.8 nm)/Pt(2.9 nm)//SiO_x at selected locations in the parameter space visualized as (b) a 2D mapping plot of χ^2 depending on the thickness of Pt d_{Pt} and thickness d_{Co} of the Co layer. (d) shows the optimal simulation, while (a) and (c) represent local minima in the χ^2 landscape.

of one Kiessig fringe at the start of the XRR curve. However, this simulation represents a decent coarse fit and is not improvable by employing the standard fitting algorithms which ultimately get stuck in this local minimum and thus preclude a successful asymmetry ratio simulation established on the corresponding structural parameters.

In order to take advantage of the excellent sensitivity of XRMR for the detection of magnetic depth profiles and minor variations of these within a samples series, the analysis has to focus extensively on every features of the reflectivity and asymmetry ratio signal. This is ultimately of higher significance than a minimization of χ^2 as stressed out by the fact that in an extreme case a straight line qualifies as a stable fit through an oscillation.

As opposed to a pure variation of the layer thickness parameters, Fig. 4.7 illustrates a selected set of XRR simulations of reflectivity data measured for the TaO_x/MgO(2.6 nm)/Ta(3.3 nm)/Co(1.8 nm)/Pt(2.9 nm)//SiO_x multilayer stack and the corresponding χ^2 map spanned by the layer thickness d_{Pt} and the roughness parameter of the Pt layer at the Co interface σ_{Pt}.

Figure 4.7(c) illustrates a fit corresponding to a local minimum at half the Pt thickness of the best-fit simulation. It roughly matches the Kiessig fringes in the first half of the plot, however, the fit lacks accuracy at larger values of the scattering vector $q > 0.45\,\text{Å}^{-1}$. Figure 4.7(d) exhibits a fit corresponding to a shallow local minimum of the χ^2 map. The quality of this fit is only minimally better than a straight line fit through the middle of the oscillations. However, it technically qualifies as a stable χ^2 minimum since a standard simplex algorithm can descend into this inescapable local minimum

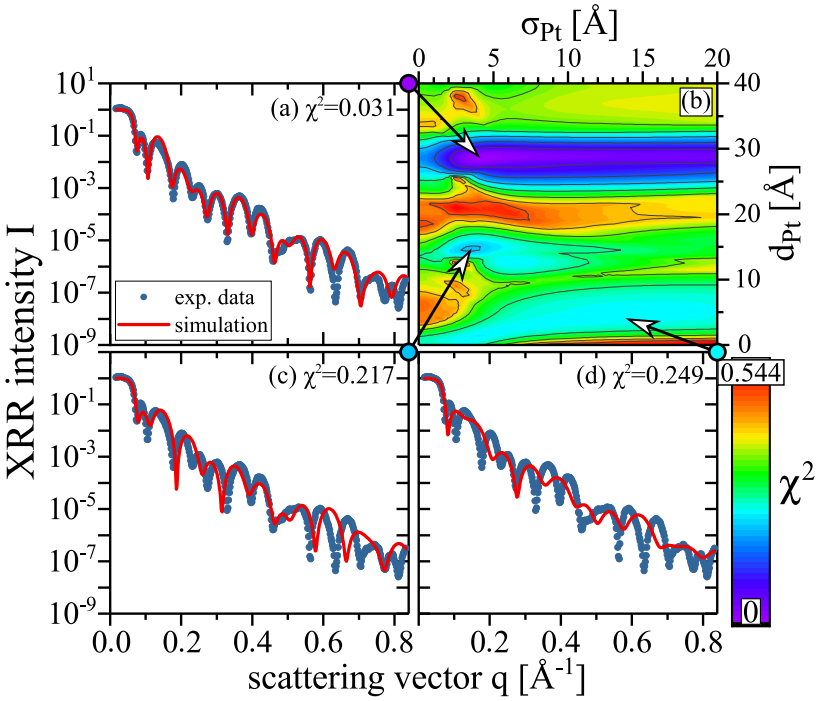

Figure 4.7: XRR intensity I and various simulations for TaO_x/MgO(2.6 nm)/Ta(3.3 nm)/Co(1.8 nm)/Pt(2.9 nm)//SiO_x at selected locations within (b) the 2D mapping plot of χ^2 depending on the thickness d and roughness σ of the Pt layer. (a) shows the optimal simulation, while (c) and (d) represent local minima in the χ^2 landscape.

of the objective function if a poor starting point is chosen.[40]

Moreover, this χ^2 landscape is highly anisotropic. While the χ^2 value is only marginally increasing when the global minimum is left along the axis defined by the roughness σ_{Pt}, the obtained thickness d_{Pt} is defined precisely by the global minimum which is steeply sloping along this axis of the map. Hence, the roughness should be defined precisely in the reflectivity simulation to use the outstanding sensitivity of XRMR to magnetic moments at interfaces to full capacity. Thus, this roughness parameter should be optimized and evaluated until the global minimum on the χ^2 landscape is unambiguously identified which can be confirmed additionally based on further methods, such as AFM or TEM measurements.

Figure 4.8 presents selected segments of the complex multi-dimensional χ^2 landscape of the TaO_x/MgO(2.6 nm)/Ta(3.3 nm)/Co(1.8 nm)/Pt(2.9 nm)//SiO_x sample. In detail, this compilation illustrates maps spanned by the Pt and Co thickness parameters, the corresponding roughness values, the extent of the magnetic depth profile along the z-direction (distance from the substrate) $d_{Pt,mag}$ and the roughness of its lower boundary $\sigma_{Pt,mag}$ as well as the magnetooptical parameters $\Delta\delta$ and $\Delta\beta$. Here, many local minima are visible obligating the experimenter to analyze the asymmetry ratio starting with heuristic algorithms which is comparable to the sectioned maps shown in Fig. 4.3 for the Pt/Fe//MgO bilayer system.

For the sake of completeness, the map depicted in Fig. 4.8(a) illustrates the same section of the parameter space which has been

[40] D. M. Olsson and L. S. Nelson. The Nelder-Mead simplex procedure for function minimization. *Technometrics*, **17** (1):45–51 (1975)

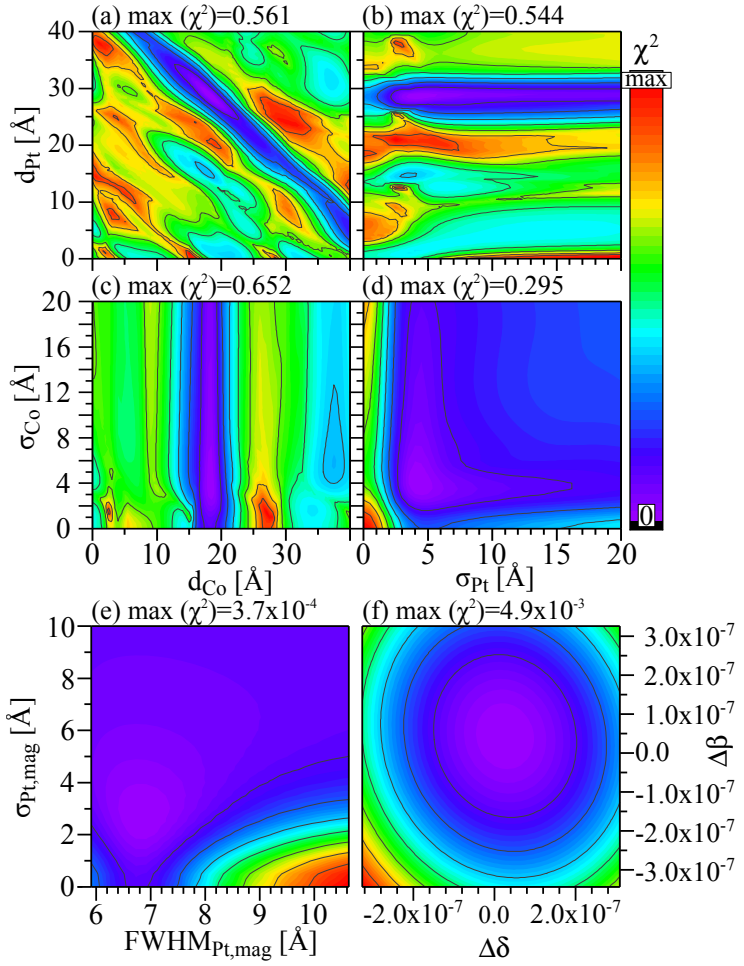

Figure 4.8: Selected 2D landscapes of the χ^2 value for TaO_x/MgO(2.6 nm)/Ta(3.3 nm)/Co(1.8 nm)/Pt(2.9 nm)//SiO_x. (a) χ^2 map plot of the thickness of the Co layer d_{Co} vs. the thickness of the Pt layer d_{Pt}. (b) χ^2 map plot of the roughness of the Pt layer σ_{Pt} vs. the thickness of the Pt layer d_{Pt}. (c) χ^2 map plot of d_{Co} vs. the roughness of the Co layer σ_{Co}. (d) χ^2 map plot of σ_{Pt} vs. σ_{Co}. (e) 2D plot of the magnetooptical simulation. The FWHM of the magnetic depth profile FWHM$_{Pt,mag}$ is plotted vs. the roughness $\sigma_{Pt,mag}$. (f) Corresponding 2D χ^2 plot of the magnetooptical parameters $\Delta\delta$ vs. $\Delta\beta$.

probed and discussed in terms of Fig. 4.6(b). Here, the axes are inverted in order to match the axes of the remaining maps. The plot of Fig. 4.8(b) is has also been discussed with regard to the analysis of the XRR simulations in Fig. 4.7. Figure 4.8(c) shows a highly anisotropic χ^2 map. The thickness d_{Co} is accurately defined by the global minimum. On the contrary, the value of χ^2 is merely increasing when the global minimum is left while probing the parameter σ_{Co}. The χ^2 2D plot shown it Fig. 4.8(d), which is based on both roughness parameters σ_{Co} and σ_{Pt}, exhibits a global minimum steeply sloping in the direction of lower roughness values. In particular, this minimum is broadened towards higher roughness values. Generally speaking, this implies a higher level of uncertainty regarding the structural roughness parameters which broaden the minimum. In this case, additional information on the interfaces is required to determine these structural parameters with an appropriate accuracy. Furthermore, an educated assessment of the real roughness parameter of the Co/Pt interface can be provided by analyzing multiple χ^2 maps, as shown in Fig. 4.8. This is, for instance, crucial for an in-depth investigation of the MPE in a complex multilayer system where the interface roughness is fundamentally affecting the magnetooptical depth profile.

The χ^2 landscape of map Fig. 4.8(e) has been generated based on a variation of the magnetic depth profile roughness $\sigma_{Pt,mag}$ in relation to the FWHM of the magnetic depth profile $FWHM_{Pt,mag}$. This effective thickness of the magnetic Pt depends on the thickness $d_{Pt,mag}$ of the initially utilized magnetic layer that becomes the magnetic depth profile $\Delta\beta$ of Fig. 4.5(e) when the magnetic roughness $\sigma_{Pt,mag}$ is taken into account. In this case, the dependence is $FWHM_{Pt,mag} = 0.0285\,nm^{-1} \cdot d^2_{Pt,mag} + 0.191 \cdot d_{Pt,mag} + 5.87\,nm$ for the TaO_x/MgO(2.6 nm)/Ta(3.3 nm)/Co(1.8 nm)/Pt(2.9 nm)//SiO_x multilayer. This 2D plot contains the global minimum. Here, the chi-squared discrepancy increases marginally in case the global minimum is left along any of the respective parameter axes. The maximum value of χ^2 on this map is 3.7×10^{-4} which is about one order of magnitude lower than the maximum χ^2 value found on the comparable parameter space for the Pt/Fe bilayer presented in Fig. 4.3(c). This plot shows a distinct global minimum and no local minima, simplifying the refinement of the magnetooptical depth profile, independent of the general χ^2 gradient, using a standard downhill fitting algorithm. In the same way, the χ^2 map which is spanned by the magnetooptical parameters $\Delta\delta$ and $\Delta\beta$, illustrated in Fig. 4.8(f), demonstrates a χ^2 well with a clear global minimum at the center. This well characteristic is similar to the χ^2 map spanned by the variation of the same magnetooptical parameters with regard to the asymmetry ratio simulation of the Pt/Fe bilayer.

Half-Heusler compound PtMnSb with and without additional Pt layer

Regarding the PtMnSb bilayer system, the need for a detailed XRR and XRMR analysis becomes obvious, e.g., in the study of the magnetic depth profile of the oxide capped half-Heulser system. Figure 4.9 shows a summary of both the reflectivity and asymmetry ratio fit results as well as the corresponding optical, density and magnetooptical depth profiles. In Fig. 4.9(a), a nearly perfect XRR fit of the experimental reflectivity scan is displayed, exhibiting merely slight deviation for scattering vectors $q > 0.2\,Å^{-1}$. Figure 4.9(b), given alongside, illustrates the corresponding optical depth profile, dominated by the homogeneously grown half-Heusler alloy. On the right flank of the profile, the AlO_x/MgO top layer mainly forms the decline of the optical depth profile at the air interface given that the intermixed light elements exhibit δ and β parameters approximately one order of magnitude below the respective values of PtMnSb at the Pt absorption edge.

Additionally, the asymmetry ratio and best-fit simulation are shown in Fig. 4.9(c). In principle, all main features of this curve are met to a satisfactory level by the best-fit simulation with the exception of one major deviation, which can be observed at the third peak in the asymmetry ratio signal. However, the nature of this deviation is highly important particularly with regard to an

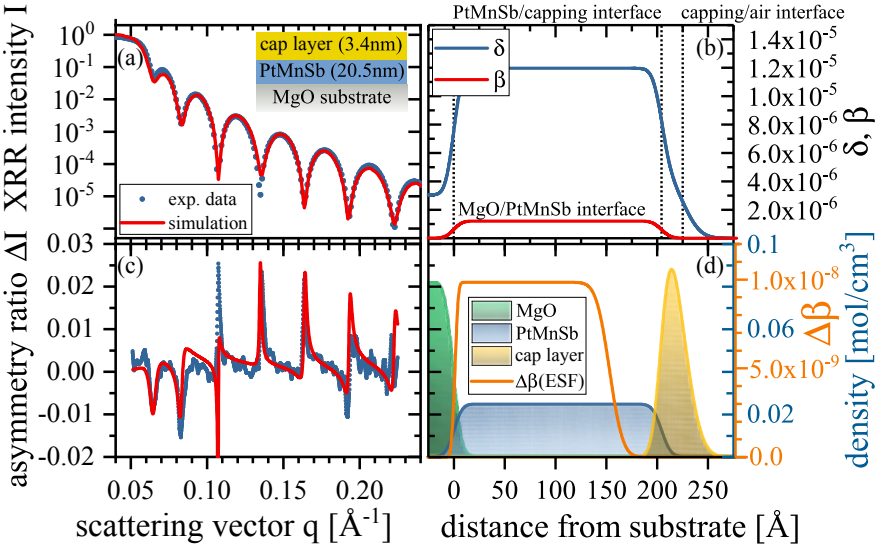

Figure 4.9: (a) XRR measurements of PtMnSb(20.5 nm) with AlO_x/MgO cap layer. (b) Magnetooptical δ and β depth profile used in the simulation. (c) Asymmetry ratio ΔI and the corresponding simulation generated with the ESF mode. (d) XRR density depth profile together with the magnetooptical $\Delta\beta$ depth profile used in the asymmetry ratio simulation in (c).

assessment of the fit quality. This aspect is discussed in detail in section 4.4.5 of this chapter. When this asymmetry ratio feature is examined individually, it becomes evident that the simulated curve peaks at an identical scattering vector but with a reduced amplitude. This effect can be partially attributed to the experimental resolution which is depending on the beamline energy.

Figure 4.9(d) combines the resulting density depth profile determined by the fit of the XRR data and the magnetooptical $\Delta\beta$ depth profile calculated based on the best-fit XRMR simulation. The magnetic depth profile shown in this combined plot is the most convincing best-fit result in consideration of the respective χ^2 maps. It shows a uniformly magnetized PtMnSb layer including an unpolarized layer at the upper interface presumably caused by intermixing and distinct oxidation.

An in-depth analysis of the χ^2 landscape of the parameters defining the magnetooptical depth profile of the lower and upper PtMnSb interface has to be conducted in order to verify a best-fit simulation result. As an exemplification of this process, the plots in the middle row, Figs. 4.10(d), (g) and (j), represent the global minimum of the χ^2 maps shown in Figs. 4.10(a) and (b). The simulation of an identical magnetic depth profile with a modification of the lower boundary, introducing a 20 Å nonmagnetic Pt layer at the interface, is visualized in the top row of Fig. 4.10. As opposed to this modification, the results of an extension of the magnetic depth profile by 40 Å at the upper boundary to match the PtMnSb interface are illustrated in the bottom row of Fig. 4.10.

When the corresponding asymmetry ratio simulations are directly compared in Figs. 4.10(f) - (h), all three form the main peaks of the asymmetry ratio equally well. However, the most striking deviation of the fitted curve from the obtained signal occurs in Fig. 4.10(f) in the intervals between the main asymmetry ratio peaks. In contrast, Figs. 4.10(g) and (h) are highly similar although

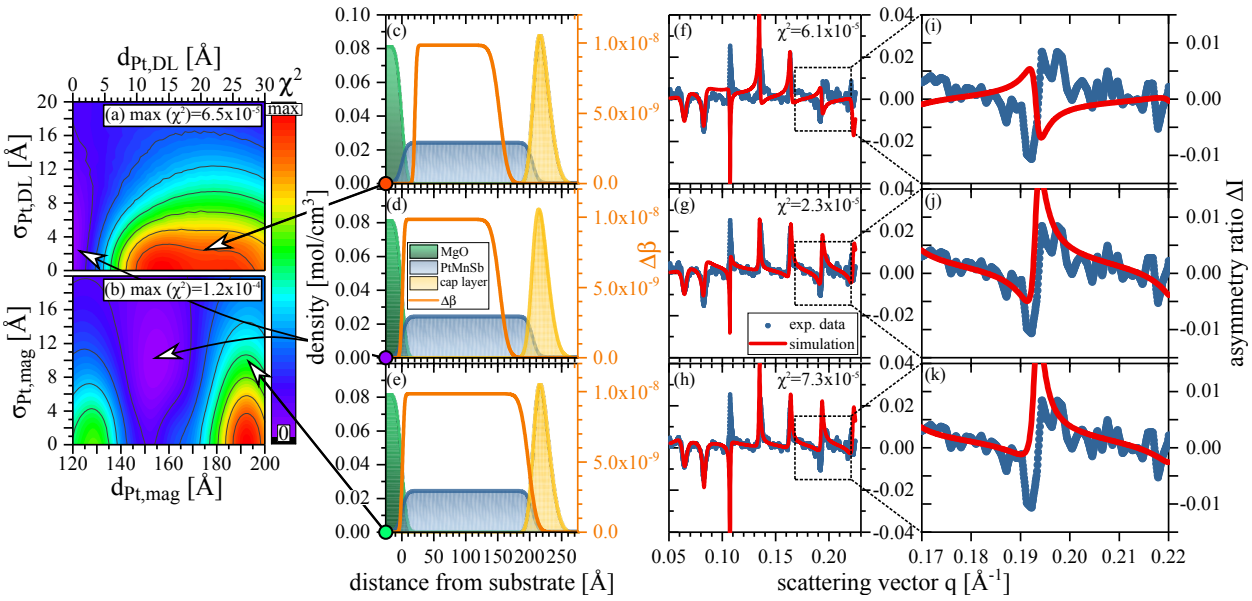

Figure 4.10: (a) and (b) show sections of the general 2D χ^2 landscape of PtMnSb(20.5 nm) with a AlO_x/MgO cap layer. In (a) the thickness of the magnetic dead layer $d_{Pt,DL}$ is plotted against the roughness of the lower magnetic interface $\sigma_{Pt,DL}$, (b) shows the thickness of the magnetic layer $d_{Pt,mag}$ vs. the roughness of the upper magnetic interface $\sigma_{Pt,mag}$. Two distinct spots of the 2D maps are choosen to compare to the corresponding asymmetry ratio simulations of the optimal fit (g). (c) - (e) show the combined density and magnetooptical $\Delta\beta$ depth profiles of (d) the optimal fit, (c) an asymmetry ratio fit with a magnetic dead layer of 20 Å at the substrate interface and (e) an extended magnetooptical depth profile by 40 Å at the upper interface. The asymmetry ratio $\Delta I(q)$ and simulated data (f) - (h) are drawn to a larger scale (i) - (k) to illustrate crucial parts of the asymmetry ratio simulation.

these simulated ratios are based on substantially different upper magnetooptical boundary positions.

In order to draw a coherent conclusion regarding the Pt magnetization depth profile based on differences in fit quality, one has to focus on minor details of the diverse XRMR simulations under consideration. The clear difference at the lower boundary of the Pt specific magnetic depth profile, which is represented in the transition from Figs. 4.10(d) to (c), significantly alters the slope of the asymmetry ratio in proximity of the main features as illustrated in the corresponding Figs. 4.10(j) and (i). An even closer look at the simulated asymmetry ratio is inevitable to determine the position of the upper boundary of the Pt specific magnetic depth profile. The exemplary shifting of this magnetic interface is illustrated in Figs. 4.10(d) and (e). The asymmetry ratio simulation of the best-fit depth profile and the extended magnetic depth profile are shown in Figs. 4.10(g) and (h), respectively. These are difficult to differentiate by eye and closely follow the measured asymmetry curve with only marginal differences which are visible at the third and sixth feature of the scan due to a reduced peak amplitude. However, these are exactly the segments of the asymmetry ratio simulation which have to be carefully taken into consideration since an appropriate fit of these features is critical for the determination of the real magnetic Pt depth profile. When the enlarged graphic parts Figs. 4.10(j) and (k) are compared, it appears that the first dip of the feature is not exactly modeled and the upwards counterpart is exaggerated in the case of the extended magnetooptical depth profile. This small difference, which is commonly but not necessarily accompanied by a reduced χ^2 value, serves to identify the most probable magnetic Pt depth profile which includes an unpolarized Pt layer at the oxide interface.

The detailed XRMR based analysis of the magnetooptical depth profile of an identical layer of 20.5 nm PtMnSb capped with 3.4 nm Pt instead of AlO_x/MgO is presented in Fig. 4.12 and discussed in the following section. In accordance with the results presented here, a potential pronounced magnetic dead layer at the substrate interface of the Pt/PtMnSb bilayer can be ruled out on the basis of an in-depth analysis of the main periodic features of the asymmetry ratio and the associated χ^2 landscape. The potential extension of the magnetic depth profile into the region of the structural Pt layer is considered here as well, although the simulated asymmetry ratio associated with an extended magnetic depth profile contains an inconspicuous however substantial deviation of data and fit. Here, the best-fit solution is associated with a magnetic depth profile closely resembling the structural half-Heusler depth profile obtained by the XRR fit with the exception of a few angstroms of unpolarized Pt at both interfaces of the PtMnSb layer.

Experimental data and simulation analysis of the Pt/PtMnSb bilayer

In order to investigate a possible static MPE in Pt and, in a more general approach, the Pt specific magnetic depth profile via XRMR, twin samples of the PtMnSb thin films have been prepared with Pt as a top layer instead of the AlO_x/MgO oxide capping (compare Fig. 4.9). The structural depth profile of this Pt/PtMnSb sample is illustrated in Fig. 4.11(a). There is an excellent agreement between the simulation produced in the ESF mode and the reflectivity scan of this bilayer. The depth profiles of the magnetooptical δ and β parameter are presented in Fig. 4.11(b). Both optical depth profiles show the interface transitions which can also be unambiguously observed in the density depth profile of this bilayer. Additionally, the best fit simulated in the ESF mode accurately reproduces the main features and the oscillations of the asymmetry ratio ΔI which are illustrated in Fig. 4.11(c). This simulation is based on the density depth profile which is shown in Fig. 4.11(d) as a function of the distance from the substrate. The resulting magnetooptical depth profile is visualized in the same plot, identifying no additional spin polarization at the Pt interface in addition to the spin polarization which is already inherent to the half-Heusler material (cf. chapter 1.7). Here, the appearance of an MPE depends predominantly on the neighboring ferromagnetic material and aside from that the interface quality.[41] The in-depth study of magnetic proximity effects in Pt on PtMnSb and the further investigation of the Pt and Mn specific magnetic depth profile are discussed in the following chapter 5 of this work.

In Fig. 4.12, an in-depth analysis of the asymmetry ratio features for the Pt(3.4 nm)/PtMnSb(20.5 nm)//MgO bilayer is shown. In the middle row of this compilation, the density profile and asymmetry ratio corresponding to the global best fit are illustrated. The global minimum is part of both χ^2 maps, depicted in Figs. 4.12(a)

[41] J. Geissler, E. Goering, F. Weigand, and G. Schütz. Interplay between chemical and magnetic roughness of Pt in a Pt/Co bilayer investigated with X-ray resonant magnetic reflectometry: Dedicated to Professor Dr. Helmut Kronmüller on the occasion of his 70th birthday. *Z. Metallkd.*, **93**(10):946–952 (2002); and T. Kuschel, C. Klewe, J.-M. Schmalhorst, F. Bertram, O. Kuschel, T. Schemme, J. Wollschläger, S. Francoual, J. Strempfer, A. Gupta, M. Meinert, G. Götz, D. Meier, and G. Reiss. Static magnetic proximity effect in Pt/$NiFe_2O_4$ and Pt/Fe bilayers investigated by x-ray resonant magnetic reflectivity. *Phys. Rev. Lett.*, **115**(9): 097401 (2015)

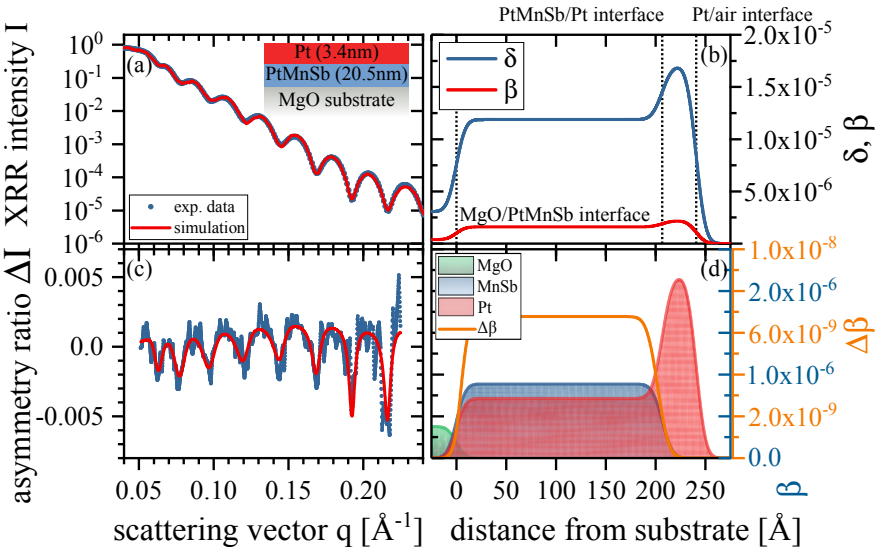

Figure 4.11: (a) XRR measurement of the Pt(3.4 nm)/PtMnSb(20.5 nm)//MgO bilayer and (b) magnetooptical δ and β depth profile used in the simulation. (c) shows the asymmetry ratio ΔI and the corresponding simulation generated in the ESF mode. The XRR density depth profile is visualized in (d) and matched to the magnetooptical $\Delta\beta$ depth profile used in the asymmetry ratio simulation (c).

and (b), which are spanned by the boundary parameters of the Pt specific magnetic depth profile. As pointed out on the map of Fig. 4.12(a), the top row of this compilation presents the simulation of an identical magnetic depth profile with an altered lower magnetic boundary position. More specifically, a magnetic dead layer of 20 Å is integrated, starting at the substrate interface position, which shifts the magnetic boundary into the PtMnSb layer as shown in Fig. 4.12(c). In order to verify the upper magnetic boundary position, the original Pt spin depth profile without this dead layer, shown in Fig. 4.12(d), is extended at the top boundary of the magnetic depth profile by 20 Å reaching into the Pt cover layer which is illustrated in Fig. 4.12(e). This characterizes a wide spin polarization of Pt, indicating a prominent static magnetic proximity effect.

The intrinsic features of the obtained asymmetry ratio have to be closely compared to the corresponding simulation, as illustrated in Figs. 4.12(f) - (h), in order to draw any conclusions regarding depth profile of the Pt specific magnetism. Consequently, a pronounced magnetic dead layer at the substrate interface has to be ruled out based on the obvious misfit of the main periodic features of the asymmetry ratio ΔI, highlighted in the magnified part of the scan shown in Fig. 4.12(i). Despite the high noise level on account of the relatively small asymmetry ratio of below 0.4 %, a realistic magnetooptical depth profile can be defined when the χ^2 landscape is carefully analyzed.

In case of a possible MPE in the Pt cover layer, the extension of the magnetic depth profile into the Pt layer is accompanied by a slight overall increase of the simulated asymmetry ratio, as shown in Figs. 4.12(j) and (k). More importantly, it also leads to an offset between data and fit which is most profound in the center of the asymmetry ratio scan. Thus, a shift in the overall shape of the fit from an upward to a downward directed course of the average

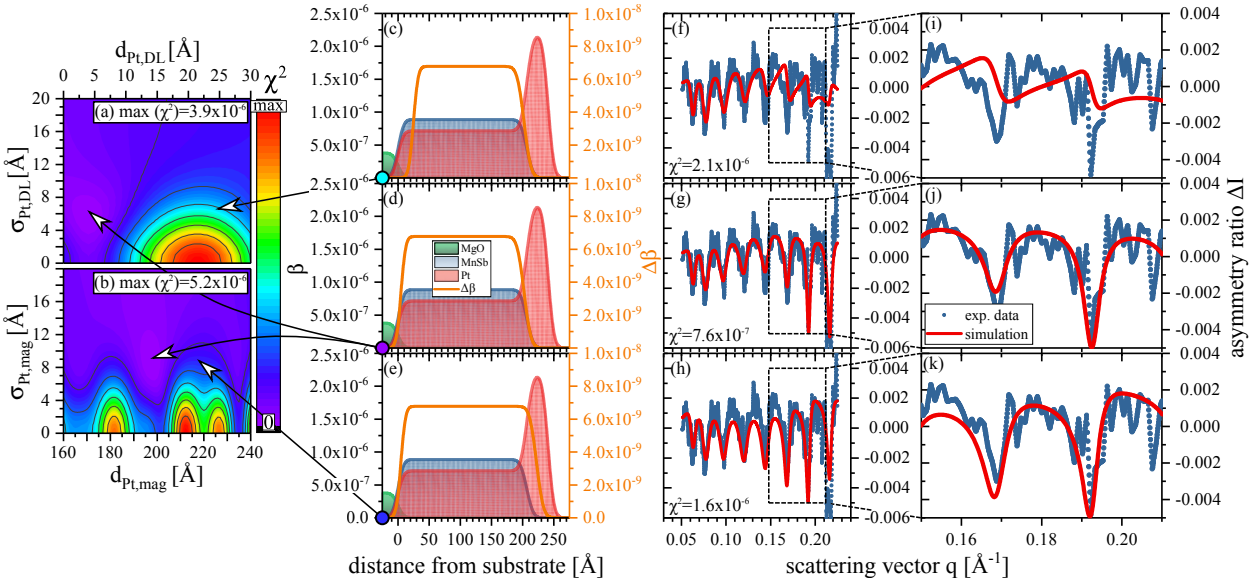

Figure 4.12: Figures (a) and (b) show sections of the general 2D χ^2 landscape of a Pt(3.4 nm)/ PtMnSb(20.5 nm)//MgO bilayer. In (a) the thickness of the magnetic dead layer $d_{Pt,DL}$ is plotted against the roughness of the lower magnetic interface $\sigma_{Pt,DL}$, (b) shows the thickness of the magnetic layer $d_{Pt,mag}$ vs. the roughness of the upper magnetic interface $\sigma_{Pt,mag}$. Two distinct spots of the 2D maps are chosen to compare to the corresponding asymmetry ratio simulations to the optimal fit (g). Figure (d) shows the optic β and magnetooptical $\Delta\beta$ parameter profiles of the optimal simulation of the asymmetry ratio ΔI (g). The profile of a simulation with an additional magnetic dead layer of 20 Å and an extended magnetic depth profile into the Pt layer resembling an MPE is plotted in Figs. (c) and (e), respectively. The asymmetry ratio plots (f) to (h) show the corresponding ratios ΔI and simulations, (i) - (k) are close-ups of crucial parts of the asymmetry ratio simulation.

curve is observable when the simulations in Figs. 4.12(g) and (h) are directly contrasted.

In general, this demonstrates that a close look at the simulated asymmetry ratio and especially the pronounced features is essential in order to study the magnetic depth profile with high accuracy. In the concrete examples discussed in this chapter, the best-fit asymmetry ratio simulation and the one corresponding to the extended magnetic depth profile are highly similar and merely show small but highly significant differences as discussed above and illustrated in Figs. 4.12(g) and (h). In general, these small deviations of the oscillatory behavior should be thoroughly evaluated and tested since an adequate fit of the asymmetry ratio is crucial for the identification of MPEs as well as magnetic death layers. Furthermore, the close analysis of multiple simulations, in order to study minor variations, e.g., of the magnetic boundary positions, provides the most accurate representation and real best fit of a realistic magnetic depth profile.

General XRMR analysis recipe procedure

The analysis of the XRMR experiments at the Pt L_3 edge discussed here has been performed following a specific course of action which can be summarized in form of a process flow diagram. On account of the wide applicability of this procedure for structurally similar thin film systems of various complexity, a general guideline for the XRMR evaluation can be created, including all fundamental options discussed in this work to achieve an improved fit convergence.

This recipe procedure is presented in the detailed flowchart shown in Fig. 4.13, visualizing a clear-cut path to optimize the simulation of the XRMR asymmetry ratio in general and determine realistic and robust magnetooptical depth profiles in complex

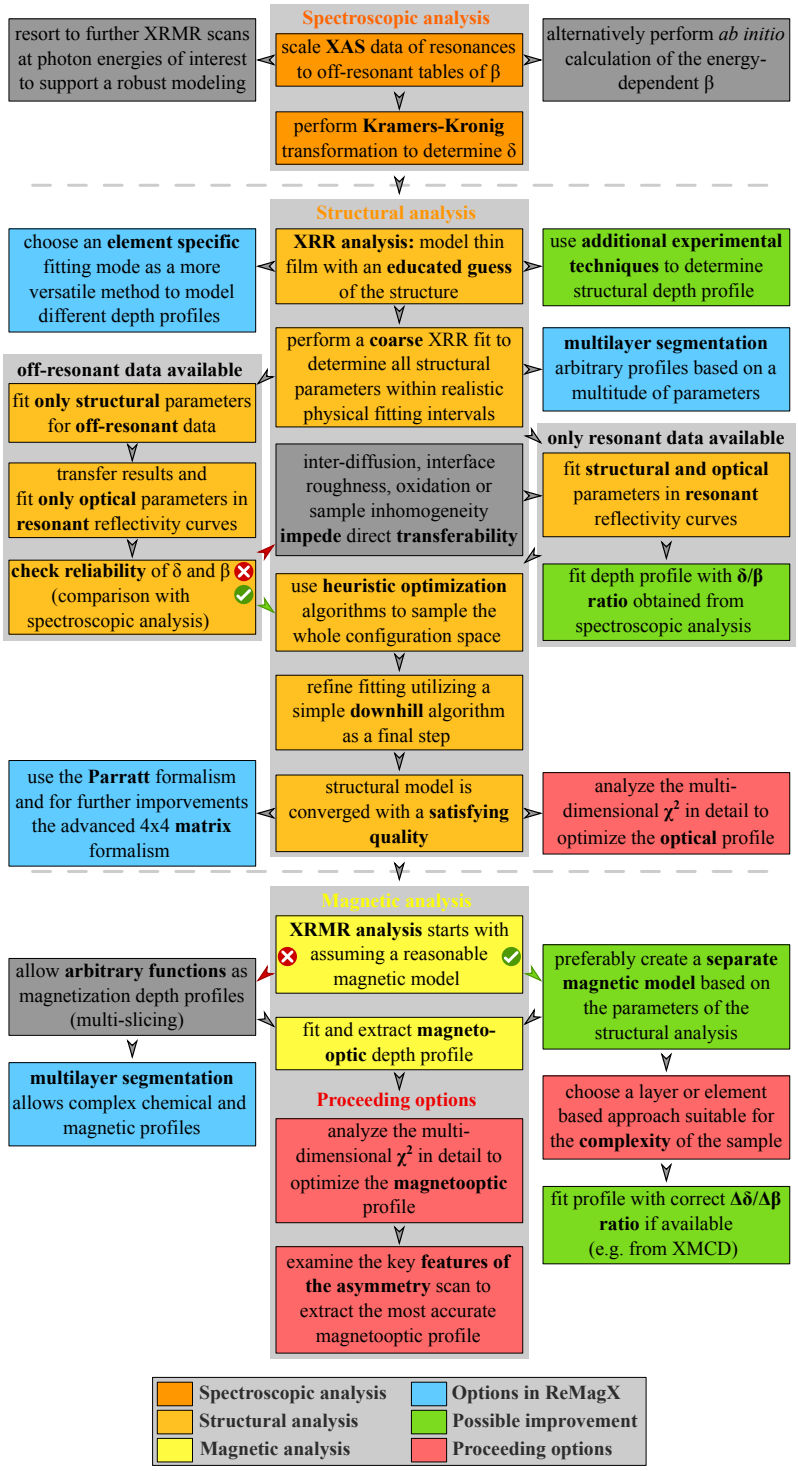

Figure 4.13: Recipe procedure for the determination a robust XRMR asymmetry ratio simulation for the bi- and multilayer systems of this work. The central blocks of the spectroscopic, structural and magnetic analysis correspond to the general steps suggested by Macke and Goering. The structural part includes the more accurate evaluation procedure using off-resonant scattering data presented by Klewe *et al.* and additionally takes into account the possibility of an impeded transferability of the structural parameters. The additional boxes demonstrate the alternative approaches and more complex analysis methods discussed here. Proceeding options regarding χ^2 landscape and asymmetry ratio feature analysis are appended in red while optional methodical alternatives are presented in grey and improvements in green, respectively. Beneficial fitting options implemented in ReMagX are shown in blue.

samples. The core of this chart is predicated on the guide for analyzing XRMR measurements discussed by Macke and Goering[42] which is extended incorporating the conclusions of this chapter with regard to the optimization of the XRMR analysis. The outlined recipe procedure is divided into three main sections, namely the spectroscopic, structural and magnetic analysis.

Starting with the spectroscopic analysis, the first step consists of scaling the resonant x-ray absorption spectrum to the tabulated

[42] S. Macke and E. Goering. Magnetic reflectometry of heterostructures. *J. Phys. Condens. Matter*, **26**(36):363201 (2014)

off-resonant values of the absorptive optical parameter β.[43] This allows to derive the corresponding dispersive part δ of the index of refraction using the Kramers-Kronig transformation. Therefore, this process necessitates a measurement of the absorption spectrum. Here, an alternative step is to make use of material specific *ab initio* calculations of the energy-dependent absorption around the edge under consideration. This is, however, increasingly difficult for complex materials when the Coulomb interaction is not negligible.

The second part of the outlined recipe procedure is the structural XRR analysis to obtain the correct thickness, roughness and optical parameters. In order to optimize this step, off-resonant XRR data is beneficial to eliminate any influence of the absorption edge on the structural model as discussed in chapter 1.1.3 and by Klewe *et al.*[44] However, the reliability of the obtained optical fitting parameters must be checked due to the fact that the direct transferability is only valid within the strict constrains and complexity level of the utilized model. Further information on material growth and composition is advantageous when evaluating the obtained parameters. Notably, the optical constants have to be checked for reliability to assess the applicability of the used model.

After the structural model has been established with a sufficient level of quality, the obtained model serves as a structural basis on which a robustly parameterized magnetic model has to be developed via the XRMR analysis. The magnetooptical depth profiles, which are obtained at this stage, should subsequently be optimized based on the established analysis of the χ^2 maps as well as the asymmetry ratio features until all algorithmic shortcomings are overcome and satisfactory fit results of the main asymmetry features are reached. Measurements at further photon energies of interest specified based on the spectroscopic analysis are helpful to separate out different models under consideration. Here, in particular XRMR scans at the L_2 edge or the inflexion point of the dichroic signal are beneficial in order to find a robust model of the magnetic depth profile.

In the flowchart discussed here, general applicable improvements are labeled in green while the advanced χ^2 map and specific asymmetry feature based proceeding options are shown in red. Additionally, options which are available in the program ReMagX are presented in blue. The basic steps of the conventional approach, specified in the center of the chart, are sufficient for most ordinary systems such as bilayer samples. It is worth noting that the multi-slicing method is usually accompanied by the introduction of a multitude of free parameters which often lead to highly complex depth profiles yet less physically feasible results. Within the scope of a detailed analysis, the extended steps beyond standard procedures are recommended for exceedingly complex multilayer systems and heterostructures.

[43] B. L. Henke, E. M. Gullikson, and J. C. Davis. X-ray interactions: photoabsorption, scattering, transmission, and reflection at $E = 50$ - $30,000$ eV, $Z = 1$ - 92. *Atomic data and nuclear data tables*, **54**(2):181–342 (1993); and C. T. Chantler. Detailed tabulation of atomic form factors, photoelectric absorption and scattering cross section, and mass attenuation coefficients in the vicinity of absorption edges in the soft X-ray ($Z = 30$ - 36, $Z = 60$ - 89, $E = 0.1$ keV - 10 keV), addressing convergence issues of earlier work. *J. Phys. Chem. Ref. Data*, **29**(4):597–1056 (2000)

[44] C. Klewe, T. Kuschel, J.-M. Schmalhorst, F. Bertram, O. Kuschel, J. Wollschläger, J. Strempfer, M. Meinert, and G. Reiss. Static magnetic proximity effect in $Pt/Ni_{1-x}Fe_x$ bilayers investigated by x-ray resonant magnetic reflectivity. *Phys. Rev. B*, **93** (21):214440 (2016)

Conclusion

In conclusion, three sample systems of increasing complexity have been investigated by means of XRMR at the Pt L_3 edge. Using these results, it is shown that various methods based on simple downhill algorithms simulating the XRMR measurements are limited when working with a complex χ^2 landscape. Here, a robust procedure for the analysis of the measured XRR and XRMR curves is determined in order to reliably obtain structural and magnetic depth profiles without exploiting further unrealistic degrees of freedom in the simulation or resorting to supplementary measurements. The software tool ReMagX is a powerful instrument when used to fit the experimental curves and model magnetooptical depth profiles based on different metaheuristic optimization algorithms as well as a detailed analysis of the asymmetry ratio features and χ^2 maps for the purpose of enhancing the agreement between the XRMR experiment and simulation.

The simple Pt/Fe bilayer is analyzed in order to point out the difference between layer and independent element based simulation methods. The ESF mode is shown to be in particular superior to the LSF mode for the independent modeling of nontrivial magnetic depth profiles. In addition, the supporting in-depth analysis of the complex multi-dimensional χ^2 landscape is introduced here as an essential instrument to accurately determine the structural and magnetooptical depth profiles.

Furthermore, the in-depth study of the dominating asymmetry ratio features is established as a powerful method of determining and evaluating supposed best-fit solutions. Both approaches are particularly important to identify physically consistent structural as well as magnetic depth profiles of nontrivial multilayers and heterostructures which has been exemplary demonstrated for a complex thin film stack including a Co/Pt interface.

In order to accurately determine the magnetic depth profiles in bilayer systems based on the half-Heusler compound PtMnSb, crucial parts of the asymmetry ratio signal have been examined and contrasted with various simulations of the asymmetry ratio to highlight the significance of even minimal deviations and underline the importance of a systematic examination of the key features to determine the most probable solution.

In this context, the effects of an oxide capping on the magnetic depth profile have been investigated in relation to the Pt capped twin sample. The effect of the capping layer on the Pt as well as Mn specific magnetic depth profile in the PtMnSb layer is discussed in-depth in the next chapter based on XRMR results analyzed by means of the established principles.

Ultimately, a recipe procedure to identify a robust XRMR asymmetry ratio simulation is presented here, in particular applicable for Pt based thin film samples.[45] However, this process is adaptable for

[45] J. Krieft, D. Graulich, A. Moskaltsova, L. Bouchenoire, S. Francoual, and T. Kuschel. Advanced data analysis procedure for hard x-ray resonant magnetic reflectivity discussed for Pt thin film samples of various complexity. *J. Phys. D: Appl. Phys.*, **53**(37):375004 (2020)

a wide range of similar multilayers and heterostructures and serves to render the excellent magnetic sensitivity and depth resolution of the XRMR technique as useful as possible.

5
Investigation of the structural and magnetic depth profiles of PtMnSb thin films

This chapter discusses the results of the structural and magnetic depth profile investigation of the various PtMnSb bilayers. These PtMnSb half-Heusler films studied in this work are either covered with the heavy metal Pt or capped with AlO_x/MgO. The bilayer systems have been studied by means of XRR, XRMR and XMCD at multiple beamlines and therefore Pt and Mn specific photon energies to create the most accurate simulation of the structural and magnetic spatial distribution and gather additional spectroscopic data to allow for a precise evaluation of magnetic characteristics. In the following paragraphs, the Mn and Pt specific structural and magnetooptical depth profiles are discussed depending on the capping material and bilayer deposition process.

Experimental and theoretical details

Four specific bilayer systems are analyzed to explore growth-dependent ways to manipulate the magnetic characteristic of the half-Heusler system, especially at the Pt, or more generally at the capping interface. All PtMnSb layers presented here have a nominal thickness of 20 nm. However, the actual layer extent obtained from the reflectivity fits slightly varies around this value due to the different capping materials and deposition processes. The structural quality of these sample systems and the relation to the stack dimensions as well as the growth process are discussed in chapter 2.

The Mn specific XRMR experiments were performed at the resonant x-ray scattering beamline 4.0.2 at the ALS (Berkeley, USA) using a 0.1 T in-plane magnetic field. Here, the XRR intensity is detected switching between left and right circularly polarized light with a DCP of (90 ± 2) %, generated by the elliptically polarizing undulator, for each step of the increasing scattering vector. The XRR and XRMR experiments in the soft x-ray regime were carried out using the resonant x-ray scattering endstation of the beamline in the

standard $\theta - 2\theta$ scattering geometry. The experimental details of the XRR and XRMR experiment in the hard x-ray regime performed at P09 beamline at PETRA III (Hamburg, Germany) can be found in section 4.3 while the theoretical details of the XRMR measurements are summarized in section 1.2. The XRMR analysis procedure is based on the established guidelines outlined in the previous section 4.4.5 of this work.

In this chapter, the structural and magnetic depth profiles of two distinct twin PtMnSb//MgO sample series with different top layers as well as one thickness series capped with Pt deposited at room temperature are comparatively analyzed. Here, the first system under investigation is the Pt/PtMnSb bilayer system with Pt deposited at room temperature (Pt_{RT}/PtMnSb). This sample is contrasted with its twin sample, for which the PtMnSb layer is grown simultaneously to the first one. The significant distinction here is the Pt growth on top of the half-Heusler structure. In this Pt/PtMnSb bilayer, the Pt is deposited at 400 °C immediately after the PtMnSb layer has been grown ($Pt_{400\,°C}$/PtMnSb). Both PtMnSb films of these samples are sputter deposited at the same time to achieve direct comparability of the half-Heusler and are hereafter referred to as series I. Moreover, the XRMR results of this twin sample series are presented here in order to directly compare the Pt and Mn specific magnetic depth profiles obtained in the soft as well as the hard x-ray regime at two different beamlines.

The first sample system of series II is the PtMnSb layer covered with the AlO_x/MgO capping (AlO_x/MgO/PtMnSb). The second system of this series is capped with Pt and, is thus, nominally identical to the first samples of series I in which the Pt capping is grown at room temperature. The Pt/PtMnSb bilayer of series II has been produced utilizing a twin sample deposition sequence with the Pt cover layer grown at room temperature subsequently to the cooling process of the half-Heusler structure and the deposition of the AlO_x/MgO capping for the twin sample. This growth of the MgO capping is usually accompanied by a minimal oxygen contamination of the sputtering chamber. The surface of the uncovered twin PtMnSb layer can therefore be exposed to a minimal oxygen partial pressure before the Pt layer is deposited after the cool-down process, which has the potential to significantly influence the immediate surface purity of the half-Heusler structure of this sample (Pt_{O_x}/PtMnSb).

The samples of the thickness series III, with nominal half-Heusler thin films of 10 nm, 15 nm and 20 nm, have been prepared following the sputter deposition procedure outlined in chapter 2 similar to the first sample of series I. All samples of this series are capped with 3 nm Pt deposited at room temperature.

The Mn near-edge XAS and XMCD spectra, evaluated in the second part of this chapter, have been measured at the ALS beamline 4.0.2 capturing absorption via the TEY and LY modes. These modes are discussed in detail in chapter 1.1.1. At this beamline, the XAS is

measured by directly detecting the sample current and the current generated by the luminescence detecting diode mounted below the sample while the x-ray photon energy is changed. The XMCD spectra have been obtained with a constant applied in-plane magnetic field of 0.1 T while the sample surface has been inclined by an angle of 30° with respect to the incoming beam and the light helicity has been switched at each specific photon energy to obtain the dichroic signal. As for the XRMR experiment, circularly polarized light has been supplied from the undulator with a DCP of (90 ± 2) %.

Results and discussion

The first sample discussed in the following is the Pt_{RT}/PtMnSb bilayer of series I. Figure 5.1(a) exemplarily illustrates the resonant XRR measurement of this Pt_{RT}(3.2 nm)/PtMnSb(19.0 nm) bilayer for a positive applied magnetic field taken with left (blue) and right (red) photon helicity and plotted against the scattering vector q. The photon energy was fixed to 649.9 eV which is directly below the Mn L_2 absorption edge. Here, the prominent Kiessig oscillations are mainly attributed to the thicker PtMnSb layer while the larger periodicity caused by the thinner Pt film on top is hard to identify by eye superposing these fringes. However, by fitting the nonmagnetic XRR curve (average of the XRR curves with opposite photon helicities) one can determine the thickness of both layers as well as the roughness values of all interfaces and the depth profile of the optical constants δ and β. The probed thin film system is schematically illustrated in the inset of Fig. 5.1(a). This idealized bilayer system is modeled in the element specific mode of ReMagX. The fit of the XRR scans determines the PtMnSb thickness to be (19.0 ± 0.2) nm with a roughness of (0.2 ± 0.1) nm on the substrate side and (0.6 ± 0.1) nm on the Pt side. The Pt layer has a thickness of (3.2 ± 0.2) nm with a surface roughness of about (0.5 ± 0.1) nm.

The XRMR asymmetry ratio ΔI in Fig. 5.1(b) is calculated according to Eq. (1.68). The close-up on the second minimum of the reflectivity curves shows a visible deviation between both curves which translates into the pronounced minimum of the asymmetry ratio shown in the enlarged region of the obtained XRMR asymmetry curve in Fig. 5.1(c). This pronounced asymmetry feature with an amplitude of about 9 % is mainly generated by the distinctive Mn spin moment of PtMnSb with a ferri- or ferromagnetic character. When the direction of the applied magnetic field is inverted, the sign of the asymmetry ratio is changed accordingly confirming the magnetic origin of the observed effect.

Figure 5.2(a) presents resonant XRR curves of the Pt_{RT}/PtMnSb bilayer taken with a positive and negative magnetic field at a photon energy of 11 567 eV, at the maximum of the Pt L_3 absorption peak. As stated for the close examination of the XRR curves at the Mn edge, the XRMR asymmetry ratio identifies even minimal devia-

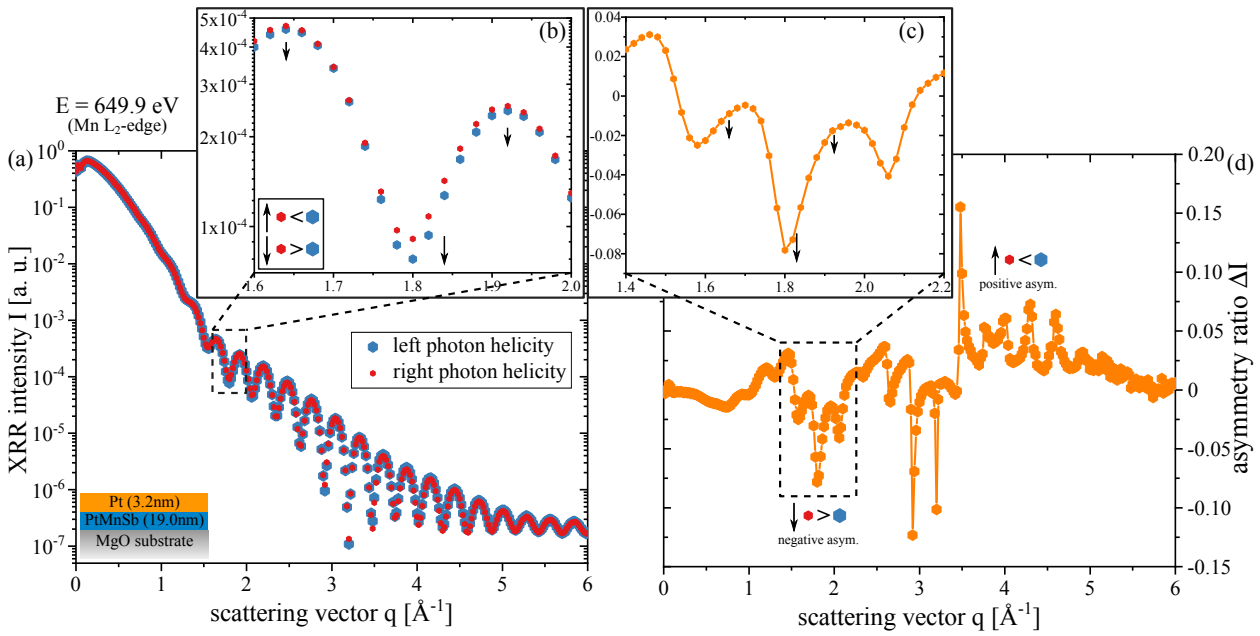

Figure 5.1: (a) XRR intensity I for the Pt_{RT}/PtMnSb bilayer for a positive applied magnetic field taken with left and right photon helicity with an energy of 649.9 eV. (b) Close-up focusing on the second minimum of the XRR oscillations. (d) XRMR asymmetry ratio ΔI derived from both XRR scans. (c) Close-up of the first major asymmetry feature centered around the q value of the minimum presented in (b).

tions of both XRR scans. This is highlighted in Fig. 5.2(b), zooming in on a minimum of the Kiessig oscillation. As illustrated by the corresponding asymmetry ratio shown in Fig. 5.2(c), the difference in both curves is most pronounced at the center of the minimum, at which the displayed asymmetry feature shows a sign change and a maximum of about 0.7 % which is almost two orders of magnitude lower than the maximum asymmetry ratios detected at Mn specific photon energies.

In an effort to confirm the magnetic origin of the Pt specific asymmetry ratio, the external magnetic field is applied perpendicular to the beam direction leading to a vanishing asymmetry ratio. In addition, a switch of the photon helicity from left to right circularly polarized changes the sign of the asymmetry ratio in accordance with Eq. (1.68).

In order to visualize the results of a combined XRR and XRMR analysis and determine the structural and magnetooptical depth profiles of all PtMnSb bilayer systems, the best-fit simulations are plotted together with the corresponding structural and magnetic depth profiles. This graphical summary of the experimental data, corresponding best-fit simulations as well as underling structural, optical and magnetooptical depth profiles as exemplarily shown in Fig. 5.3 is the basis for any further analysis of the XRMR results and has therefore been created for every sample discussed in this work.

The impact of different capping layers on the magnetic interface properties of the PtMnSb half-Heusler system will be addressed hereafter. First, the magnetic depth profile of the standard Pt_{RT}/PtMnSb bilayer is discussed in relation to the series I twin sample $Pt_{400\,°C}$/PtMnSb with a Pt capping immediately grown after the PtMnSb deposition. Additionally, the change from a heavy

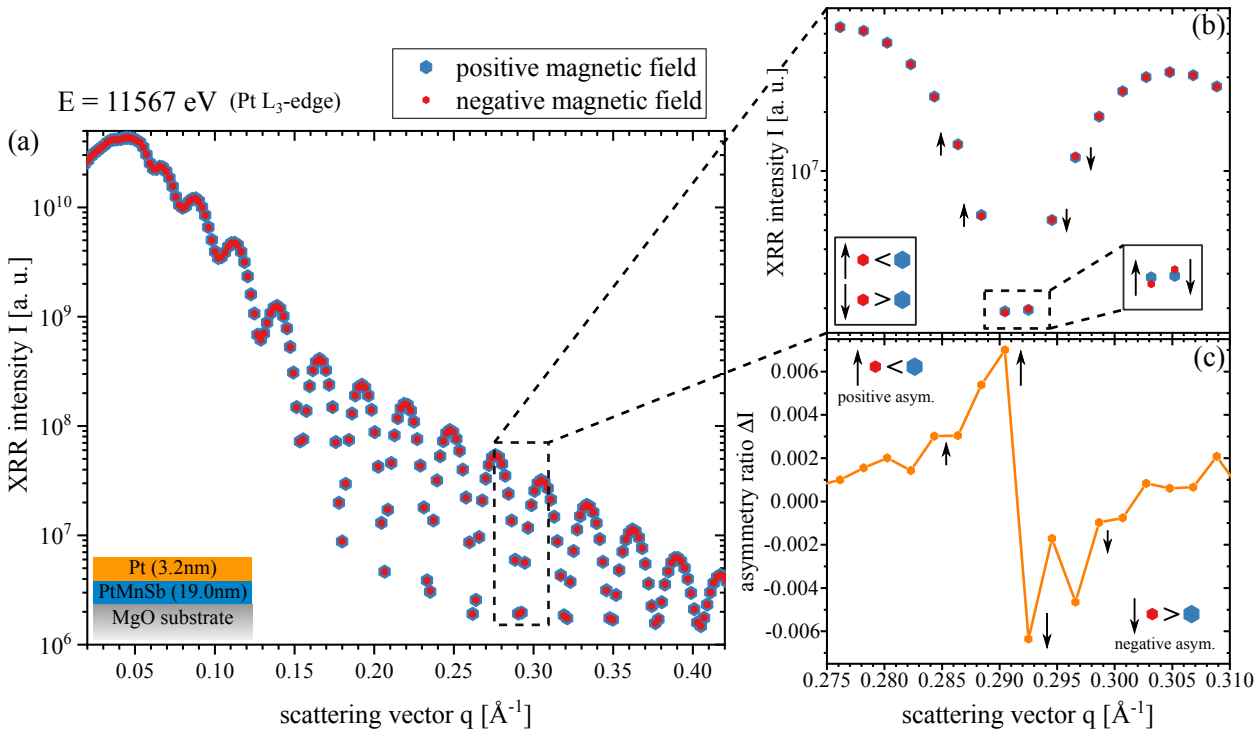

Figure 5.2: (a) XRR intensity I for the Pt_{RT}/PtMnSb bilayer taken with left circularly polarized light at a photon energy of 11 567 eV for a magnetic field applied with a positive and negative polarity. (b) Close-up focusing on a distinctive minimum of the XRR oscillations indicating (c) the XRMR asymmetry ratio ΔI derived from both XRR scans.

metal to an insulating oxide significantly alters the interface quality and its magnetic properties. Therefore, the samples of series II, discussed in chapter 4.4.3 with regard to the optimization of the XRMR analysis procedure, are included in this comparison amended by the soft x-ray Mn specific XRMR results in order to study the influence of the capping material and deposition sequence of nominally identical bilayers on the Mn and Pt specific magnetic characteristics of the half-Heuser system.

Magnetic depth profiles of the Pt_{RT}/PtMnSb bilayer

The soft and hard x-ray magnetic reflectometry results of the Pt_{RT}/PtMnSb bilayer are discussed in the following. Figure 5.3 serves as a paradigm for the graphical summary of the XRMR results, where the hard x-ray scan of the XRR intensity I is presented with the corresponding best-fit simulation in Fig. 5.3(a). Here, the best fit almost perfectly matches the obtained XRR data with only marginal deviations as far as the end of the fitting window at a scattering vector of $q = 0.5\,\text{Å}^{-1}$.

The optical depth profile presented in Fig. 5.3(b) is based on constant δ and β values in the homogeneously grown half-Heusler alloy, dropping down sharply towards the MgO interface matching the determined interface roughness. At the Pt/PtMnSb interface the dispersion δ increases while the absorption β decreases equally according to the interface roughness forming a small plateau in both cases before dropping off to zero at the top Pt surface.

In Fig. 5.3(c), the asymmetry ratio ΔI is plotted, for which the

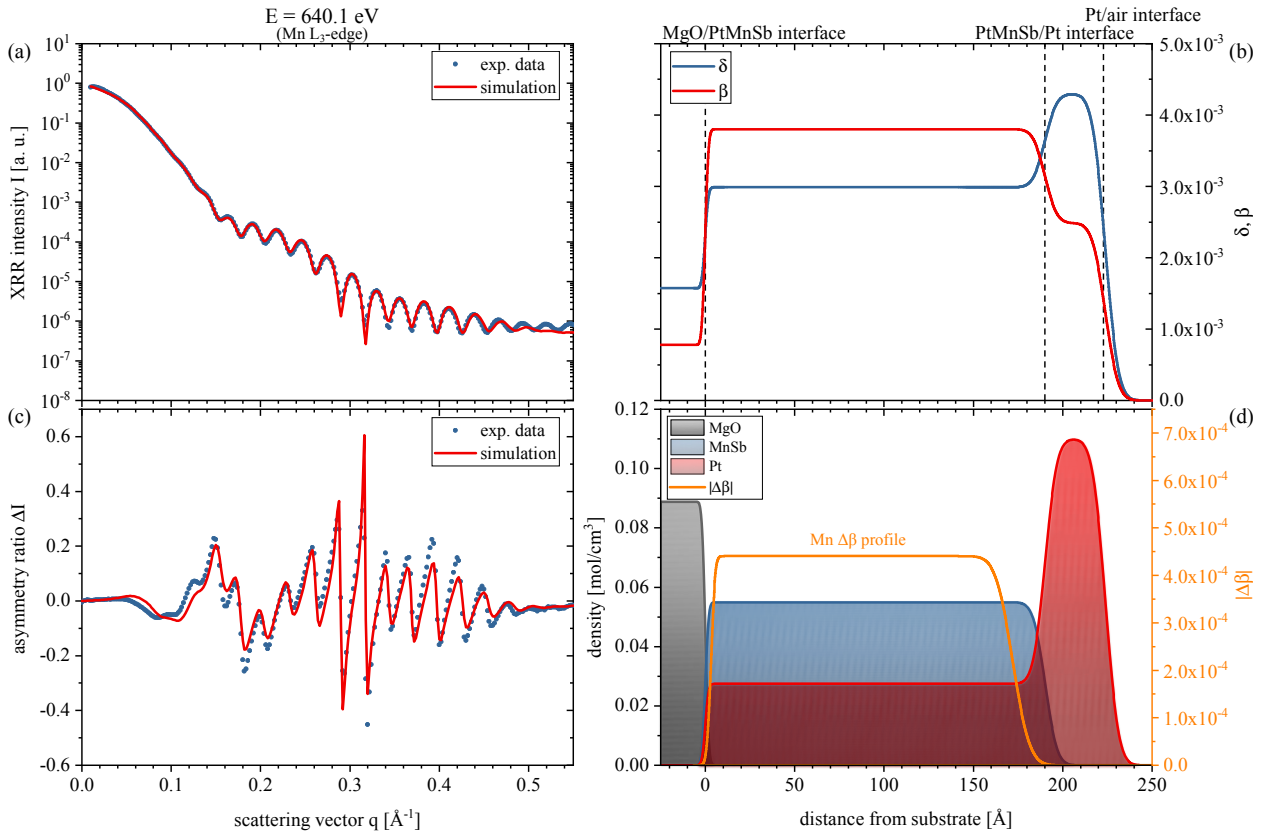

Figure 5.3: XRR and XRMR measurement and simulation result at a photon energy of 640.1 eV for the Pt_{RT}(3.2 nm)/PtMnSb(19.0 nm) bilayer. (a) XRR intensity I and corresponding simulation resulting in (b) the optical δ and β depth profiles. (c) XRMR asymmetry data and fit resulting in the $\Delta\beta$ depth profile shown in (d) in relation to the structural density depth profile.

best-fit simulation accurately reproduces every feature of this pronounced asymmetry ratio of up to 50 % with almost no deviations. The results of the reflectivity and asymmetry ratio simulation are combined to create Fig. 5.3(d) which presents the determined structural density depth profile in addition to the magnetooptical $\Delta\beta$ depth profile. The value and shape of this depth profile define the magnetic absorption which is the dominating characteristic in the process of simulating the XRMR asymmetry ratio in close energetic vicinity of an absorption edge. The determined $\Delta\beta$ distribution directly visualizes the thickness of the spin-polarized, in this case Mn specific, region of the thin PtMnSb film.

The structural density depth profile shown in Fig. 5.3(d) is the foundation of the XRR simulation. Here, the density values of the layer plateaus are fixed to literature values using the ESF mode of ReMagX. For instance, the top Pt layer has been shown to crystallize quasi-epitaxially on the ordered PtMnSb in a (001) oriented fcc structure.[1] This cubic structure has a density of 21.45 g/cm^3, determined for bulk material,[2] which can be converted to 0.11 mol/cm^3. This value is set as density of the top layer in the simulation which is modulated at the interfaces according to the roughness. The elements constituting the PtMnSb half-Heusler are considered separately within this mode of analysis. The density of each element is set to the theoretical value determined by the *ab initio* structure calculations presented in chapter 1.7 which is confirmed by the

[1] J. Krieft, J. Mendil, M. H. Aguirre, C. O. Avci, C. Klewe, K. Rott, J.-M. Schmalhorst, G. Reiss, P. Gambardella, and T. Kuschel. Co-sputtered PtMnSb thin films and PtMnSb/Pt bilayers for spin-orbit torque investigations. *Phys. Status Solidi Rapid Res. Lett.*, **11**(4): 1600439 (2017)

[2] W. M. Haynes. *CRC handbook of chemistry and physics*. CRC press (2014)

structural analysis discussed in section 2.4. The density of each half-Heulser element is set to $0.0275\,\mathrm{mol/cm^3}$ following this calculation based on an ideal stoichiometric composition. The density depth profile of each element is then coupled to the other two during the XRMR simulation sharing both interface roughness values.

Since the individual elements are displayed on top of each other in a molar density depth profile, the different depth profiles for Pt on the one hand as well as Mn and Sb on the other hand must be separated to allow for a clear display. Thus, the latter elements are combined into a MnSb depth profile through a simple addition which still displays the correct density when MnSb is interpreted as a two atomic composite. The density of the MgO substrate is equally fixed to a literature value of $0.0888\,\mathrm{mol/cm^3}$ based on a density of $3.58\,\mathrm{g/cm^3}$.[3]

[3] Manufactory Data-Sheet, *MgO substrate*, CrysTec GmbH Kristalltechnologie

The main fitting parameters in the evaluation of the XRR data are therefore the thickness and roughness values of each modeled layer and interface, respectively, as well as the optical constants δ and β of the Mn specific layer profile. Since the photon energy is at or close to the absorption edge the literature values do not apply. However, the parameters resulting from the simulation are checked for consistency with the XAS, respectively Kramers-Kronig based calculations. This process is discussed in detail in section 5.7 of this work. The optical parameters of all other elements are set to the values given by the Chantler tables[4] for the f' and f'' components as starting parameters of the fit. In the second step, the optical parameters of these remaining elements are allowed to slightly deviate from the literature values to achieve a satisfying fit quality.

[4] C. T. Chantler. Theoretical form factor, attenuation, and scattering tabulation for $Z = 1$ - 92 from $E = 1$ - 10 eV to $E = 0.4$ - 1.0 MeV. *J. Phys. Chem. Ref. Data*, **24**(1):71–643 (1995)

Based on the obtained structural model, the independent magnetic model is introduced by assuming a homogeneous magnetization of the ferromagnetically ordered Mn moments in the PtMnSb layer. The magnetic asymmetry ratio is then fitted by varying the magnetooptical parameters $\Delta\beta$ and $\Delta\delta$. Since the magnetic depth profile of the sample can differ from the chemical depth profile, a potential magnetic dead layer is modeled by introducing a layer of zero magnetic density at the substrate interface. The extent of this dead layer as well as the magnetic depth profile including its thickness and both magnetic interface roughness values are subsequently fitted in combination with a refinement of the magnetooptical parameters.

The XRMR asymmetry ratios ΔI of this $\mathrm{Pt_{RT}}(3.2\,\mathrm{nm})/\mathrm{PtMnSb}(19.0\,\mathrm{nm})$ bilayer measured in the soft x-ray regime at the Mn L_2 and L_3 absorption edges with specific photon energies of 639.3 eV, 640.1 eV and 651.2 eV are shown in Fig. 5.4. In addition, the fixed-q_z scan as well as the XMCD signal in comparison to the plateau values of the magnetooptical $\Delta\beta$ depth profiles are illustrated. In order to determine a pronounced magnetooptical contrast and thus a high asymmetry ratio which is readily identifiable, the optimal photon energies for the XRMR experiment have been determined beforehand based on this scan. Here, certain photon energies at

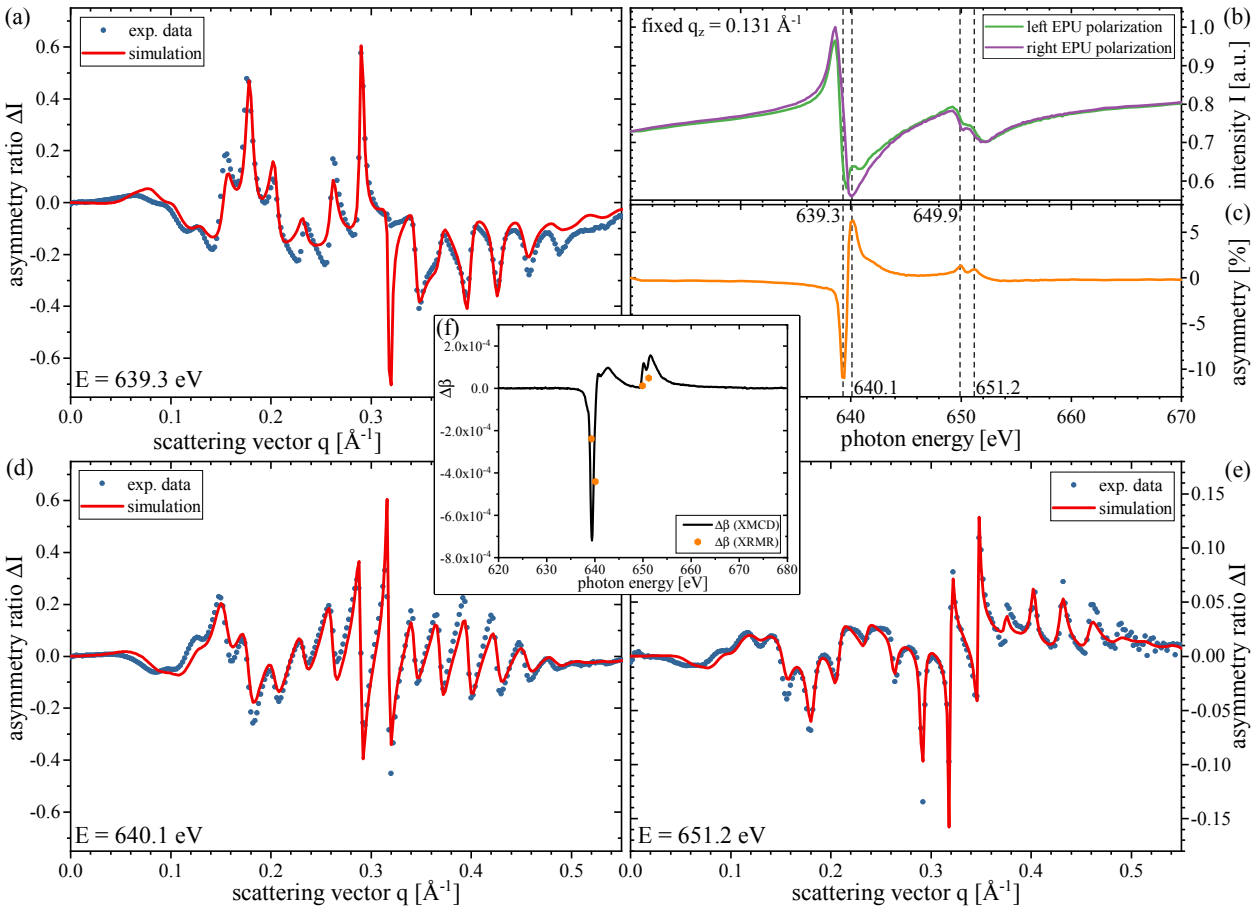

Figure 5.4: XRMR asymmetry ratios ΔI of the Pt_{RT}(3.2 nm)/PtMnSb(19.0 nm) bilayer taken close to the Mn L_2 and L_3 absorption edges with specific photon energies of (a) 639.3 eV, (d) 640.1 eV and (e) 651.2 eV. (b) XRR intensity I measured for varying photon energy at a fixed scattering vector $q_z = 0.131\,\text{Å}^{-1}$ with left and right circular polarization providing (c) the asymmetry ratio as a function of energy at fixed q_z. (f) Magnetooptical parameter $\Delta\beta$ derived from the XMCD signal compared to the plateau values of the $\Delta\beta$ depth profiles determined by the XRMR simulations of the asymmetry ratios.

specific points of interest, such as the relevant absorption edges, the inflexion point of the spectroscopy signal or points of strong dichroic response in general are chosen as outlined in the recipe procedure 4.13 to separate out different models and thus improve the robustness of the simulated magnetic depth profiles.

An energy-dependent measurement of the magnetic response at a fixed scattering vector q_z is presented in Fig. 5.4(b). The resulting asymmetry ratio of this data taken with left and right circularly polarized light is shown in Fig. 5.4(c). The experiment was performed at a fixed scattering vector $q_z = 0.131\,\text{Å}^{-1}$ which is close to the first pronounced minimum of the XRR Kiessig fringes. The dashed lines mark the photon energies at which the XRMR measurements were performed. The experimental XRMR data, along with the respective simulations, are presented in Fig. 5.4(a), (d) and (e) while the remaining scan at a photon energy of 649.9 eV is shown in the close-up XRMR analysis featured in Fig. 5.1. The central graphic Fig. 5.4(f) illustrates the magnetooptical parameter $\Delta\beta$ derived from the XMCD signal in relation to the plateau values of the $\Delta\beta$ depth profiles determined by the fitting process of the XRMR asymmetry ratios. This plot confirms that the magnetooptical absorptive correction $\Delta\beta$ used in the simulations is in close agreement to the obtained magnetic circular dichroism spectra of this sample. The

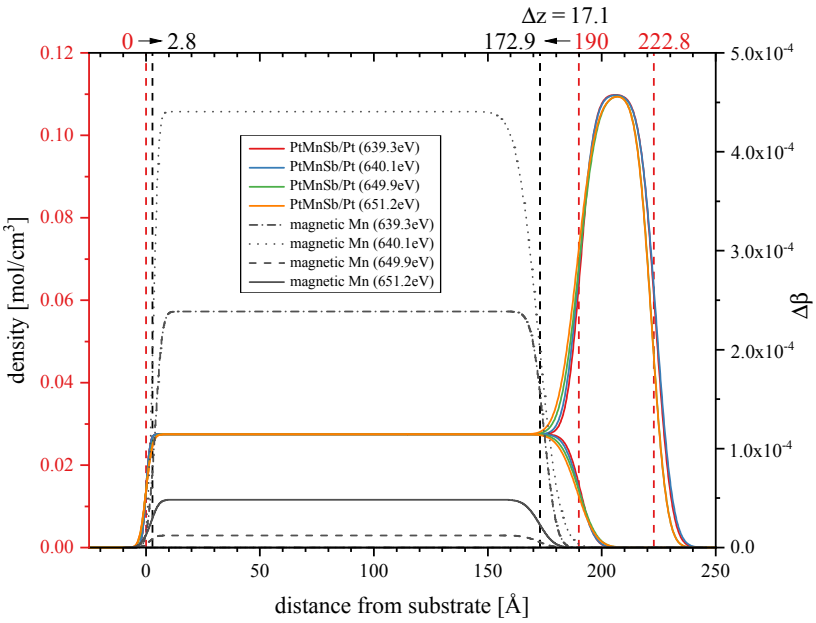

Figure 5.5: Comparison of simulated Pt_{RT}/PtMnSb structural density and magnetooptical depth profiles obtained from the XRR and subsequent XRMR analysis of the Pt_{RT}(3.2 nm)/PtMnSb(19.0 nm) bilayer for varying photon energies around the Mn $L_{2,3}$ absorption edge. The black lines illustrate the depth profile of the magnetic Mn as a result of the scan at the specified photon energy. The dashed vertical lines mark the averaged position of the individual depth profile boundary.

spectra of the dispersive correction $\Delta\delta$ can be calculated via the Kramers-Kronig integral relations. The results are also in excellent agreement with the magnetooptical constants determined by these simulations as discussed in detail in section 5.8 of this chapter.

Figure 5.5 shows the results of the XRMR analysis at the specified photon energies in the soft x-ray regime for the Pt_{RT}/PtMnSb bilayer. Here, the independently obtained structural and magnetic depth profiles corresponding to the fits shown in Fig. 5.4 are combined to illustrate the Mn specific spin polarization and to discuss the magnetic dead layers of this bilayer system.

Here, the thickness of the PtMnSb layer is determined to be 190.0 Å within a standard deviation or average deviation from the mean of 0.6 Å. The PtMnSb//MgO interface has an rms roughness value of 1.8 Å with a standard deviation of 0.4 Å while the top Pt/PtMnSb interface is significantly rougher with a value of 5.8 Å and a standard deviation of 0.8 Å. The Pt capping layer has an average lateral extent of 32.8 Å with a standard deviation of 1.5 Å while the top interface shows a roughness of 5.5 Å with a standard deviation of 0.6 Å. All four magnetic depth profiles show the characteristic top and bottom magnetic dead layers. The position of the magnetic boundary is found at an average distance to the substrate interface of 2.8 Å with a parameter specific standard deviation of 1.3 Å. The depth profile's drop towards this dead layer is as abrupt as for the related bilayer system with a boundary roughness of 2.3 Å obtained constantly over all simulations with a standard deviation of 0.5 Å. The top boundary of the magnetooptical depth profile is positioned at an average distance of 172.9 Å from the substrate. This value found to be equally uniform over all XRMR scans represented by a standard deviation of 1.0 Å. The top interface of the magnetic depth profile has a rms roughness of about $2-3$ times

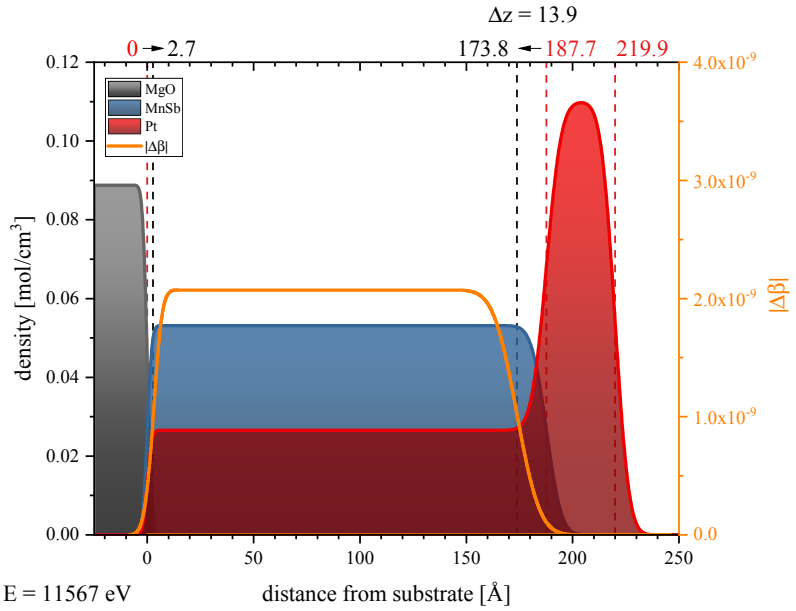

Figure 5.6: Structural density and Pt specific magnetooptical $\Delta\beta$ depth profile obtained for Pt_{RT}/PtMnSb from the XRMR scan with a photon energy at the Pt L_3 absorption edge.

higher than the bottom interface with a value of 7.1 Å and a standard deviation of 1.3 Å. The upper Mn specific magnetic dead layer has therefore a lateral extend of 17.1 Å with a standard deviation of 1.3 Å.

In a second step, the Pt specific magnetic depth profile has been investigated utilizing a specialized hard x-ray beamline as discussed in section 4.3. The results shown here have been obtained from the XRR and XRMR scans with a photon energy at the Pt L_3 absorption edge. This experiment has been conducted at the hard x-ray PETRA III beamline P09 at DESY. As illustrated in Fig. 5.6, this Pt_{RT}(3.2 nm)/PtMnSb(18.8 nm) bilayer system shows the expected magnetic dead layers at both PtMnSb interfaces. The minimal structural differences, in comparison to the results of the soft x-ray experiment, are mainly attributed to the inevitable variation of the probed sample section placed in the x-ray focus for the Mn and Pt specific XRMR scans. The consequence of this comparative XRMR study at multiple beamlines on the results is discussed at length in the next section of this chapter.

The lower magnetic dead layer at the high quality PtMnSb//MgO interface has a minimal lateral extent of 2.7 Å which is about the same value as for the Mn specific dead layer of this bilayer. The top magnetic dead layer at the Pt interface is determined to have a lateral extent of 13.9 Å. The magnetic boundary is positioned at a distance of 173.8 Å from the substrate interface and shows a rms roughness of 8.6 Å. In combination both Pt specific magnetic dead layers reduce the share of spin polarized Pt within the PtMnSb to 91.2 % of the layer.

Moreover, the Pt specific magnetooptical $\Delta\beta$ depth profiles presented in Fig. 5.6 are directly compared to the Mn specific

magnetic results in the next section. This is especially important in order to highlight the characteristic systematic differences in the observed atom specific magnetic depth profiles and develop a quantitative profile correlation which is directly influenced by the structural bilayer properties.

Mn and Pt specific magnetic depth profiles in comparison for the Pt_{RT}/ PtMnSb bilayer

Figure 5.7 directly contrasts the results of the XRMR investigation of the Pt_{RT}/PtMnSb bilayer obtained in the soft x-ray regime at the Mn L_3 absorption edge with the results of the hard x-ray Pt specific asymmetry analysis based on the XRMR measurement at the Pt L_3 absorption edge. A discussed in chapter 1.2, those measurements had to be performed at different synchrotrons due to the specific photon energy requirements.

The XRR results shown in Figs. 5.7(a) and (c) obtained at both characteristic absorption edges could be fitted almost perfectly and thus provided the structural density depth profiles shown in this illustration which are the basis of the subsequent simulation of the corresponding asymmetry ratios. Here, the XRR and XRMR simulation has been performed as discussed in section 1.2 within the framework of the results presented in Fig. 5.3. The individual layers are defined and coupled in the same way while the fitting algorithms determine the same free structural and optical parameters. Based on this structural model which is converged with a satisfying quality, the magnetic model assumes a homogeneous magnetization of the PtMnSb layer with optional magnetic dead layers at both interfaces. As discussed in chapter 1.2, the anomalous scattering factors as well as the structural characteristic of the magnetic depth profile are free parameters during the fitting procedure.

The magnetic XRMR curve measured in the soft x-ray regime at a photon energy of 640.1 eV, close to the Mn L_3 absorption edge, is presented in Fig. 5.7(c). Again, a nearly perfect fit is obtained based on this well defined magnetic depth profile. The $\Delta\beta$ depth profile is shown in relation to the structural density depth profile in Fig. 5.7(d).

A minimal shift of the lower boundary of the magnetic depth profile with respect to the chemical interface is observed. This indicates a small Mn specific magnetic dead layer close to the substrate interface. Theoretically, the same result could be obtained in case of a thin layer of an antiferromagnetic phase forming at the interface since the circularly dichroic XRMR response is equivalent to a nonmagnetic dead layer. The experiment performed at 640.1 eV provides an optical PtMnSb depth profile with a thickness of 19.2 nm and an interface rms roughness of 1.4 Å on the side of the substrate and an expectable higher value of 5.2 Å at the Pt interface.

When this chemical density depth profile measured at the ALS beamline 4.0.2 is compared to the one obtained by investigating the

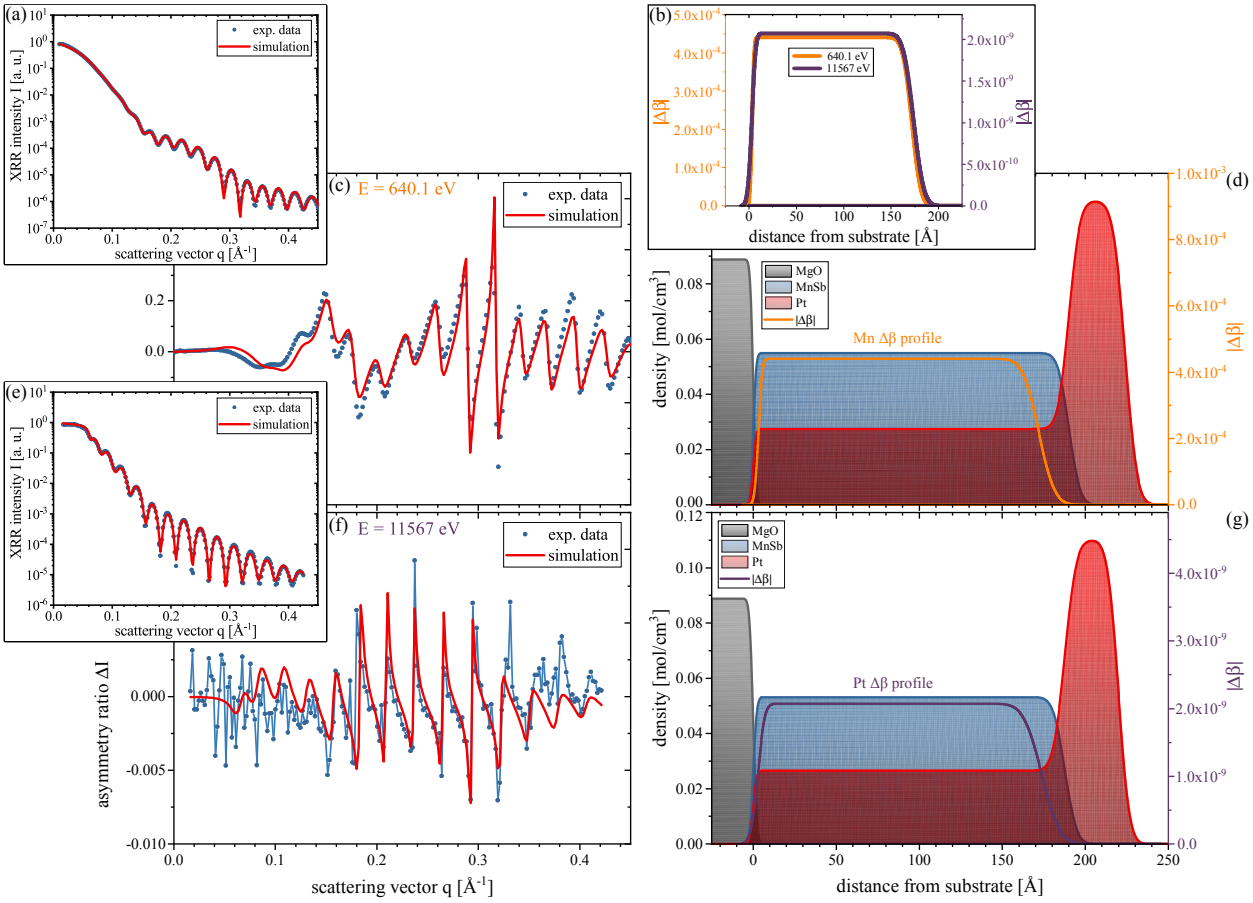

Figure 5.7: Direct comparison of the XRR intensity I and asymmetry ratio ΔI for the Pt_{RT}/PtMnSb bilayer. (a) XRR scan and simulation at the Mn specific photon energy of 640.1 eV and (c) the associated asymmetry ratio ΔI and simulation. (e) XRR scan and simulation at the Pt specific photon energy of 11 567 eV and (f) the associated asymmetry ratio ΔI and simulation. (d) and (g) show the structural density and $\Delta\beta$ depth profiles determined by the simulation. The resulting magnetooptical $\Delta\beta$ depth profiles are directly compared in (b).

same sample three month later at the hard x-ray P09 beamline at PETRA III, the results are nicely reproduced. This substantiates the excellent chemical as well as sub-monolayer structural sensitivity of this non-destructive reflectivity technique. The analysis of the DESY measurement performed at 11 567 eV close to the Pt L_3 absorption edge provides a PtMnSb density depth profile with a thickness of 18.8 nm and an interface roughness of 1.7 Å on the side of the substrate and 5.4 Å at the Pt interface, respectively. The small difference regarding the observed half-Heusler thickness could be attributed to the fact that a different spot of the thin film sample is probed during each experiment. Although the sample was centered in the experiment the exact focus position does vary due to the beamline characteristics. Additionally, the XRR experiment at high photon energies is predominately performed at grazing incidence to work with the required scattering vectors while the soft x-ray experiments utilizes a large fraction of the available scattering angle θ. This directly determines the focus size of the x-ray beam as discussed in chapter 1.1.3.

As shown by the AFM analysis presented in Fig. 2.6, the FWHM of the height distribution of a 10 nm PtMnSb in the relatively small scanning area of 1 µm^2 is 1.9 nm. Based on a minimal focus spot size of 100 µm × 100 µm the XRR measurement probes a much

larger area and thus the corresponding simulation yields an average value over the illuminated thin film surface area. Since the beam footprint at low θ angles used within the hard x-ray regime exceeds the sample size for a significant part of the reflectivity curve, the measurement is less localized and includes the border areas of the thin-film system. Although the deposition process is optimized to prevent structural sample inhomogeneities, shadowing effects do occur at the outermost regions of the substrate surface due to the sample fixture. Overall, this edge thinning effect and the general inhomogeneity due to the underlining grain structure observed during sample growth account for the thickness variation of the PtMnSb layer. However, these effects do not influence the roughness values and de facto the fit evaluation of both reflectivity experiments reveals identical values as outlined above.

The quantitative determination of the magnetooptical depth profiles is highly element specific based on the energy of selected electronic transitions. The asymmetry ratios taken at the Mn and Pt specific photon energies shown in Figs. 5.7(c) and (f) provide the optical depth profiles shown in relation to the chemical depth profiles based on the XRR results in 5.7(d) and (g). With the exception of the $\Delta\beta$ depth profile plateau value, which depends on the magnetooptical characteristics of the respective absorption edge, the general form is nearly identical. Both $\Delta\beta$ depth profiles are brought into direct contrast with each other in Fig. 5.7(b) to highlight the minor depth profile variations. When the depth profiles are quantified, the Pt specific depth profile is marginally wider with a lateral extent of 171 Å in comparison to the 169 Å of the Mn specific magnetic depth profile. The boundary of the Pt specific magnetic depth profile on the side of the substrate is positioned at 2.7 Å with a rms roughness of 3.4 Å which is marginally closer to the substrate than the lower boundary of the Mn specific depth profile. Here, the magnetic interface is positioned at a distance of 3.1 Å from the substrate interface with a roughness value of 1.8 Å. Hence, the magnetic dead layer in terms of the Mn magnetic moments is 0.4 Å wider and significantly less rough than the magnetic dead layer obtained for the Pt magnetic moments. The same effect can be observed at the upper interface of the magnetic depth profile. Here, the Mn specific boundary is positioned at a distance of 172 Å from the substrate with a roughness of 7.5 Å while the Pt specific boundary is found at 173.8 Å with a roughness of 8.6 Å. Again, the magnetic dead layer of the Mn moments is formed about 2 Å before the one regarding the Pt magnetic moments in relation to the substrate interface position and forms a slightly rougher magnetic interface.

These minimal discrepancies of the Mn and Pt specific layers are certainly close to the actual experimental accuracy, in particular due to the relatively low observable asymmetry ratio in the hard x-ray regime. However, the relation of the structural parameters for the Mn and Pt specific magnetic depth profiles is striking in its simi-

larities at both magnetic interfaces. One reason for this extended Pt specific magnetic depth profile by a few angstrom in relation to the magnetic Mn moments could be a marginal MPE. The immediate proximity to the outermost magnetic Mn atoms induces a Pt spin polarization extending the magnetic depth profile of the half-Heusler structure into a region, in which the Mn magnetic moments are arranged into a compensated state. These magnetic dead or reduced-magnetization phases usually form at an interface due to intermixing, structural disorder or a chemical alteration of the interfacial surface layer. Additionally, the magnetic coupling in the surface region can become highly frustrated which results in a depletion of the ferromagnetic properties. Due to a proximity induced spin polarization, the Pt might stay polarized in the first few monolayers of the Mn specific magnetic dead layer regions while the Mn loses its polarization due to the discussed mechanisms.

The Pt_{RT}/PtMnSb bilayer discussed here has been produced utilizing the standard procedure, for which the Pt cover layer is grown subsequently to the cooling process of the deposited half-Heusler structure at room temperature. However, the Pt deposition temperature has a substantial influence of the Pt/PtMnSb interface quality predominantly due to interdiffusion processes. Thus, the soft and hard x-ray based results for the $Pt_{400\,°C}$/PtMnSb sample are presented in the following section of this work to demonstrate basic ways of manipulating the magnetic Mn and Pt specific depth profiles based on growth induced structural changes.

Magnetic depth profiles of the $Pt_{400\,°C}$/PtMnSb bilayer

The second PtMnSb bilayer system discussed in this chapter is a twin sample of the previously presented one with the exception of the Pt deposition temperature which significantly influences the capping layer and top interface of the half-Heusler structure. Figure 5.8 summarizes the soft x-ray results of the XRMR analysis for this $Pt_{400\,°C}$(2.8 nm)/PtMnSb(19.2 nm) bilayer. The Pt layer of this thin film system has been grown at the half-Heusler sputtering temperature after the PtMnSb had been deposited on the MgO substrate with a few seconds delay due to the sputter source and plasma processing. The photon energies for the XRMR analysis were determined based on the energy-dependent measurements of the magnetic response. The fixed-q_z scan is shown in Fig. 5.8(b) performed at a scattering vector of $q_z = 0.131\,\text{Å}^{-1}$, obtaining the corresponding asymmetry for both circular beam polarizations presented in Fig. 5.8(c). For each edge of the Mn $L_{2,3}$ absorption spectrum, one characteristic feature of the asymmetry curve was chosen to provide a photon energy with a high asymmetry response and thus optimize the signal-to-noise ratio as well as the simulation accuracy.

The XRMR data obtained at a photon energy of 639.7 eV and the best-fit simulation are displayed in Fig. 5.8(e). Here, the agree-

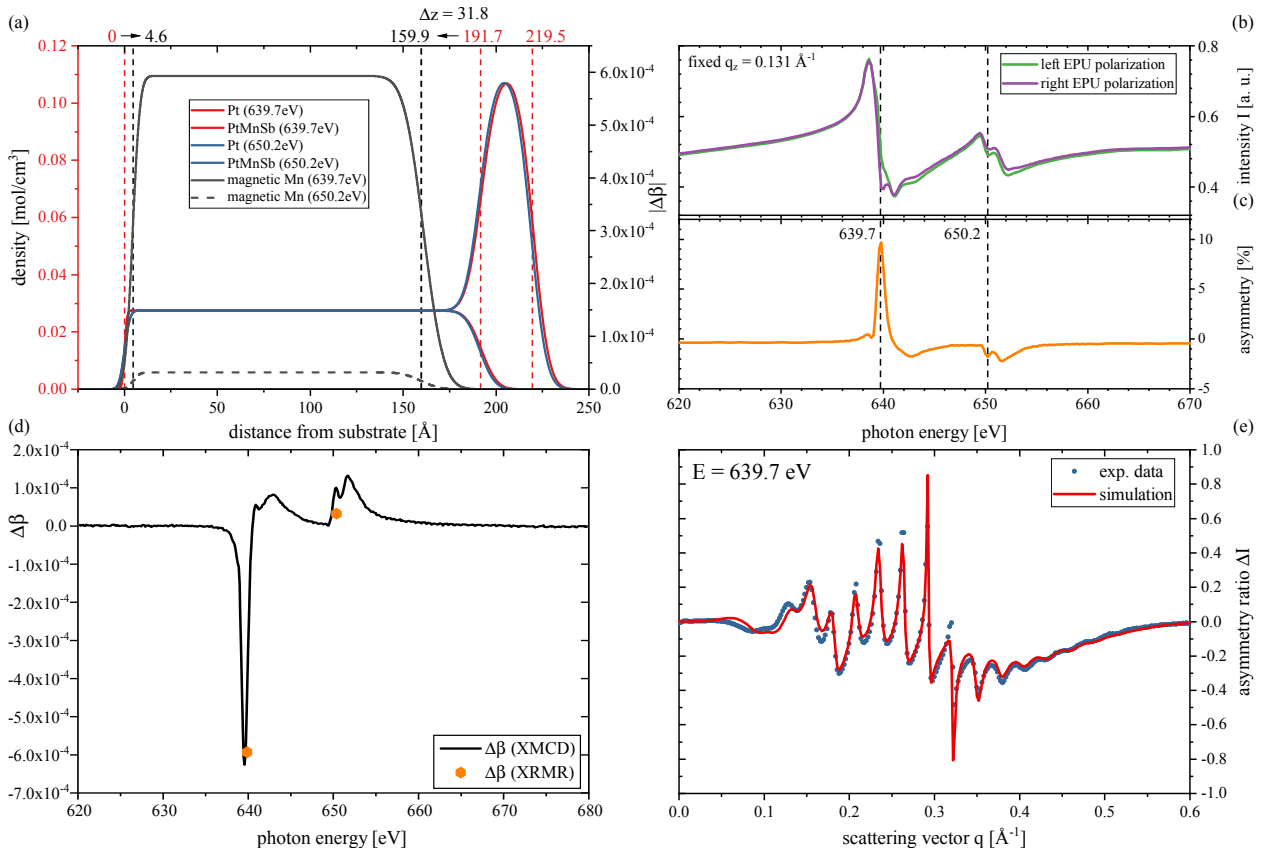

Figure 5.8: (a) Structural density depth profile of the $Pt_{400\,°C}$/PtMnSb bilayer determined by the XRMR analysis and the magnetooptical depth profile $\Delta\beta$ used in the simulation of the asymmetry ratio (e). (b) Photon energy-dependent XRR intensity measurement for left and right circularly polarized light and corresponding asymmetry (c) at a fixed scattering vector $q_z = 0.131\,\text{Å}^{-1}$. (d) Magnetooptical parameter $\Delta\beta$ derived from the XMCD signal in relation to the simulated PtMnSb $\Delta\beta$ plateau value shown in (a).

ment between the experimental and simulated asymmetry ratio at the Mn L_3 absorption edge is almost perfect. Although the x-ray wavelength at this energy is 19.38 Å, the accuracy which is usually achievable, e.g., within the thickness determination of a quasi-perfect crystalline layer, is below 0.5 Å. This excellent depth resolution is a major asset of XRR and XRMR technique since it enables the user to obtain details of the structural and magnetic depth profiles far beyond the Abbe diffraction limit. This principle is commonly known from ellipsometry methods, for which the resolution lies effectively within the sub-nanometer regime although visible light, with a wavelength of up to four orders of magnitude above the detection limit, is utilized.[5]

The resulting structural density depth profile, determined by the XRMR analysis and the magnetooptical depth profile $\Delta\beta$ used in the simulation of the asymmetry ratio, are shown in Fig. 5.8(a). This graphic combines the structural and magnetic information obtained from the XRR and XRMR measurements at 639.7 eV as well as 650.2 eV. The density depth profiles which are independently simulated based on both scans are nearly indistinguishable confirming the sub-angstrom accuracy of the employed reflectivity technique. For instance, the thickness of the covering Pt layer is determined to be 28.0 Å based on the Mn L_3 XRR curve, while the fit of the Mn L_2 data results in a value of 27.7 Å. The lower Pt interface

[5] M. Losurdo and K. Hingerl. *Ellipsometry at the Nanoscale*. Springer (2013)

has a rms roughness of 3.2 Å in the density depth profile obtained at the Mn L_3 edge and a similar value of 2.9 Å at the Mn L_2 edge. The variation of the top Pt interface is found to be below the experimental accuracy as well. While the interface position varies by 1.2 Å, the interface roughness is identical in both simulations with a rms value of 6.4 Å. Although the beamline optics are generally optimized to produce high beam stability, beam drifts and to some extent vibrations can cause a minimal focus displacement. Since the undulator, optics and in particular the beamline monochromator are actively driven to change the photon energy, a small beam drift is more likely to occur between measurement at different absorption edges. Therefore, a small change of the illuminated sample area can lead to measurement averaging over a marginally different layer texture and composition. This shift of the probed sample area corresponds to the obtained structural parameters, of which the average rms roughness is unchanged yet the PtMnSb thickness is slightly altered due to a minimal thickness gradient towards the sample edges.

Besides the structural density depth profile, Fig. 5.8(a) shows the magnetooptical depth profiles obtained from the simulation of the asymmetry ratio simulations at 639.7 eV as well as 650.2 eV. Both depth profiles are highly similar in form and differ only in their plateau value by about an order of magnitude due to the edge specific absorption characteristics illustrated by the XMCD signal shown in Fig. 5.8(d). This graphic shows the $\Delta\beta$ values derived from the magnetic circular dichroism spectra in comparison to the XRMR based simulated plateau values which nicely fit the expected $\Delta\beta$ relation.

The magnetooptical depth profiles obtained at both photon energies reveal a small Mn specific magnetic dead layer at the substrate interface. The boundary of the magnetic depth profile is positioned at a distance of 4.6 Å. The standard deviation of this dead layer thickness between both independent measurements is merely 0.3 Å. This lower interface has an rms roughness value of 3.0 Å with a standard deviation of 0.2 Å. The magnetic dead layer at the side of the Pt cover layer is determined with slightly less accuracy due to the relation to the structurally minimally less well defined Pt interface. Here, the upper magnetic interface is positioned at a distance of 159.9 Å from the substrate with a standard deviation of 1.1 Å, while the averaged magnetic depth profile obtained from both scans drops off 31.8 Å below the Pt/PtMnSb interface. The thickness of this upper magnetic dead layer has a standard deviation in both measurements of 0.5 Å. Therefore, the $Pt_{400\,°C}$/PtMnSb bilayer forms a significant Mn specific magnetic dead layer at the top side of the PtMnSb layer. Consequently, the extent of this magnetic dead layer is increased by a factor of two in comparison to the Pt_{RT}/PtMnSb twin bilayer discussed previously.

The formation of this nonmagnetic region with an extent of 32 Å is likely facilitated by the high Pt deposition temperature.

The growth process at elevated temperatures promotes significant interdiffusion at the interface and alters the chemical composition and structural order. Additionally, interfacial lattice-strain can lead to magnetic frustration or local antiferromagnetic ordering, all inducing a loss of the ferromagnetic properties. In general, the origin of a magnetic dead layer can in many cases be attributed to a combination of different contributing effects. The most common factors are interface mixing effects with a progressive stoichiometry loss of the magnetic material towards the interface, structural coupling as well as lattice strain, phase separation and intrinsic electronic changes at the interface.[6]

The magnetic dead layer on the substrate side is significantly smaller with an extent of only about 5 Å. This abrupt drop of the observable Mn magnetic moment represented by the $\Delta\beta$ depth profile is supposedly caused by lattice strain induced by the minimal lattice mismatch between the MgO substrate and the half-Heusler structure as well as interdiffusion processes due to the high deposition temperature in combination with a marginal oxidation of the PtMnSb interface layer. Although the surface roughness is usually an important factor for the dead layer formation,[7] the small rms roughness value (1.7 Å) of the substrate interface suggests that oxygen contamination at the PtMnSb//MgO interface is the main source for the reduction of the spin polarization. This chemical deterioration results in a hybridization of Mn and O in the outermost atomic layers at the PtMnSb//MgO interface reducing the net magnetic moment.[8]

Due to the extended scale of the experiment, probing the asymmetry ratio at multiple distinct photon energies per Mn absorption edge, the overall measurement time is significantly higher compared to a single reflectivity experiment. The elongated measurement time and in particular the numerous changes of the photon energy increases the probability of a beam drift. This slightly increases the overall variance of the structural and magnetooptical parameters in comparison to the twin sample results presented in the next section since it has been analyzed at only one photon energy per Mn specific absorption edge.

In accordance to the previously obtained results regarding localization of Mn magnetic moments, the magnetic depth profiles obtained at the Pt L_3 absorption edge show an increased magnetic dead layer at the Pt/PtMnSb interface when the Pt is grown at elevated temperatures. The structural density and Pt specific magnetooptical $\Delta\beta$ depth profile of this system are shown in Fig. 5.9. The reflectivity scans which serve as a basis for the XRR and XRMR simulation have also been performed at the Pt L_3 specific photon energy.

The thickness of the PtMnSb layer is determined to be 18.8 nm based on the XRR scan at this absorption edge which is identical to the value for the bilayer system shown in Fig. 5.6. This confirms the identical sputtering parameters and growth conditions em-

[6] L. F. Kourkoutis, J. Song, H. Hwang, and D. Muller. Microscopic origins for stabilizing room-temperature ferromagnetism in ultrathin manganite layers. *Proceedings of the National Academy of Sciences*, **107**(26):11682–11685 (2010); E. Moon, P. Balachandran, B. J. Kirby, D. Keavney, R. Sichel-Tissot, C. Schleputz, E. Karapetrova, X. Cheng, J. M. Rondinelli, and S. May. Effect of interfacial octahedral behavior in ultrathin manganite films. *Nano Lett.*, **14**(5):2509–2514 (2014); J. A. Mundy, Y. Hikita, T. Hidaka, T. Yajima, T. Higuchi, H. Y. Hwang, D. A. Muller, and L. F. Kourkoutis. Visualizing the interfacial evolution from charge compensation to metallic screening across the manganite metal–insulator transition. *Nat. Commun.*, **5**(1):1–6 (2014); and F. Song, Å. Monsen, Z. Li, J. Wells, and E. Wahlström. The layer-by-layer stoichiometry of $La_{0.7}Sr_{0.3}MnO_3/SrTiO_3$ thin films and interfaces. *Surface and Interface Analysis*, **45**(7):1144–1147 (2013)

[7] S. Cardoso, P. Freitas, Z. Zhang, P. Wei, N. Barradas, and J. Soares. Electrode roughness and interfacial mixing effects on the tunnel junction thermal stability. *J. Appl. Phys.*, **89**(11):6650–6652 (2001)

[8] S.-H. Shen, D.-S. Lee, C.-W. Cheng, W.-J. Chan, and G. Chern. The correlation between magnetic dead layer and perpendicular magnetic anisotropy in MgO/CoFeB/Ta top structure. *IEEE Transactions on Magnetics*, **55**(2):1–5 (2018); and H. K. Gweon, S. J. Yun, and S. H. Lim. A very large perpendicular magnetic anisotropy in Pt/Co/MgO trilayers fabricated by controlling the MgO sputtering power and its thickness. *Scientific reports*, **8**(1):1266 (2018)

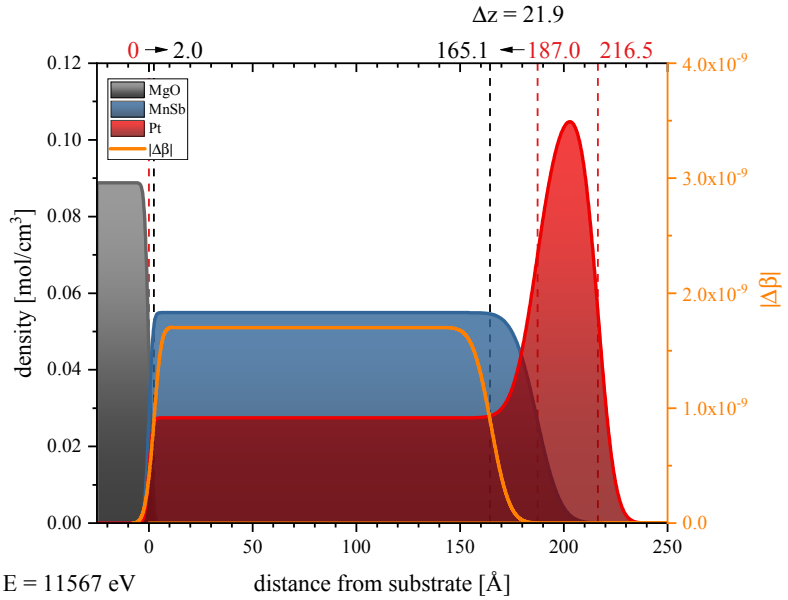

Figure 5.9: Structural density and Pt specific magnetooptical $\Delta\beta$ depth profile obtained for $Pt_{400\,°C}$/PtMnSb from the XRMR scan with a photon energy at the Pt L_3 absorption edge.

ployed within the thin film deposition of both half-Heusler layers. However, due to the different applied temperatures during the Pt deposition process, one can observe an increased roughness of the Pt/PtMnSb interface for the hot deposited bilayer. The rms roughness of this boundary in the Pt specific simulation is 8.1 Å. Similarly, the total lateral extent of the covering Pt is effectively reduced by a few tenth of a nanometer while the roughness to the top Pt interface significantly increases due to the higher deposition temperature. The most interesting aspect of this direct comparison between both bilayer systems is the transformation of the magnetooptical depth profile due to these structural changes mainly related to the interface quality.

Here, the Pt specific magnetooptical depth profile shows the characteristic magnetic dead layers. The lower one at the substrate sets the magnetic boundary at a distance of 2.0 Å in relation to the structural interface which is merely 0.7 Å smaller than in the standard Pt_{RT}/PtMnSb bilayer. The small difference can be attributed to the measurement and simulation accuracy of the XRMR data in the hard x-ray regime. Here, minimal asymmetry ratios on the order of 0.01 and below have to be taken into consideration for a precise XRMR evaluation. The step-by-step procedure to analyze these small XRMR asymmetry signals in the most reliably and qualitatively consistent form is outlined in chapter 4 of this work.

The upper boundary of the Pt specific magnetic depth profile is positioned at a distance of 165.1 Å from the substrate interface and shows an rms roughness of 7.0 Å which is just marginally lower than the roughness obtained in the Pt_{RT}/PtMnSb bilayer. The magnetic interface position however is significantly farther away for the Pt/PtMnSb interface in this bilayer with hot grown Pt. Figure 5.9 shows a magnetic dead layer at the Pt cover layer

with a lateral extent of 21.9 Å. This is almost twice the thickness as obtained in the Pt_{RT}/PtMnSb bilayer system and it substantiates the significant effect of the Pt growth conditions of the Mn and Pt specific spin polarization within the half-Heusler system. Here, the combination of both Pt specific magnetic dead layers in this PtMnSb system reduces the share of the spin polarized Pt to 84.9 % of the half-Heusler structure. The change of the Pt deposition temperature and the immediate growth subsequent to the PtMnSb layer thus reduces the magnetic depth profile in this half-Heusler structure of the same thickness by more than 6 % or 7 Å. In the next section, the Pt specific magnetooptical $\Delta\beta$ depth profiles shown in Fig. 5.9 are directly compared to the Mn specific XRMR results.

Mn and Pt specific magnetic depth profiles in comparison for the $Pt_{400\,°C}$/PtMnSb bilayer

The graphical compilation of Fig. 5.10 serves as a direct comparison of the experimental XRR and XRMR results of the $Pt_{400\,°C}$/PtMnSb bilayer system at the Mn and Pt characteristic absorption edges. More specifically, the results obtained with a photon energy of 650.2 eV at the Mn L_2 absorption edge are contrasted with the results obtained at the Pt L_3 absorption edge. The Mn specific asymmetry ratio and corresponding best-fit simulation are shown in Fig. 5.10(c). Further scans close to the Mn $L_{2,3}$ absorption edge, the related fixed-q_z scans and XMCD spectrum as well as the corresponding structural density depth profiles are discussed with regard to Fig. 5.8.

The structural density and $\Delta\beta$ depth profiles are determined based on the XRR scan, shown in Fig. 5.10(a), and the asymmetry simulation. Both structural and magnetic depth profiles are illustrated in Fig. 5.10(d). The Pt specific results are presented in the bottom row of this compilation, in which Fig. 5.10(e) shows the XRR and Fig. 5.10(f) the XRMR scan, and corresponding best fit, obtained at a photon energy of 11 567 eV. Due to the more than one order of magnitude lower asymmetry ratio and therefore significantly smaller signal-to-noise ratio, a less unambiguous and clear featured asymmetry signal is detected. The best-fit simulation is shown here, for which the reliability of the result is checked based on the χ^2 optimization discussed in chapter 4.4.5. The corresponding magnetooptical $\Delta\beta$ depth profile in relation to the obtained structural density depth profile is presented in Fig. 5.10(g). A direct comparison is drawn in Fig. 5.10(b) between both $\Delta\beta$ depth profiles obtained at the Pt L_3 as well as the Mn L_2 absorption edge. Here, the relationship of both magnetooptical contours is consistent with the Pt and Mn specific magnetic depth profiles identified in the standard Pt/PtMnSb bilayer system presented in Fig. 5.7. In both cases the Pt specific magnetic depth profile is slightly wider than the Mn specific magnetic depth profile, while both depth profiles are indicating a larger magnetic dead layer at the Pt/PtMnSb in-

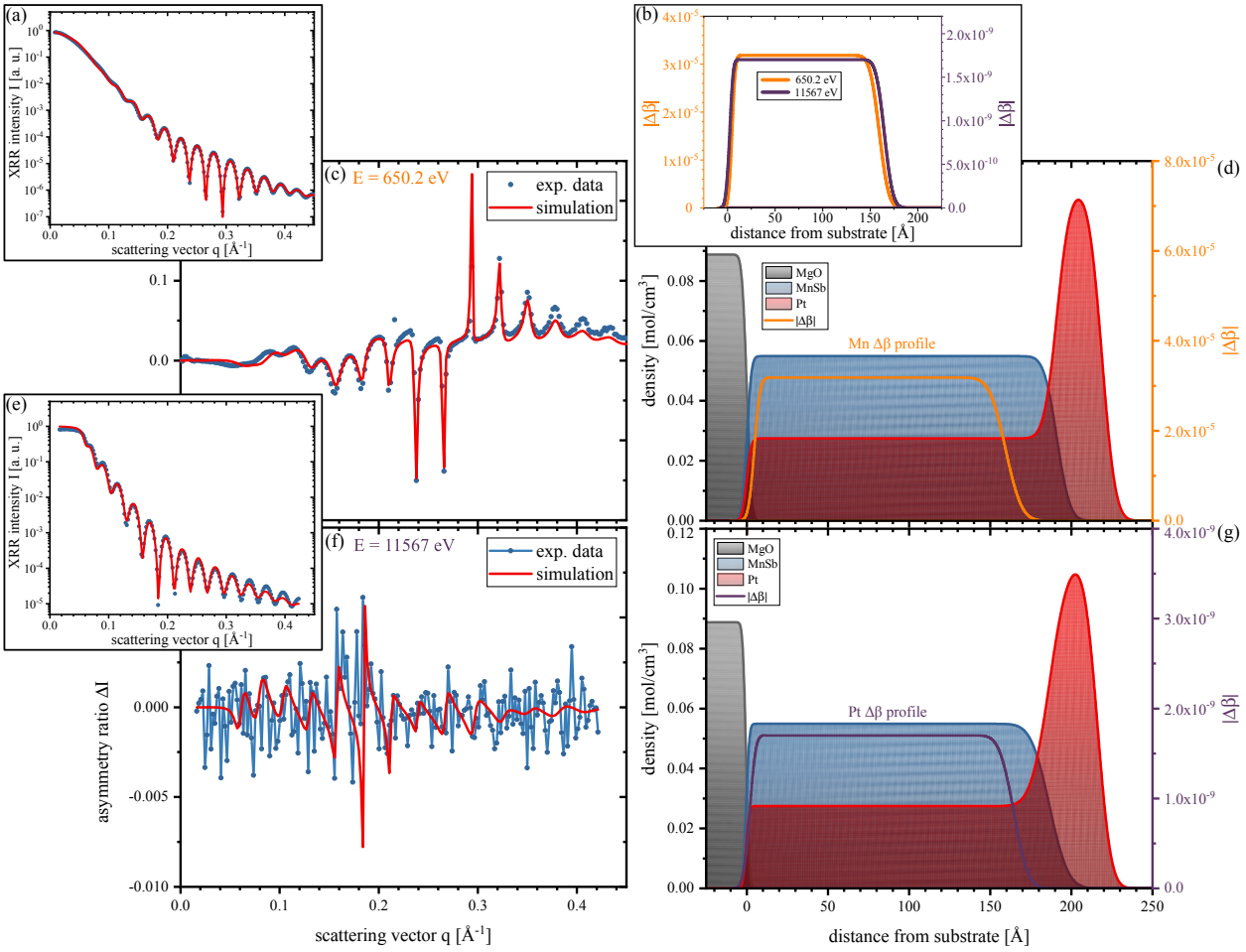

Figure 5.10: Direct comparison of the XRR intensity I and asymmetry ratio ΔI for the $Pt_{400\,°C}$/PtMnSb bilayer. (a) XRR scan and simulation at the Mn specific photon energy of 650.21 eV and (c) the associated asymmetry ratio ΔI and simulation. (e) XRR scan and simulation at the Pt specific photon energy of 11 567 eV and (f) the associated asymmetry ratio ΔI and simulation. (d) and (g) show the structural density and $\Delta\beta$ depth profiles determined by the simulation. The resulting magnetooptical $\Delta\beta$ depth profiles are directly compared in (b).

terface due to the hot deposited Pt capping. More precisely, the Pt specific depth profile exhibits a lower magnetic boundary at a distance of 2.0 Å in relation to the structural substrate interface. This boundary has a rms roughness value of 3.1 Å. The bottom magnetic boundary is therefore similar to the Mn specific lower boundary of the magnetooptical $\Delta\beta$ depth profile. However, the small magnetic dead layer at the substrate interface has a lateral extent of 4.6 Å in case of the Mn specific depth profile. Consequently, the lower magnetic dead layer specified by the scan at the Pt absorption edge is 2.6 Å smaller than the Mn specific version.

A similar picture can be found when the magnetic dead layers at the Pt interface are characterized. Here, the Mn specific $\Delta\beta$ depth profile exhibits a top boundary at a distance of 159.6 Å with a roughness value of 7.8 Å. In contrast, the Pt specific upper magnetic boundary is determined to be positioned at a distance of 165.1 Å from the substrate interface and exhibits a rms roughness of 7 Å. Since the obtained structural density depth profile is slightly different at both absorption edges, the top magnetic dead layer should also be defined in relation to the Pt/PtMnSb interface of each simulated density depth profile. Here, the Mn specific upper magnetic

dead layer starts 31.8 Å below the Pt interface while the Pt specific upper magnetic dead layer has an extent of 21.9 Å. However, this difference is also based on the slight variations of the determined optical depth profile since both experiments probe different spots of the sample surface. The combination of both Pt specific magnetic dead layers reduces the share of spin polarized Pt within this PtMnSb to 87.2 % of the layer.

In consideration of the fact that the asymmetry ratio at the Pt absorption edge is particularly noisy for this bilayer system, the Mn depth profile has been determined with a significantly higher accuracy, corresponding to the experimental XRMR resolution. The Pt specific magnetic depth profile should be ranked less accurate due to the less pronounced minima in the χ^2 landscapes of the asymmetry fit. However, the direct comparison of the resulting magnetooptical $\Delta\beta$ depth profiles shows the same overall correlation as observed for the standard bilayer illustrated in Fig. 5.7. The bottom magnetic dead layer is almost identical for both sample systems within the measurement accuracy of about 1.5 Å. In particular the relation of the Mn specific to the Pt specific depth profile is highly similar with a marginally larger distance to the substrate interface in case of the Mn specific depth profile in both systems.

Furthermore, the standard bilayer shows a top magnetic boundary at a distance of 172.9 Å from the substrate in case of Mn and 173.8 Å in case of Pt. The magnetic dead layer related to the Mn magnetic moments thus forms about 1 Å before the one regarding the Pt magnetic moments. In comparison to the bilayer with hot deposited Pt, for which the top magnetic boundary is at a distance of 159.9 Å in case of Mn and 165.1 Å in case of Pt, the half-Heusler forms a significantly larger top magnetic dead layer when the Pt layer is deposited at the PtMnSb growth temperature. Here, the Mn specific ferromagnetic ordering is vanishing at a distance of about 13 Å closer to the substrate, while the Pt specific spin polarization is lost at a distance of about 9 Å closer to the MgO interface. The rms roughness of all top magnetic boundaries is however comparable and merely varies between 7 Å and 8.6 Å.

The XRMR measurement of this $Pt_{400\,°C}$/PtMnSb bilayer shows a particular small signal-to-noise ratio and is therefore presented in an enlarged form in Fig. 5.11(a). Here, the asymmetry ratio ΔI and best-fit simulation is shown in detail to highlight the agreement of the main asymmetry features and the overall oscillatory pattern. When the main features of the asymmetry ratio are again examined in detail, as shown in the close-up of Fig. 5.11(b), a general correlation of sub-noise asymmetry signal and best-fit simulation can be observed.

Moreover, one can directly compare the parameters of the Mn and Pt specific magnetic depth profiles of this bilayer. As summarized by Table 5.1 and magnetic dead layer specific in Table 5.2, the share of the Mn spin polarization is 81.0 % of the full half-Heusler structure which is about 4 % below the obtained value regarding

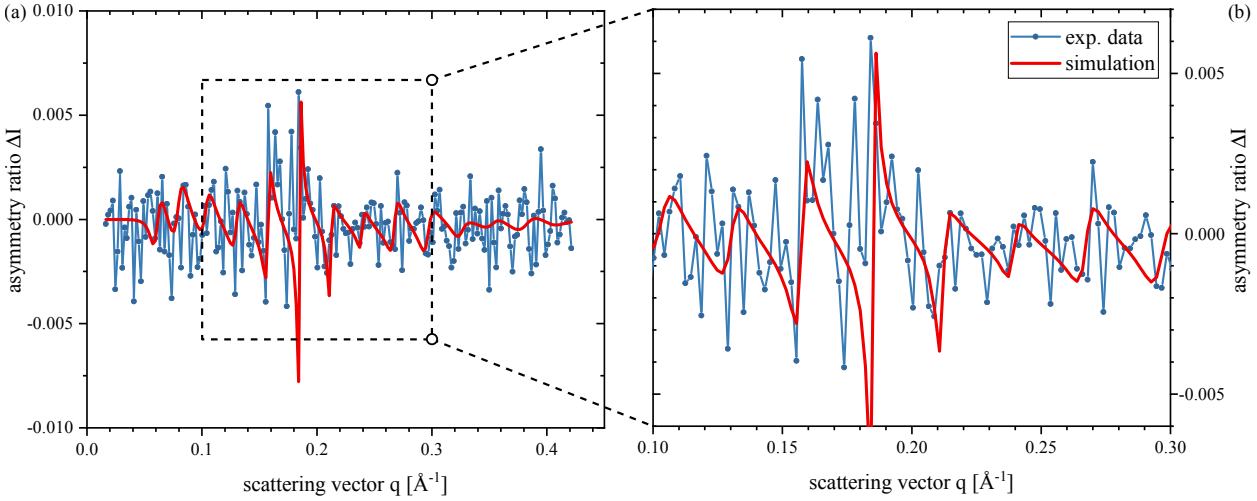

Figure 5.11: (a) Asymmetry ratio ΔI and simulation measured for the $Pt_{400\,°C}$/PtMnSb bilayer using the Pt specific photon energy of 11 567 eV. (b) Enlarged view of the asymmetry ratio ΔI and simulation presented in (a) in the scattering vector range between 0.1 and 0.3 Å^{-1}.

the Pt magnetic moment. Comparing the extents of the magnetic dead layers for each particular type of atom, one finds a similar picture as revealed for the standard sample in Fig. 5.7. Here, the magnetic dead layer obtained at the Mn absorption edge shifts the magnetic boundary to a distance of 4.6 Å from the substrate. This dead layer is therefore 2.6 Å wider than the depth profile representing the Pt spin polarization.

The same disparity between Mn and Pt specific depth profiles can be observed at the Pt/PtMnSb interface, however the effect inducing an extended Pt magnetic depth profile is much more pronounced. The extent of the Mn specific upper magnetic dead layer was found to be 31.8 Å while the Pt specific depth profile has a magnetic boundary positioned 21.9 Å below the structural PtMnSb interface. Under consideration of the small determined structural variation of the interface position, one obtains an atom-specific difference of the magnetic depth profile of about 5 Å at the Pt interface.

This characteristic difference of the Pt magnetooptical depth profile in relation to the distribution of intrinsic Mn magnetic moments within the PtMnSb structure can be attributed to the same effects discussed with regards to the direct depth profile comparison based on Fig. 5.7. The main effect is a small MPE, for which the magnetic Mn atoms induce a Pt spin polarization extending the magnetic depth profile of the PtMnSb structure into an adjacent layer in which the Mn magnetic moments are arranged into a compensated state due to the Pt-growth induced structural deficits. The Mn specific magnetic depth profile shows a reduced-magnetization phase which forms due to the intermixing, structural disorder or a chemical alteration of the Pt/PtMnSb interface. This process is increased when the Pt cover layer is sputter deposited at 400 °C subsequent to the half-Heusler growth. Thus, the Mn spin polarization observable by XRMR is suppressed in the interface region and the magnetic boundary is shifted up to about 3 nm

inside of the nominal PtMnSb structure. Due to the proximity induced spin polarization the Pt remains polarized in the first few monolayers or up to 10 Å of the Mn specific magnetic dead layer regions while the discussed mechanisms lead to a loss of the Mn spin polarization.

Magnetic depth profiles of the PtMnSb thin film with AlO_x/MgO capping

Figure 5.12 shows an overview of the combined XRMR results for the AlO_x/MgO/PtMnSb(20.8 nm) sample of series II. Here, five specific photon energies close to the Mn $L_{2,3}$ absorption edge were used to obtain a refined picture of the Mn specific magnetooptical sample state. Figure 5.12(d) presents a photon energy-dependent XRR intensity measurement for left and right circularly polarized light and fixed scattering vector q_z.

The relative intensity of the L_3 and L_2 edges is sensitive to the spin state since the edges are split by the spin-orbit coupling of the $2p^5$ configuration which is created when a $2p$ electron is excited. The L_3 edge at lower photon energy is corresponding to the $^2P_{3/2}$ excited state while the higher energy L_2 edge is defined by the $^2P_{1/2}$ term. Based on the state degeneracy, the L_3 absorption edge in general has twice the edge jump of the L_2 edge. This edge jump proportion roughly translates to the relation of empirically observable asymmetry ratios. The asymmetry ratio obtained from the photon energy-dependent XRR intensity measurement at a fixed scattering vector $q_z = 0.131\,\text{Å}^{-1}$ is presented below the corresponding intensity plot in Fig. 5.12(e) and shows a maximum of $\sim 42\,\%$ about 1 eV below the L_3 absorption edge. At the L_2 edge, the obtained asymmetry ratio falls narrowly short of $\sim 20\,\%$.

In general, the momentum transfer for the fixed-q_z scan is selected based on the reflectivity curve. As illustrated in Fig. 5.1, the value is set to provide a high asymmetry response in combination with a high overall XRR intensity. The energy-dependent measurement with a fixed momentum transfer consequently results in a profile close to a $L_{2,3}$ absorption edge spectrum which is slightly modified due to the dispersive part. The fixed-q_z scan presented in Fig. 5.12(e) shows distinct features close to both edges. Here, multiple photon energies yielding a high asymmetry ratio are chosen for detailed XRMR measurements and the corresponding simulation of the asymmetry ratio. The selected photon energies are marked in Figs. 5.12(d) and (e).

All XRMR asymmetry ratio scans and the respective fits are shown in the Figs. 5.12(a) - (c), (f) and (g). Every simulated asymmetry ratio provides a good agreement with the experimental result. The major asymmetry features are fitted almost perfectly while the only visible discrepancy can be found in the scan with a photon energy of 638.4 eV. Here, the particularly pronounced oscillatory pattern found in the asymmetry response is matched

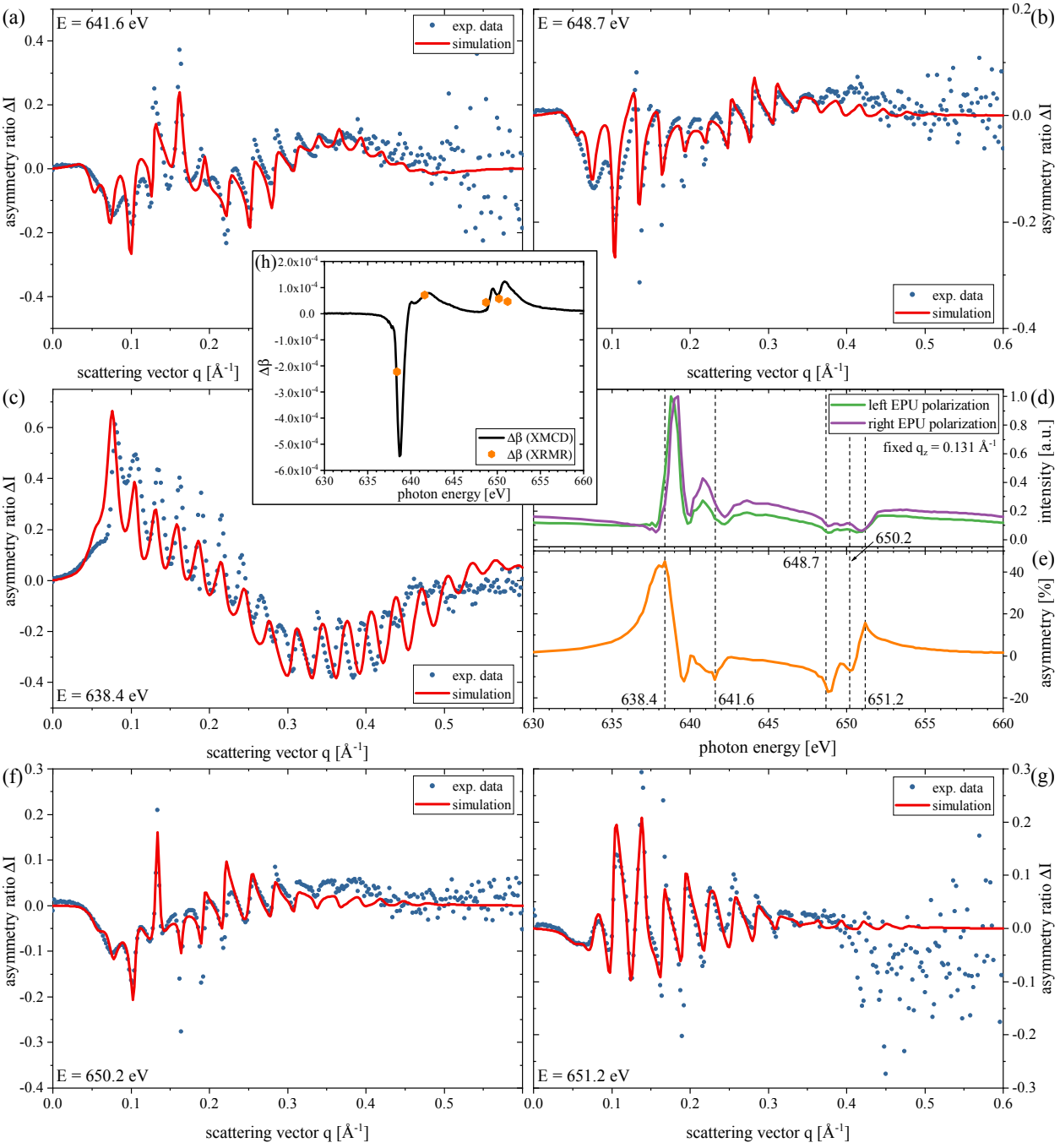

Figure 5.12: Overview of the XRMR results for the PtMnSb(20.8 nm) sample capped with AlO_x/MgO. (a) - (c), (f) and (g) show XRMR asymmetry ratios ΔI and the best-fit simulations obtained at varying photon energies around the Mn $L_{2,3}$ absorption edge. (d) Photon energy-dependent XRR intensity measurement for left and right circularly polarized light and corresponding asymmetry (c) at a fixed scattering vector $q_z = 0.131\,\text{Å}^{-1}$. (h) Magnetooptical parameter $\Delta\beta$ derived from the XMCD signal in relation to the obtained PtMnSb $\Delta\beta$ plateau values.

in the underlining course. However, the exact height of the ΔI amplitude is underestimated in the first half of this asymmetry scan culminating in a pattern mismatch at the point of transition of the overall slope around $q_z = 0.28\,\text{Å}^{-1}$.

Beside this variation of measurement and best fit, the remaining XRMR asymmetries and fits are in accordance, at which the noise level significantly increases around $q_z = 0.4\,\text{Å}^{-1}$. This effect, based on the drop in intensity of the Kiessig fringes in the reflectivity curve, should not mislead the simulation by assuming the presence of visible features in this region of the XRMR asymmetry ratio.

The reasonable approach is to restrict the fitting algorithm to a window of the asymmetry scan with an acceptable signal-to-noise ratio. For instance, the asymmetry ratios presented in Fig. 5.12 are fitted up to a scattering vector of $q_z = 0.45\,\text{Å}^{-1}$ while the rest of the scan is not taken into account when the χ^2 value is determined. However, the large noise can in theory obscure a potential magnetic response at high scattering vectors yet the best-fit solutions obtained from all XRMR simulations presented here suggest no pronounced asymmetry ratios at high momentum transfers. The inset Fig. 5.12(h) shows magnetooptical parameter $\Delta\beta$ derived from the XMCD signal compared to the PtMnSb $\Delta\beta$ plateau values of the XRMR based profiles. Here, all obtained values for the absorptive part of the magnetooptical depth profile closely follow the relation given by the XMCD signal.

Figure 5.13 summarizes the structural and magnetooptical depth profiles of this AlO_x/MgO/PtMnSb sample obtained from the five asymmetry ratio scans at different photon energies which are presented in Fig. 5.12. The density depth profiles simulated based on the XRR scans close to the Mn L_2 as well as the L_3 absorption edge are again compared to the magnetic depth profiles based on the asymmetry fits to identify and quantify the magnetic dead layer within the half-Heulser PtMnSb layer. The thickness of this layer is 20.8 nm, determined with a small standard deviation over all XRR simulations of 1.8 Å. The average rms roughness of the top PtMnSb layer is 6.5 Å with a standard deviation of only 1.1 Å. The substrate interface is equally well defined over all five separate measurements with a roughness value of 4.5 Å and a standard deviation of 1.3 Å.

The magnetooptical depth profile within this PtMnSb layer has a lateral extent of 17.2 nm determined with a standard deviation over all five scans of 1.9 Å. Here, the lower boundary is positioned at a distance of 21.5 Å from the substrate interface identified with a relatively high standard deviation of 3.4 Å. The upper magnetic boundary is placed at 19.4 nm in relation to the substrate interface. The position of this magnetic interface is varying just as much between all five scan with a standard deviation of 3.5 Å. A higher precision is found in the determination of the upper interface roughness with an average value of 5.7 Å and a standard deviation of only 1.4 Å.

The magnetic dead layers at the substrate side and in proximity to the AlO_x/MgO can be defined based on this averaged interface positions. Here, the magnetic dead layer at the bottom of the PtMnSb layer is much more pronounced than in the previously discussed sample series. The average lateral extent of 2.2 nm is a factor of 5 to 8 larger than for the Pt/PtMnSb bilayers presented in Figs. 5.5 and 5.8, respectively. This discrepancy may be attributed to a MgO substrate of significantly worse quality. Since the Pt capped samples discussed in this chapter were grown in a separate sample series, a different batch of MgO substrates was utilized for the sample series of the AlO_x/MgO sample presented here. Although each

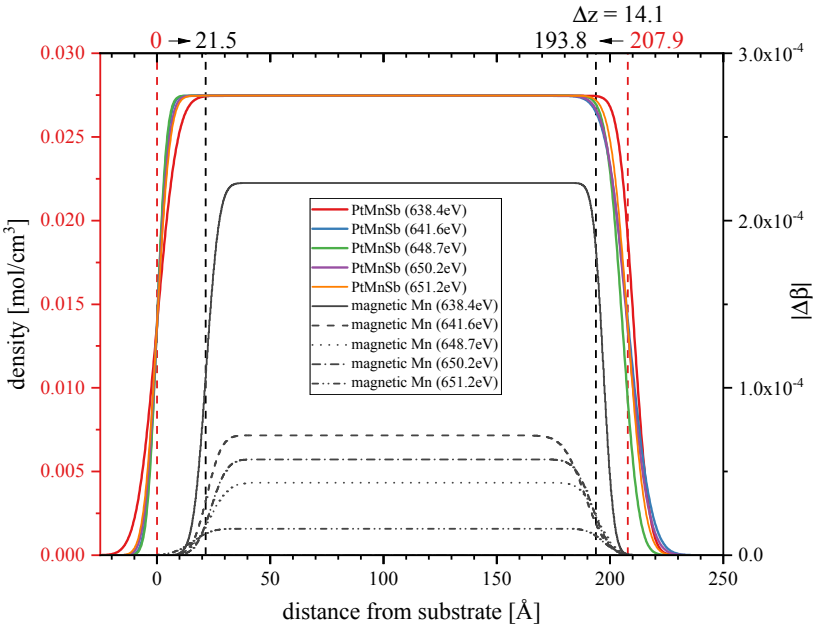

Figure 5.13: Comparison of simulated PtMnSb structural density and magnetooptical depth profiles obtained from the XRR and subsequent XRMR analysis of the PtMnSb(20.8 nm) sample capped with AlO_x/MgO for varying photon energies around the Mn $L_{2,3}$ absorption edge.

substrate was cleaned by different organic solvents and annealed at a high temperatures prior to the PtMnSb deposition process, in order to remove impurities at the surface layer, a substrate miscut or interface defilement due to surface milling can significantly increase the structural roughness of the substrate interface. This assumption is verified by the average roughness of the substrate interface obtained from the XRR fits of the five independent XRMR experiments. The average rms roughness of 4.5 Å is 2.5 times higher than the average interface roughness of the Pt capped series (1.8 Å). Based on this increased interface impurity, a higher degree of oxidative contamination in combination with an increased level of interdiffusion occurs during and after the half-Heulser deposition at elevated temperatures.

The thickness of the upper magnetic dead layer is on a comparable level with the one of the foremost discussed standard Pt_{RT}/PtMnSb bilayer system. The average position of the upper Mn specific magnetic boundary is 14.1 Å below the mean capping/PtMnSb interface position. Here, the higher variance of the PtMnSb thickness and the upper magnetic boundary position lead to a higher uncertainty regarding the magnetic dead layer extent than for the Pt capped systems. The standard deviation of the upper magnetic boundary at 19.4 nm from the substrate is 3.4 Å over all measurements. When all XRR and XRMR simulations at the specific photon energies are considered independently, one obtains an upper magnetic dead layer thicknesses between 11 Å and 19 Å corresponding to a standard deviation of 3.5 Å over all energies. This higher discrepancy in comparison to the well defined structural and magnetic depth profiles of the Pt capped systems can certainly be attributed to the lower level of interface quality

obtained for the AlO_x/MgO capped samples. Due to increased intermixing, structural disorder and oxidation of the top atomic PtMnSb layers, one can observe a decline of the ferromagnetic properties. The reduced interface quality suggests oxygen contamination at the PtMnSb//MgO interface as primary reason for the reduction of spin polarization. This chemical alteration leads to the formation of Mn-O hybrid states in the magnetic dead layer region reducing the net magnetic moment.

Mn and Pt specific magnetic depth profiles in comparison for the PtMnSb thin film with AlO_x/MgO capping

Figure 5.14 visualizes the direct comparison of the simulated PtMnSb structural density and the magnetooptical $\Delta\beta$ depth profiles obtained from the XRR and subsequent XRMR analysis of the AlO_x/MgO/PtMnSb sample with photon energies at the Pt L_3 as well as Mn L_2 absorption edges. This sample shows a particularly rough MgO substrate interface as discussed with regard to Fig. 5.13. Since the MgO substrate turns out to be an unreliable point of reference for a comparison of the XRMR results obtained at Mn, respectively Pt specific photon energies during different experimental beamline sessions, the capping/PtMnSb interface is matched here. Although nominally the same sample has been analyzed in both sessions, the relatively poor substrate quality in combination with a substantial temporal distance between both experiments at the ALS and DESY beamlines, causes a significant difference in the structural modeling of the substrate interface based on these results. Moreover, a change of the exact sample section focused during the reflectivity experiments can evoke substantial differences in the obtained optical depth profiles based on the actual variation due to an imperfect growth process on a substrate which may exhibit increased roughness and accretion of contaminants due to a miscut induced step structure.

When the framework is shifted to match the PtMnSb interface at the capping side, a shift of the relative MgO interface position by 5.5 Å is observed. This is illustrated in Fig. 5.14(a) for both depth profiles based on measurements at 11 567 eV, respectively 651.2 eV in the Mn specific soft x-ray regime. The depth profiles of the AlO_x/MgO nearly overlap with a marginally higher surface roughness obtained in the Pt specific asymmetry simulation. When the magnetic $\Delta\beta$ depth profiles of both Mn and Pt specific scans are compared within the established PtMnSb interface based framework, the expected relation is confirmed in case of the lower magnetic boundary. Figure 5.14(b) illustrates this $\Delta\beta$ comparison, for which the Pt specific boundary is positioned at a distance of 9 Å from the substrate with a rms roughness of merely 2.3 Å. In contrast, the Mn specific boundary is found at a distance of 15.4 Å and shows a roughness of 6.8 Å. A much higher difference can be observed at the top magnetic boundary in this system. Here, the

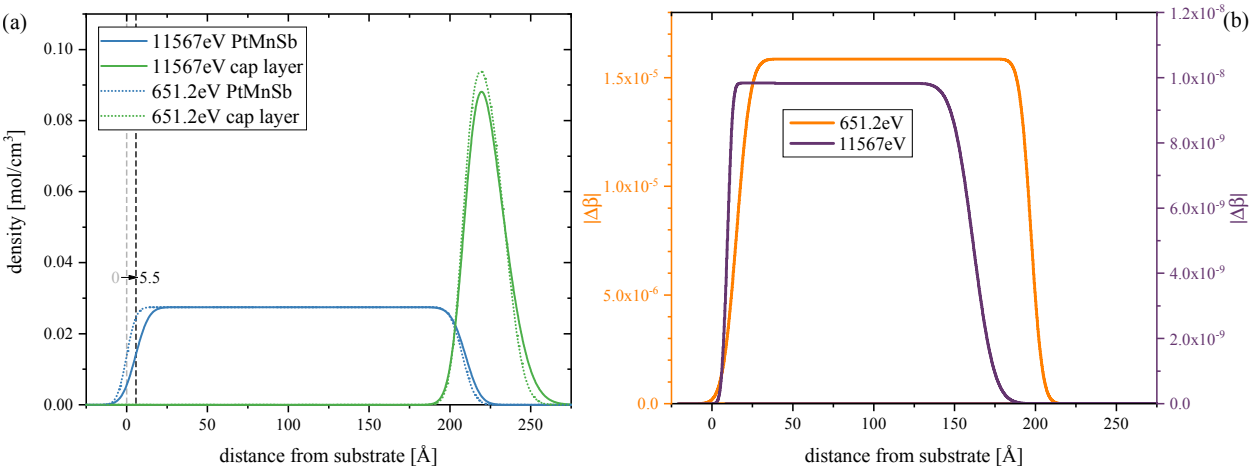

Figure 5.14: (a) Simulated PtMnSb structural density and (b) magnetooptical $\Delta\beta$ depth profiles obtained from the XRR and subsequent XRMR analysis of the AlO_x/MgO/PtMnSb sample with the Mn (651.2 eV) and Pt (11 567 eV) specific photon energies.

Pt specific boundary is found at a position of 161.5 Å from the substrate which is about 34 Å below the Mn specific boundary obtained at this photon energy of 651.2 eV. This indicates a significant difference in the atom specific magnetic dead layer thickness caused by the oxide capping of this sample system.

This consequence of the AlO_x/MgO capping on the magnetic properties of the PtMnSb, especially in the upper interface region, is analyzed in more detail, under consideration of both soft and hard x-ray specific results, in Fig. 5.15. This graphical compilation of all obtained structural and magnetooptical depth profiles confirms the key observations made based on the exemplary comparison of the two specific photon energies at the Mn and Pt absorption edges. Figure 5.15(a) shows the structural density depth profiles of the PtMnSb(20.8 nm) sample capped with AlO_x/MgO for photon energies around the Mn $L_{2,3}$ absorption edges in grey and the depth profile simulated based on the Pt L_3 absorption edge data in red. The Pt specific magnetooptical $\Delta\beta$ depth profile is marked by the dashed line in direct relation to all structural depth profiles.

When the Pt specific density depth profile, which has been shifted to fit the interface of the depth profile based on the XRMR scan at 651.2 eV, is compared to the average interface position, a minimal deviation of about 2 Å is observed. This is close to the experimental resolution for the analysis of the soft x-ray data. The Pt specific magnetic dead layer thickness is defined in relation to this averaged interface position. The lower magnetic dead layer has an extent of 9 Å while the upper magnetic interface is positioned 46 Å below the AlO_x/MgO capping interface. This significant change in the $\Delta\beta$ depth profile in relation to the results obtained at the Mn $L_{2,3}$ absorption edges is highlighted in Fig. 5.15(b). Here, the magnetooptical depth profiles obtained by the XRMR analysis of this AlO_x/MgO capped PtMnSb layer, which have been presented in relation to the structural depth profiles in Fig. 5.13, are directly compared with the Pt specific depth profile.

The Mn specific dead layer at the substrate has an average thick-

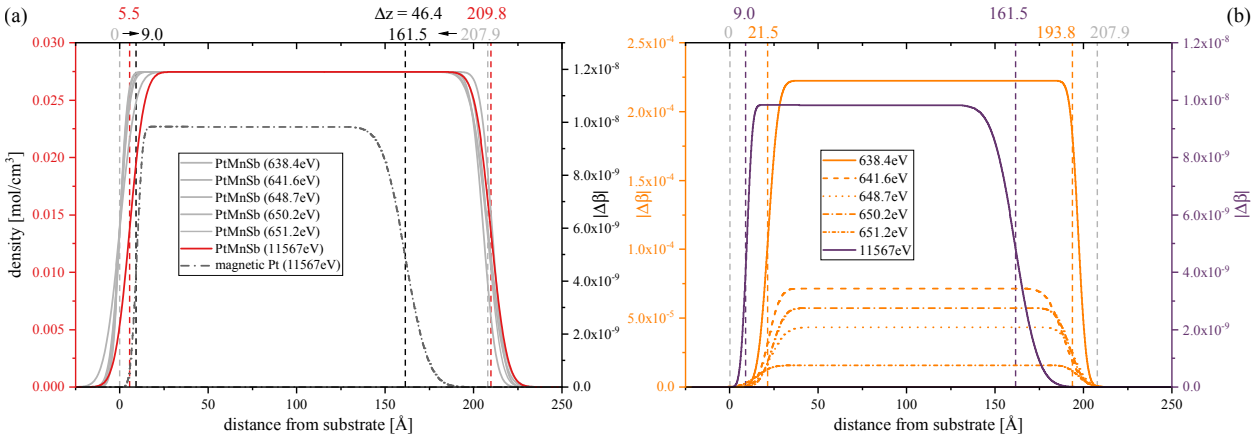

Figure 5.15: (a) Comparison of the structural density depth profiles of the AlO_x/MgO/PtMnSb sample for photon energies around the Mn $L_{2,3}$ absorption edge (grey) and at the Pt L_3 absorption edge (red), in relation to the Pt specific magnetooptical $\Delta\beta$ depth profile (dashed line). (b) The Pt specific magnetooptical $\Delta\beta$ depth profile contrasted with all Mn specific depth profiles shown in Fig. 5.13.

ness of 21.5 Å, while the Pt specific magnetic dead layer has an extent of only 9 Å in relation to the substrate determined in the fixed interface framework. In principle, this result fits the dead layer relation obtained for the Pt capped twin sample, for which the Mn specific dead layer has a thickness of 21 Å and the Pt lower magnetic boundary is observed in proximity yet significantly closer to the substrate at a distance of 17 Å. The top magnetic dead layer of the AlO_x/MgO capped PtMnSb layer is however strongly influenced by the interdiffusion, oxidation and the consequential transformation of dominant ordering structure of the Mn magnetic moment.

In contrast to the upper Mn specific magnetic dead layer, which has a thickness of 14.1 Å, the upper Pt magnetic boundary forms 46.4 Å below the PtMnSb interface on the side of the oxide capping. The chemical alteration of the half-Heusler crystal structure and the reduction of the ferromagnetic ordering of the Mn magnetic moments significantly influences the Pt spin polarization. Based on this extended Pt specific magnetic dead layer it can be assumed that the half-Heusler unit cell is modified due to these interface effects far deeper into the PtMnSb layer than presumed on the basis of the results for the Mn specific dead layer. Supposedly, the ordering of the Mn magnetic moment is sustained by a long range magnetic ordering maintained by Mn oxide impurities. At the same time the Pt spin polarization is lost due to the degradation of the half-Heusler structure in the upper region of the PtMnSb layer which is directly affected by the AlO_x/MgO capping.

Magnetic depth profiles of the Pt_{O_x}/PtMnSb bilayer

The PtMnSb half-Heusler layer of the previously discussed AlO_x/MgO capped sample has been prepared in the same deposition process simultaneously to the one of the twin sample capped with Pt. The results of this Pt_{O_x}/PtMnSb bilayer of series II are summarized in Fig. 5.16. This graphic compilation shows the energy-dependent scan with fixed momentum transfer in Fig. 5.16(b) and the corre-

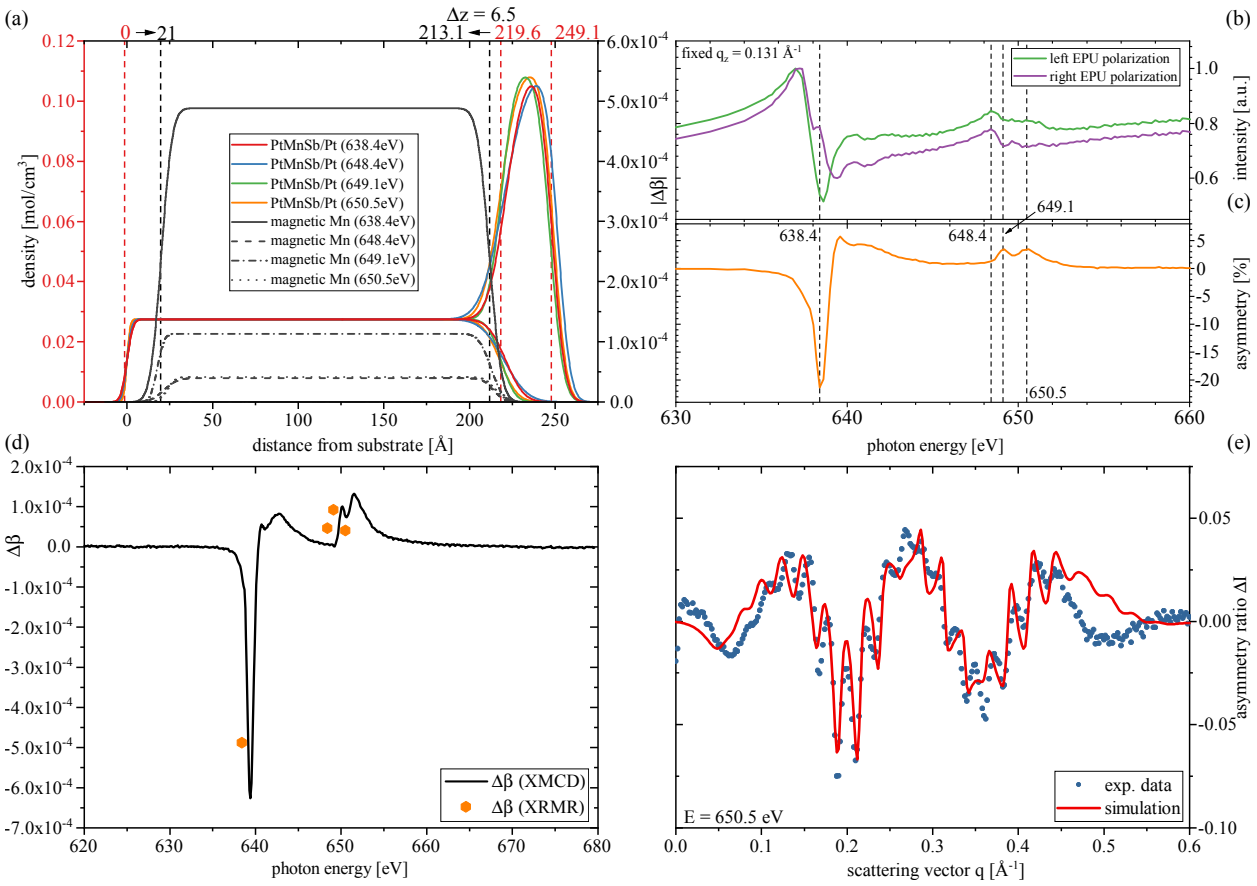

Figure 5.16: (a) Comparison of simulated structural density and magnetooptical depth profiles obtained from the XRR and subsequent XRMR analysis of the Pt_{O_x}/PtMnSb bilayer for varying photon energies around the Mn $L_{2,3}$ absorption edge. (b) Photon energy-dependent XRR intensity measurement for left and right circularly polarized light and corresponding asymmetry (c) at a fixed scattering vector $q_z = 0.131\,\text{Å}^{-1}$. (d) Magnetooptical parameter $\Delta\beta$ derived from the XMCD signal in relation to the obtained PtMnSb $\Delta\beta$ plateau values shown in (a). (e) XRMR asymmetry ratio and simulation measured with a specific photon energy of 650.5 eV.

sponding asymmetry in Fig. 5.16(c). One of the obtained magnetic asymmetry signals which was measured at a photon energy of 650.5 eV in the vicinity of the Mn L_2 absorption edge is exemplary shown in Fig. 5.16(e). Here, with the exception of the last drop of the oscillation amplitude for a scattering vector larger than $q_z = 0.45\,\text{Å}^{-1}$, the asymmetry ratio is reasonably well fit. The fit of the higher order oscillatory asymmetry features on top of the base signal oscillation is in accordance with the obtained asymmetry ratio. Small deviations can be observed at maximum amplitude, were the correct higher order oscillatory feature is merely implied by the best-fit asymmetry ratio.

The magnetooptical depth profile obtained from this analysis of the XRMR experiment conducted with a beamline energy of 650.5 eV is a part of the structural and magnetooptical depth profile comparison presented in Fig. 5.16(a) including the results obtained at the other specified photon energies. Figure 5.16(d) illustrates the $\Delta\beta$ parameter in dependence of the photon energy derived from the XMCD signal. The PtMnSb $\Delta\beta$ plateau values of the XRMR based profiles are shown in direct comparison and nicely follow the course of the dichroic response.

The average PtMnSb depth profile resulting from these independent simulations has a thickness of 22.0 nm, accurately determined

with a standard deviation of 1.7 Å. On top of this PtMnSb half-Heusler structure, the Pt capping layer has an average extent of 2.9 nm while the standard deviation of this structural parameter is 1.8 Å. The interface of the PtMnSb layer on the side of this Pt capping, which was deposited at room temperature like the sample visualized in Fig. 5.5, shows an average rms roughness of 7.8 Å with a standard deviation of 2.2 Å. These roughnesses are comparable to the previously discussed bilayer due to the identical sputter deposition process. The substrate roughness is slightly lower (2.3 Å) than for the previously presented AlO_x/MgO/PtMnSb system of series II. This improved roughness indicates a slightly smoother MgO interface or in general a higher substrate quality in comparison to the twin sample, deposited on a MgO substrate of the same production series. In order to complete the evaluation of the structural roughnesses, the top Pt interface has an rms roughness of 5.9 Å with a standard deviation of 0.6 Å. The top layer roughness is therefore identical within the given accuracy for all samples discussed in this chapter.

The influence of the heavy metal capping relative to the insulating oxide capping on the magnetic properties can be studied by comparing the magnetoopical depth profiles illustrated in Fig. 5.16(a) with the depth profiles of the twin sample presented in Fig. 5.13. Here, the lower boundary of the Mn specific magnetic depth profile can be found at 21 Å from the substrate interface with a standard deviation over all four photon energies of 2.3 Å. The roughness of this magnetic interface is determined to be 4.4 Å independently simulated with a standard deviation of 1.5 Å. This lower magnetic dead layer within the PtMnSb compound is therefore very similar to the one obtained within the sample capped with AlO_x/MgO. The PtMnSb layer of both samples were deposited simultaneously on substrates of the same batch which was likely produced under identical manufacturing conditions. The quality of the substrate used for the twin sample production is therefore identical, however as discussed in relation to both Pt capped samples of the first series presented in this chapter, the quality between deposition series may vary on the scale of XRMR significance.

The twin samples of series II show a lower magnetic dead layer of 21.5 Å and 21.0 Å, respectively, while the solely Pt capped samples of series I have substrate bound magnetic dead layers of 4.6 Å and 2.8 Å, respectively. Since the deposition conditions are nominally identical with only a slight difference in deposition temperature due to aging phenomena of the substrate holder, the substrate interface quality is the main factor determining the lateral extent of the lower magnetic dead layer.

The top magnetic dead layer of this sample has to be quantified in relation to the obtained structural interface, in particular since this position is influenced by the interface characteristics. In the Pt_{O_x}/PtMnSb sample of series II, the upper magnetic boundary is positioned at a distance of 213.1 Å relative to the substrate interface

as illustrated in Fig. 5.16(a). This value is accurately determined by the various measurements within a standard deviation of 2.1 Å.

Although the PtMnSb layer of both twin samples was deposited simultaneously, the thickness of the half-Heuser structure slightly varies depending on the capping layer. The PtMnSb layer in the AlO_x/MgO capped sample has a thickness of 20.8 nm while the Pt capped version shows a lateral extent of 21.9 nm. On the one hand, this difference of about 1 nm can be attributed to a slightly reduced PtMnSb thickness due to the reactive oxide capping which decreases the optical parameters in the interface region based on these light element induced structural disorder in the immediate interface region. On the other hand, this thickness disparity of both density depth profiles is reinforced by intermixing and chemical alteration at the interfacial surface layer during the deposition of the Pt cover layer. Here, steps and dislocations at the interface as well as a gradual stoichiometric transition from pure PtMnSb to Pt due to the formation of polycrystalline transition zones can nominally increase the obtained PtMnSb thickness. The island based Volmer-Weber growth mode discussed in chapter 2.4 suggests a Pt replenishment effect at the interface for epitaxial grains of different half-Heusler thickness.

The homogeneous growth of thicker and therefore smoother half-Heusler structures is locally confined. For PtMnSb above a thickness of $\sim$ 15 nm the grains become significantly larger and more defect-free, which is confirmed by the discussed STEM images (see Figs. 2.10 and 2.21). Since the obtained density depth profile constitutes an average over all illuminated grains, one has to expect a different outcome for the situation when those grains get equalized by a Pt cover layer in relation to the covering by light metal oxides. The decisive factor here is the structural density in relation to the half-Heusler system within the transition zone. The Pt cover layer therefore slightly increases the average thickness of the PtMnSb based on an intermixing and structural transitioning effect. This is directly visible based on all XRR simulations presented for this sample. The significant influence of the covering layer on the half-Heusler layer termination is particularly evident when both density depth profiles of heavy and light element covering are directly compared, resulting in the obtained difference of both density depth profiles.

Moreover, this structural difference has a direct influence on the magnetic interface properties. As illustrated in Fig. 5.13, the top magnetic dead layer with a thickness of 14.1 Å can be found in direct proximity to the AlO_x/MgO interface of the PtMnSb layer. In contrast, the magnetic dead layer at the Pt/PtMnSb interface has an average thickness of merely 6.5 Å as illustrated in Fig. 5.16(a). The main reason for this extended magnetooptical depth profile is certainly the structural termination of the PtMnSb layer through the deposition of Pt atoms. The formation of a small transition zone in combination with interdiffusion and the general in-plane averaging

effect of this reflectivity method lead to a delayed decline of the Mn specific magnetism in relation to the AlO_x/MgO capped PtMnSb structure.

Mn and Pt specific magnetic depth profiles in comparison for the Pt_{O_x}/ PtMnSb bilayer

Figure 5.17 summarizes the optical and magnetooptical XRR and XRMR results of the Pt_{O_x}/PtMnSb bilayer. The structural density depth profile obtained at a photon energy of 11 567 eV is illustrated in a direct comparison to the depth profile obtained at 638.4 eV. When the structural density depth profiles are normalized in relation to the Pt/PtMnSb interface instead of the substrate interface as it is usually the case, the results of both beamlines are in accordance with each other. Due to the significant difference in the obtained substrate interface, this form of structural representation is more reliable and allows for a comparison of the optical and magnetooptical depth profile. When the interface properties of the substrate are subject to change, for reasons of chemical alternation, inhomogeneous sample growth in combination with a shift of the exact probing x-ray focus position or other effects, the bilayer system is quantifiable in relation to the Pt/PtMnSb interface even though the MgO interface does not serve as a stable point of reference.

Figure 5.17(b) shows the Mn and Pt specific structural density depth profiles, for which the one obtained at 638.4 eV is shifted by 12.1 Å to match the Pt/PtMnSb interface position determined by the XRMR experiment at a photon energy of 11 567 eV. This shift leads to an agreement of the Pt density depth profile within measurement accuracy. The roughness of the matched interface is nearly identical in both independent simulations with a rms value of 8.3 Å and 8.9 Å, respectively. Due to this interface matching, the nominal position of the PtMnSb//MgO interface differs by 12.1 Å as illustrated by the dashed lines.

The obtained magnetooptical $\Delta\beta$ depth profiles, for which the Pt depth profile has been shifted in the same frame of reference as the corresponding optical depth profile, are shown in Fig. 5.17(a) in direct comparison to the Mn specific depth profile based on the XRMR scan at 638.4 eV. The structural density depth profile of the Pt specific XRMR scan is integrated into the framework of Fig. 5.16, presenting the comparison of simulated structural density and magnetooptical depth profiles obtained from the XRR and subsequent XRMR analysis of the Pt_{O_x}/PtMnSb bilayer for varying photon energies around the Mn $L_{2,3}$ absorption edge. The combined graphic of Fig. 5.17(c) illustrates all Mn and Pt specific density depth profile as well as the $\Delta\beta$ depth profile at the Pt L_3 absorption edge. This classifies the Pt specific magnetic depth profile boundaries in relation to both frames of reference and specifies the magnetic dead layers at the substrate and Pt interfaces. More specifically, the lower magnetic dead layer has an

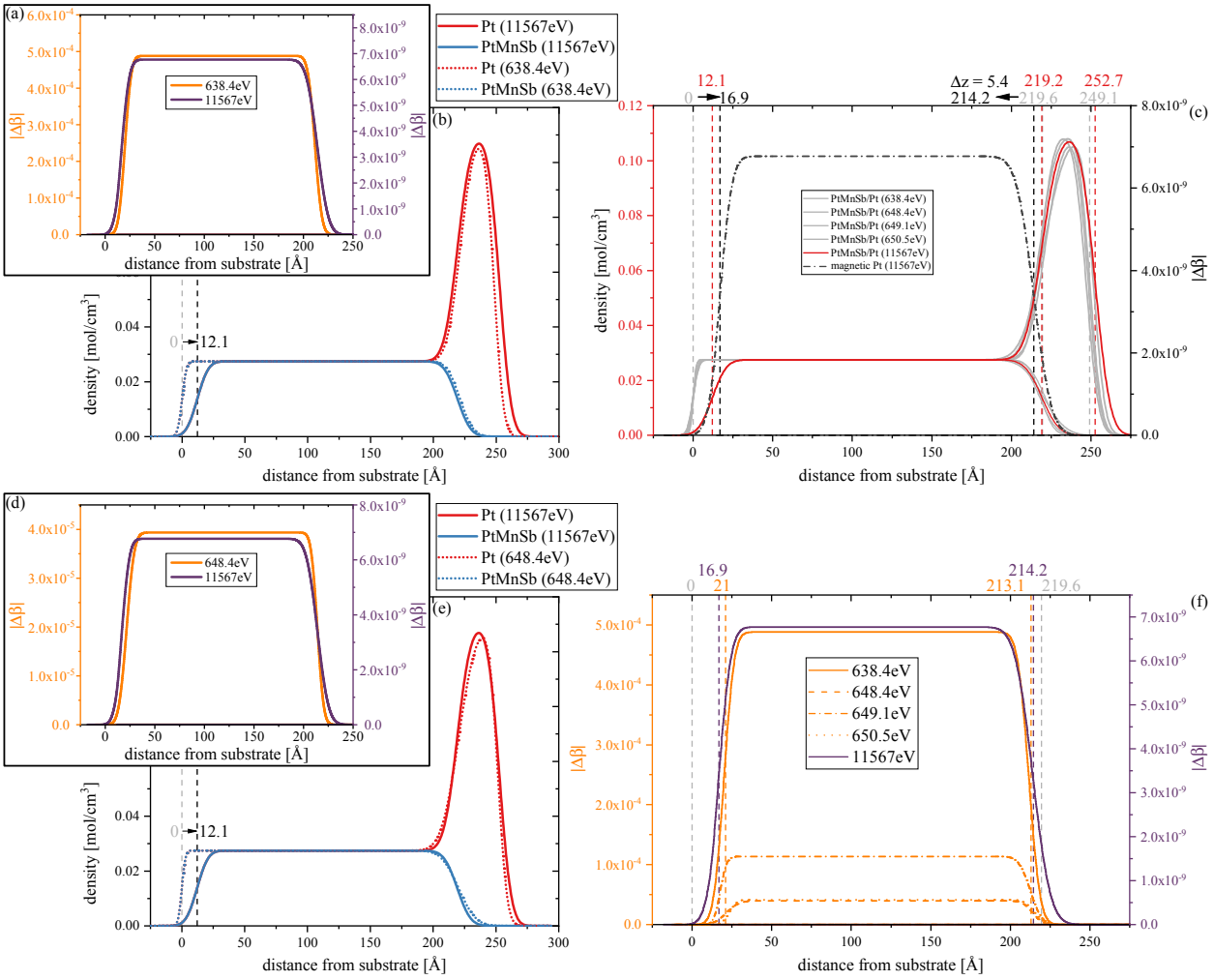

Figure 5.17: (a) Direct comparison of the Pt and Mn specific magnetooptical $\Delta\beta$ depth profiles of the Pt_{O_x}/PtMnSb bilayer. (b) Structural density depth profile obtained at a photon energy of 11 567 eV in direct comparison to the depth profile obtained at 638.4 eV (dotted line). (e) Respective comparison of the depth profile obtained at 648.4 eV (dotted line). (d) Direct comparison of the resulting magnetooptical $\Delta\beta$ depth profiles for both asymmetry scans at the energies shown in (e). (c) Simulated Pt/PtMnSb structural density depth profiles at various energies, Mn specific (grey) and Pt specific (red), in relation to the $\Delta\beta$ depth profile at the Pt L_3 absorption edge (dashed line). (f) The Pt specific magnetooptical $\Delta\beta$ depth profile contrasted with all Mn specific depth profiles shown in Fig. 5.16.

extent of 16.9 Å in the same frame of reference as all previously discussed results at the Mn $L_{2,3}$ absorption edges. The top magnetic dead layer shows a thickness of 5.4 Å in relation to the Pt/PtMnSb interface which is 1.1 Å smaller than the Mn specific dead layer. This nicely fits the results obtained by the direct depth profile comparison illustrated in Fig. 5.17(a). Here, the Pt specific upper magnetic boundary is positioned at marginally larger distance from the substrate than the Mn specific version.

An identical result is found based on the XRMR data obtained close to the Mn L_2 absorption edge at 648.4 eV. The Pt specific density depth profile is fixed within the Pt/PtMnSb interface based framework, leading to a nominal MgO interface shift by the same distance of 12.1 Å. In this additional exemplary depth profile comparison between Mn and Pt specific results shown in Fig. 5.17(e), the top PtMnSb interface as well as the capping Pt layer demonstrate a matching structural depth profile with minimal roughness deviations. An equivalent discontinuity of the substrate interface is observed due to the previously mentioned MgO surface quality issues. The Mn and Pt specific magnetooptical

depth profiles simulated based on these structural results are again presented in Fig. 5.17(d) revealing the well-established characteristic relation between both types of atomic magnetic moment. Here, the difference of the upper magnetic boundary position is 1.4 Å which is in perfect accordance with the calculated dead layer thickness. At the lower magnetic interface on the side of the MgO substrate the Pt specific boundary is positioned at a distance of 16.9 Å for the substrate, while the Mn specific result based on the 648.4 eV scan determined the lower boundary at a distance of 22 Å. The lower magnetic dead layer obtained at this energy at the Mn edge is therefore about 5 Å wider than the Pt specific dead layer. This is most probably a direct result of a pronounced static MPE in the interface region of this half-Heulser system. Here, the Mn specific ferromagnetism is reduced due to chemical alteration and interface induced disorder.

Figure 5.17(f) summarizes all $\Delta\beta$ depth profiles obtained for this sample. Here, the Pt specific magnetooptical $\Delta\beta$ depth profile is contrasted with the Mn specific depth profiles shown in Fig. 5.16. The overall depth profile shape is nearly identical with equivalent rms roughness values for both magnetic boundaries. The average magnetic dead layer at the MgO interface is found to have a thickness of 21 Å while the Pt depth profile shows a dead layer with an extent of 16.9 Å. The upper magnetic dead layer is marked in relation to the average structural Pt/PtMnSb interface position. Mirroring the boundary relation at the substrate interface, a slightly smaller Pt specific dead layer can be observed. It shows an extent of 5.4 Å while the Mn specific dead layer has a thickness of 6.5 Å, which is also based on the MPE in the Pt evoked by the Mn specific ferromagnetic characteristics of the half-Heusler structure losing its magnetic phase ordering in vicinity of the structural interface.

Summary of the magnetic reflectivity of PtMnSb

The following charts summarize the structural and magnetooptical depth profile parameters for all four samples discussed in this chapter. Table 5.1 specifies the PtMnSb thickness d_{PtMnSb} as well as the corresponding structural roughness on the side of the substrate σ_s and the capping layer σ_c. Furthermore, it sums up the optical

Table 5.1: Specific parameters of the averaged structural and magnetooptical depth profiles obtained from the XRR and XRMR asymmetry simulations.

XRMR simulation results [Å]

Sample	Series	d_{PtMnSb}	σ_s	σ_c	$d_{\mathrm{Mn,mag}}$	$\sigma_{\mathrm{Mn,mag(s)}}$	$\sigma_{\mathrm{Mn,mag(c)}}$
Pt_{RT}/PtMnSb	I	190.0	1.8	5.8	170.1	3.4	7.1
$Pt_{400\,^\circ C}$/PtMnSb	I	191.7	1.7	6.4	155.3	3.0	7.8
AlO_x/MgO/PtMnSb	II	207.9	4.5	6.5	172.3	5.7	5.8
Pt_{O_x}/PtMnSb	II	219.6	2.3	7.8	192.1	4.4	5.6

Mn specific magnetic dead layer results [Å]

Sample	Series	$d_{\mathrm{Mn,MDL(s)}}$	$\sigma_{\mathrm{Mn,mag(s)}}$	$d_{\mathrm{Mn,MDL(c)}}$	$\sigma_{\mathrm{Mn,mag(c)}}$	Mn mag. ratio [%]
Pt_{RT}/PtMnSb	I	2.8	3.4	17.1	7.1	89.5
$Pt_{400\,^{\circ}C}$/PtMnSb	I	4.6	3.0	31.8	7.8	81.0
AlO_x/MgO/PtMnSb	II	21.5	5.7	14.1	5.8	82.9
Pt_{O_x}/PtMnSb	II	21.0	4.4	6.5	5.6	87.5

Table 5.2: Specific parameters of Mn specific magnetic dead layers obtained from the XRR and XRMR asymmetry simulations.

and magnetooptical depth profile parameters obtained by the XRR and XRMR asymmetry simulations. The lateral extent of the Mn magnetic depth profile $d_{\mathrm{Mn,mag}}$ and the rms roughness values of the upper $\sigma_{\mathrm{Mn,mag(c)}}$ and lower magnetic boundary $\sigma_{\mathrm{Mn,mag(s)}}$ are tabulated. These parameters are the average over all XRR and XRMR simulations, respectively, based on all experiments at the various Mn $L_{2,3}$ absorption edge specific photon energies.

The Mn specific magnetic dead layer results can be found in Tab. 5.2. Here, the thickness of the magnetic dead layer at the substrate interface $d_{\mathrm{Mn,MDL(s)}}$ is listed as well as the lateral extent of the magnetic dead layer below the PtMnSb capping layer interface $d_{\mathrm{Mn,MDL(c)}}$. The corresponding roughnesses of these magnetic boundaries are listed in the column labeled $\sigma_{\mathrm{Mn,mag(s)}}$ and $\sigma_{\mathrm{Mn,mag(c)}}$, respectively. The ratio of magnetic Mn to nonmagnetic Mn within the PtMnSb layer is given according to the relative thickness of the combined magnetic dead layers $d_{\mathrm{Mn,MDL(s)}}$ and $d_{\mathrm{Mn,MDL(c)}}$ to the structural PtMnSb thickness d_{PtMnSb}.

The Pt_{O_x}/PtMnSb bilayer of the deposition series II exhibits a significantly larger magnetic dead layer at the substrate than the nominally identical bilayer of series I. This difference is attributed to the slightly varying substrate quality between both sample series as discussed at length in this chapter. The minimal oxygen contamination of the sputtering chamber, following the growth of the MgO capping, however does not negatively influence the extent of the magnetic dead layer at the Pt/PtMnSb interface. It can be assumed that the surface of the uncovered twin PtMnSb layer is therefore only negligibly exposed to oxygen, which is originating from the MgO sputtering plasma filling the chamber before the Pt deposition. The immediate surface purity of the PtMnSb half-Heusler structure is not negatively influenced which is confirmed by the analysis of the LY and TEY XAS data presented in section 5.6 of this work.

The specific parameters of the Pt specific magnetic dead layers obtained from the consecutive simulations of the XRR and XRMR asymmetry ratio, based on the scans performed at the Pt L_3 absorption edge, are summarized in Tab. 5.3. Here, the thickness of both magnetic dead layers at the substrate as well as the capping interface can be found for all sample systems discussed in this chapter. The rms roughness values of the corresponding magnetic bound-

Pt specific magnetic dead layer results [Å]

Sample	Series	$d_{\mathrm{Pt,MDL(s)}}$	$\sigma_{\mathrm{Pt,mag(s)}}$	$d_{\mathrm{Pt,MDL(c)}}$	$\sigma_{\mathrm{Pt,mag(c)}}$	Pt mag. ratio [%]
$\mathrm{Pt_{RT}/PtMnSb}$	I	2.7	3.4	13.9	8.6	91.2
$\mathrm{Pt_{400\,°C}/PtMnSb}$	I	2.0	3.1	21.9	7.0	87.2
$\mathrm{AlO_x/MgO/PtMnSb}$	II	9.0	2.3	46.4	10.3	73.4
$\mathrm{Pt_{O_x}/PtMnSb}$	II	16.9	6.1	5.4	5.0	89.9

Table 5.3: Specific parameters of Pt specific magnetic dead layers obtained from the XRR and XRMR asymmetry simulations.

aries are listed next to the specific dead layer extent. Here, the ratio of magnetic Pt to nonmagnetic Pt within the half-Heusler layer is given according to the relative thickness of the combined magnetic dead layers $d_{\mathrm{Pt,MDL(s)}}$ and $d_{\mathrm{Pt,MDL(c)}}$ to the structural PtMnSb thickness d_{PtMnSb}. In accordance with the direct comparison of the Mn and Pt specific $\Delta\beta$ depth profiles of all Pt/PtMnSb thin film systems presented in this chapter, the share of Pt in a ferromagnetically ordered state within the half-Heusler layer is slightly higher than the share of Mn contributing to the net magnetic moment of the PtMnSb layer. Both nominally identical bilayers covered by Pt deposited at room temperature show a Pt specific magnetic ratio which is about 2 % higher than the Mn specific one listed in Tab. 5.2.

The $\mathrm{Pt_{400\,°C}/PtMnSb}$ bilayer shows a considerably higher share of magnetized Pt which is 6 % above the obtained Mn ratio. This difference is presumably caused by the increased intermixing and structural disorder at the Pt/PtMnSb interface. Here, the MPE is complemented by the direct alloying in the transition zone. Magnetic Mn atoms induce a Pt spin polarization, extending the magnetic depth profile of the structurally intact PtMnSb structure into an adjacent layer, in which the Mn magnetic moments are arranged into a compensated state due to the Pt growth and intermixing induced structural alterations. The Mn spin polarization observable by XRMR is therefore suppressed in the transition zone and the magnetic boundary is shifted up to about 3 nm inside of the nominal PtMnSb structure. Due to the proximity induced spin polarization the Pt remains polarized in the first few monolayers of the Mn specific magnetic dead layer regions while the mechanisms mentioned above lead to the local reduction of the Mn specific spin polarization.

An inverse effect can be observed in the oxide covered PtMnSb thin film. The $\mathrm{AlO_x/MgO/PtMnSb}$ sample exhibits a significantly higher share of Mn than Pt contributing to the net magnetic moment. This difference of up to 9.5 % is attributed to the chemical alteration at the PtMnSb interface in combination with an increasing hybridization of Mn and O in the outermost atomic layers. Here, the ordering of the Mn magnetic moment is most likely sustained by a long range magnetic ordering based on Mn oxide impurities. At the same time, the Pt spin polarization vanishes in

this region due to the degradation of the half-Heusler structure in the upper region of the PtMnSb layer which is directly affected by the AlO_x/MgO capping.

PtMnSb thickness dependence

In this section, the PtMnSb thickness dependence of the magnetooptical depth profiles will be discussed in detail. All PtMnSb samples of varying thickness presented as part of this comparison have been deposited within the same deposition series. This is essential to guarantee a direct structural comparability in order to analyze the explicit thickness-dependent influences on the magnetic properties.

In Fig. 5.18, the simulated structural density and magnetooptical depth profiles are displayed for three PtMnSb layers of increasing thickness capped each with Pt at room temperature. The results for the Pt(2.7 nm)/PtMnSb(9.7 nm) bilayer is presented in red, while the results for the intermediate Pt(2.7 nm)/PtMnSb(16.2 nm) bilayer are presented in blue. The thickest bilayer of this series, with the density depth profile illustrated in yellow, consists of PtMnSb(21.7 nm) also covered with 2.7 nm of Pt. The black solid and dashed lines mark the magnetooptical $\Delta\beta$ depth profile of the corresponding bilayer systems. The XRMR analysis was preformed based on the hard XRR experiments conducted at the Pt L_3 absorption edge, at which the photon energy is tuned to the maximum dichroic response. The magnetooptical depth profiles discussed in this section are therefore Pt specific.

Here, the distance of the magnetooptical depth profile boundary in relation to the PtMnSb interfaces is illustrated by the vertical lines, with the type of lines corresponding to the depth profile of the respective half-Heusler thickness. The interface-sided boundary of the magnetooptical depth profiles is equivalent within a standard deviation of 1.6 Å. Therefore, the average distance of 9.4 Å in relation to the substrate interface is indicated by the black dashed line. The magnetooptical depth profile of the Pt(2.7 nm)/PtMnSb(9.7 nm) bilayer shows an upper boundary 96.8 Å above the substrate interface as indicated by the solid line. This relative abrupt decline of $\Delta\beta$ in relation to the distance from the substrate is centered 7 Å below the Pt/PtMnSb interface position determined by the structural XRR simulation. The magnetooptical depth profile is consequently marginally smaller than the structural PtMnSb density depth profile.

When the PtMnSb thickness is increased to 16.2 nm, the magnetic depth profile boundary at the substrate side is unchanged within the simulation accuracy as expected for samples produced under identical growth conditions within the sputtering process. The structural depth profile of the covering Pt layer is almost identical showing a smooth transition with a low roughness as discussed in

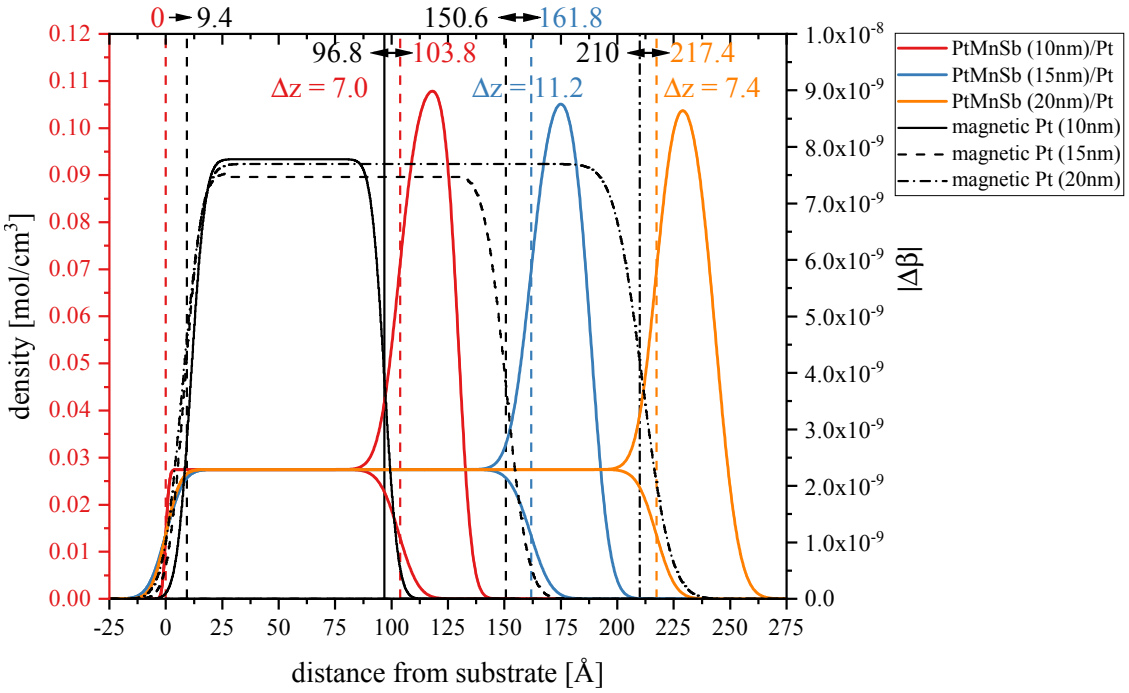

Figure 5.18: Comparison of simulated structural density and magnetooptical depth profiles obtained from the XRR and subsequent XRMR analysis at the Pt L_3 absorption edge of the Pt/PtMnSb bilayers with a nominal PtMnSb thickness of 10 nm, 15 nm and 20 nm. The exact interface position is indicated by the dashed line of the corresponding color. The boundary of the magnetic $\Delta\beta$ depth profile for each layer thickness is marked by the dashed line (average over all lower boundaries) on the substrate side and the line of the corresponding pattern on the Pt side.

chapter 2.4. However, the magnetooptical $\Delta\beta$ depth profile exhibits an upper boundary with a slightly higher distance of 11.2 Å in relation to the structural Pt/PtMnSb interface.

The last sample in this thickness series shows comparable structural top layer Pt as well as Pt/PtMnSb interface properties. The magnetic $\Delta\beta$ depth profile drops of at the Pt interface less abruptly due to the slightly higher roughness of the upper magnetic depth profile boundary. This leads to a marginal magnetic contribution of Pt atoms which are structurally allocate to the Pt top layer. Here, the nominal boundary of the $\Delta\beta$ depth profile is placed 7 Å below the structural Pt/PtMnSb interface.

At large, this thickness series confirms the existence of a small and sharply confined magnetic dead layer on both PtMnSb interfaces. The dead layer at the substrate interface has a size of 9.4 Å which is almost independent of the sample thickness as indicated by the relatively small standard deviation of 1.6 Å. In contrast, the Pt specific magnetic dead layer at the Pt/PtMnSb interface starts on average 8.5 Å below the structural interface with a slightly higher standard deviation of 2.3 Å. Therefore, one has to conclude that the extent of both Pt magnetic dead layers in relation to the structural interface position is nearly identical whereupon the upper boundary is marginally less consistent throughout the thickness series. However, the general form of the magnetooptical depth profile is consistent with a comparable share of magnetic dead layer at both PtMnSb interfaces as well as an almost constant $\Delta\beta$ plateau value of $\sim 7.5 \times 10^{-9}$ obtained from all XRMR simulations.

This picture of the thickness-independent Pt specific magnetic dead layer characteristic changes when the twin samples of this thickness series capped with AlO_x/MgO are analyzed by the same

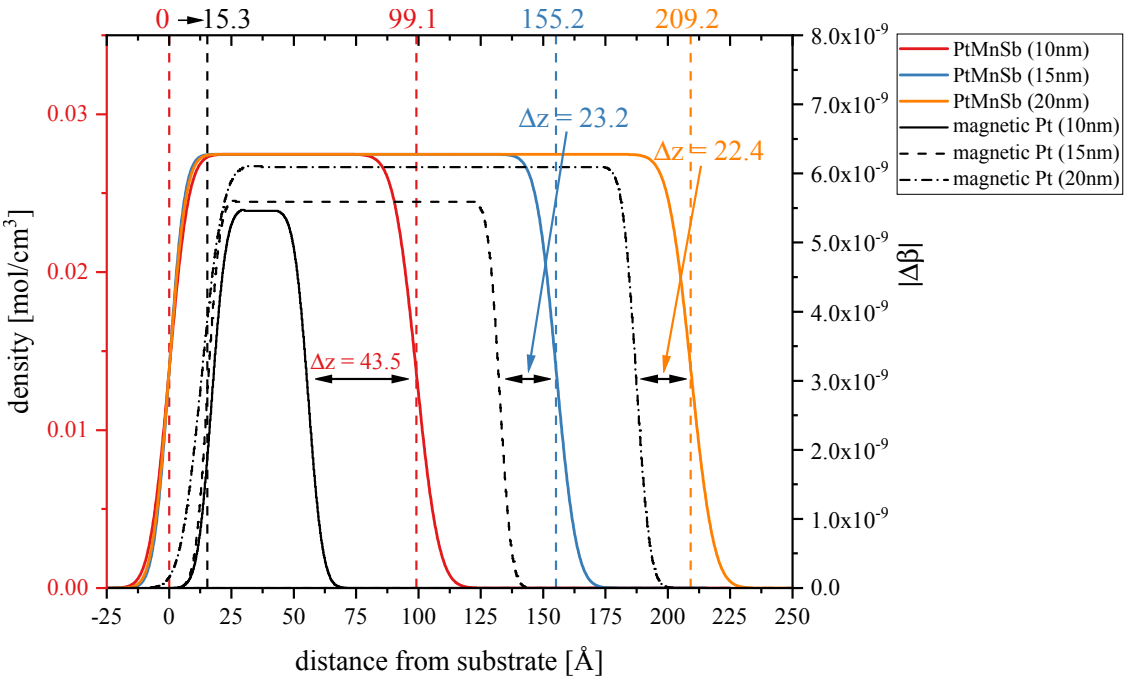

Figure 5.19: Comparison of simulated structural density and Pt specific magnetooptical depth profiles obtained from the XRR and subsequent XRMR analysis of the PtMnSb layers with a nominal thickness of 10 nm, 15 nm and 20 nm capped with AlO_x/MgO. The exact interface position is indicated by the dashed line of the corresponding color. The average boundary of the magnetic $\Delta\beta$ depth profile on the substrate side is marked by the dashed line. The distance of the upper depth profile boundary to the corresponding capping/PtMnSb interface is marked by the black arrows.

XRR and XRMR methodology. Figure 5.19 illustrates the results for this PtMnSb thickness series. Here, the magnetooptical depth profiles are again presented by the black lines with the type of lines indicating the affiliation with the structural density depth profile. The vertical dashed lines mark the exact position of the capping/PtMnSb interface. In relation to this position the black arrows mark the extent of the upper magnetic dead layer within the PtMnSb half-Heusler.

Regarding the structural density depth profile, the most striking difference, in comparison to the Pt capped samples, is the obtained thickness of the nominally equivalent PtMnSb layers. The nominal 10 nm PtMnSb sample capped with Pt exhibits an interface at a distance of 104 Å in relation to the substrate. On the contrary, the layer capped with AlO_x/MgO forms an interface at a distance of 99 Å. This discrepancy is consistent throughout the thickness series. While the 10 nm PtMnSb sample capped with AlO_x/MgO is structurally simulated to be 5 Å thinner than the Pt capped twin sample, the nominal 15 nm PtMnSb layer is about 7 Å thinner. The thickest nominal 20 nm layer forms an interface at a distance of 209 Å which is about 8 Å thinner than the Pt capped sample version. This structural difference potentially occurs based on atomic interdiffusion within the sputtering process or subsequent oxidation of the interface due to unintended *in situ* plasma oxidation during the MgO deposition process.

Overall, the magnetooptical depth profiles of the AlO_x/MgO capped samples are significantly narrower than those of the corresponding Pt capped twin samples. As for the Pt capped bilayer systems, the boundary of the Pt specific magnetic depth profile on the substrate side is equivalent throughout this thickness series.

The average bottom boundary distance is 15.3 Å from the substrate interface with a standard deviation of 2 Å. The magnetic dead layer on the substrate side is about 6 Å wider than for the Pt capped bilayers. Although this difference is only just outside the measurement accuracy, it is significant. However, the plateau value of these $\Delta\beta$ depth profiles is about 30 % lower than for the Pt capped series, which indicates an overall reduced magnetization. This is accompanied by a lesser magnetic response in the XRMR experiment and overall a smaller asymmetry ratio. Consequently, the XRMR simulations of the magnetooptical depth profile are based on data with a higher signal-to-noise ratio which can aggravate the exact determination of the dead layer boundary depending on the accuracy of the corresponding asymmetry feature fits.

Nonetheless, the Pt specific magnetic dead layer on the side of the AlO_x/MgO capping layer shows a significant dependency on the PtMnSb layer thickness. The thin nominal 10 nm layer exhibits an upper magnetic dead layer of 43.5 Å, while the thicker nominal 15 nm and 20 nm layers show a magnetooptical depth profile with an upper boundary about 23.2 Å, respectively 22.4 Å, below the structural interface position. This observation is in line with the analysis of the half-Heuser layer growth as discussed in relation to the PtMnSb thickness in chapter 2.4. The thinner 10 nm samples show the homogeneous Frank-van der Merwe growth mode (PtMnSb on PtMnSb) resulting in a closed layer. However, the TEM images reveal a transition zone at the interface as well as misoriented grains which leads to a defective quasi-amorphous interface. When the AlO_x/MgO capping layer is deposited on this imperfect half-Heusler structure, the more distinctive interdiffusion and oxidation interferes in the formation of the magnetic Mn lattice hampering the half-Heusler magnetism.

The thicker bilayer samples exhibit quasi layer-by-layer growth. The islands formed during the deposition are closed up with increasing thickness. The PtMnSb interface features merely some steps and dislocations with an almost perfect match to the Pt cover layer. This considerably reduces the interfacial roughness level and interdiffusion when the half-Heusler film is subsequently capped with AlO_x/MgO. The roughness of the magnetooptical depth profile is equivalent for all samples independent of thickness or capping layer. The lower boundary has an average roughness value of 5.3 Å with a standard deviation of 1.1 Å. Due to the different oxidizing capping layer, the upper magnetoopical boundary shows a higher variation with an average roughness of 5.6 Å and a standard deviation of 2.1 Å.

Magnetic dead layer based on the probe of the magnetic moment

The magnetic moment of various sputter deposited PtMnSb bilayer series has been additionally investigated by SQUID and

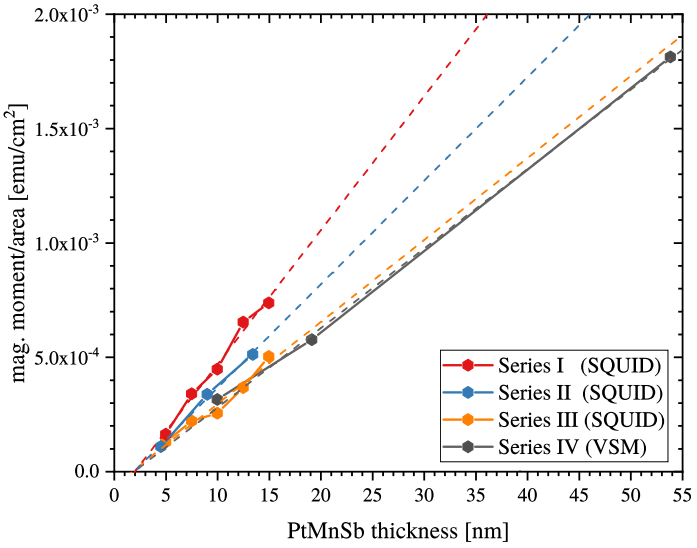

Figure 5.20: Plot to determine the magnetic dead layer thickness within PtMnSb films. The magnetic moment of various PtMnSb sample series is obtained from SQUID or VSM measurement. Each area-normalized series is independently processed by linear least-square fitting. The intercept of the linear fit on the x-axis determines the combined thickness of the top and bottom magnetic dead layers.

VSM experiments. Figure 5.20 shows the area normalized thickness-dependent results for three PtMnSb sample series of varying half-Heusler thickness subjected to SQUID experiments and one series analyzed by VSM measurements. Here, the linear extrapolation to the x-axis can be utilized to determine the overall magnetic dead layer thickness of each deposition series directly as the intercept. Series I and III as well as the series probed via VSM (IV) are PtMnSb layers capped with the heavy metal Pt, while series II is capped with AlO_x/MgO. This method of determining the correct magnetic dead layer thickness is less accurate than the XRMR based methods, mainly do to the relatively high error associated with the magnetic moment in the VSM experiments of up to 5 % and the series specific normalization of each obtained moment relative to the measured area of the probed sample cut.

The average magnetic dead layer thickness determined over all plotted series is 1.88 nm with a standard deviation of 1.1 Å. Notably, the series based on AlO_x/MgO capped PtMnSb layers (II) shows a combined dead layer thickness of 1.90 nm, which is about 0.2 Å wider than the averaged value for the Pt_{RT}/PtMnSb bilayers. This can be seen when the x-axis intercept region of these plots is significantly enlarged as presented in Fig. 5.21. Here, Fig. 5.21(b) is a close-up of Fig. 5.20, highlighting the x-axis intercept of each series fit. The intercept region is further enlarged in Fig. 5.21(a) to illustrate the obtained thickness values of the PtMnSb magnetic dead layers for each sample series. In both graphics, the grey shaded region indicates the range of obtained magnetic dead layer thicknesses by this method based on all SQUID and VSM series.

The Pt_{RT}/PtMnSb bilayers analyzed by the linear extrapolation presented in Fig. 5.21 have been prepared under the same sputter deposition conditions as the sample featured in Fig. 5.5 in chapter 5.2.1. The structural density and magnetooptical depth profiles obtained from the XRR and subsequent XRMR analysis of the Pt_{RT}/PtMnSb bilayer, which is the basis of this summarizing illus-

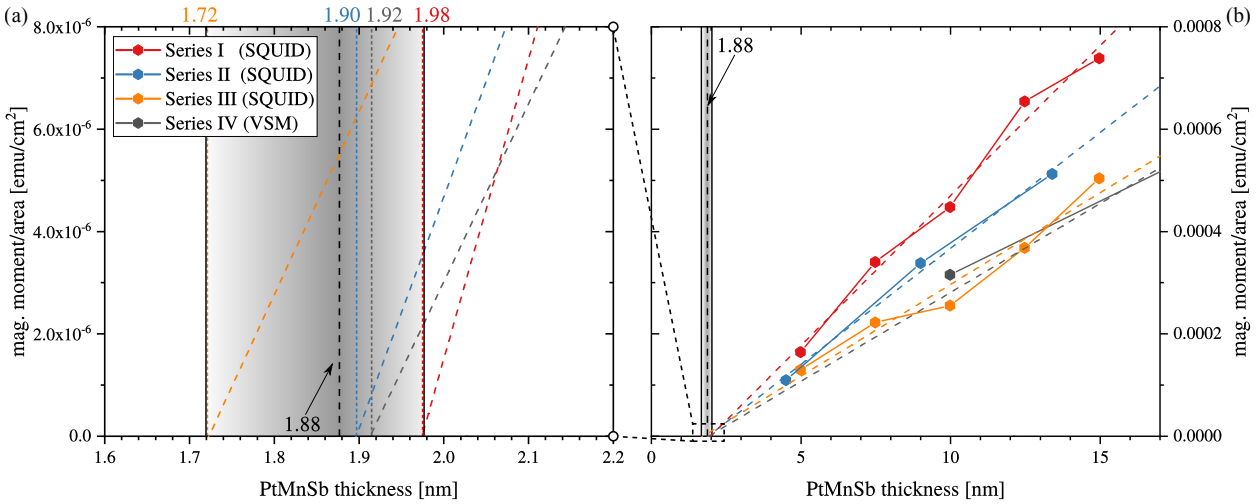

Figure 5.21: The graphic (b) is a close-up of Fig. 5.20 highlighting the x-axis intercept of each series fit. This specific region is again enlarged in the plot (a), illustrating the specific obtained thickness values of the PtMnSb magnetic dead layers. The mean x-axis intercept is located at a thickness of 1.88 nm while the range of obtained dead layer thicknesses using these SQUID and VSM series is indicated by the grey shaded region.

tration, shows a layer specific combined magnetic dead layer of 19.9 Å. In particular, the Mn specific magnetic depth profile shows a dead layer of 2.8 Å at the substrate interface and a dead layer of 17.1 Å at the Pt/PtMnSb interface. The combined magnetic dead layer thickness is therefore in accordance with the thickness obtained from the extrapolation of the plot of the thickness dependent magnetic moment.

Here, the methodical accuracy has to be considered in the evaluation of the obtained magnetic moment as well as the series, respectively linear fit, specific error in the localization of the x-axis intercept. The averaged standard error of the linear regression regarding the intercept position is about 0.4 Å. However, one has to consider the measurement accuracy which yields a combined variable uncertainty of about 1.7 Å. Thus, the value and corresponding margin of error obtained by identifying the intercept point is (1.88 ± 0.17) nm which is in accordance with the combined extent of both magnetic dead layers (1.99 nm) within the simulated magnetic depth profile of Fig. 5.5. The XRMR investigation of the Pt_{RT}/PtMnSb bilayer system is therefore within the margin of error of the magnetic dead layer determination based on this alternative probe of the magnetic moment.

Comparison of XRMR and XMCD results

The total electron yield XAS, luminescence yield XAS as well as both corresponding XMCD spectra at the Mn $L_{2,3}$ absorption edge of the Pt_{RT}/PtMnSb bilayer are summarized in Figure 5.22(a). The XMCD signals shown here, based on the TEY and LY, are multiplied by a factor of 2 to allow for a comparison of the distinct spectral features. Here, the XMCD spectrum is defined as $I_+ - I_-$, with I_+ and I_- specifying the absorption intensity based on a parallel and antiparallel direction of the magnetization, opposite

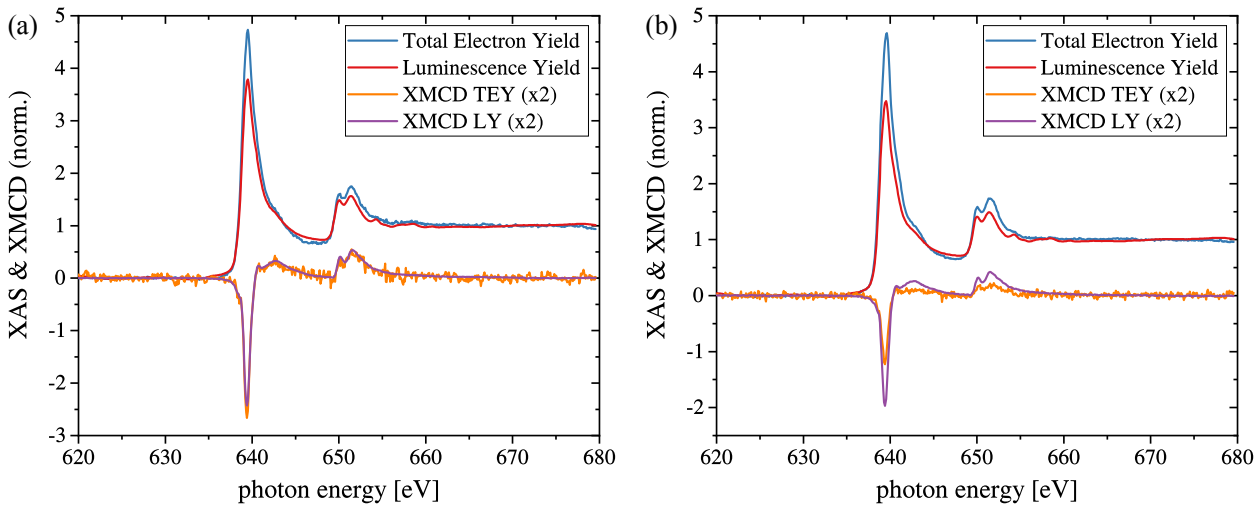

Figure 5.22: (a) Mn x-ray absorption near-edge spectrum of the Pt_{RT}/PtMnSb bilayer, measured by TEY and LY. The corresponding XMCD signals derived from TEY and LY are multiplied by 2 to compare the distinct spectral shape. (b) XAS and XMCD data (TEY and LY) at the Mn edge of the $Pt_{400\,°C}$/PtMnSb bilayer.

to the majority spin direction, in relation to the photon spin. The XMCD spectra obtained by TEY are inverted to allow for a direct comparison with the LY results.

An unambiguous multiplet structure can be observed in both Mn $2p$ XAS spectra shown in Fig. 5.22(a). These near-edge Mn $L_{2,3}$ spectra consist of characteristic features representing the absorption in the core excitation regions. The Mn $2p_{3/2}$ core excitation produces a distinct peak structure at the Mn L_3 absorption edge. This sharp XAS peak shows a pronounced shoulder structure towards higher photon energies. Both TEY and LY spectra form a clear doublet structure at the Mn L_2 absorption edge which is a general feature of the Mn $2p_{1/2}$ core excitation. This overall shape of the Mn near-edge region is characteristic of the Mn-Sb covalent bonding in the PtMnSb compound.

The XMCD spectra, derived from the TEY and LY absorption measurements, are presented together with the XAS data in Fig. 5.22(a). Here, a sharp negative peak is visible at the $2p_{3/2}$ core excitation region. This feature is followed by a smaller positive peak structure following the L_3 absorption edge towards higher energies in the same excitation region. In the subsequent $2p_{1/2}$ core excitation region, the XMCD signal shows a small positive double peak feature similar to the one observed in the XAS curve. This overall significant XMCD spectrum is characteristic of the large Mn specific magnetic moment in the probed PtMnSb layer which has a theoretical moment of about 3.8 μ_B per Mn atom based on the *ab initio* calculations discussed in chapter 1.7.

The *ab initio* calculations by Kimura *et al.* of the XMCD spectra for this Mn transition, based on the assumption of a magnetized high spin Mn $3d^5$ configuration in the ground state, reproduce the essential features presented here. Furthermore, these spectra can be analyzed based on the DOS and band hybridization which is discussed in detail for this specific PtMnSb structure in chapter 1.7. In general, the occupation and spin polarization of the ground

states as well as the orbital contribution to the magnetic moment have a direct influence on the spectral shape of the Mn 2p signal.

First-principles calculations to determine the spin polarized density of states of the PtMnSb compound reveal a significant intra-atomic exchange splitting of the Mn 3d states. This gives rise to a nearly occupied majority spin state as well as a nearly unoccupied minority spin state. As stated in chapter 1.7 of this work on the clarification of the spin-dependent electronic structures of the PtMnSb half-Heusler, the Ni 3d and Pt 5d states are almost fully occupied for both spin directions. Additionally, just as the spin-orbit splitting, electrostatic interactions, DOS and corresponding bandwidth, the band hybridization plays an important role for the interpretation of features of the XAS and XMCD signals. In this material the hybridization between the minority-spin Mn 3d and the Ni 3d or Pt 5d states has to be considered as weak. Additionally, the hybridization between the neighboring Mn atoms is equally small based on the large atomic distance.[9] This leads to a narrow bandwidth of the unoccupied minority spin state[10] which is visible in the narrow spectral shape of the Mn $L_{2,3}$ absorption edge of the Pt/PtMnSb bilayer as seen in Fig. 5.22. The direct comparison with the *ab initio* calculated signal shows that all basic features of the obtained spectra for the PtMnSb sample can be qualitatively found in the simulated Mn 2p XAS and XMCD spectra which assume a high spin-polarized Mn $3d^5$ ground state configuration.

Figure 5.22(b) illustrates XAS and XMCD at the Mn $L_{2,3}$ absorption edge of the $Pt_{400\,°C}$/PtMnSb bilayer. The overall shape of the XAS curve is identical to the previously discussed spectra in both Mn $2p_{3/2}$ and $2p_{1/2}$ core excitation regions. However, the XAS signal obtained by luminescence yield is slightly smaller compared to the sample capped with Pt grown at room temperature. More significantly, the XMCD spectra obtained via the different detection modes are different for this bilayer. This is particularity noticeable since those TEY and LY are almost identical for the standard Pt/PtMnSb bilayer, as seen in 5.22(a), with the exception of a higher signal-to-noise ratio of the LY signal. Here, the probing depth of the spectroscopy mode has a significant impact on the obtained spectra since the magnetic characteristics of the surface region and in particular the Pt/PtMnSb interface is dominating the TEY response. The reduced XMCD signal clearly indicates a reduced Mn spin polarization at the top of the PtMnSb layer when the Pt is deposited at higher temperatures. This result is in good agreement with the XRMR based analysis of the magnetic depth profile presented in section 5.2.3. A detailed analysis of the XMCD spectra based on the sample magnetization relation to the probing depth of both modes is outlined in the next section 5.7 of this chapter.

For both samples discussed so far, a clear multiplet contribution can be observed at the Mn $L_{2,3}$ absorption edge. This aspect is subject to significant change when the PtMnSb is covered by AlO_x/MgO instead of Pt. Figure 5.23(a) shows XAS and XMCD

[9] A. Kimura, S. Suga, T. Shishidou, S. Imada, T. Muro, S.-Y. Park, T. Miyahara, T. Kaneko, and T. Kanomata. Magnetic circular dichroism in the soft-x-ray absorption spectra of Mn-based magnetic intermetallic compounds. *Phys. Rev. B*, **56**(10):6021 (1997)

[10] S. Youn and B. Min. Effects of the spin-orbit interaction in Heusler compounds: Electronic structures and Fermi surfaces of NiMnSb and PtMnSb. *Phys. Rev. B*, **51**(16):10436 (1995)

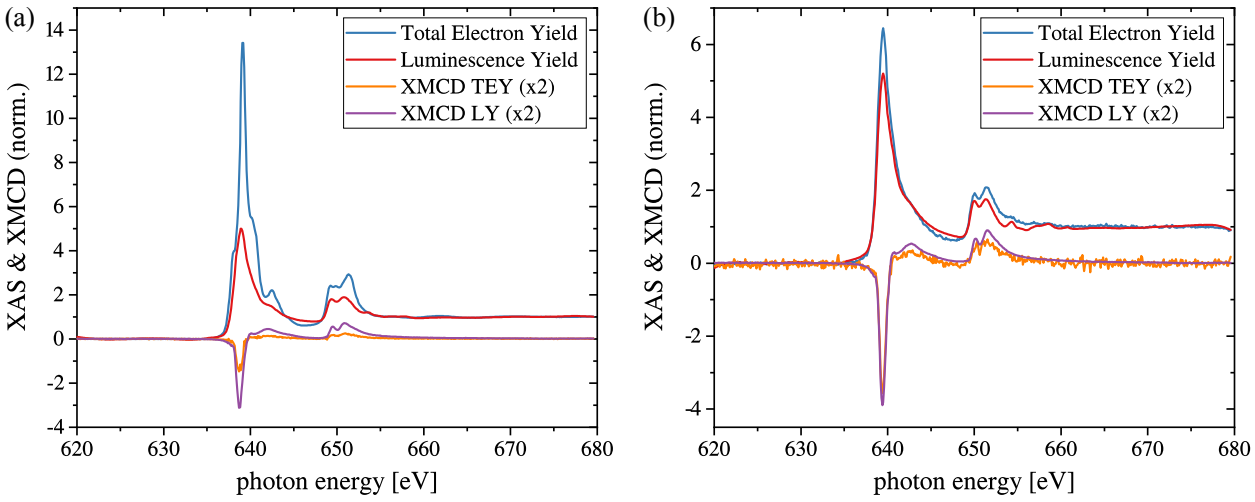

Figure 5.23: (a) Mn x-ray absorption near-edge spectrum of the PtMnSb layer capped with AlO_x/MgO measured by TEY and LY. The corresponding XMCD signals derived from TEY and LY are multiplied by 2 to compare the distinct spectral shape. (b) XAS and XMCD data (TEY and LY) at the Mn edge of the Cr buffered Pt_{RT}/PtMnSb bilayer.

spectra of the AlO_x/MgO/PtMnSb sample obtained by TEY and LY measurements. Both spectra exhibit significant deviation from the observed spectral structure of the Pt capped samples mainly due to the modifications of the Mn electronic properties. The XAS signal still shows a multiplet contribution, however the peak shape, in particular at the L_2 absorption edge, deviates from the spectra of the Pt covered PtMnSb layers. This indicates a variation of the Mn 3*d* states when checked against a perfect PtMnSb structure with a clean interface. The cover layer of MgO and AlO_x alters the chemical bonding of the Mn in the interface region. When the XMCD spectra are compared to the previously discussed dichroic response of the Pt capped layers, a significant reduction of the signal intensity can be observed. This results from the MgO in direct contact to the top PtMnSb layer which leads to a chemical interaction with the Mn changing the electronic and magnetic properties. The dominant Mn-Sb hybridization is altered due to the Mg and O interdiffusion diluting the characteristic multiplet structure. Here, the reduced XMCD signal leads to the assumption of a vanishing magnetization in the PtMnSb interface region, especially since the TEY signal is about a factor of 2 weaker than the LY XMCD response. Only the spin-polarized Mn states within the PtMnSb contribute to the observed dichroism. There is no change of the essential features of the XMCD spectrum, merely a reduced intensity due to the antiferromagnetic or paramagnetic compounds forming in the interface region. The most probable candidates are Mn oxides which do not significantly contributed to the dichrioic response.

Additionally, peaks and variations of the shoulder profiles in both core excitation regions are visible in the XAS signals. These most likely emerge due to the chemically altered interface region. The TEY result shows typical features related to the formation of Mn oxides, predominately in the shoulder region of the Mn L_3 absorption edge. The 3*d* electrons in these insulating Mn oxides are less itinerant and therefore the overall structure of the Mn

Spin and Orbital Magnetic Moment [μ_B]

Sample	Series	m_{spin} (LY)	m_{spin} (TEY)	$m_{orb.}$ (LY)	$m_{orb.}$ (TEY)
Pt_{RT}/PtMnSb	I	1.81	1.34	-0.23	-0.06
$Pt_{400\,°C}$/PtMnSb	I	1.54	0.55	-0.19	0.01
AlO_x/MgO/PtMnSb	II	1.55	0.33	-0.24	0.01
Pt_{RT}/PtMnSb/Cr	III	2.08	1.34	-0.29	0.04

Table 5.4: Spin and orbital magnetic moment obtained via sum rule analysis of XAS and XMCD Mn $L_{2,3}$ absorption edge spectroscopy performed at room temperature.

$2p$ XAS is much more narrow. Depending on the Mn oxidation state additional peaks appear in the XAS curve, while the one in the L_3 shoulder is characteristic for the Mn^{2+} oxidation state. The reduced XMCD signal and the change of the $2p_{3/2}$ and $2p_{1/2}$ features suggests a combined contribution to the XAS response of a structurally intact PtMnSb main and a chemically and magnetically altered interface layer. The exact size of the PtMnSb interface layer can be estimated based on the XRMR results presented in chapter 5.2.5 and a comparison of the LY and TEY result for each sample which is discussed in section 5.8.

Figure 5.23(b) shows XAS and XMCD spectra obtained in TEY and LY detection mode at the Mn edge of the Pt/PtMnSb bilayer buffered with a 30 nm Cr layer. The Pt capping layer was deposited at room temperature. This sample is structurally equivalent to the one probed to obtain the spectra presented in Fig. 5.22(a), with the exception that the PtMnSb layer is separated from the MgO interface. This buffer layer can improve the crystallinity and structural quality of the epitaxial interface layer. It further prohibits intermixing and chemical alteration of the interfacial surface layer which induces magnetic disorder in the immediate interface region as revealed by the small magnetic dead layer obtained from the XRMR analysis in chapter 5.2.1. As expected, the overall spectral shape of XAS and XMCD spectra for the Cr buffered bilayer is nearly identical to the standard sample. The only noticeable difference is the slightly increased XMCD signal of the buffered sample which implies a larger Mn atomic moment in the half-Heulser compound. This can be due to a reduction of the small dead layer at the interface as well as a marginally higher structural ordering which directly translates to an enhanced saturation magnetization and accordingly a higher overall Mn specific atomic moment in the PtMnSb.[11] The spin and orbital magnetic moment of the different PtMnSb half-Heusler systems, determined based on the Mn $L_{2,3}$ XAS and XMCD spectra of the differently deposited sample systems, are listed in Tab. 5.4.

[11] Z. Wen, T. Kubota, and K. Takanashi. Optimization of half-Heusler PtMnSb alloy films for spintronic device applications. *J. Phys. D: Appl. Phys.*, **51** (43):435002 (2018)

Comparison of the XRMR and XAS based optical results

The obtained x-ray absorption spectra can be utilized to determine the optical constants based on tabulated energy-dependent atomic scattering data.[12] The atomic scattering factors are the basis for the calculation of the refraction index for a defined compound material such as PtMnSb. Those element specific values are obtained from an experimental measurement of the atomic photoabsorption cross section. These absorption measurements provide values for the imaginary or absorptive part of the atomic scattering factor. The real or dispersive part is calculated from these absorption measurements using the Kramers-Kronig integral relations as defined in Eqs. (1.24) and (1.25).

[12] B. L. Henke, E. M. Gullikson, and J. C. Davis. X-ray interactions: photoabsorption, scattering, transmission, and reflection at $E = 50$ - $30,000$ eV, $Z = 1$ - 92. *Atomic data and nuclear data tables*, **54** (2):181–342 (1993)

In general, the optical constants are highly sensitive to the atomic configuration and thus the immediate atomic environment, e.g., in a specific compound. The interaction with neighboring atoms creates a fine structure which is smoothed out in the tabulated data. In the vicinity of an absorption edge, the absorption intensity spectra shows significant deviations, most noticeable the Henke table does not yield an L_2 edge jump. This uncertainty of the optical data tables in this near-edge region, based on the atomic like assumptions, has to be corrected by a precise determination of the optical constants for the Pt/PtMnSb bilayer system. The Pt/PtMnSb bilayers serve as a prime example for this procedure, since a wide range of XRR and XRMR measurements at multiple energies close to the Mn absorption edges allow for an in-depth comparison of XRR optical depth profiles and absorption spectroscopy results.

In this work, the Mn x-ray near-edge absorption spectrum is measured for two opposite circular polarizations with an applied magnetic field of 0.5 T. The LY spectrum measured for the Pt_{RT}/PtMnSb bilayer can be adjusted to fit the edge jump and slope of the absorptive part β calculated based on the tabulated data for the corresponding PtMnSb compound. This XAS based refinement of the calculated energy-dependent β values is illustrated in Fig. 5.24(b). Here, compound specific literature values of the absorption coefficient β are shown in grey while the XAS, illustrated in green, is adjusted to fit the theoretical edge jump and slop. In a next step the literature values are replaced in the near-edge region ($620 - 680$ eV) by the adjusted XAS based β values. The result is shown in Fig. 5.24(a) with the tabulated values for the PtMnSb compound presented in a wider range from 400 to 1200 eV. Additionally to the XAS correction at the Mn L_2 and L_3 absorption edges, these values are marginally adjusted to fit the β value obtained from the off-resonant XRMR measurement at 1000 eV. The simulation of the off-resonant reflectivity thus serves as gauge to calibrate the measured absorption data. In both graphics, Figs. 5.24(a) and (b), the β results obtained from the XRR simulations at the Mn absorption edges are shown by the orange dots.

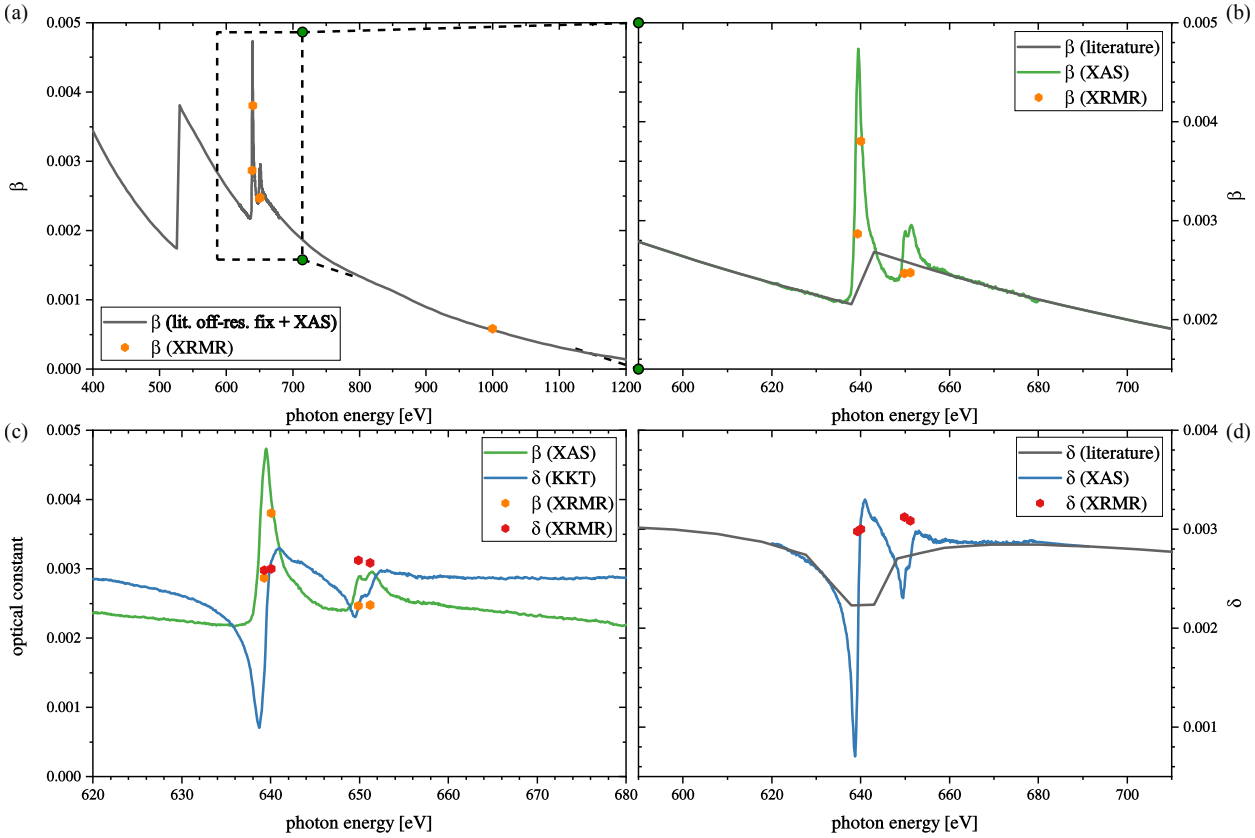

Figure 5.24: (a) Optical constant β of PtMnSb based on the element specific tabulated index of refraction [Henke et al., 1993]. These values are slightly adjusted to match the obtained results of the off-resonant XRMR scan and corrected at the Mn $L_{2,3}$ absorption edge by the XAS data. (b) The literature values of the absorption coefficient β and the XAS data adjusted to fit the theoretical edge jump and slop. (c) The optical constants β derived from the XAS data and δ calculated by the Kramers-Kronig transformation. The results obtained from the XRR simulations are shown by the orange and red dots, respectively. (d) The literature values of the dispersion coefficient δ derived by the Kramers-Kronig transformation and adjusted to fit the theoretical progression.

These determined constants of the absorptive part, corresponding to the plateau values of the optical β depth profile given by the XRR simulation, nicely fit the XAS corrected literature values.

The optical constant δ, representing the dispersive part, is derived by means of the Kramers-Kronig transformation as discussed in chapter 1.1.3. Therefore, the obtained XAS is normalized and slope corrected to get rid of experimental offsets. The resulting absorption data is fitted to the theoretical edge jump and subsequently the Kramers-Kronig transformation is performed. The resulting curve of the real part of the refractive index at the absorption edges is then adjusted to fit the broader curse of the tabulated δ values for the PtMnSb compound. This corrected δ spectrum is shown in Fig. 5.24(d) and significantly refines the characteristics of the tabulated δ data at the absorption edge. Here, the δ values obtained from the various XRR simulations at the specific energies, detailed in Fig. 5.4, are shown by the red dots. These are the plateau values of the simulated optical δ depth profile representing the PtMnSb layer. The optical δ and β depth profiles obtained from the XRR simulation at a specific photon energy of 640.1 eV for the Pt(3.2 nm)/PtMnSb(19.0 nm) bilayer is shown in Fig. 5.3. The optical depth profiles form a distinct plateau between the PtMnSb//MgO and the Pt/PtMnSb interface, defining the PtMnSb specific optical parameters. Since the XAS is normalized to the Mn specific edge, which dominated the energy-dependent course, the contributions to

the spectrum by the MgO substrate and the thin Pt cover layer are accounted for when the spectrum is adjusted to the tabulated data.

Figure 5.24(c) summarizes the results of the absorption spectroscopy and subsequent determination of the optical constants. It shows the optical parameter β derived from the XAS data and the near-edge course of δ calculated by the Kramers-Kronig transformation. The results obtained from the XRR simulations are illustrated by the orange and red dots, respectively. Here, all optical parameters determined based on the optical depth profiles are close to or in good agreement with the XAS and literature based calculation.

Comparison of the XRMR and XMCD based magnetooptical results

This section serves to compare the XRMR and XMCD based results with regard to the magnetic characteristic of the presented PtMnSb thin films. The obtained depth profiles are checked for consistency with the parameters determined by XAS and the obtained magnetic dead layers are validated in accordance with the TEY and LY dichroic responses as theoretically described in section 1.3 of this work. By following the derivation of Eq.(1.89), the optical constant $\Delta\beta$ can be determined directly based on the XMCD spectrum in the LY mode which is a bulk sensitive direct transmission probe as presented in chapter 1.1.1.

Figure 5.25 illustrates the combined XRMR and XMCD results obtained in the LY mode for the PtMnSb(19.0 nm) sample covered with Pt(3.2 nm) deposited at RT. The structural density depth profile and the magnetooptical depth profile $\Delta\beta$, which has already been discussed in section 5.2.1, is shown in Fig. 5.25(a). The detailed analysis of the absorption spectroscopy results is illustrated on the right side of this graphical compilation. Fig. 5.25(b) shows the Mn x-ray absorption near-edge spectrum measured by LY using circularly polarized light at an angle of incidence of 30° and with an applied magnetic field of 0.5 T. The XMCD signal is generated by switching the light helicity at each point of photon energy. The dashed red line below the XAS signals for both helicities I_+ and I_- represents the standard background which consists of a defined step at each absorption edge. The background is subtracted for the process of sum-rule calculation to quantify the magnetic spin and orbital moments. Each step of the background is centered at the inflection point of the XAS signal while the step ratio is fixed at 2:1. The resulting background subtracted and angle of incident as well as polarization corrected XAS spectrum are shown in Fig. 5.25(a). This signal is subsequently integrated to determine the parameter r which represents a central factor in the sum-rule analysis as discussed in chapter 1.1.1.

The corresponding XMCD difference signal is shown in Fig. 5.25(d). It completely matches the spectral shape of the PtMnSb reference

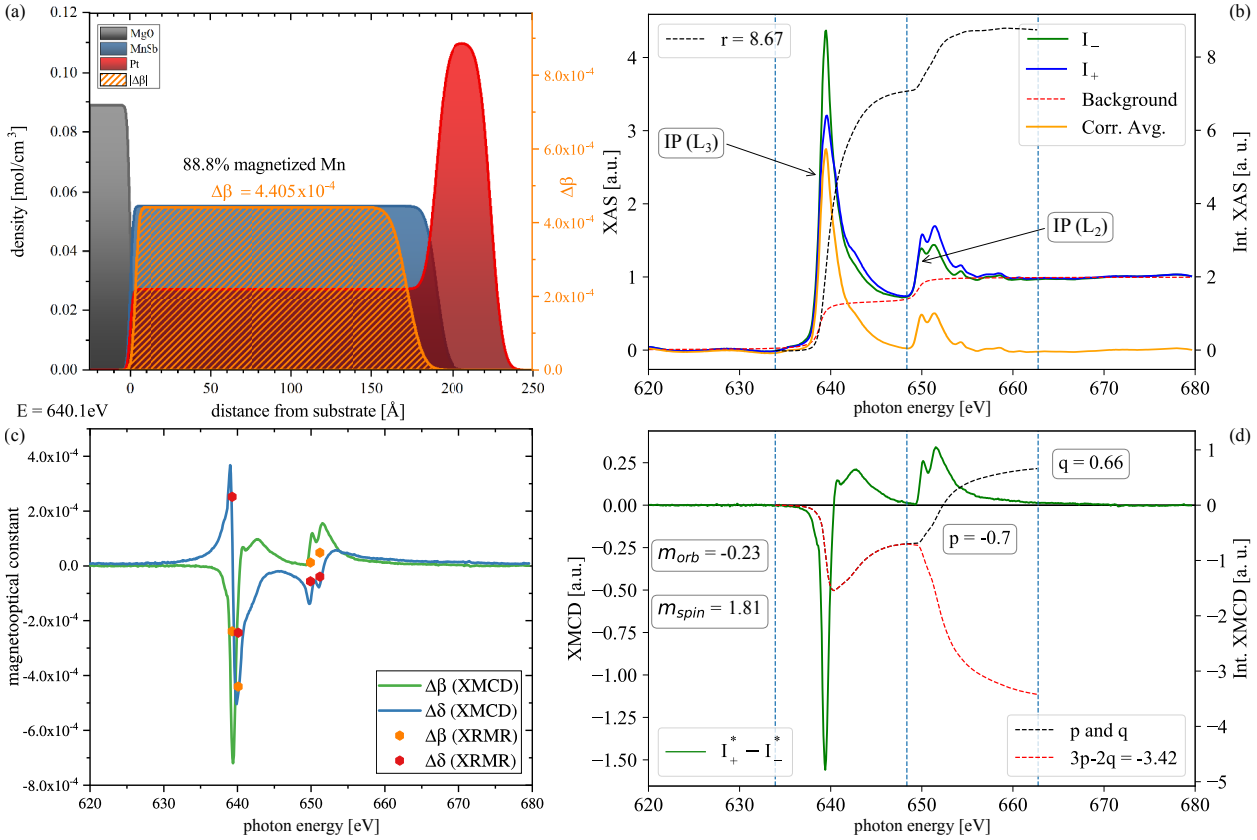

Figure 5.25: (a) Structural density and the magnetooptical $\Delta\beta$ depth profile of the PtMnSb(19.0 nm) sample covered with Pt(3.2 nm) deposited at RT. (b) Mn x-ray near-edge absorption spectrum measured by LY for two opposite circular polarizations with an applied magnetic field of 0.5 T. The red line represents the standard two-step background which is subtracted for the sum-rule calculation and positioned based on the inflexion points on the low energy side of both L_3 and L_2 resonances. The dashed black line represents the integration of the corrected XAS spectrum. (c) The magnetooptical constants $\Delta\beta$ derived from the XMCD data shown in (d) and $\Delta\delta$ calculated by the Kramers-Kronig transformation. The results obtained from the various XRMR simulations are presented by the orange and red dots, respectively. The integrated p, q and r parameters are included in the sum rule equations.

signal discussed in chapter 1.7 and is subjected to the sum-rule analysis in order to determine the magnetic spin and orbital moments. The integrated XMCD signal over the L_3 edge and the combined L_3 and L_2 range, respectively, is given by p and q, as defined in Eqs. (1.4) to (1.6). The exact integration interval is marked by the vertical dashed lines, while the resulting integrated XMCD signal is shown in Fig. 5.25(b) with the obtained parameters p and q explicitly labeled. According to the sum-rules, the results have to be multiplied by the number of $3d$ holes given by $n_\mathrm{h} = (10 - n_{3d})$ which yields $n_\mathrm{h} = 4.64$ following the spin-polarized DOS calculations of chapter 1.7. The obtained corrected spin magnetic moment for the ferromagnetically ordered Mn in this Pt/PtMnSb bilayer is $m_\mathrm{spin} = (1.81 \pm 0.10)\ \mu_\mathrm{B}/\mathrm{atom}$ while the resulting orbital magnetic moment is $m_\mathrm{orb.} = (-0.23 \pm 0.10)\ \mu_\mathrm{B}/\mathrm{atom}$.

The magnetic depth profile presented as a result of the XRMR analysis in Fig. 5.25(a) displays a share of 88.8 % ferromagnetic Mn within the PtMnSb half-Heusler structure. Since the absorption spectroscopy in the LY mode probes the entire thin film sample, the average Mn specific spin magnetic moment within the magnetic depth profile determined by the XRMR analysis is significantly higher. Therefore, the corrected value, based on the share of magnetized Mn, for the spin magnetic moment in the determined magnetic region is therefore $m_\mathrm{spin} = (2.06 \pm 0.10)\ \mu_\mathrm{B}/\mathrm{atom}$.

Figure 5.25(c) shows the magnetooptical constants $\Delta\beta$ derived

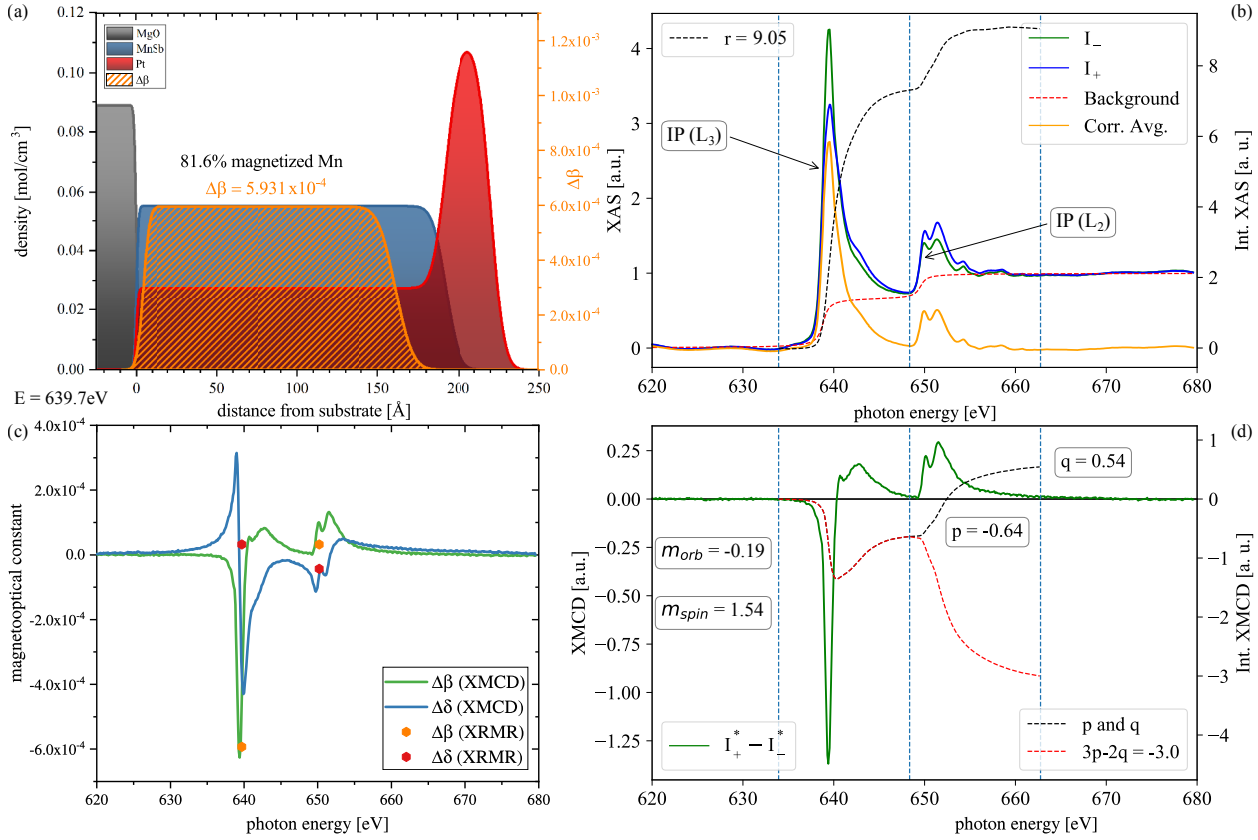

Figure 5.26: (a) Structural density and the magnetooptical $\Delta\beta$ depth profile of the $Pt_{400\,°C}$/PtMnSb bilayer. (b) Mn x-ray near-edge absorption spectrum measured by LY for two opposite circular polarizations with an applied magnetic field of 0.5 T. The red line represents the standard two-step background which is subtracted for the sum-rule calculation. The dashed black line represents the integration of the corrected XAS spectrum. (c) The magnetooptical constants $\Delta\beta$ derived from the XMCD data shown in (d) and $\Delta\delta$ calculated by the Kramers-Kronig transformation. The results obtained from the various XRMR simulations are presented by the orange and red dots, respectively. The integrated p, q and r parameters are included in the sum rule equations.

from the XMCD data shown in Fig. 5.25(d) and the corresponding $\Delta\delta$ constant calculated using the Kramers-Kronig calculus described in Eqs. (1.24) and (1.25). Here, the results are directly compared with the magnetooptical parameters obtained from the various magnetic reflectivity simulations which are presented in Fig. 5.5. These parameters, indicated by the orange and red dots, respectively, are in excellent agreement with the magnetooptical constants determined based on the XMCD spectra by means of Eqs. (1.81) to (1.90) which have been discussed previously in this chapter.

In an analog way, the $Pt_{400\,°C}$(2.8 nm)/PtMnSb(19.2 nm) bilayer was studied by means of XMCD. The results in comparison to the XRMR based structural and magnetic depth profile are shown in Fig. 5.26. Here, the presented $\Delta\beta$ depth profile obtained at a photon energy of 639.7 eV captures 81.6 % of the PtMnSb structural density depth profile. The sum-rule analysis, determining the spin and orbital magnetic moment, is illustrated in Fig. 5.26(d). It yields a spin magnetic moment for the ferromagnetic Mn in this Pt/PtMnSb bilayer of $m_{\mathrm{spin}} = (1.54 \pm 0.10)\ \mu_{\mathrm{B}}$/atom while the orbital moment is calculated to be close to zero with a value of $m_{\mathrm{spin}} = (-0.19 \pm 0.10)\ \mu_{\mathrm{B}}$/atom. In combination with the depth profile of magnetized Mn in the half-Heusler, the share corrected value for the spin magnetic moment is $m_{\mathrm{spin}} = (1.89 \pm 0.10)\ \mu_{\mathrm{B}}$/atom, which is 8 % lower than the value obtained for the standard Pt/PtMnSb bilayer. Therefore, this value, which is

corrected for the extend of the Mn specific magnetic dead layers, shows a slightly reduced magnetic moment in the ferromagnetic phase of the PtMnSb thin film structure when the Pt cover layer is deposited at higher temperatures. In almost the same manner as the extended upper magnetic dead layer, this effect is probably caused by an increased intermixing inducing structural disorder in the half-Heusler system. However, the obtained difference of the share corrected magnetic moment is merely about 2 times higher than the experimental XMCD accuracy, which shows that the actual magnetized share of the PtMnSb forms a qualitatively identical magnetic phase while the main difference is the magnetic dead layer thickness at the Pt/PtMnSb interface which is highly significant as discussed in section 5.3.

The magnetooptical constants $\Delta\beta$ derived from the XMCD data are shown in Fig. 5.26(c). The corresponding $\Delta\delta$ values are calculated by the Kramers-Kronig transformation. The magnetooptical parameters obtained from the XRMR analysis of the bilayer system are again presented by the orange and red dots, which almost exactly fit the constants specified by the magnetic circular dichroism.

The XMCD experiment measured in the TEY mode is highly surface sensitive with a probing depth in a general range of 2 to 10 nm depending on material and surface properties. Although the fundamental scattering processes contributing to the electrons escaping from the sample as a result of the cascade process initiated by the initial absorption of a photon are exactly predictable, it is very difficult to account for all possible event combinations. Thus, the exact probing depth can usually only be roughly estimated especially for a complex oxide based capping structure.

In general, the XMCD signal obtained in TEY is consisting, on the one hand, of excited elastic photoelectrons as well as Auger electrons due to the core hole decay and, on the other hand, of lower energy electrons cascaded by inelastic scattering processes. These events determine the mean probing depth which is a combination of the escape distance of all type of electrons. Here, the elastic electrons are contributing notably based on the inelastic mean free path of the Auger electrons.[13] In the photon energy range close to the Mn L_2 and L_3 absorption edges the mean free path can be determined by the universal curve of the mean free path of electrons in solids as a function of their energy. This curve shown in Fig. 5.27 provides values of about 10 Å. The contribution of the lower energy electrons to the probing depth is however crucially dependent on the material since the transport properties of these electrons vary in particular between metal or insulator systems.

For instance, low energy electrons are able to lose energy through inelastic scattering processes in metal systems when interacting with valence-band electrons. When the electrons are excited in an insulator material, low level conduction band electrons exhibit no effective mechanism to lose energy, e.g., via a scattering process. In case these conduction band electrons are positioned above the

[13] S. Gota, M. Gautier-Soyer, and M. Sacchi. Fe 2*p* absorption in magnetic oxides: Quantifying angular-dependent saturation effects. *Phys. Rev. B*, **62**(7):4187 (2000)

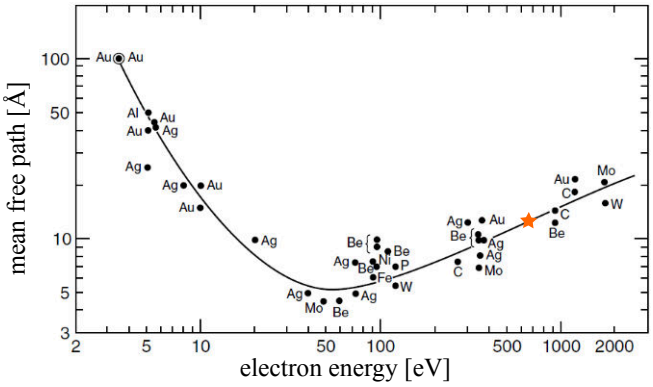

Figure 5.27: Universal curve of the escape depth as a function of the electron kinetic energy based on Ref. [Somorjai, 1981]. The orange star marks the relevant value for the Mn $L_{2,3}$ absorption edge.

vacuum level, they can be emitted from the sample and increase the total electron yield. This is a common process in material systems featuring a large band gap. This shows that the TEY probing depth is a highly material-dependent characteristic especially in thin films systems combining various metallic, half-metallic and insulating layers.

When calculating the Auger electron range (AER) in a system, one has to take into account the electron stopping power of the material initiating the inelastic scattering processes. As shown by Ashley *et al.* the energy-dependent stopping powers are comparable for various metals.[14] The effective ranges for Auger electrons, defining the distance over which one Auger electron of a specific energy interacts within the sample, in relation to the kinetic energy can be derived from the characteristic stopping power. It is shown by Frazer *et al.* that the direct contributions of Auger electrons to the TEY signal in metals such as Cr is relatively small. In the soft x-ray regime, primary Auger electron experience a substantial energy loss within 5 Å of the sample surface. Here, the AER is one of many factors characterizing the maximum probing depths. In systems with a pure insulating capping layer the low energy electrons are unable to interact with the valence band electrons in a scattering process as it is the predominant mechanism in metals leading to a larger escape depth. Figure 5.29(b) shows the maximum probing depth (MPD) and AER as a function of Auger electron initial kinetic energy. It illustrates the close connection of the MPD to the AER for the lower energy range below ∼400 eV.

The divergence between the MPD and the AER with increasing core energy indicates a significant increase in the contribution from multiple electron scattering events at higher energies. In this total electron yield experiment at higher energies above ∼400 eV, the cascading electrons generated by inelastic scattering increases significantly for higher initial Auger electron kinetic energies of the soft x-ray regime. Thus, a precise specification of the Auger electron interactions with the top layer material of the thin film is important for a correct assessment of the MPD.

Here, another method to determine the exact MPD beyond a simple estimation of the AER is presented based on the detailed

[14] J. Ashley, C. Tung, R. Ritchie, and V. Anderson. Calculations of mean free paths and stopping powers of low energy electrons (⩽ 10 keV) in solids using a statistical model. *IEEE Trans. Nucl. Sci.*, **23**(6):1833–1837 (1976)

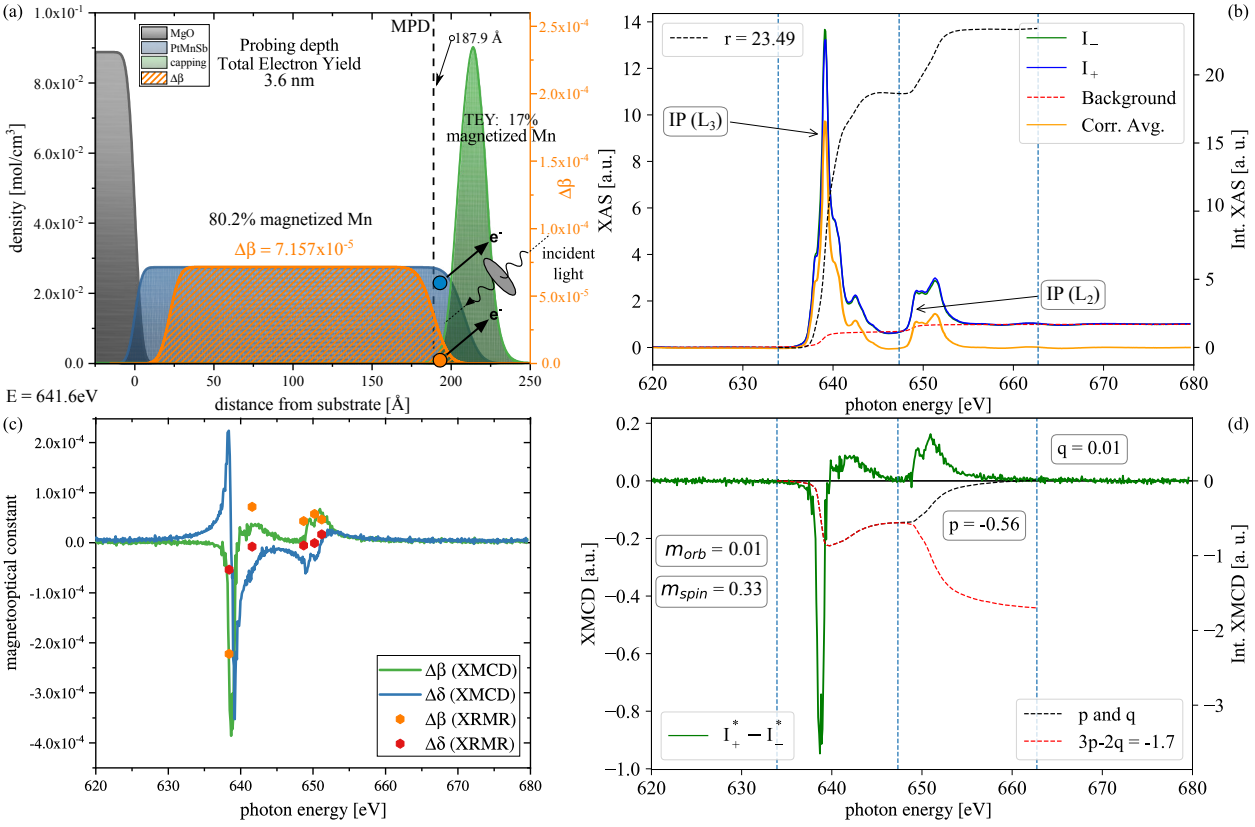

Figure 5.28: (a) Structural density and the magnetooptical $\Delta\beta$ depth profile of the PtMnSb(20.8 nm) sample capped with AlO_x/MgO. (b) Mn x-ray near-edge absorption spectrum measured by TEY for two opposite circular polarizations with an applied magnetic field of 0.5 T. The red line represents the standard two-step background which is subtracted for the sum-rule calculation. The dashed black line represents the integration of the corrected XAS spectrum. (c) The magnetooptical constants $\Delta\beta$ derived from the XMCD data shown in (d) and $\Delta\delta$ calculated by the Kramers-Kronig transformation. The results obtained from the various XRMR simulations are presented by the orange and red dots, respectively. The integrated p, q and r parameters are included in the sum rule equations.

evaluation of the magnetic depth profiles which have been determined by the XRMR analysis. Figure 5.28 shows the structural density depth profile and the corresponding magnetooptical $\Delta\beta$ depth profile of the PtMnSb(20.8 nm) sample capped with AlO_x/MgO in combination with the sum-rule analysis of the Mn x-ray near-edge absorption spectrum measured by the TEY method. Since the magnetic dead layers of this PtMnSb thin film are precisely determined by the XRMR analysis and the Pt/PtMnSb bilayers show coherent results in reflectivity and absorption spectroscopy, the exact probing depth of the TEY can be determined.

This process is exemplary visualized in Fig. 5.28(a). Here, the structural density depth profile and the magnetooptical $\Delta\beta$ depth profile of the XRMR scan at a photon energy of 641.6 eV are shown. The XRMR analysis of the magnetic depth profile determines that a share of 80.2 % of the Mn specific magnetic moment is ferromagnetically ordered within the PtMnSb layer. Here, the assumed probing depth of the total electron yield XMCD is well within the range of the upper magnetic dead layer. Therefore, one has to explicitly take the roughness of the upper magnetic boundary into account to determine the real probing depth based on the comparison with the LY results. The AlO_x/MgO/PtMnSb sample shows a Mn spin magnetic moment of $m_{spin} = (1.55 \pm 0.10)\ \mu_B$/atom, as discussed in chapter 5.6. According to the Mn specific magnetic depth profile obtained from the XRMR analysis, the share corrected value of the

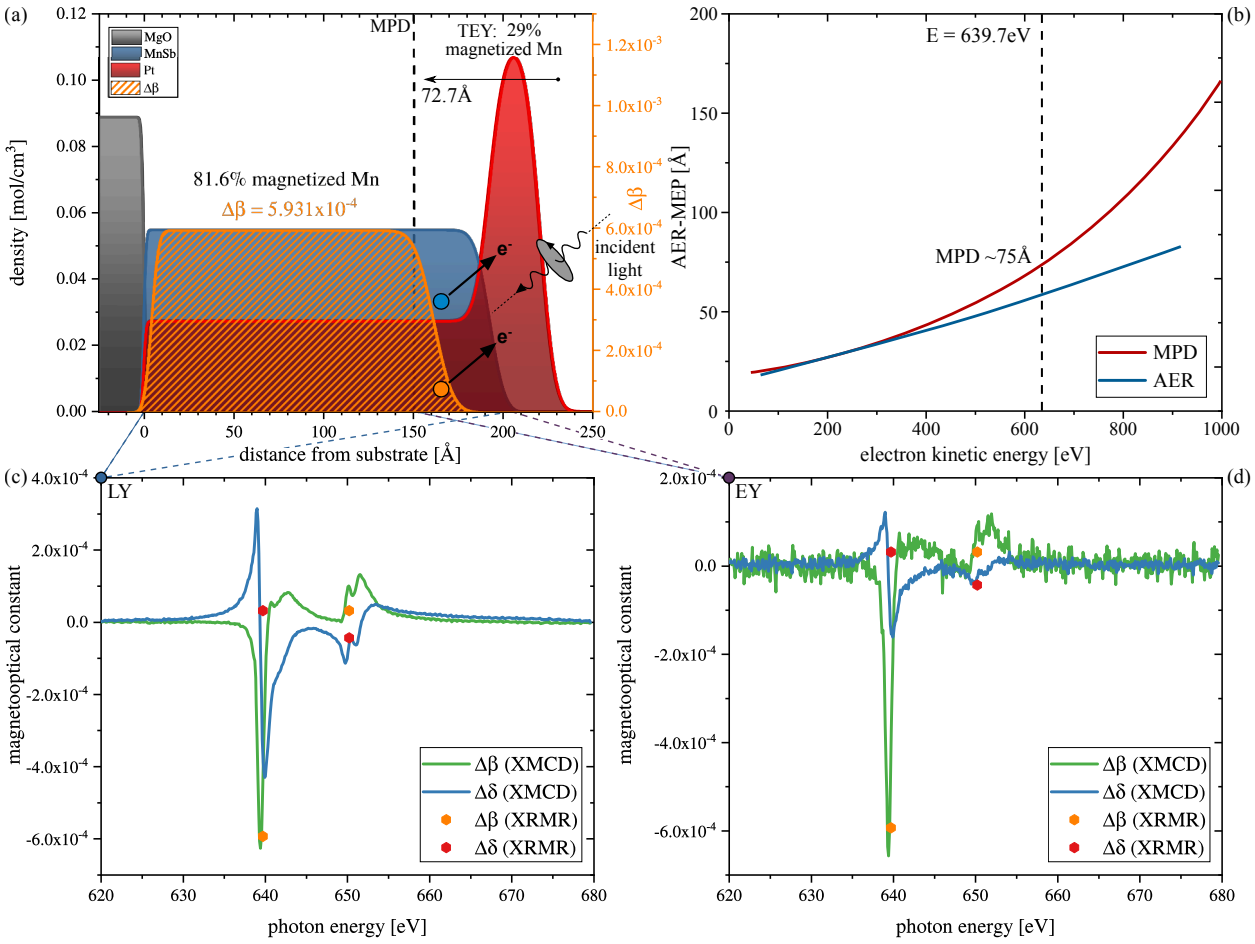

Figure 5.29: (a) Structural density and the magnetooptical $\Delta\beta$ depth profile of the $Pt_{400\,°C}$/PtMnSb bilayer. (b) MPD and AER as a function of Auger electron initial kinetic energy based on Ref. [Frazer et al., 2003]. (c) The magnetooptical constants $\Delta\beta$ derived from the LY XMCD data and $\Delta\delta$ calculated by the Kramers-Kronig transformation. (d) The magnetooptical constants $\Delta\beta$ derived from the EY XMCD data and $\Delta\delta$ calculated by the Kramers-Kronig transformation. The results obtained from the various XRMR simulations are presented by the orange and red dots, respectively.

ferromagnetic phase is consequently $m_{spin} = (1.93 \pm 0.10)\ \mu_B$/atom. The magnetic moment obtained from the TEY measurement is therefore 17 % of the share corrected value obtained from the LY experiment which translates to an equivalent share of ferromagnetically ordered Mn within the TEY probing depth. Hence, the TEY probes the PtMnSb layer up to a distance of 187.9 Å from the substrate. Including the AlO_x/MgO capping layer, the TEY probing depth is therefore 3.6 nm in this particular oxide capped thin film system.

The MPD with regard to the Pt/PtMnSb is exemplary calculated here based on the PtMnSb thin film covered with hot deposited Pt. The results are presented in Fig. 5.29. This sample shows a share of 81.6 % for the Mn specific magnetic depth profile which leads to a share corrected spin magnetic moment of $m_{spin} = (1.89 \pm 0.10)\ \mu_B$/atom. The obtained moment by the TEY measurement is $m_{spin} = (0.55 \pm 0.10)\ \mu_B$/atom and thus this mode probes a layer of the PtMnSb system with 29 % of the Mn ordered ferromagnetically. Assuming a uniform distribution of Mn within the PtMnSb thin film, the maximum TEY probing depth is 72.7 Å. The Mn specific magnetic depth profile of the PtMnSb is therefore only affecting the magnetic contribution to the electron yield signal within the first

1.3 nm above the MPD. The remaining 3.2 nm of the magnetic dead layer are not contributing to the magnetic dichroism response in the TEY.

Bases on this calculated MPD the magnetooptical constants $\Delta\beta$ can be derived from the LY as well as the TEY XMCD signal. This magnetooptical constant and the corresponding $\Delta\delta$ spectrum, calculated by the Kramers-Kronig transformation are illustrated in bottom row of Fig. 5.29. The magnetooptical constants derived from the LY scan are shown in Fig. 5.29(c) while the TEY result, corrected for the share of magnetically ordered Mn within the probing range, is presented in Fig. 5.29(d). The results obtained from the various XRMR simulations, discussed in-depth in section 5.2.3 of this work, are in excellent agreement with the magnetooptical spectra calculated based on the XMCD results obtained in both LY as well as TEY mode. This is only achievable when the characteristics of the magnetic depth profile obtained from the precise XRMR measurement are taken into account and connected with the exactly determined MPD as outlined in this chapter.

Conclusion

The complementary spectroscopic studies outlined in the previous sections clearly support the results of the magnetic reflectivity performed on the various PtMnSb samples, summarized in section 5.3 of this work. First of all, the XRMR analysis of the PtMnSb thickness series shows consistent magnetic depth profiles which overall scale with the structural extent of the half-Heusler layer. Both Pt and oxide capped series confirm the existence of a well defined magnetic dead layer, bordering both the substrate as well as the top interface of the PtMnSb layer.

The extent of these magnetic dead layers is in line with the previously discussed, nominally 20 nm samples with an equivalent capping process, which have been investigated in detail in the first sections of this chapter. The size of the obtained magnetic dead layers for the varying PtMnSb layer extent is comparable and almost independent of the sample thickness on both interfaces for all samples of the Pt capped PtMnSb series. Here, the lower magnetic dead layer is, in a first approximation, identical for all samples of the thickness series while the upper magnetic dead layer shows a slightly higher variation. The results for the magnetic depth profiles in the AlO_x/MgO capped series are in line with these observation with the exception of a slightly wider magnetic dead layer at the substrate side and a significant dependency of the upper magnetic dead layer on the thickness of the PtMnSb layer.

This has to be attributed to the increased interdiffusion and oxidation at the capping interface in combination with the development of a pronounced transition zone at the thinner layers forming a defective and quasi-amorphous interface. The extent of the Pt spe-

cific magnetic depth profile is therefore reduced in relation to the structural interface position. The layer-by-layer growth, higher quality and reduced roughness of the structural Pt/PtMnSb interface thus directly translates to a smaller magnetic dead layer.

The spin polarization of the half-Heusler region, covered by the magnetic depth profile, is however not significantly influenced by the interface properties, as shown by the stable magnetooptical $\Delta\beta$ depth profiles with comparable plateau values over all samples within the respective thickness series. The average plateau value of the oxide capped series is about 20 % lower than for the Pt/PtMnSb thickness series which in combination with the different dead layer extent nicely fits the obtained results of the XMCD based study.

The investigation of the magnetic dead layer by probing the magnetic moment via SQUID and VSM measurements reveals an average extent of 1.88 nm. This value is in accordance with the XRMR based results and confirms the slightly wider Mn specific magnetic dead layers in case of an oxide capped PtMnSb structure.

The direct comparison of the XRMR and XMCD studies of the PtMnSb bilayers shows consistent results. Here, the expected multiplet structure is found in the Mn $2p$ XAS curve, characteristic for the PtMnSb compound. Furthermore, the direct comparison to the *ab initio* spectra confirms the high spin-polarized $3d^5$ ground state configuration of the half-Heusler. When the XAS and XMCD signal for bilayers of different capping are contrasted, a clear deviation of the observed spectral structure is observed due to the increased chemical alteration of the Mn bonding. The difference of the obtained Mn specific spin magnetic moment can be clearly attributed to the varying magnetic dead layer thickness, in direct relation to the specific deposition process of the PtMnSb bilayer. Here, the magnetic moment is reduced by growing the Pt capping at elevated temperature or replacing the Pt by the discussed AlO_x/MgO version. The XMCD results are quantitatively in agreement with the reduced magnetic depth profile of the respective samples.

When these XAS results of the resonances are utilized to determine the magnetooptical absorption parameters as well as the corresponding dispersive constants via the Kramers-Kronig integral relations, the good agreement between both studies is substantiated. Moreover, the determined plateau values of the optical β and δ depth profile, given by the fundamental XRR simulations of the XRMR analysis, match the XAS corrected literature values at both characteristic Mn L_2 and L_3 absorption edges.

Additionally, the difference of the XMCD results obtained in the TEY and LY mode is analyzed quantitatively in order to determine the MPE of the TEY measurement in relation to the capping material. This process is based on the characterization of the magnetic depth profile by the XRMR study which allows for the consideration of the exact magnetic dead layer thickness when comparing both XAS techniques.

The magnetooptical constants derived from the LY as well as

the TEY XMCD signal are used to confirm the results of the XRMR simulation since both $\Delta\beta$ and $\Delta\delta$ are considered free parameters during the fit of the asymmetry ratio. The obtained magnetooptical results are consistent within the experimental margin of error as illustrated by the exemplary plots in Fig. 5.28 for the TEY and Fig. 5.29 for the LY. This latter figure also illustrates the consistency between the MPD determination by the method outlined in this chapter and the expected results based on the specific literature regarding the AER in this bilayer systems. Overall, this broad range of consistency checks confirms the XRMR results of this work and substantiates the qualitative and quantitative characterization of the element specific magnetic depth profile in the half-Heusler structure, demonstrating and improving an essential aspect of the current spintronic research.

6
Publications and Conferences

Publications

- J. Krieft, J. Mendil, M. H. Aguirre, C. O. Avci, C. Klewe, K. Rott, J.-M. Schmalhorst, G. Reiss, P. Gambardella, and T. Kuschel. Co-sputtered PtMnSb thin films and PtMnSb/Pt bilayers for spin-orbit torque investigations. *Phys. Status Solidi Rapid Res. Lett.*, **11**(4):1600439 (2017)

- T. Huebner, U. Martens, J. Walowski, A. Boehnke, J. Krieft, C. Heiliger, A. Thomas, G. Reiss, T. Kuschel, and M. Münzenberg. Enhancement of thermovoltage and tunnel magneto-Seebeck effect in CoFeB-based magnetic tunnel junctions by variation of the $MgAl_2O_4$ and MgO barrier thickness. *Phys. Rev. B*, **96**(21): 214435 (2017)

- O. Reimer, D. Meier, M. Bovender, L. Helmich, J.-O. Dreessen, J. Krieft, A. S. Shestakov, C. H. Back, J.-M. Schmalhorst, A. Hütten, G. Reiss, and T. Kuschel. Quantitative separation of the anisotropic magnetothermopower and planar Nernst effect by the rotation of an in-plane thermal gradient. *Sci. Rep.*, **7**:40586 (2017)

- R. Klett, J. Schönle, A. Becker, D. Dyck, K. Borisov, K. Rott, D. Ramermann, B. Büker, J. Haskenhoff, J. Krieft, T. Huebner, O. Reimer, C. Shekhar, J.-M. Schmalhorst, A. Hütten, C. Felser, W. Wernsdorfer, and G. Reiss. Proximity-Induced Superconductivity and Quantum Interference in Topological Crystalline Insulator SnTe Thin-Film Devices. *Nano Lett.*, **18**(2):1264–1268 (2018)

- J. Krieft, Z. Li, A. V. Singh, S. Regmi, A. Rastogi, A. Srivastava, Z. Galazka, T. Mewes, A. Gupta, and T. Kuschel. Vectorial observation of the spin Seebeck effect in epitaxial $NiFe_2O_4$ thin films with various magnetic anisotropy contributions. *Appl. Phys. Lett.*, **114**(23): 232404 (2019)

- J. Krieft, D. Graulich, A. Moskaltsova, L. Bouchenoire, S. Francoual, and T. Kuschel. Advanced data analysis procedure for hard x-ray resonant magnetic reflectivity discussed for Pt thin

film samples of various complexity. *J. Phys. D: Appl. Phys.*, **53**(37): 375004 (2020)

- A. Moskaltsova, J. Krieft, D. Graulich, T. Matalla-Wagner, S. Francoual, and T. Kuschel. Impact of the magnetic proximity effect in Pt on the total magnetic moment of Pt/Co/Ta trilayers studied by x-ray resonant magnetic reflectivity. *AIP Advances*, **10**(1):015154 (2020)

- D. Dyck, A. Becker, J. Koo, T. Matalla-Wagner, J. Krieft, and G. Reiss. Anomalous Hall Effect and Magnetoresistance in Sputter-Deposited Magnetic Weyl Semimetal Co_2TiGe Thin Films. *Phys. Status Solidi B*, 2000067 (2020)

- S. Emori, C. Klewe, J.-M. Schmalhorst, J. Krieft, P. Shafer, Y. Lim, D. A. Smith, A. Sapkota, A. Srivastava, C. Mewes, Z. Jiang, B. Khodadadi, H. Elmkharram, J. J. Heremans, E. Arenholz, G. Reiss, and T. Mewes. Element-Specific Detection of Sub-Nanosecond Spin-Transfer Torque in a Nanomagnet Ensemble. *Nano Lett.*, **20**(11):7828–7834 (2020)

- D. Graulich, J. Krieft, A. Moskaltsova, J. Demir, T. Peters, T. Pohlmann, J. Wollschläger, J. R. Linares Mardegan, S. Francoual, and T. Kuschel. Quantitative comparison of the magnetic proximity effect in Pt detected by XRMR and XMCD. *in submission*

Conferences

- J. Krieft *et al.* Experimental analysis of the anomalous Hall effect arising from noncollinear antiferromagnetism in MnIr thin films. *DPG Spring Meeting*, Regensburg (2016)

- J. Krieft *et al.* Co-sputtered PtMnSb thin films and PtMnSb/Pt bilayers for spin-orbit torque investigations. *633th WE-Heraeus Seminar "Spin Orbit Dynamics"*, Bad Honnef (2017)

- J. Krieft *et al.* Co-sputtered PtMnSb thin films and PtMnSb/Pt bilayers for spin-orbit torque investigations. *Spin Mechanics 4*, Lake Louise (2017)

- J. Krieft *et al.* Spin depth profiles of PtMnSb thin films and PtMnSb/Pt bilayers investigated by x-ray resonant reflectivity. *ESRF Special XMaS User Meeting*, Grenoble (2017)

- J. Krieft *et al.* Co-sputtered PtMnSb thin films and PtMnSb/Pt bilayers for spin-orbit torque investigations. *DPG Spring Meeting*, Dresden (2017)

- J. Krieft *et al.* Vectorial magnetometry using longitudinal spin Seebeck effect measurements in Pt/NFO/MGO films. *SIP of the MINT center*, University of Alabama, Tuscaloosa (2017)

- J. Krieft *et al.* Vectorial observation of the spin Seebeck effect in $NiFe_2O_4$ thin films on differently oriented lattice-matched substrates. *Spin Caloritronics IX*, Columbus (2018)
- J. Krieft *et al.* Advantages and limits of hard x-ray resonant magnetic reflectivity discussed for Pt thin film samples of various complexity. *DESY Photon Science Users' Meeting*, Hamburg (2019)

Acknowledgments

At this point, I would like to express my sincere gratitude to my supervisor Prof. Dr. Günter Reiss for giving me the opportunity to work with state-of-the-art laboratory equipment and write this dissertation. I owe my greatest gratitude to Dr. Timo Kuschel, who was instrumental in defining the path of the presented research work and provided continuous mentoring, knowledge and motivation.

Besides my advisors, I would like to thank Dr. Jan Schmalhorst for his insightful comments, advice, and support. I thank my fellow colleagues from the work group Thin Films & Physics of Nanostructures at Bielefeld University for the inspiring discussions and their encouragement. In particular, I thank Dr. Karsten Rott for his technical expertise and many helpful discussions and Aggi Windmann for her professional support with the academic bureaucracy.

My sincere thanks also goes to Prof. Dr. Arunava Gupta, who has provided access to the laboratory and research facilities of his work group during my three month stay at the University of Alabama. This thesis would not have been possible without the opportunity conduct experiments at the various brilliant synchrotron radiation facilities. I must show my gratitude for the opportunity to work at the Advanced Light Source (ALS), Berkeley, USA. Furthermore, I would like to acknowledge DESY, Hamburg, Germany, a member of the Helmholtz Association HGF, and the European Synchrotron Radiation Facility (ESRF), Grenoble, France for the provision of experimental facilities.

I would like to thank the resident beamline staff, in particular Dr. Padraic Shafer, Dr. Christoph Klewe, Dr. Sonia Francoual, and Dr. Laurence Bouchenoire at the ALS beamline 4.0.2, DESY beamline P09 and the beamline BM28 at the ESRF for technical support as well as Dominik Graulich, Anastasiia Moskaltsova, Dr. Panagiota Bougiatioti, Tobias Pohlmann and Dr. Johannes Mendil for their assistance and many helpful discussions during the beamtimes. Special thanks go to Sebastian Macke for providing software support of the fitting tool ReMagX.

Bibliography

H. Akasaka and M. Sato. Process and apparatus for simultaneous erasure and recording in magneto-optical recording, (1989). US Patent 4,853,912.

M. Althammer, S. Meyer, H. Nakayama, M. Schreier, S. Altmannshofer, M. Weiler, H. Huebl, S. Geprägs, M. Opel, R. Gross, D. Meier, C. Klewe, T. Kuschel, J.-M. Schmalhorst, G. Reiss, L. Shen, A. Gupta, Y.-T. Chen, G. E. W. Bauer, E. Saitoh, and S. T. B. Goennenwein. Quantitative study of the spin Hall magnetoresistance in ferromagnetic insulator/normal metal hybrids. *Phys. Rev. B*, **87**(22):224401 (2013).

M. Althammer, A. V. Singh, T. Wimmer, Z. Galazka, H. Huebl, M. Opel, R. Gross, and A. Gupta. Current direction anisotropy of the spin Hall magnetoresistance in nickel ferrite thin films with bulk-like magnetic properties. *arXiv:1811.04696*, (2018).

V. P. Amin and M. D. Stiles. Spin transport at interfaces with spin-orbit coupling: Phenomenology. *Phys. Rev. B*, **94**:104420 (2016). DOI: 10.1103/PhysRevB.94.104420.

K. Ando and E. Saitoh. Inverse spin-Hall effect in palladium at room temperature. *J. Appl. Phys.*, **108**(11):113925 (2010).

J.-P. Ansermet. Perpendicular transport of spin-polarized electrons through magnetic nanostructures. *J. Phys. Condens. Matter*, **10**(27): 6027 (1998).

W. Antel Jr, M. Schwickert, T. Lin, W. O'Brien, and G. Harp. Induced ferromagnetism and anisotropy of Pt layers in Fe/Pt (001) multilayers. *Phys. Rev. B*, **60**(18):12933 (1999).

A. Antonyan, S. Pyo, H. Jung, and T. Song. Embedded MRAM Macro for eFlash Replacement. In *2018 IEEE International Symposium on Circuits and Systems (ISCAS)*, pages 1–4. IEEE, (2018).

U. Arp, F. Federmann, E. Kallne, B. Sonntag, and S. Sorensen. Absorption resonances in the $2p$ threshold of manganese atoms. *J. Phys. B*, **25**(18):3747 (1992).

J. Ashley, C. Tung, R. Ritchie, and V. Anderson. Calculations of mean free paths and stopping powers of low energy electrons ($\leqslant$ 10 keV) in solids using a statistical model. *IEEE Trans. Nucl. Sci.*, **23**(6):1833–1837 (1976).

E. Attaran and P. J. Grundy. The magnetic, magneto-optical and structural properties of PtMnSb thin films. *J. Magn. Magn. Mater.*, **78**(1):51–55 (1989).

C. O. Avci, K. Garello, A. Ghosh, M. Gabureac, S. F. Alvarado, and P. Gambardella. Unidirectional spin Hall magnetoresistance in ferromagnet/normal metal bilayers. *Nat. Phys.*, **11**(7):570–575 (2015).

C. O. Avci, A. Quindeau, C.-F. Pai, M. Mann, L. Caretta, A. S. Tang, M. C. Onbasli, C. A. Ross, and G. S. Beach. Current-induced switching in a magnetic insulator. *Nat. Mater.*, **16**(3):309 (2017).

N. Awaji, K. Noma, K. Nomura, S. Doi, T. Hirono, H. Kimura, and T. Nakamura. Soft X-ray Resonant Magnetic Reflectivity Study on Induced Magnetism in $[Fe_{70}Co_{30}/Pd]_n$ Super-Lattice Films. *J. Phys. Conf. Ser.*, **83**(1):012034 (2007).

P. Bach, A. S. Bader, C. Rüster, C. Gould, C. R. Becker, G. Schmidt, L. W. Molenkamp, W. Weigand, C. Kumpf, E. Umbach, R. Urban, G. Woltersdorf, and B. Heinrich. Molecular-beam epitaxy of the half-Heusler alloy NiMnSb on (In, Ga) As/InP (001). *Appl. Phys. Lett.*, **83**(3):521–523 (2003).

M. N. Baibich, J. M. Broto, A. Fert, F. N. Van Dau, F. Petroff, P. Etienne, G. Creuzet, A. Friederich, and J. Chazelas. Giant magnetoresistance of (001)Fe/(001)Cr magnetic superlattices. *Phys. Rev. Lett.*, **61**(21):2472 (1988).

J. Balluff, K. Diekmann, G. Reiss, and M. Meinert. High-throughput screening for antiferromagnetic Heusler compounds using density functional theory. *Phys. Rev. Mater.*, **1**(3):034404 (2017).

R. Bansal, N. Chowdhury, and P. Muduli. Proximity effect induced enhanced spin pumping in Py/Gd at room temperature. *Appl. Phys. Lett.*, **112**(26):262403 (2018).

M. Baral and A. Chakrabarti. Half-metallicity versus symmetry in half-Heusler alloys based on Pt, Ni, and Co: An ab initio study. *Phys. Rev. B*, **99**(20):205136 (2019).

G. E. W. Bauer, E. Saitoh, and B. J. van Wees. Spin caloritronics. *Nat. Mater.*, **11**(5):391–399 (2012).

E. Beaurepaire, F. Scheurer, G. Krill, and J.-P. Kappler. *Magnetism and Synchrotron Radiation*, volume 34. Springer Berlin, Germany (2001).

L. Berger. Side-jump mechanism for the Hall effect of ferromagnets. *Phys. Rev. B*, **2**(11):4559 (1970).

J. Bertinshaw, S. Brück, D. Lott, H. Fritzsche, Y. Khaydukov, O. Soltwedel, T. Keller, E. Goering, P. Audehm, D. L. Cortie, W. D. Hutchison, Q. M. Ramasse, M. Arredondo, R. Maran, V. Nagarajan, F. Klose, and C. Ulrich. Element-specific depth profile of

magnetism and stoichiometry at the $La_{0.67}Sr_{0.33}MnO_3/BiFeO_3$ interface. *Phys. Rev. B*, **90**(4):041113 (2014).

G. Binasch, P. Grünberg, F. Saurenbach, and W. Zinn. Enhanced magnetoresistance in layered magnetic structures with antiferromagnetic interlayer exchange. *Phys. Rev. B*, **39**:4828–4830 (1989).

M. Björck, G. Andersson, B. Sanyal, M. Hedlund, and A. Wildes. Segregation and interdiffusion in (Fe, Co)/Pt superlattices. *Phys. Rev. B*, **79**(8):085428 (2009).

E. Blackburn, C. Sanchez-Hanke, S. Roy, D. Smith, J.-I. Hong, K. Chan, A. Berkowitz, and S. Sinha. Pinned Co moments in a polycrystalline permalloy/CoO exchange-biased bilayer. *Phys. Rev. B*, **78**(18):180408 (2008).

J. Bobo, P. Johnson, M. Kautzky, F. Mancoff, E. Tuncel, R. White, and B. Clemens. Optical spectroscopy investigations of half metallic ferromagnetic Heusler alloy thin films: PtMnSb, NiMnSb, and CuMnSb. *J. Appl. Phys.*, **81**(8):4164–4166 (1997).

G. Bona, F. Meier, M. Taborelli, E. Bucher, and P. Schmidt. Spin polarized photoemission from NiMnSb. *Solid State Commun.*, **56**(4): 391–394 (1985).

C. Borca, T. Komesu, H.-K. Jeong, P. A. Dowben, D. Ristoiu, C. Hordequin, J. Nozieres, J. Pierre, S. Stadler, and Y. Idzerda. Evidence for temperature dependent moments ordering in ferromagnetic NiMnSb (100). *Phys. Rev. B*, **64**(5):052409 (2001).

M. Born and E. Wolf. *Principles of optics: Electromagnetic theory of propagation, interference and diffraction of light*. Elsevier (2013).

S. Bosu, Y. Sakuraba, K.-i. Uchida, K. Saito, T. Ota, E. Saitoh, and K. Takanashi. Spin Seebeck effect in thin films of the Heusler compound Co_2MnSi. *Phys. Rev. B*, **83**(22):224401 (2011).

L. Bouchenoire, S. Brown, P. Thompson, J. Duffy, J. Taylor, and M. Cooper. Performance of phase plates on the XMaS beamline at the ESRF. *J. Synchrotron Radiat.*, **10**(2):172–176 (2003).

L. Bouchenoire, S. Brown, P. Thompson, M. Cain, M. Stewart, and M. Cooper. Development of a novel piezo driven device for fast helicity reversal experiments on the XMaS Beamline. *AIP Conf. Proc.*, **879**(1):1679–1682 (2007).

P. Bougiatioti, C. Klewe, D. Meier, O. Manos, O. Kuschel, J. Wollschläger, L. Bouchenoire, S. D. Brown, J.-M. Schmalhorst, G. Reiss, and T. Kuschel. Quantitative disentanglement of the spin Seebeck, proximity-induced, and ferromagnetic-induced anomalous Nernst effect in normal-metal–ferromagnet bilayers. *Phys. Rev. Lett.*, **119**(22):227205 (2017).

V. Brabers. *Handbook of magnetic materials*, volume 8. Elsevier, New York, NY, USA (1995).

V. Brabers. Progress in spinel ferrite research. *Handb. Magn. Mater.*, **8**:189–324 (1995).

W. H. Bragg and W. L. Bragg. The reflection of X-rays by crystals. *Proc. R. Soc. Lond. A*, **88**(605):428–438 (1913).

A. Bratkovsky. Tunneling of electrons in conventional and half-metallic systems: Towards very large magnetoresistance. *Phys. Rev. B*, **56**(5):2344 (1997).

S. Brown, L. Bouchenoire, D. Bowyer, J. Kervin, D. Laundy, M. Longfield, D. Mannix, D. Paul, A. Stunault, P. Thompson, M. J. Cooper, C. A. Lucas, and W. G. Stirling. The XMaS beamline at ESRF: Instrumental developments and high-resolution diffraction studies. *J. Synchrotron Radiat.*, **8**(6):1172–1181 (2001).

S. Brück, S. Macke, E. Goering, X. Ji, Q. Zhan, and K. M. Krishnan. Coupling of Fe and uncompensated Mn moments in exchange-biased Fe/MnPd. *Phys. Rev. B*, **81**(13):134414 (2010).

S. Cardoso, P. Freitas, Z. Zhang, P. Wei, N. Barradas, and J. Soares. Electrode roughness and interfacial mixing effects on the tunnel junction thermal stability. *J. Appl. Phys.*, **89**(11):6650–6652 (2001).

P. Carra and M. Altarelli. Dichroism in the x-ray absorption spectra of magnetically ordered systems. *Phys. Rev. Lett.*, **64**(11):1286 (1990).

P. Carra, B. Thole, M. Altarelli, and X. Wang. X-ray circular dichroism and local magnetic fields. *Phys. Rev. Lett.*, **70**(5):694 (1993).

F. Casper, T. Graf, S. Chadov, B. Balke, and C. Felser. Half-Heusler compounds: novel materials for energy and spintronic applications. *Semicond. Sci. Tech.*, **27**(6):063001 (2012).

C. T. Chantler. Theoretical form factor, attenuation, and scattering tabulation for $Z = 1$ - 92 from $E = 1$ - 10 eV to $E = 0.4$ - 1.0 MeV. *J. Phys. Chem. Ref. Data*, **24**(1):71–643 (1995).

C. T. Chantler. Detailed tabulation of atomic form factors, photoelectric absorption and scattering cross section, and mass attenuation coefficients in the vicinity of absorption edges in the soft X-ray ($Z = 30$ - 36, $Z = 60$ - 89, $E = 0.1$ keV - 10 keV), addressing convergence issues of earlier work. *J. Phys. Chem. Ref. Data*, **29**(4):597–1056 (2000).

J. Chazalviel. Spin-dependent Hall effect in semiconductors. *Phys. Rev. B*, **11**(10):3918 (1975).

J. Chazalviel and I. Solomon. Experimental evidence of the anomalous Hall effect in a nonmagnetic semiconductor. *Phys. Rev. Lett.*, **29**(25):1676 (1972).

C. Chen, F. Sette, Y. Ma, and S. Modesti. Soft-x-ray magnetic circular dichroism at the $L_{2,3}$ edges of nickel. *Phys. Rev. B*, **42**(11):7262 (1990).

C. Chen, Y. Idzerda, H.-J. Lin, N. Smith, G. Meigs, E. Chaban, G. Ho, E. Pellegrin, and F. Sette. Experimental confirmation of the X-ray magnetic circular dichroism sum rules for iron and cobalt. *Phys. Rev. Lett.*, **75**(1):152 (1995).

Y.-T. Chen, S. Takahashi, H. Nakayama, M. Althammer, S. T. Goennenwein, E. Saitoh, and G. E. Bauer. Theory of spin Hall magnetoresistance. *Phys. Rev. B*, **87**(14):144411 (2013).

V. Cherepanov, I. Kolokolov, and V. L'vov. The saga of YIG: Spectra, thermodynamics, interaction and relaxation of magnons in a complex magnet. *Phys. Rep.*, **229**(3):81–144 (1993).

A. Chernyshov, M. Overby, X. Liu, J. K. Furdyna, Y. Lyanda-Geller, and L. P. Rokhinson. Evidence for reversible control of magnetization in a ferromagnetic material by means of spin–orbit magnetic field. *Nat. Phys.*, **5**(9):656–659 (2009).

C. Chien. *The Hall effect and its applications*. Springer Science & Business Media (2013).

A. Chumak, V. Vasyuchka, A. Serga, and B. Hillebrands. Magnon spintronics. *Nat. Phys.*, **11**(6):453 (2015).

C. Ciccarelli, L. Anderson, V. Tshitoyan, A. J. Ferguson, F. Gerhard, C. Gould, L. W. Molenkamp, J. Gayles, J. Železnỳ, L. Šmejkal, Z. Yuan, J. Sinova, F. Freimuth, and T. Jungwirth. Room-temperature spin-orbit torque in NiMnSb. *Nat. Phys.*, **12**:855–860 (2016).

B. Cox, R. Tahir-Kheli, and R. Elliott. Thin films of itinerant-electron ferromagnets on a nonmagnetic metallic substrate. *Phys. Rev. B*, **20** (7):2864 (1979).

C. Daboo, J. A. C. Bland, R. J. Hicken, A. J. R. Ives, M. J. Baird, and M. J. Walker. Vectorial magnetometry with the magneto-optic Kerr effect applied to Co/Cu/Co trilayer structures. *Phys. Rev. B*, **47**: 11852–11859 (1993).

J. Daillant and A. Gibaud. *X-ray and Neutron Reflectivity: Principles and Applications*, volume 770. Springer, Berlin (2008).

A. Dane, A. Veldhuis, D. De Boer, A. Leenaers, and L. Buydens. Application of genetic algorithms for characterization of thin layered materials by glancing incidence X-ray reflectometry. *Physica B*, **253**(3-4):254–268 (1998).

F. de Bergevin. The interaction of x-rays (and neutrons) with matter. In *X-ray and Neutron Reflectivity*, pages 1–57. Springer, (2009).

D. De Boer, A. Leenaers, and W. Van den Hoogenhof. Glancing-incidence x-ray analysis of thin-layered materials: A review. *X-Ray Spectrometry*, **24**(3):91–102 (1995).

J. H. de Boer and E. J. Verwey. Semi-conductors with partially and with completely filled 3*d*-lattice bands. *Proc. Phys. Soc.*, **49**(4S):59 (1937).

F. M. De Groot. Dips and peaks in fluorescence yield X-ray absorption are due to state-dependent decay. *Nat. Chem.*, **4**(10): 766–767 (2012).

R. A. De Groot, F. M. Mueller, P. G. Van Engen, and K. H. J. Buschow. New class of materials: half-metallic ferromagnets. *Phys. Rev. Lett.*, **50**(25):2024 (1983).

S. Doi, K. Nomura, N. Awaji, N. Hosoito, R. Yamagishi, and M. Suzuki. Magnetization profile of Ir in a MnIr/CoFe exchange bias system evaluated by hard x-ray resonant magnetic reflectivity. *J. Appl. Phys.*, **106**(12):123919 (2009).

M. I. Dyakonov and V. I. Perel. Current-induced spin orientation of electrons in semiconductors. *Phys. Lett. A*, **35**(6):459–460 (1971).

H. Ebert and G. Schütz. Theoretical and experimental study of the electronic structure of PtMnSb. *J. Appl. Phys.*, **69**(8):4627–4629 (1991).

C. Ederer, M. Komelj, M. Fähnle, and G. Schütz. Theory of induced magnetic moments and x-ray magnetic circular dichroism in Co-Pt multilayers. *Phys. Rev. B*, **66**(9):094413 (2002).

W. Eerenstein, T. Palstra, T. Hibma, and S. Celotto. Diffusive motion of antiphase domain boundaries in Fe_3O_4 films. *Phys. Rev. B*, **68**(1): 014428 (2003).

F. Elder, A. Gurewitsch, R. Langmuir, and H. Pollock. Radiation from electrons in a synchrotron. *Phys. Rev.*, **71**(11):829 (1947).

S. Emori, C. Klewe, J.-M. Schmalhorst, J. Krieft, P. Shafer, Y. Lim, D. A. Smith, A. Sapkota, A. Srivastava, C. Mewes, Z. Jiang, B. Khodadadi, H. Elmkharram, J. J. Heremans, E. Arenholz, G. Reiss, and T. Mewes. Element-Specific Detection of Sub-Nanosecond Spin-Transfer Torque in a Nanomagnet Ensemble. *Nano Lett.*, **20**(11): 7828–7834 (2020).

J. L. Erskine and E. Stern. Calculation of the M_{23} magneto-optical absorption spectrum of ferromagnetic nickel. *Phys. Rev. B*, **12**(11): 5016 (1975).

U. Fano. Effects of configuration interaction on intensities and phase shifts. *Phys. Rev.*, **124**(6):1866 (1961).

G. Felcher, R. Hilleke, R. Crawford, J. Haumann, R. Kleb, and G. Ostrowski. Polarized neutron reflectometer: A new instrument to measure magnetic depth profiles. *Rev. Sci. Instrum.*, **58**(4):609–619 (1987).

E. Fermi. *Nuclear physics: a course given by Enrico Fermi at the University of Chicago*. University of Chicago Press (1950).

A. Fert. Transport in magnetic alloys: Scattering asymmetries (anisotropic scattering, skew scattering, side-jump). *Physica B+C*, **86**: 491–500 (1977).

J. Fink, E. Schierle, E. Weschke, and J. Geck. Resonant elastic soft x-ray scattering. *Rep. Prog. Phys.*, **76**(5):056502 (2013).

B. H. Frazer, B. Gilbert, B. R. Sonderegger, and G. De Stasio. The probing depth of total electron yield in the sub-keV range: TEY-XAS and X-PEEM. *Surf. Sci.*, **537**(1-3):161–167 (2003).

A. Fresnel. *Mémoires de l'Académie*, **11**:393 (1823).

W. Friedrich, P. Knipping, and M. Laue. Interferenzerscheinungen bei Röntgenstrahlen. *Ann. Phys.*, **346**(10):971–988 (1913).

Y. Fujii. Recent Developments in the X-Ray Reflectivity Analysis for Rough Surfaces and Interfaces of Multilayered Thin Film Materials. *J. Mater.*, **2013** (2013).

P. Fulde. *Electron correlations in molecules and solids*, volume 100. Springer Science & Business Media (2012).

I. Galanakis. Surface properties of the half-and full-Heusler alloys. *J. Phys. Condens. Matter*, **14**(25):6329 (2002).

I. Galanakis, P. Dederichs, and N. Papanikolaou. Origin and properties of the gap in the half-ferromagnetic Heusler alloys. *Phys. Rev. B*, **66**(13):134428 (2002).

I. Galanakis, P. Mavropoulos, and P. H. Dederichs. Electronic structure and Slater–Pauling behaviour in half-metallic Heusler alloys calculated from first principles. *J. Phys. D: Appl. Phys.*, **39**(5): 765 (2006).

S. D. Ganichev, E. L. Ivchenko, V. V. Bel'Kov, S. A. Tarasenko, M. Sollinger, D. Weiss, W. Wegscheider, and W. Prettl. Spin-galvanic effect. *Nature*, **417**(6885):153–156 (2002).

K. Garello, I. M. Miron, C. O. Avci, F. Freimuth, Y. Mokrousov, S. Blügel, S. Auffret, O. Boulle, G. Gaudin, and P. Gambardella. Symmetry and magnitude of spin-orbit torques in ferromagnetic heterostructures. *Nat. Nanotechn.*, **8**(8):587–593 (2013).

J. Geissler, E. Goering, M. Justen, F. Weigand, G. Schütz, J. Langer, D. Schmitz, H. Maletta, and R. Mattheis. Pt magnetization profile in a Pt/Co bilayer studied by resonant magnetic x-ray reflectometry. *Phys. Rev. B*, **65**(2):020405 (2001).

J. Geissler, E. Goering, F. Weigand, and G. Schütz. Interplay between chemical and magnetic roughness of Pt in a Pt/Co bilayer

investigated with X-ray resonant magnetic reflectometry: Dedicated to Professor Dr. Helmut Kronmüller on the occasion of his 70th birthday. *Z. Metallkd.*, **93**(10):946–952 (2002).

S. Geprägs, S. Meyer, S. Altmannshofer, M. Opel, F. Wilhelm, A. Rogalev, R. Gross, and S. T. Goennenwein. Investigation of induced Pt magnetic polarization in $Pt/Y_3Fe_5O_{12}$ bilayers. *Appl. Phys. Lett.*, **101**(26):262407 (2012).

F. Gerhard, C. Schumacher, C. Gould, and L. W. Molenkamp. Control of the magnetic in-plane anisotropy in off-stoichiometric NiMnSb. *J. Appl. Phys.*, **115**(9):094505 (2014).

M. Ghimire, Sandeep, T. Sinha, and R. Thapa. First principles study of the electronic and magnetic properties of semi-Heusler alloys NiXSb (X= Ti, V, Cr and Mn). *J. Alloys Compd.*, **509**(41):9742–9752 (2011).

J. Giapintzakis, C. Grigorescu, A. Klini, A. Manousaki, V. Zorba, J. Androulakis, Z. Viskadourakis, and C. Fotakis. Low-temperature growth of NiMnSb thin films by pulsed-laser deposition. *Appl. Phys. Lett.*, **80**(15):2716–2718 (2002).

A. Gibaud and G. Vignaud. Specular reflectivity from smooth and rough surfaces. In *X-ray and Neutron Reflectivity*, pages 85–131. Springer, Berlin, Germany, (2009).

M. Gibert, M. Viret, P. Zubko, N. Jaouen, J.-M. Tonnerre, A. Torres-Pardo, S. Catalano, A. Gloter, O. Stéphan, and J.-M. Triscone. Interlayer coupling through a dimensionality-induced magnetic state. *Nat. Commun.*, **7**:11227 (2016).

F. J. Giessibl. Advances in atomic force microscopy. *Rev. Mod. Phys.*, **75**(3):949 (2003).

S. Gota, M. Gautier-Soyer, and M. Sacchi. Fe 2p absorption in magnetic oxides: Quantifying angular-dependent saturation effects. *Phys. Rev. B*, **62**(7):4187 (2000).

T. Graf, C. Felser, and S. S. Parkin. Simple rules for the understanding of Heusler compounds. *Prog. Solid State Ch.*, **39**(1):1–50 (2011).

G.-Y. Guo, S. Murakami, T.-W. Chen, and N. Nagaosa. Intrinsic spin Hall effect in platinum: First-principles calculations. *Phys. Rev. Lett.*, **100**(9):096401 (2008).

H. K. Gweon, S. J. Yun, and S. H. Lim. A very large perpendicular magnetic anisotropy in Pt/Co/MgO trilayers fabricated by controlling the MgO sputtering power and its thickness. *Scientific reports*, **8**(1):1266 (2018).

J. Hannon, G. Trammell, M. Blume, and D. Gibbs. X-ray resonance exchange scattering. *Phys. Rev. Lett.*, **61**(10):1245 (1988).

K. Hanssen, P. Mijnarends, L. Rabou, and K. Buschow. Positron-annihilation study of the half-metallic ferromagnet NiMnSb: Experiment. *Phys. Rev. B*, **42**(3):1533 (1990).

D. Haskel, G. Srajer, J. Lang, J. Pollmann, C. Nelson, J. Jiang, and S. Bader. Enhanced interfacial magnetic coupling of Gd/Fe multilayers. *Phys. Rev. Lett.*, **87**(20):207201 (2001).

J. Hauser. Magnetic proximity effect. *Phys. Rev.*, **187**(2):580 (1969).

W. M. Haynes. *CRC handbook of chemistry and physics*. CRC press (2014).

B. L. Henke, E. M. Gullikson, and J. C. Davis. X-ray interactions: photoabsorption, scattering, transmission, and reflection at $E = 50$ - 30,000 eV, $Z = 1$ - 92. *Atomic data and nuclear data tables*, **54**(2): 181–342 (1993).

F. Heusler. Über magnetische Manganlegierungen. *Verh. Dtsch. Phys. Ges.*, **5**:219 (1903).

J. E. Hirsch. Spin hall effect. *Phys. Rev. Lett.*, **83**(9):1834 (1999).

V. Holy, J. Kubena, I. Ohlidal, K. Lischka, and W. Plotz. X-ray reflection from rough layered systems. *Phys. Rev. B*, **47**(23):15896 (1993).

M. Hoppe, S. Döring, M. Gorgoi, S. Cramm, and M. Müller. Enhanced ferrimagnetism in auxetic $NiFe_2O_4$ in the crossover to the ultrathin-film limit. *Phys. Rev. B*, **91**(5):054418 (2015).

N. Hosoito, T. Ohkochi, K. Kodama, and M. Suzuki. Charge and induced magnetic structures of au layers in Fe/Au bilayer and Fe/Au/Fe trilayer films by resonant x-ray magnetic reflectivity at the Au L_3 absorption edge. *J. Phys. Soc. Jpn.*, **83**(2):024704 (2014).

S.-Y. Huang, X. Fan, D. Qu, Y. Chen, W. Wang, J. Wu, T. Chen, J. Xiao, and C. Chien. Transport magnetic proximity effects in platinum. *Phys. Rev. Lett.*, **109**(10):107204 (2012).

T. Huebner, U. Martens, J. Walowski, A. Boehnke, J. Krieft, C. Heiliger, A. Thomas, G. Reiss, T. Kuschel, and M. Münzenberg. Enhancement of thermovoltage and tunnel magneto-Seebeck effect in CoFeB-based magnetic tunnel junctions by variation of the $MgAl_2O_4$ and MgO barrier thickness. *Phys. Rev. B*, **96**(21): 214435 (2017).

M. Hytch, M. Walls, and J.-P. Chevalier. Measurement of roughness and diffuseness of interfaces. *Ultramicroscopy*, **83**(3-4):217–225 (2000).

T. Inukai, M. Matsuoka, and K. Ono. Magneto-optical properties of vacuum-deposited PtMnSb thin films. *Appl. Phys. Lett.*, **49**(1):52–53 (1986).

M. Isasa, S. Vélez, E. Sagasta, A. Bedoya-Pinto, N. Dix, F. Sánchez, L. E. Hueso, J. Fontcuberta, and F. Casanova. Spin Hall Magnetoresistance as a Probe for Surface Magnetization in $Pt/CoFe_2O_4$ Bilayers. *Phys. Rev. Appl.*, **6**(3):034007 (2016).

D. Iwanenko and I. Pomeranchuk. On the maximal energy attainable in a betatron. *Phys. Rev.*, **65**(11-12):343 (1944).

F. Jedema, H. Heersche, A. Filip, J. Baselmans, and B. Van Wees. Electrical detection of spin precession in a metallic mesoscopic spin valve. *Nature*, **416**(6882):713 (2002).

W. H. Jefferys and J. O. Berger. Ockham's Razor and Bayesian Analysis. *Am. Sci.*, **80**(1):64–72 (1992).

P. Jensen, H. Dreyssé, and M. Kiwi. Magnetic reordering in the vicinity of a ferromagnetic/antiferromagnetic interface. *Eur. Phys. J. B*, **46**(4):541–551 (2005).

M. Julliere. Tunneling between ferromagnetic films. *Phys. Lett. A*, **54**(3):225–226 (1975).

T. Jungwirth, Q. Niu, and A. MacDonald. Anomalous Hall effect in ferromagnetic semiconductors. *Phys. Rev. Lett.*, **88**(20):207208 (2002).

T. Jungwirth, X. Marti, P. Wadley, and J. Wunderlich. Antiferromagnetic spintronics. *Nat. Nanotechn.*, **11**(3):231–241 (2016).

Y. Kajiwara, K. Harii, S. Takahashi, J.-i. Ohe, K.-i. Uchida, M. Mizuguchi, H. Umezawa, H. Kawai, K. Ando, K. Takanashi, S. Maekawa, and E. Saitoh. Transmission of electrical signals by spin-wave interconversion in a magnetic insulator. *Nature*, **464**(7286):262 (2010).

M. Kallmayer, H. Schneider, G. Jakob, H. Elmers, B. Balke, and S. Cramm. Interface magnetization of ultrathin epitaxial $Co_2FeSi(110)/Al_2O_3$ films. *J. Phys. D: Appl. Phys.*, **40**(6):1552 (2007).

H. C. Kandpal, C. Felser, and R. Seshadri. Covalent bonding and the nature of band gaps in some half-Heusler compounds. *J. Phys. D: Appl. Phys.*, **39**(5):776 (2006).

C. Kao, J. Hastings, E. Johnson, D. Siddons, G. Smith, and G. Prinz. Magnetic-resonance exchange scattering at the iron L II and L III edges. *Phys. Rev. Lett.*, **65**(3):373 (1990).

R. Karplus and J. Luttinger. Hall effect in ferromagnetics. *Phys. Rev.*, **95**(5):1154 (1954).

T. Kasuya. A theory of metallic ferro-and antiferromagnetism on Zener's model. *Prog. Theor. Phys.*, **16**(1):45–57 (1956).

Y. Kato, R. C. Myers, A. C. Gossard, and D. D. Awschalom. Observation of the spin Hall effect in semiconductors. *Science*, **306**(5703):1910–1913 (2004).

M. Katsnelson, V. Y. Irkhin, L. Chioncel, A. Lichtenstein, and R. A. de Groot. Half-metallic ferromagnets: From band structure to many-body effects. *Rev. Mod. Phys.*, **80**(2):315 (2008).

M. C. Kautzky and B. M. Clemens. Epitaxial Growth of (001)- and (111)-oriented PtMnSb Films and Multilayers. In *MRS Proceedings*, volume 384, page 109. Cambridge Univ Press, (1995).

M. C. Kautzky and B. M. Clemens. Structure and magneto-optical properties of epitaxial PtMnSb (001) on W (001)/MgO (001). *Appl. Phys. Lett.*, **66**(10):1279–1281 (1995).

M. C. Kautzky, F. B. Mancoff, J.-F. Bobo, P. R. Johnson, R. L. White, and B. M. Clemens. Investigation of possible giant magnetoresistance limiting mechanisms in epitaxial PtMnSb thin films. *J. Appl. Phys.*, **81**(8):4026–4028 (1997).

A. Kehlberger, K. Richter, M. C. Onbasli, G. Jakob, D. H. Kim, T. Goto, C. A. Ross, G. Götz, G. Reiss, T. Kuschel, and M. Kläui. Enhanced magneto-optic Kerr effect and magnetic properties of $CeY_2Fe_5O_{12}$ epitaxial thin films. *Phys. Rev. Appl.*, **4**(1):014008 (2015).

H. Kiessig. Interferenz von Röntgenstrahlen an dünnen Schichten. *Ann. Phys.*, **402**(7):769–788 (1931).

H. Kiessig. Untersuchungen zur Totalreflexion von Röntgenstrahlen. *Ann. Phys.*, **402**(6):715–768 (1931).

T. Kikkawa, K.-i. Uchida, Y. Shiomi, Z. Qiu, D. Hou, D. Tian, H. Nakayama, X.-F. Jin, and E. Saitoh. Longitudinal spin Seebeck effect free from the proximity Nernst effect. *Phys. Rev. Lett.*, **110**(6): 067207 (2013).

D.-O. Kim, K. M. Song, Y. Choi, B.-C. Min, J.-S. Kim, J. W. Choi, and D. R. Lee. Asymmetric magnetic proximity effect in a Pd/Co/Pd trilayer system. *Sci. Rep.*, **6**:25391 (2016).

S. J. Kim, W. C. Kim, C. S. Kim, and S. W. Lee. Moessbauer studies of superexchange interactions in $NiFe_2O_4$. *J. Korean Phys. Soc.*, **36**(6): 430–434 (2000).

A. Kimura, S. Suga, T. Shishidou, S. Imada, T. Muro, S.-Y. Park, T. Miyahara, T. Kaneko, and T. Kanomata. Magnetic circular dichroism in the soft-x-ray absorption spectra of Mn-based magnetic intermetallic compounds. *Phys. Rev. B*, **56**(10):6021 (1997).

C. Kittel. On the theory of ferromagnetic resonance absorption. *Phys. Rev.*, **73**(2):155 (1948).

M. Kiwi. Origin of the magnetic proximity effect. *Mater. Res. Soc. Symp. Proc.*, **746** (2002).

M. Kiwi and M. Zuckermann. The Proximity Effect for Weak Itinerant Ferro-and Antiferro-Magnets. In *Proc. of the 19-th Conf. on Magnetism and Magnetic Materials*, volume 18, page 347, (1973).

R. Klett, J. Schönle, A. Becker, D. Dyck, K. Borisov, K. Rott, D. Ramermann, B. Büker, J. Haskenhoff, J. Krieft, T. Huebner, O. Reimer, C. Shekhar, J.-M. Schmalhorst, A. Hütten, C. Felser, W. Wernsdorfer, and G. Reiss. Proximity-Induced Superconductivity and Quantum Interference in Topological Crystalline Insulator SnTe Thin-Film Devices. *Nano Lett.*, **18**(2):1264–1268 (2018).

C. Klewe, T. Kuschel, J.-M. Schmalhorst, F. Bertram, O. Kuschel, J. Wollschläger, J. Strempfer, M. Meinert, and G. Reiss. Static magnetic proximity effect in $Pt/Ni_{1-x}Fe_x$ bilayers investigated by x-ray resonant magnetic reflectivity. *Phys. Rev. B*, **93**(21):214440 (2016).

J. Kondo. Anomalous Hall effect and magnetoresistance of ferromagnetic metals. *Prog. Theor. Exp. Phys*, **27**(4):772–792 (1962).

L. F. Kourkoutis, J. Song, H. Hwang, and D. Muller. Microscopic origins for stabilizing room-temperature ferromagnetism in ultrathin manganite layers. *Proceedings of the National Academy of Sciences*, **107**(26):11682–11685 (2010).

E. Kravtsov, D. Haskel, S. Te Velthuis, J. Jiang, and B. Kirby. Complementary polarized neutron and resonant x-ray magnetic reflectometry measurements in Fe/Gd heterostructures: Case of inhomogeneous intralayer magnetic structure. *Phys. Rev. B*, **79**(13): 134438 (2009).

J. Krieft, J. Mendil, M. H. Aguirre, C. O. Avci, C. Klewe, K. Rott, J.-M. Schmalhorst, G. Reiss, P. Gambardella, and T. Kuschel. Co-sputtered PtMnSb thin films and PtMnSb/Pt bilayers for spin-orbit torque investigations. *Phys. Status Solidi Rapid Res. Lett.*, **11**(4): 1600439 (2017).

J. Krieft, D. Graulich, A. Moskaltsova, L. Bouchenoire, S. Francoual, and T. Kuschel. Advanced data analysis procedure for hard x-ray resonant magnetic reflectivity discussed for Pt thin film samples of various complexity. *J. Phys. D: Appl. Phys.*, **53**(37):375004 (2020).

T. Kuschel, H. Bardenhagen, H. Wilkens, R. Schubert, J. Hamrle, J. Pištora, and J. Wollschläger. Vectorial magnetometry using magnetooptic Kerr effect including first-and second-order contributions for thin ferromagnetic films. *J. Phys. D: Appl. Phys.*, **44**(26): 265003 (2011).

T. Kuschel, C. Klewe, J.-M. Schmalhorst, F. Bertram, O. Kuschel, T. Schemme, J. Wollschläger, S. Francoual, J. Strempfer, A. Gupta, M. Meinert, G. Götz, D. Meier, and G. Reiss. Static magnetic proximity effect in $Pt/NiFe_2O_4$ and Pt/Fe bilayers investigated by x-ray resonant magnetic reflectivity. *Phys. Rev. Lett.*, **115**(9):097401 (2015).

T. Kuschel, C. Klewe, P. Bougiatioti, O. Kuschel, J. Wollschläger, L. Bouchenoire, S. Brown, J. Schmalhorst, D. Meier, and G. Reiss. Static Magnetic Proximity Effect in Pt Layers on Sputter-Deposited $NiFe_2O_4$ and on Fe of Various Thicknesses Investigated by XRMR. *IEEE Trans. Magn.*, **52**:4500104 (2016).

J. C. Lagarias, J. A. Reeds, M. H. Wright, and P. E. Wright. Convergence properties of the Nelder–Mead simplex method in low dimensions. *SIAM J. Optim.*, **9**(1):112–147 (1998).

D. Lee, S. Sinha, D. Haskel, Y. Choi, J. Lang, S. Stepanov, and G. Srajer. X-ray resonant magnetic scattering from structurally and magnetically rough interfaces in multilayered systems. I. Specular reflectivity. *Phys. Rev. B*, **68**(22):224409 (2003).

K. Lenz, S. Zander, and W. Kuch. Magnetic proximity effects in antiferromagnet/ferromagnet bilayers: The impact on the Néel temperature. *Phys. Rev. Lett.*, **98**(23):237201 (2007).

J. Li, M. Jia, Z. Ding, J. Liang, Y. Luo, and Y. Wu. Pt-enhanced anisotropic magnetoresistance in Pt/Fe bilayers. *Phys. Rev. B*, **90**(21): 214415 (2014).

N. Li, S. Schäfer, R. Datta, T. Mewes, T. Klein, and A. Gupta. Microstructural and ferromagnetic resonance properties of epitaxial nickel ferrite films grown by chemical vapor deposition. *Appl. Phys. Lett.*, **101**(13):132409 (2012).

Z. Li, J. Krieft, A. V. Singh, S. Regmi, A. Rastogi, A. Srivastava, Z. Galazka, T. Mewes, A. Gupta, and T. Kuschel. Vectorial observation of the spin Seebeck effect in epitaxial NiFe2O4 thin films with various magnetic anisotropy contributions. *Appl. Phys. Lett.*, **114**(23): 232404 (2019).

L. Liu, T. Moriyama, D. Ralph, and R. Buhrman. Spin-torque ferromagnetic resonance induced by the spin Hall effect. *Phys. Rev. Lett.*, **106**(3):036601 (2011).

L. Liu, C.-F. Pai, Y. Li, H. W. Tseng, D. C. Ralph, and R. A. Buhrman. Spin-torque switching with the giant spin Hall effect of tantalum. *Science*, **336**(6081):555–558 (2012).

H. Lord and R. Parker. Electrical resistivity of nickel ferrite. *Nature*, **188**(4754):929 (1960).

M. Losurdo and K. Hingerl. *Ellipsometry at the Nanoscale*. Springer (2013).

M. Lovell and R. Richardson. Analysis methods in neutron and X-ray reflectometry. *Curr. Opin. Colloid Interface Sci.*, **4**(3):197–204 (1999).

Y. Lu, J. Cai, S. Huang, D. Qu, B. Miao, and C. Chien. Hybrid magnetoresistance in the proximity of a ferromagnet. *Phys. Rev. B*, **87**(22):220409 (2013).

U. Lüders, M. Bibes, J.-F. Bobo, M. Cantoni, R. Bertacco, and J. Fontcuberta. Enhanced magnetic moment and conductive behavior in $NiFe_2O_4$ spinel ultrathin films. *Phys. Rev. B*, **71**(13): 134419 (2005).

U. Lüders, A. Barthelemy, M. Bibes, K. Bouzehouane, S. Fusil, E. Jacquet, J.-P. Contour, J.-F. Bobo, J. Fontcuberta, and A. Fert. $NiFe_2O_4$: A versatile spinel material brings new opportunities for spintronics. *Adv. Mater.*, **18**(13):1733–1736 (2006).

M. Luysberg, R. Sofin, S. Arora, and I. Shvets. Strain relaxation in $Fe_3O_4/MgAl_2O_4$ heterostructures: Mechanism for formation of antiphase boundaries in an epitaxial system with identical symmetries of film and substrate. *Phys. Rev. B*, **80**(2):024111 (2009).

S. Lyo and T. Holstein. Side-jump mechanism for ferromagnetic Hall effect. *Phys. Rev. Lett.*, **29**(7):423 (1972).

L. Ma, L. Lang, J. Kim, Z. Yuan, R. Wu, S. Zhou, and X. Qiu. Spin diffusion length and spin Hall angle in $Pd_{1-x}Pt_x$/YIG heterostructures: Examination of spin relaxation mechanism. *Phys. Rev. B*, **98** (22):224424 (2018).

S. Macke. ReMagX - x-ray magnetic reflectivity tool. www.remagx.org.

S. Macke and E. Goering. Magnetic reflectometry of heterostructures. *J. Phys. Condens. Matter*, **26**(36):363201 (2014).

S. Macke, A. Radi, J. E. Hamann-Borrero, A. Verna, M. Bluschke, S. Brück, E. Goering, R. Sutarto, F. He, G. Cristiani, M. Wu, E. Benckiser, H.-U. Habermeier, G. Logvenov, N. Gauquelin, G. A. Botton, A. P. Kajdos, S. Stemmer, G. A. Sawatzky, M. W. Haverkort, B. Keimer, and V. Hinkov. Element specific monolayer depth profiling. *Adv. Mater.*, **26**(38):6554–6559 (2014).

O. Madelung, U. Rössler, and M. Schulz. Ternary compounds, organic semiconductors. *Landolt-Börnstein–Group III Condensed Matter*, **41** (2000).

C. Majkrzak. Neutron scattering studies of magnetic thin films and multilayers. *Physica B*, **221**(1-4):342–356 (1996).

D. Margulies, F. Parker, M. Rudee, F. Spada, J. Chapman, P. Aitchison, and A. Berkowitz. Origin of the anomalous magnetic behavior in single crystal Fe_3O_4 films. *Phys. Rev. Lett.*, **79**(25):5162 (1997).

T. Matsui, N. Iketani, K. Morii, and Y. Nakayama. The effect of stacking patterns and annealing conditions on phase evolution by solid-state reactions of thin multilayered Pt/Mn/Sb films. *Mat. Chem. Phys.*, **36**(1-2):106–111 (1993).

K. I. McKinnon. Convergence of the Nelder–Mead Simplex Method to a Nonstationary Point. *SIAM J. Optim.*, **9**(1):148–158 (1998).

D. Meier, T. Kuschel, L. Shen, A. Gupta, T. Kikkawa, K. Uchida, E. Saitoh, J. M. Schmalhorst, and G. Reiss. Thermally driven spin and charge currents in thin NiFe2O4/Pt films. *Phys. Rev. B*, **87**(5): 054421 (2013).

D. Meier, D. Reinhardt, M. van Straaten, C. Klewe, M. Althammer, M. Schreier, S. T. B. Goennenwein, A. Gupta, M. Schmid, C. H. Back, J.-M. Schmalhorst, T. Kuschel, and G. Reiss. Longitudinal spin Seebeck effect contribution in transverse spin Seebeck effect experiments in Pt/YIG and Pt/NFO. *Nat. Commun.*, **6**:8211 (2015).

M. Meinert, J.-M. Schmalhorst, G. Reiss, and E. Arenholz. Ferrimagnetism and disorder of epitaxial $Mn_{2-x}Co_xVAl$ Heusler compound thin films. *J. Phys. D: Appl. Phys.*, **44**(21):215003 (2011).

H.-C. Mertins, F. Schäfers, X. Le Cann, A. Gaupp, and W. Gudat. Faraday rotation at the 2*p* edges of Fe, Co, and Ni. *Phys. Rev. B*, **61** (2) (2000).

C. Mewes and T. Mewes. *Handbook of Nanomagnetism*. Pan Stanford (2015).

T. Mewes, H. Nembach, M. Rickart, and B. Hillebrands. Separation of the first-and second-order contributions in magneto-optic Kerr effect magnetometry of epitaxial FeMn/NiFe bilayers. *J. Appl. Phys.*, **95**(10):5324–5329 (2004).

I. M. Miron, G. Gaudin, S. Auffret, B. Rodmacq, A. Schuhl, S. Pizzini, J. Vogel, and P. Gambardella. Current-driven spin torque induced by the Rashba effect in a ferromagnetic metal layer. *Nat. Mater.*, **9**(3):230–234 (2010).

I. M. Miron, K. Garello, G. Gaudin, P.-J. Zermatten, M. V. Costache, S. Auffret, S. Bandiera, B. Rodmacq, A. Schuhl, and P. Gambardella. Perpendicular switching of a single ferromagnetic layer induced by in-plane current injection. *Nature*, **476**(7359): 189–193 (2011).

J. Moodera and R. Meservey. Magnetic proximity effect in thin films of Ni on nonmagnetic metals. *Phys. Rev. B*, **29**(6):2943 (1984).

E. Moon, P. Balachandran, B. J. Kirby, D. Keavney, R. Sichel-Tissot, C. Schleputz, E. Karapetrova, X. Cheng, J. M. Rondinelli, and S. May. Effect of interfacial octahedral behavior in ultrathin manganite films. *Nano Lett.*, **14**(5):2509–2514 (2014).

J. E. Moore. The birth of topological insulators. *Nature*, **464**(7286): 194 (2010).

M. Morota, Y. Niimi, K. Ohnishi, D. Wei, T. Tanaka, H. Kontani, T. Kimura, and Y. Otani. Indication of intrinsic spin Hall effect in 4*d* and 5*d* transition metals. *Phys. Rev. B*, **83**(17):174405 (2011).

V. Moruzzi and P. Marcus. Magnetism in fcc rhodium and palladium. *Phys. Rev. B*, **39**(1):471 (1989).

O. Mosendz, J. Pearson, F. Fradin, G. Bauer, S. Bader, and A. Hoffmann. Quantifying spin Hall angles from spin pumping: Experiments and theory. *Phys. Rev. Lett.*, **104**(4):046601 (2010).

A. Moskaltsova, J. Krieft, D. Graulich, T. Matalla-Wagner, S. Francoual, and T. Kuschel. Impact of the magnetic proximity effect in Pt on the total magnetic moment of Pt/Co/Ta trilayers studied by x-ray resonant magnetic reflectivity. *AIP Advances*, **10**(1):015154 (2020).

N. F. Mott. The scattering of fast electrons by atomic nuclei. *Proc. R. Soc. Lond. A*, **124**(794):425–442 (1929).

A. Mukhopadhyay, S. K. Vayalil, D. Graulich, I. Ahmed, S. Francoual, A. Kashyap, T. Kuschel, and P. S. A. Kumar. Asymmetric modification of the magnetic proximity effect in Pt/Co/Pt trilayers by the insertion of a Ta buffer layer. *arXiv:1911.12187*, (2019).

J. A. Mundy, Y. Hikita, T. Hidaka, T. Yajima, T. Higuchi, H. Y. Hwang, D. A. Muller, and L. F. Kourkoutis. Visualizing the interfacial evolution from charge compensation to metallic screening across the manganite metal–insulator transition. *Nat. Commun.*, **5**(1):1–6 (2014).

N. Nagaosa, J. Sinova, S. Onoda, A. H. MacDonald, and N. P. Ong. Anomalous hall effect. *Rev. Mod. Phys.*, **82**(2):1539 (2010).

R. Nagel, C. Alof, A. Balogh, W. Arnoldbik, and D. Boerma. Study of magnetic multilayers by RBS with nanometer resolution. *Nucl. Instrum. Methods Phys. Res. B*, **183**(1-2):140–145 (2001).

H. Nakayama, M. Althammer, Y.-T. Chen, K.-i. Uchida, Y. Kajiwara, D. Kikuchi, T. Ohtani, S. Geprägs, M. Opel, S. Takahashi, R. Gross, G. E. W. Bauer, S. T. B. Goennenwein, and E. Saitoh. Spin Hall magnetoresistance induced by a nonequilibrium proximity effect. *Phys. Rev. Lett.*, **110**(20):206601 (2013).

J. A. Nelder and R. Mead. A simplex method for function minimization. *Comput. J.*, **7**(4):308–313 (1965).

L. Neumann, D. Meier, J. Schmalhorst, K. Rott, G. Reiss, and M. Meinert. Temperature dependence of the spin Hall angle and switching current in the nc-W (O)/CoFeB/MgO system with perpendicular magnetic anisotropy. *Appl. Phys. Lett.*, **109**(14):142405 (2016).

L. Névot and P. Croce. Caractérisation des surfaces par réflexion rasante de rayons X. Application à l'étude du polissage de quelques verres silicates. *Rev. Phys. Appl.*, **15**(3):761–779 (1980).

R. G. Newton. Optical theorem and beyond. *Am. J. Phys.*, **44**(7):639–642 (1976).

L. Offernes, P. Ravindran, and A. Kjekshus. Electronic structure and chemical bonding in half-Heusler phases. *J. Alloys Compd.*, **439**(1-2): 37–54 (2007).

Y. Ohnuma, M. Matsuo, and S. Maekawa. Spin transport in half-metallic ferromagnets. *Phys. Rev. B*, **94**(18):184405 (2016).

R. Ohyama, T. Koyanagi, and K. Matsubara. Magneto-optical Kerr effect of rf-sputtered PtMnSb thin films. *J. Appl. Phys.*, **61**(6): 2347–2352 (1987).

D. M. Olsson and L. S. Nelson. The Nelder-Mead simplex procedure for function minimization. *Technometrics*, **17**(1):45–51 (1975).

P. Oppeneer. *Handbook of Magnetic Materials*, volume 13. Elsevier, Amsterdam (2001).

N. Papanikolaou, R. Zeller, and P. Dederichs. Conceptual improvements of the KKR method. *J. Phys. Condens. Matter*, **14**(11):2799 (2002).

L. G. Parratt. Surface Studies of Solids by Total Reflection of X-Rays. *Phys. Rev.*, **95**(2):359 (1954).

D. Pesin and A. H. MacDonald. Spintronics and pseudospintronics in graphene and topological insulators. *Nat. Mater.*, **11**(5):409 (2012).

A. Pimpinelli and J. Villain. *Physics of Crystal Growth*, volume 19. Cambridge University Press (1998).

M. Przybylski, J.-M. Tonnerre, F. Yildiz, H. Tolentino, and J. Kirschner. Non-collinear magnetic profile in $(Rh/Fe_{1-x}Co_x)_2/Rh$ (001) bilayer probed by polarized soft x-ray resonant magnetic reflectivity. *J. of Appl. Phys.*, **111**(7):07C103 (2012).

O. Rader, E. Vescovo, J. Redinger, S. Blügel, C. Carbone, W. Eberhardt, and W. Gudat. Fe-induced magnetization of Pd: The role of modified Pd surface states. *Phys. Rev. Lett.*, **72**(14):2247 (1994).

O. Reimer, D. Meier, M. Bovender, L. Helmich, J.-O. Dreessen, J. Krieft, A. S. Shestakov, C. H. Back, J.-M. Schmalhorst, A. Hütten, G. Reiss, and T. Kuschel. Quantitative separation of the anisotropic magnetothermopower and planar Nernst effect by the rotation of an in-plane thermal gradient. *Sci. Rep.*, **7**:40586 (2017).

R. M. Rowan-Robinson, A. Stashkevich, Y. Roussigné, M. Belmeguenai, S.-M. Chérif, A. Thiaville, T. Hase, A. Hindmarch, and D. Atkinson. The interfacial nature of proximity-induced magnetism and the Dzyaloshinskii-Moriya interaction at the Pt/Co interface. *Sci. Rep.*, **7**(1):16835 (2017).

S. Roy, M. Fitzsimmons, S. Park, M. Dorn, O. Petracic, I. V. Roshchin, Z.-P. Li, X. Batlle, R. Morales, A. Misra, X. Zhang, K. Chesnel, J. B. Kortright, S. K. Sinha, and I. K. Schuller. Depth profile of uncompensated spins in an exchange bias system. *Phys. Rev. Lett.*, **95**(4):047201 (2005).

S. Roy, C. Sanchez-Hanke, S. Park, M. Fitzsimmons, Y. Tang, J. Hong, D. J. Smith, B. Taylor, X. Liu, M. Maple, A. E. Berkowitz, C.-C. Kao, and S. K. Sinha. Evidence of modified ferromagnetism at a buried Permalloy/CoO interface at room temperature. *Phys. Rev. B*, **75**(1):014442 (2007).

M. A. Ruderman and C. Kittel. Indirect exchange coupling of nuclear magnetic moments by conduction electrons. *Phys. Rev.*, **96**(1):99 (1954).

E. Saitoh, M. Ueda, H. Miyajima, and G. Tatara. Conversion of spin current into charge current at room temperature: Inverse spin-Hall effect. *Appl. Phys. Lett.*, **88**(18):182509 (2006).

J. Sakurai and J. Napolitano. *Modern Quantum Mechanics*. Cambridge University Press (2017).

G. Schütz, W. Wagner, W. Wilhelm, P. Kienle, R. Zeller, R. Frahm, and G. Materlik. Absorption of circularly polarized x-rays in iron. *Phys. Rev. Lett.*, **58**(7):737 (1987).

G. Schütz, R. Wienke, W. Wilhelm, W. Zeper, H. Ebert, and K. Spörl. Spin-dependent x-ray absorption in Co/Pt multilayers and $Co_{50}Pt_{50}$ alloy. *J. Appl. Phys.*, **67**(9):4456–4458 (1990).

M. Schwickert, R. Coehoorn, M. Tomaz, E. Mayo, D. Lederman, W. O'Brien, T. Lin, and G. Harp. Magnetic moments, coupling, and interface interdiffusion in Fe/V (001) superlattices. *Phys. Rev. B*, **57**(21):13681 (1998).

L. Sève, N. Jaouen, J. Tonnerre, D. Raoux, F. Bartolomé, M. Arend, W. Felsch, A. Rogalev, J. Goulon, C. Gautier, and J. F. Bérar. Profile of the induced 5*d* magnetic moments in Ce/Fe and La/Fe multilayers probed by x-ray magnetic-resonant scattering. *Phys. Rev. B*, **60**(13):9662 (1999).

J. Shan, P. Bougiatioti, L. Liang, G. Reiss, T. Kuschel, and B. J. van Wees. Nonlocal magnon spin transport in NiFe2O4 thin films. *Appl. Phys. Lett.*, **110**(13):132406 (2017).

J. Shan, A. Singh, L. Liang, L. Cornelissen, Z. Galazka, A. Gupta, B. van Wees, and T. Kuschel. Enhanced magnon spin transport in $NiFe_2O_4$ thin films on a lattice-matched substrate. *Appl. Phys. Lett.*, **113**(16):162403 (2018).

S.-H. Shen, D.-S. Lee, C.-W. Cheng, W.-J. Chan, and G. Chern. The correlation between magnetic dead layer and perpendicular magnetic anisotropy in MgO/CoFeB/Ta top structure. *IEEE Transactions on Magnetics*, **55**(2):1–5 (2018).

M. Sigalas and D. Papaconstantopoulos. Calculations of the total energy, electron-phonon interaction, and Stoner parameter for metals. *Phys. Rev. B*, **50**(11):7255 (1994).

A. Y. Silov, P. A. Blajnov, J. H. Wolter, R. Hey, K. H. Ploog, and N. S. Averkiev. Current-induced spin polarization at a single heterojunction. *Appl. Phys. Lett.*, **85**(24):5929–5931 (2004).

A. V. Singh, B. Khodadadi, J. B. Mohammadi, S. Keshavarz, T. Mewes, D. S. Negi, R. Datta, Z. Galazka, R. Uecker, and A. Gupta. Bulk single crystal-like structural and magnetic characteristics of epitaxial spinel frrite thin films with elimination of antiphase boundaries. *Adv. Mater.*, **29**(30):1701222 (2017).

J. Sinova, D. Culcer, Q. Niu, N. Sinitsyn, T. Jungwirth, and A. MacDonald. Universal intrinsic spin Hall effect. *Phys. Rev. Lett.*, **92**(12): 126603 (2004).

J. Sinova, S. O. Valenzuela, J. Wunderlich, C. Back, and T. Jungwirth. Spin hall effects. *Rev. Mod. Phys.*, **87**(4):1213 (2015).

J. Smit. The spontaneous Hall effect in ferromagnetics II. *Physica*, **24** (1-5):39–51 (1958).

J. Smith and H. Beljers. Ferromagnetic resonance absorption in $BaFe_{12}O_{19}$, a highly anisotropic crystal. *Phillips Res. Rep.*, **10**(2): 113–130 (1955).

G. A. Somorjai. *Chemistry in Two Dimensions: Surfaces*. Cornell University Press (1981).

F. Song, Å. Monsen, Z. Li, J. Wells, and E. Wahlström. The layer-by-layer stoichiometry of $La_{0.7}Sr_{0.3}MnO_3/SrTiO_3$ thin films and interfaces. *Surface and Interface Analysis*, **45**(7):1144–1147 (2013).

D. Stearns. The scattering of x-rays from nonideal multilayer structures. *J. Appl. Phys.*, **65**(2):491–506 (1989).

J. Stöhr. X-ray magnetic circular dichroism spectroscopy of transition metal thin films. *J. Electron Spectrosc. Relat. Phenom.*, **75**:253–272 (1995).

J. Stöhr. Exploring the microscopic origin of magnetic anisotropies with X-ray magnetic circular dichroism (XMCD) spectroscopy. *J. Magn. Magn. Mater.*, **200**(1-3):470–497 (1999).

J. Stöhr and H. Siegmann. *Magnetism: From fundamentals to Nanoscale Dynamics. 2006*. Springer Berlin, Germany .

J. Stöhr and H. C. Siegmann. Magnetism. *Solid-State Sciences. Springer, Berlin, Heidelberg*, **5** (2006).

E. C. Stoner. Collective electron ferronmagnetism. *Proc. Royal Soc. A*, **165**(922):372–414 (1938).

E. C. Stoner. Collective electron ferromagnetism II. Energy and specific heat. *Proc. Royal Soc. A*, **169**(938):339–371 (1939).

G. Sundaram and Q. Niu. Wave-packet dynamics in slowly perturbed crystals: Gradient corrections and Berry-phase effects. *Phys. Rev. B*, **59**(23):14915 (1999).

M. Suzuki, H. Muraoka, Y. Inaba, H. Miyagawa, N. Kawamura, T. Shimatsu, H. Maruyama, N. Ishimatsu, Y. Isohama, and Y. Sonobe. Depth profile of spin and orbital magnetic moments in a subnanometer Pt film on Co. *Phys. Rev. B*, **72**(5):054430 (2005).

Z. Szotek, W. Temmerman, D. Ködderitzsch, A. Svane, L. Petit, and H. Winter. Electronic structures of normal and inverse spinel ferrites from first principles. *Phys. Rev. B*, **74**(17):174431 (2006).

S. Takahashi and S. Maekawa. Spin current, spin accumulation and spin Hall effect. *Sci. Technol. Adv. Mater.*, **9**(1):014105 (2008).

S. Takahashi, E. Saitoh, and S. Maekawa. Spin current through a normal-metal/insulating-ferromagnet junction. *J. Phys.: Conf. Ser.*, **200**(6):062030 (2010).

C. Tanaka, J. Nowak, and J. Moodera. Magnetoresistance in ferromagnet-insulator-ferromagnet tunnel junctions with half-metallic ferromagnet NiMnSb compound. *J. Appl. Phys.*, **81**(8): 5515–5517 (1997).

C. T. Tanaka, J. Nowak, and J. S. Moodera. Spin-polarized tunneling in a half-metallic ferromagnet. *J. Appl. Phys.*, **86**(11):6239–6242 (1999).

T. Tanaka, H. Kontani, M. Naito, T. Naito, D. S. Hirashima, K. Yamada, and J. Inoue. Intrinsic spin hall effect and orbital Hall effect in 4*d* and 5*d* transition metals. *Phys. Rev. B*, **77**(16):165117 (2008).

X. Tao, Q. Liu, B. Miao, R. Yu, Z. Feng, L. Sun, B. You, J. Du, K. Chen, S. Zhang, L. Zhang, Z. Yuan, D. Wu, and H. Ding. Self-consistent determination of spin Hall angle and spin diffusion length in Pt and Pd: The role of the interface spin loss. *Sci. Adv.*, **4** (6):eaat1670 (2018).

P. M. Tedrow and R. Meservey. Spin-dependent tunneling into ferromagnetic nickel. *Phys. Rev. Lett.*, **26**(4):192 (1971).

T. N. Theis and H.-S. P. Wong. The end of Moore's law: A new beginning for information technology. *Comput. Sci. Eng.*, **19**(2):41 (2017).

B. Thole, P. Carra, F. Sette, and G. van der Laan. X-ray circular dichroism as a probe of orbital magnetization. *Phys. Rev. Lett.*, **68** (12):1943 (1992).

J. Tiilikainen, J. Tilli, V. Bosund, M. Mattila, T. Hakkarainen, V.-M. Airaksinen, and H. Lipsanen. Nonlinear fitness–space–structure adaptation and principal component analysis in genetic algorithms: an application to x-ray reflectivity analysis. *J. Phys. D: Appl. Phys.*, **40**(1):215 (2006).

J. Tiilikainen, V. Bosund, J.-M. Tilli, J. Sormunen, M. Mattila, T. Hakkarainen, and H. Lipsanen. Genetic algorithm using independent component analysis in x-ray reflectivity curve fitting of periodic layer structures. *J. Phys. D: Appl. Phys.*, **40**(19):6000 (2007).

J. Tiilikainen, J.-M. Tilli, V. Bosund, M. Mattila, T. Hakkarainen, J. Sormunen, and H. Lipsanen. Accuracy in x-ray reflectivity analysis. *J. Phys. D: Appl. Phys.*, **40**(23):7497 (2007).

M. Tolan. *X-ray Scattering from Soft-Matter Thin Films: Materials Science and Basic Research*. Springer, Berlin (1999).

J. Tonnerre, L. Sève, D. Raoux, G. Soullié, B. Rodmacq, and P. Wolfers. Soft X-ray resonant magnetic scattering from a magnetically coupled Ag/Ni multilayer. *Phys. Rev. Lett.*, **75**(4):740 (1995).

J. Tonnerre, L. Sève, A. Barbara-Dechelette, F. Bartolomé, D. Raoux, V. Chakarian, C. Kao, H. Fischer, S. Andrieu, and O. Fruchart. Soft x-ray resonant magnetic reflectivity study of thin films and multilayers. *J. Appl. Phys.*, **83**(11):6293–6295 (1998).

L. Tröger, D. Arvanitis, K. Baberschke, H. Michaelis, U. Grimm, and E. Zschech. Full correction of the self-absorption in soft-fluorescence extended X-ray-absorption fine structure. *Phys. Rev. B*, **46**(6):3283 (1992).

W.-K. Tse and S. D. Sarma. Intrinsic spin Hall effect in the presence of extrinsic spin-orbit scattering. *Phys. Rev. B*, **74**(24):245309 (2006).

Y. Tserkovnyak, A. Brataas, and G. E. Bauer. Enhanced Gilbert damping in thin ferromagnetic films. *Phys. Rev. Lett.*, **88**(11):117601 (2002).

K.-i. Uchida, S. Takahashi, K. Harii, J. Ieda, W. Koshibae, K. Ando, S. Maekawa, and E. Saitoh. Observation of the spin Seebeck effect. *Nature*, **455**(7214):778–781 (2008).

K.-i. Uchida, H. Adachi, T. Ota, H. Nakayama, S. Maekawa, and E. Saitoh. Observation of longitudinal spin-Seebeck effect in magnetic insulators. *Appl. Phys. Lett.*, **97**(17):172505 (2010).

K.-i. Uchida, J. Xiao, H. Adachi, J.-i. Ohe, S. Takahashi, J. Ieda, T. Ota, Y. Kajiwara, H. Umezawa, H. Kawai, G. E. W. Bauer, S. Maekawa, and E. Saitoh. Spin seebeck insulator. *Nat. Mater.*, **9**(11):894 (2010).

K.-i. Uchida, M. Ishida, T. Kikkawa, A. Kirihara, T. Murakami, and E. Saitoh. Longitudinal spin Seebeck effect: from fundamentals to applications. *J. Phys. Condens. Matter.*, **26**(34):343202 (2014).

K.-i. Uchida, H. Adachi, T. Kikkawa, A. Kirihara, M. Ishida, S. Yorozu, S. Maekawa, and E. Saitoh. Thermoelectric Generation Based on Spin Seebeck Effects. *Proc. IEEE*, **104**(10, SI):1946–1973 (2016).

A. Ulyanenkov and S. Sobolewski. Extended genetic algorithm: application to x-ray analysis. *J. Phys. D: Appl. Phys.*, **38**(10A):A235 (2005).

S. O. Valenzuela and M. Tinkham. Direct electronic measurement of the spin Hall effect. *Nature*, **442**(7099):176 (2006).

G. van der Laan. Soft x-ray resonant magnetic scattering of magnetic nanostructures. *C. R. Phys.*, **9**(5-6):570–584 (2008).

G. van der Laan and B. Thole. Strong magnetic x-ray dichroism in 2*p* absorption spectra of 3*d* transition-metal ions. *Phys. Rev. B*, **43** (16):13401 (1991).

G. van der Laan, B. T. Thole, G. A. Sawatzky, J. B. Goedkoop, J. C. Fuggle, J.-M. Esteva, R. Karnatak, J. Remeika, and H. A. Dabkowska. Experimental proof of magnetic x-ray dichroism. *Phys. Rev. B*, **34**(9):6529 (1986).

P. G. Van Engen, K. H. J. Buschow, R. Jongebreur, and M. Erman. PtMnSb, a material with very high magneto-optical Kerr effect. *Appl. Phys. Lett.*, **42**(2):202–204 (1983).

W. Van Roy, J. De Boeck, B. Brijs, and G. Borghs. Epitaxial NiMnSb films on GaAs (001). *Appl. Phys. Lett.*, **77**(25):4190–4192 (2000).

L. d. Van Uitert. Dc resistivity in the nickel and nickel zinc ferrite system. *J. Chem. Phys.*, **23**(10):1883–1887 (1955).

A. Verna, B. A. Davidson, Y. Szeto, A. Y. Petrov, A. Mirone, A. Giglia, N. Mahne, and S. Nannarone. Measuring magnetic profiles at manganite surfaces with monolayer resolution. *J. Magn. Magn. Mater.*, **322**(9-12):1212–1216 (2010).

E. Verwey and E. Heilmann. Physical properties and cation arrangement of oxides with spinel structures I. Cation arrangement in spinels. *J. Chem. Phys.*, **15**(4):174–180 (1947).

G. Vignale. Ten years of spin Hall effect. *J. Supercond. Nov. Magn.*, **23**(1):3 (2010).

P. Wadley, B. Howells, J. Železnỳ, C. Andrews, V. Hills, R. P. Campion, V. Novák, K. Olejník, F. Maccherozzi, S. S. Dhesi, S. Y. Martin, T. Wagner, J. Wunderlich, F. Freimuth, Y. Mokrousov, J. Kuneš, J. S. Chauhan, M. J. Grzybowski, A. W. Rushforth, K. W. Edmonds, B. L. Gallagher, and T. Jungwirth. Electrical switching of an antiferromagnet. *Science*, **351**:587–590 (2016).

Y. Wang, W. Lin, D. Qu, Q. Ma, Y. Zhang, Y. Li, S. Yang, and C. Chien. Voltage-Controlled Sensitivity of the Spin Seebeck Effect in $Pt/Y_3Fe_5O_{12}/MgO/(PbMg_{1/3}Nb_{2/3}O_3)_{0.7}(PbTiO_3)_{0.3}$ Multiferroic Heterostructures. *Phys. Rev. Appl.*, **10**(1):014004 (2018).

K. Watanabe. On New Ferromagnetic Intermetallic Compounds PtMnSn and PtMnSb. *J. Phys. Soc. Jap.*, **28**(2):302–307 (1970).

M. Weiler, M. Althammer, F. D. Czeschka, H. Huebl, M. S. Wagner, M. Opel, I.-M. Imort, G. Reiss, A. Thomas, R. Gross, and S. T. B. Goennenwein. Local Charge and Spin Currents in Magnetothermal Landscapes. *Phys. Rev. Lett.*, **108**(10):106602 (2012).

Z. Wen, T. Kubota, and K. Takanashi. Optimization of half-Heusler PtMnSb alloy films for spintronic device applications. *J. Phys. D: Appl. Phys.*, **51**(43):435002 (2018).

H. Wende and C. Antoniak. X-ray magnetic dichroism. In *Magnetism and Synchrotron Radiation*, pages 145–167. Springer, Berlin, Germany, (2010).

J. Wijngaard, C. Haas, and R. De Groot. Origin of the difference in the magneto-optical Kerr effect between PtMnSb and NiMnSb. *Phys. Rev. B*, **40**(13):9318 (1989).

F. Wilhelm, P. Poulopoulos, H. Wende, A. Scherz, K. Baberschke, M. Angelakeris, N. Flevaris, and A. Rogalev. Systematics of the Induced Magnetic Moments in 5*d* Layers and the Violation of the Third Hund's Rule. *Phys. Rev. Lett.*, **87**(20):207202 (2001).

S. Wolf, D. Awschalom, R. Buhrman, J. Daughton, S. Von Molnar, M. Roukes, A. Y. Chtchelkanova, and D. Treger. Spintronics: a spin-based electronics vision for the future. *Science*, **294**(5546): 1488–1495 (2001).

Y. Wu, B. Wu, Z. Wei, Z. Zhou, C. Zhao, Y. Xiong, S. Tou, S. Yang, B. Zhou, and Y. Shao. Structural, half-metallic and elastic properties of the half-Heusler compounds NiMnM (M= Sb, As and Si) and IrMnAs from first-principles calculations. *Intermetallics*, **53**:26–33 (2014).

J. Wunderlich, B. Kaestner, J. Sinova, and T. Jungwirth. Experimental observation of the spin-Hall effect in a two-dimensional spin-orbit coupled semiconductor system. *Phys. Rev. Lett.*, **94**(4): 047204 (2005).

Y. Xu, Y. Yang, K. Yao, B. Xu, and Y. Wu. Self-current induced spin-orbit torque in FeMn/Pt multilayers. *Sci. Rep.*, **6** (2016).

T. Yang, B. Liu, F. Pan, J. Luo, and K. Tao. Polarization of Pd atoms in Ni/Pd magnetic multilayers. *J. Phys. Condens. Matter*, **7**(6):1121 (1995).

K. Yosida. Magnetic properties of Cu-Mn alloys. *Phys. Rev.*, **106**(5): 893 (1957).

S. Youn and B. Min. Effects of the spin-orbit interaction in Heusler compounds: Electronic structures and Fermi surfaces of NiMnSb and PtMnSb. *Phys. Rev. B*, **51**(16):10436 (1995).

H. Zabel. X-ray and neutron reflectivity analysis of thin films and superlattices. *Appl. Phys. A*, **58**(3):159–168 (1994).

K. Zafar, P. Audehm, G. Schütz, E. Goering, M. Pathak, K. Chetry, P. LeClair, and A. Gupta. Cr magnetization reversal at the CrO_2/RuO_2 interface: Origin of the reduced GMR effect. *Phys. Rev. B*, **84**(13):134412 (2011).

J. Zak, E. Moog, C. Liu, and S. Bader. Universal approach to magneto-optics. *J. Magn. Magn. Mater.*, **89**(1-2):107–123 (1990).

S. Zhang. Spin Hall effect in the presence of spin diffusion. *Phys. Rev. Lett.*, **85**(2):393 (2000).

J. M. Ziman. *Electrons and phonons: the theory of transport phenomena in solids*. Oxford university press (2001).

M. Zuckermann. The proximity effect for weak itinerant ferromagnets. *Solid State Commun.*, **12**(7):745–747 (1973).

M. Zwiebler, J. Hamann-Borrero, M. Vafaee, P. Komissinskiy, S. Macke, R. Sutarto, F. He, B. Büchner, G. Sawatzky, L. Alff, et al. Electronic depth profiles with atomic layer resolution from resonant soft x-ray reflectivity. *New J. Phys.*, **17**(8):083046 (2015).